BioMed Research International

Quantitative Biomedical Imaging: Techniques and Clinical Applications

Guest Editors: Guang Jia, Steven B. Heymsfield, Jinyuan Zhou, Guang Yang, and Yukihisa Takayama

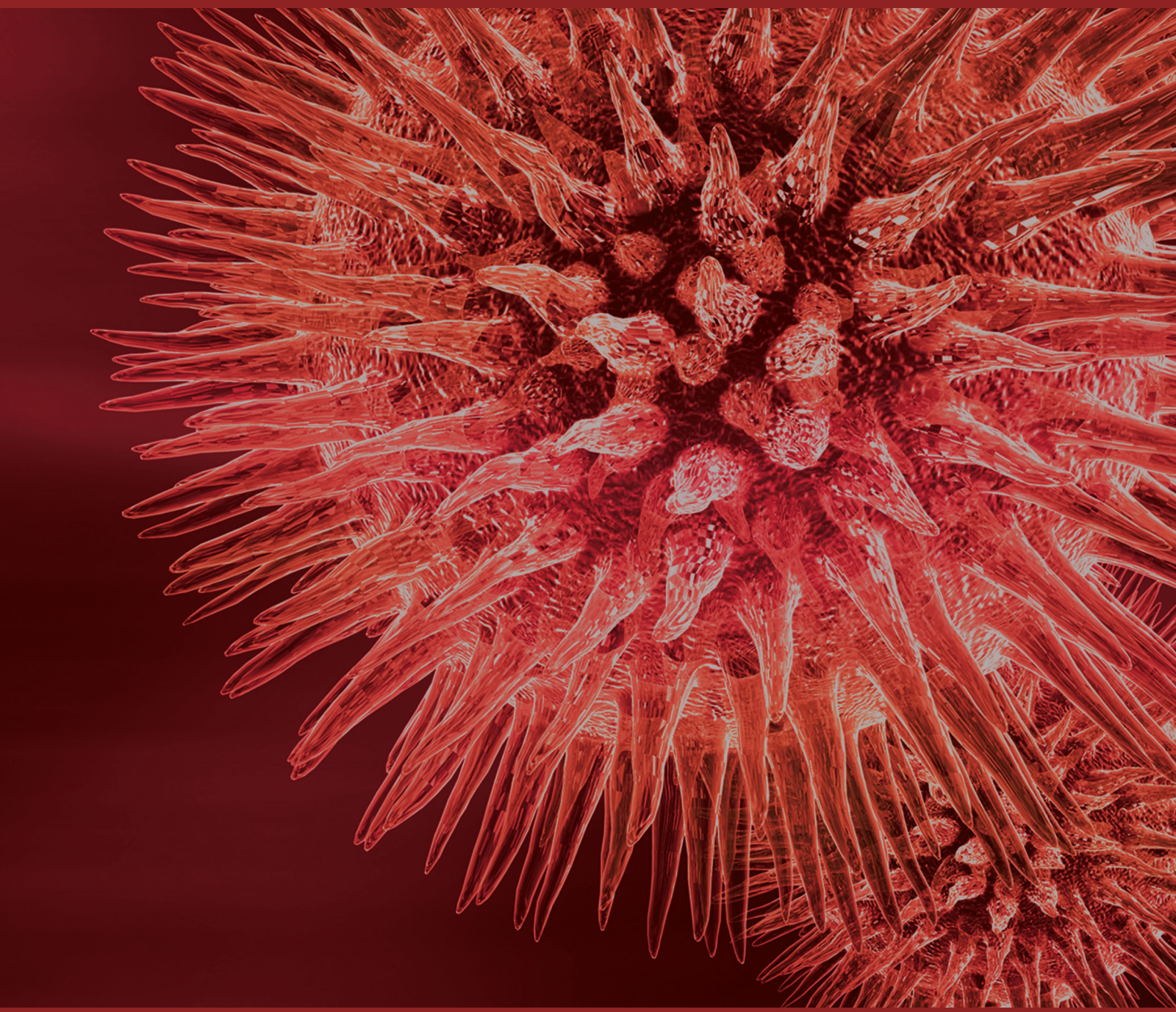

Quantitative Biomedical Imaging: Techniques and Clinical Applications

BioMed Research International

Quantitative Biomedical Imaging: Techniques and Clinical Applications

Guest Editors: Guang Jia, Steven B. Heymsfield, Jinyuan Zhou, Guang Yang, and Yukihisa Takayama

Contents

Hindawi Publishing Corporation
BioMed Research International
Volume 2016, Article ID 3080965, 2 pages
http://dx.doi.org/10.1155/2016/3080965

Editorial

Quantitative Biomedical Imaging: Techniques and Clinical Applications

Guang Jia,[1] Steven B. Heymsfield,[2] Jinyuan Zhou,[3] Guang Yang,[4] and Yukihisa Takayama[5]

[1] *Medical and Health Physics Program, Department of Physics and Astronomy, Louisiana State University, Baton Rouge, LA 70803, USA*
[2] *Laboratory of Metabolism-Body Composition, Pennington Biomedical Research Center, Baton Rouge, LA 70808, USA*
[3] *Department of Radiology, Johns Hopkins University, Baltimore, MD 21287, USA*
[4] *Shanghai Key Laboratory of Magnetic Resonance, Department of Physics, East China Normal University, Shanghai 200062, China*
[5] *Department of Radiology Informatics and Network, Graduate School of Medical Sciences, Kyushu University, Fukuoka 812-8582, Japan*

Correspondence should be addressed to Guang Jia; gjia@lsu.edu

Received 20 June 2016; Accepted 20 June 2016

For decades, cross-sectional biomedical images have been generated from various modalities, including computed tomography (CT), three-dimensional tomosynthesis, ultrasound, magnetic resonance imaging (MRI), single photon emission computed tomography (SPECT), and positron emission tomography (PET). Many advanced quantitative imaging methods have been developed, such as perfusion MRI/CT, diffusion tensor/weighted MRI, functional MRI (fMRI), ultrasound/MR elastography, dynamic PET, and dynamic contrast enhanced MRI. There is great variability across imaging platforms, imaging techniques, postprocessing software, and imaging readers. There is an unmet clinical need for improving the value and practicality of quantitative biomedical imaging.

Systematic reviews of a quantitative biomedical imaging method will improve researchers' understanding and skills in utilizing these methods. For example, arterial spin labeling (ASL) is a noninvasive MRI modality capable of measuring blood perfusion without the use of a contrast agent. E. Vaghefi and B. Pontré reviewed the technical aspects of ASL and their implications for its optimum adaptation for retinal blood perfusion monitoring, as well as ASL application in human ocular blood flow assessment.

Cross-system/site/vendor/platform/software/reader comparisons of a quantitative biomedical imaging method are crucial. C. Brodén et al. compared 3D-CT to standard radiostereometric analysis for measuring migration of acetabular cups in total hip arthroplasty. G. J. Pelgrim et al. evaluated the capability of MRI and CT to perform myocardial perfusion quantification, previously only achievable with PET.

Reproducibility and reliability assessments of quantitative biomedical imaging methods are necessary steps. The current 2D tagging cardiac MRI technique requires multiple breath holds to cover the whole heart and cannot show the 3D motion of the left ventricle. Y. Amano et al. evaluated the feasibility of fast 3-breath-hold 3D tagging for the assessment of the circumferential strain in patients with hypertrophic myocardial diseases. A. R. Yu et al. investigated the optimal PET energy window for 124I PET based on image characteristics of reconstructed PET. The energy window of 350~750 keV was proposed as the optimal energy window, although 400~590 keV was obtained as the highest noise equivalent count rate.

Pathophysiological validation and computer simulation are crucial to understanding a quantitative biomedical imaging method. U. Klose et al. confirmed the strong dependence of the whole brain apparent diffusion coefficient (ADC) MRI histograms on the age of the examined subjects. The proposed model can be used to characterize changes of the whole brain ADC histogram in certain diseases under consideration of age effects. Z. Krajnc et al. quantitatively evaluated growth plates around the knees in adolescent soccer players utilizing the diffusion-weighted MRI. Diffusion-weighted imaging measurements indicate increased cellularity in growth plates around knees in football players most prominent in proximal tibia medial region after intense training. D. Shimamoto

et al. evaluated whether the diagnostic performance of Gd-EOB-DTPA-enhanced MRI in evaluating liver function and pathology is improved by considering liver volume. They found that the inclusion of liver volume may improve Gd-EOB-DTPA-based predictions of liver function but not predictions of liver pathology. F. F. Schröder et al. analyzed preoperative CT images of patients who underwent pancreatoduodenectomy (PD) or pylorus preserving PD and investigated predictors for postoperative pancreatic fistula and postoperative severe complications.

Physical and virtual phantom for quality check/assurance will improve our knowledge of a quantitative biomedical imaging method. Characterization of lesion formation and restoration by imaging features is a novel field of research in multiple sclerosis. R. K. Verma et al. investigated statistical differences with MR perfusion imaging features that reflect the dynamics of Gadolinium uptake in multiple sclerosis lesions using dynamic texture parameter analysis. Brain tissue segmentation in MRI is useful for a wide range of applications. F. Baselice et al. proposed a brain joint segmentation and classification algorithm based on proton density and relaxation times, instead of the acquired gray level image.

Computer assisted analysis and diagnosis will facilitate the clinical adoption of single or multiparametric/modality imaging methods. In order to accurately diagnose acute appendicitis, K. B. Kim et al. proposed a method to extract the appendix automatically by using a series of image processing and self-organizing maps that learn typical shape patterns of the appendix from US. The analysis and interpretation of high-resolution CT images of the chest in the presence of interstitial lung disease are a time-consuming task which requires experience. V. Vasconcelos et al. proposed a computer-aided diagnosis (CAD) scheme to assist radiologists in the differentiation of lung patterns associated with interstitial lung disease and with healthy lung parenchyma. Indirect immunofluorescence is the gold standard for the diagnosis of autoimmune diseases. A. B. Elgaaied et al. introduced the AIDA Project (Autoimmunity: Diagnosis Assisted by Computer) developed in the framework of an Italy-Tunisia, cross-border cooperation and its preliminary results. J. Jeong et al. proposed a CAD algorithm with a simplified false-positive reduction scheme for microcalcification clusters in reconstructed digital breast tomosynthesis images. M. Larobina et al. investigated the feasibility of automatically training supervised methods, such as k-nearest neighbor and principal component discriminant analysis, to segment the four subcortical brain structures: caudate, thalamus, pallidum, and putamen. Their results demonstrate that atlas-guided training is an effective way to automatically define a representative and reliable training dataset, thus giving supervised methods the chance to successfully segment brain MRI images without the need for user interaction.

Development of a translational imaging method from preclinical to clinical patient care may require additional steps to simplify the paradigm, to improve image quality, or to reengineer the hardware. The usefulness of ADC MRI as a quantitative imaging tool has motivated several studies that have investigated the reliability and reproducibility of ADC estimates. M. Alipoor et al. proposed a new experiment design method that is based on minimizing the determinant of the covariance matrix of the estimated parameters. S. Aootaphao et al. proposed the X-ray scattering correction method for improving soft tissue images on the large flat panel detector of portable cone beam CT (CBCT). The reconstructed images with their proposed scatter correction show significant improvement on image quality. Thus, the proposed scatter correction technique has a high potential to detect soft tissues in the brain. S.-S. Han et al. evaluated the availability of software-based correction of mandibular plane for the vertical measurement of the mandible in CBCT. G. Wang et al. developed high-field permanent magnetic circuit of 1.2 T and 1.5 T with novel magnetic focusing and curved surface correction. They have obtained high quality images of mice using their small animal micro-MRI instruments.

Imaging-based big data and network systems may be used to promote hardware and software standards in quantitative biomedical imaging. Using the data from the Osteoarthritis Initiative, M. Zhang et al. developed a rapid cartilage damage quantification method for the lateral tibiofemoral compartment using MRI. M. Zhang et al. evaluated the influence of MRI sequence on the relationship between bone marrow lesions volume and pain. They compared quantitative assessments of bone marrow lesions on intermediate-weighted fat suppressed (IW FS) turbo spin echo and 3-dimensional dual echo steady state (3D DESS) sequences. They found that bone marrow lesion quantification on IW FS offers better validity and statistical power than bone marrow lesion quantification on a 3D DESS sequence.

Finally, it is crucial to develop novel quantitative biomedical imaging biomarkers for diseases, such as shear-wave ultrasound elastography (SWE). SWE is thought to be useful for quantitatively evaluating tissue hardness. However, it remains unclear what types of pathology affect tissue hardness. T. Fukuhara et al. elucidated the correlation between shear-wave velocity (SWV) and fibrosis in thyroid. Small muscle cells of the cavernosum play an important role in erection. J.-J. Zhang et al. investigated the feasibility of shear-wave US elastography on evaluating the level of small muscle cells in penis quantitatively. Liver disease associated with cystic fibrosis (CFLD) is the second cause of mortality in these patients. T. Cañas et al. found that shear-wave elastography in the right hepatic lobe is a noninvasive technique useful to detect CFLD in their sample of patients. They found that splenic SWV values are higher in cystic fibrosis patients, without any clinical consequence. Last but not least, V. Rajagopalan and E. P. Pioro studied the potential role of brain parenchymal fraction as a relatively simple quantitative MRI measure for distinguishing amyotrophic lateral sclerosis phenotypes.

Guang Jia
Steven B. Heymsfield
Jinyuan Zhou
Guang Yang
Yukihisa Takayama

Hindawi Publishing Corporation
BioMed Research International
Volume 2016, Article ID 5909741, 6 pages
http://dx.doi.org/10.1155/2016/5909741

Research Article

Accuracy and Precision of Three-Dimensional Low Dose CT Compared to Standard RSA in Acetabular Cups: An Experimental Study

Cyrus Brodén,[1] Henrik Olivecrona,[1] Gerald Q. Maguire Jr.,[2] Marilyn E. Noz,[3] Michael P. Zeleznik,[4] and Olof Sköldenberg[5]

[1]*Department of Molecular Medicine and Surgery, Karolinska Institutet, 17176 Stockholm, Sweden*
[2]*School of Information and Communication Technology, KTH Royal Institute of Technology, 16440 Stockholm, Sweden*
[3]*Department of Radiology, New York University School of Medicine, New York, NY 10016, USA*
[4]*School of Computing, College of Engineering, University of Utah, Salt Lake City, UT 84109, USA*
[5]*Department of Clinical Sciences, Danderyd Hospital, Karolinska Institutet, 18288 Stockholm, Sweden*

Correspondence should be addressed to Cyrus Brodén; cyrus.broden@gmail.com

Received 4 December 2015; Revised 30 May 2016; Accepted 1 June 2016

Academic Editor: Yukihisa Takayama

Background and Purpose. The gold standard for detection of implant wear and migration is currently radiostereometry (RSA). The purpose of this study is to compare a three-dimensional computed tomography technique (3D CT) to standard RSA as an alternative technique for measuring migration of acetabular cups in total hip arthroplasty. *Materials and Methods*. With tantalum beads, we marked one cemented and one uncemented cup and mounted these on a similarly marked pelvic model. A comparison was made between 3D CT and standard RSA for measuring migration. Twelve repeated stereoradiographs and CT scans with double examinations in each position and gradual migration of the implants were made. Precision and accuracy of the 3D CT were calculated. *Results*. The accuracy of the 3D CT ranged between 0.07 and 0.32 mm for translations and 0.21 and 0.82° for rotation. The precision ranged between 0.01 and 0.09 mm for translations and 0.06 and 0.29° for rotations, respectively. For standard RSA, the precision ranged between 0.04 and 0.09 mm for translations and 0.08 and 0.32° for rotations, respectively. There was no significant difference in precision between 3D CT and standard RSA. The effective radiation dose of the 3D CT method, comparable to RSA, was estimated to be 0.33 mSv. *Interpretation*. Low dose 3D CT is a comparable method to standard RSA in an experimental setting.

1. Introduction

Radiostereometric Analysis (RSA) is the gold standard for precise monitoring of micromovements of orthopaedic joint implants [1–4]. However, since not every hospital does have the stereoradiographic facilities needed for doing standard RSA imaging, it is therefore important to consider alternative techniques to follow prosthesis migration over time.

Current computed tomography (CT) scanners can routinely provide high-resolution volume data with voxels of submillimeter size in all dimensions. Therefore, the potential exists for detecting the small tantalum beads implanted as RSA markers in CT volumes with reasonable accuracy, and then this data can be used to calculate the marker positions.

At the Karolinska Institute a three-dimensional (3D) CT technique (3D CT) has been developed that could potentially detect migration and subsequent osteolysis in hip prostheses [5, 6]. The aim of this study was to validate this low dose 3D CT as a tool for migration assessment of acetabular components in total hip arthroplasty (THA).

2. Materials and Methods

2.1. Experimental Setup. A plastic model of the human pelvis (Sawbones, Vashon, WA, USA) was marked with nine 1.0 mm tantalum beads. To simulate a typical marker configuration in THA, the markers were placed in the periacetabular bone using the same procedure as when marking a patient during

surgery. We used two implants mounted consecutively to the pelvic model: a cemented (Müller Exceed™, Biomet, Warsaw, Indiana, USA) and an uncemented (T.O.P.®, Waldemar LINK GmbH & Co. KG, Hamburg, Germany) acetabular cup. They were implanted in the model after being marked with tantalum beads in a circular fashion in the periphery of the opening of the polyethylene liner. The cups were held by a jig that allowed translations in x-, y-, and z-axis by 1.0 mm increments. Each cup could also be rotated in 1.0° increments about the x-axis as shown in Figure 1. Six positions for each cup relative to the pelvic model were chosen. For each position we added translation and/or rotation to the cup to simulate a movement of the component relative to the pelvic model. For each position a double examination of RSA and a double examination of CT were conducted. Within each scan in a double examination the model was moved without changing the position of the cup relative to the pelvic model in order to simulate movement of a patient between the two examinations.

The following procedure was performed to measure the migration of the implant in relation to the model: (1) the pelvic phantom including the jig was placed in the RSA calibration cage at the point of intersection of the central radiograms above the RSA calibration cage, (2) one set of radiographs was taken (position 1_{RSA}, series 1_{RSA}), (3) the calibration cage, the X-ray tubes, and the phantom were repositioned (without moving any of the phantom's components), (4) one set of radiographs was taken (position 1_{RSA}, series 2_{RSA}), (5) the model was moved (without moving any of the phantom's components) to the CT table, (6) one CT scan was done (position 1_{CT}, series 1_{CT}), (7) the phantom was repositioned (without moving the cup in relation to the pelvis) in the CT scanner, (8) one CT scan was done (position 1_{CT}, series 2_{CT}), and (9) the prosthesis was moved 1.0 mm in relation to the pelvis, along the x- or y-axis and rotated 1.0° around the x-axis to simulate migration of the implant. This resulted in all migrations being along the x-, y-, and z-axes for translations and about the x-, y-, and z-axes for rotations. Steps (1) to (9) were repeated a total of 6 times for each cup, giving us, for each RSA and CT examination, position 1, series 1 and 2; position 2, series 1 and 2; and so on.

2.2. The RSA Method. Uniplanar calibration cage (Cage 43; RSA Biomedical AB, Umea, Sweden) was used. Digital radiographs (Bucky Diagnostic; Philips, Eindhoven, the Netherlands) were then taken using 2 X-ray sources angled at 40° to each other. The exposure was set to 125 kV and 2.5 mAs for each X-ray tube. The measurement and migration analyses were done with the UmRSA 6.0 computer software (RSA Biomedical, Umea, Sweden).

The stereoradiographs that composed the RSA examinations were conducted by an experienced radiologic nurse and a physician with extensive experience using RSA did the analysis. The condition number and the mean error were calculated. The condition number assesses the distribution of markers and should be below 100–110 to be reliable [4]. The mean error represents the stability of the markers and is acceptable if it is under 0.35 mm [7, 8]. In our study, all condition numbers were below 100 and all mean errors below 0.30 mm.

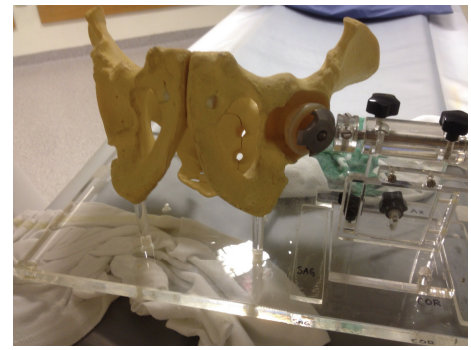

Figure 1: Pelvic model with jig holding the cemented cup in place for the examinations. The jig allows precise translations in x-, y-, and z-axis by 1.0 mm increments and rotations in 1.0° increments about the x-axis.

2.3. The 3D CT Method. For each position, two CT scans were obtained. All volumes were acquired using the same scout view. A clinical CT scanner (Discovery CT750HD, GE Healthcare, USA) was used. Images were acquired at 120 kVp, 10 mAs. The scanner software did not permit reducing the mAs more. Volumes were reconstructed with an in-plane resolution of 0.6 ∗ 0.6 mm at 0.3 mm increments.

2.4. Image Analysis. In order to easily compare two CT volumes, it is helpful if they are viewed simultaneously in the same spatial alignment. For this we used a 3D volume image processing tool which includes functions for volume registration, fusion, and data analysis [5, 6]. This registration algorithm has been described previously and extensively validated [9–11]. The semiautomated image registration procedure has a graphical interface and is used to perform landmark-based fusion of two volumes. In first step, one of the two volumes of a pair was spatially aligned with the second volume (the reference volume). The spatially aligned volume is called the transformed volume. This transformation is possible by using landmarks chosen manually on the cohomologous tantalum beads in the pelvis of the two volumes as shown in Figure 2 [5, 6]. The program used these manually designated preliminary landmarks as starting points for an automated process that calculated the best fit center of the tantalum beads and designated the final landmarks at the centroid of each bead before the transformation. The transformed volume could then be compared to the reference volume. In a second step, we utilize the markers in both cups of the paired volumes (as landmarks) in order to perform a numerical analysis to calculate precision and accuracy. All the measurements were done by a physician experienced in the CT method who was different from person who did the RSA analysis.

2.5. Precision. The precision of a measurement is "the degree to which repeated measurements under unchanged conditions show the same results" [12, 13]. Precision was calculated

Figure 2: Volume fusion of the transformed and reference volume. In this experiment the relative movement of the cup is zero. The overlapping pattern between the two examinations indicates that the surface representations are closer than the smallest voxel elements and that visually the precision of this method is good.

as the difference between the double measurements (series 1 and 2) at one predetermined position of the cup relative to the pelvic model. For instance, for x-translation (xt), $d_{\text{prec}_{xt}} = xt_{p_{1:1}} - xt_{p_{1:2}}$, where $d_{\text{prec}_{xt}}$ is the difference between position 1 series 1 ($p_{1:1}$) and position 1 series 2 ($p_{1:2}$) [13]. If the precision of the modality were perfect, then the difference between these two positions would be null. When viewing the two images, this would look like a perfect fusion between the two implants, since no movement between the implants relative to the pelvic model occurred between these scans (Figure 2).

For the precision measurements, we used as many tantalum beads as could be visualized in each modality. In the 3D CT mode we used nine markers for bone and nine markers for the prosthesis for the cemented cup. For the uncemented cup, we used nine markers for bone and twelve for the prosthesis. For the standard RSA we used six markers for the cemented and four markers for the uncemented cup. This reduced number of markers was due to the fact that the standard RSA method suffered from marker occlusion, even in our experimental setting.

2.6. Accuracy. The definition of accuracy is "the degree of closeness between a measured value and the true value and contains both random and systemic errors" [12, 13]. The accuracy of standard RSA was, in this laboratory setting, assumed to be perfect; that is, standard RSA measures the true migration of the implant [14]. The standard RSA measurements were therefore used as the gold standard measurements when we calculated the accuracy of the 3D CT method. For assessing accuracy we had to use only the tantalum beads that could be visualized in both modalities. We used six tantalum beads with the cemented cup and four with the uncemented cup and seven markers for bone with both cups. In a first step, migration was calculated pairwise in positions 1-2, 3-4, and 5-6 to get independent measurements, in both RSA and CT.

In RSA. For instance, for x-translation, $\text{RSA}_{xt_{1\text{-}2}} = xt_{p_1} - xt_{p_2}$, where $\text{RSA}_{xt_{1\text{-}2}}$ is the migration of the prosthesis from positions 1 (p_1) and 2 (p_2)

In CT. Consider the following: $\text{CT}_{xt_{1\text{-}2}} = xt_{p_1} - xt_{p_2}$, where $\text{CT}_{xt_{1\text{-}2}}$ is the migration of the cup from positions 1 (p_1) and 2 (p_2).

The difference between the migration values of the two modalities should ideally be zero if the accuracy is perfect; that is, $d_{\text{accurCT}_{xt}} = \text{RSA}_{xt_{1\text{-}2}} - \text{CT}_{xt_{1\text{-}2}} = 0$, where $d_{\text{accurCT}_{xt}}$ is the accuracy for the x-translation.

2.7. Radiation. The CT effective dose was calculated using the manufacturer stated dose length product (DLP mGy-cm) and combining this with the normalized effective dose DLP conversion factor (k mSV/(mGy-cm)) for the human pelvis [15]. The RSA effective dose was estimated with a Monte Carlo simulation using a software program xDose in our hospital developed by the National Radiological Protection Board [16].

2.8. Statistics. We calculated precision and accuracy for translations and rotations in the x-, y-, and z-axes. The data was first examined to determine if it followed a normal (Gaussian) distribution by histograms, box, density, and quantile-quantile plots so that the standard deviation (SD) could be used. We calculated the precision for standard RSA and 3D CT as 2.45 $*$ SD (6 degrees of freedom (d.o.f.)) of the difference between the double examinations (d_{prec}). The 95% quantile for the t-distribution with 6 d.o.f. is 2.45, and this was chosen for precision since only random errors are included in precision measurements. We calculated the accuracy for 3D CT using the root mean square error (RMS) as 2.57 $*$ RMS (5 d.o.f.). This gives a measure of the magnitude of a varying quantity and was chosen since the difference between the standard RSA and the 3D CT method could be both positive and negative. The 95% quantile for the t-distribution with 5 d.o.f. is 2.57 and was chosen because accuracy involves both systemic and random errors. SPSS 22 for Mac was used for all statistical calculations.

3. Results

The precision for 3D CT was comparable to standard RSA, ranging between 0.01 and 0.09 mm for translations and 0.06 and 0.29° for rotations. For standard RSA, the precision ranged from 0.04 to 0.09 mm for translations and 0.08 to 0.32° for rotations, respectively (Table 1). All markers (twelve for the uncemented and nine for the cemented cup) could be used for 3D CT whereas six and four markers were used for standard RSA for the cemented and uncemented cups, respectively.

The accuracy ranged from 0.07 to 0.32 mm for translations and 0.21 to 0.82° for rotation for the 3D CT method (Table 2). The measurements for the uncemented cup had lower accuracy. This was explained by the fact that the same rigid body model was used when comparing the two methods and via standard RSA we could only identify 4 (out of 9) markers.

Table 1: Precision of 3D CT compared to standard RSA.

	Standard RSA				3D CT			
	2.45 ∗ SD	Mean	Min	Max	2.45 ∗ SD	Mean	Min	Max
Uncemented cup								
Translation (mm)								
x	0.07	0.00	−0.03	0.05	0.01	0.00	0.00	0.01
y	0.05	0.02	−0.02	0.04	0.04	−0.01	−0.04	0.00
z	0.09	0.03	−0.02	0.09	0.09	−0.01	−0.09	0.01
Rotation (°)								
x	0.22	−0.05	−0.15	0.12	0.10	−0.01	−0.10	0.01
y	0.13	0.00	−0.10	0.05	0.06	−0.02	−0.05	0.00
z	0.08	0.00	−0.03	0.05	0.21	−0.07	−0.21	0.01
Cemented cup								
Translation (mm)								
x	0.08	0.00	−0.04	0.05	0.04	−0.01	−0.03	0.00
y	0.04	0.00	−0.02	0.02	0.04	−0.01	−0.04	0.00
z	0.09	0.00	−0.05	0.05	0.06	−0.02	−0.06	0.00
Rotation (°)								
x	0.19	−0.03	−0.16	0.06	0.14	−0.02	−0.11	0.02
y	0.32	0.02	−0.17	0.14	0.29	−0.14	−0.24	0.02
z	0.12	0.02	−0.03	0.10	0.27	−0.05	−0.27	0.02

Table 2: Accuracy for 3D CT.

	2.57 ∗ RMS	Mean	Min	Max
Uncemented cup				
Translation (mm)				
x	0.29	0.05	−0.11	0.19
y	0.28	−0.06	−0.13	0.05
z	0.32	0.04	−0.06	0.26
Rotation (d)				
x	0.82	−0.15	−0.56	0.17
y	0.71	−0.18	−0.52	0.06
z	0.43	−0.04	−0.22	0.10
Cemented cup				
Translation (mm)				
x	0.19	0.01	−0.17	0.17
y	0.07	0.01	−0.08	0.07
z	0.08	0.00	−0.10	0.07
Rotation (d)				
x	0.21	0.01	−0.15	0.28
y	0.44	0.05	−0.43	0.49
z	0.26	−0.01	−0.33	0.22

The landmark designation procedure in the 3D CT was rapid and required less than five minutes per volume. Since the 3D volumes could be freely rotated and viewed from arbitrary angles, it was easy to differentiate between tantalum beads. In contrast, in standard RSA tantalum beads were harder to identify than in 3D CT. The effective radiation dose was estimated to be on an average 0.33 mSv per scan for the 3D CT method and 0.1 mSv for standard RSA.

4. Discussion

To our knowledge, this is the first study comparing a 3D CT and a RSA method. There have however been numerous publications based on our CT method used for other applications such as acetabular loosening, motion analysis of disc replacements, and cup wear [5, 6, 17]. Numerous publications on RSA have shown that it can be used as an early detector of migration of an implant, which is an early sign for risk of revision [18, 19]. RSA has therefore been suggested to play a role in evidence based introduction of new implants. For knee implants, migration of the tibia component of more than 1.6 mm during the first year is unacceptable and indicates a high risk for revision [19]. For hip stems the prediction of failure of implants is due to the shape of the implant. Migration exceeding 0.85 mm within the first six months is a predictor for implant failure for anatomical cemented stems [20].

Our aim in this phantom study using a pelvic model was to compare our new 3D CT method with standard RSA in terms of precision and accuracy in order to see if this new method could be used to detect early signs of loosening of a prosthetic implant in patients who also have implanted markers. It could therefore provide an alternative for evidence based introduction of new implants. We found comparable precision for 3D CT compared to standard RSA in acetabular components for THA. In standard RSA, even in our experimental setting, both our cups, but especially the uncemented cup, suffered from marker occlusion, that is, not being able to use all tantalum beads. This problem is common in RSA studies, especially around uncemented acetabular components; hence other RSA alternatives have been developed to solve this problem such as model based RSA [21–23].

We also found a high degree of accuracy for the 3D CT method when using standard RSA as the gold standard. In

the uncemented cup we could only use four tantalum beads that could be visualized on both images in standard RSA and thus only these markers could be used when comparing migration between methods. These markers did not form an optimal stable rigid body for 3D CT; therefore the results of the accuracy of the uncemented cup were not as satisfying as those for the cemented cup.

In this model study, the radiation dose was comparable to RSA. The radiation dose in CT is highly dependent on the machine and the protocol used for the examination. In this case, the average effective dose was estimated to be 0.33 mSv. This is a low dose and can be compared to the RSA effective dose estimated to be 0.1 mSv in this study.

CT is easily acquired and the examination can be performed on any modern CT scanner. The acquisition is fast, and patient positioning in the scanner is not vital, since the volume can be transformed into an arbitrary spatial orientation for viewing and processing.

There are several potential benefits from using CT as opposed to RSA. It greatly speeds up the marking process, since marker identification becomes trivial when utilizing powerful, interactive 2D and 3D visualization tools applied to the CT volume data. This enables 3D evaluation of marker configuration and distribution. In addition to reporting the relative motion numerically, the CT method gives immediate visual feedback in both 2D and 3D, with volumes displayed either side by side or fused. The quality of the registration, in this case based on the markers attached to the bone, as well as the relative movement, could be visually evaluated. Any point in these volumes can be accessed and designated, so there is potential for studying the relative movement at any location. Another advantage is that landmarks can be added on structures other than tantalum beads, if the stability of the rigid body is not sufficient [24]. Another advantage of 3D CT could be the simultaneous evaluation of, for example, osteolysis in clinical cases which has not been evaluated in this experimental study.

Disadvantages of the proposed method are that it is new and relatively untested for this application and has not been validated as much as RSA. Additionally, it requires user interaction which could vary from one operator to another. To our knowledge, there is no commercially available 3D CT software at present.

The limitation of our study was that we did not use an instrument that could directly measure migration of the implant for comparison with the 3D CT method. Instead we used the RSA method as a gold standard that has a documented small error in precision and accuracy [4].

5. Conclusion

In conclusion, 3D CT has comparable precision to standard RSA and an acceptable accuracy. This CT method could potentially be used to evaluate patients with RSA markers, thus avoiding the inability to evaluate these patients over time due to the lack of facilities for doing stereoradiographs. Further, the effective dose associated with CT is becoming comparable to that of two planar X-rays. However, further clinical studies with the 3D CT method on patients are necessary before it can be used as an alternative method to RSA.

Disclosure

Some of this material has been presented at the 2015 Orthopaedic Surgery Conference in Falun, Sweden.

Competing Interests

No competing interests are declared.

Authors' Contributions

Cyrus Brodén prepared the model for scanning, performed the model studies, did the analysis of model, and wrote the major part of the paper. Henrik Olivecrona and Olof Sköldenberg initiated the study, prepared the model for scanning, performed the model studies, did the analysis of model, and wrote the paper. Gerald Q. Maguire Jr., Marilyn E. Noz, and Michael P. Zeleznik participated in writing the software, analyzing the data, and writing the paper.

Acknowledgments

The authors thank Lise-Lotte Widmark for help in performing the CT and RSA examinations.

References

[1] G. Selvik, "Roentgen stereophotogrammetry. A method for the study of the kinematics of the skeletal system," *Acta Orthopaedica Scandinavica, Supplement*, vol. 232, pp. 1–51, 1989.

[2] J. Kärrholm, B. Borssén, G. Löwenhielm, and F. Snorrason, "Does early micromotion of femoral stem prostheses matter? 4–7-year stereoradiographic follow-up of 84 cemented prostheses," *The Journal of Bone & Joint Surgery—British Volume*, vol. 76, no. 6, pp. 912–917, 1994.

[3] L. Ryd, B. E. J. Albrektsson, L. Carlsson et al., "Roentgen stereophotogrammetric analysis as a predictor of mechanical loosening of knee prostheses," *The Journal of Bone & Joint Surgery—British Volume*, vol. 77, no. 3, pp. 377–383, 1995.

[4] E. R. Valstar, R. Gill, L. Ryd, G. Flivik, N. Börlin, and J. Kärrholm, "Guidelines for standardization of radiostereometry (RSA) of implants," *Acta Orthopaedica*, vol. 76, no. 4, pp. 563–572, 2005.

[5] H. Olivecrona, L. Olivecrona, L. Weidenhielm et al., "A new technique for diagnosis of acetabular cup loosening using computed tomography: preliminary experience in 10 patients," *Acta Orthopaedica*, vol. 79, no. 3, pp. 346–353, 2008.

[6] P. Svedmark, F. Lundh, G. Németh et al., "Motion analysis of total cervical disc replacements using computed tomography: preliminary experience with nine patients and a model," *Acta Radiologica*, vol. 52, no. 10, pp. 1128–1137, 2011.

[7] I. Söderkvist and P.-Å. Wedin, "Determining the movements of the skeleton using well-configured markers," *Journal of Biomechanics*, vol. 26, no. 12, pp. 1473–1477, 1993.

[8] I. Söderkvist and P.-Å. Wedin, "On condition numbers and algorithms for determining a rigid body movement," *BIT*, vol. 34, no. 3, pp. 424–436, 1994.

[9] M. E. Noz, G. Q. Maguire Jr., M. P. Zeleznik, E. L. Kramer, F. Mahmoud, and J. Crafoord, "A versatile functional-anatomic image fusion method for volume data sets," *Journal of Medical Systems*, vol. 25, no. 5, pp. 297–307, 2001.

[10] L. Olivecrona, J. Crafoord, H. Olivecrona et al., "Acetabular component migration in total hip arthroplasty using CT and a semiautomated program for volume merging," *Acta Radiologica*, vol. 43, no. 5, pp. 517–527, 2002.

[11] R. J. T. Gorniak, E. L. Kramer, G. Q. Maguire Jr., M. E. Noz, C. J. Schettino, and M. P. Zeleznik, "Evaluation of a semiautomatic 3D fusion technique applied to molecular imaging and MRI brain/frame volume data sets," *Journal of Medical Systems*, vol. 27, no. 2, pp. 141–156, 2003.

[12] J. Ranstam, "Methodological note: accuracy, precision, and validity," *Acta Radiologica*, vol. 49, no. 1, pp. 105–106, 2008.

[13] O. Sköldenberg, T. Eisler, A. Stark, O. Muren, N. Martinez-Carranza, and L. Ryd, "Measurement of the migration of a focal knee resurfacing implant with radiostereometry," *Acta Orthopaedica*, vol. 85, no. 1, pp. 79–83, 2014.

[14] E. R. Valstar, H. A. Vrooman, S. Toksvig-Larsen, L. Ryd, and R. G. H. H. Nelissen, "Digital automated RSA compared to manually operated RSA," *Journal of Biomechanics*, vol. 33, no. 12, pp. 1593–1599, 2000.

[15] AAPM, "The measurement, reporting, and management of radiation dose in CT," Report of AAPM Task Group 23 of the Diagnostic Imaging Council CT Committee 96, American Association of Physicists in Medicine, College Park, Md, USA, 2008.

[16] P. Andreo, "Monte Carlo techniques in medical radiation physics," *Physics in Medicine and Biology*, vol. 36, no. 7, pp. 861–920, 1991.

[17] D. Goldvasser, M. E. Noz, G. Q. Maguire, H. Olivecrona, C. R. Bragdon, and H. Malchau, "A new technique for measuring wear in total hip arthroplasty using computed tomography," *Journal of Arthroplasty*, vol. 27, no. 9, pp. 1636–1640.e1, 2012.

[18] J. Kärrholm, "Radiostereometric analysis of early implant migration—a valuable tool to ensure proper introduction of new implants," *Acta Orthopaedica*, vol. 83, no. 6, pp. 551–552, 2012.

[19] B. G. Pijls, E. R. Valstar, K.-A. Nouta et al., "Early migration of tibial components is associated with late revision," *Acta Orthopaedica*, vol. 83, no. 6, pp. 614–624, 2012.

[20] F. Bottner, E. Su, B. Nestor, B. Azzis, T. P. Sculco, and M. Bostrom, "Radiostereometric analysis: the hip," *HSS Journal*, vol. 1, no. 1, pp. 94–99, 2005.

[21] B. L. Kaptein, E. R. Valstar, B. C. Stoel, P. M. Rozing, and J. H. C. Reiber, "A new type of model-based Roentgen stereophotogrammetric analysis for solving the occluded marker problem," *Journal of Biomechanics*, vol. 38, no. 11, pp. 2330–2334, 2005.

[22] T. Baad-Hansen, S. Kold, B. L. Kaptein, and K. Søballe, "High-precision measurements of cementless acetabular components using model-based RSA: An Experimental Study," *Acta Orthopaedica*, vol. 78, no. 4, pp. 463–469, 2007.

[23] M. Stilling, S. Kold, S. de Raedt, N. T. Andersen, O. Rahbek, and K. Soballe, "Superior accuracy of model-based radiostereometricanalysis for measurement of polyethylene wear: a phantom study," *Bone and Joint Research*, vol. 1, no. 8, pp. 180–191, 2012.

[24] H. Olivecrona, L. Weidenhielm, L. Olivecrona et al., "A new CT method for measuring cup orientation after total hip arthroplasty: a study of 10 patients," *Acta Orthopaedica Scandinavica*, vol. 75, no. 3, pp. 252–260, 2004.

Hindawi Publishing Corporation
BioMed Research International
Volume 2016, Article ID 8651573, 8 pages
http://dx.doi.org/10.1155/2016/8651573

Research Article

Three-Dimensional Computer-Aided Detection of Microcalcification Clusters in Digital Breast Tomosynthesis

Ji-wook Jeong,[1] Seung-Hoon Chae,[1] Eun Young Chae,[2] Hak Hee Kim,[2] Young-Wook Choi,[3] and Sooyeul Lee[1]

[1]*SW·Content Research Laboratory, Electronics & Telecommunications Research Institute, 218 Gajeongno, Yuseong-gu, 34129 Daejeon, Republic of Korea*
[2]*Department of Radiology and Research Institute of Radiology, Asan Medical Center, University of Ulsan College of Medicine, 88 Olympic-ro 43-gil, Songpa-gu, 05505 Seoul, Republic of Korea*
[3]*Advanced Medical Device Research Division, Korea Electrotechnology Research Institute, 111 Hanggaul-ro, Sangnok-gu, Ansan-si, 15588 Gyeonggi-do, Republic of Korea*

Correspondence should be addressed to Ji-wook Jeong; jwj@etri.re.kr

Received 10 September 2015; Revised 12 February 2016; Accepted 17 February 2016

Academic Editor: Guang Jia

We propose computer-aided detection (CADe) algorithm for microcalcification (MC) clusters in reconstructed digital breast tomosynthesis (DBT) images. The algorithm consists of prescreening, MC detection, clustering, and false-positive (FP) reduction steps. The DBT images containing the MC-like objects were enhanced by a multiscale Hessian-based three-dimensional (3D) objectness response function and a connected-component segmentation method was applied to extract the cluster seed objects as potential clustering centers of MCs. Secondly, a signal-to-noise ratio (SNR) enhanced image was also generated to detect the individual MC candidates and prescreen the MC-like objects. Each cluster seed candidate was prescreened by counting neighboring individual MC candidates nearby the cluster seed object according to several microcalcification clustering criteria. As a second step, we introduced bounding boxes for the accepted seed candidate, clustered all the overlapping cubes, and examined. After the FP reduction step, the average number of FPs per case was estimated to be 2.47 per DBT volume with a sensitivity of 83.3%.

1. Introduction

Recently, there have been several reports that the acquisition of several projection views (PVs) of the compressed breast using a conventional full-field digital mammography (FFDM) detector is sufficient to reconstruct the total DBT images at a total radiation dose comparable to that used in mammography [1, 2]; however, the reconstructed 3D DBT volume contains artifacts from missing information, regardless of the reconstruction technique applied [3–5]. Despite these shortcomings, it is expected that DBT can reduce the overlapping breast tissue effect, which is usually considered to be a limiting factor for lesion detection and characterization in FFDM [1, 6, 7].

There has been a controversy as to whether or not the cancer detection performance through prospective clinical trials has found an increase in sensitivity with a moderate increase in the call-back rate [8–10]. As a consistent second reader, CADe may be helpful by detecting lesions in DBT missed by radiologists owing to the large volume of the image data, as well as a number of other factors [11]. The detection of MCCs in DBT volumes by radiologists may be more difficult compared with mammography for two reasons: the number of MCs on each reconstructed slice will be fewer than the total number of MC clusters, making it less apparent. CADe may be of particular interest in DBT for MC detection by adopting a maximum intensity projection (MIP) method. MCs may appear blurred from many factors including an inaccurate system geometry, focal spot motion, and patient motion. There have been several feasibility studies recently regarding CADe for MC detection in DBT [12, 13].

It is also important to reduce the number of false negatives during the search for MCCs in a 3D DBT volume, which may be more demanding than for mammograms. For these

reasons, CADe may play an even more important role in MC detection in DBT than in mammography by automatically searching for MCCs in a 3D DBT image volume within a relatively short period of time. There have been a number of studies regarding the development of CADe techniques for the detection of masses in DBT [11, 14–17]. Compared with the detection of masses, preliminary researches regarding the detection of MCCs on DBT have been reported [12, 18–23].

Reiser and coworkers back-projected binarized PVs containing detected MCs into a 3D volume to conduct an MIP transformation for second-stage detection [18]. Features were extracted and a false-positive (FP) reduction step was conducted with a sensitivity of 86% with 1.3 FP clusters per DBT volume. Bernard and others developed a detection algorithm of MCCs on filtered back-projection reconstructed slices [21] enhanced by convolving the image volume with a Mexican hat wavelet with a sensitivity of 85% at an average of 1.4 FP marks per breast volume. Park and coworkers detected MCCs on both individual PVs with a sensitivity of 70% at an average of 3.99 FPs per volume and individual reconstructed slices with a sensitivity of 86% at an average of 15.9 FPs per volume [19]. Sahiner and coworkers investigated the detection of MCCs in the reconstructed DBT volume using an enhanced-modulated 3D multiscale calcification response function and SNR enhancement [13].

In this paper, a simple and efficient FP reduction scheme coupled with a detection algorithm for MCCs in a reconstructed DBT volume using 3D objectness- and SNR-enhanced images is suggested [13, 23]. For a dataset of two-view DBTs of 69 breasts with or without MCCs, a view-based sensitivity of 83.3% was achieved at 2.47 FPs per DBT volume.

2. Data Acquisition

The patient recruitment protocol was approved by IRB. Breast imaging patients of the breast imaging research laboratory at Asan Medical Center (Seoul, Korea) who were recommended for breast biopsy based on suspicious mammographic breast masses and microcalcifications were eligible. Written informed consent was obtained from each patient. We acquired the DBT scans of 15 PV images over a ±21 angular range in 2.8 increments through a step-and-shoot operation using the prototype DBT system for breast imaging research fabricated by KERI (Ansan, Korea) [25]. The DBT system has a flat panel digital detector with dimensions of 14.40 cm × 25.92 cm and a pixel pitch of 0.0748 mm × 0.0748 mm [26–28]. The 3D DBT volumes were reconstructed at a 1 mm slice interval with a pixel pitch of 0.1 mm × 0.1 mm using the FDK filtered back-projection reconstruction technique [29]. DBT scans of the 69 breasts were acquired in both craniocaudal and mediolateral oblique views prior to a biopsy and the location of the biopsy-proven MCC was marked by an experienced radiologist using clinical mammograms and the biopsy report as references. A total of 19 MCCs were identified on the 138 DBT scans.

3. Prescreening Step

The MCs are first enhanced using a multiscale Hessian enhancement with an object-type response function and an SNR enhancement with combination of several simple digital filters in the reconstructed DBT volume ($\mathrm{Im}(x, y, z)$) [13]. Then, the resulting Hessian-based object-type response volume is again voxel-wise convolved with the SNR-enhanced volume, and a connected-component segmentation process [30] is performed to extract the clustering seed objects for the MCCs, which are described in Section 5. Before the prescreening step, we subsampled the DBT images in the x-y direction by 10 and the maximum grey level value was chosen as a representative value to reduce the computational load; its effect on the detection accuracy is discussed later in this paper.

3.1. Multiscale Object-Type Response. There is an observation that all three eigenvalues of the Hessian matrix [30, 31] near the center of a spherically symmetric lesion with positive contrast are given negative and are nearly equal to each other in the case of spherical shape, whereas the Hessian matrix for voxels that are a part of other types of shapes, such as lines or planes, will give unequal eigenvalues. In practice, to optimize the Hessian enhancement process for objects at different scales and reduce the computational noise from the estimation of second-order derivatives in the Hessian operator calculations, the image $I(x, y, z)$ is first convolved with a 3D Gaussian smoothing filter giving a smoothed image $G(x, y, z)$ and Hessian matrix $H_{\varepsilon\delta}$ setup as follows:

$$H_{\varepsilon\delta} = \frac{\partial^2 G(x, y, z)}{\partial\varepsilon\partial\delta}, \tag{1}$$

where (ε, δ) is chosen among the Cartesian axes of x, y, and z, alternatively. Then, the Hessian matrix ($H_{\alpha\beta}$; $\alpha, \beta \in \{x, y, z\}$) is diagonalized and the eigenvalues $\{(\lambda_1, \lambda_2, \lambda_3) \mid 0 \geq \lambda_3 \geq \lambda_2 \geq \lambda_1\}$ are specified in ascending order.

To enhance a spherically symmetric object, a response $O(\{\lambda_i\}; \sigma)$ at a Gaussian scale σ is defined using

$$O(\{\lambda_i\}; \sigma) = \left(1 - \exp\left(-\frac{{\lambda_1}^2}{2\alpha^2 |\lambda_2\lambda_3|}\right)\right) \cdot \left(1 - \exp\left(-\frac{{\lambda_1}^2 + {\lambda_2}^2 + {\lambda_3}^2}{2\gamma^2}\right)\right), \tag{2}$$

where the selected values for the objectness parameters of α and γ are 0.1 and 3.0, respectively [32]. We find that the selection of typically chosen functional type for an object response is enough to give sufficiently accurate detection results comparable to other researches.

Then, a response vector $R = \{O(\lambda_{\sigma 1}), O(\lambda_{\sigma 2}), \ldots, O(\lambda_{\sigma N})\}$ at multiple scales $\{\sigma\} = \{\sigma 1, \sigma 2, \ldots, \sigma N\}$ is obtained at every (x, y, z). In this study, we chose $N = 3$ to reduce the computational load. After the optimal index for scale $i^* = \arg\max_i \{O(\lambda_{\sigma i})\}$ was estimated, the multiscale object-type response (MOR) at every voxel of (x, y, z) was then evaluated as $O(x, y, z) = O({\lambda_{\sigma i}}^*)$. Figure 1(b) illustrates

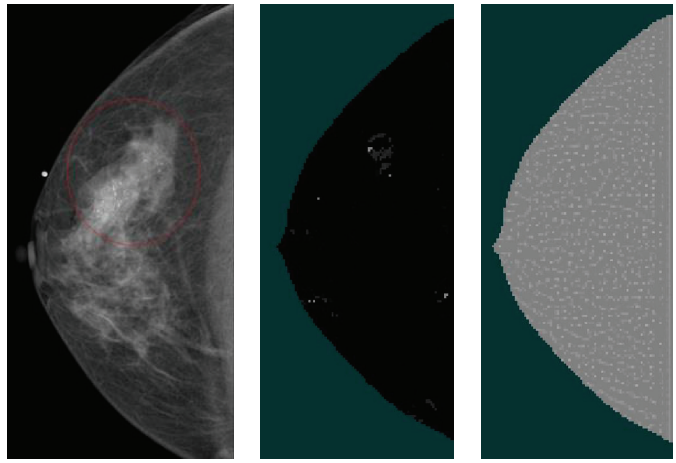

(a) (b) (c)

Figure 1: (a) A mammogram containing MCCs. The ROI drawn by a radiologist is shown in the red circle. (b) A multiscale Hessian-enhanced image. (c) An SNR-enhanced image.

the filtering process to enhance the objectness using the multiscale Hessian matrix.

3.2. 3D SNR Enhancement. From the clinical observations, many visible MCs are closely related with grey level fluctuations, and we introduced an SNR enhancement preprocessing step to each two-dimensional DBT slice independently. It consists of a combination of three linear mean filters centered at the calcification candidate, F_1, F_2, and F_3, of sizes $M_1 \times M_1$, $M_2 \times M_2$, and $M_3 \times M_3$, respectively, where $M_1 = 15$, $M_2 = 7$, and $M_3 = 3$, to define a single band-pass filter before convolution with the image and extracting the signal intensity relative to the slowly varying background image intensity [13]. In order to remove an artifact resulting from the inclusion of pixels right near the candidate pixel, F_2 is subtracted from F_1 filter. Then, the combined band-pass filter was convolved with DBT volume as illustrated in Figure 1(c). Overall block diagram for our CADe system of MCCs in DBT images is given in Figure 2.

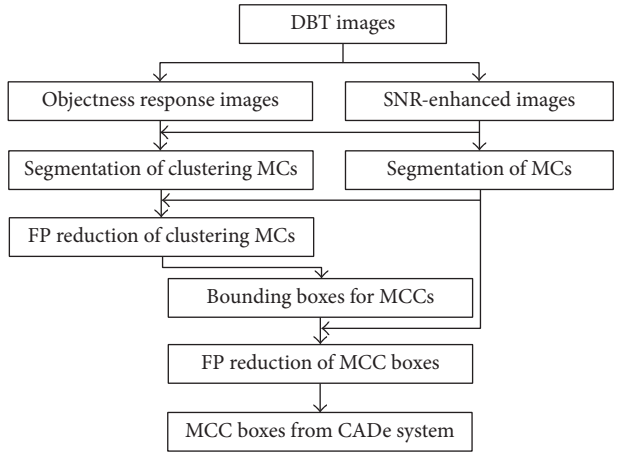

Figure 2: The block diagram of our CADe system.

4. MCC Detection

In the MCC detection step, we firstly weighted $O(x, y, z)$ with SNR-enhanced voxel value of $\mathrm{SNR}(x, y, z)$, where $\mathrm{SNR}(x, y, z)$ is given by $\mathrm{SNR}(x, y, z) = I(x, y, z) \otimes F(x, y)$, and $F(x, y)$ is a resulting 2D digital filter in order to obtain the multiscale objectness response (MOR). Since both the multiscale calcification response and the SNR enhancement are intended to highlight the MCs, it may be expected that their product will improve the microcalcification detection.

Over $\mathrm{MOR}(x, y, z)$, a connected-component segmentation technique was performed to detect about 500 connected objects as the initial seed objects [30, 33]. Voxels that were above the binarizing threshold were marked and grouped into 3D connected objects to give a labeled image. The labeled image was again converted to the labeled map to examine the shape attributes of each segmented and labeled object. The initial threshold was chosen to be relatively high enough to detect only about 500 connected objects, which are defined as cluster seed objects below as exemplified in Figure 3.

The noise around each individual MC candidate was estimated using the $\mathrm{SNR3D}(x, y, z)$ images as follows. The squared noise level $\sigma^2(x, y, z)$ at each input voxel of $\mathrm{SNR}(x, y, z)$ was evaluated from the standard deviation of the grey level value distribution in the neighborhood of that pixel. The SNR of the MC candidate was then calculated as the ratio of $\sigma^2(x, y, z)$ and the local mean value $m_{\mathrm{loc}}(x, y, z)$ at the same voxel as follows:

$$\mathrm{SNR3D}\,(x, y, z) = \frac{\sigma^2\,(x, y, z)_{\mathrm{SNR}(x,y,z)}}{m_{\mathrm{loc}}\,(x, y, z)_{\mathrm{SNR}(x,y,z)}}, \tag{3}$$

where the subscripts indicate the corresponding local operator performed on the given 3D image. The individual MC candidates were also labeled using a connected-component segmentation algorithm and an SNR threshold value of 3.2

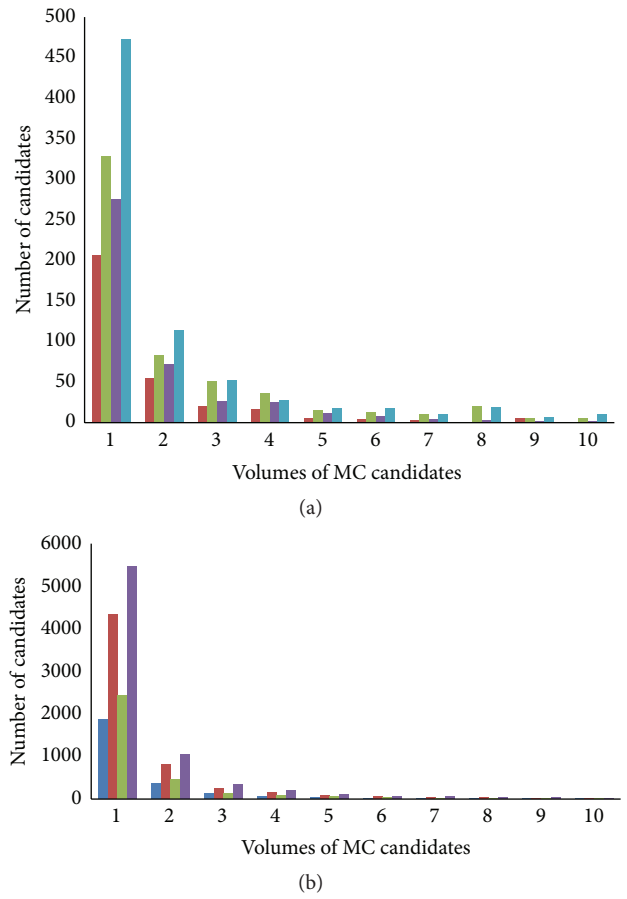

FIGURE 3: (a) Volume distributions of segmented candidates from (a) MOR image and (b) SNR image. Blue, brown, green, and violet colored bars are for RMLO, LMLO, RCC, and LCC modalities of a DBT image, respectively.

was chosen for the binarization of the SNR3D(x, y, z) image to locate about 5,000 MC candidates, independent of the cluster seed object detection process.

Then, an MC clustering process was applied to choose the MCC candidates as follows. Note that only the clustering seed objects segmented from the MOR images were considered as the clustering center. Starting with each cluster seed object, individual MC candidates satisfying the clustering criteria of their distances being within 5 mm from the cluster center were included as cluster members. Figure 4 shows a snapshot of our MCC detection system before MC clustering and FP reduction step.

5. False-Positive Reduction

As a first step to reduce the FPs for the MCC candidates, we applied a rule-based classifier with two rules related to the voxel sum of the individual MCs and the number of cluster seed candidates in the neighborhood of the candidate cluster. The voxels of individual MC candidates within a 5 mm radius of the cluster seed candidate were counted and the first rule specifies that if this number is less than 9, the cluster seed candidate will be eliminated. We also counted the number of nearby cluster seed candidates within a 5 mm radius of the cluster candidate under consideration. The second rule specifies that if this number is less than 2, the cluster candidate will be eliminated.

Second, the cubes minimally containing the MCs were generated and clustered for a further FP reduction. To qualify the clustered MCs, a bounding cube was generated for each accepted seed candidate. The overlapping cubes were combined and examined to determine whether the number of combined cubes is larger than one. Next, we examined the number and voxel sum of the included individual MC candidates contained in each cube. When the number of the included individual MC candidates within the resulting MCC cube was less than 80 or the total volume of the MC candidates was less than 140 mm^3, the combined cube was eliminated.

In this study, a suggested MCC candidate on the DBT image was considered as true positive, if the overlapped volume between the annotated gold standard and the detected MCC candidate is larger than zero, to simplify the volumetric analysis between them. Further improvement of the FP reduction algorithm using the elaborated volumetric analysis as a next step will be reported in the near future.

6. Results and Discussion

As shown in Figure 4, our detection and screening system for the MCCs in DBT successfully suggests the outlining range of inspection. Using view-based scoring, the average number of FPs using the datasets was estimated to be 2.47 per DBT volume at an 83.3% sensitivity, which was found to be comparable with other pioneering researches [12, 13]. In particular, it is notable that the FPs for the DBT volumes with MCCs proven to be positive were found to be 2.24, lower than 2.56 for the DBT volumes without an MCC [34]. It is noted that our CADe system gives less FPs with the true-positive lesion marking than with normal breast images, indicating that our algorithm should be improved further to give the lower specificity or less FPs with the same sensitivity results. It is well known that the higher rate of FPs of the breast cancer diagnosis usually leads to increased psychological and economical burden, meaning that the patients undergo unnecessary and exhaustive diagnostic procedures. It is also notable that the clinical criterion of FPs per case for CADe based on any commercial medical imaging modality is eventually under or about to be one-per-case, and the mammography CADe of the breast cancer has been proven to satisfy such a criterion. Our results compared with the clinical gold standards marked by a radiologist (as exemplified in Figure 5) indicate that the feasibility of automated detection algorithm of MCCs in reconstructed DBT volumes coupled with the relatively simplified clustering and FP reduction algorithm, however, is also necessary to fine-tune the prescreening parameters to reduce the number of FPs.

In principle, our approach basically utilizes the combination of two microcalcification enhancement processes: (1)

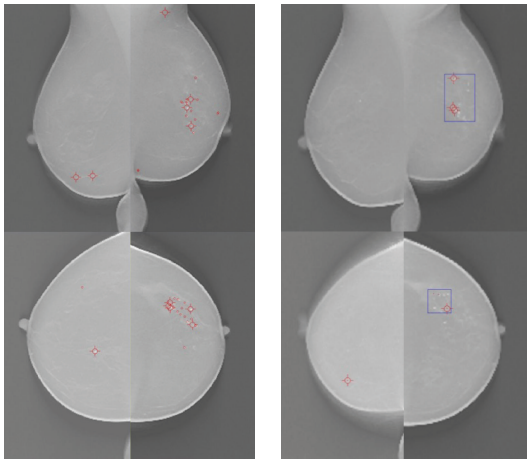

(a) (b)

Figure 4: Snapshots of our MCC detection system (a) before and (b) after clustering step. Red circles are for the clustering MC candidates extracted from an MOR image after the prescreening step based on the analysis of the individual MC candidates extracted from an SNR image. Blue square means a bounding box after the prescreening step. Left top, right top, left bottom, and right bottom images are for RLMO, LMLO, RCC, and LCC modalities of a DBT image.

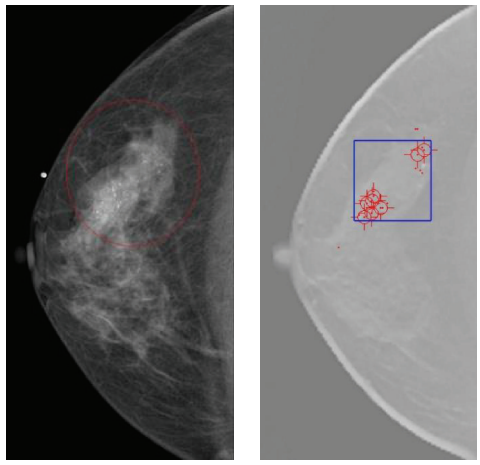

(a) (b)

Figure 5: (a) A mammogram containing MCCs. The ROI drawn by a radiologist is shown in the red circle. (b) A DBT slice with the suggested MCC bounding cube. The blue square containing the MCCs was automatically determined during the CADe calculation. Red dots or circles indicate the MC seed objects before the FP reduction step.

3D objectness enhancement of the MC response based on a multiscale Hessian analysis and (2) SNR enhancement based on a combination of linear boxcar filters. The FPs per DBT volume were counted from the dataset after two FP reduction steps, and the free response receiver operating characteristics (FROC) curve for the detection system is shown in Figure 6. The area under the FROC curve normalized to 20.44 FPs per DBT volume at a sensitivity of 100.0% was estimated to be 0.88 [35–38], implying that our results are in quite reasonable agreement with previous researches in spite of several assumptions and the setting of the evaluation parameters [39–41], however, giving slow convergence of the sensitivity as FPs increase.

Our CADe system contains a large number of parameters for prescreening, clustering, and FP reduction stages. In this preliminary study, we focused on the effect of the FP reduction threshold parameters. The binarizing threshold values for the MOR volume and the SNR-enhanced volume were chosen empirically, implying that further studies with a larger DBT image set to optimize the control parameters may improve the MC detection performance [42–44].

The MOR function used in this study was introduced for spherically symmetric objects; however, pathology-proven MCs will have a variety of shapes, including elongated, stellated, and irregular shapes. In addition, the interplanar artifacts resulting from the adopted limited-angle reconstruction

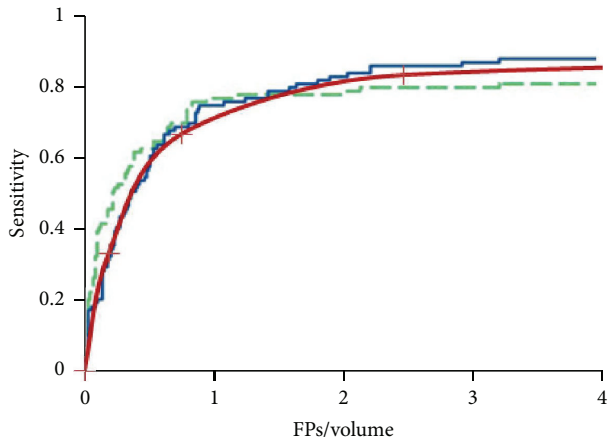

Figure 6: The overall performance of the MCC detection and FP reduction algorithm in terms of the FROC curve. Solid brown line is for the ROC using our CADe algorithm. Solid blue and dashed green lines are for the ROCs using the FP reduction algorithm involving convolution neural network features with the DBT volume and the digital mammography [24].

algorithm to obtain DBT image may distort the shape of the MCs in the depth direction and influence the performance of the applied segmentation method probably giving lower sensitivity of MCC detection [22]. Further studies regarding the anisotropic properties of the SNR distribution in the depth direction are also desired.

It should be commented that there have been some notable reports regarding MC detection on PVs [18, 19]. The MC detection on each two-dimensional PV is supposed to be independent of the specific reconstruction method, meaning that its detection results can be compared without the interplanar artifacts originating from the incomplete reconstruction algorithm for the DBT images. Tomosynthesis reconstruction with multiple noisy PVs can play a role in the prescreening step in the clinical MC detection approach by increasing the SNR of the targets.

It is notable that several pioneering reports involving various imaging modalities, such as three-dimensional DBT volume itself [24] and the planar projection view images [45], have been published up to now; however, the CADe for DBT images seems to be not outperforming that for digital mammography within near future. It is also worth commenting that, recently, there has been a report of a multimodal joint-CADe algorithm involving both DBT and projection view images [46].

Further research using the independently acquired DBT volume dataset is in progress to validate our proposed FP reduction algorithm.

7. Conclusion

We developed a CADe system with a simplified FP reduction scheme for the detection of MCCs in reconstructed DBT volumes. The result of our proposed MCC detection algorithm is a promising approach, giving detection results comparable to other researches. Ongoing researches include further optimization of the FP reduction parameters using a large dataset and the 2D-3D hybridized detection on both PVs and the reconstructed volume. It is expected that, with further study on the CADe algorithm to improve the detection accuracy, the CADe system may play the role of a second reader by assisting radiologists in the detection of MCCs in DBT in the near future.

Competing Interests

The authors declare that they have no competing interests.

Acknowledgments

This research was supported by the R&D Convergence Program (Grant CAP-13-3-KERI) of NST (National Research Council of Science & Technology) of Republic of Korea.

References

[1] L. T. Niklason, B. T. Christian, L. E. Niklason et al., "Digital tomosynthesis in breast imaging," *Radiology*, vol. 205, no. 2, pp. 399–406, 1997.

[2] S. Suryanarayanan, A. Karellas, S. Vedantham et al., "Comparison of tomosynthesis methods used with digital mammography," *Academic Radiology*, vol. 7, no. 12, pp. 1085–1097, 2000.

[3] Y. Chen, J. Y. Lo, and J. T. Dobbins III, "Importance of point-by-point back projection correction for isocentric motion in digital breast tomosynthesis: relevance to morphology of structures such as microcalcifications," *Medical Physics*, vol. 34, no. 10, pp. 3885–3892, 2007.

[4] E. Y. Sidky, X. Pan, I. S. Reiser, R. M. Nishikawa, R. H. Moore, and D. B. Kopans, "Enhanced imaging of microcalcifications in digital breast tomosynthesis through improved image-reconstruction algorithms," *Medical Physics*, vol. 36, no. 11, pp. 4920–4932, 2009.

[5] Y. Lu, H.-P. Chan, J. Wei, and L. M. Hadjiiski, "Selective-diffusion regularization for enhancement of microcalcifications in digital breast tomosynthesis reconstruction," *Medical Physics*, vol. 37, no. 11, pp. 6003–6014, 2010.

[6] I. Andersson, D. M. Ikeda, S. Zackrisson et al., "Breast tomosynthesis and digital mammography: a comparison of breast cancer visibility and BIRADS classification in a population of cancers with subtle mammographic findings," *European Radiology*, vol. 18, no. 12, pp. 2817–2825, 2008.

[7] G. Gennaro, A. Toledano, C. Di Maggio et al., "Digital breast tomosynthesis versus digital mammography: a clinical performance study," *European Radiology*, vol. 20, no. 7, pp. 1545–1553, 2010.

[8] T. W. Freer and M. J. Ulissey, "Screening mammography with computer-aided detection: prospective study of 12,860 patients in a community breast center," *Radiology*, vol. 220, no. 3, pp. 781–786, 2001.

[9] R. L. Birdwell, P. Bandodkar, and D. M. Ikeda, "Computer-aided detection with screening mammography in a university hospital setting," *Radiology*, vol. 236, no. 2, pp. 451–457, 2005.

[10] B. Brancato, N. Houssami, D. Francesca et al., "Does computer-aided detection (CAD) contribute to the performance of digital mammography in a self-referred population?" *Breast Cancer Research and Treatment*, vol. 111, no. 2, pp. 373–376, 2008.

[11] H.-P. Chan, J. Wei, B. Sahiner et al., "Computer-aided detection system for breast masses on digital tomosynthesis mammograms: preliminary experience," *Radiology*, vol. 237, no. 3, pp. 1075–1080, 2005.

[12] S. Bernard, S. Muller, and J. Onativia, "Computer-aided microcalcification detection on digital breast tomosynthesis data: a preliminary evaluation," in *Digital Mammography*, E. A. Krupinski, Ed., vol. 5116 of *Lecture Notes in Computer Science*, pp. 151–157, 2008.

[13] B. Sahiner, H.-P. Chan, L. M. Hadjiiski et al., "Computer-aided detection of clustered microcalcifications in digital breast tomosynthesis: a 3D approach," *Medical Physics*, vol. 39, no. 1, pp. 28–39, 2012.

[14] I. Reiser, R. M. Nishikawa, M. L. Giger et al., "Computerized detection of mass lesions in digital breast tomosynthesis images using two- and three dimensional radial gradient index segmentation," *Technology in Cancer Research and Treatment*, vol. 3, no. 5, pp. 437–441, 2004.

[15] I. Reiser, R. M. Nishikawa, M. L. Giger et al., "Computerized mass detection for digital breast tomosynthesis directly from the projection images," *Medical Physics*, vol. 33, no. 2, pp. 482–491, 2006.

[16] H.-P. Chan, J. Wei, Y. Zhang et al., "Computer-aided detection of masses in digital tomosynthesis mammography: comparison of three approaches," *Medical Physics*, vol. 35, no. 9, pp. 4087–4095, 2008.

[17] S. Singh, G. D. Tourassi, J. A. Baker, E. Samei, and J. Y. Lo, "Automated breast mass detection in 3D reconstructed tomosynthesis volumes: a featureless approach," *Medical Physics*, vol. 35, article 3626, 2008.

[18] I. Reiser, R. M. Nishikawa, A. V. Edwards et al., "Automated detection of microcalcification clusters for digital breast tomosynthesis using projection data only: a preliminary study," *Medical Physics*, vol. 35, no. 4, pp. 1486–1493, 2008.

[19] S. C. Park et al., "Applying a 2D based CAD scheme for detecting micro-calcification clusters using digital breast tomosynthesis images: an assessment," in *Proceedings of the Medical Imaging 2008: Computer-Aided Diagnosis*, vol. 6915 of *Proceedings of SPIE*, pp. 71–78, San Diego, Calif, USA, February 2008.

[20] H.-P. Chan, B. Sahiner, J. Wei, L. M. Hadjiiski, C. Zhou, and M. A. Helvie, "Digital breast tomosynthesis: computerized detection of microcalcifications in reconstructed breast volume using a 3D approach," in *Medical Imaging: Computer-Aided Diagnosis*, vol. 7624 of *Proceedings of SPIE*, pp. 1–8, March 2010.

[21] S. Bernard, S. Muller, and J. Onativia, "Computer-aided microcalcification detection on digital breast tomosynthesis data: a preliminary evaluation," in *Digital Mammography*, vol. 5116 of *Lecture Notes in Computer Science*, pp. 151–157, 2008.

[22] Y. Zhang, H.-P. Chan, B. Sahiner et al., "A comparative study of limited-angle cone-beam reconstruction methods for breast tomosynthesis," *Medical Physics*, vol. 33, article 3781, 2006.

[23] J.-W. Jeong, S.-H. Chae, S. Lee, E. Y. Chae, H. H. Kim, and Y.-W. Choi, "Simplified false-positive reduction in computer-aided detection scheme of clustered microcalcifications in digital breast tomosynthesis," in *Medical Imaging 2015: Computer-Aided Diagnosis, 941426*, vol. 9414 of *Proceedings of SPIE*, 6 pages, March 2015.

[24] R. K. Samala, H.-P. Chan, Y. Lu, L. Hadjiiski, J. Wei, and M. Helvie, "Comparison of computer-aided detection of clustered microcalcifications in digital mammography and digital breast tomosynthesis," in *Medical Imaging 2015: Computer-Aided Diagnosis, 94140K*, vol. 9414 of *Proceedings of SPIE*, 7 pages, March 2015.

[25] T. Wu, R. H. Moore, E. A. Rafferty, and D. B. Kopans, "A comparison of reconstruction algorithms for breast tomosynthesis," *Medical Physics*, vol. 31, no. 9, pp. 2636–2647, 2004.

[26] X. Cao, K. Ma, R. Lian, and Q. Zhang, "Hardware implementation on the weight calculation of iterative algorithm for CT image reconstruction," *ETRI Journal*, vol. 35, no. 5, pp. 931–934, 2013.

[27] S.-H. Son, N. Simonov, H.-J. Kim, J.-M. Lee, and S.-I. Jeon, "Preclinical prototype development of a microwave tomography system for breast cancer detection," *ETRI Journal*, vol. 32, no. 6, pp. 901–910, 2010.

[28] M. Park, B. G. Chae, H.-E. Kim et al., "Digital holographic display system with large screen based on viewing window movement for 3D video service," *ETRI Journal*, vol. 36, no. 2, pp. 232–241, 2014.

[29] I. A. Feldkamp, L. C. Davis, and J. W. Kress, "Practical cone-beam algorithm," *Journal of the Optical Society of America A*, vol. 1, no. 6, pp. 612–619, 1984.

[30] Insight Software Consortium, *The ITK Software Guide*, 2005, http://www.itk.org.

[31] Y. Sato, C.-F. Westin, A. Bhalerao et al., "Tissue classification based on 3D local intensity structures for volume rendering," *IEEE Transactions on Visualization and Computer Graphics*, vol. 6, no. 2, pp. 160–180, 2000.

[32] L. Antiga, "Generalizing vesselness with respect to dimensionality and shape," *The Insight Journal*, vol. 3, 2007.

[33] A. Huang, H.-M. Liu, C.-W. Lee, C.-Y. Yang, and Y.-M. Tsang, "On concise 3-D simple point characterizations: a marching cubes paradigm," *IEEE Transactions on Medical Imaging*, vol. 28, no. 1, pp. 43–51, 2009.

[34] J. Ge, B. Sahiner, L. M. Hadjiiski et al., "Computer aided detection of clusters of microcalcifications on full field digital mammograms," *Medical Physics*, vol. 33, no. 8, pp. 2975–2988, 2006.

[35] M. A. Helvie, L. Hadjiiski, E. Makariou et al., "Sensitivity of noncommercial computer-aided detection system for mammographic breast cancer detection: a pilot clinical trial," *Radiology*, vol. 231, no. 1, pp. 208–214, 2004.

[36] T. E. Cupples, J. E. Cunningham, and J. C. Reynolds, "Impact of computer-aided detection in a regional screening mammography program," *American Journal of Roentgenology*, vol. 185, no. 4, pp. 944–950, 2005.

[37] M. J. Morton, D. H. Whaley, K. R. Brandt, and K. K. Amrami, "Screening mammograms: interpretation with computer-aided detection—prospective evaluation," *Radiology*, vol. 239, no. 2, pp. 375–383, 2006.

[38] J. J. Fenton, S. H. Taplin, P. A. Carney et al., "Influence of computer-aided detection on performance of screening mammography," *The New England Journal of Medicine*, vol. 356, no. 14, pp. 1399–1409, 2007.

[39] D. Gur, G. S. Abrams, D. M. Chough et al., "Digital breast tomosynthesis: observer performance study," *American Journal of Roentgenology*, vol. 193, no. 2, pp. 586–591, 2009.

[40] S. P. Poplack, T. D. Tosteson, C. A. Kogel, and H. M. Nagy, "Digital breast tomosynthesis: initial experience in 98 women with abnormal digital screening mammography," *American Journal of Roentgenology*, vol. 189, no. 3, pp. 616–623, 2007.

[41] A. P. Smith, E. A. Rafferty, and L. Niklason, "Clinical performance of breast tomosynthesis as a function of radiologist experience level," in *Digital Mammography*, E. A. Krupinski, Ed., vol. 5116 of *Lecture Notes in Computer Science*, pp. 61–66, 2008.

[42] D. Gur, J. H. Sumkin, H. E. Rockette et al., "Changes in breast cancer detection and mammography recall rates after the introduction of a Computer-aided detection system," *Journal of the National Cancer Institute*, vol. 96, no. 3, pp. 185–190, 2004.

[43] J. C. Dean and C. C. Ilvento, "Improved cancer detection using computer-aided detection with diagnostic and screening mammography: prospective study of 104 cancers," *American Journal of Roentgenology*, vol. 187, no. 1, pp. 20–28, 2006.

[44] M. Gromet, "Comparison of computer-aided detection to double reading of screening mammograms: review of 231,221 mammograms," *American Journal of Roentgenology*, vol. 190, no. 4, pp. 854–859, 2008.

[45] R. K. Samala, H.-P. Chan, Y. Lu, L. M. Hadjiiski, J. Wei, and M. A. Helvie, "Digital breast tomosynthesis: computer-aided detection of clustered microcalcifications on planar projection images," *Physics in Medicine and Biology*, vol. 59, no. 23, pp. 7457–7477, 2014.

[46] R. K. Samala, H.-P. Chan, Y. Lu, L. M. Hadjiiski, J. Wei, and M. A. Helvie, "Computer-aided detection system for clustered microcalcifications in digital breast tomosynthesis using joint information from volumetric and planar projection images," *Physics in Medicine and Biology*, vol. 60, no. 21, pp. 8457–8479, 2015.

Hindawi Publishing Corporation
BioMed Research International
Volume 2016, Article ID 5206268, 10 pages
http://dx.doi.org/10.1155/2016/5206268

Research Article

Automatic Extraction of Appendix from Ultrasonography with Self-Organizing Map and Shape-Brightness Pattern Learning

Kwang Baek Kim,[1] Doo Heon Song,[2] and Hyun Jun Park[3]

[1]*Department of Computer Engineering, Silla University, Busan 46958, Republic of Korea*
[2]*Department of Computer Games, Yong-in Songdam College, Yongin 17145, Republic of Korea*
[3]*Department of Computer Engineering, Pusan National University, Busan 46241, Republic of Korea*

Correspondence should be addressed to Kwang Baek Kim; gbkim@silla.ac.kr

Received 3 December 2015; Accepted 2 March 2016

Academic Editor: Yoshito Tsushima

Accurate diagnosis of acute appendicitis is a difficult problem in practice especially when the patient is too young or women in pregnancy. In this paper, we propose a fully automatic appendix extractor from ultrasonography by applying a series of image processing algorithms and an unsupervised neural learning algorithm, self-organizing map. From the suggestions of clinical practitioners, we define four shape patterns of appendix and self-organizing map learns those patterns in pixel clustering phase. In the experiment designed to test the performance for those four frequently found shape patterns, our method is successful in 3 types (1 failure out of 45 cases) but leaves a question for one shape pattern (80% correct).

1. Introduction

Appendicitis, one of the most common surgical abdominal emergences, is an inflammation of the appendix that can be classified into early appendicitis, gangrenous appendicitis, gangrenous appendicitis, chronic appendicitis, and acute appendicitis according to its development stage [1]. Typically, the illness begins with vague midabdominal discomfort followed by nausea, anorexia, and indigestion and within several hours the pain migrates to the right lower quadrant [2]. Examination at this point shows localized tenderness to one-finger palpation and perhaps slight muscular guarding. Rebound or percussion tenderness (the latter provides the same information more humanely) may be elicited in the same area [3].

Often the site of maximum tenderness is located at McBurney's point, at which lies two-thirds along a line from the umbilicus to the anterior superior iliac spine [4]. However, there are various kinds of difficulties in the diagnosis of acute appendicitis especially for high false-positive diagnosis rate in women aged between 20 and 40 [5] and women in pregnancy because the nausea, vomiting, and abdominal pain of appendicitis can also be features of pregnancy and physical examination may not be reliable in them [6].

Recent studies advocate the use of medical imaging to reduce the rate of negative appendectomies [7]. Among available imaging modalities such as ultrasonography (US), computed tomography (CT), and magnetic resonance imaging (MRI), US may be especially useful where there are equivocal clinical signs or an indeterminate diagnostic score. In these situations, US may improve diagnostic accuracy by reducing the number of false negatives and therefore prevent unnecessary surgery [8]. US examination should be the first imaging test performed, particularly among the pediatric and young adult populations [9], who represent the main targets for appendicitis, and in pregnant patients.

Among known sonographic findings of acute appendicitis, a threshold of 6 mm diameter of the appendix under compression is the most accurate US finding for appendicitis [10]. Thus, the critical point, 6 mm of the diameter of the appendix, is a crucial factor in decision making for appendectomy. As a result, the measurement error of 1 mm near the critical point may lead doctors to a serious misdiagnosis [2].

While the reliability of US in diagnosing acute appendicitis is much improved to be matched with that of CT or MRI [6], current naked eye examination of the US has limitations in accurate measurement in cases of unclear delineation of the appendix with thick abdomen and in cases showing ill-defined borders of the appendix by surrounding tissues and its intrinsic operator subjectivity [2].

Thus, there are growing needs for an intelligent decision making tool for more accurate diagnosis by artificial intelligence technology and careful image processing and analyzing algorithms. Unfortunately, there are few tools for the practitioners to use with credibility to date. A preliminary study applies several histogram thresholding methods in detecting appendix [11] but that method is weak when the brightness contrast is not very high and will have potential information loss in edge linking procedure.

Pixel clustering methods [2, 12, 13] are designed to enhance the brightness contrast and form an appendix object from US by using fuzzy binarization [12] or forming object with K-means clustering [13], ART2 neural learning, and fuzzy ART [2] to overcome the subjectivity of US analysis and to extract appendix automatically with high accuracy.

While the recent result [2] demonstrates its superiority in successful extraction rate (high sensitivity) with fuzzy ART over other pixel clustering methods, failed extraction cases suggest that there might be a close relationship between the shape of the appendix in the image and the brightness distribution of the surrounding environments. Thus, in this paper, we propose a more efficient method to extract appendix area correctly by using self-organizing map (SOM) algorithm [14] in the critical pixel clustering process instead of fuzzy ART. SOM shares its structural stability with fuzzy ART as it is relatively not sensitive to the setting of vigilance parameter but it is also a nonlinear, ordered, smooth mapping of high dimensional data onto the regular, low-dimensional array [15]. SOM is an unsupervised learning neural network tool used in many medical image analysis applications successfully [16, 17]. Another advantage of SOM in object clustering over fuzzy ART in this medical application is that SOM can learn more coherent clusters than fuzzy ART in pixel clustering such that it is less sensitive to the shape of the appendix with respect to the brightness distribution of its surroundings. Medical experts suggest that there can be four distinctive shape-brightness types in consideration and those types cover most clinical appendicitis cases in practice. Thus, our method is expected to show more stable performance than previous attempts for various shape patterns of appendices in the US images. Our experiment is designed with respect to such clinical observations in this paper.

Knowing that the appendix is located at the lower organ area below the bottom fascia line, we conduct a series of image processing techniques to find the fascia line correctly and limit the region of interest to form the appendix object accurately. Figure 1 demonstrates the overall process of our method.

The first step of our automatic extraction methodology is to enhance the brightness contrast by ends-in search stretching [18]. Knowing that the appendix is below fascia area, our method tries to find and remove the fascia area to limit the region of interest. In this part, the bottom fascia lines are carefully treated with cubic spline interpolation [19] such that the lines are correctly connected. The appendix area is then extracted from that image by applying SOM algorithm to form the target object and then the boundary lines are refined by 8-directional contour tracking again.

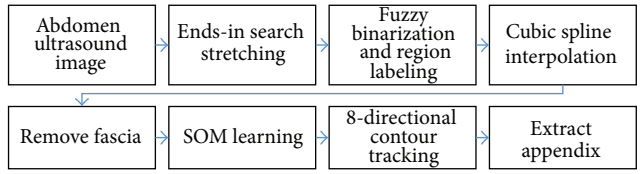

Figure 1: Process of appendix extraction.

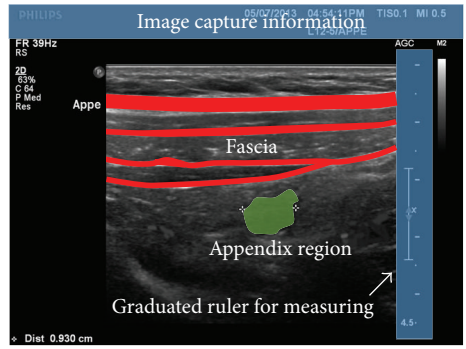

Figure 2: Typical input ultrasound image.

2. Removing Fascia Area after Stretching

As shown in Figure 2, abdomen ultrasound image consists of image filming information on the above and measurement information on the right and the abdomen image at the center. In the abdomen image, there are fascia area including muscles and appendix area below the fascia. Appendix has the shape of a circle or flat oval.

Usually the size of appendix is between 6 mm and 12 mm. After ends-in search stretching for enhancing the brightness contrast and removing unnecessary measuring ruler part from input US as we did in [12], we set up the fuzzy membership function for binarization for our region of interest (ROI). Unlike [12], in this paper, we apply trapezoidal membership function as shown in Figure 3, where I_{Max} and I_{Min} denote the brightest and the darkest pixel of the ROI, respectively, and let T be the average of I_{Max} and I_{Min}. Then, (1) defines the upper bound of trapezoid that has membership degree 1 as interval $[I_s, I_e]$

$$I_s = \frac{T}{3}, \qquad I_e = 2I_s. \tag{1}$$

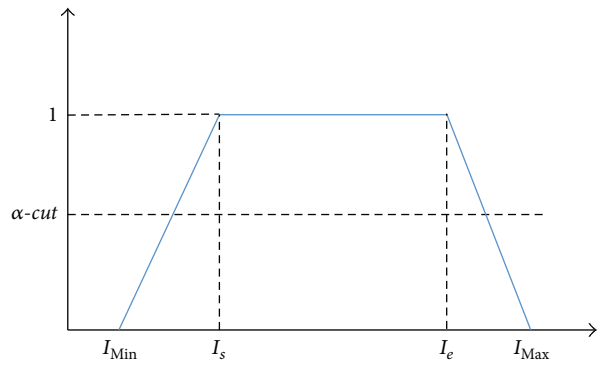

Figure 3: Membership function for fuzzy binarization.

The whole membership degree over interval $[I_{\text{Min}}, I_s, I_e, I_{\text{Max}}]$ is defined as

$$\begin{aligned} &\text{if } \left(I_{\text{Min}} < I \le I_s\right) \text{ then } \frac{I - I_s}{I_s - I_{\text{Min}}} + 1 \\ &\text{if } \left(I_s < I \le I_e\right) \text{ then } \mu(I) = 1.0 \\ &\text{if } \left(I_e < I \le I_{\text{Max}}\right) \text{ then } \mu(I) = \frac{I - I_e}{I_{\text{Max}} - I_e} + 1. \end{aligned} \tag{2}$$

α-cut is the median of the interval (0.5) in this paper since there is no specific preference.

The effect of fuzzy binarization is shown in Figure 4.

From the result of fuzzy binarization, we apply 8-directional contour tracking algorithm [18] to extract fascia boundary lines. Fascia has the shape of a horizontally long thin object; thus we extract such object that is long enough (longer than 1/3 of the width of the ROI in this paper) as fascia. Figure 5 shows results of 8-directional contour tracking.

Unfortunately, the binarized noiseless image may have disconnected fascia area due to the brightness difference of that area. In order to reconnect them, cubic spline interpolation [19] is applied. Figure 6 demonstrates the effect of cubic spline interpolation.

Then we remove such fascia area so that the refined ROI is focused on the extraction of appendix.

3. Extracting Appendix with Self-Organizing Map

SOM algorithm is a time-efficient unsupervised learning algorithm that maps complex multi-dimensional data onto a 2-dimensional space without predefined number of clusters or correlation between data. Like fuzzy ART, SOM also is not sensitive to the setting of vigilance parameter but the arrangement of nodes (neurons) may concern its performance. The usual arrangement of nodes is two-dimensional regular spacing in a hexagonal or rectangular grid as shown in Figure 7 and we choose hexagonal arrangement in this paper.

Since the shape of our target object, appendix, has oval shape, it is more natural to use hexagonal arrangement than rectangular ones. In this quantification process using SOM, we let our SOM learn sufficiently many times in repetition. Algorithm 1 summarizes our adoption of SOM in this paper.

Step 1: Initialize weights
  $w \leftarrow$ random value
Step 2: Set topological neighborhood and learning rate
  $\gamma \leftarrow$ integer
  $\alpha \leftarrow$ small number $(0 < \alpha < 1)$
Step 3: While stop condition is not satisfied,
  do Steps 4–8
  Step 4: For each input x
    do Steps 5–8
    Step 5: Compute distance
      $D(j) = \sum_i (w_{ji} - x_i)^2$
    Step 6: Find winner neuron y_j
    Step 7: Update weights within radius
      $w_{ji}^{k+1} = w_{ji}^k + \alpha \left[x_i - w_{ji}^k\right]$
    Step 8: Reduce learning rate and radius
    Step 9: Test stop condition

Algorithm 1: SOM learning algorithm.

The effect of quantification by SOM learning is as shown in Figure 8.

The last part of the appendix extraction process is again 8-directional contour tracking [18]. Figure 9 shows an example of appendix extraction and Figure 9(c) represents a snapshot of implemented software.

4. Experiment and Analysis

The system is implemented in Visual Studio 2010 C# with Intel(R) Core(TM) i7-2600 CPU @ 3.40 GHz and 4 GB RAM PC. Sixty images containing appendicitis supplied by Busan Paik Hospital and Busan National University Medical Center, Korea, are used in this experiment. The actual system gives some characteristic features of extracted appendix as shown in Figure 9(c).

Medical experts in this field suggest that there are a few shape-brightness pattern types of appendices found in clinical practice. Four patterns shown in Figure 10 are what they observe most frequently. Appendix in type A represents an oval appendix whose surroundings are brighter than

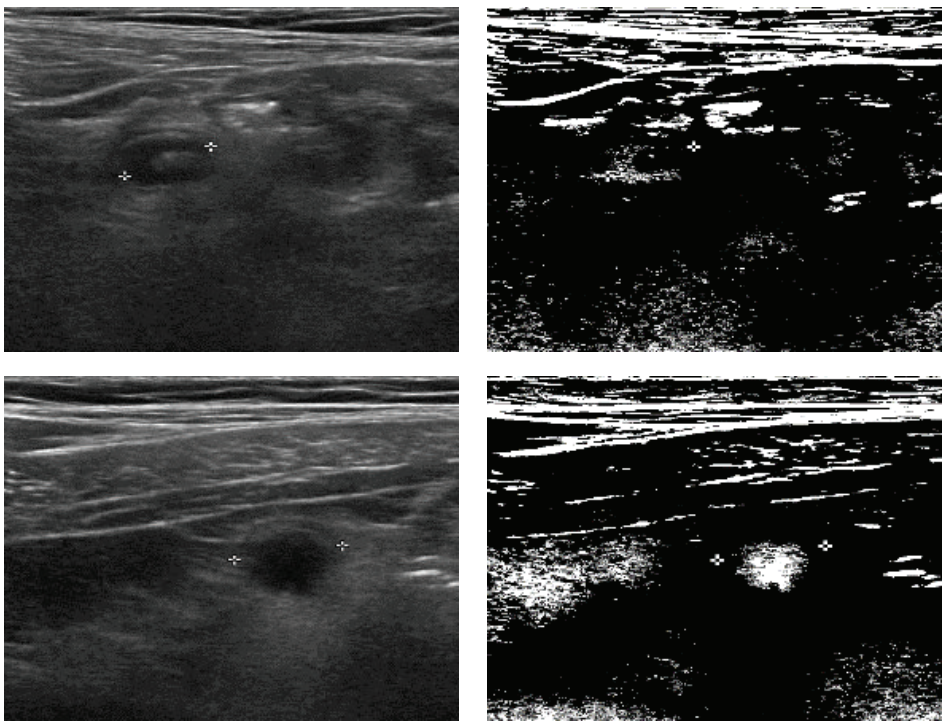

(a) Input image (ROI) (b) Fuzzy-binarized

Figure 4: Effect of fuzzy binarization.

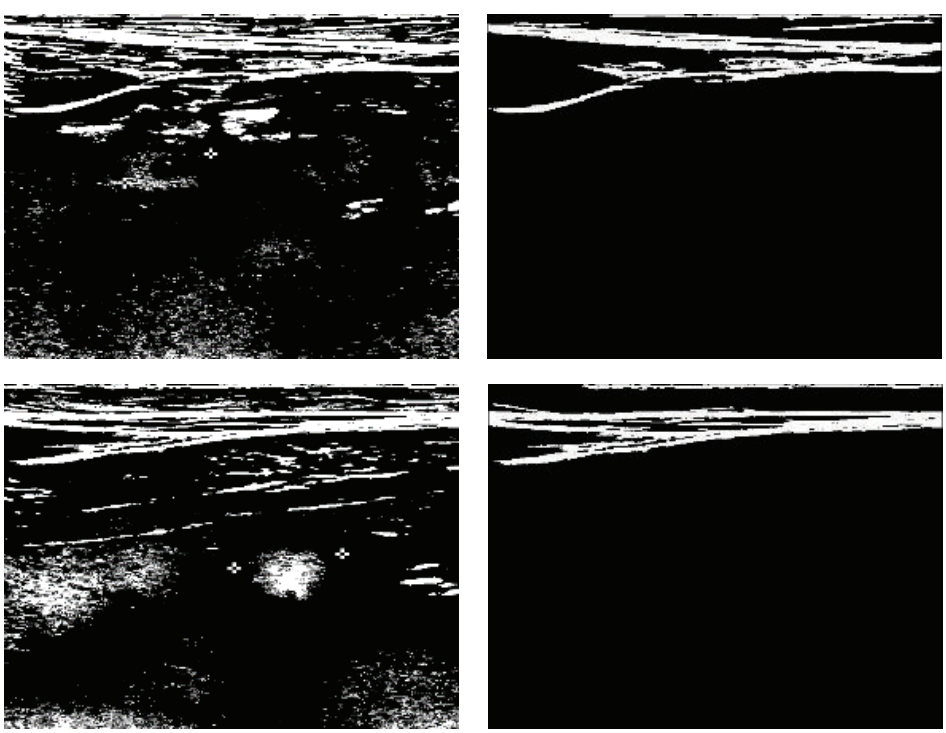

(a) Input (b) Fascia extracted

Figure 5: Extracting fascia lines with contour tracking.

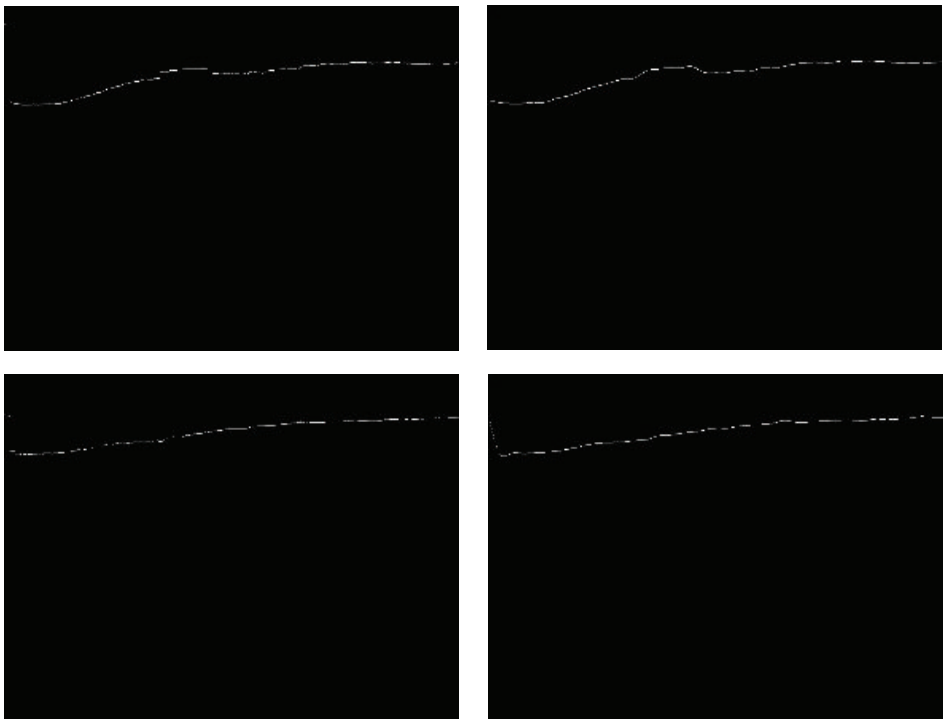

(a) Fascia after tracking (b) Fascia after cubic spline

Figure 6: Extraction of fascia boundary line.

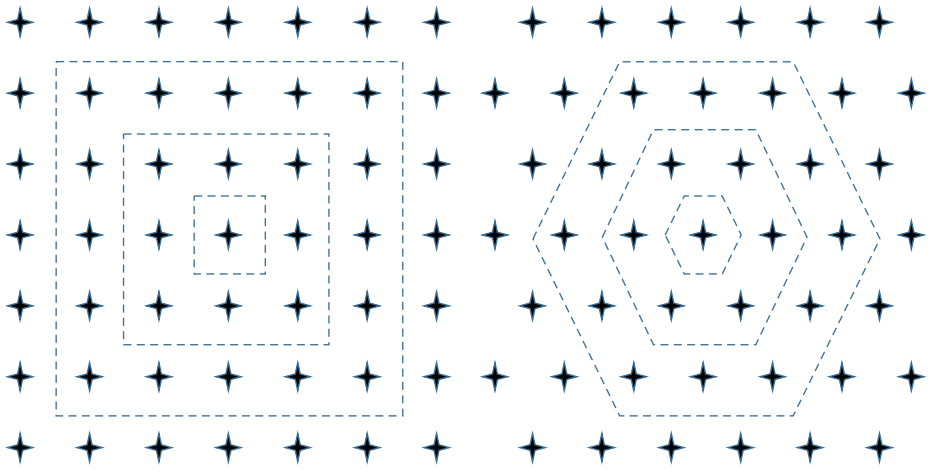

(a) Rectangular type (b) Hexagonal type

Figure 7: Node arrangement for SOM learning.

the appendix area. Type B represents a hooked shape of appendix. Type C represents also an oval shape appendix but the brightness of the appendix is much lower than the surroundings. Type D, which is the hardest to extract in this experiment, represents a long oval shape appendix whose brightness contrast is very low compared with surroundings. For type D, thus, the shape is more important than the brightness contrast in naked eye inspection but the automatic procedure will suffer the most.

In experiment, we arrange 15 DICOM US images for each type. Figure 11 demonstrates the successful and failed extraction cases for each pattern type.

Apparently, type C is the easiest and type D is the hardest for both human expert and the software. Table 1 summarizes

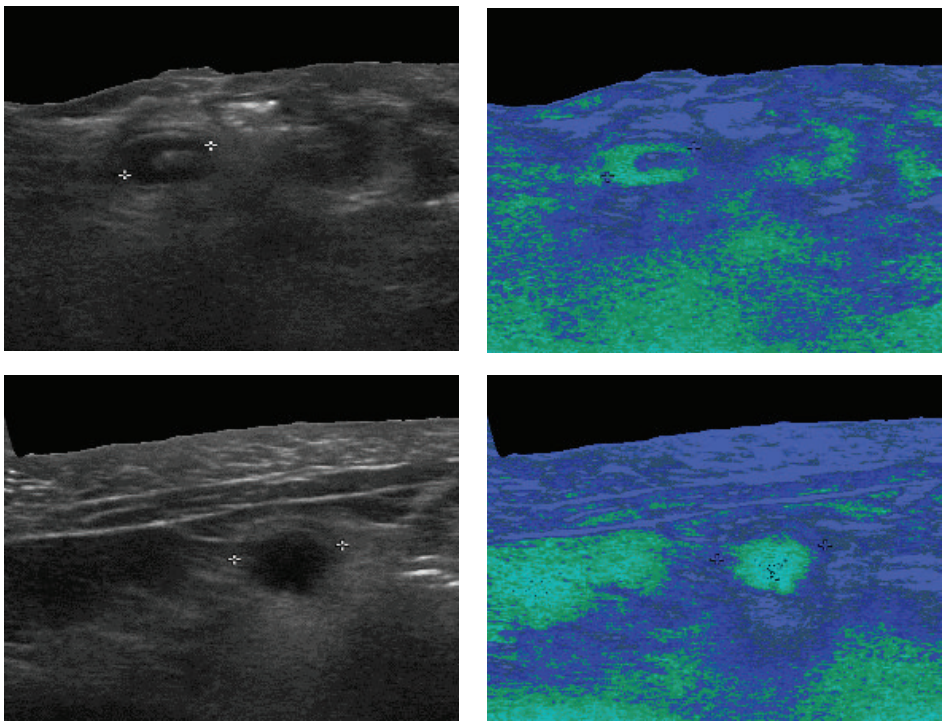

(a) Below fascia ROI (b) Quantized by SOM

Figure 8: The effect of quantization by SOM.

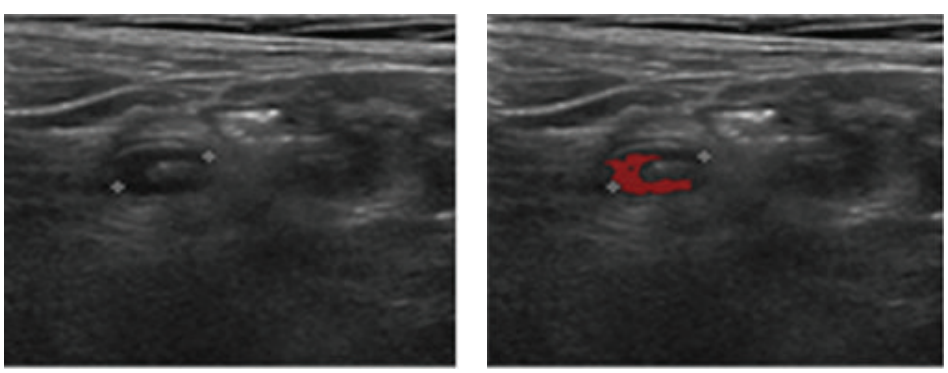

(a) Input image (b) Appendix extracted

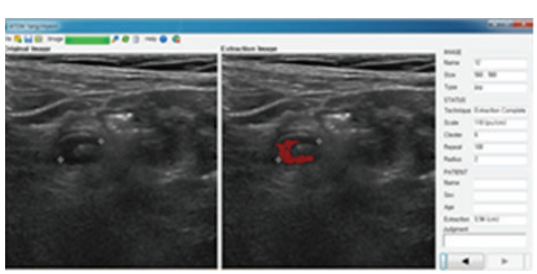

(c) Snapshot of the implemented software

Figure 9: Automatic extraction of appendix: example.

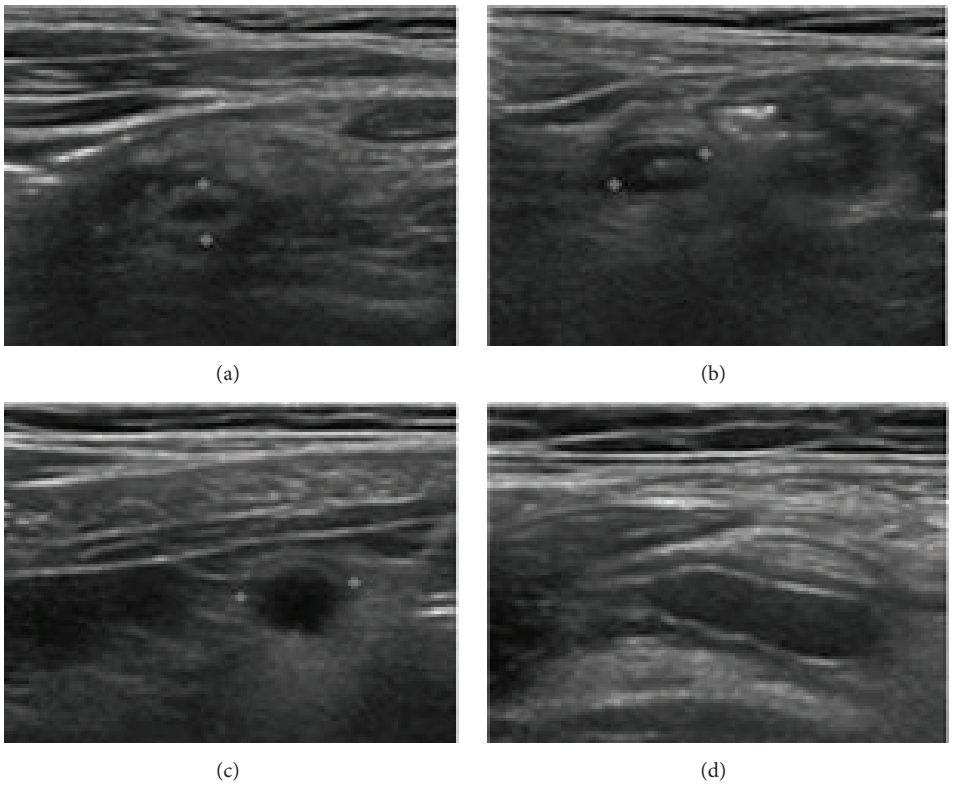

(a) (b) (c) (d)

Figure 10: Shape-brightness patterns of appendices.

Table 1: Appendix extraction results.

Type	Previous [2]	Ext. rate	Proposed	Ext. rate
A	13	86.7%	15	100.0%
B	12	80.0%	14	93.3%
C	15	100.0%	15	100.0%
D	9	60.0%	12	80.0%
Total	49	81.7%	56	93.3%

the experimental result of our proposed algorithm comparing with previous fuzzy ART approach [2].

The success and failure decision in this experiment is made by the agreement of multiple medical doctors. In our experiment, there is no true negative input image; thus the specificity is the extraction rate (ext. rate) in Table 1.

As one can see from Table 1, type C is easy for both algorithms but, in other types, the proposed SOM based learning improves the specificity compared with that of fuzzy ART. The result supports the observation that although fuzzy ART is also a method that is not sensitive to the vigilance parameter settings, low brightness contrast would limit the power of ART learning in clustering phase. In that sense, we confirm that the SOM learning is more stable in clustering. Figure 12 demonstrates the difference between previous approach [2] and proposed method in quantization (upper image) and the extraction result (lower image).

5. Conclusion

In this paper, we propose a method to extract appendix automatically by using a series of image processing algorithms and self-organizing map that learns typical shape patterns of appendix from US. Accurate extraction of appendix area from such appendicitis cases could be critical when the patient is a woman in pregnancy or a young child when that is found as acute appendicitis. Developing such software that extracts target appendix automatically with high accuracy is much needed to avoid operator subjectivity and to sustain high reliability.

The proposed software adopts SOM learning such that it learns the shape patterns and shows stable performance in extracting target appendix accurately in most cases through carefully designed experiment. Extracted appendix results were shown to multiple medical experts and it is regarded as correct extraction when two or more human experts agree that the output from the software is sufficiently accurate. In that regard, our proposed software correctly extracted target appendix of various patterns in 56 cases out of 60 given cases (93.35%) and is completely successful in two out of four types of shape patterns. Such performance is a good improvement from our previous fuzzy ART based methodology. However, the shape type D that has very long oval shape with weak brightness contrast from surroundings still has room for improvement as being only successful in 80% of the given cases.

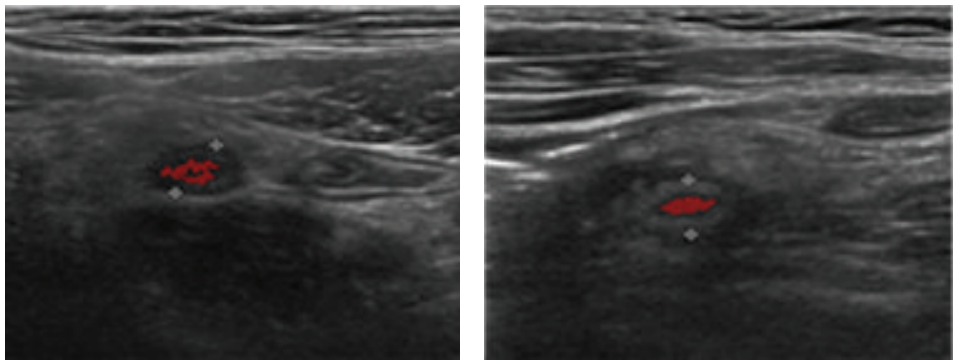

(a) Type A, both successes

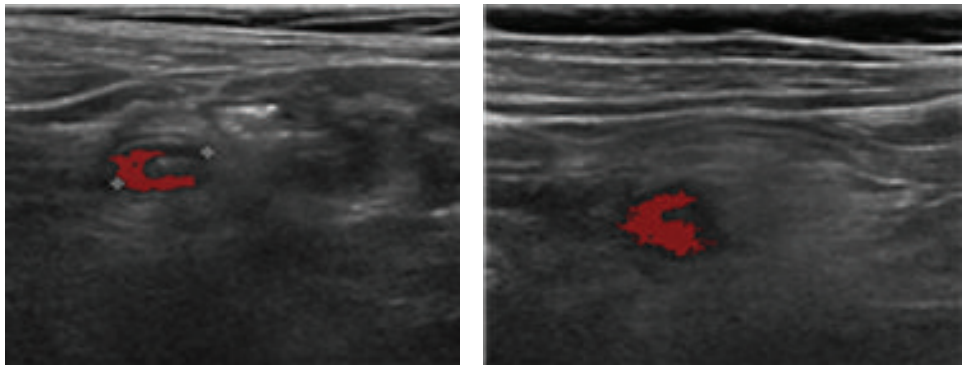

(b) Type B, both successes

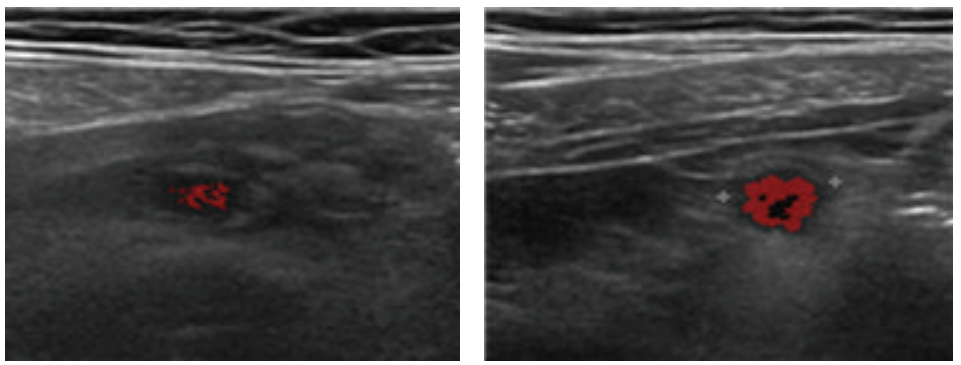

(c) Type C, both successes

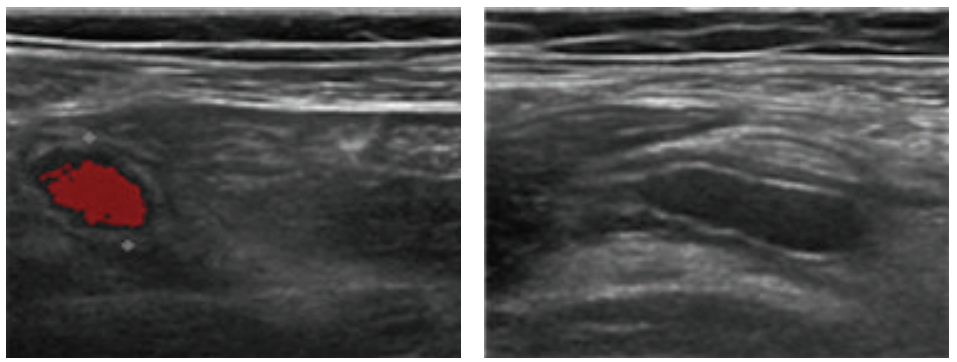

(d) Type D, success and failure

Figure 11: Appendices extractions with respect to the shape patterns.

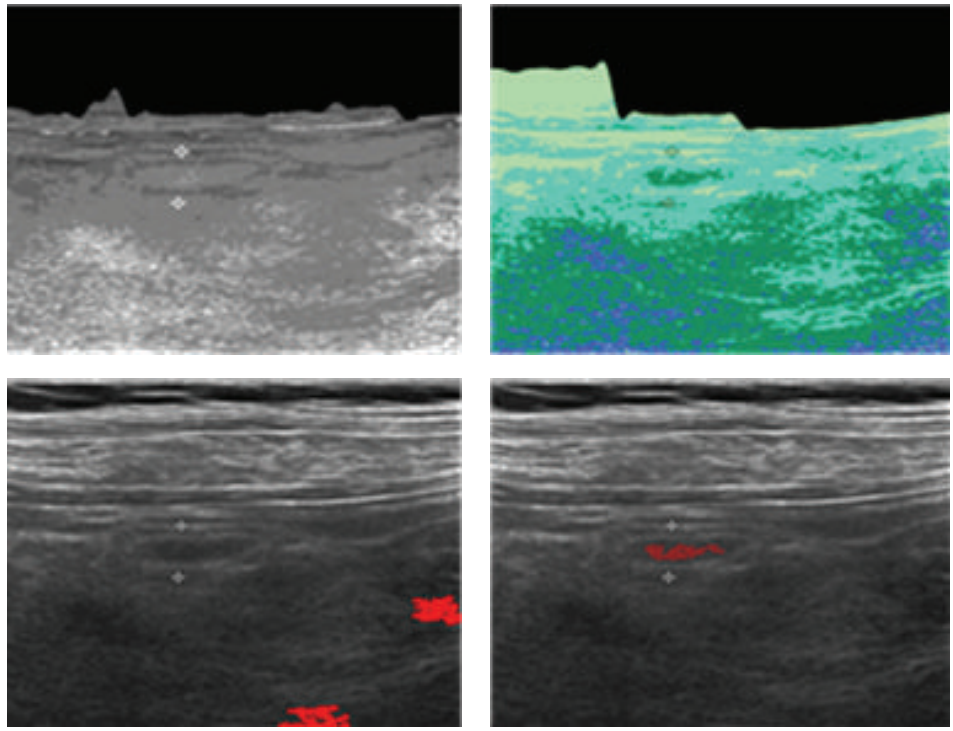

(a) Previous [2] (b) Proposed

Figure 12: Direct comparison of appendices extraction.

Competing Interests

The authors declare that they have no competing interests.

References

[1] F. W. Kremkau, *Diagnostic Ultrasound: Principles and Instruments*, WB Saunders Company, London, UK, 2001.

[2] K. B. Kim, H. J. Park, D. H. Song, and S.-S. Han, "Developing an intelligent automatic appendix extraction method from ultrasonography based on fuzzy ART and image processing," *Computational and Mathematical Methods in Medicine*, vol. 2015, Article ID 389057, 10 pages, 2015.

[3] D. Longo, A. Fauci, D. Kasper, and S. Hauser, *Harrison's Principles of Internal Medicine*, McGraw-Hill, New York, NY, USA, 18th edition, 2011.

[4] C. A. Grover and G. Sternbach, "Charles McBurney: McBurney's point," *The Journal of Emergency Medicine*, vol. 42, no. 5, pp. 578–581, 2012.

[5] G. M. Doherty, *CURRENT Diagnosis & Treatment: Surgery*, McGraw-Hill, New York, NY, USA, 13th edition, 2010.

[6] G. M. Israel, N. Malguria, S. McCarthy, J. Copel, and J. Weinreb, "MRI vs. ultrasound for suspected appendicitis during pregnancy," *Journal of Magnetic Resonance Imaging*, vol. 28, no. 2, pp. 428–433, 2008.

[7] J. R. L. Wild, N. Abdul, J. E. Ritchie, B. Rud, S. Freels, and R. L. Nelson, "Ultrasonography for diagnosis of acute appendicitis," *Cochrane Database of Systematic Reviews*, no. 2, Article ID CD010402, 2013.

[8] K. M. Jang, K. Lee, M.-J. Kim et al., "What is the complementary role of ultrasound evaluation in the diagnosis of acute appendicitis after CT?" *European Journal of Radiology*, vol. 74, no. 1, pp. 71–76, 2010.

[9] N. H. Park, H. E. Oh, H. J. Park, and J. Y. Park, "Ultrasonography of normal and abnormal appendix in children," *World Journal of Radiology*, vol. 3, no. 4, pp. 85–91, 2011.

[10] N. Kessler, C. Cyteval, B. Gailix et al., "Appendicitis: evaluation of sensitivity, specificity, and predictive values of US, Doppler US, and laboratory findings," *Radiology*, vol. 230, no. 2, pp. 472–478, 2004.

[11] M. Wider, Y. M. Myint, and E. Supriyanto, "Comparison of histogram thresholding methods for ultrasound appendix image extraction," *International Journal of Computers*, vol. 5, no. 11, pp. 542–549, 2011.

[12] S. I. Park and K. B. Kim, "Extraction of appendix from ultrasonographic images with fuzzy binarization technique," *International Journal of Bio-Science and Bio-Technology*, vol. 5, no. 4, pp. 139–147, 2013.

[13] S. I. Park, H. J. Park, and K. B. Kim, "Appendix analysis from ultrasonography with cubic spline interpolation and K-means clustering," *International Journal of Bio-Science and Bio-Technology*, vol. 7, no. 1, pp. 1–10, 2015.

[14] J. A. Kangas, T. K. Kohonen, and J. T. Laaksonen, "Variants of self-organizing maps," *IEEE Transactions on Neural Networks*, vol. 1, no. 1, pp. 93–99, 1990.

[15] J. Vesanto and E. Alhoniemi, "Clustering of the self-organizing map," *IEEE Transactions on Neural Networks*, vol. 11, no. 3, pp. 586–600, 2000.

[16] K.-B. Kim, S. Kim, and G.-H. Kim, "Vector quantizer of medical image using wavelet transform and enhanced SOM algorithm,"

Neural Computing & Applications, vol. 15, no. 3-4, pp. 245–251, 2006.

[17] P.-L. Chang and W.-G. Teng, "Exploiting the self-organizing map for medical image segmentation," in *Proceedings of the 20th IEEE International Symposium on Computer-Based Medical Systems (CBMS '07)*, pp. 281–286, Maribor, Slovenia, June 2007.

[18] R. C. Gonzalez and R. E. Woods, *Digital Image Processing*, Prentice-Hall, Upper Saddle River, NJ, USA, 2nd edition, 2002.

[19] A. S. V. R. Kanth and Y. N. Reddy, "Cubic spline for a class of singular two-point boundary value problems," *Applied Mathematics and Computation*, vol. 170, no. 2, pp. 733–740, 2005.

Hindawi Publishing Corporation
BioMed Research International
Volume 2016, Article ID 3067123, 8 pages
http://dx.doi.org/10.1155/2016/3067123

Research Article

Comparison of Imaging Characteristics of ^{124}I PET for Determination of Optimal Energy Window on the Siemens Inveon PET

A Ram Yu,[1] Hee-Joung Kim,[2] Sang Moo Lim,[3] and Jin Su Kim[3,4,5]

[1]*Laboratory Animal Center, OSONG Medical Innovation Foundation, Osong, Chungbuk 28160, Republic of Korea*
[2]*Department of Radiological Science, College of Health Science, Yonsei University, Wonju 26493, Republic of Korea*
[3]*Molecular Imaging Research Center, Korea Institute of Radiological and Medical Sciences, Seoul 01812, Republic of Korea*
[4]*Korea Drug Development Platform Using Radio-Isotope (KDePRI), Seoul 01812, Republic of Korea*
[5]*Radiological and Medico-Oncological Sciences, University of Science and Technology (UST), Seoul 01812, Republic of Korea*

Correspondence should be addressed to Jin Su Kim; jinsukim601@gmail.com

Received 3 December 2015; Revised 4 February 2016; Accepted 7 February 2016

Academic Editor: Guang Jia

Purpose. ^{124}I has a half-life of 4.2 days, which makes it suitable for imaging over several days over its uptake and washout phases. However, it has a low positron branching ratio (23%), because of prompt gamma coincidence due to high-energy γ-photons (602 to 1,691 keV), which are emitted in cascade with positrons. *Methods.* In this study, we investigated the optimal PET energy window for ^{124}I PET based on image characteristics of reconstructed PET. Image characteristics such as nonuniformities, recovery coefficients (RCs), and the spillover ratios (SORs) of ^{124}I were measured as described in NEMA NU 4-2008 standards. *Results.* The maximum and minimum prompt gamma coincidence fraction (PGF) were 33% and 2% in 350~800 and 400~590 keV, respectively. The difference between best and worst uniformity in the various energy windows was less than 1%. The lowest SORs of ^{124}I were obtained at 350~750 keV in nonradioactive water compartment. *Conclusion.* Optimal energy window should be determined based on image characteristics. Our developed correction method would be useful for the correction of high-energy prompt gamma photon in ^{124}I PET. In terms of the image quality of ^{124}I PET, our findings indicate that an energy window of 350~750 keV would be optimal.

1. Introduction

PET is a widely used noninvasive diagnostic modality for imaging functional and biochemical phenomena *in vivo*. The imaging of glucose metabolism using ^{18}F-FDG is a routinely used PET imaging technique. The imaging of the hypoxia, perfusion, and proliferation is also possible using commonly used PET radionuclides, such as ^{11}C, ^{13}N, ^{15}O, and ^{18}F [1, 2]. Recently, the use of ^{124}I has increased, since it is useful for pretherapeutic PET dosimetry and for studying monoclonal antibody kinetics to predict ^{131}I activity distributions [3–5]. ^{124}I could be used to investigate lengthy biological processes due to its long half-life (4.2 days), which makes it suitable for imaging over several days during the biological uptake and washout phases of radiolabeled antibodies [6, 7]. Characteristics of ^{124}I were compared with ^{18}F in Table 1. ^{124}I has a low positron branching ratio (23%). High-energy γ-photons (602–1,691 keV) are emitted in a cascade with positrons, and a low positron branching ratio leads to decrease sensitivity. If high-energy γ-photons are recorded within the energy window, a prompt gamma coincidence, due to high-energy γ-photons, generates false coincidence. In addition, prompt gamma coincidence contributed to the detection of spurious background activity [8, 9].

Furthermore, high-energy gammas are emitted in cascade with positrons. These lead to spurious coincidences and reduction of image quality [10, 11]. Although several research groups have studied the quantification and correction of prompt gamma coincidence for ^{124}I PET [9, 10, 12–14], the quantification of ^{124}I PET remains challenging. Because prompt gamma coincidence due to high-energy γ-photons was emitted in ^{124}I PET, optimal PET acquisition settings

Table 1: Characteristics of ^{124}I in comparison with ^{18}F.

	^{124}I	^{18}F
Half-life	4.18 day	109.74 min
Max. positron energy (keV)	2,138	635
Branching ratio (%)	23	97
Gamma energy (keV)	511 (23%) 602 (60%) 722 (10%) 1,691 (11%)	511 (97%)

were required to improve image quality. Other papers were studied count based evaluation and did not consider the prompt gamma coincidence correction [8, 10, 15]. So, they suggest use of relatively narrow energy window in order to exclude high-energy gamma prompt photons. Although the NECR was used to assess the image quality of PET, recently there was a report that SNR of reconstructed image cannot be predicted by the NECR especially on the PET image using iterative reconstruction method [16, 17]. Because raw data may not follow a Poisson distribution due to dead time, thus, the use of the NECR may be limited [16, 18].

In contrast, we proposed prompt gamma coincidence correction method in a previous study [19]; we could successfully correct the prompt gamma photon in ^{124}I. Our developed method was applied to reconstructed image not count based NECR metric. Therefore, optimal energy window in ^{124}I PET should be determined on reconstructed image. In this study, we assessed the image quality of reconstructed PET to determine the optimal energy window in ^{124}I PET with various parameters on Siemens Inveon PET (Siemens Medical Solutions, USA) [20–22]. Image qualities such as nonuniformity, recovery coefficient, and spillover ratio were assessed according to NEMA NU 4-2008.

2. Materials and Methods

2.1. System Description. The Inveon system was preclinical system with high sensitivity and high resolution. The detector consists of 64 detector blocks with a 16.1 cm of ring diameter and 12.7 cm of axial FOV. The crystal size is 1.51 × 1.51 × 10 mm^3 and the crystal pitch is 1.59 mm. The packing fraction is 92% [15, 20–22].

2.2. Correction of Prompt Gamma Coincidence of ^{124}I. Recently, we developed the method for determination of prompt gamma coincidence fraction of ^{124}I [19]. Briefly, the process of measurement of sensitivity and prompt gamma coincidence fraction were described as follows; to measure the prompt gamma coincidence fraction, we measured the sensitivities of ^{124}I and ^{18}F using NEMA NU 2 like sensitivity phantom (length: 12.7 cm) [23]. Source activities were 506 kBq for ^{124}I and 673 kBq for ^{18}F, respectively. Sensitivities were measured at the condition below 1% dead time loss. PET data was collected for 5 min using 1~5 aluminum sleeves of 1 mm thickness and different diameters. Intrinsic and background activities were measured for 1 hr and subtracted from total prompt counts within every energy window set. Branching ratio corrected sensitivities of ^{124}I and ^{18}F were also calculated. Sensitivities and prompt gamma coincidence fraction were calculated with various energy windows. Prompt gamma coincidence fractions (PGFs) were predicted using the following equation:

$$\text{PGF} = \frac{\left(\text{branching ratio corrected value of } ^{124}\text{I sensitivity} - \text{branching ratio corrected value of } ^{18}\text{F sensitivity}\right)}{\text{branching ratio corrected value of } ^{124}\text{I sensitivity}}. \quad (1)$$

We determined prompt gamma coincidence fraction at various energy windows. The lower level discriminator (LLD) was fixed at 350 keV to minimize the effect of intrinsic radioactivity due to the presence of ^{176}Lu [24, 25]. Because adjustment of the upper level discriminator (ULD) was influential for the assessment of prompt gamma coincidence due to the high-energy single γ-photons of ^{124}I (602 to 1,691 keV), the ULD was increased in steps of 25 or 50 keV from 550 keV to 800 keV. Energy window of 400~590 keV was also included to compare the result with previous study [8]. To perform the prompt gamma coincidence correction [19], we derived the sinogram for the scatter component and then multiplied by a PGF. The prompt gamma coincidence corrected emission sinogram was then determined as follows:

$$\begin{aligned}&\text{Prompt gamma coincidence-corrected emission sinogram}\\ &= \text{emission sinogram} - \left(\text{scatter sinogram} \times \text{PGF}\right).\end{aligned} \quad (2)$$

2.3. Image Quality. NECR is the metric based on measured PET count rate. Therefore, we assessed image quality on reconstructed ^{124}I PET image to determine the optimal ^{124}I PET energy window. Image qualities such as nonuniformity, recovery coefficient (RC), and spillover ratio (SOR) were measured according to NEMA NU 4-2008. The NEMA NU 4-2008 image quality phantom (length 50 mm, diameter 30 mm, and volume 20.7 mL) is consisted of three parts in cylindrical. Space of the center is uniform region (length 15 mm, diameter 30 mm) and this part means actual signal to noise of imaging equipment. The upper part of the uniform region is cold region that has two empty spaces (length 15 mm, inner diameter 8 mm, and outer diameter 10 mm). One space fills air and the other space fills nonradioactive water. Although both cylinders are nonradioactive, scattered photons, nonzero positron range, and random or other effects may cause the reconstructed images to display activity in these compartments. So measurement of spillover ratio from

cold region displays accuracy of scatter correction. Bottom of the cylinder (length 20 mm, diameter 30 mm) has five fillable rods with diameters of 1, 2, 3, 4, and 5 mm and center of each rod is 7 mm from the cylinder axis. This part serves recovery coefficient.

According to the NEMA NU 4-2008 guideline, 20 min of scan time and 3.7 MBq of ^{18}F were needed. Because ^{124}I has a lower positron branching ratio compared to that of ^{18}F, longer scan time and higher activity of ^{124}I were needed to avoid the bias due to the difference of positron number when image quality was compared. In the study of Disselhorst and coworkers, a corrected scan time of 4700 s and activity of 14.4 MBq were used for ^{124}I PET, because equal positron numbers were needed for proper comparison as the branching ratios of ^{124}I and ^{18}F were different [11]. In our present study, we also used 4700 s of PET scan time and 14.4 MBq of ^{124}I to maintain the same level of positron numbers when image characteristics of ^{124}I were investigated. The image quality phantom was placed in the center of the scanner FOV and PET data was acquired at various energy windows settings to determine the optimal PET energy window. The lower level discriminator was fixed at 350 keV, and the higher level discriminator was increased in steps of 25 or 50 keV steps from 550 keV to 800 keV. The timing window was set to 3.432 nsec. 3D list mode PET data were sorted into sinogram using FORE and reconstructed using 2D FBP with a ramp filter. The pixel size of reconstructed images was $0.776 \times 0.776\,\text{mm}^2$. Attenuation correction was performed using ^{57}Co point source [26]. Normalization, scatter correction (SC), prompt gamma coincidence correction, and dead time correction were also applied.

2.3.1. Nonuniformity. To measure nonuniformity, a volume of interest (VOI) (length 10 mm, diameter 22.5 mm) was drawn at the center of the uniform region. The values of the means and standard deviations (SD) in this VOI were measured. Nonuniformity (NU) was expressed as percentage SD (%SD: standard deviation divided by mean multiplied by 100%).

2.3.2. Recovery Coefficient. The five radioactive source fillable rods (diameters 1, 2, 3, 4, and 5 mm) in the bottom of the cylinder (length 20 mm, diameter 30 mm) were used to determine RCs. To determine the RCs, circular ROI of twice the rod diameter was drawn around each rod. Maximum values and SDs were measured for each profile. RC was defined as the ratio between the measured maximum values in rods and the mean value in the uniform area. %SD of RCs were calculated using the following equation:

$$\%\text{SD}_{\text{RC}} = 100 \times \sqrt{\left(\frac{\text{SD}_{\text{line profile}}}{\text{Mean}_{\text{line profile}}}\right)^2 + \left(\frac{\text{SD}_{\text{uniform region}}}{\text{Mean}_{\text{uniform region}}}\right)^2}. \quad (3)$$

2.3.3. Spillover Ratio. The upper part of the uniform region was a cold region consisting of two empty spaces (length 15 mm, inner diameter 8 mm, and outer diameter 10 mm). One empty space was for air and the other space was for nonradioactive water. To calculate the SOR, two cylindrical VOIs (length 7.5 mm, diameter 4 mm) were drawn in the air and nonradioactive water filled compartments. The half size of the water or nonradioactive compartments was used to minimize the effect of the longer positron range of ^{124}I in ROI analysis [11]. SOR was defined as the ratio between the mean value of a cold cylinder and the mean value of the uniform area. The effect of prompt gamma coincidence due to high-energy γ-photons (602 keV to 1,691 keV) emitted from ^{124}I was assessed in terms of SOR for different PET acquisition energy windows.

2.4. Noise Equivalent Count Rate. In another previous study, an optimal energy window for ^{124}I small animal imaging was determined using NECR [8]. In our present study, we also calculated NECRs using Monte Carlo simulation [27] to compare the result of image quality assessment on reconstructed image.

Inveon consists of 16 modules providing 80 full crystal rings with an axial length of 127 mm and a ring diameter of 161 mm. Size and pitch of crystal are $1.51 \times 1.51 \times 10\,\text{mm}^3$ and 1.59 mm. Energy resolution was 14.5% and coincidence window was set to 3.432 ns [20]. NEMA NU 4 mouse phantom (diameter = 2.5 cm, length = 7 cm) was placed at the center. ^{124}I source simulated all the physical process during emission and interaction of positrons. NECR was then calculated as the following equation:

$$\text{NECR} = \frac{T^2}{T + S + 2fR + f\text{PGF}}, \quad (4)$$

where T, S, R, PGF, and f are prompt gamma coincidence corrected true, scatter, random, and prompt gamma coincidence fraction and average fraction of the projection taken up by the object. Simulation for NECR was repeated under various energy windows. The lower level discriminator was fixed at 350 keV, and the higher level energy discriminator was increased in steps of 25 keV from 550 keV to 800 keV. Energy window of 400~590 keV was also included. Source activity was 1 MBq to 50 MBq for measurement of NECR.

3. Results

3.1. Prompt Gamma Coincidence Fraction of ^{124}I. The branching ratio uncorrected ^{124}I sensitivities in representative energy window were 1.57, 1.78, 2.04, 2.26, and 1.31% within the energy window of 350~550, 350~600, 350~650, 350~750, and 400~590 keV, respectively. The branching ratio uncorrected ^{18}F sensitivities were 6.44, 6.51, 6.54, 6.61, and 5.43% within the energy window of 350~550, 350~600, 350~650, 350~750, and 400~590 keV, respectively. The branching ratio corrected sensitivities were 9.83% for ^{124}I and 6.81% for ^{18}F within an energy window of 350~750 keV and timing window of 3.432 ns. The difference between "branching ratio corrected" and "branching ratio uncorrected" sensitivities was the portion of prompt gamma coincidence fraction. The PGF was 31% at 350~750 keV. The PGFs were presented in Table 2.

Table 2: Prompt gamma coincidence fraction (PGF) at different energy window settings.

Energy window (keV)	PGF
350~550	0.03
350~600	0.13
350~625	0.19
350~650	0.24
350~675	0.26
350~700	0.27
350~725	0.29
350~750	0.31
350~775	0.32
350~800	0.33
400~590	0.02

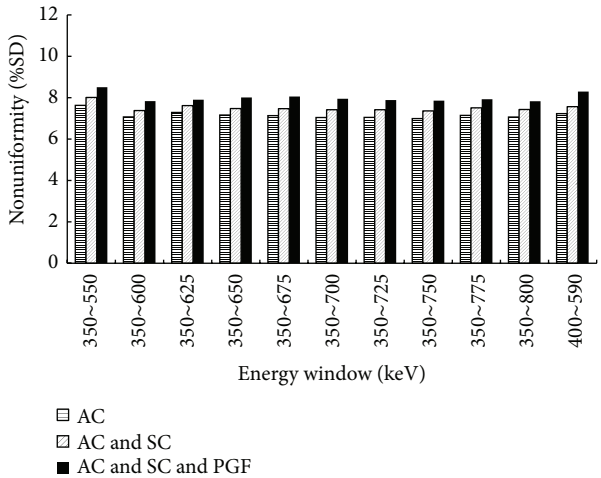

Figure 1: Nonuniformity (%SD) in the uniform region of the NEMA NU 4 image quality phantom.

The maximum and minimum PGF were 33% and 2% in 350~800 and 400~590 keV, respectively.

3.2. Image Quality

3.2.1. Nonuniformity. The nonuniformity of the NEMA NU 4 image quality phantom for ^{124}I was shown in Figure 1. The highest and the lowest nonuniformities were 7.63% and 6.99% within energy windows of 350~550 and 350~750 keV, respectively. The difference of nonuniformity with the various energy windows was <1%. When SC and PGF were applied, nonuniformity was slightly worse. The mean difference was 0.35 and 0.84 percentage point when applying SC and PGF correction, respectively, compared to applying only AC.

3.2.2. RC. The RC and %SD of RC values of the different rods were shown in Table 3. For ^{124}I PET, 1 mm sized rod was not discernible on the image. Therefore the RC for a 1 mm sized rod was not calculated. The representative values of RC within an energy window of 350~750 keV were as follows. RCs were 0.27, 0.41, 0.54, and 0.67 for 2, 3, 4, and 5 mm rods, respectively.

3.2.3. SOR. SORs in the air and nonradioactive water compartments were shown in Table 4 with different energy windows. The lowest SOR value was obtained within an energy window of 350~700 and 350~750 keV in air and water, respectively. The lowest SOR values in air and water compartments were −6.47% and 0.26% at 350~700 and 350~750 keV, respectively. Negative value of SOR after scatter correction was due to bias scaling of single scatter simulation algorithm which was reported in Disselhorst and colleagues' study [11]. The highest SOR value was obtained within an energy window of 350~650 keV in both air and water. When SC was compared with AC, SOR values were decreased by roughly 4.28 percentage point in air and by 6.74 percentage point in water. When PGF was compared with AC, SOR values were decreased by roughly 7.66 percentage point in air and by 12.79 percentage point in water.

Considering the actual mouse experimental conditions, the weighted SOR (wSOR) was calculated using the following equation:

$$\text{wSOR} = \sqrt{f_{\text{air}} \cdot \text{SOR}_{\text{air}}{}^2 + f_{\text{water}} \cdot \text{SOR}_{\text{water}}{}^2}. \quad (5)$$

The weighting factor of f_{air} and f_{water} represents the ratio of the volume occupied by the air and water, respectively, in mouse whole body. The value of f_{air} was the ratio of lung volume in mouse carcass which was calculated using organ density and mass for mouse model (f_{air}: 0.027, f_{water}: 0.973) [28]. Considering the actual mouse experimental conditions, air (lung)/water fractions were determined. The minimum value of the wSOR was assumed to be the desired point, and the corresponding energy window was the optimal energy window. The lowest wSOR value was obtained within an energy window of 350~750 keV for reconstructed images when AC, SC, and PGF corrections were applied (Table 4).

3.3. Noise Equivalent Count Rate. Figure 2(a) shows the NECR curve in different energy windows. The highest NECR was obtained at 400~590 keV. The 2nd highest NECR was found at 350~600 keV and the NECR was decreased as the ULD was increased (Figure 2). Figure 2(b) showed which energy window has the maximum of the NECR. The NECR was calculated with 5 MBq of ^{124}I, the actual activity of injecting the mouse. The LLD was first fixed at 350 keV, and the ULD was increased in 25 keV steps starting at 550 keV until 800 keV. The normalized NECR curves were generated with optimized energy windows. Individual NECR was normalized with the value of NECR at 350~600 keV. Normalized value of NECR with varying ULD was plotted in Figure 2(b).

4. Discussion

In this study, we measured the PET sensitivity and image quality parameters of ^{124}I in order to identify an optimal energy window for ^{124}I imaging. We can find that PGF was

Table 3: Recovery coefficients and %SD values for 5 different rods.

Rod diameter* (mm)	2		3		4		5	
	RC†	%SD‡	RC	%SD	RC	%SD	RC	%SD
FBP								
350~550	0.23	32.90	0.36	44.09	0.53	50.20	0.64	65.26
350~600	0.24	29.89	0.39	40.54	0.50	46.35	0.62	63.38
350~625	0.27	33.43	0.40	45.78	0.52	47.42	0.62	62.90
350~650	0.27	31.06	0.38	42.24	0.49	46.74	0.63	62.11
350~675	0.22	27.41	0.38	42.26	0.60	45.78	0.60	61.49
350~700	0.25	28.95	0.40	41.27	0.57	46.76	0.67	61.51
350~725	0.26	30.60	0.37	40.65	0.52	47.11	0.65	62.01
350~750	0.27	31.20	0.41	44.30	0.54	46.57	0.67	61.64
350~775	0.24	29.34	0.41	41.95	0.57	47.07	0.65	62.14
350~800	0.23	25.71	0.41	41.56	0.55	46.94	0.68	62.98
400~590	0.24	32.66	0.37	43.36	0.49	49.37	0.66	66.94

*For ^{124}I PET, RC could not be calculated for a 1 mm rod size, because this rod was not discernible by ^{124}I PET.
†RC: recovery coefficient.
‡%SD: percent standard deviation.

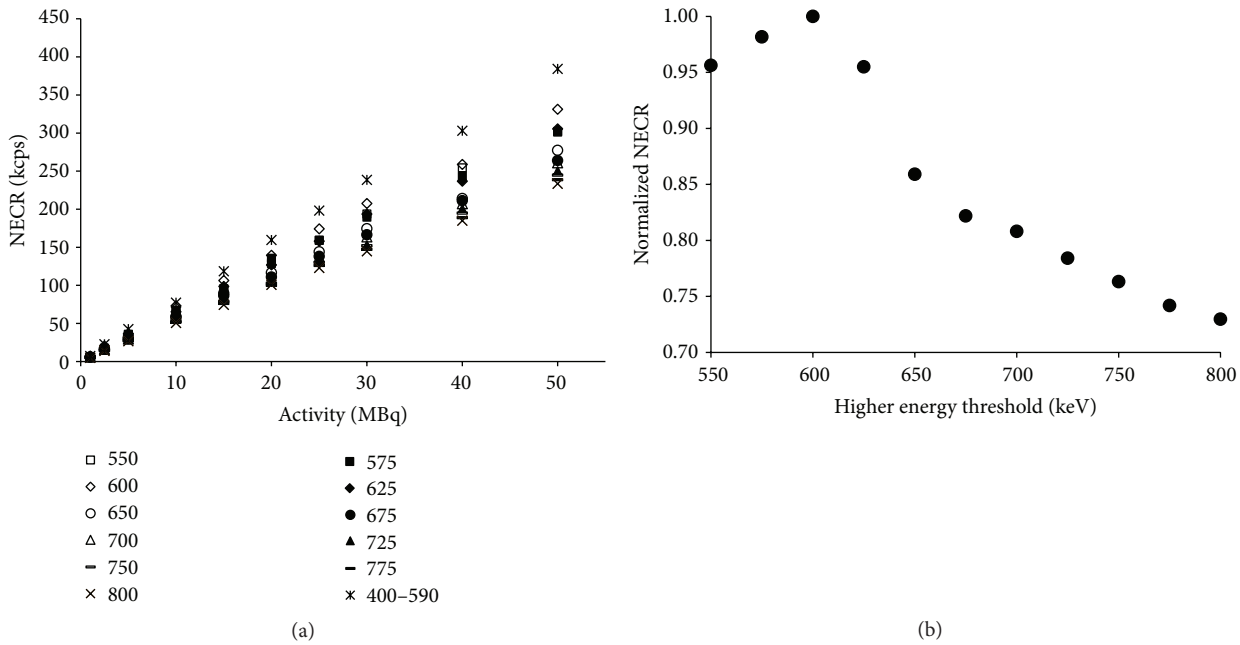

Figure 2: NECR curve for different energy windows (a) at the lower threshold was 350 keV in all cases except 400~590 keV. Normalized NECR variation according to ULD (b).

increased with wider energy windows (Table 2). PGF at 350~550 and 400~590 keV was almost zero. This result is consistent with the other paper [8].

Nonuniformity was increased within narrower energy window. The highest and the lowest nonuniformities were 7.63% and 6.99% within energy windows of 350~550 and 350~750 keV, respectively. The difference between the lowest and the highest nonuniformities with various energy windows was <0.6 percentage point. When SC and PGF were performed, nonuniformity became slightly worsened due to reduced measured count within corresponding energy windows. This tendency for increase of nonuniformity after SC has been previously reported [11]. The difference of nonuniformity was 0.35 percentage point whether the scatter correction is performed or not. When PGF was performed, the difference of nonuniformity was larger than SC (0.84 percentage point).

The RCs of the 4 different rods were shown in Table 3. In this study, since a 1 mm diameter rod was not discernible by ^{124}I PET, we could not calculate the RC of a 1 mm diameter for ^{124}I. This was due to the properties of limit resolution of ^{124}I. A low RC value means low detectability in small hot regions

Table 4: Spillover ratio in air and water compartments with attenuation, scatter, and single gamma photon correction applied.

Energy window	Air	Water	wSOR[‡]
350~550	−5.03	1.01	1.30
350~600	−4.33	1.26	1.43
350~625	−3.40	1.80	1.86
350~650	−2.68	2.87	2.86
350~675	−4.14	2.15	2.22
350~700	−6.47	0.79	1.32
350~725	−5.85	0.39	1.03
350~750	−5.54	0.26	0.95
350~775	−5.77	1.58	1.83
350~800	−5.41	2.36	2.49
400~590	−5.75	1.40	1.67
Mean difference[*]	4.28	6.74	N/A[§]
Mean difference[†]	7.66	12.79	N/A

[*]Mean difference: mean difference of spillover ratio between attenuation correction and attenuation and scatter correction.
[†]Mean difference: mean difference of spillover ratio between attenuation correction and attenuation and scatter and single gamma photon correction.
[‡]Weighted SOR (wSOR).
[§]Not applicable.

(<1 mm diameter) for ^{124}I PET due to higher positron range than ^{18}F. According to Bao et al.'s report, the RCs of ^{18}F were 0.17, 0.48, 0.72, 0.84, and 0.93 mm for 1, 2, 3, 4, and 5 mm rods, respectively [22]. The difference of RCs between ^{124}I and ^{18}F was about 30% compared with Bao et al.'s paper. These were associated with the reduced spatial resolution. The FWHMs (full width at half maximum) were reported to be 2.38 mm and 1.81 mm for ^{124}I and ^{18}F, respectively (about 30% difference) [11]. Regarding the effect of the energy window, RCs were not significantly different within the energy windows ($p > 0.05$). RC was dependent on the spatial resolution. %SD of RC was increased for wider energy windows. When SC and PGF were applied, RCs were not significantly changed ($p > 0.05$). This was well accordant with a previous study [11].

SORs in the nonradioactive water and air compartments were shown in Table 4. The lowest SOR value was obtained within an energy window of 350~700 and 350~750 keV in air and water, respectively. The highest SOR value was obtained within an energy window of 350~650 keV in both air and water. After PGF correction, SORs were improved by 7.66 percentage point and 12.79 percentage point at air and nonradioactive water compared to the value of SOR after AC. In this present study, we compared multiple parameters for the assessment of image quality for determination of optimal PET energy window of ^{124}I. Because sensitivity and nonuniformity simply depend on PET count statistics, RC was not changed with different energy windows. Therefore, assessment of SOR would be more crucial for determination of optimal PET acquisition window. In particular, for ^{124}I PET, single gamma photons also should be considered for the analysis of SOR. The SOR was improved after single gamma photon correction; our proposed correction method was reasonably suitable for correction of single gamma photon. Although SOR in water included the effects of scatter and positron range, SOR in air reflected only scattered photons; because the positron range in air was more than 1 m, almost no annihilations occurred in air [11]. Thus, the value of SOR in the water was more important than in air. For ^{124}I PET, image quality was found to be affected by SOR for various energy windows and prompt gamma photon correction. We calculated wSOR to determine the optimal energy window considering the composition ratio of air and water. The best value of wSOR was obtained with an energy window of 350~750 keV.

The NECR has been commonly proposed to find optimal parameters of PET scanners. Therefore, in another previous study, optimal energy windows for ^{124}I small animal imaging with the Inveon PET system were determined based on NECR [8]. In our NECR result, the optimized ULD was determined to be 600 keV, among our experimental design of energy window setting. This is the most similar ULD proposed in other experiments (590 keV) [8]. Additionally, the highest NECR was obtained at 400~590 keV. This result was in agreement with the other study [8].

Optimal energy windows based on NECR were determined to be 350~600 keV in present study and 400~590 keV in the other study. The values of wSOR were 1.43 and 1.67 with an energy window of 350~600 keV and 400~590 keV, respectively. The values of wSOR with an energy window of 350~600 keV and 400~590 keV were not lowest when energy window was determined based on NECR. The lowest wSOR values were 0.95 with an energy window of 350~750 keV. This was because NECR did not account for possible count rate bias such as the systematic mispositioning of data because of spatial pile-up effects [29]. This phenomenon was more prominent for ^{124}I due to the emissions of high-energy gamma photons. Therefore, evaluation of image quality was necessary to choose the appropriate energy window. Optimal energy window was determined by considering the analysis of SOR. Although the PGF was increased with wider energy windows, the best SOR was showed in 350~750 keV. As applying the prompt gamma correction, conditions that guarantee the count rate to some extent were optimal energy window. In this study to determine the energy window, our interest is not count based evaluation but reconstructed image quality based evaluation. We have proposed a relatively wide energy window; it means the proposed correction method considering PGF was useful to quantify the ^{124}I PET. Therefore, there was a big difference between our proposed method (prompt gamma correction method) and NECR metric. According to our proposed method, energy window "350–750 keV" was best energy window. Although this energy window was wider, prompt gamma coincidence could be corrected using our proposed prompt gamma correction method and this result was assessed using image quality from the reconstructed PET data. Therefore, we could use wider energy window for ^{124}I.

5. Conclusion

The present study described the image characteristics to suggest an energy window of ^{124}I. Optimal energy window should be determined based on image characteristics and the SOR was important factor to determine the optimal

energy window in ^{124}I PET. Our developed prompt gamma correction method would be useful for the quantification of ^{124}I PET.

Competing Interests

The authors declare that there are no competing interests regarding the publication of this paper.

Acknowledgments

This work was supported by the Korea Science and Engineering Foundation (KOSEF) (no. 2015001667 (PI, Joo Hyun Kang) and no. 1711026888 (PI, Kook-Hyun Yu)) and Health Technology R&D (no. HO15C0003 (PI, Jin Su Kim)).

References

[1] M. Bruehlmeier, U. Roelcke, P. A. Schubiger, and S. M. Ametamey, "Assessment of hypoxia and perfusion in human brain tumors using PET with ^{18}F-fluoromisonidazole and ^{15}O-H_2O," *Journal of Nuclear Medicine*, vol. 45, no. 11, pp. 1851–1859, 2004.

[2] M. Castellani, A. Colombo, R. Giordano et al., "The role of PET with ^{13}N-ammonia and ^{18}F-FDG in the assessment of myocardial perfusion and metabolism in patients with recent AMI and intracoronary stem cell injection," *Journal of Nuclear Medicine*, vol. 51, no. 12, pp. 1908–1916, 2010.

[3] W. Jentzen, R. Weise, J. Kupferschläger et al., "Iodine-124 PET dosimetry in differentiated thyroid cancer: recovery coefficient in 2D and 3D modes for PET(/CT) systems," *European Journal of Nuclear Medicine and Molecular Imaging*, vol. 35, no. 3, pp. 611–623, 2008.

[4] W. Jentzen, R. F. Hobbs, A. Stahl, J. Knust, G. Sgouros, and A. Bockisch, "Pre-therapeutic ^{124}I PET(/CT) dosimetry confirms low average absorbed doses per administered ^{131}I activity to the salivary glands in radioiodine therapy of differentiated thyroid cancer," *European Journal of Nuclear Medicine and Molecular Imaging*, vol. 37, no. 5, pp. 884–895, 2010.

[5] D. S. Lee and J. C. Paeng, "Molecular nuclear cardiac imaging," *Korean Journal of Nuclear Medicine*, vol. 38, no. 2, pp. 175–179, 2004.

[6] S. Pandey, A. Venugopal, R. Kant, R. Coleman, and J. Mukherjee, " ^{124}I-Epidepride: a PET radiotracer for extended imaging of dopamine D2/D3 receptors," *Nuclear Medicine and Biology*, vol. 41, no. 5, pp. 426–431, 2014.

[7] A. M. S. Braghirolli, W. Waissmann, J. B. da Silva, and G. R. dos Santos, "Production of iodine-124 and its applications in nuclear medicine," *Applied Radiation and Isotopes*, vol. 90, pp. 138–148, 2014.

[8] N. Anizan, T. Carlier, C. Hindorf, J. Barbet, and M. Bardiès, "Acquisition setting optimization and quantitative imaging for ^{124}I studies with the Inveon microPET-CT system," *EJNMMI Research*, vol. 2, article 7, 2012.

[9] R. A. Gregory, C. A. Hooker, M. Partridge, and G. D. Flux, "Optimization and assessment of quantitative ^{124}I imaging on a Philips Gemini dual GS PET/CT system," *European Journal of Nuclear Medicine and Molecular Imaging*, vol. 36, no. 7, pp. 1037–1048, 2009.

[10] S. Vandenberghe, "Three-dimensional positron emission tomography imaging with ^{124}I and ^{86}Y," *Nuclear Medicine Communications*, vol. 27, no. 3, pp. 237–245, 2006.

[11] J. A. Disselhorst, M. Brom, P. Laverman et al., "Image-quality assessment for several positron emitters using the NEMA NU 4-2008 standards in the siemens inveon small-animal PET scanner," *Journal of Nuclear Medicine*, vol. 51, no. 4, pp. 610–617, 2010.

[12] S. Surti, R. Scheuermann, and J. S. Karp, "Correction technique for cascade gammas in ^{124}I imaging on a fully-3D, time-of-flight PET scanner," *IEEE Transactions on Nuclear Science*, vol. 56, no. 3, pp. 653–660, 2009.

[13] M. Lubberink, A. Van Schie, H. W. A. M. De Jong, G. A. M. S. Van Dongen, and G. J. J. Teule, "Acquisition settings for PET of ^{124}I administered simultaneously with therapeutic amounts of ^{131}I," *Journal of Nuclear Medicine*, vol. 47, no. 8, pp. 1375–1381, 2006.

[14] W. Jentzen, "Experimental investigation of factors affecting the absolute recovery coefficients in iodine-124 PET lesion imaging," *Physics in Medicine and Biology*, vol. 55, no. 8, pp. 2365–2398, 2010.

[15] D. Taleb, M. A. Bahri, G. Warnock et al., "Performance measurements of the MicroPET FOCUS 120 for iodine-124 imaging," *IEEE Transactions on Nuclear Science*, vol. 59, no. 5, pp. 1868–1878, 2012.

[16] T. Chang, G. Chang, J. W. Clark Jr., R. H. Diab, E. Rohren, and O. R. Mawlawi, "Reliability of predicting image signal-to-noise ratio using noise equivalent count rate in PET imaging," *Medical Physics*, vol. 39, no. 10, pp. 5891–5900, 2012.

[17] C. C. Watson, M. E. Casey, B. Bendriem et al., "Optimizing injected dose in clinical PET by accurately modeling the counting-rate response functions specific to individual patient scans," *Journal of Nuclear Medicine*, vol. 46, no. 11, pp. 1825–1834, 2005.

[18] D. W. Wilson, B. M. W. Tsui, and H. H. Barrett, "Noise properties of the EM algorithm. II. Monte Carlo simulations," *Physics in Medicine and Biology*, vol. 39, no. 5, pp. 847–871, 1994.

[19] J. S. Kim and A. R. Yu, "Determination of single gamma photon fraction of ^{124}I PET," *Journal of Instrumentation*, vol. 10, no. 3, p. p03006, 2015.

[20] C. C. Constantinescu and J. Mukherjee, "Performance evaluation of an Inveon PET preclinical scanner," *Physics in Medicine and Biology*, vol. 54, no. 9, pp. 2885–2899, 2009.

[21] A. R. Yu, J. S. Kim, K. M. Kim et al., "Performance measurement of siemens inveon PET scanner for small animal imaging," *Korean Journal of Medical Physics*, vol. 21, no. 2, pp. 145–152, 2010.

[22] Q. Bao, D. Newport, M. Chen, D. B. Stout, and A. F. Chatziioannou, "Perfrmance evalution of the inveon dedicated PET preclinical tomograph based on the NEMA NU-4 standards," *Journal of Nuclear Medicine*, vol. 50, no. 3, pp. 401–408, 2009.

[23] J. S. Kim, J. S. Lee, K. C. Im et al., "Performance measurement of the microPET focus 120 scanner," *Journal of Nuclear Medicine*, vol. 48, no. 9, pp. 1527–1535, 2007.

[24] S. Yamamoto, H. Horii, M. Hurutani, K. Matsumoto, and M. Senda, "Investigation of single, random, and true counts from natural radioactivity in LSO-based clinical PET," *Annals of Nuclear Medicine*, vol. 19, no. 2, pp. 109–114, 2005.

[25] A. L. Goertzen, Y. S. Joon, and C. J. Thompson, "Imaging of weak-source distributions in LSO-based small-animal PET scanners," *Journal of Nuclear Medicine*, vol. 48, no. 10, pp. 1692–1698, 2007.

[26] M. A. Bahri, A. Plenevaux, G. Warnock, A. Luxen, and A. Seret, "NEMA NU4-2008 image quality performance report for the micropet focus 120 and for various transmission and reconstruction methods," *Journal of Nuclear Medicine*, vol. 50, no. 10, pp. 1730–1738, 2009.

[27] A. R. Yu, J. S. Kim, K. M. Kim et al., "Optimal PET acquisition setting of ^{124}I with Siemens Inveon PET: ccomparative simulation study with ^{18}F and microPET R4," in *Proceedings of the IEEE Nuclear Science Symposium Conference Record (NSS/MIC '09)*, pp. 2666–2668, IEEE, Orlando, Fla, USA, October 2009.

[28] W. H. Miller, C. Hartmann-Siantar, D. Fisher et al., "Evaluation of beta-absorbed fractions in a mouse model for ^{90}Y, ^{188}Re, ^{166}Ho, ^{149}Pm, ^{64}Cu, and ^{177}Lu radionuclides," *Cancer Biotherapy and Radiopharmaceuticals*, vol. 20, no. 4, pp. 436–449, 2005.

[29] R. D. Badawi, P. Domigan, O. Johnson et al., "Count-rate dependent event mispositioning and NEC in PET," *IEEE Transactions on Nuclear Science*, vol. 51, no. 1, pp. 41–45, 2004.

Hindawi Publishing Corporation
BioMed Research International
Volume 2016, Article ID 6240504, 13 pages
http://dx.doi.org/10.1155/2016/6240504

Review Article

Application of Arterial Spin Labelling in the Assessment of Ocular Tissues

E. Vaghefi[1] and B. Pontré[2]

[1]*School of Optometry, University of Auckland, Auckland 1023, New Zealand*
[2]*Department of Anatomy with Radiology, University of Auckland, Auckland 1023, New Zealand*

Correspondence should be addressed to E. Vaghefi; e.vaghefi@auckland.ac.nz

Received 5 November 2015; Accepted 7 February 2016

Academic Editor: Guang Jia

Arterial spin labelling (ASL) is a noninvasive magnetic resonance imaging (MRI) modality, capable of measuring blood perfusion without the use of a contrast agent. While ASL implementation for imaging the brain and monitoring cerebral blood flow has been reviewed in depth, the technique is yet to be widely used for ocular tissue imaging. The human retina is a very thin but highly stratified structure and it is also situated close to the surface of the body which is not ideal for MR imaging. Hence, the application of MR imaging and ASL in particular has been very challenging for ocular tissues and retina. That is despite the fact that almost all of retinal pathologies are accompanied by blood perfusion irregularities. In this review article, we have focused on the technical aspects of the ASL and their implications for its optimum adaptation for retinal blood perfusion monitoring. Retinal blood perfusion has been assessed through qualitative or invasive quantitative methods but the prospect of imaging flow using ASL would increase monitoring and assessment of retinal pathologies. The review provides details of ASL application in human ocular blood flow assessment.

1. Ocular Blood Perfusion Quantification

Our sense of vision is critically dependent on all the components of our eye to function cohesively, so we will have a clear image of the outside world. The retina is the light-sensitive tissue that is lined on the inside surface of the eye and contains nerve cells, which convert incoming light into electrical impulses (Figure 1). Anatomically, retina is a highly stratified tissue, consisting of multiple cell types organized into its layered structure. Each layer of the retina performs distinct and yet interdependent functions, which in conclusion support the phototransduction process [1]. Briefly and moving from inside in contact with the vitreous outside, these are the inner limiting membrane, nerve fibre layer, ganglion cell layer, the inner plexiform layer, inner nuclear layer, the outer plexiform layer, outer nuclear layer, the external limiting membrane inner/outer segment of photoreceptors, and the retinal pigment epithelium. Like all the other tissues in the human body, the retinal layers of different cell types need oxygen, and hence blood supply, to survive.

The two major sources of blood supply to the mammalian retina are the retinal and the choroidal blood vessels [2]. The choroidal vascular bed receives the bigger blood flow of about 65–85% of the total blood flow and the remaining 15–35% flows to the retina through the central retinal artery [3]. While the choroidal circulation is vital for the maintenance of the outer retina and particularly the photoreceptors, the retinal vasculature nourishes the inner retinal layers. The arterial input to the eye is derived from the internal carotid artery and includes central retinal artery, the short and long posterior ciliary arteries, and the anterior ciliary arteries. Venous outflow from the eye is primarily via the vortex veins and the central retinal vein. The choroidal arteries arise from long and short posterior ciliary arteries and each of the posterior ciliary arteries breaks up into fan-shaped lobules of capillaries that supply localized regions of the choroid. The arteries pierce the sclera around the optic nerve and fan out to form the three vascular layers in the choroid: outer (most scleral), medial, and inner (nearest Bruch's membrane of the pigment epithelium) layers of blood vessels [4, 5]. Any

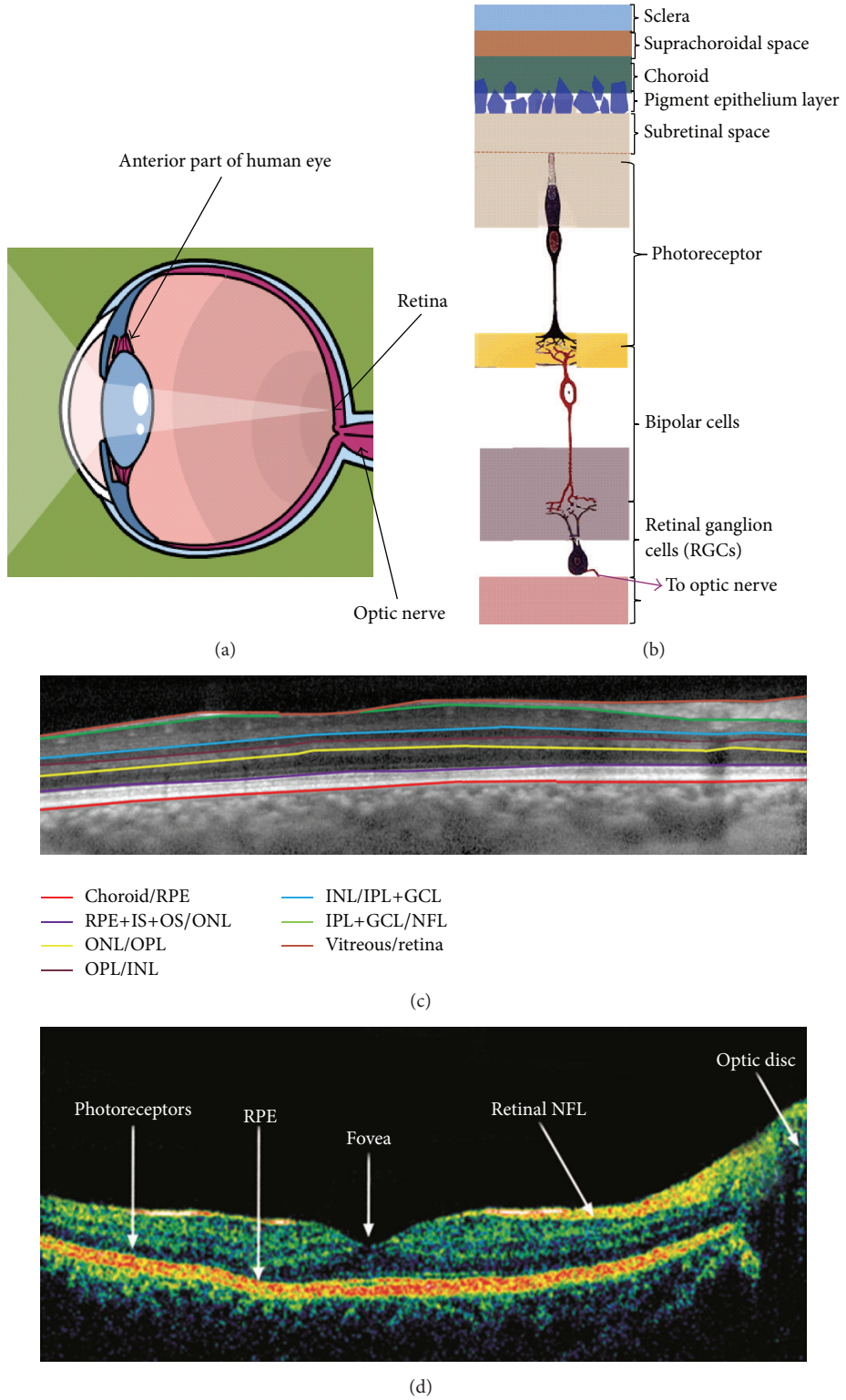

FIGURE 1: The layered structure of the retina. (a) General anatomy of the eye, including the retina lining the back of the eye; and (b) the cellular component of retinal stratified structure. (c) The segmented raw retinal OCT image overlaid with seven identified boundaries. (d) Raw OCT image of the retina.

deficiency of either of these two retinal circulations could result in blood perfusion alterations in the retina which is linked to several retinal pathologies [6].

Perfusion allows for the delivery of oxygen and nutrients to tissues by means of blood flow and it is one of the most fundamental physiological parameters [7]. Disorders correlated with blood perfusion such as stroke account for much of the medical morbidity in industrialized nations, and blood flow alterations also commonly accompany other pathophysiological changes such as cancer, epilepsy, and neurodegenerative diseases [8]. Hence, the measurements of perfusion have direct diagnostic value. Tissue perfusion is usually measured using a diffusible tracer that can be exchanged between the vascular compartment and tissue [9]. Conventional fluid flow describes the volume of liquid passing a given point per unit of time and has a unit of mL/min. However, perfusion flow is a more useful physiological measure. Perfusion flow is the volume of fluid (i.e., blood) passing in and out of a given weight of tissue per unit of time. That is because the cerebral and retinal blood flow should be distinguished as a rate for a specific tissue weight [10].

There are many methods of measuring blood perfusion, including methods based on computed tomography (CT), laser Doppler, single-photon emission computed tomography (SPECT), and MRI. The majority of these techniques require the injection of an exogenous tracer that acts to alter the signal intensity as the contrast agent moves through the blood, allowing the quantification of tissue perfusion. Both CT and SPECT techniques provide high sensitivity to perfusion [11] but are unsuitable for serial studies requiring multiple examinations owing to the use of ionising radiation. MRI techniques using gadolinium based contrast agents (GBCA) also provide high sensitivity while avoiding the use of ionising radiation. However, the risks associated with GBCA such as nephrogenic systemic fibrosis (NSF) make such techniques unsuitable in at-risk patients. The use of contrast agents that are not gadolinium based such as fluorinated halocarbons [12], deuterated water ($2H_2O$) [13, 14], and 17O-water [14] has been investigated. The use of arterial spin labelling (ASL) techniques eliminates the requirement for externally administered agents and exploits the advantages offered by MRI-based techniques [15, 16].

2. ASL

The primary benefit of ASL over other MRI-based techniques is that the use of the blood itself as a tracer eliminates the risks associated with GCBA and other exogenous tracers. As a result, ASL is of most use in cases where the use of an exogenous contrast agent is contraindicated [17] or in cases where patients require multiple perfusion assessments in a single study [18]. In studies of the eye, for example, it may be appropriate to assess perfusion under a variety of conditions during the same study, making techniques based on exogenous contrast agents undesirable [19, 20].

ASL requires that the arterial blood supplying the tissues of interest is labelled by modifying its magnetization. Image contrast is affected by the presence of the labelled blood in the imaging volume. Acquiring an image of the tissues of interest after a sufficient delay time to allow the labelled blood to enter the imaging volume results in a decrease in signal related to the local tissue perfusion. Comparing the labelled images to those acquired without the labelled blood allows regional variations in tissue perfusion to be identified. Further, this signal can be modelled to determine the tissue perfusion at each voxel. In both the qualitative and the quantitative applications of ASL, the resulting signal depends on the tissue properties, timing considerations, and imaging parameters. For this reason, ASL techniques used in any study need to be specifically optimized for the tissue of interest [21, 22].

2.1. Applications of ASL. In a clinical setup, ASL can be grouped with other anatomical (e.g., spin-lattice T1 or spin-spin T2) or functional (e.g., fMRI) imaging sequences in order to provide a comprehensive assessment of the imaged organ [23]. To date, the major clinical applications of the ASL have been focused on studying the brain and its disorders [24]. Several studies have used ASL to detect regional hypoperfusion in patients suffering from Alzheimer's dementia ([25, page 2000], [26]) or frontotemporal dementia [27, 28]. Epilepsy is another neurological disorder in which ASL can be applied for diagnosis and management. Interictal hypoperfusion measured by ASL has been shown to correlate with interictal hypometabolism ([29, 30], [31, page 200]). ASL has also been used in conjunction with other modalities to monitor the diagnosis and treatment effects of several brain affective disorders such as depression [30, 32], schizophrenia [33], Parkinson [34], and hypoperfusion of prefrontal cortex [35]. Furthermore and combined with fMRI, ASL is proved to be an appealing approach for imaging brain activations during long time scale processes and more ecological paradigms such as motor learning [36], emotion or mental states [37–39], mood changes [40, 41], and natural vision [42]. The utility of ASL in detection of migraine [43, 44] and focal seizure [44] has also been demonstrated in several case reports. ASL can be combined with fMRI to look at brain's oxygenation and functionality since it provides absolute quantification of brain blood perfusion and is less susceptible to baseline drift and motion artefact [45, 46]. Finally, since ASL is reagent-free it has become an appealing technique in paediatric studies, as a biomarker for functional brain development in both healthy populations and developmental disorders [47, 48].

Apart from the field of brain research, new applications of ASL are being investigated around the world. Preliminary studies of the applicability of ASL in the cardiovascular investigations [49] and its related pathologies such as stroke have been looked at [50, 51]. ASL has also been obtained from postischemic extremities in patients with peripheral vascular disease [49]. The kidney is another highly perfused tissue where ASL has also been used [52]. Lastly, since tumorous tissue usually has higher perfusion than healthy tissue, ASL has been applied for detection and grading of tumours [53, 54]. One reason for the spread of ASL's clinical usage has been the verification of its measurements against previously stablished flowmetry methods.

ASL MRI has been validated against other quantitative technologies such as Dynamic Susceptibility-Weighted

Contrast-Enhanced MRI [55–57], PET scan, and using different exogenous contrast agents [58, 59]. Furthermore, since ASL image contrast is not based on susceptibility effects, it could be used to study regions of high static field inhomogeneity [60–62]. This property of ASL is especially valuable while imaging highly layered structures such as the eye's retina [63, 64].

ASL implementations are now commercially available on all major MRI platforms and their reproducibility has been confirmed by several multicentre studies [46, 65]. However, before applying this technique in the clinic, many of its technical parameters have to be studied and optimized. Here we are going to review the effects of a number of these factors on the quality of the ASL measurements.

2.2. Technical Considerations. Early implementations of ASL used a series of short labelling pulses (PASL), to label the arterial blood [66–68]. The shorter pulses mitigate the SAR issues and high power deposition, but the nonadiabatic nature of the labelling pulses results in decreased labelling efficiency and lower ASL signal.

The next generation of ASL implementations is known as continuous ASL (CASL) [16]. In CASL schemes, the blood that passes through the labelling slab is continuously affected and allows blood magnetization to reach a steady-state, maximising the signal difference between the labelled and control conditions [69]. However, this labelling scheme leads to increased magnetization transfer effects that would decrease the accuracy of the measurements. The long labelling pulses used in CASL are particularly problematic in higher field strength systems. At these higher fields, specific absorption rate (SAR) is increased, leading to higher amounts of RF energy being absorbed and potentially increasing local heating in tissues. Longer RF pulses, like those used in CASL, also lead to increased SAR, exacerbating any potential heating occurring in patients [44, 70].

The latest implementation of ASL in many modern applications is the pseudo-continuous ASL (pCASL) (Figure 2), which is used to overcome the limitations of PASL and CASL [15, 60]. Rather than using a single continuous labelling pulse like CASL, 1000 or more shaped magnetization pulses are very rapidly applied to label the arterial blood. Compared to CASL, pCASL provides superior labelling efficiency and is compatible with modern body coil RF transmission hardware that is now ubiquitous on clinical MRI scanners. In practice, the signal-to-noise ratio (SNR) of the pCASL implementation is higher than other methods due to two reasons. Firstly, in pCASL implementation the temporal duration of the labelled slab is longer which in turn leads to larger volume of labelled blood that is delivered to the tissue, leading to an increased SNR. Secondly, even for an interval of equal temporal duration, it has been shown that the labelled magnetization delivered to the blood is higher using pCASL [71].

Over the past decade, there has been a general trend to the use of higher field strength systems owing to the higher overall SNR. Theoretically, the expected ASL signal will increase proportional to the strength of the main magnetic field. Wang et al. [69] studied the effects of the magnet field strength on the implementation of ASL to quantify

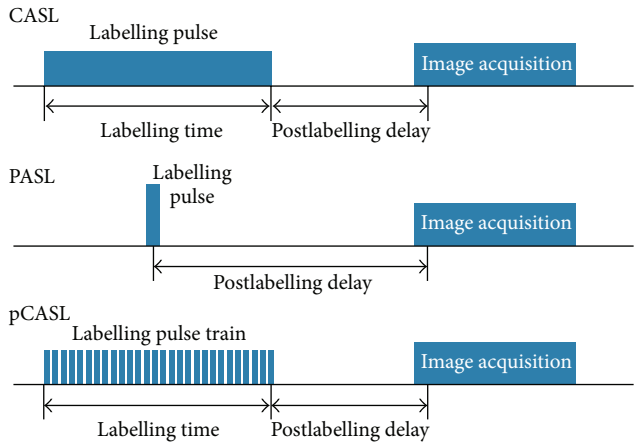

Figure 2: Different implementations of ASL pulse sequence for MR, continuous (CASL), pulsed (PASL), and pseudo-continuous (pCASL) technique.

the cerebral blood flow. They reported that, using similar pulse sequences, a 4 T magnet generated more than twice the amount of ASL signal compared to a 1.5 T magnet, consistent with the theoretical expectations. Other studies have used 7 T magnet strength to apply ASL to human brain [72, 73]; however, it has been noted that since these high strengths are much more susceptible to off-resonance fields especially at the tagging location, a robust prescan procedure is needed to optimize the ASL parameters [74].

In all forms of ASL, ideally the labelling pulse will result in perfect and complete labelling of the arterial blood. In this ideal case, all of the blood passing through the imaging volume will contribute to the ASL signal. However, in magnets with clinical field strengths, the lifetime of the magnetically tagged blood is about 1300–1750 ms. The labelling lifetime along with the timing delays used in the pulse sequence will influence labelling efficiency. The postlabelling delay time (the delay between the labelling pulse train and acquisition) needs to be set so that the labelled blood arrives at the tissue of interest when it is acquired. Shorter delays can be used to reduce scan time but come at the expense of potentially inefficient labelling since the labelled blood has not had sufficient time to arrive at the imaging slice. A longer delay could be used to ensure that more labelled blood perfuses the tissues of interest but labelling efficiency may be reduced owing to T1 relaxation effects [75].

Aside from timing and protocol-specific effects, labelling efficiencies in ASL also depend on the hardware used. Higher magnetic field strength systems provide increased efficiency in ASL studies [76] owing to the increase in overall SNR as well as the lengthening of T1 in tissues [70]. The multichannel head coils have been shown to increase the SNR of the ASL scans [77] and allow for the use of parallel imaging techniques [45]. The coil arrays used in parallel imaging can be exploited to decrease the echo time (TE) and maximise the signal from tissues with very short T2, such as the retina [78]. The higher SNR achieved by using multichannel coils has also been shown to provide more accurate quantification of tissue perfusion [79–81]. The gain in SNR is also mentioned when

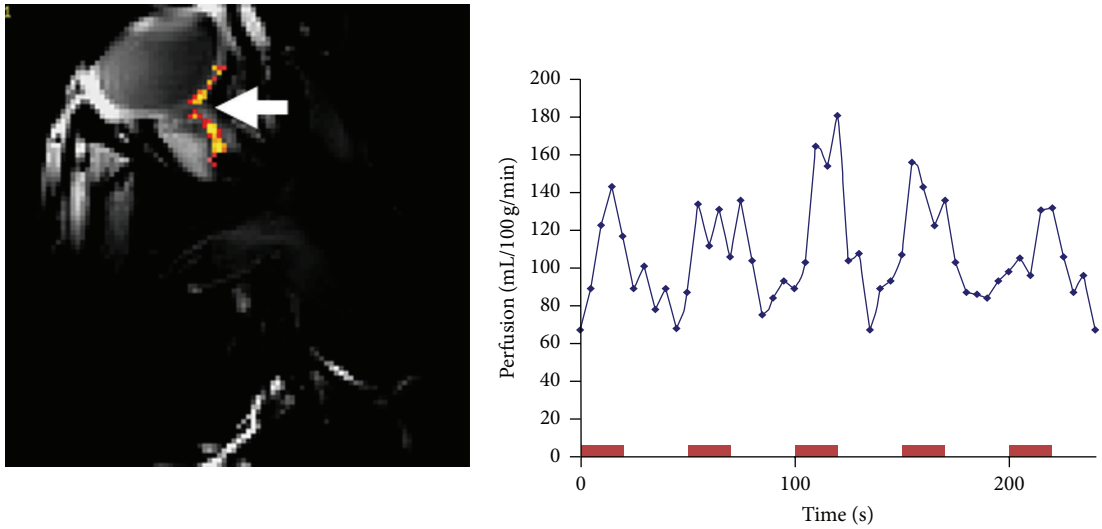

(a) (b)

Figure 3: (a) Statistical map extracted from our ASL dataset is showing the correlation map of voxels (arrow) activated to the visual stimulus ($Z > 3.23$). (b) ASL perfusion signal in mL/100 g/min units is extracted from active voxels shown on (a) over the time course of our experiment. Red blocks denote the periods of light stimulation.

surface coils are used in conjunction with standard head coils, imaging the brain, the kidney, and the eye [82].

Similar to other MRI techniques, ASL is also sensitive to motion and susceptibility artefacts. Motion artefacts are an issue in all MR imaging techniques owing to the effectively long scan times, resulting in difficulties for some patients to remain still throughout the examination. In ASL, misregistration resulting from motion between the control and labelled data can cause local or global changes in ASL signal not related to tissue perfusion [83–85]. Magnetic field inhomogeneities are problematic in EPI-based protocols such as ASL where the long echo trains used can result in image distortions or significant signal loss. Field inhomogeneities will also affect the labelling efficiency, particularly in pCASL techniques owing to the nonadiabatic nature of the labelling pulses [22]. Artefacts specific to ASL studies, such as enhanced T1 shortening owing to the presence of gadolinium based contrast agents, and insufficient suppression of intravascular spins can also result in suboptimal image quality [83–85].

Fortunately, many of these issues can be partially mitigated by the use of background suppression [86, 87]. Blood labelling in ASL is inherently inefficient with only 1-2% of the spins in the blood contributing to the signal, so the use of effective background suppression will increase ASL signal-to-noise ratio and sensitivity and result in improved quantification of perfusion measures. In order to incorporate background suppression in ASL implementation, an initial saturation pulse is applied to the imaging region. This saturation pulse is then followed by carefully timed magnetization inversion pulses. Such combination results in the longitudinal magnetization of the static target tissue being close to zero at the time of image acquisition. Meanwhile, the tagged arterial blood water molecules that are passing through the target tissue have not experienced the initial saturation pulse, but only the inversion pulses [88–90]. Hence, the ASL perfusion signal is preserved, while the static tissue signal is nearly eliminated.

2.3. Applicability of ASL in the Eye. The mammalian retina is found to have a high rate of perfusion [91–94], which is required for the maintenance of the physiological homeostasis in the highly compartmented ultrastructure of the retina. Retina is the most metabolically active tissue in the human body [95] and is highly sensitive to the local perfusion rates of the retinal and choroidal circulations. The choroidal arteries, which feed the outer retina, arise from the posterior ciliary arteries that penetrate the sclera around the optic nerve [4]. Simultaneously, the retinal vasculature network is branched from the central retina artery and feeds the deeper layers of the retina. The central retina artery itself receives its blood supply from the Circle of Willis, which is formed by an arterial polygon and supplies the blood of the eye and the brain.

The retinal circulation has no autonomic innervation and is regulated by local factors [6] while the choroidal circulation is not autoregulated and is mainly controlled by sympathetic innervation [96]. Using a 9 T Phillips magnet in a preliminary study, we have previously shown that ASL can be applied to image this nonregulated blood flow in the retina (Figure 3). The perfusion rates of the blood in retina have been tried to be measured using other methods, including laser speckle [97], ultrasound combined with enhanced depth imaging OCT [98], high frequency immersion ultrasound [99], OCT Angiography [100, 101], Doppler OCT [102], ultrahigh speed swept source/Fourier domain OCT [103], and laser Doppler flowmetry [104]. Most of these techniques have not been transformed to the clinical setup, due to their limitations in sensitivity, reproducibility, and accuracy. However, the perfusion rates of the retinal and choroidal circulations are of clinical importance as they are altered and affected in many of the common retinal pathologies.

Several studies have shown that, within retina, the outer segments of the photoreceptors are the most metabolically active [105, 106]. Due to such high demand of blood perfusion, the ability to regulate steady blood flow in the retina is essential for the health of this tissue. Normal blood flow within the retina and choroidal vasculatures is altered in a number of retinal disorders that affect the overall vision.

Diabetic retinopathy (DR) is an ocular manifestation of diabetes which disturbs the normal retinal vasculature function and often leads to capillary occlusion and if left untreated to vascular proliferation [107, 108]. By the time that the manifestation of DR becomes clinically observable, irreversible changes to the retinal vasculature network have already occurred. These changes (i.e., proliferation of the retinal vasculature) are in response to the tissue hypoxia which is known to occur in DR; however, the exact time when hypoxia begins is as yet unknown [109]. In ophthalmic clinical studies, it has been shown that retinal blood flow is reduced before and in the early stages of DR [110–112]. This initial flow reduction is then followed by an increase in retinal blood flow, possibly due to the release of vascular endothelial growth factor (VEGF), which in turn leads to proliferative retinopathy [113, 114].

Glaucoma is a term encompassing a group of disorders of the eye which generally damage the optic nerve. Often the onset and progression of glaucoma are accompanied by an increase in the intraocular pressure (IOP) of the patient. There is evidence that there is a relationship between ocular perfusion and damage progression in patients with glaucoma [115]. There is further evidence that an eye with elevated IOP could experience conditions similar to those suffering from reduced retinal perfusion [105, 116]. Due to the effective autoregulation in the retinal circulation, the decreased perfusion pressure of the eye suffering from glaucoma does not affect the PO_2 of the inner retina [117]. On the other hand, the choroidal blood flow was shown to be decreased in glaucoma, resulting in hypoxic conditions at the photoreceptors [116].

Retinopathy of prematurity (ROP) is affecting premature infants and it is marked by abnormal growth of blood vessel in the retina. ROP progresses firstly by delayed retinal vascular growth after birth and partial regression of existing vessels. This is then followed by neovascularization induced by hypoxia [118]. ROP was first associated with exposure to high levels of oxygen after the initial description of the disease [119]. In order to maintain healthy and sufficient blood perfusion levels in premature infants, currently supplemental oxygen is closely monitored [120]. The current clinical treatment to stop the progression of this condition is the indirect laser photocoagulation to bring the perfusion rates of the retina towards normal levels [121].

Retinal detachment is a condition that could occur due to various often advanced pathologies of the retina. In this condition, the retinal tissue peels away from the RPE [122]. During retinal detachment progression, the photoreceptor segments are separated from their supporting vasculature. This process leads to lower oxygen values at the photoreceptors site, inducing local hypoxic conditions and increasing the cell death rate under this condition. It has been shown that retinal detachment is correlated by altered choroidal perfusion rates [123].

3. Application of ASL in Animal Models

The ASL modality is capable of noninvasively quantifying blood perfusion in scanned tissues. A recent study showed that ASL could provide sufficient resolution and SNR to accurately measure the different blood flow of the retinal and choroidal circulations in mice eyes [63]. Furthermore, the same study showed that ASL can correctly quantify the changes of blood flow modulated by anaesthetics in their animal model. It was mentioned that the retinal blood flow changed from 1.3 ± 0.44 to 0.88 ± 0.22 mL/g/min and choroidal blood flow changed from 7.7 ± 2.1 to 4.3 ± 1.9 mL/g/min due to anaesthesia.

In a following study, a mouse model of diabetic retinopathy was imaged with ASL [124]. The blood flows of the mice were quantified at early and late time points after onset of hyperglycemia. It has been reported that the choroidal blood flow was reduced by 20% in the diabetic group compared with the control group after 10 weeks. After 30 weeks, it was observed that both choroidal and retinal blood flows were notably lower in the mice model of diabetic retinopathy. The visual performance of these animals was also found to be significantly worsened.

In the third study from the same authors, changes in retinal and choroidal blood flows of the mouse model of retinitis pigmentosa were measured with ASL [125]. Here it was observed that the retinal blood flow was decreased consistently and significantly through the course of the study. The same effect was not observed in the choroidal blood flow though.

Reference [126] measured the retinal and cerebral blood flows in rats under light and dark adapted conditions using ASL. These measurements were then reconfirmed with fluorescent microspheres. The choroidal blood flow was measured at $64.8 \pm 29\ \mu$L/min during dark adaptation and $66.0 \pm 17.8\ \mu$L/min during light adaptation condition. Retinal BF was $11.6 \pm 2.9\ \mu$L/min during light adaptation and between 8.2 and 9.9 μL/min under dark adapted environment. A 10 Hz flickering light stimulation was also applied which led to significantly higher retinal blood flow but not the choroidal blood flow $13.5 \pm 3.2\ \mu$L/min.

ASL was utilized to obtain high resolution blood flow measurements of rat models of retinitis pigmentosa [127]. A CASL pulse sequence and an 11.7 T small animal MRI were combined with customized surface coil to implement the ASL technique here. It was hence possible to have $44 * 44\ \mu$m in-plane resolution and differentiate between retinal and choroidal circulations in rats' retinas. This study found that choroidal and retinal circulations have different susceptibility to progressive retinal degeneration in this animal model.

A follow-up study looked at applying ASL to look at the effects of acute hypertension on the choroidal and retinal blood flows, in a rat model [128]. In this study, an autoregulatory behaviour was observed in the retinal blood circulation, while a baroregulation response was imaged in the choroid vasculature. The authors believe that their animal model was

useful in studying retinal and choroidal vascular dysregulation.

The most human-like implementation of ASL in animal models was done using eight baboons and a 3-Tesla clinical scanner [129]. The retinal blood flow was measured under normal and hypercapnia conditions in these animals. It was found that base blood flow from the posterior retina was 83 ± 30 mL/100 g/min while in hypercapnia this was increased by 25 ± 9%.

The above-mentioned studies have established the applicability and accuracy of ASL blood in studying the models of different retinal conditions. Next, we are reviewing the application of the ASL to human tissue.

4. Application of ASL in Human Retinal Tissue

One of the first studies that have used a conventional standard and commercially available 3 T clinical magnet to investigate the feasibility of measuring blood flow of the human retina using ASL was done by [130]. Here, the blood flow measurements were obtained in five healthy individuals using an 8-channel array head coil. A CASL was used in this study and the labelling was placed 5 cm below the optic nerve to invert the magnetization of the blood in the carotid arteries below the Circle of Willis. The inverting pulse duration was varied between 500 and 2000 ms to optimize the sequence for achieving maximum SNR. Additionally, background suppression technique was also employed in order to improve the quality of the obtained results. The two main sources of image artefact in ophthalmic MRI are ocular motion artefact and partial volume effects [131, 132]. The former is due to involuntary eye movement and the latter is due to the proximity of the eye to the surface of the body. In the [130] study, these artefacts are minimized by usage of a fixation target and blink-synced image acquisition. The blood flow estimation was performed using a single-compartment model [133, 134]. Using this model and assuming labelling efficiency of 0.85, brain-blood water partition coefficient of 0.9 g/mL [135], and longitudinal relaxation rate of 0.67 s^{-1} for the retinal tissue [136, 137], the measured blood flow to a section of the retina around the fovea was measured at 1.75 ± 0.54 $\mu L/mm^2/min$.

A follow-up investigation tried to differentiate between the human retinal and choroidal blood flow, in a clinical setup [138]. Four healthy individuals were scanned by ASL under normocarbia (partial end-tidal pressure values = 40 mmHg) and hypercarbia (partial end-tidal pressure values = 50 mmHg) conditions. The MRI setup was similar to a previous study [130] but a pCASL pulse sequence was applied here. Using a similar single-compartment model and parameter assumption as before, the baseline blood flow was measured at 1.55 ± 0.17 $\mu L/mm^2/min$. This value increased during hypercarbia to 1.96 ± 0.18 $\mu L/mm^2/min$. Overall, hypercarbia caused a 26% relative increase of blood flow from the normal condition which is calculated to be 6.7% increase in the blood flow per 1 mmHg. This study, by controlling the breathing conditions, showed that when the clinical ASL does not have the spatial resolution to differentiate the retinal and choroidal blood flows, the obtained measurements are dominated by the latter vascular blood flow.

A similar but separate study was performed on 5 healthy subjects under normal and hypercapnia conditions [139]. Eye fixation and queued breathing techniques were employed to minimize the motion artefact. The ASL labelling plane was placed 7 cm below the optic nerve, and ASL background suppression was also employed. The background suppression pulse timing for ASL of the human retina is investigated in depth and optimized in a later publication [90]. Here it was measured that the group-averaged peak blood flow value was at 93 ± 31 mL/(100 mL min). Furthermore, profiles of blood flow from sclera to vitreous and across the thickness of the retina showed that under hypercapnia condition flows were increased from 93 ± 31 to 104 ± 35 mL/(100 mL min).

One study investigated the levels of blood perfusion in retina during rest and exercise [140]. This study used a 3 T magnet combined with a custom-made surface coil and a pCASL pulse sequence. Using this ASL setup and measuring four young healthy volunteers, it was found that, compared to the resting state (60 ± 5 beats per minute and arterial pressure of 78 ± 5 mmHg), the retinal blood perfusion increased by 25% ± 7% and ocular perfusion pressure increased by 25% ± 6% in the exercise mode.

The same authors investigate the patients suffering from retinitis pigmentosa with similar ASL implementation [141]. The authors measured basal blood flow of 142 ± 16 mL/100 mL/min (or 1.14 ± 0.13 $\mu L/mm^2/min$) in the posterior retinal-choroid in the control group and 70 ± 19 mL/100 mL/min (or 0.56 ± 0.15 $\mu L/mm^2/min$) in the retinitis pigmentosa group. This revealed a significant reduction of blood perfusion in patients compared to controls.

A recent study looked at the effect of aging on choroidal blood circulation, using pCASL and 3 T magnet, scanning 17 normal subjects (24–68 years old) [142]. This study found that choroidal blood flow was negatively correlated with age, declining 2.7 mL/100 mL/min each year, while it was not correlated with perfusion pressure, arterial pressure, or intraocular pressure. This age dependence of choroidal perfusion was only observed in central retina, but not at its periphery.

5. Conclusion

ASL is a versatile and noninvasive imaging technique that is used to estimate tissue perfusion without the use of endogenous tracers. Although the main application of ASL remains the measurement of cerebral blood perfusion, this technique is gradually being adopted in other organs as well. Owing to the nature of the tissues, noninvasive techniques are required to assess pathologies of the eye. While other MRI-based techniques such as T1 and T2 weighted imaging [143], diffusion tensor imaging [144, 145], and contrast-enhanced imaging [146–148] have been used to look at the dynamic physiology of the ocular tissue, ASL shows promise as a technique to assess pathologies of the retina. Here at the University of Auckland, we are implementing new pCASL modalities in our Siemens SKYRA 3 T magnet. While we are still optimizing our approach, our preliminary data are promising (Figure 4).

We are aiming to study the blood perfusion of the retina in healthy and diseased subjects, by using our optimized ASL

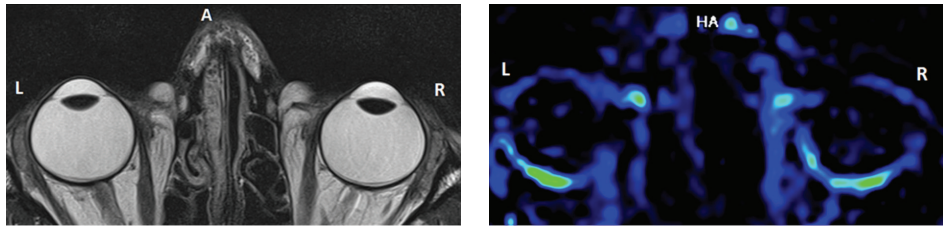

(a) (b)

Figure 4: (a) High resolution T2 weighted anatomical image, used to locate the tissue of interest (i.e., the retina) in order to apply the ASL sequence. (b) The perfusion-weighted image calculated from the application of 2D ASL sequence. The choroid layer in the back of the eye is clearly highlighted, showing the detection of blood perfusion into this vasculature bed.

routine in the very near future. This review article sets the scene for our upcoming research articles, presenting novel research into ocular perfusion.

Competing Interests

The authors of this paper do not have any association with a commercial organisation or any financial interest in a product that may give rise to the perception of a potential conflict of interests.

Acknowledgments

The authors wish to thank Dr. Monica Acosta from the Department of Physiology, University of Auckland, for her insights into compilation of this paper.

References

[1] J. D. Reynolds and S. E. Olitsky, *Pediatric Retina*, Springer, 2010.

[2] A. Lens, S. C. Nemeth, and J. K. Ledford, *Ocular Anatomy and Physiology*, SLACK Incorporated, Thorofare, NJ, USA, 2008.

[3] D. Abramson, *Blood Vessels and Lymphatics in Organ Systems*, Academic Press, 2012.

[4] H. R. Zhang, "Scanning electron-microscopic study of corrosion casts on retinal and choroidal angioarchitecture in man and animals," *Progress in Retinal and Eye Research*, vol. 13, no. 1, pp. 243–270, 1994.

[5] J. W. Kiel, *The Ocular Circulation*, Integrated Systems Physiology: From Molecule to Function to Disease, Morgan & Claypool Life Sciences, San Rafael, Calif, USA, 2010.

[6] C. J. Pournaras, E. Rungger-Brändle, C. E. Riva, S. H. Hardarson, and E. Stefansson, "Regulation of retinal blood flow in health and disease," *Progress in Retinal and Eye Research*, vol. 27, no. 3, pp. 284–330, 2008.

[7] G.-H. Jahng, K.-L. Li, L. Ostergaard, and F. Calamante, "Perfusion magnetic resonance imaging: a comprehensive update on principles and techniques," *Korean Journal of Radiology*, vol. 15, no. 5, pp. 554–577, 2014.

[8] P. B. Barker, X. Golay, and G. Zaharchuk, *Clinical Perfusion MRI: Techniques and Applications*, Cambridge University Press, 2013.

[9] J. G. Webster, *The Physiological Measurement Handbook*, CRC Press, Philadelphia, Pa, USA, 2014.

[10] J. G. Cunha-Vaz, *Diabetic Retinopathy*, World Scientific, 2011.

[11] G. Mariani, L. Bruselli, T. Kuwert et al., "A review on the clinical uses of SPECT/CT," *European Journal of Nuclear Medicine and Molecular Imaging*, vol. 37, no. 10, pp. 1959–1985, 2010.

[12] S. M. Eleff, M. D. Schnall, L. Ligetti et al., "Concurrent measurements of cerebral blood flow, sodium, lactate, and high-energy phosphate metabolism using 19F, 23Na, 1H, and 31P nuclear magnetic resonance spectroscopy," *Magnetic Resonance in Medicine*, vol. 7, no. 4, pp. 412–424, 1988.

[13] J. A. Detre, V. H. Subramanian, M. D. Mitchell et al., "Measurement of regional cerebral blood flow in cat brain using intracarotid $2H_2O$ and ^2H NMR imaging," *Magnetic Resonance in Medicine*, vol. 14, no. 2, pp. 389–395, 1990.

[14] J. J. H. Ackerman, C. S. Ewy, N. N. Becker, and R. A. Shalwitz, "Deuterium nuclear magnetic resonance measurements of blood flow and tissue perfusion employing $2H_2O$ as a freely diffusible tracer," *Proceedings of the National Academy of Sciences of the United States of America*, vol. 84, no. 12, pp. 4099–4102, 1987.

[15] J. A. Detre, J. S. Leigh, D. S. Williams, and A. P. Koretsky, "Perfusion imaging," *Magnetic Resonance in Medicine*, vol. 23, no. 1, pp. 37–45, 1992.

[16] D. S. Williams, J. A. Detre, J. S. Leigh, A. P. Koretsky, and D. S. Williams, "Magnetic resonance imaging of perfusion using spin inversion of arterial water," *Proceedings of the National Academy of Sciences of the United States of America*, vol. 89, no. 1, pp. 212–216, 1992.

[17] A. Li, C. S. Wong, M. K. Wong, C. M. Lee, and M. C. Au Yeung, "Acute adverse reactions to magnetic resonance contrast media—gadolinium chelates," *British Journal of Radiology*, vol. 79, no. 941, pp. 368–371, 2006.

[18] S. Paradiso, D. L. Johnson, N. C. Andreasen et al., "Cerebral blood flow changes associated with attribution of emotional valence to pleasant, unpleasant, and neutral visual stimuli in a PET study of normal subjects," *American Journal of Psychiatry*, vol. 156, no. 10, pp. 1618–1629, 1999.

[19] A. Longo, M. Geiser, and C. E. Riva, "Subfoveal choroidal blood flow in response to light-dark exposure," *Investigative Ophthalmology and Visual Science*, vol. 41, no. 9, pp. 2678–2683, 2000.

[20] G. Fuchsjäger-Mayrl, E. Polska, M. Malec, and L. Schmetterer, "Unilateral light-dark transitions affect choroidal blood flow in both eyes," *Vision Research*, vol. 41, no. 22, pp. 2919–2924, 2001.

[21] D. C. Alsop, J. A. Detre, X. Golay et al., "Recommended implementation of arterial spin-labeled Perfusion MRI for clinical applications: a consensus of the ISMRM perfusion study group and the European consortium for ASL in dementia," *Magnetic Resonance in Medicine*, vol. 73, no. 1, pp. 102–116, 2015.

[22] S. Aslan, F. Xu, P. L. Wang et al., "Estimation of labeling efficiency in pseudocontinuous arterial spin labeling," *Magnetic Resonance in Medicine*, vol. 63, no. 3, pp. 765–771, 2010.

[23] M. A. Brown and R. C. Semelka, *MRI: Basic Principles and Applications*, John Wiley & Sons, Hoboken, NJ, USA, 2003.

[24] E. T. Petersen, I. Zimine, Y.-C. L. Ho, and X. Golay, "Non-invasive measurement of perfusion: a critical review of arterial spin labelling techniques," *British Journal of Radiology*, vol. 79, no. 944, pp. 688–701, 2006.

[25] D. C. Alsop, J. A. Detre, and M. Grossman, "Assessment of cerebral blood flow in Alzheimer's disease by spin-labeled magnetic resonance imaging," *Annals of Neurology*, vol. 47, no. 1, pp. 93–100, 2000.

[26] N. A. Johnson, G.-H. Jahng, M. W. Weiner et al., "Pattern of cerebral hypoperfusion in Alzheimer disease and mild cognitive impairment measured with arterial spin-labeling MR imaging: initial experience," *Radiology*, vol. 234, no. 3, pp. 851–859, 2005.

[27] A. T. Du, G. H. Jahng, S. Hayasaka et al., "Hypoperfusion in frontotemporal dementia and Alzheimer disease by arterial spin labeling MRI," *Neurology*, vol. 67, no. 7, pp. 1215–1220, 2006.

[28] W. T. Hu, Z. Wang, V. M.-Y. Lee, J. Q. Trojanowski, J. A. Detre, and M. Grossman, "Distinct cerebral perfusion patterns in FTLD and AD," *Neurology*, vol. 75, no. 10, pp. 881–888, 2010.

[29] R. L. Wolf, D. C. Alsop, I. Levy-Reis et al., "Detection of mesial temporal lobe hypoperfusion in patients with temporal lobe epilepsy by use of arterial spin labeled perfusion MR imaging," *American Journal of Neuroradiology*, vol. 22, no. 7, pp. 1334–1341, 2001.

[30] S. Lui, L. M. Parkes, X. Huang et al., "Depressive disorders: focally altered cerebral perfusion measured with arterial spin-labeling MR imaging," *Radiology*, vol. 251, no. 2, pp. 476–484, 2009.

[31] Y.-M. Lim, Y.-W. Cho, S. Shamim et al., "Usefulness of pulsed arterial spin labeling MR imaging in mesial temporal lobe epilepsy," *Epilepsy Research*, vol. 82, no. 2-3, pp. 183–189, 2008.

[32] B. Duhameau, J.-C. Ferré, P. Jannin et al., "Chronic and treatment-resistant depression: a study using arterial spin labeling perfusion MRI at 3 Tesla," *Psychiatry Research. Neuroimaging*, vol. 182, no. 2, pp. 111–116, 2010.

[33] L. Scheef, C. Manka, M. Daamen et al., "Resting-state perfusion in nonmedicated schizophrenic patients: a continuous arterial spin-labeling 3.0-T MR study," *Radiology*, vol. 256, no. 1, pp. 253–260, 2010.

[34] K. J. Black, J. M. Koller, M. C. Campbell, D. A. Gusnard, and S. I. Bandak, "Quantification of indirect pathway inhibition by the adenosine A_{2a} antagonist SYN115 in Parkinson disease," *The Journal of Neuroscience*, vol. 30, no. 48, pp. 16284–16292, 2010.

[35] R. W. Freudenmann, M. Kölle, A. Huwe et al., "Delusional infestation: neural correlates and antipsychotic therapy investigated by multimodal neuroimaging," *Progress in Neuro-Psychopharmacology and Biological Psychiatry*, vol. 34, no. 7, pp. 1215–1222, 2010.

[36] I. R. Olson, H. Rao, K. S. Moore, J. Wang, J. A. Detre, and G. K. Aguirre, "Using perfusion fMRI to measure continuous changes in neural activity with learning," *Brain and Cognition*, vol. 60, no. 3, pp. 262–271, 2006.

[37] J. Wang, H. Rao, G. S. Wetmore et al., "Perfusion functional MRI reveals cerebral blood flow pattern under psychological stress," *Proceedings of the National Academy of Sciences of the United States of America*, vol. 102, no. 49, pp. 17804–17809, 2005.

[38] J. Wang, M. Korczykowski, H. Rao et al., "Gender difference in neural response to psychological stress," *Social Cognitive and Affective Neuroscience*, vol. 2, no. 3, pp. 227–239, 2007.

[39] J. Lim, W.-C. Wu, J. Wang, J. A. Detre, D. F. Dinges, and H. Rao, "Imaging brain fatigue from sustained mental workload: an ASL perfusion study of the time-on-task effect," *NeuroImage*, vol. 49, no. 4, pp. 3426–3435, 2010.

[40] S. J. Gillihan, H. Rao, J. Wang et al., "Serotonin transporter genotype modulates amygdala activity during mood regulation," *Social Cognitive and Affective Neuroscience*, vol. 5, no. 1, pp. 1–10, 2009.

[41] D. J. J. Wang, H. Rao, M. Korczykowski et al., "Cerebral blood flow changes associated with different meditation practices and perceived depth of meditation," *Psychiatry Research: Neuroimaging*, vol. 191, no. 1, pp. 60–67, 2011.

[42] H. Rao, J. Wang, K. Tang, W. Pan, and J. A. Detre, "Imaging brain activity during natural vision using CASL perfusion fMRI," *Human Brain Mapping*, vol. 28, no. 7, pp. 593–601, 2007.

[43] J. M. Pollock, A. R. Deibler, J. H. Burdette et al., "Migraine associated cerebral hyperperfusion with arterial spin-labeled MR imaging," *American Journal of Neuroradiology*, vol. 29, no. 8, pp. 1494–1497, 2008.

[44] J. M. Pollock, A. R. Deibler, T. G. West, J. H. Burdette, R. A. Kraft, and J. A. Maldjian, "Arterial spin-labeled magnetic resonance imaging in hyperperfused seizure focus: a case report," *Journal of Computer Assisted Tomography*, vol. 32, no. 2, pp. 291–292, 2008.

[45] M. A. Griswold, P. M. Jakob, R. M. Heidemann et al., "Generalized autocalibrating partially parallel acquisitions (GRAPPA)," *Magnetic Resonance in Medicine*, vol. 47, no. 6, pp. 1202–1210, 2002.

[46] E. T. Petersen, K. Mouridsen, and X. Golay, "The QUASAR reproducibility study, part II: results from a multi-center arterial spin labeling test-retest study," *NeuroImage*, vol. 49, no. 1, pp. 104–113, 2010.

[47] J. Wang, D. J. Licht, G.-H. Jahng et al., "Pediatric perfusion imaging using pulsed arterial spin labeling," *Journal of Magnetic Resonance Imaging*, vol. 18, no. 4, pp. 404–413, 2003.

[48] K. K. Oguz, X. Golay, F. B. Pizzini et al., "Sickle cell disease: continuous arterial spin-labeling perfusion MR imaging in children," *Radiology*, vol. 227, no. 2, pp. 567–574, 2003.

[49] W.-C. Wu, E. Mohler III, S. J. Ratcliffe, F. W. Wehrli, J. A. Detre, and T. F. Floyd, "Skeletal muscle microvascular flow in progressive peripheral artery disease: assessment with continuous arterial spin-labeling perfusion magnetic resonance imaging," *Journal of the American College of Cardiology*, vol. 53, no. 25, pp. 2372–2377, 2009.

[50] S. Warach, J. F. Dashe, and R. R. Edelman, "Clinical outcome in ischemic stroke predicted by early diffusion-weighted and perfusion magnetic resonance imaging: a preliminary analysis," *Journal of Cerebral Blood Flow and Metabolism*, vol. 16, no. 1, pp. 53–59, 1996.

[51] J. A. Chalela, D. C. Alsop, J. B. Gonzalez-Atavales, J. A. Maldjian, S. E. Kasner, and J. A. Detre, "Magnetic resonance perfusion imaging in acute ischemic stroke using continuous arterial spin labeling," *Stroke*, vol. 31, no. 3, pp. 680–687, 2000.

[52] D. A. Roberts, J. A. Detre, L. Bolinger et al., "Renal perfusion in humans: MR imaging with spin tagging of arterial water," *Radiology*, vol. 196, no. 1, pp. 281–286, 1995.

[53] R. L. Wolf, J. Wang, S. Wang et al., "Grading of CNS neoplasms using continuous arterial spin labeled perfusion MR imaging at

3 Tesla," *Journal of Magnetic Resonance Imaging*, vol. 22, no. 4, pp. 475–482, 2005.

[54] T. Noguchi, T. Yoshiura, A. Hiwatashi et al., "Perfusion imaging of brain tumors using arterial spin-labeling: correlation with histopathologic vascular density," *American Journal of Neuroradiology*, vol. 29, no. 4, pp. 688–693, 2008.

[55] M.-A. Weber, M. Günther, M. P. Lichy et al., "Comparison of arterial spin-labeling techniques and dynamic susceptibility-weighted contrast-enhanced MRI in perfusion imaging of normal brain tissue," *Investigative Radiology*, vol. 38, no. 11, pp. 712–718, 2003.

[56] M.-A. Weber, C. Thilmann, M. P. Lichy et al., "Assessment of irradiated brain metastases by means of arterial spin-labeling and dynamic susceptibility-weighted contrast-enhanced perfusion MRI: initial results," *Investigative Radiology*, vol. 39, no. 5, pp. 277–287, 2004.

[57] D. J. J. Wang, J. R. Alger, J. X. Qiao et al., "The value of arterial spin-labeled perfusion imaging in acute ischemic stroke: comparison with dynamic susceptibility contrast-enhanced MRI," *Stroke*, vol. 43, no. 4, pp. 1018–1024, 2012.

[58] R. P. Bokkers, J. P. Bremmer, B. N. van Berckel et al., "Arterial spin labeling perfusion MRI at multiple delay times: a correlative study with $H_2{}^{15}O$ positron emission tomography in patients with symptomatic carotid artery occlusion," *Journal of Cerebral Blood Flow & Metabolism*, vol. 30, no. 1, pp. 222–229, 2009.

[59] G. Xu, H. A. Rowley, G. Wu et al., "Reliability and precision of pseudo-continuous arterial spin labeling perfusion MRI on 3.0 T and comparison with ^{15}O-water PET in elderly subjects at risk for Alzheimer's disease," *NMR in Biomedicine*, vol. 23, no. 3, pp. 286–293, 2010.

[60] K. K. Kwong, D. A. Chesler, R. M. Weisskoff et al., "MR perfusion studies with T1-weighted echo planar imaging," *Magnetic Resonance in Medicine*, vol. 34, no. 6, pp. 878–887, 1995.

[61] V. W. Y. Wong, T. Y. Y. Lai, P. T. H. Lam, and D. S. C. Lam, "Prioritization of cataract surgery: visual analogue scale versus scoring system," *ANZ Journal of Surgery*, vol. 75, no. 7, pp. 587–592, 2005.

[62] W. Dai, D. Garcia, C. De Bazelaire, and D. C. Alsop, "Continuous flow-driven inversion for arterial spin labeling using pulsed radio frequency and gradient fields," *Magnetic Resonance in Medicine*, vol. 60, no. 6, pp. 1488–1497, 2008.

[63] E. R. Muir, *Magnetic resonance imaging of retinal physiology and anatomy in mice [Ph.D. thesis]*, Georgia Institute of Technology, Atlanta, Ga, USA, 2010.

[64] H. Kolb, "Simple anatomy of the retina," in *Webvision: The Organization of the Retina and Visual System*, H. Kolb, E. Fernandez, and R. Nelson, Eds., University of Utah Health Sciences, Salt Lake City, Utah, USA, 1995.

[65] S. Gevers, M. J. van Osch, R. P. H. Bokkers et al., "Intra- and multicenter reproducibility of pulsed, continuous and pseudo-continuous arterial spin labeling methods for measuring cerebral perfusion," *Journal of Cerebral Blood Flow and Metabolism*, vol. 31, no. 8, pp. 1706–1715, 2011.

[66] S.-G. Kim, "Quantification of relative cerebral blood flow change by flow-sensitive alternating inversion recovery (FAIR) technique: Application to functional mapping," *Magnetic Resonance in Medicine*, vol. 34, no. 3, pp. 293–301, 1995.

[67] E. C. Wong, R. B. Buxton, and L. R. Frank, "Implementation of quantitative perfusion imaging techniques for functional brain mapping using pulsed arterial spin labeling," *NMR in Biomedicine*, vol. 10, no. 4-5, pp. 237–249, 1997.

[68] R. R. Edelman and Q. Chen, "EPISTAR MRI: multislice mapping of cerebral blood flow," *Magnetic Resonance in Medicine*, vol. 40, no. 6, pp. 800–805, 1998.

[69] J. Wang, D. C. Alsop, L. Li et al., "Comparison of quantitative perfusion imaging using arterial spin labeling at 1.5 and 4.0 Tesla," *Magnetic Resonance in Medicine*, vol. 48, no. 2, pp. 242–254, 2002.

[70] J. Wang, Y. Zhang, R. L. Wolf, A. C. Roc, D. C. Alsop, and J. A. Detre, "Amplitude-modulated continuous arterial spin-labeling 3.0-T perfusion MR imaging with a single coil: feasibility study," *Radiology*, vol. 235, no. 1, pp. 218–228, 2005.

[71] E. C. Wong, R. B. Buxton, and L. R. Frank, "A theoretical and experimental comparison of continuous and pulsed arterial spin labeling techniques for quantitative perfusion imaging," *Magnetic Resonance in Medicine*, vol. 40, no. 3, pp. 348–355, 1998.

[72] B. Roy, R. Awasthi, A. Bindal et al., "Comparative evaluation of 3-dimensional pseudocontinuous arterial spin labeling with dynamic contrast-enhanced perfusion magnetic resonance imaging in grading of human glioma," *Journal of Computer Assisted Tomography*, vol. 37, no. 3, pp. 321–326, 2013.

[73] L. E. Nordin, T.-Q. Li, J. Brogren et al., "Cortical responses to amphetamine exposure studied by pCASL MRI and pharmacokinetic/pharmacodynamic dose modeling," *NeuroImage*, vol. 68, pp. 75–82, 2013.

[74] W.-M. Luh, S. L. Talagala, T.-Q. Li, and P. A. Bandettini, "Pseudo-continuous arterial spin labeling at 7 T for human brain: estimation and correction for off-resonance effects using a Prescan," *Magnetic Resonance in Medicine*, vol. 69, no. 2, pp. 402–410, 2013.

[75] J. M. Pollock, H. Tan, R. A. Kraft, C. T. Whitlow, J. H. Burdette, and J. A. Maldjian, "Arterial spin-labeled MR perfusion imaging: clinical applications," *Magnetic Resonance Imaging Clinics of North America*, vol. 17, no. 2, pp. 315–338, 2009.

[76] X. Golay and E. T. Petersen, "Arterial spin labeling: benefits and pitfalls of high magnetic field," *Neuroimaging Clinics of North America*, vol. 16, no. 2, pp. 259–268, 2006.

[77] K. P. Pruessmann, M. Weiger, M. B. Scheidegger, and P. Boesiger, "SENSE: sensitivity encoding for fast MRI," *Magnetic Resonance in Medicine*, vol. 42, no. 5, pp. 952–962, 1999.

[78] T. Q. Duong and E. R. Muir, "Magnetic resonance imaging of the retina," *Japanese Journal of Ophthalmology*, vol. 53, no. 4, pp. 352–367, 2009.

[79] H. Raoult, J. Petr, E. Bannier et al., "Arterial spin labeling for motor activation mapping at 3T with a 32-channel coil: reproducibility and spatial accuracy in comparison with BOLD fMRI," *NeuroImage*, vol. 58, no. 1, pp. 157–167, 2011.

[80] H. Raoult, J.-Y. Gauvrit, J. Petr et al., "Innovations in functional MR imaging of the brain: arterial spin labeling and diffusion," *Journal de Radiologie*, vol. 92, no. 10, pp. 878–888, 2011.

[81] T. Tjandra, J. C. W. Brooks, P. Figueiredo, R. Wise, P. M. Matthews, and I. Tracey, "Quantitative assessment of the reproducibility of functional activation measured with BOLD and MR perfusion imaging: implications for clinical trial design," *NeuroImage*, vol. 27, no. 2, pp. 393–401, 2005.

[82] S.-H. Park, D. J. J. Wang, and T. Q. Duong, "Balanced steady state free precession for arterial spin labeling MRI: initial experience for blood flow mapping in human brain, retina, and kidney," *Magnetic Resonance Imaging*, vol. 31, no. 7, pp. 1044–1050, 2013.

[83] A. R. Deibler, J. M. Pollock, R. A. Kraft, H. Tan, J. H. Burdette, and J. A. Maldjian, "Arterial spin-labeling in routine clinical

practice, part 1: technique and artifacts," *American Journal of Neuroradiology*, vol. 29, no. 7, pp. 1228–1234, 2008.

[84] A. R. Deibler, J. M. Pollock, R. A. Kraft, H. Tan, J. H. Burdette, and J. A. Maldjian, "Arterial spin-labeling in routine clinical practice, part 2: hypoperfusion patterns," *American Journal of Neuroradiology*, vol. 29, no. 7, pp. 1235–1241, 2008.

[85] A. R. Deibler, J. M. Pollock, R. A. Kraft, H. Tan, J. H. Burdette, and J. A. Maldjian, "Arterial spin-labeling in routine clinical practice. Part 3. Hyperperfusion patterns," *American Journal of Neuroradiology*, vol. 29, no. 8, pp. 1428–1435, 2008.

[86] W. T. Dixon, M. Sardashti, M. Castillo, and G. P. Stomp, "Multiple inversion recovery reduces static tissue signal in angiograms," *Magnetic Resonance in Medicine*, vol. 18, no. 2, pp. 257–268, 1991.

[87] F. Q. Ye, J. A. Frank, D. R. Weinberger, and A. C. McLaughlin, "Noise reduction in 3D perfusion imaging by attenuating the static signal in arterial spin tagging (ASSIST)," *Magnetic Resonance in Medicine*, vol. 44, no. 1, pp. 92–100, 2000.

[88] D. M. Garcia, G. Duhamel, and D. C. Alsop, "Efficiency of inversion pulses for background suppressed arterial spin labeling," *Magnetic Resonance in Medicine*, vol. 54, no. 2, pp. 366–372, 2005.

[89] W. Dai, P. M. Robson, A. Shankaranarayanan, and D. C. Alsop, "Reduced resolution transit delay prescan for quantitative continuous arterial spin labeling perfusion imaging," *Magnetic Resonance in Medicine*, vol. 67, no. 5, pp. 1252–1265, 2012.

[90] N. Maleki, W. Dai, and D. C. Alsop, "Optimization of background suppression for arterial spin labeling perfusion imaging," *Magnetic Resonance Materials in Physics, Biology and Medicine*, vol. 25, no. 2, pp. 127–133, 2012.

[91] J. B. Hickam, H. O. Sieker, and R. Frayser, "Studies of retinal circulation and AV oxygen difference in man," *Transactions of the American Clinical and Climatological Association*, vol. 71, pp. 34–44, 1960.

[92] J. B. Hickam and R. Frayser, "Studies of the retinal circulation in man: observations on vessel diameter, arteriovenous oxygen difference, and mean circulation time," *Circulation*, vol. 33, no. 2, pp. 302–316, 1966.

[93] F. C. Delori, "Noninvasive technique for oximetry of blood in retinal vessels," *Applied Optics*, vol. 27, no. 6, pp. 1113–1125, 1988.

[94] A. Alm and A. Bill, "Ocular and optic nerve blood flow at normal and increased intraocular pressures in monkeys (*Macaca irus*): a study with radioactively labelled microspheres including flow determinations in brain and some other tissues," *Experimental Eye Research*, vol. 15, no. 1, pp. 15–29, 1973.

[95] N. D. Wangsa-Wirawan and R. A. Linsenmeier, "Retinal oxygen: fundamental and clinical aspects," *Archives of Ophthalmology*, vol. 121, no. 4, pp. 547–557, 2003.

[96] C. Delaey and J. Van de Voorde, "Regulatory mechanisms in the retinal and choroidal circulation," *Ophthalmic Research*, vol. 32, no. 6, pp. 249–256, 2000.

[97] Y. Tamaki, M. Araie, E. Kawamoto, S. Eguchi, and H. Fujii, "Non-contact, two-dimensional measurement of tissue circulation in choroid and optic nerve head using laser speckle phenomenon," *Experimental Eye Research*, vol. 60, no. 4, pp. 373–383, 1995.

[98] M. Kim, S. S. Kim, H. J. Kwon, H. J. Koh, and S. C. Lee, "Association between choroidal thickness and ocular perfusion pressure in young, healthy subjects: enhanced depth imaging optical coherence tomography study," *Investigative Ophthalmology and Visual Science*, vol. 53, no. 12, pp. 7710–7717, 2012.

[99] D. J. Coleman, R. H. Silverman, A. Chabi et al., "High-resolution ultrasonic imaging of the posterior segment," *Ophthalmology*, vol. 111, no. 7, pp. 1344–1351, 2004.

[100] Y. Jia, S. T. Bailey, D. J. Wilson et al., "Quantitative optical coherence tomography angiography of choroidal neovascularization in age-related macular degeneration," *Ophthalmology*, vol. 121, no. 7, pp. 1435–1444, 2014.

[101] Y. Jia, E. Wei, X. Wang et al., "Optical coherence tomography angiography of optic disc perfusion in glaucoma," *Ophthalmology*, vol. 121, no. 7, pp. 1322–1332, 2014.

[102] Y. Wang, B. A. Bower, J. A. Izatt, O. Tan, and D. Huang, "Retinal blood flow measurement by circumpapillary Fourier domain Doppler optical coherence tomography," *Journal of Biomedical Optics*, vol. 13, no. 6, Article ID 064003, 2008.

[103] B. Baumann, B. Potsaid, M. F. Kraus et al., "Total retinal blood flow measurement with ultrahigh speed swept source/Fourier domain OCT," *Biomedical Optics Express*, vol. 2, no. 6, pp. 1539–1552, 2011.

[104] J. M. Harazny, U. Raff, J. Welzenbach et al., "New software analyses increase the reliability of measurements of retinal arterioles morphology by scanning laser Doppler flowmetry in humans," *Journal of Hypertension*, vol. 29, no. 4, pp. 777–782, 2011.

[105] V. A. Alder, J. Ben-Nun, and S. J. Cringle, "PO2 profiles and oxygen consumption in cat retina with an occluded retinal circulation," *Investigative Ophthalmology and Visual Science*, vol. 31, no. 6, pp. 1029–1034, 1990.

[106] R. G. Buttery, C. F. L. Hinrichsen, W. L. Weller, and J. R. Haight, "How thick should a retina be? A comparative study of mammalian species with and without intraretinal vasculature," *Vision Research*, vol. 31, no. 2, pp. 169–187, 1991.

[107] V. Patel, S. Rassam, R. Newsom, J. Wiek, and E. Kohner, "Retinal blood flow in diabetic retinopathy," *British Medical Journal*, vol. 305, no. 6855, pp. 678–683, 1992.

[108] E. M. Kohner, V. Patel, and M. B. Salwan, "Role of blood flow and impaired autoregulation in the pathogenesis of diabetic retinopathy," *Diabetes*, vol. 44, no. 6, pp. 603–607, 1995.

[109] A. P. Adamis, J. W. Miller, M.-T. Bernal et al., "Increased vascular endothelial growth factor levels in the vitreous of eyes with proliferative diabetic retinopathy," *American Journal of Ophthalmology*, vol. 118, no. 4, pp. 445–450, 1994.

[110] T. Kawagishi, Y. Nishizawa, M. Emoto et al., "Impaired retinal artery blood flow in IDDM patients before clinical manifestations of diabetic retinopathy," *Diabetes Care*, vol. 18, no. 12, pp. 1544–1549, 1995.

[111] S. Konno, G. T. Feke, A. Yoshida, N. Fujio, D. G. Goger, and S. M. Buzney, "Retinal blood flow changes in type I diabetes. A long-term, follow-up study," *Investigative Ophthalmology and Visual Science*, vol. 37, no. 6, pp. 1140–1148, 1996.

[112] A. C. Clermont, L. P. Aiello, F. Mori, L. M. Aiello, and S.-E. Bursell, "Vascular endothelial growth factor and severity of nonproliferative diabetic retinopathy mediate retinal hemodynamics in vivo: a potential role for vascular endothelial growth factor in the progression of nonproliferative diabetic retinopathy," *American Journal of Ophthalmology*, vol. 124, no. 4, pp. 433–446, 1997.

[113] G. T. Feke, H. Tagawa, A. Yoshida et al., "Retinal circulatory changes related to retinopathy progression in insulin-dependent diabetes mellitus," *Ophthalmology*, vol. 92, no. 11, pp. 1517–1522, 1985.

[114] J. E. Grunwald, C. E. Riva, S. H. Sinclair, A. J. Brucker, and B. L. Petrig, "Laser Doppler velocimetry study of retinal circulation

in diabetes mellitus," *Archives of Ophthalmology*, vol. 104, no. 7, pp. 991–996, 1986.

[115] D. Gherghel, S. Orgül, K. Gugleta, M. Gekkieva, and J. Flammer, "Relationship between ocular perfusion pressure and retrobulbar blood flow in patients with glaucoma with progressive damage," *American Journal of Ophthalmology*, vol. 130, no. 5, pp. 597–605, 2000.

[116] C. M. Yancey and R. A. Linsenmeier, "Oxygen distribution and consumption in the cat retina at increased intraocular pressure," *Investigative Ophthalmology and Visual Science*, vol. 30, no. 4, pp. 600–611, 1989.

[117] C. E. Riva, J. E. Grunwald, and B. L. Petrig, "Autoregulation of human retinal blood flow. An investigation with laser doppler velocimetry," *Investigative Ophthalmology and Visual Science*, vol. 27, no. 12, pp. 1706–1712, 1986.

[118] J. Chen and L. E. H. Smith, "Retinopathy of prematurity," *Angiogenesis*, vol. 10, no. 2, pp. 133–140, 2007.

[119] N. Ashton, "Pathological basis of retrolental fibroplasia," *British Journal of Ophthalmology*, vol. 38, no. 7, pp. 385–396, 1954.

[120] V. E. Kinsey, H. J. Arnold, R. E. Kalina et al., "PaO_2 levels and retrolental fibroplasia: a report of the cooperative study," *Pediatrics*, vol. 60, no. 5, pp. 655–668, 1977.

[121] E. J. Chung, J. H. Kim, H. S. Ahn, and H. J. Koh, "Combination of laser photocoagulation and intravitreal bevacizumab (Avastin®) for aggressive zone I retinopathy of prematurity," *Graefe's Archive for Clinical and Experimental Ophthalmology*, vol. 245, no. 11, pp. 1727–1730, 2007.

[122] C. D. Regillo and W. E. Benson, *Retinal Detachment: Diagnosis and Management*, Lippincott-Raven, 1998.

[123] A. Gaudric, M. Sterkers, and G. Coscas, "Retinal detachment after choroidal ischemia," *American Journal of Ophthalmology*, vol. 104, no. 4, pp. 364–372, 1987.

[124] E. R. Muir, R. C. Rentería, and T. Q. Duong, "Reduced ocular blood flow as an early indicator of diabetic retinopathy in a mouse model of diabetes," *Investigative Ophthalmology and Visual Science*, vol. 53, no. 10, pp. 6488–6494, 2012.

[125] E. R. Muir, B. De La Garza, and T. Q. Duong, "Blood flow and anatomical MRI in a mouse model of retinitis pigmentosa," *Magnetic Resonance in Medicine*, vol. 69, no. 1, pp. 221–228, 2013.

[126] Y.-Y. I. Shih, L. Wang, B. H. De La Garza et al., "Quantitative retinal and choroidal blood flow during light, dark adaptation and flicker light stimulation in rats using fluorescent microspheres," *Current Eye Research*, vol. 38, no. 2, pp. 292–298, 2013.

[127] G. Li, B. De La Garza, Y.-Y. I. Shih, E. R. Muir, and T. Q. Duong, "Layer-specific blood-flow MRI of retinitis pigmentosa in RCS rats," *Experimental Eye Research*, vol. 101, pp. 90–96, 2012.

[128] G. Li, Y.-Y. I. Shih, J. W. Kiel, B. De La Garza, F. Du, and T. Q. Duong, "MRI study of cerebral, retinal and choroidal blood flow responses to acute hypertension," *Experimental Eye Research*, vol. 112, pp. 118–124, 2013.

[129] Y. Zhang, H.-Y. Wey, O. S. E. Nateras, Q. Peng, B. H. De La Garza, and T. Q. Duong, "Anatomical, blood oxygenation level-dependent, and blood flow MRI of nonhuman primate (baboon) retina," *Magnetic Resonance in Medicine*, vol. 66, no. 2, pp. 546–554, 2011.

[130] N. Maleki, W. Dai, and D. C. Alsop, "Blood flow quantification of the human retina with MRI," *NMR in Biomedicine*, vol. 24, no. 1, pp. 104–111, 2011.

[131] A. Lemke, F. B. Laun, D. Simon, B. Stieltjes, and L. R. Schad, "An in vivo verification of the intravoxel incoherent motion effect in diffusion-weighted imaging of the abdomen," *Magnetic Resonance in Medicine*, vol. 64, no. 6, pp. 1580–1585, 2010.

[132] J. V. Hajnal, D. J. Bryant, L. Kasuboski et al., "Use of fluid attenuated inversion recovery (FLAIR) pulse sequences in MRI of the brain," *Journal of Computer Assisted Tomography*, vol. 16, no. 6, pp. 841–844, 1992.

[133] R. B. Buxton, L. R. Frank, E. C. Wong, B. Siewert, S. Warach, and R. R. Edelman, "A general kinetic model for quantitative perfusion imaging with arterial spin labeling," *Magnetic Resonance in Medicine*, vol. 40, no. 3, pp. 383–396, 1998.

[134] K. Zierler, "A critique of compartmental analysis," *Annual Review of Biophysics and Bioengineering*, vol. 10, no. 1, pp. 531–562, 1981.

[135] P. Herscovitch and M. E. Raichle, "What is the correct value for the brain-blood partition coefficient for water?" *Journal of Cerebral Blood Flow and Metabolism*, vol. 5, no. 1, pp. 65–69, 1985.

[136] H. Lu, C. Clingman, X. Golay, and P. C. M. van Zijl, "Determining the longitudinal relaxation time (T1) of blood at 3.0 Tesla," *Magnetic Resonance in Medicine*, vol. 52, no. 3, pp. 679–682, 2004.

[137] N. Maleki, W. Dai, and D. C. Alsop, "A systematic approach to optimizing background suppression for arterial spin labeling perfusion imaging," *Proceedings of the International Society for Magnetic Resonance in Medicine*, vol. 16, p. 1929, 2008.

[138] N. Maleki, D. C. Alsop, W. Dai et al., "The effect of hypercarbia and hyperoxia on the total blood flow to the retina as assessed by magnetic resonance imaging," *Investigative Ophthalmology and Visual Science*, vol. 52, no. 9, pp. 6867–6874, 2011.

[139] Q. Peng, Y. Zhang, O. S. E. Nateras, M. J. P. van Osch, and T. Q. Duong, "MRI of blood flow of the human retina," *Magnetic Resonance in Medicine*, vol. 65, no. 6, pp. 1768–1775, 2011.

[140] Y. Zhang, O. S. Emeterio Nateras, Q. Peng, C. A. Rosende, and T. Q. Duong, "Blood flow MRI of the human retina/choroid during rest and isometric exercise," *Investigative Ophthalmology and Visual Science*, vol. 53, no. 7, pp. 4299–4305, 2012.

[141] Y. Zhang, J. M. Harrison, O. S. E. Nateras, S. Chalfin, and T. Q. Duong, "Decreased retinal–choroidal blood flow in retinitis pigmentosa as measured by MRI," *Documenta Ophthalmologica*, vol. 126, no. 3, pp. 187–197, 2013.

[142] O. S. Emeterio Nateras, J. M. Harrison, E. R. Muir et al., "Choroidal blood flow decreases with age: an MRI study," *Current Eye Research*, vol. 39, no. 10, pp. 1059–1067, 2014.

[143] E. Vaghefi, B. P. Pontre, M. D. Jacobs, and P. J. Donaldson, "Visualizing ocular lens fluid dynamics using MRI: manipulation of steady state water content and water fluxes," *American Journal of Physiology—Regulatory Integrative and Comparative Physiology*, vol. 301, no. 2, pp. R335–R342, 2011.

[144] E. Vaghefi and P. J. Donaldson, "An exploration into diffusion tensor imaging in the bovine ocular lens," *Frontiers in Physiology*, vol. 4, p. 33, 2013.

[145] E. Vaghefi, B. Pontre, P. J. Donaldson, P. J. Hunter, and M. D. Jacobs, "Visualization of transverse diffusion paths across fiber cells of the ocular lens by small animal MRI," *Physiological Measurement*, vol. 30, no. 10, pp. 1061–1073, 2009.

[146] E. Vaghefi, K. Walker, B. P. Pontre, M. D. Jacobs, and P. J. Donaldson, "Magnetic resonance and confocal imaging of solute penetration into the lens reveals a zone of restricted extracellular space diffusion," *The American Journal of Physiology—Regulatory Integrative and Comparative Physiology*, vol. 302, no. 11, pp. R1250–R1259, 2012.

[147] E. Vaghefi, B. P. Pontre, K. L. Walker, and P. J. Donaldson, "Visualisation of solute fluxes in the lens reveals a barrier to extracellular diffusion," in *International Conference on the Lens*, Kailua-Kona, Hawaii, USA, 2012.

[148] E. Vaghefi and M. D. Jacobs, "Uptake and distribution of gadolinium in the ocular lens," in *Proceedings of the 30th Annual International Conference of the IEEE Engineering in Medicine and Biology Society (EMBS '08)*, pp. 843–846, Vancouver, Canada, 2008.

Hindawi Publishing Corporation
BioMed Research International
Volume 2016, Article ID 1734190, 12 pages
http://dx.doi.org/10.1155/2016/1734190

Review Article

Quantitative Myocardial Perfusion with Dynamic Contrast-Enhanced Imaging in MRI and CT: Theoretical Models and Current Implementation

G. J. Pelgrim,[1,2] A. Handayani,[1,2] H. Dijkstra,[1,2] N. H. J. Prakken,[1,2] R. H. J. A. Slart,[1,3] M. Oudkerk,[1] P. M. A. Van Ooijen,[1,2] R. Vliegenthart,[1,2] and P. E. Sijens[1,2]

[1] *University Medical Center Groningen, Center for Medical Imaging North-East Netherlands (CMI-NEN), University of Groningen, Hanzeplein 1, 9713 GZ Groningen, Netherlands*
[2] *University Medical Center Groningen, Department of Radiology, University of Groningen, Hanzeplein 1, 9713 GZ Groningen, Netherlands*
[3] *University Medical Center Groningen, Department of Nuclear Medicine and Molecular Imaging, University of Groningen, Hanzeplein 1, 9713 GZ Groningen, Netherlands*

Correspondence should be addressed to G. J. Pelgrim; g.j.pelgrim@umcg.nl

Received 4 December 2015; Accepted 11 February 2016

Academic Editor: Sebastian Kelle

Technological advances in magnetic resonance imaging (MRI) and computed tomography (CT), including higher spatial and temporal resolution, have made the prospect of performing absolute myocardial perfusion quantification possible, previously only achievable with positron emission tomography (PET). This could facilitate integration of myocardial perfusion biomarkers into the current workup for coronary artery disease (CAD), as MRI and CT systems are more widely available than PET scanners. Cardiac PET scanning remains expensive and is restricted by the requirement of a nearby cyclotron. Clinical evidence is needed to demonstrate that MRI and CT have similar accuracy for myocardial perfusion quantification as PET. However, lack of standardization of acquisition protocols and tracer kinetic model selection complicates comparison between different studies and modalities. The aim of this overview is to provide insight into the different tracer kinetic models for quantitative myocardial perfusion analysis and to address typical implementation issues in MRI and CT. We compare different models based on their theoretical derivations and present the respective consequences for MRI and CT acquisition parameters, highlighting the interplay between tracer kinetic modeling and acquisition settings.

1. Introduction

Myocardial perfusion imaging (MPI) is commonly used to investigate myocardial ischemia. While different modalities for MPI have different diagnostic accuracy, the overall accuracy to diagnose hemodynamically significant coronary artery disease (CAD) is good [1]. Analysis of MPI results in the clinical setting is mostly performed by visual evaluation of presence and pattern of hypoenhancement of the myocardium during first-pass of intravenously injected contrast. Presence of regions with normal perfusion is essential for this method to work. This is a limitation for diagnosis of patients with multivessel disease or balanced ischemia [2]. MPI can only distinguish multivessel disease and balanced ischemia when quantitative measures of myocardial perfusion are provided.

Positron emission tomography (PET) was the first technique to establish quantitative measures for perfusion. In PET, time-resolved acquisition of the first-pass of tracer uptake and direct quantification of tracer concentration were developed. With those parameters quantified, tracer kinetic modeling (1-compartment or 2-compartment modeling) could be applied to produce independent estimates of perfusion in stress and rest, known as absolute perfusion measurement (mL/g/min). This technique has been validated using microsphere comparison [2–4]. Furthermore, added

clinical value beyond relative and visual perfusion analysis has been demonstrated [5–8]. The myocardial perfusion reserve (MPR), calculated from PET-derived perfusion measurement at stress and rest, was shown to be an important predictor of cardiovascular events [9–11].

A limitation of cardiac PET is the relatively high cost and the need for an on-site cyclotron, depending on the tracer. Recent developments with the new ^{18}F-tracer flurpiridaz or other improved tracers could obviate the need for an on-site cyclotron. Flurpiridaz has shown good linearity of myocardial uptake with perfusion at a large flow range, excellent myocardial retention, low background noise in adjacent organs, and a relatively long half-life (110 min) [12].

Magnetic resonance imaging (MRI) and computed tomography (CT) imaging could be important modalities to compete with PET for the complete workup of cardiac patients. Recent developments have sparked interest for myocardial perfusion quantification using these techniques. State-of-the-art MRI and CT have better spatial and temporal resolution compared to PET. Integration of MRI and CT into current workup for coronary artery disease (CAD) also profits from their wider availability, lower costs, and increasing clinical role in comprehensive diagnosis of CAD. The validity and noninferiority of MRI and CT compared to PET measurements need to be demonstrated before a decision regarding the preference for MRI or CT over PET for myocardial perfusion quantification can be reached. Lack of standardized acquisition and modeling protocols for myocardial perfusion acquisition have complicated comparison between studies and modalities.

The aim of this study is to provide insight into the tracer kinetic models in absolute myocardial perfusion quantification, and their implementation requirements for CT and MRI. A further aim was to analyze the factors that influence myocardial perfusion quantification.

2. Myocardial Perfusion Imaging in MRI and CT

Perfusion refers to the delivery of blood to the tissue via the intravascular capillary pathway. Perfusion imaging uses dynamic contrast-enhanced acquisition to observe the first-pass dynamics of contrast agent delivery into the tissue of interest over time. For myocardial perfusion quantification, the first-pass contrast dynamics at the respective supplying artery or other arterial input sites should be captured as well. The typical arterial input sites for myocardial perfusion are the left ventricular cavity in MRI or the descending aorta in CT.

2.1. Contrast Agent. MRI and CT use different agents (gadolinium and nonionic iodine, resp.) to acquire contrast in the myocardial perfusion scans: both small molecules (<1 kDa, typical particle diameters of 0.82 nm for gadolinium dimeglumine and 1.4 nm of iohexol) that distribute to the interstitial space and generally do not enter the intracellular space. Actually, MRI contrast agents do interact with the intracellular space by changing the relaxivity of water that diffuses freely into the cell. The diffusion constants for MRI and CT contrast agents are roughly similar: 2.7×10^{-2} m^2/s for gadolinium dimeglumine, and 2.5×10^{-2} m^2/s for iohexol [13, 14]. Although the nonionic iodine contrast agents typically have a much higher viscosity compared to gadolinium, neither CT nor MRI contrast agents have significant effects on the viscosity of the blood stream [15, 16]. Gadolinium-based contrast agents have limited linearity of contrast enhancement to contrast concentration, with higher dose resulting in blood signal saturation [17, 18]. A typical dose of gadolinium contrast for visual and quantitative analysis is 0.05 mmol/kg at an injection rate of 4-5 mL/s. Dosages as low as 0.03 mmol/kg body weight have been recommended to prevent contrast saturation both in the myocardium and in the arterial input function [19]. Iodine-based contrast agents on the other hand have more straightforward and steady linearity of contrast enhancement to contrast concentration, which greatly simplifies absolute quantification [20]. In myocardial perfusion studies with multidetector CT, iodine contrast agents are administered at an injection rate of 3–5 mL/s and a volume of 60–70 mL [21, 22]. The resulting lengthy administration of CT contrast (longer than the first-pass of diffusion), however, violates the principles of indicator dilutor theory and will affect the accuracy of quantification.

2.2. Acquisition of Myocardial Perfusion Imaging. In MRI, myocardial perfusion imaging is mainly based on T1-weighted pulse sequences, where interactions of paramagnetic gadolinium (Gd^{3+}) with surrounding water molecules result in lower T1 relaxation times of the protons involved, resulting in signal enhancement showing as hyperintensity on the T1-weighted image, reflecting the distribution of gadolinium [23]. The current protocol allows acquisition of three myocardial short-axis slices at every heartbeat with a typical spatial resolution of $1.5 \times 1.5 \times 10\,\text{mm}^3$, performed during 50–60 consecutive heartbeats. In dynamic contrast-enhanced MRI, temporal resolution generally is in the order of 1 sec (1-2 cardiac cycles). Recently introduced advanced accelerated imaging sequences achieve whole heart 3D perfusion MRI with a voxel resolution of $2.3 \times 2.3 \times 5\,\text{mm}^3$, although with their reduced temporal resolution not a substitute for quantitative estimation of myocardial blood flow [24]. In CT, with dynamic shuttling mode acquisition, whole heart coverage with higher spatial resolution can be obtained ($0.3 \times 0.3 \times 5\,\text{mm}^3$) at every 2-3 heartbeats [22]. In contrast, CT scanners with wider detectors, of up to 16 cm, can achieve whole heart acquisition in a single heartbeat [25]. In both methods, perfusion imaging is performed over 20–30 consecutive heartbeats. CT has a high temporal resolution. The latest generation of dual-source CT scanners has a temporal resolution per acquisition of approximately 63 ms. However, dual-source CT scanners need to shuttle between two positions, resulting in a time interval in-between scans of once every second heartbeat and, for high heart rhythms, once every three cardiac cycles. The 256- and 320-slice CT scanners have lower temporal resolution per acquisition (in the order of 135 ms), but these scanners do not have to shuttle between two positions in order to acquire information about the whole

heart, providing the opportunity to image at every heartbeat (at the cost of higher dose). A limitation in CT, and especially also in dynamic CT perfusion studies, is that the radiation dose is directly related to the number of images acquired. For a thorough overview of CT perfusion acquisition techniques one is referred to the review by Rossi et al. [26].

2.3. Why Use Modeling in MRI and CT. In theory, tissue perfusion can be inferred from the apparent contrast enhancement without any complex modeling, assuming that the contrast agent is hemodynamically inert. This hypothesis holds true if two criteria are met with (1) a linear relationship between contrast enhancement and contrast concentration (*ex vivo* linearity) and (2) a linear relationship between apparent contrast enhancement and *perfusion* (*in vivo/uptake* linearity).

Ex vivo linearity is present in PET tracers as well as in CT iodine-based contrast agents regardless of their concentrations and in MR gadolinium only up to a certain concentration limit [17, 18]. *In vivo/uptake* linearity is limited in case of extravasating contrast agent. Most contrast agents in perfusion imaging do not only flow to the intravascular space but also distribute to the extracellular extravascular space (EES). Only in case EES extraction fraction is constant within the range of physiological perfusion flow, the apparent contrast enhancement will be linear to perfusion, as is the case with ^{15}O-water and ^{18}F-flurpiridaz in PET. However, in most tracers such as ^{13}N-ammonia [12, 23, 27], ^{82}Rb-rubidium [12, 23], gadolinium [23, 28–30], and iodine [23, 31, 32], the extraction fractions decrease nonlinearly with increasing perfusion, causing reduced *in vivo/uptake* linearity.

To correct for the effect of these extravasating tracers or contrast agents on contrast enhancement, tracer kinetic modeling attempts to separate the dynamics of contrast agent in the intravascular space and the EES over time to yield more accurate perfusion estimation. These modeling techniques have been successfully applied in PET myocardial perfusion imaging with different tracers, including ^{13}N-ammonia and ^{82}Rb-rubidium [33]. It is theoretically feasible to implement the same principles in MRI and CT, using tracer kinetic modeling.

3. Tracer Kinetic Modeling

Tracer kinetic modeling essentially relates the dynamics of tracer or contrast agent concentration in tissue (myocardium) to that in the supplying artery referred to as arterial input function (AIF). The contrast dynamics over time are obtained by tracing the myocardium and AIF voxels from the dynamic contrast-enhanced acquisition (Figure 1).

The mathematical relation between contrast dynamics in the tissue and in the AIF is represented by an impulse response function (IRF) (Figure 2). As a result of a one unit-amplitude of an infinitely narrow input bolus (impulse bolus) in the arterial inlet (Figure 2(a)), contrast retention will occur in the tissue with a certain dynamic proportion in time, defined as IRF (Figure 2(b)). In a perfusion imaging study, the AIF can be considered as a train of time-shifted and magnitude-scaled impulse boluses (Figure 2(c)) producing a corresponding train of time-shifted and magnitude-scaled IRFs in the tissue (Figure 2(d)). An iterative curve-fitting operation called deconvolution can then be applied to reconstruct the IRF from the AIF and tissue enhancement curves. Since deconvolution may lead to more than one mathematically suitable solution, it is necessary to restrict the operation by requiring the IRF to follow a certain parameterized formulation specific for each perfusion model. Therefore, perfusion flow is estimated from those IRF parameters providing the best fit at deconvolution.

4. Different Tracer Kinetic Models

Tracer kinetic models for absolute myocardial perfusion quantification can be classified into three model groups: distributed parameter, compartmental, and indicator dilution theory approaches, each of which has been developed into more specific models. For thorough explanation of the distributed parameter and compartmental models one is referred to the technical paper by Sourbron and Buckley and two manuscripts by Jerosch-Herold for the indicator dilution theory approach [34–36]. In the present overview those modeling approaches are solely compared on the basis of physical interpretation of their respective IRF.

For extravasating contrast agents as used in MRI and CT, contrast agent molecules distribute across two spaces, that is, the intravascular space and the EES (Figure 3). Each space is defined by volume, rate, and transit time parameters. The relative intravascular plasma space is defined as the intravascular plasma volume relative divided by total tissue volume (v_p). The intravascular flow rate (F) equals the blood perfusion rate per unit of volume of tissue and the mean capillary transit time (MTT_c) is the ratio between the blood volume and the tissue blood perfusion rate. Similarly, the tissue interstitial volume (v_e) is the sum of extravascular extracellular space (EES) volume contained in a volume of tissue. The two-way exchange rate to and from the EES is called the permeability-surface product, PS, and the MTT_e is the mean transit time for the EES. Additionally, an extraction fraction (E) describes the proportion of the contrast agent distributing to the EES. IRF is affected by the inflow of contrast (perfusion), two-way exchange of contrast between plasma and the EES, extraction fraction, and permeability. High-order perfusion models take into account such dynamics as completely as possible, although assumptions remain and additional variables do not necessarily yield more accurate results. The lower order models assume some parameters or dynamics to be negligible compared to others, thus simplifying the model. In Figure 4 each modeling approach is illustrated, with the formulation presented in Table 1.

5. Models Based on Axially Distributed Parameters

5.1. Distributed Parameter Model. This model takes into account the most detailed aspects of contrast dynamics at the tissue level. It assumes contrast concentration within the

Table 1: Tracer kinetic model formulation.

Model	Output parameters	Impulse response function (IRF)
Distributed parameter	F, PS, MTT_c, MTT_e, v_p, v_e	Not available in time domain
Tissue homogeneity	F, E, MTT_c, v_p, v_e	
Adiabatic approximation of tissue homogeneity	F, E, MTT_c, v_p, v_e (assuming $v_p \ll v_e$)	See Figure 5(a) $\mathrm{IRF}(t) = \begin{cases} F, & 0 < t \le \frac{F}{v_p} \\ EF \exp^{-(EF/v_e)(t)}, & t > \frac{F}{v_p} \end{cases}$
2-compartment	F, PS, v_p, v_e	See Figure 5(b) $\mathrm{IRF}(t) = F \exp^{-(F/v_p)(t)} + \mathrm{PS} \exp^{-(\mathrm{PS}/v_e)(t)}$
1-compartment (Extended Toft's)	K_{trans}, v_p, v_e	See Figure 5(c) $\mathrm{IRF}(t) = K_{\mathrm{trans}} \exp^{-(K_{\mathrm{trans}}/v_e)(t)} + v_p \partial(t)$
1-compartment (Toft's)	K_{trans}, v_e (assuming $v_p \ll v_e$)	See Figure 5(d) $\mathrm{IRF}(t) = K_{\mathrm{trans}} \exp^{-(K_{\mathrm{trans}}/v_e)(t)}$
Fermi	F, MTT_c, k (in extravasating contrast agent, only F is of physiological value)	See Figure 5(e) $\mathrm{IRF}(t) = \frac{F}{\exp^{k(t-\mathrm{MTT}_c)} + 1}$
Model-independent deconvolution	F (estimated as initial IRF magnitude)	No specific formulation

F: perfusion rate.
PS: extracellular extravascular space (EES) exchange rate.
MTT_c: capillary mean transit time.
MTT_e: EES mean transit time.
v_p: EES volume fraction.
v_e: intravascular plasma volume fraction.
K_{trans}: compound transfer constant (perfusion and EES exchange).
k: venous clearance rate for intravascular contrast agent.

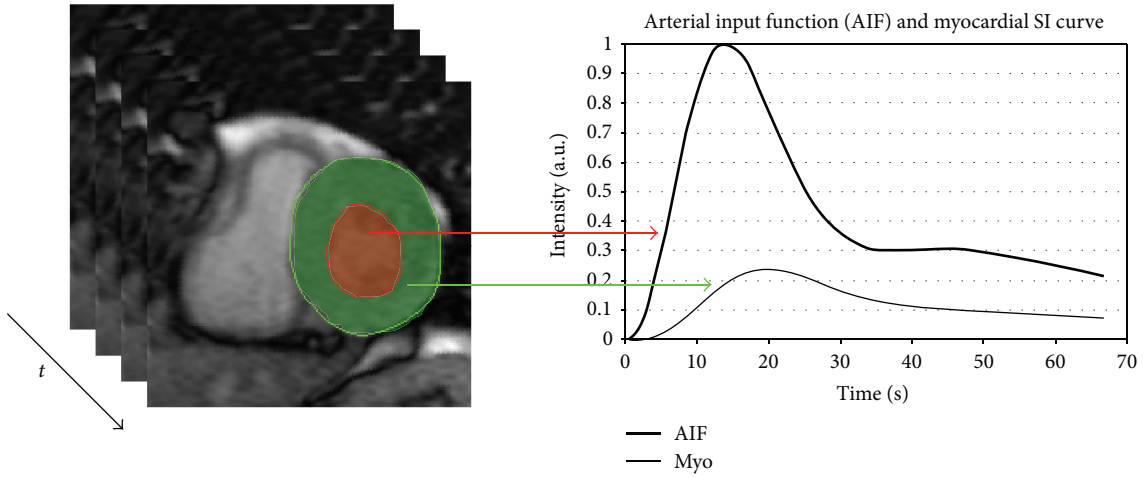

Figure 1: Myocardial (green voxels) and arterial input function (red voxels) tracing to produce contrast dynamics time curves.

intravascular space and EES to be varying temporally and axially along the longitudinal direction of the perfusion flow (Figure 4(a)). As such, the model is able to estimate every volume, rate, and time parameter specified in the intravascular and the interstitial space, as well as the extraction fraction. The distributed parameter model has been applied to estimate MRI stress/rest myocardial perfusion in healthy volunteers [37].

5.2. Tissue Homogeneity Model. This model by Johnson and Wilson assumes that the contrast concentration only varies longitudinally in the intravascular space and not in the EES (Figure 4(b)) [38]. With this assumption, the model loses the ability to estimate the time parameter of the EES (MTT_e) but can still estimate the other intravascular and EES parameters. These two axially distributed models require special numerical treatments for model fitting (i.e., multiple or Laplace-domain fitting) due to their complexity [39, 40].

5.3. Adiabatic Approximation of Tissue Homogeneity Model. Developed by Lawrence and Lee, this model further simplifies the tissue homogeneity model by assuming that the contrast

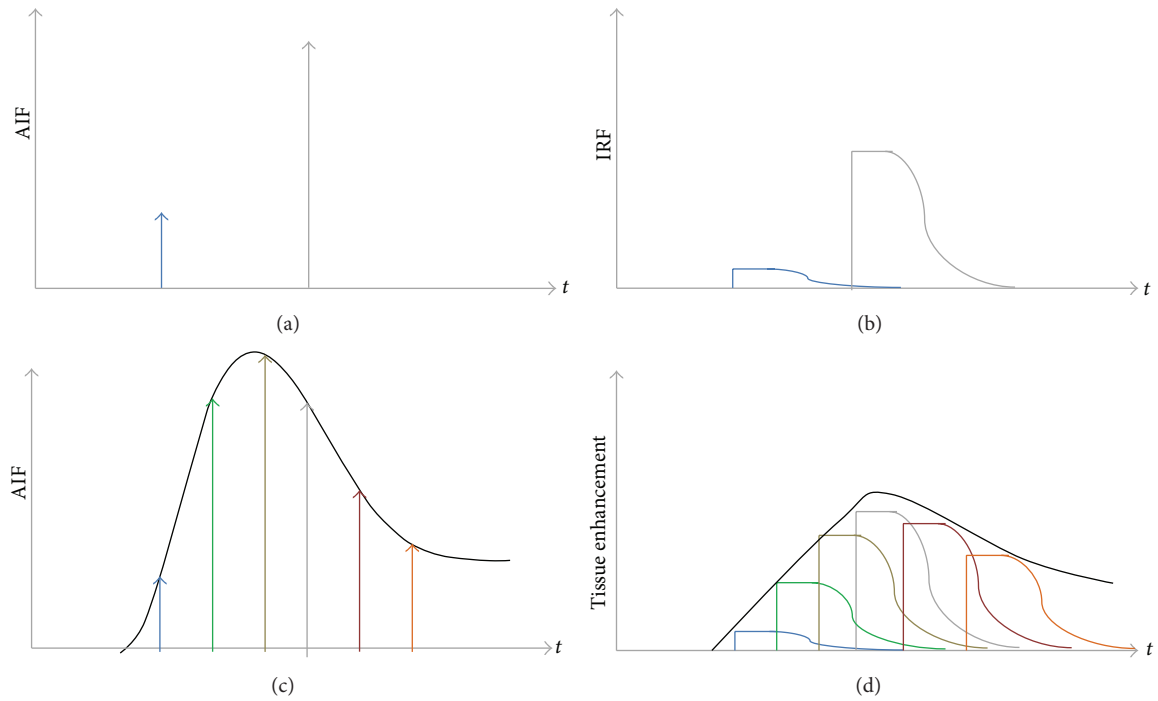

FIGURE 2: Single arterial inlets are shown with different magnitude scale in different time instance (a) and the respective magnitude-scaled impulse response function (IRF) in the tissue (b). A contrast bolus can be modeled as trains of arterial inlets (c), producing trains of magnitude-scaled IRF in the tissue (d). Deconvolution aims to reconstruct the IRF that fits the relation between the red and green lines in (c) and (d), respectively.

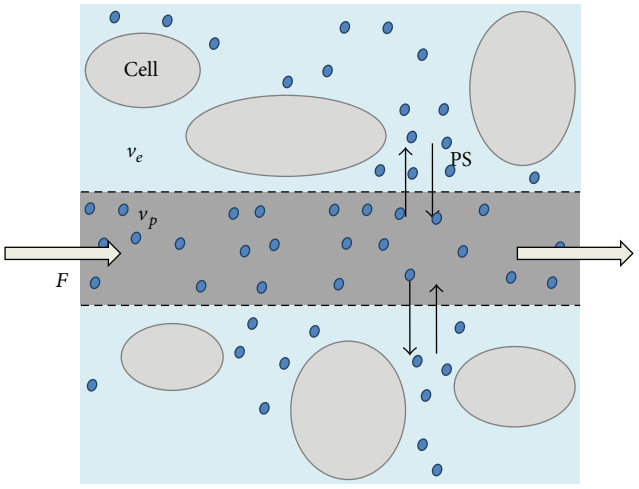

FIGURE 3: Illustration of contrast agent (blue dots) distribution in the tissue: v_p is the plasma volume within the intravascular space, v_e is the extravascular extracellular space, F is the perfusion flow within the intravascular space, and PS is the permeability-surface exchange rate between v_p and v_e. Another parameter, the extraction fraction (E), denotes the proportion of contrast agent exchanged to the extravascular extracellular space.

exchange between the intravascular space and the EES only takes place in the venous outlet [41]. Therefore, the rate of concentration change in the EES is much slower than in the intravascular space (Figure 4(c)). Adiabatic model fitting can be performed as a standard time-domain deconvolution with IRF, as specified in Table 1: height and length of the plateau correspond to perfusion flow and capillary mean transit time (MTT_c), respectively, while the decay rate of the monoexponential function represents the venous clearance. This model was first proposed in brain studies but has been used in oncological and cardiac studies afterwards [42–46].

5.4. Implementation Issues. The main limitations for axially distributed models are (1) the need of a fast acquisition rate to support MTT_c estimation and (2) the more complicated and noise-sensitive fitting methods. Faster perfusion produces shorter MTT_c, requiring more compact contrast bolus to accurately capture the MTT_c from the contrast dynamics.

6. Models Based on Compartments

The main difference between the compartmental and axially distributed model lies in the assumption that intravascular and EES contrast agent concentrations only vary with time, and not axially (Figures 4(d) and 4(e)). Because the axial contrast concentration gradient is considered negligible, transit time cannot be estimated, limiting the modeling results to the volume and rate parameters.

6.1. 2-Compartmental and 1-Compartmental Model. The typical IRF of a 2-compartment model takes the shape of a biexponential function, without an initial plateau for the capillary inflow phase due to the absence of transit time

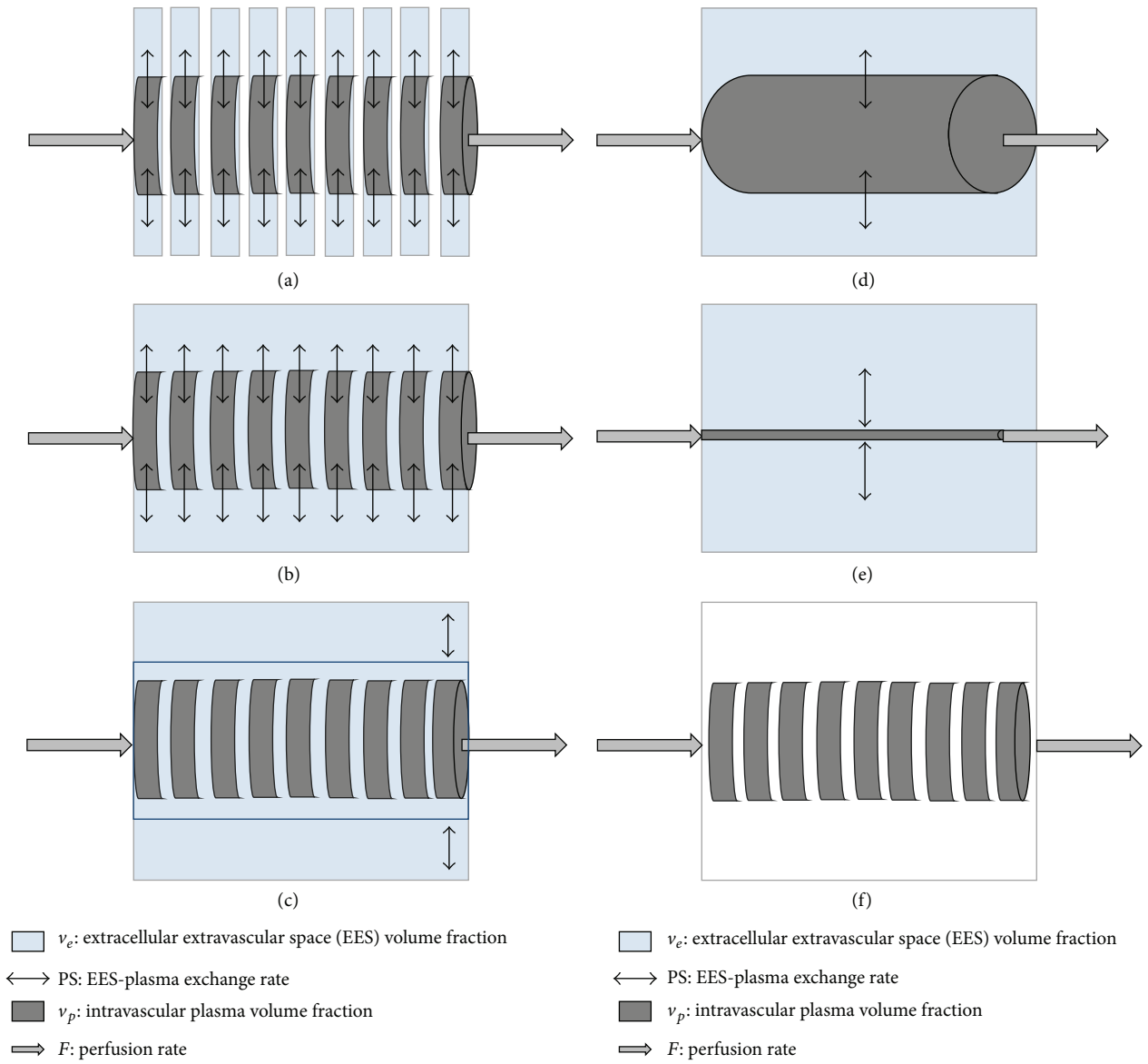

Figure 4: Schematic representation of different tracer kinetic models: (a) distributed parameter model, (b) tissue homogeneity model, (c) adiabatic approximation of tissue homogeneity model, (d) 2-compartment model, (e) 1-compartment (Toft's) model, and (f) Fermi model.

estimation. The faster-decaying exponential refers to the transfer towards the EES while the slower exponential refers to the transfer from the EES. On the other hand, the IRF of a 1-compartment model takes the shape of a monoexponential function. The maximum magnitude of the IRF corresponds to K_{trans}, a compound tissue transfer constant formulated by multiplying perfusion (F) by the contrast extraction fraction (E) [47]. Three main 1-compartmental models are distinguished.

6.2. Toft's Models. The basic Toft's model refers specifically to immediate and complete tracer extraction fraction ($E = 1$) and negligible v_p compared to v_e, such that K_{trans} represents perfusion flow [47]. Since v_p is not negligible in the myocardium, one study applied an Extended Toft's model where v_p is added to the original IRF [47, 48]. However, it has been argued that, under the Extended Toft's model, K_{trans} is closer to the EES exchange rate than to the perfusion flow [49].

6.3. Patlak Model. The Patlak model includes only data portions from the early phase of contrast arrival, when the contrast agent has not significantly filled the EES yet. Here, EES contrast concentration is not adequate to cause diffusion of contrast molecules back to the intravascular space. Under this assumption, v_e and v_p can be considered a single compartment with a single transfer rate (K_{trans}) [50]. The temporal growth in the EES contrast concentration will be linear to the rate of contrast transfer to the EES (K_{trans}) and the AIF contrast concentration. Therefore, K_{trans}

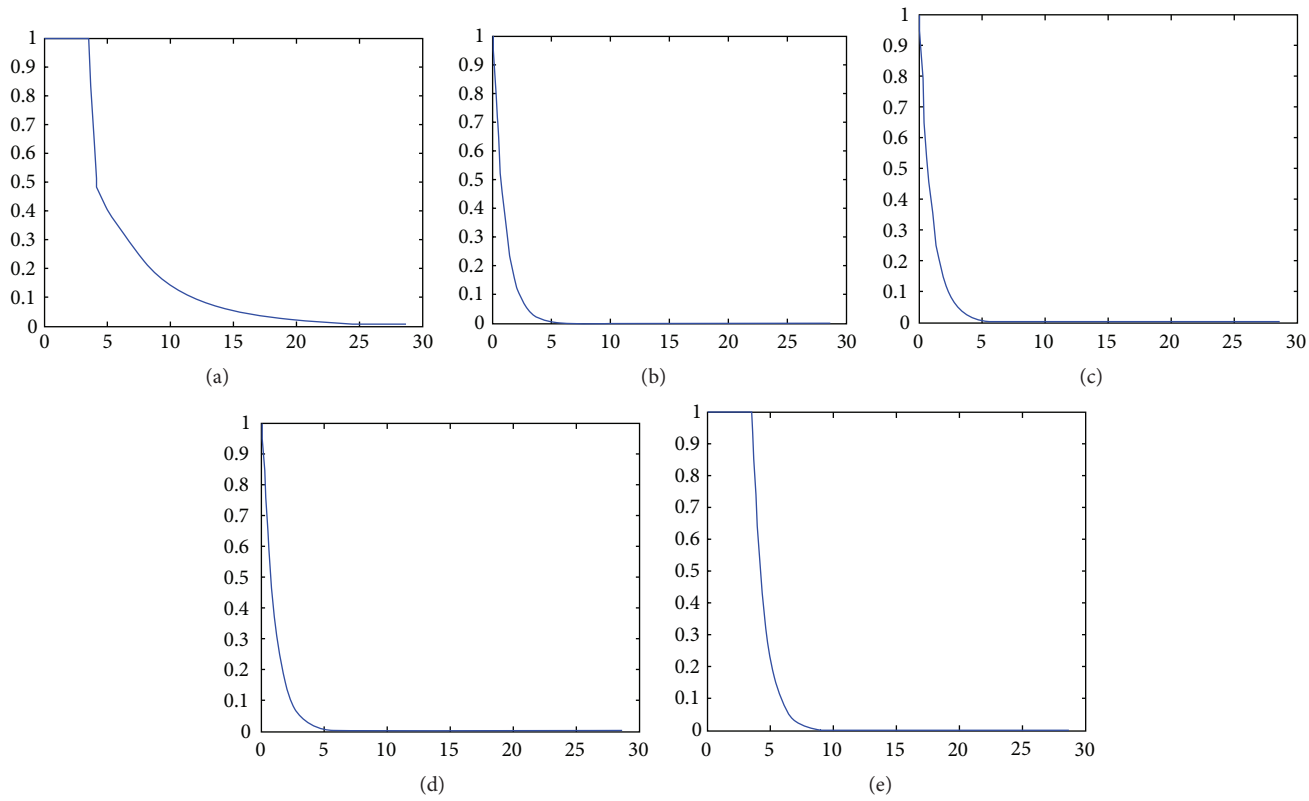

Figure 5

of the Patlak model can be reconstructed from the slope of a correlation map between tissue contrast concentration and the area under the curve of the AIF. However, care should be taken to make sure that only appropriate data portions are used. The Patlak model has been used in human MRI studies of myocardial perfusion, with an acquisition rate matching every heartbeat, as well as in animals with the acquisition rate matching every other heartbeat [30, 48, 51].

6.4. Maximum Slope Method. The maximum slope method is derived from exactly the same assumptions as the Patlak model, therefore requiring the same portion of data points and suffering the same concerns. The Patlak-equivalent K_{trans} is derived by normalizing the maximum slope of the tissue concentration to the maximum (peak) concentration of the AIF. The tissue maximal upslope is calculated by linear fitting while the AIF peak is derived from gamma-variate fitting. The method has been implemented in an older study based on electron-beam CT as well as in more recent myocardial perfusion studies with dual-source CT [21, 52–54].

6.5. Implementation Issues. The main critique on the 1-compartment model is that K_{trans} is a multiplication of extraction fraction (E) and perfusion instead of a sole perfusion (F) indicator. A limited number of MRI studies have shown a nonlinearly decreasing extraction suggesting a limited range of K_{trans} proportionality with perfusion if this parameter is to be derived from gadolinium [18, 28–30]. Correcting K_{trans} for the extraction fraction (E) improved the correlation between Patlak-derived K_{trans} and microsphere perfusion in an animal experiment [51].

7. Models Based on Indicator Dilution Theory

7.1. The Fermi Model. The Fermi model was initially developed for studies with a purely intravascular indicator. Assuming an axially varying contrast concentration in the intravascular space, it was observed that the IRF of an intravascular indicator resembled the shape of the Fermi function [19, 55]. The amplitude, width of initial plateau, and subsequent curve decay rate of the fitted Fermi function represent perfusion, capillary mean transit time, and venous clearance rate, respectively (Table 1). For extravasating tracers, the validity of the Fermi model holds as long as the tracer concentration in the EES is substantially lower than in the intravascular space ($c_e \ll c_p$), a condition assumed to be attainable in the first-pass of tracer circulation [36]. The Fermi model has been used in many MR human and animal studies [2, 36, 56–60] and it has been used in one CT porcine study [32].

7.2. Model-Independent Deconvolution. The previous perfusion models have been driven by specific physical assumptions on the distribution of contrast agent in the tissue, culminating into exact IRF formulation. A model-independent approach attempts to overcome these tissue-specific assumption problems by applying more generic mathematical constraints in the IRF calculation. With the central-volume principle applied in the indicator dilution theory, the initial

magnitude of the IRF is then assumed as perfusion regardless of the shape of the IRF [19, 35]. Studies with high data quality have shown excellent agreement of model-independent deconvolution with true perfusion (simulation study) and microspheres (porcine study, $n = 3$), as well as with PET in healthy volunteers ($n = 5$) [35, 61].

7.3. Implementation Issues. Since the indicator dilution approach does not presume any separation between the intravascular and the EES contrast dynamics, its perfusion estimation is uncorrected for EES exchange. Therefore, the same concern as in 1-compartment models, that is, the consistency of perfusion representation over the physiological range of perfusion, also applies to indicator dilution theory models.

8. Influence of Different Acquisition Settings

In the previous paragraphs, the different perfusion models were discussed. Those models offer different degrees of perfusion evaluation. When more accurate quantification of perfusion is desired, consequently, more detailed information of contrast dynamics is required. This leads to more demanding acquisition settings (i.e., faster acquisition rate, higher contrast-to-noise ratio). As a result, more detailed models are more sensitive to noise, because a small change in the contrast dynamics will have more impact on the parameter estimations.

8.1. Key Acquisition Factors. Jerosch-Herold performed a thorough review on specific MRI requirements [19]. Minimal requirements of several general key acquisition/image quality parameters that influence the output of tracer kinetic models are listed here.

(1) A compact contrast bolus is needed to ensure that the contrast dynamics contains information as requested by the modeling. An increasingly dispersed bolus is known to cause increasing perfusion underestimation and variability, especially at higher flow rate [62]. As a rough guidance, the contrast bolus should be compact enough to accommodate a clear definition of the peak enhancement in the AIF as well as in the tissue (and even more compact in case of the use of the axially distributed model). A gadolinium injection rate of at least 3 mL/s, and optimally 4 mL/s, has been recommended for MRI myocardial perfusion assessment [18, 63]. More prominent bolus dispersion can be expected in CT due to the typically larger injected contrast volume.

(2) In order to estimate the flow rate and transit time parameters, a sufficiently fast acquisition rate (temporal resolution) is needed to capture the fastest change described by the model. When only the flow rate parameter is analyzed, the minimum scan interval is determined by the time-to-peak (TTP) of the AIF. When both rate and transit time parameters are concerned, the mean capillary transit time (MTT_c) determines the minimum scan interval. In other tissues a considerable underestimation was found when the temporal resolution was reduced, with both CT and MRI [62, 64–68].

(3) In order to estimate volume parameters, the acquisition period should be at least within the order of the transit time parameter of the concerned volume, to ensure proper capture of the arrival and clearance of contrast agent.

(4) In-plane spatial resolution should be adequate to prevent partial volume effects, especially if voxel-wise tracer kinetic modeling is to be applied. In the data acquisition this means that voxels are best small and isotropic (cubic rather than rectangular, etc.). This is hard to realize in MRI where the in-plane spatial resolution is approximately 5 times lower than in CT (1.5×1.5 mm versus 0.3×0.3 mm) with slice thickness much larger than in-plane resolution. In post-processing, the quantification resolution particularly worsens due to partial volume effects in CT where investigators have typically analyzed the CT perfusion in slices thicker than the native resolution.

(5) Signal-to-noise ratio (SNR) concerns the total variability in the contrast dynamics. Small variations in contrast dynamics may influence the precision of tracer kinetic modeling. The use of higher Tesla machines in MRI may provide better SNR without compromising spatiotemporal resolution, although inherent problems with RF homogeneity can adversely impact quantification. Implementation of higher tube current in CT can also improve SNR by reducing variability in contrast dynamics and the error in model fitting [19, 55]. A disadvantage of higher tube current is the increase in radiation dose. A decrease in tube voltage could increase SNR, because of the K-edge of iodine, which lies around 35 kV. If possible, a lower tube voltage would be beneficial for contrast scans and additionally lowers radiation dose [69].

9. Clinical Implication and Conclusion

Regarding the choice of model used, we suggest that one should use the simplest possible model that can explain the contrast dynamics. It is worth noting that the use of higher-order models will only be beneficial when the acquisition is optimized to capture the additional contrast dynamic details requested by the model. Considering the current imaging and contrast administration setup for MRI and CT myocardial perfusion imaging, the 1-compartmental and Fermi models seem to be the most technically applicable. Axially distributed models require an acquisition rate at the order of MTT_c and a sufficiently compact bolus to identify the capillary inflow phase. Balancing such demand with clinical requirements for spatial resolution and coverage could be problematic. Apart from optimal data quality, model-independent deconvolution also requires knowledge for selection of the regularization parameter, which may not be available in every imaging center.

Issues for clinical adoption go beyond the accuracy of the quantitative myocardial perfusion value itself. The assumptions made by each model are coupled with the theoretical pitfalls we have tried to identify in our appraisal.

The major complication with quantitative MR perfusion is in the limited linearity of contrast enhancement to contrast concentration, requiring lower dose of gadolinium, thus compromising the accuracy of visual analysis as well as the precision of perfusion estimation. CT perfusion on the

other hand greatly simplifies quantification efforts by offering a linear relationship between contrast enhancement and concentration. However, current CT imaging setup suffers reduced image quality due to the shuttling mode acquisition and limited temporal resolution as well as acquisition period due to the radiation dose constraint; both reduce the precision and accuracy of perfusion estimation.

Limited studies have mentioned instability issues of higher-order models. More investigations are required [37, 70]. Reproducibility of perfusion values is highly related to the imaging quality, where specific issues such as acquisition/reconstruction artifacts need to be taken care of in both modalities before implementing the model.

An important issue for the clinical setting would be to establish the expected physiological variability across different subjects, so that the usability of quantitative myocardial perfusion in diagnostic or sequential observation setting can be verified. Quantitative PET studies for instance have shown considerable heterogeneity in myocardial perfusion of healthy volunteers, related to factors such as age, gender, rate-pressure product, and other hemodynamic factors [71, 72]. Furthermore, in the presence of COPD and hypertension, the value of myocardial perfusion reserve has been shown to be impaired without regional myocardial ischemia [73–75]. The spectrum of physiological variability in myocardial perfusion should also be investigated with MRI and CT if myocardial perfusion quantification is to be adopted in clinical practice.

Studies investigating the performance of quantitative MRI and CT myocardial perfusion imaging in detecting CAD have been conducted with different reference standards, that is, stenosis diameter, derived from either quantitative CT or invasive coronary angiography, fractional flow reserve, or even visual analysis of SPECT myocardial perfusion. None of these reference parameters actually capture the same functional phenomenon as myocardial perfusion. The anatomical aspect of a stenosis does not describe its functional relevance, while fractional flow reserve, even though being a functional parameter, indicates the hemodynamics of the focal coronary lesion rather than its systemic effect on myocardial microcirculation. The quantitative relationship between myocardial perfusion and the above parameters, therefore, can be expected to be affected by broader physiological variability, which may be better captured by quantitative analysis than by visual assessment. However, the superiority of quantitative myocardial perfusion over mere visual analysis for diagnosis of hemodynamically significant CAD still needs to be proven.

Competing Interests

The authors declare that there is no conflict of interests regarding the publication of this paper.

Acknowledgments

R. Vliegenthart is supported by a grant from the Netherlands Organization for Scientific Research.

References

[1] C. Jaarsma, T. Leiner, S. C. Bekkers et al., "Diagnostic performance of noninvasive myocardial perfusion imaging using single-photon emission computed tomography, cardiac magnetic resonance, and positron emission tomography imaging for the detection of obstructive coronary artery disease: a meta-analysis," *Journal of the American College of Cardiology*, vol. 59, no. 19, pp. 1719–1728, 2012.

[2] G. Morton, A. Chiribiri, M. Ishida et al., "Quantification of absolute myocardial perfusion in patients with coronary artery disease: comparison between cardiovascular magnetic resonance and positron emission tomography," *Journal of the American College of Cardiology*, vol. 60, no. 16, pp. 1546–1555, 2012.

[3] W. G. Kuhle, G. Porenta, S.-C. Huang et al., "Quantification of regional myocardial blood flow using 13N-ammonia and reoriented dynamic positron emission tomographic imaging," *Circulation*, vol. 86, no. 3, pp. 1004–1017, 1992.

[4] Y. Choi, S.-C. Huang, R. A. Hawkins et al., "Quantification of myocardial blood flow using 13N-ammonia and PET: comparison of tracer models," *Journal of Nuclear Medicine*, vol. 40, no. 6, pp. 1045–1055, 1999.

[5] H. Gewirtz, "PET measurement of adenosine stimulated absolute myocardial blood flow for physiological assessment of the coronary circulation," *Journal of Nuclear Cardiology*, vol. 19, no. 2, pp. 347–354, 2012.

[6] S. A. Kajander, E. Joutsiniemi, M. Saraste et al., "Clinical value of absolute quantification of myocardial perfusion with ^{15}O-water in coronary artery disease," *Circulation: Cardiovascular Imaging*, vol. 4, no. 6, pp. 678–684, 2011.

[7] M. F. Di Carli, S. Dorbala, J. Meserve, G. El Fakhri, A. Sitek, and S. C. Moore, "Clinical myocardial perfusion PET/CT," *Journal of Nuclear Medicine*, vol. 48, no. 5, pp. 783–793, 2007.

[8] T. H. Schindler, H. R. Schelbert, A. Quercioli, and V. Dilsizian, "Cardiac PET imaging for the detection and monitoring of coronary artery disease and microvascular health," *JACC Cardiovascular Imaging*, vol. 3, no. 6, pp. 623–640, 2010.

[9] R. H. J. A. Slart, C. J. Zeebregts, H. L. Hillege et al., "Myocardial perfusion reserve after a PET-driven revascularization procedure: a strong prognostic factor," *Journal of Nuclear Medicine*, vol. 52, no. 6, pp. 873–879, 2011.

[10] R. A. Tio, A. Dabeshlim, H.-M. J. Siebelink et al., "Comparison between the prognostic value of left ventricular function and myocardial perfusion reserve in patients with ischemic heart disease," *Journal of Nuclear Medicine*, vol. 50, no. 2, pp. 214–219, 2009.

[11] L. E. Juárez-Orozco, J. Glauche, E. Alexanderson et al., "Myocardial perfusion reserve in spared myocardium: correlation with infarct size and left ventricular ejection fraction," *European Journal of Nuclear Medicine and Molecular Imaging*, vol. 40, no. 8, pp. 1148–1154, 2013.

[12] J. Maddahi, "Properties of an ideal PET perfusion tracer: new PET tracer cases and data," *Journal of Nuclear Cardiology*, vol. 19, supplement 1, pp. S30–S37, 2012.

[13] M. J. Gordon, K. C. Chu, A. Margaritis, A. J. Martin, C. R. Ethier, and B. K. Rutt, "Measurement of Gd-DTPA diffusion through PVA hydrogel using a novel magnetic resonance imaging method," *Biotechnology and Bioengineering*, vol. 65, no. 4, pp. 459–467, 1999.

[14] N. Nair, W.-J. Kim, R. D. Braatz, and M. S. Strano, "Dynamics of surfactant-suspended single-walled carbon nanotubes in a centrifugal field," *Langmuir*, vol. 24, no. 5, pp. 1790–1795, 2008.

[15] C. Irace, S. Tamburini, B. Bertucci, M. S. Franceschi, and A. Gnasso, "Effects of iodinated contrast media on common carotid and brachial artery blood flow and wall shear stress," *European Radiology*, vol. 16, no. 12, pp. 2721–2727, 2006.

[16] W. H. Reinhart, B. Pleisch, L. G. Harris, and M. Lütolf, "Influence of contrast media (iopromide, ioxaglate, gadolinium-DOTA) on blood viscosity, erythrocyte morphology and platelet function," *Clinical Hemorheology and Microcirculation*, vol. 32, no. 3, pp. 227–239, 2005.

[17] W. Utz, T. Niendorf, R. Wassmuth, D. Messroghli, R. Dietz, and J. Schulz-Menger, "Contrast-dose relation in first-pass myocardial MR perfusion imaging," *Journal of Magnetic Resonance Imaging*, vol. 25, no. 6, pp. 1131–1135, 2007.

[18] M. Ishida, H. Sakuma, S. Murashima et al., "Absolute blood contrast concentration and blood signal saturation on myocardial perfusion MRI: Estimation from CT data," *Journal of Magnetic Resonance Imaging*, vol. 29, no. 1, pp. 205–210, 2009.

[19] M. Jerosch-Herold, "Quantification of myocardial perfusion by cardiovascular magnetic resonance," *Journal of Cardiovascular Magnetic Resonance*, vol. 12, article 57, 2010.

[20] J. P. B. O'Connor, P. S. Tofts, K. A. Miles, L. M. Parkes, G. Thompson, and A. Jackson, "Dynamic contrast-enhanced imaging techniques: CT and MRI," *British Journal of Radiology*, vol. 84, no. 2, pp. S112–S120, 2011.

[21] F. Bamberg, R. Hinkel, R. P. Marcus et al., "Feasibility of dynamic CT-based adenosine stress myocardial perfusion imaging to detect and differentiate ischemic and infarcted myocardium in an large experimental porcine animal model," *International Journal of Cardiovascular Imaging*, vol. 30, no. 4, pp. 803–812, 2014.

[22] G. Bastarrika, L. Ramos-Duran, U. J. Schoepf et al., "Adenosine-stress dynamic myocardial volume perfusion imaging with second generation dual-source computed tomography: concepts and first experiences," *Journal of Cardiovascular Computed Tomography*, vol. 4, no. 2, pp. 127–135, 2010.

[23] M. Salerno and G. A. Beller, "Noninvasive assessment of myocardial perfusion," *Circulation: Cardiovascular Imaging*, vol. 2, no. 5, pp. 412–424, 2009.

[24] R. Jogiya, S. Kozerke, G. Morton et al., "Validation of dynamic 3-dimensional whole heart magnetic resonance myocardial perfusion imaging against fractional flow reserve for the detection of significant coronary artery disease," *Journal of the American College of Cardiology*, vol. 60, no. 8, pp. 756–765, 2012.

[25] Y. Kikuchi, N. Oyama-Manabe, M. Naya et al., "Quantification of myocardial blood flow using dynamic 320-row multidetector CT as compared with ^{15}O-H_2O PET," *European Radiology*, vol. 24, no. 7, pp. 1547–1556, 2014.

[26] A. Rossi, D. Merkus, E. Klotz, N. Mollet, P. J. de Feyter, and G. P. Krestin, "Stress myocardial perfusion: imaging with multidetector CT," *Radiology*, vol. 270, no. 1, pp. 25–46, 2014.

[27] H. R. Schelbert, M. E. Phelps, S. C. Huang et al., "N-13 ammonia as an indicator of myocardial blood flow," *Circulation*, vol. 63, no. 6, pp. 1259–1272, 1981.

[28] C. Y. Tong, F. S. Prato, G. Wisenberg et al., "Measurement of the extraction efficiency and distribution volume for Gd- DTPA in normal and diseased canine myocardium," *Magnetic Resonance in Medicine*, vol. 30, no. 3, pp. 337–346, 1993.

[29] X. Li, C. S. Springer Jr., and M. Jerosch-Herold, "First-pass dynamic contrast-enhanced MRI with extravasating contrast reagent: evidence for human myocardial capillary recruitment in adenosine-induced hyperemia," *NMR in Biomedicine*, vol. 22, no. 2, pp. 148–157, 2009.

[30] M. Ishida, T. Ichihara, M. Nagata et al., "Quantification of myocardial blood flow using model based analysis of first-pass perfusion MRI: extraction fraction of Gd-DTPA varies with myocardial blood flow in human myocardium," *Magnetic Resonance in Medicine*, vol. 66, no. 5, pp. 1391–1399, 2011.

[31] J. M. Canty Jr., R. M. Judd, A. S. Brody, and F. J. Klocke, "First-pass entry of nonionic contrast agent into the myocardial extravascular space. Effects on radiographic estimates of transit time and blood volume," *Circulation*, vol. 84, no. 5, pp. 2071–2078, 1991.

[32] E. Daghini, A. N. Primak, A. R. Chade et al., "Evaluation of porcine myocardial microvascular permeability and fractional vascular volume using 64-slice helical computed tomography (CT)," *Investigative Radiology*, vol. 42, no. 5, pp. 274–282, 2007.

[33] A. Saraste, S. Kajander, C. Han, S. V. Nesterov, and J. Knuuti, "PET: is myocardial flow quantification a clinical reality?" *Journal of Nuclear Cardiology*, vol. 19, no. 5, pp. 1044–1059, 2012.

[34] S. P. Sourbron and D. L. Buckley, "Tracer kinetic modelling in MRI: estimating perfusion and capillary permeability," *Physics in Medicine and Biology*, vol. 57, no. 2, pp. R31–R33, 2012.

[35] M. Jerosch-Herold, C. Swingen, and R. T. Seethamraju, "Myocardial blood flow quantification with MRI by model-independent deconvolution," *Medical Physics*, vol. 29, no. 5, pp. 886–897, 2002.

[36] M. Jerosch-Herold, N. Wilke, A. E. Stillman, and R. F. Wilson, "Magnetic resonance quantification of the myocardial perfusion reserve with a Fermi function model for constrained deconvolution," *Medical Physics*, vol. 25, no. 1, pp. 73–84, 1998.

[37] D. A. Broadbent, J. D. Biglands, A. Larghat et al., "Myocardial blood flow at rest and stress measured with dynamic contrast-enhanced MRI: comparison of a distributed parameter model with a fermi function model," *Magnetic Resonance in Medicine*, vol. 70, no. 6, pp. 1591–1597, 2013.

[38] J. A. Johnson and T. A. Wilson, "A model for capillary exchange," *The American Journal of Physiology*, vol. 210, no. 6, pp. 1299–1303, 1966.

[39] T. S. Koh, D. L. H. Cheong, and Z. Hou, "Issues of discontinuity in the impulse residue function for deconvolution analysis of dynamic contrast-enhanced MRI data," *Magnetic Resonance in Medicine*, vol. 66, no. 3, pp. 886–892, 2011.

[40] A. Garpebring, N. Ostlund, and M. Karlsson, "A novel estimation method for physiological parameters in dynamic contrast-enhanced MRI: application of a distributed parameter model using Fourier-domain calculations," *IEEE Transactions on Medical Imaging*, vol. 28, no. 9, pp. 1375–1383, 2009.

[41] K. S. St Lawrence and T.-Y. Lee, "An adiabatic approximation to the tissue homogeneity model for water exchange in the brain. II. Experimental validation," *Journal of Cerebral Blood Flow and Metabolism*, vol. 18, no. 12, pp. 1378–1385, 1998.

[42] S. Bisdas, G. Konstantinou, K. Surlan-Popovic et al., "Dynamic contrast-enhanced CT of head and neck tumors: comparison of first-pass and permeability perfusion measurements using two different commercially available tracer kinetics models," *Academic Radiology*, vol. 15, no. 12, pp. 1580–1589, 2008.

[43] V. Goh, S. Halligan, and C. I. Bartram, "Quantitative tumor perfusion assessment with multidetector CT: are measurements from two commercial software packages interchangeable?" *Radiology*, vol. 242, no. 3, pp. 777–782, 2007.

[44] A. So, J. Hsieh, J.-Y. Li, J. Hadway, H.-F. Kong, and T.-Y. Lee, "Quantitative myocardial perfusion measurement using CT Perfusion: a validation study in a porcine model of reperfused acute myocardial infarction," *International Journal of Cardiovascular Imaging*, vol. 28, no. 5, pp. 1237–1248, 2012.

[45] A. So, G. Wisenberg, A. Islam et al., "Non-invasive assessment of functionally relevant coronary artery stenoses with quantitative CT perfusion: preliminary clinical experiences," *European Radiology*, vol. 22, no. 1, pp. 39–50, 2012.

[46] M. Jerosch-Herold, N. Wilke, Y. Wang et al., "Direct comparison of an intravascular and an extracellular contrast agent for quantification of myocardial perfusion," *International Journal of Cardiac Imaging*, vol. 15, no. 6, pp. 453–464, 1999.

[47] P. S. Tofts, G. Brix, D. L. Buckley et al., "Estimating kinetic parameters from dynamic contrast-enhanced T(1)- weighted MRI of a diffusable tracer: Standardized quantities and symbols," *Journal of Magnetic Resonance Imaging*, vol. 10, no. 3, pp. 223–232, 1999.

[48] N. A. Pack and E. V. R. DiBella, "Comparison of myocardial perfusion estimates from dynamic contrast-enhanced magnetic resonance imaging with four quantitative analysis methods," *Magnetic Resonance in Medicine*, vol. 64, no. 1, pp. 125–137, 2010.

[49] S. P. Sourbron and D. L. Buckley, "On the scope and interpretation of the Tofts models for DCE-MRI," *Magnetic Resonance in Medicine*, vol. 66, no. 3, pp. 735–745, 2011.

[50] C. S. Patlak, R. G. Blasberg, and J. D. Fenstermacher, "Graphical evaluation of blood-to-brain transfer constants from multiple-time uptake data," *Journal of Cerebral Blood Flow and Metabolism*, vol. 3, no. 1, pp. 1–7, 1983.

[51] T. Ichihara, M. Ishida, K. Kitagawa et al., "Quantitative analysis of first-pass contrast-enhanced myocardial perfusion MRI using a Patlak plot method and blood saturation correction," *Magnetic Resonance in Medicine*, vol. 62, no. 2, pp. 373–383, 2009.

[52] F. Bamberg, R. Hinkel, F. Schwarz et al., "Accuracy of dynamic computed tomography adenosine stress myocardial perfusion imaging in estimating myocardial blood flow at various degrees of coronary artery stenosis using a porcine animal model," *Investigative Radiology*, vol. 47, no. 1, pp. 71–77, 2012.

[53] F. Bamberg, E. Klotz, T. Flohr et al., "Dynamic myocardial stress perfusion imaging using fast dual-source CT with alternating table positions: initial experience," *European Radiology*, vol. 20, no. 5, pp. 1168–1173, 2010.

[54] R. G. Gould, M. J. Lipton, M. T. McNamara, R. E. Sievers, S. Koshold, and C. B. Higgins, "Measurement of regional myocardial blood flow in dogs by Ultrafast CT," *Investigative Radiology*, vol. 23, no. 5, pp. 348–353, 1988.

[55] M. Bindschadler, D. Modgil, K. R. Branch, P. J. La Riviere, and A. M. Alessio, "Comparison of blood flow models and acquisitions for quantitative myocardial perfusion estimation from dynamic CT," *Physics in Medicine and Biology*, vol. 59, no. 7, pp. 1533–1556, 2014.

[56] O. M. Muehling, N. M. Wilke, P. Panse et al., "Reduced myocardial perfusion reserve and transmural perfusion gradient in heart transplant arteriopathy assessed by magnetic resonance imaging," *Journal of the American College of Cardiology*, vol. 42, no. 6, pp. 1054–1060, 2003.

[57] T. F. Christian, A. H. Aletras, and A. E. Arai, "Estimation of absolute myocardial blood flow during first-pass MR perfusion imaging using a dual-bolus injection technique: comparison to single-bolus injection method," *Journal of Magnetic Resonance Imaging*, vol. 27, no. 6, pp. 1271–1277, 2008.

[58] T. F. Christian, D. W. Rettmann, A. H. Aletras et al., "Absolute myocardial perfusion in canines measured by using dual-bolus first-pass MR imaging," *Radiology*, vol. 232, no. 3, pp. 677–684, 2004.

[59] L.-Y. Hsu, D. W. Groves, A. H. Aletras, P. Kellman, and A. E. Arai, "A quantitative pixel-wise measurement of myocardial blood flow by contrast-enhanced first-pass CMR perfusion imaging: microsphere validation in dogs and feasibility study in humans," *JACC: Cardiovascular Imaging*, vol. 5, no. 2, pp. 154–166, 2012.

[60] C. A. Miller, J. H. Naish, M. P. Ainslie et al., "Voxel-wise quantification of myocardial blood flow with cardiovascular magnetic resonance: Effect of variations in methodology and validation with positron emission tomography," *Journal of Cardiovascular Magnetic Resonance*, vol. 16, article 11, 2014.

[61] N. A. Pack, E. V. R. DiBella, T. C. Rust et al., "Estimating myocardial perfusion from dynamic contrast-enhanced CMR with a model-independent deconvolution method," *Journal of Cardiovascular Magnetic Resonance*, vol. 10, article 52, 2008.

[62] E. Henderson, B. K. Rutt, and T.-Y. Lee, "Temporal sampling requirements for the tracer kinetics modeling of breast disease," *Magnetic Resonance Imaging*, vol. 16, no. 9, pp. 1057–1073, 1998.

[63] R. Gebker, C. Jahnke, I. Paetsch et al., "MR myocardial perfusion imaging with k-space and time broad-use linear acquisition speed-up technique: feasibility study," *Radiology*, vol. 245, no. 3, pp. 863–871, 2007.

[64] D. Spira, J. D. Gerlach, S. M. Spira, M. Schulze, A. Sauter, and M. Horger, "Effect of scan time on perfusion and flow extraction product (K-trans) measurements in lung cancer using low-dose volume perfusion CT (VPCT)," *Academic Radiology*, vol. 19, no. 1, pp. 78–83, 2012.

[65] C. S. Ng, A. G. Chandler, W. Wei et al., "Effect of sampling frequency on perfusion values in perfusion CT of lung tumors," *American Journal of Roentgenology*, vol. 200, no. 2, pp. W155–W162, 2013.

[66] V. Goh, J. Liaw, C. I. Bartram, and S. Halligan, "Effect of temporal interval between scan acquisitions on quantitative vascular parameters in colorectal cancer: implications for helical volumetric perfusion CT techniques," *American Journal of Roentgenology*, vol. 191, no. 6, pp. W288–W292, 2008.

[67] Y. Cao, D. Li, Z. Shen, and D. Normolle, "Sensitivity of quantitative metrics derived from DCE MRI and a pharmacokinetic model to image quality and acquisition parameters," *Academic Radiology*, vol. 17, no. 4, pp. 468–478, 2010.

[68] L. E. Kershaw and H.-L. M. Cheng, "Temporal resolution and SNR requirements for accurate DCE-MRI data analysis using the AATH model," *Magnetic Resonance in Medicine*, vol. 64, no. 6, pp. 1772–1780, 2010.

[69] M. Fujita, K. Kitagawa, T. Ito et al., "Dose reduction in dynamic CT stress myocardial perfusion imaging: comparison of 80-kV/370-mAs and 100-kV/300-mAs protocols," *European Radiology*, vol. 24, no. 3, pp. 748–755, 2014.

[70] F. Schwab, M. Ingrisch, R. Marcus et al., "Tracer kinetic modeling in myocardial perfusion quantification using MRI," *Magnetic Resonance in Medicine*, vol. 73, no. 3, pp. 1206–1215, 2015.

[71] J. Czernin, P. Müller, S. Chan et al., "Influence of age and hemodynamics on myocardial blood flow and flow reserve," *Circulation*, vol. 88, no. 1, pp. 62–69, 1993.

[72] S. Sdringola, N. P. Johnson, R. L. Kirkeeide, E. Cid, and K. L. Gould, "Impact of unexpected factors on quantitative

myocardial perfusion and coronary flow reserve in young, asymptomatic volunteers," *JACC: Cardiovascular Imaging*, vol. 4, no. 4, pp. 402–412, 2011.

[73] S. Nakamori, K. Onishi, M. Ishida et al., "Myocardial perfusion reserve is impaired in patients with chronic obstructive pulmonary disease: a comparison to current smokers," *European Heart Journal Cardiovascular Imaging*, vol. 15, no. 2, pp. 180–188, 2014.

[74] H. Nakajima, K. Onishi, T. Kurita et al., "Hypertension impairs myocardial blood perfusion reserve in subjects without regional myocardial ischemia," *Hypertension Research*, vol. 33, no. 11, pp. 1144–1149, 2010.

[75] K. Kawecka-Jaszcz, D. Czarnecka, A. Olszanecka et al., "Myocardial perfusion in hypertensive patients with normal coronary angiograms," *Journal of Hypertension*, vol. 26, no. 8, pp. 1686–1694, 2008.

Hindawi Publishing Corporation
BioMed Research International
Volume 2016, Article ID 2073076, 9 pages
http://dx.doi.org/10.1155/2016/2073076

Research Article

Computer-Assisted Classification Patterns in Autoimmune Diagnostics: The AIDA Project

Amel Benammar Elgaaied,[1] Donato Cascio,[2] Salvatore Bruno,[2] Maria Cristina Ciaccio,[2] Marco Cipolla,[2] Alessandro Fauci,[2] Rossella Morgante,[2] Vincenzo Taormina,[2] Yousr Gorgi,[3] Raja Marrakchi Triki,[1] Melika Ben Ahmed,[4] Hechmi Louzir,[4] Sadok Yalaoui,[5] Sfar Imene,[3] Yassine Issaoui,[1] Ahmed Abidi,[1] Myriam Ammar,[1] Walid Bedhiafi,[1] Oussama Ben Fraj,[1] Rym Bouhaha,[1] Khouloud Hamdi,[1] Koudhi Soumaya,[1] Bilel Neili,[1] Gati Asma,[1] Mariano Lucchese,[6] Maria Catanzaro,[6] Vincenza Barbara,[6] Ignazio Brusca,[7] Maria Fregapane,[7] Gaetano Amato,[8] Giuseppe Friscia,[9] Trai Neila,[3] Souayeh Turkia,[3] Haouami Youssra,[3] Raja Rekik,[4] Hayet Bouokez,[5] Maria Vasile Simone,[10] Francesco Fauci,[10] and Giuseppe Raso[2]

[1] *Faculté des Sciences, Université de Tunis El Manar, 1088 Tunis, Tunisia*
[2] *Dipartimento di Fisica e Chimica, Università Degli Studi di Palermo, 90128 Palermo, Italy*
[3] *Hôpital Charles Nicolle, 1006 Tunis, Tunisia*
[4] *Institut Pasteur, 1002 Tunis, Tunisia*
[5] *Hôpital Ariana, 2080 Tunis, Tunisia*
[6] *Ospedale S. Antonio Abate, 91016 Trapani, Italy*
[7] *Ospedale Buccheri La Ferla Fatebenefratelli, 90123 Palermo, Italy*
[8] *Ospedale Civico, 90121 Palermo, Italy*
[9] *Ospedale di Sciacca, 92019 Agrigento, Italy*
[10] *CyclopusCAD srl, 90128 Palermo, Italy*

Correspondence should be addressed to Donato Cascio; donato.cascio@unipa.it

Received 11 September 2015; Revised 24 November 2015; Accepted 17 January 2016

Academic Editor: Dimitrios P. Bogdanos

Antinuclear antibodies (ANAs) are significant biomarkers in the diagnosis of autoimmune diseases in humans, done by mean of Indirect ImmunoFluorescence (IIF) method, and performed by analyzing patterns and fluorescence intensity. This paper introduces the AIDA Project (autoimmunity: diagnosis assisted by computer) developed in the framework of an Italy-Tunisia cross-border cooperation and its preliminary results. A database of interpreted IIF images is being collected through the exchange of images and double reporting and a Gold Standard database, containing around 1000 double reported images, has been settled. The Gold Standard database is used for optimization of a CAD (Computer Aided Detection) solution and for the assessment of its added value, in order to be applied along with an Immunologist as a second Reader in detection of autoantibodies. This CAD system is able to identify on IIF images the fluorescence intensity and the fluorescence pattern. Preliminary results show that CAD, used as second Reader, appeared to perform better than Junior Immunologists and hence may significantly improve their efficacy; compared with two Junior Immunologists, the CAD system showed higher Intensity Accuracy (85,5% versus 66,0% and 66,0%), higher Patterns Accuracy (79,3% versus 48,0% and 66,2%), and higher Mean Class Accuracy (79,4% versus 56,7% and 64.2%).

1. Introduction

Autoimmune diseases are due to a reaction of the immune system to self-antigens, occurring through tolerance breakage. The targeted antigens could be common to all kinds of cells or organ specific, and their recognition by humoral or cellular immune effectors could lead to diversified symptoms, depending on pathology [1–3].

There are over 80 different AID, and collectively they are amongst the most prevalent diseases in the US, affecting at least 7% of the population. Because most AID are chronic and incurable, from a public health perspective they constitute a major health problem which, besides causing individual suffering, has high societal costs [4]. These diseases can affect people of all ages and both sexes, with a higher frequency in women of child-bearing age. The autoimmune diseases are multifactorial, and their risk factors are genetic and environmental. The combination of risk factors may vary from one population to another, generating different epidemiological profiles.

Presence of autoantibodies in patient sera has in itself a value of diagnosis, and the ascertaining of their titer and specificity helps to confirm the autoimmune disease and its follow-up. The search of autoantibodies in sera is based on a routine technique performed by Immunologists and on Indirect ImmunoFluorescence (IIF) [5].

The IIF is the Gold Standard for the diagnosis of autoimmune diseases. IIF is a test having high sensitivity, but only analytical and not diagnostic specificity, since the positivity for ANA does not automatically confirm the presence of autoimmune disease; indeed the ANA may be present even in healthy subjects. Furthermore, the quality of the response is strongly influenced by Reader's experience, by the quality of reagents used for testing (characteristics of the cell substrate or fluorochrome-labeled anti-human immunoglobulins used), and by other local factors. As regards the methods immunochemical alternatives, they have the major advantage of being more easily automated and do not require great expertise in interpretation of the results. By contrast the number of antigenic specificities reportable in the test is certainly lower than that detectable on Hep-2 cells and also the integrity of the antigenic epitopes theoretically detectable is not always preserved [6]. The binding of autoantibodies on HEp-2 cells is revealed by fluorescent antibodies to human immunoglobulin. The fluorescence pattern observed on the microscope (Homogeneous, Fine Speckled, Coarse Speckled, Nucleolar, Centromere, Nuclear Dots, etc.) is specific according to the nature of the self-antigen and its location in the cell.

The main disadvantage of IIF technique is its subjectivity in the interpretation of results, highly depending on the experience of the operator. The difficulty of IIF diagnosis technique is related to the distinction of very similar fluorescence patterns (such as Fine Speckled and Coarse Speckled patterns) and to the subjectivity of the observer. For that reason, two Senior Immunologists (double reading) with strong experience in fluorescent image interpretation are quite often needed. However, this condition is not respected in all immunology laboratories involved in diagnosis.

The introduction of new modern approaches, based on computer systems, is an economic and effective support for the diagnosis of autoimmune diseases [7, 8].

Nowadays the need within the scientific community for a large database of IIF images reported out by medical experts is on the increase. Its use could be related to various purposes: training of young Immunologists, epidemiological studies, diagnosis, and so forth. Storing, processing, and sharing such data necessarily require computer techniques [9]. Moreover, computing support is needed in order to avoid difficulties of IIF images interpretation. As already happening with other medical areas facing the same kind of problems (e.g., Radiology), the second Reader could be replaced by a CAD (Computer Aided Detection) solution [10, 11]. In this paper, computer-assisted diagnosis on IIF images, as performed in the AIDA Project, is presented and discussed.

2. The AIDA Project

The AIDA (autoimmunity: diagnosis assisted by computer) Project has been financed by a EU cross-border cooperation Italy-Tunisia, involving four teams in Sicily and four teams in Tunis, as presented below.

The aim of the AIDA Project is the applications of ICT for the analysis and interpretation of IIF images.

The AIDA Project has two main specific objectives:

(i) the creation of a large database of IIF images, interpreted with the contribution of Italian and Tunisian hospitals;

(ii) the evaluation of the added value of CAD, with cooperation from an Immunologist as a second Reader in detection of autoantibodies.

These specific objectives are being achieved through the production of a set of expected results:

(i) the improvement of organizational and decisional processes of public health policies that will lead to construction of an interinstitutional horizontal partnership (between health facilities) and vertical partnership (region/province/university/ASP),

(ii) the creation of a database of IIF tests images including medical report data,

(iii) application and validation of computer expert systems to support IIF diagnosis in all hospitals involved,

(iv) cooperation between Sicily and Tunisia in research and training within the field of immunology and medical imaging,

(v) conduction of epidemiological studies in autoimmune diseases within regions geographically close though traditionally different in terms of customs and lifestyle,

(vi) increase in employment opportunities within health applied ICT, such as distribution activities, production, and services within this area of expertise, both in Tunisia and in Sicily.

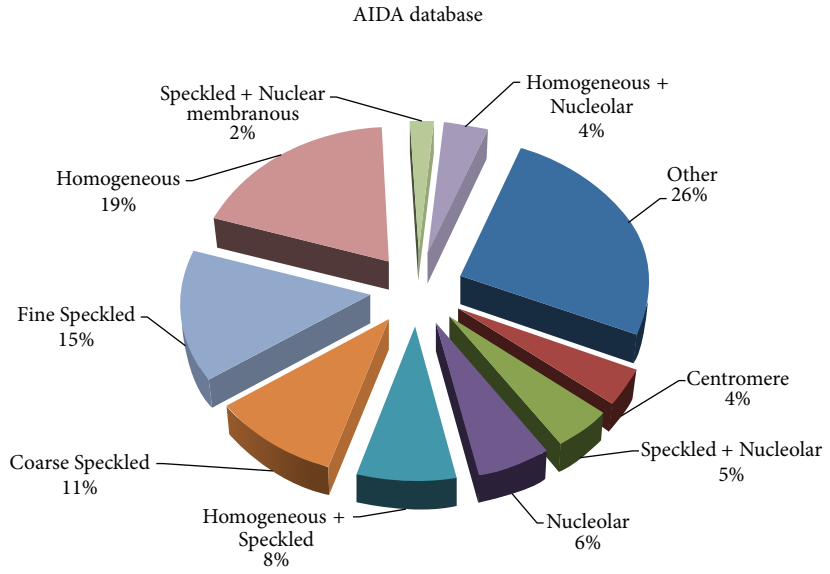

Figure 1: Distribution of IIF patterns in the AIDA database (number of images 14393).

3. Materials and Methods

3.1. IIF Technique and Protocol. As reported in this paper, within the context of the project, the IIF technique has been applied to HEp-2 cells using patients sera selected from immunology laboratories for detection of autoantibodies. Manufacturers of kits and instruments employed for ANA testing in AIDA were different site-to-site; the following automated systems solution for the processing of Indirect ImmunoFluorescence tests has been used: IF Sprinter from Euroimmun, NOVA from INOVA diagnostic, Helios from Aesku.

Serial dilutions were carried out and the dilution of 1/80 was considered positive. After incubation of the 1/80 serum dilution, bound antibodies are revealed by fluorescent antibodies to human immunoglobulin. HEp-2 images have been acquired by means of a unit consisting of a fluorescence microscope (40-fold magnification) coupled with a 50 W mercury vapor lamp and a digital camera. The camera has a CCD sensor equipped with pixel size that equals 3.2 μm × 3.2 μm. The images have 24-bit color depth and are stored in low compression jpeg format. The negativity or positivity of the serum is established along with the fluorescence pattern (Homogeneous, Fine Speckled, Coarse Speckled, Nucleolar, Centromere, Nuclear Dots, etc.) reflecting the autoantibodies specificity. One image has been taken for negative sera and three images have been taken for positive sera.

3.2. Database. Using a uniform approach, three Tunisian immunology services (Pasteur, Charles Nicolle, and Ariana) and four Sicilian ones (ASP-Trapani, Buccheri La Ferla, Civico, and Sciacca) contributed to collection of images of IIF test on HEp-2 cells. These images correspond to the routine IIF technique performed in the different hospitals for autoimmune diseases diagnosis and were thus reported by Senior Immunologists. A total of 5762 sera of patients addressed for diagnosis of autoimmune disease were involved in this study, as indicated in Table 1. Each image and related report was stored in a common database created in the context of AIDA Project. The database stored the contents of two years' activity and reached a total amount of 14393 stored images. This number is very high compared to public IIF images databases available worldwide (public dataset can be downloaded after proper registration, on site: http://i3a2014.unisa.it/).

Table 1: Number of sera and images.

Number of patients	Results of IIF test	Number of selected images	Total images
5762	4316 Positive	12947	14393

A portion of the database utilized is composed of negative images (1446, corresponding to approximately 10%), that is, images whose fluorescence values are not to be associated with autoimmunity problems; 10% of negative cases were considered a satisfactory percentage, in terms of statistics and value purposes, for both Immunologists and the CAD.

The remaining images were classified into different patterns (according to the physician reporting); the distribution rates are shown in Figure 1. In a second step, 6974 images were anonymously exchanged between partners in full respect of ethics and for the purpose of blind double reporting by Senior or Junior Immunologists. The Junior Immunologists are Ph.D. students (3) and are fundamental Immunologists (1). The four young Immunologists (*Juniors*), all coming from the Tunis Faculty of Sciences, were involved as Readers of images already reported by the experts (*Seniors*). In this first study on the benefits of using the CAD for the correct interpretation of IIF test, we wanted to investigate how the system can be a helpful tool to Junior Immunologists.

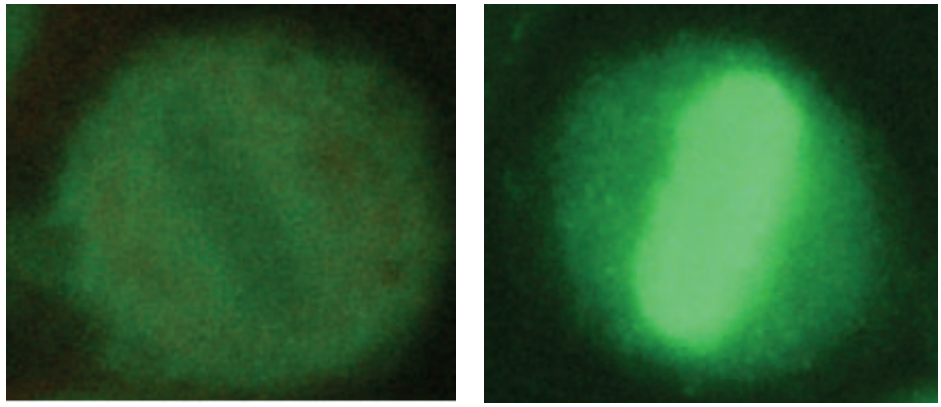

(a) (b)

Figure 2: Examples of negative and positive mitosis ((a) and (b), resp.).

3.3. Statistics Calculation. The Accuracy and the Mean Class Accuracy (MAC) are adopted in this work as measures of the performance [12].

Let CCR_k be the correct classification rate for class k determined as follows:

$$\mathrm{CCR}_k = \frac{T_k}{N_k}, \tag{1}$$

where T_k is the number of correct identifications of class k, while N_k is the total number of elements of class k. The Accuracy is defined by

$$\text{Accuracy} = \frac{\sum_k \mathrm{CCR}_k \cdot N_k}{\sum_k N_k}. \tag{2}$$

The MAC is determined by

$$\mathrm{MAC} = \frac{1}{k}\sum_k \mathrm{CCR}_k. \tag{3}$$

Chi-square test was used to check the relationship between the two classification systems. To test the strength of agreement, interrater agreement statistics was conducted [13]. McNemar test was performed to check the difference for paired proportions. p values of less than 0.05 were considered significant.

3.4. CAD Immuno. Computer Aided Diagnosis (CAD) systems are widely used for different tasks within medicine such as second reading, increasing the diagnosis speed, and training physicians for special task. One of such systems is proposed in recent days for automatic HEp-2 images classification, which is important for detection of antibodies in human serum. In the AIDA Project the *CyclopusCAD Immuno* software was used, powered by CyclopusCAD ltd., a spin-off of University of Palermo [14–18]. It consists of a computer system for image analysis using artificial intelligence methods, of which some are proprietary [19, 20]. The performance comparison between CyclopusCAD Immuno and several automated systems for IIF analysis was presented in a recent paper by Gorgi et al. [21].

3.5. Medical Context. For each well the diagnostic procedure consists of fluorescence intensity classification, mitotic cells recognition, and staining pattern classification for interphase cells. Interestingly, all these steps can be formulated as pattern recognition problems. The medical doctor evaluates the fluorescence intensity of the sample classifying it into three classes, named negative, intermediate, and positive.

Such classification is important since it affects staining pattern identification for interphase cells, which is performed only on positive or intermediate samples. Mitotic cells recognition aims at verifying the presence of at least a cell in mitosis within the image analyzed. Mitotic cells may exhibit two fluorescence patterns. The first, named as negative mitosis, is characterized by a fluorescent cell body while the collapsed chromosomes mass, located in the middle part of the cell, does not exhibit a fluorescent patter or has a weak fluorescence. With the second pattern, reported as positive mitosis, we observe the opposite situation: that is, the cell body is weakly fluorescent or nonfluorescent, while the chromosomes mass is fluorescent. Figure 2 shows examples of negative and positive mitosis. The third step of the IIF diagnostic procedure aims at recognizing the staining pattern of interphase cells. HEp-2 samples with nonnegative fluorescence intensity may reveal different staining patterns, relevant for diagnostic purposes. The patterns classification is performed by the topographic survey of the nuclear fluorescence during the cell cycle. In particular, the chromatin positivity in the phases of the cycle preceding the cell division indicates the possible presence of a Homogeneous pattern. However, this positivity of the chromatin must be differentiated with respect to the case where the chromatin positivity is present in a Centromere pattern. On the contrary, the chromatin negativity is used to direct the classification to those patterns characterized by such negativity (Speckled, Nucleolar) (see also http://www.anapatterns.org/).

The most frequent and clinically useful staining patterns are represented in Figure 3.

It is worth observing how the mitotic cell recognition step is important for two reasons: first, the presence of at least one mitotic cell confirms with medical doctors the correctness

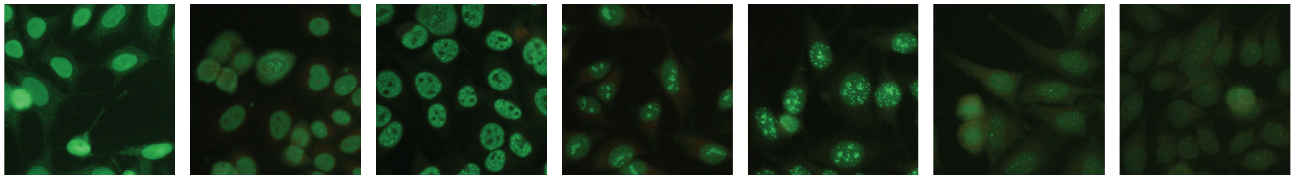

Figure 3: IIF images with different staining patterns (from left to right: Homogeneous, Fine Speckled, Coarse Speckled, Nucleolar, Centromere, Nuclear Dots, and Nuclear Pore Complex).

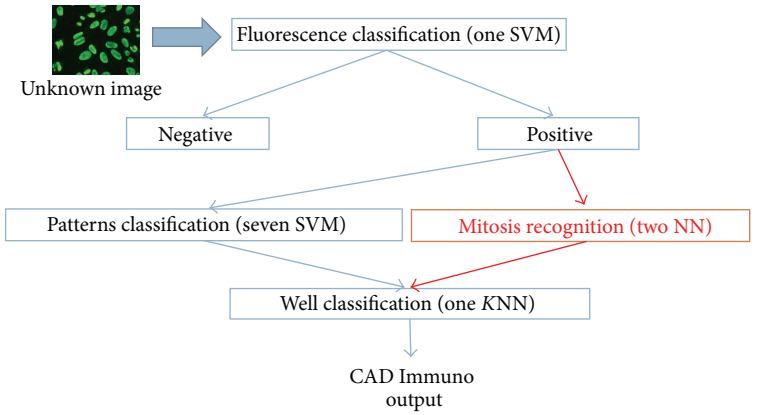

Figure 4: CyclopusCAD Immuno working flow: the system aims to reproduce the operations flow made by Immunologist and described in Section 3.5, by making a classification of fluorescence only for nonnegative images, and by operating a patterns classification and a mitosis classification; it will then be using the results of these classifications to provide a final output.

of well preparation, so that the well is discarded if no cell in mitosis is detected; second, the information on the fluorescence pattern of mitotic cells can be used to improve the ability to discriminate between similar stainings of interphase cells [22].

3.6. CAD Workflow. The CAD Immuno is able to identify, on IIF images, the fluorescence intensity and the fluorescence pattern. In particular, the analysis of fluorescence images for the positive/negative detection is carried out using a Support Vector Machine (SVM) classifier. The system is able to recognize the following fluorescence patterns: Homogeneous, Fine Speckled, Coarse Speckled, Nucleolar, Centromere, Nuclear Dots, and Nuclear Pore Complex. The system searches and classifies positive mitosis and negative mitosis within the image. The classification of mitosis occurs by using two Neural Network (NN) classifiers. The final decision-making process for the detection of fluorescence pattern is achieved by using a K-Nearest Neighbors (K-NN) classifier, having nine inputs (seven outputs of patterns classifiers and two mitosis classifiers). Figure 4 shows the CAD Immuno working flow.

In several multiclass classification problems, it is preferable to use a number of classifiers equal to the number of classes and each classifier is trained to discriminate a class from all the others (binary approach) [23]. In this system, in addition to differentiating the classification stage by implementing seven classifiers for seven classes of staining patterns, the preprocessing, segmentation, and feature extraction steps are differentiated as well. The CAD Immuno here presented adopts a nonstandard pipeline for supervised image classification.

Figure 5 shows the flow of operations adopted in this work; the generic new image is simultaneously processed by seven processes, obtaining seven separate outputs representing how the cell resembles each of the 7 classes analyzed in this work. The choice of methods, features, and parameters was performed automatically, using the Mean Class Accuracy (MCA) as a "figure of merit." The parameters involved are tuned using a cross validation scheme. The main benefit of this pipeline consists in offering of a good explanatory faculty, based on an easily explainable principle.

3.7. Features. Cells patterns analysis clearly shows that differences between classes are mainly based on the presence and distribution of bright/dark structures: numbers, sizes (areas), intensity, and colors. It seems natural to use features providing an analysis of texture and more specifically features able to deal with bright/dark speckle-like structure description.

Different staining patterns can be characterized by a limited set of attributes describing the spatial relationships between pixels values and main image variations occurring in each cell type; this information is generally obtained by mean of textural analysis techniques. These techniques can be grouped into two major categories: (i) statistical methods describing the distribution of grey-levels in the image and (ii) frequency domain measurements of image variations [24–26]. To achieve the objective of robust classification, we

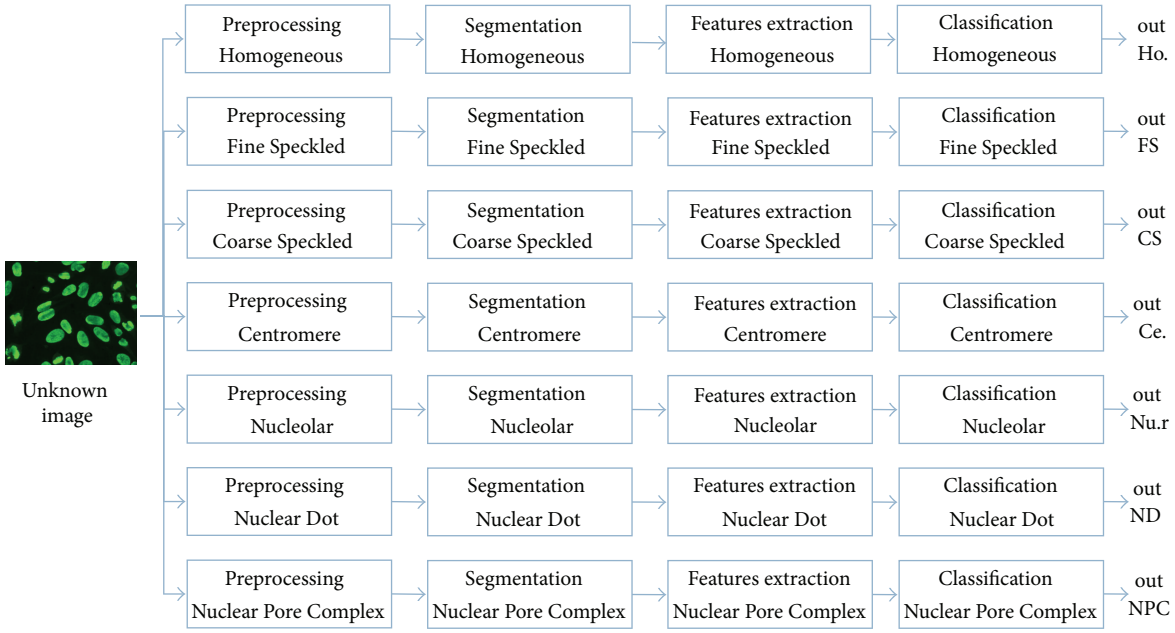

Figure 5: Pipeline of patterns classification method: the generic new image is simultaneously processed by seven processes, thus obtaining seven separate outputs showing how the cell resembles each of the 7 classes analyzed in this work; as an example, out Ho. represents the degree of similarity between the unknown image and the Homogeneous images.

Table 2: Level of concordance between two Senior Immunologist Readers of 589 wells.

		Senior 1							
		Negative	Homog.	Fine S.	Coarse S.	Nucleol.	Centrom.	Dot	TOT
Senior 2	Negative	**117**	6	10	5	3			141
	Homog.	5	**110**	15	3	1			134
	Fine S.	26	22	**49**	24	1			122
	Coarse S.	23	4	20	**67**				114
	Nucleol.	1				**38**			39
	Centrom.						**31**		31
	Dot					1		**7**	8
	TOT	172	142	94	99	44	31	7	**589**

combined several discriminative visual features known to be effective for cell classifications with a robust and scalable multiclass boosting. All classifiers, developed in this project by CyclopusCAD, use a large number (108) of extracted features, able to fully characterize the HEp-2 cells. In more detail, four quantization levels [27] were analyzed (256, 128, 64, and 32), and for each of them the following 27 features have been extracted [28].

(i) Intensity Based Features (9). They include mean value, standard deviation, ratio of standard deviation to the mean value, entropy, moment of inertia, skewness, kurtosis, and entropy of the contours gradient.

(ii) Geometry-Based Features (8). They include mean radius, standard deviation of radius, maximum radius, ratio of the standard deviation to the mean value, circularity, anisotropy, fractal index, and eccentricity.

(iii) Shape-Morphological-Based Features (8). They include area, perimeter, convex area, convex deficiency, solidity, compactness, roundness, and Euler's number.

(iv) Descriptors-Based Features (2). They include entropy of HOG (Histogram of Oriented Gradients) and entropy of HAG (Histogram of Amplitude Gradients).

4. Results and Discussion

In order to evaluate the concordance level, a subsample of 589 wells (each of them with 3 images), reported by two Senior Immunologists, was analyzed. The results are shown in Table 2 and revealed a concordance level around 71% (Cohen's K statistic was 0.64). The maximum level of concordance has been obtained for the Centromere pattern. The lower concordance level is observed with the Fine Speckled pattern. This concordance level represents the difficulty of

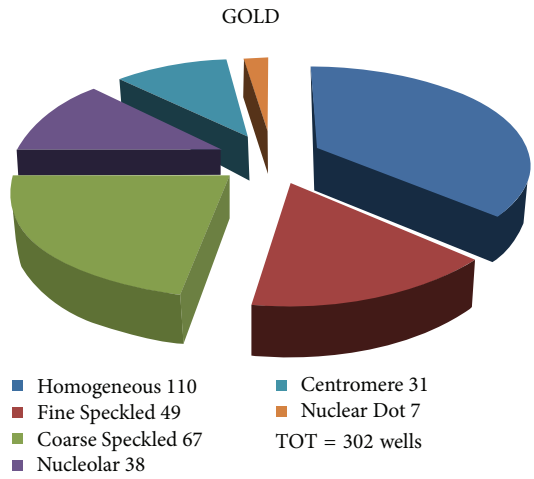

Figure 6: Distribution of IIF patterns in the Gold Standard database (number of images 1006 and number of wells 302).

interpretation of IIF images and the obvious need for a double reading and for Gold Standard. Taking only images into account, with a concordance of interpretation between the two Senior Immunologists, a subsample database was then extracted containing 1006 images, representing all types of patterns (302 wells corresponding to 906 images) and including negative tests (100 images).

In this Gold Standard database, the distribution of the different patterns is given in Figure 6. The overall approach is resumed in Table 3.

Our objective is to evaluate the added value of the CAD used as a second Reader. We first tested CAD performance *stand-alone* in comparison with two Junior Immunologists. Four young fundamental Immunologists (*Juniors*) were involved as Readers of images already reported by the experts (*Seniors*). Before being compared to the CAD, the reporting concordances of these Junior Readers were compared with each other and to those of a Senior Immunologist. As shown in Table 4, and as expected, the concordance level between Junior and Senior Immunologists was lower than that observed when comparing only Seniors. The only exception to this is with Reader 4, who is a more experienced fundamental Immunologist but has never been involved in diagnosis.

We also compared the Junior Readers with one another. We looked at two pairs: Juniors 1 and 2 against Juniors 3 and 4. The results indicate, for each pair, a concordance level that is near to the mean concordance of a Senior.

In another step we assessed the performance of two Juniors reporting on Gold Standard wells (each of them with 3 images). Accuracy was established by considering intensity on one hand and patterns on the other.

We then compared this performance to that of the CAD, which gave better results than Junior Immunologists, as shown in Tables 5 and 6.

Compared with the two Readers, CyclopusCAD Immuno software showed higher Intensity Accuracy (versus Junior 1 $p = 0.016$, versus Junior 2 $p = 0.016$), higher Patterns Accuracy (versus Junior 1 $p < 0.0001$, versus Junior 2 $p = 0.1$), and higher MAC (versus Junior 1 $p = 0.0026$, versus Junior 2 $p = 0.057$).

In a last step we assessed the performance improvement of the Junior Immunologist reports with the support of

Table 3: Number of IIF images in AIDA database: with one or two reports among which a Gold Standard sample with concordant reporting was extracted.

	Images		
	With 1 report	With 2 reports	*Gold Standard*
Positive	12947	6274	906
Negative	1446	700	100
Total	**14393**	6974	1006

Table 4: Percent of reporting concordance of Junior Immunologist versus Senior or Junior Immunologist.

Concordance% of Juniors versus Seniors				
Junior Readers	1	2	3	4
Number of wells	117	169	174	141
Concordance	37,6%	53,2%	42,5%	72,3%
Mean	45,8%		57,4%	
Concordance% of Junior versus Junior				
Juniors pair	1 versus 2		3 versus 4	
Number of wells	265		219	
Concordance	46,8%		68,5%	

Table 5: Comparison of CAD and Junior reporting using Gold Standard images as reference.

Readers	Intensity	Patterns		
	Accuracy	Accuracy	Mean accuracy	Cohen's *K*
Junior 1	66,0%	48,0%	56,7%	0,36
Junior 2	66,0%	66,2%	64,2%	0,58
CAD	**85,5%**	**79,3%**	**79,4%**	**0,36**

Table 6: Accuracy and mean accuracy of CAD compared to Gold Standard used as reference.

CAD	Homog.	Fine S.	Coarse S.	Nucleol.	Centrom.	Dot	Other	ACC	MAC
Homog.	**81,1**%	9,5%	6,8%	2,7%	0,0%	0,0%	0,0%		
Fine S.	6,5%	**54,8**%	16,1%	19,4%	3,2%	0,0%	0,0%		
Coarse S.	0,0%	9,6%	**80,8**%	3,8%	3,8%	1,9%	0,0%		
Nucleol.	3,3%	10,0%	0,0%	**86,7**%	0,0%	0,0%	0,0%	**79,3**%	**79,4**%
Centrom.	3,4%	3,4%	0,0%	3,4%	**89,7**%	0,0%	0,0%		
Dot	0,0%	0,0%	16,7	0,0%	0,0%	**83,3**%	0,0%		
Other	0,0%	0,0%	0,0%	0,0%	0,0%	0,0%	**0,0**%		

Table 7: Accuracy of Junior reporting with the support of the CAD using Gold Standard images as reference.

Readers	Intensity	Patterns		
	Accuracy	Accuracy	Mean accuracy	Cohen's K
Junior 1	76,0%	69,5%	73,9%	0,61
Junior 2	66,0%	68,2%	66,3%	0,60

the CAD. The increase in accuracy, reported in Table 7, is observed particularly for Junior Reader 1.

With respect to the performance of Junior 1,

(i) Intensity Accuracy varied from 66% to 76%, showing an increase ($p = 0.21$);

(ii) Patterns Accuracy varied from 48% to 69.5% and was significantly increased ($p = 0.002$);

(iii) MAC varied from 56.7% to 73.9% and was significantly increased ($p = 0.02$);

(iv) Cohen's K varied from 0,36 to 0,61.

With respect to the performance of Junior 2,

(i) Intensity Accuracy showed no variation;

(ii) Patterns Accuracy varied from 66.2% to 68.2%, showing a low significance increase ($p = 0.81$);

(iii) MAC varied from 64.2% to 66.3, showing a low significance increase ($p = 0.79$);

(iv) Cohen's K varied from 0,58 to 0,60.

5. Conclusions

In this paper the AIDA Project and its preliminary results are presented. The AIDA Project initiative in Italy and Tunis suggests that a joint effort by Health Professionals, Scientific Societies, and patients' associations can make a difference. Even before its closure the preliminary results produced by the AIDA Project are very encouraging. The size of the database, with around 14500 images and each with their respective report, is the biggest within the field of Indirect ImmunoFluorescence applied to autoimmune diseases diagnosis in the world. Additionally we have compiled around 1000 images with two concordant reports established by immunology experts and including different patterns, which have composed our first Gold Standard database. This has been the basis for "learning" of the *CyclopusCAD Immuno* software. This Gold Standard database has proven to be of great interest and has been considered for use as reference to evaluate Junior and Fundamental Immunologists and CAD performance. The automatic CAD system used and optimized in the AIDA Project has been described and its performance was evaluated.

In this work the results in terms of performance of Junior Immunologists, CAD, and Immunologists with the aid of CAD have also been reported. The CAD system showed higher Intensity Accuracy (85,5% versus 66,0% and 66,0%), higher Patterns Accuracy (79,3% versus 48,0% and 66,2%), and higher MAC (79,4% versus 56,7% and 64.2%).

Another objective of this project is to evaluate the added value of the CAD used as a second Reader. The analysis conducted here showed that the CAD support improves the performances of Junior Immunologists up to as much as 45%, as highlighted by the comparisons reported on Tables 5 and 7.

Considering the concordance level between Fundamental Immunologists evaluated at 71%, the CAD seems to bring the same level of performance. Indeed, when compared to Gold Standard, the CAD showed a mean accuracy of 85% for intensity evaluation and 79% for pattern recognition.

With these preliminary results, we can conclude that the objectives of the project are being reached with the demonstration that the CAD shows a higher performance than Junior Immunologists and equivalent results with Immunology Experts. In a further step, the Gold Standard database should be enriched, including the addition of more double reported and triple reported images. With such a high number of images of high-quality reporting, we would be able to improve the CAD performance and our quality assessment approach in order to offer a product of high confidence that could be used as second Reader to student learning and to remote diagnosis.

Disclaimer

This document was produced with the financial assistance of the European Union in the frame of the ENPI CT Italy-Tunisia 2007–2013. The views expressed herein can in no way be taken to reflect the official opinion of the European Union. Sole responsibility for the views, interpretations, or conclusions contained in this document lies with the authors. Neither the European Commission nor Management

Structures of the Program can be held responsible for the accuracy, completeness, or use of the information contained herein.

Conflict of Interests

The authors declare that there is no conflict of interests regarding the publication of this paper.

Acknowledgments

The authors thank Dr. Marcella Zanetti for the excellent work and organizational support. The authors thank the Department of Health of the Sicilian Region (Italy) and the Public Health Department of Tunis (Tunisia) for the support provided.

References

[1] M. J. Fritzler, "Toward a new autoantibody diagnostic orthodoxy: understanding the bad, good and indifferent," *Autoimmunity Highlights*, vol. 3, no. 2, pp. 51–58, 2012.

[2] R. Tozzoli, N. Bizzaro, E. Tonutti et al., "Guidelines for the laboratory use of autoantibody tests in the diagnosis and monitoring of autoimmune rheumatic diseases," *American Journal of Clinical Pathology*, vol. 117, no. 2, pp. 316–324, 2002.

[3] N. Bizzaro and A. Wiik, "Appropriateness in anti-nuclear antibody testing: from clinical request to strategic laboratory practice," *Clinical and Experimental Rheumatology*, vol. 22, no. 3, pp. 349–355, 2004.

[4] The Autoimmune Diseases Coordinating Committee (National Institutes of Health), *Progress in Autoimmune Diseases Research*, 2005.

[5] N. Bizzaro, A. Antico, S. Platzgummer et al., "Automated antinuclear immunofluorescence antibody screening: a comparative study of six computer-aided diagnostic systems," *Autoimmunity Reviews*, vol. 13, no. 3, pp. 292–298, 2014.

[6] N. Agmon-Levin, J. Damoiseaux, C. Kallenberg et al., "International recommendations for the assessment of autoantibodies to cellular antigens referred to as anti-nuclear antibodies," *Annals of the Rheumatic Diseases*, vol. 73, no. 1, pp. 17–23, 2014.

[7] R. Hiemann, T. Büttner, T. Krieger, D. Roggenbuck, U. Sack, and K. Conrad, "Challenges of automated screening and differentiation of non-organ specific autoantibodies on HEp-2 cells," *Autoimmunity Reviews*, vol. 9, no. 1, pp. 17–22, 2009.

[8] A. Willitzki, R. Hiemann, V. Peters et al., "New platform technology for comprehensive serological diagnostics of autoimmune diseases," *Clinical and Developmental Immunology*, vol. 2012, Article ID 284740, 8 pages, 2012.

[9] S. Tangaro, R. Bellotti, F. De Carlo et al., "MAGIC-5: an Italian mammographic database of digitised images for research," *Radiologia Medica*, vol. 113, no. 4, pp. 477–485, 2008.

[10] S. Ciatto, D. Cascio, F. Fauci et al., "Computer-assisted diagnosis (CAD) in mammography: comparison of diagnostic accuracy of a new algorithm (Cyclopus[5], Medicad) with two commercial systems," *La Radiologia Medica*, vol. 114, no. 4, pp. 626–635, 2009.

[11] D. Cascio, F. Fauci, M. Iacomi et al., "Computer-aided diagnosis in digital mammography: comparison of two commercial systems," *Imaging in Medicine*, vol. 6, no. 1, pp. 13–20, 2014.

[12] A. Rigon, F. Buzzulini, P. Soda et al., "Novel opportunities in automated classification of antinuclear antibodies on HEp-2 cells," *Autoimmunity Reviews*, vol. 10, no. 10, pp. 647–652, 2011.

[13] J. Cohen, "A coefficient of agreement for nominal scales," *Educational and Psychological Measurement*, vol. 20, no. 1, pp. 37–46, 1960.

[14] D. Cascio, R. Magro, F. Fauci, M. Iacomi, and G. Raso, "Automatic detection of lung nodules in CT datasets based on stable 3D mass-spring models," *Computers in Biology and Medicine*, vol. 42, no. 11, pp. 1098–1109, 2012.

[15] L. Vivona, D. Cascio, F. Fauci, and G. Raso, "Fuzzy technique for microcalcifications clustering in digital mammograms," *BMC Medical Imaging*, vol. 14, no. 1, article 23, 18 pages, 2014.

[16] M. Iacomi, D. Cascio, F. Fauci, and G. Raso, "Mammographic images segmentation based on chaotic map clustering algorithm," *BMC Medical Imaging*, vol. 14, article 12, 2014.

[17] F. Fauci, A. La Manna, D. Cascio et al., "A fourier based algorithm for microcalcifications enhancement in mammographic images," in *Proceedings of the IEEE Nuclear Science Symposium and Medical Imaging Conference Record*, pp. 4388–4391, Anaheim, Calif, USA, October-November 2012.

[18] D. Cascio, V. Taormina, M. Cipolla, F. Fauci, M. Vasile, and G. Raso, "HEp-2 cell classification with heterogeneous classes-processes based on k-nearest neighbours," in *Proceedings of the 1st Workshop on Pattern Recognition Techniques for Indirect Immunofluorescence Images*, pp. 10–15, Stockholm, Sweden, August 2014.

[19] D. Cascio, F. Fauci, R. Magro, and G. Raso, "Method for processing biomedical images," Patent WO 2007/119204 A2, 2007.

[20] D. Cascio, F. Fauci, and G. Raso, "Metodo di template matching per l'analisi di immagini mediche," Patent in Italy PA2012A000019, 2012.

[21] Y. Gorgi, T. Dhaouadi, I. Sfar et al., "Comparative study of human and automated screening for antinuclear antibodies by immunofluorescence on HEp-2 cells," *International Journal of Statistics in Medical Research*, vol. 4, no. 3, pp. 270–276, 2015.

[22] A. Bradwell, R. Stokes, and G. Johnson, *Atlas of HEp-2 Patterns and Laboratory Techniques*, Binding Site, Birmingham, UK, 1995.

[23] J. Furnkranz, "Round robin classification," *Journal of Machine Learning Research*, vol. 2, no. 4, pp. 721–747, 2002.

[24] G. L. Masala, S. Tangaro, B. Golosio et al., "Comparative study of feature classification methods for mass lesion recognition in digitized mammograms," *Nuovo Cimento C*, vol. 30, no. 3, pp. 305–316, 2007.

[25] L. Vivona, D. Cascio, R. Magro, F. Fauci, and G. Raso, "A fuzzy logic C-means clustering algorithm to enhance microcalcifications clusters in digital mammograms," in *Proceedings of the IEEE Nuclear Science Symposium and Medical Imaging Conference (NSS/MIC '11)*, pp. 3048–3050, Valencia, Spain, October 2011.

[26] G. L. Masala, B. Golosio, P. Oliva et al., "Classifiers trained on dissimilarity representation of medical pattern: a comparative study," *Nuovo Cimento C*, vol. 28, no. 6, pp. 905–912, 2005.

[27] P. Perner, H. Perner, and B. Müller, "Mining knowledge for HEp-2 cell image classification," *Artificial Intelligence in Medicine*, vol. 26, no. 1-2, pp. 161–173, 2002.

[28] D. Cascio, V. Taormina, M. Cipolla, S. Bruno, F. Fauci, and G. Raso, "A multi-process systems for HEp-2 cells classification based on SVM," *Pattern Recognition Letters*, vol. 74, pp. 10–17, 2016.

Hindawi Publishing Corporation
BioMed Research International
Volume 2016, Article ID 8659298, 11 pages
http://dx.doi.org/10.1155/2016/8659298

Research Article

Development of High-Field Permanent Magnetic Circuits for NMRI/MRI and Imaging on Mice

Guangxin Wang,[1] Huantong Xie,[2] Shulian Hou,[3] Wei Chen,[1] and Xiuhong Yang[3]

[1]*College of Science, North China University of Science and Technology, Tangshan 063000, China*
[2]*Shanghai Shining Global Science and Education Equipment Corporation, Ltd., Shanghai 201806, China*
[3]*Fundamental Medical College, North China University of Science and Technology, Tangshan 063000, China*

Correspondence should be addressed to Shulian Hou; houshulian@163.com

Received 15 October 2015; Revised 24 January 2016; Accepted 27 January 2016

Academic Editor: Guang Jia

The high-field permanent magnetic circuits of 1.2 T and 1.5 T with novel magnetic focusing and curved-surface correction are developed. The permanent magnetic circuit comprises a magnetic yoke, main magnetic steel, nonspherical curved-surface magnetic poles, plugging magnetic steel, and side magnetic steel. In this work, a novel shimming method is proposed for the effective correction of base magnetic field (B_0) inhomogeneities, which is based on passive shimming on the telescope aspheric cutting, grinding, and fine processing technology of the nonspherical curved-surface magnetic poles and active shimming adding higher-order gradient coils. Meanwhile, the magnetic resonance imaging dedicated alloy with high-saturation magnetic field induction intensity and high electrical resistivity is developed, and nonspherical curved-surface magnetic poles which are made of the dedicated alloy have very good anti-eddy-current effect. In addition, the large temperature coefficient problem of permanent magnet can be effectively controlled by using a high quality temperature controller and deuterium external locking technique. Combining our patents such as gradient coil, RF coil, and integration computer software, two kinds of small animal Micro-MRI instruments are developed, by which the high quality MRI images of mice were obtained.

1. Introduction

Magnetic resonance imaging (MRI) has become more and more important for clinical and basic medicine. MRI technology has many important characteristics, such as noninvasive, high soft tissue contrast, and can provide distinct anatomical information of lesions. It has significant advantage in functional imaging, especially. In addition, a lot of medical researches have to be done on animals such as rats and mice. Therefore, the research and development of small animal MRI instrument are becoming more and more urgent. It is well known that the stronger magnetic field can provide a higher signal-to-noise ratio (SNR) and images with good quality [1]. However, the optimum field strength remains unknown and depends upon many factors such as leakage magnet, image inhomogeneities, and eddy currents induced by fast switching gradients of the magnetic field gradients. At present, the mainstream of small animal MRI pieces of equipment with the magnetic field strength ≥7 T [2, 3] is generally produced on the basis of superconductor technology. Moreover, the price of these pieces of equipment is very high, and the laboratories in some universities cannot afford them. Actually, it is not necessary to perform small animals imaging by using ultra-high-field MRI instrument. For permanent magnet type MRI instrument, when the magnetic field strength is about 1.5 T, it can meet the requirements of small animal structure imaging and preliminary functional imaging.

B_0 magnet is the most important part of permanent magnet type MRI instrument. Currently, the magnetic field strength of B_0 magnet is generally less than 1 T. In order to increase magnetic field intensity, reduce leakage magnet, and achieve shimming, some researchers have adopted different methods, such as adding yokes [4], pole shoes [5], and

shim rings [6] in B_0 magnet. It is reported that B_0 magnet can generally be improved by the optimization of magnetic pole shapes [7], adding adjustable shim pieces to the C-shaped magnetic poles [8], and changing magnet yokes [9]. At present, a 0.6 T MRI instrument with bore 450 mm was developed successfully [10]. The research and development of 1.0 T MRI system is also reported [11, 12]. When the magnetic field strength of cylindrical permanent magnet is up to 1.5 T, it is very difficult to install the compensation coils and solve the problem of base magnetic field uniformity. Yamada et al. [13] investigated the potential of such systems in functional MR imaging (fMRI) of somatosensory cortex activity elicited by forepaw stimulation in medetomidine-sedated rats by using a 1.5 T compact imager. Haishi et al. [14] developed a 2.0 T permanent magnetic circuit for NMR/MRI and obtained MRI image of a human finger in vivo. Moreover, the images of a live animal are not obtained in this reference. Tamada et al. [15] also developed a 2.0 T permanent magnet using a biplanar single-channel shim coil, but the mass of this kind of permanent magnet is bigger, and the space utilization of B_0 magnet is lower. Therefore, the increase of B_0 magnetic field in keeping large utilization efficiency of magnetic space is very important for upgrading permanent magnetic circuit for NMRI/MRI. The Magnetic Materials Research Center of Shin-Etsu Chemical Co., Ltd., has successfully developed the world's largest large-scale magnetic circuit for a Halbach type permanent magnet with a total weight of approximately 9.5 tons [16]. Although it is the largest permanent magnetic circuit generating a strong magnetic field, it will be used mainly on the production processes for MR sensor for use in MRAMs (magnetoresistance random access memories) and encoders for position detection. Moreover, our developed 1.2 T and 1.5 T permanent magnetic circuits for a half-Halbach type permanent magnet are used mainly for small animal Micro-MRI instruments.

Shimming is also a key problem in the development of permanent magnetic circuit [17–20], which consists of the passive shimming and the active shimming. The passive shimming technology is invented in the early 1990s [17]. To date, the passive shimming of permanent magnet mainly draws from one of the superconducting magnets [21]. There is no special shimming method tailored to the characteristics of permanent magnet, and the shimming mainly depends on experiences. So the shimming of permanent magnet has not made a substantial progress. At present, many optimization methods [22–29] on permanent magnet shimming are proposed, such as linear programming method [22], dynamic programming method [23], linear integer programming method [24], mixed integer programming method [25], successive approximation method [26], and other passive shimming technologies [27–29]. In order to realize the shimming of permanent magnet, the working space should be away from shim pieces, which produced an uneven local small magnetic field. Therefore, the effective working space will become small. This is also a primary factor restricting the development of permanent magnet. At present, it is reported that shimming method adding thin iron pieces is often used. Owing to the edge effect on thin iron piece shimming, the effective shimming space becomes small and the efficiency reduces. In the study, we adopted the passive shimming method of cutting, grinding, and fine processing technology in realizing the homogeneity field. The active shimming of permanent magnet is generally obtained by adding several high-order current coils. These coils may correct the complex inhomogeneity of B_0 magnet. Tamada et al. [30] proposed a new planar single-channel shim coil in the magnet gap. The coil design is based on the superposition of multiple circular currents and the stream function method. In this study, the active shimming is obtained by adding higher-order current coils in the remaining spaces of RF coil and gradient coil, which not only achieves the shimming but also saves the magnetic field space.

The eddy current problem in permanent magnet is also very prominent due to the existence of more ferromagnetic materials. The eddy current will increase when ferromagnetic pieces and magnetic yokes are directly connected to permanent magnetic circuit [31–34]. At present, the active self-shielding [31–33] is a most competent method on solving the eddy current. The active self-shielding gradient coil may be obtained by installing a shielding coil outside gradient coil. When the current phases of self-shielding coil and gradient coil remain strictly the same, the eddy current of superconducting magnet may effectively be eliminated. However, it is not suitable for permanent magnet to install large active self-shielding coil because the active self-shielding coil takes up a lot of space. Making an anti-eddy-current board is currently a popular method of reducing the eddy current for permanent magnet instrument [34]. Moreover, the anti-eddy-current board will occupy valuable working space. Therefore, it is also not an ideal method of reducing eddy current.

To solve these problems, we made the improvement from three aspects according to the characteristic of permanent magnet. (1) The improvement on B_0 magnet of permanent magnetic circuit: in order to increase the magnetic field strength of B_0 magnet, the space efficiency, and uniformity, high-field permanent magnet system with magnetic focusing and curved-surface correction is developed. (2) The improvement on the shimming of B_0 magnet: self-developed novel shimming scheme is based on passive shimming and active shimming. In the passive shimming, the traditional passive shimming method adding shim pieces is subverted, and the cutting, grinding, and fine processing technology of magnetic poles is adopted for realizing the homogeneity field. The active shimming method adding higher-order coils is proposed, which helps reduce the shimming difficult and saves the working space. (3) The improvement of the anti-eddy-current technology on B_0 magnet: a new magnetic pole is formed by connecting alloy magnetic pole with main magnetic steel together. The nonspherical curved-surface magnetic poles made of the self-developed MRI dedicated alloy replaced pole pieces and anti-eddy-current board. The MRI dedicated alloy is a kind of high electrical impedance permanent magnet material, which may effectively reduce the eddy current. By using the above technologies, along with gradient coil [35], RF coil [36], and integration computer software [37], 1.2 T and 1.5 T small animal Micro-MRI instruments (Figure 1) are developed, by which the high quality MRI images of mice were obtained.

(a) (b)

Figure 1: MRI systems with 1.2 T (a) and 1.5 T (b) permanent magnetic circuits.

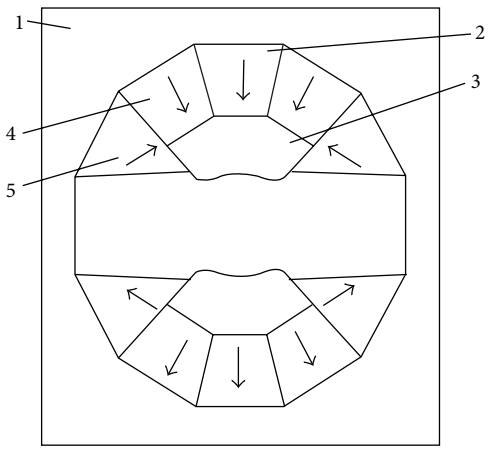

Figure 2: Cross-section schematic of permanent magnetic circuit. 1, magnetic yoke, 2, main magnetic steel, 3, nonspherical curved-surface magnetic poles, 4, plugging magnetic steel, and 5, side magnetic steel. The arrows represent the direction of magnetic susceptibility of magnetic steel.

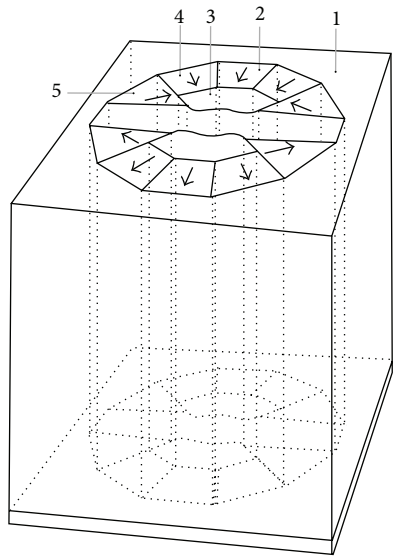

Figure 3: Cross-sectional stereogram of permanent magnetic circuit.

2. Development of Permanent MRI Instrument

2.1. The Design of Permanent Magnetic Circuit. The cross-section schematic and stereogram of permanent magnet circuit are shown in Figures 2 and 3, respectively. Herein the nonspherical curved-surface magnetic poles made of the magnetic resonance imaging dedicated alloy are two saddle-type rotary curved surfaces, have the same shapes, and are symmetrically distributed at the center of the magnetic yoke. Two pieces of main magnetic steel (MMS) are, respectively, positioned behind the two magnetic poles; the plugging magnetic steel is deviated from the center position and is, respectively, positioned behind the two magnetic poles and positioned on the two side surfaces of the main magnetic steel; the side magnetic steel is, respectively, positioned on the side surfaces of the two magnetic poles and arranged on the outer side of the plugging magnetic steel. The main magnetic steel and the plugging magnetic steel are made of permanent magnet materials with high coercive force; the side magnetic steel is made of permanent magnet materials with higher coercive force; the coercive force of the side magnetic steel is over 20 percent higher than that of the main magnetic steel.

The specific sizes of permanent magnetic circuit are determined by the inverse design of magnetic field distribution, and the design generally consists of three stages. First, the magnetic field distribution of permanent B_0 magnet is determined within the magnetic field theory. Second, the magnetic circuit and the sizes of permanent magnet and ferromagnetic parts are determined according to magnetic properties of special alloy and NdFeB material, magnet working gap, and magnetic flux density (see Figure 4). In order to correct the error causing more simplified processing, the structure parameters of permanent B_0 magnet are further optimized by means of MATLAB simulation. At last, the

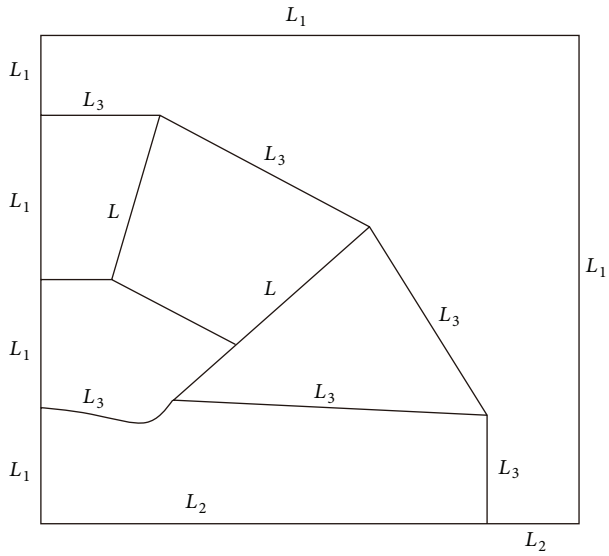

Figure 4: The boundary schematic of selected 1/4 permanent magnet in computation. L_1 is the boundary parallel to magnetic induction lines. L_2 denotes the symmetrical boundary perpendicular to magnetic induction lines. L_3 denotes the border between two materials such as iron and NdFeB, air and NdFeB, magnetic poles alloy and NdFeB, and magnetic poles alloy and air. L is the boundary of magnetizing current.

exact sizes of permanent magnetic circuit are determined on the basis of the experiments of magnetic field design and permanent magnetic circuit manufacture. Considering high symmetry of closed permanent magnet circuit, the sizes of two-dimensional permanent magnet circuit are determined firstly, by which the ones of three-dimensional permanent magnet circuit are deduced. The electromagnetic field equation of the simplified main magnet model is given as in [38]. We only drew boundary schematic of symmetric permanent magnetic circuits in Figures 9 and 10. $\Omega(L_1 \cup L_2 \cup L_3 \cup L)$ in (1) denotes the entire solution domain:

$$\frac{\partial}{\partial x}\left(\nu\frac{\partial A}{\partial x}\right) + \frac{\partial}{\partial y}\left(\nu\frac{\partial A}{\partial y}\right) = 0, \quad \Omega\left(L_1 \cup L_2 \cup L_3 \cup L\right), \tag{1}$$

$$A = 0, \quad L_1, \tag{2}$$

$$\frac{\partial A}{\partial r} = 0, \quad L_2, \tag{3}$$

$$\left(\nu\frac{\partial A}{\partial n}\right)_{L_3^+} = \left(\nu\frac{\partial A}{\partial n}\right)_{L_3^-}, \quad L_3, \tag{4}$$

$$\left(\nu\frac{\partial A}{\partial n}\right)_{L^+} - \left(\nu\frac{\partial A}{\partial n}\right)_{L^-} = j, \quad L, \tag{5}$$

where A is the undetermined magnetic vector potential. The reluctivity ν is equal to the reciprocal of the permeability μ. μ denotes the relative permeability of permanent magnetic material along the easy magnetization direction. The permeability μ is regarded as the permeability of vacuum μ_0 in computation. j is the density of bound current. It is very difficult to obtain analytical solutions of the above equations. The sizes of magnetic poles and side magnets are obtained using the finite element method and the CUDAGPU software. The objective function of utilization coefficient on permanent magnet is given as

$$M = \frac{\int \upsilon_c \left|B_c\right|^2 dV}{\int \upsilon_m \left|J_0{}^2\right| dV}, \tag{6}$$

where υ_c denotes the space area between two poles of B_0 magnet, B_c is the magnetic density, υ_m denotes the volume of space occupied permanent magnet, and J_0 is the modulus of residual magnetization vector in permanent magnetic material. In practical design, we selected the utilization coefficient as large as possible ($M = 0.7$). The permanent magnet is made of N50-type high-grade steel (residual magnetic flux $B_r = 1.4$ T) [39]. Based on numerical calculation and manufacturing experience, the angles between main magnetic steel, nonspherical curved-surface magnetic poles, plugging magnetic steel, and side magnetic steel are determined. The sizes of each part of 1.2 T and 1.5 T permanent circuits are also determined. Their specific sizes may be seen in Figures 5, 9, and 10 and Tables 1–3.

The shape and structure schematic of nonspherical curved-surface magnetic poles is demonstrated in Figure 5. The magnetic poles (3 in Figure 2) with saddle-type rotary curved surfaces are symmetrically distributed at the center of the magnetic yoke. The closest distance d between two magnetic poles is the magnetic poles gap, x is the distance from a location point on the curved surface to the center of the magnet, and y is the distance between the corresponding location points of two rotating curved surfaces. In designing the curved-surface magnetic poles, the magnetic poles gap (d) must have higher precision at any angle. The relative error of d is less than 0.0003 mm (0.3 μm). The two curved surfaces must have higher symmetry, and the relative error is less than 0.0003 mm (0.3 μm). And the two curved surfaces must be high symmetrical on the center dotted line, whose relative error is less than 0.0005 mm (0.5 μm). In Table 1, the size of magnetic poles with saddle-type rotary curved surfaces is demonstrated by using the quadratic interpolation. The data error in Table 1 is generally less than 0.1%. By the adoption of a magnetic focusing technology, high-field 1.2–2.1 T intensity can be achieved. The uniform field of a magnet is corrected by the curved surfaces, so that extremely high space efficiency and more than ten times the uniformity are achieved.

2.2. B_0 Magnet Shimming. The highly homogeneous magnetic field is required in permanent magnet type MRI system. The basic magnetic field cannot meet the high uniformity requirement of MRI systems, so it is rather important to achieve the shimming of B_0 magnet. At present, the shimming methods mainly include the active shimming and the passive shimming. The passive shimming adding ferromagnetic pieces is a popular method of achieving permanent magnet shimming. Moreover, the uneven local small magnetic field generating shim pieces seriously interferes with the basic magnetic field. In order to weaken the interference of

Table 1: The size of magnetic poles with saddle-type rotary curved surfaces. d is the magnetic poles gap, x is the distance from a location point on the curved surface to the center of the magnet, and y is the distance between the corresponding location points of two rotating curved surfaces.

x/d	0.00	0.4	0.8	1.2	1.6	2.0	2.4	2.8	3.2	3.24	3.28	3.32	3.36	3.4	3.52
y/d	1.08	1.076	1.063	1.042	1.014	1.0	1.0	1.023	1.18	1.21	1.24	1.27	1.30	1.34	1.46

Table 2: The size of permanent magnetic circuit with the magnetic field strength 1.5 T. x is the distance from a location point on the curved surface to the center of the magnet. y is the distance between the corresponding location points of two rotating curved surfaces. The units of x and y are mm.

x	0	12	24	36	48	60	72	84	96	97.2	98.4	99.6	100.8	102
y	43.2	43.04	42.54	41.69	40.56	40.0	40.0	40.93	47.38	48.41	49.53	50.74	52.05	53.46

Table 3: The size of permanent magnetic circuit with the magnetic field strength 1.2 T. x is the distance from a location point on the curved surface to the center of the magnet. y is the distance between the corresponding location points of two rotating curved surfaces. The units of x and y are mm.

x	0	28	56	84	112	140	168	196	224	226.8	229.6	232.4	235.2	238
y	75.6	75.32	74.44	72.95	70.98	70.0	70.0	71.63	82.91	84.72	86.67	88.80	91.08	93.55

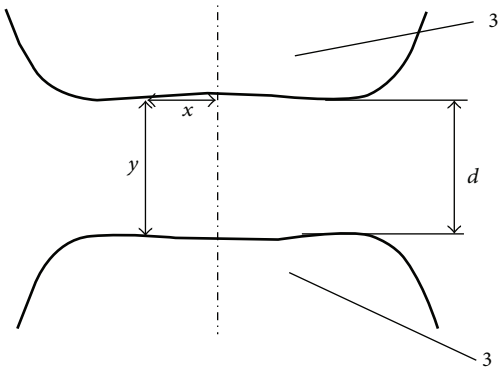

Figure 5: The shape and structure schematic of nonspherical curved-surface magnetic poles is demonstrated. The magnetic poles (see label 3 in Figure 2) with saddle-type rotary curved surfaces are symmetrically distributed at the center of the magnetic yoke.

the local small magnetic field, the working space should be away from these shim pieces. Therefore, the effective working space and the space utilization efficiency will greatly decrease. In keeping the invariable working space, the magnetic gap should become large, which will lead to the decrease of the magnetic field strength. It is well known that the utilization space of permanent magnet is proportional to the cube of B_0 magnet sizes. The magnetic steel mass will greatly increase for keeping the same base magnetic field, which also increases the difficulty of manufacturing permanent magnet system. In addition, the mutual interference between ferromagnetic pieces and magnetic poles will further increase the difficulty of achieving the shimming of permanent magnet. The above factors are also the main reasons hindering the breakthrough of high-field permanent Micro-MRI instrument so far. In this study, the cutting, grinding, and polishing techniques of aspheric optical components were transplanted to the processing of magnetic poles surface and the shimming practice, by which the shimming difficulty of permanent magnet is reduced.

The good shimming is dependent on a high-precision measurement technology. In order to achieve high-accuracy shimming of permanent magnet, it is necessary to have a high-precision measurement technology. In designing permanent magnet system, the magnetic field data of 2048 collected points are measured point by point by using frequency-spectrum method, and then the processing plan is determined according to measuring magnetic field data of these points. In the practical work, measurement and high-precision processing may be carried out synchronously without the interferences of shim pieces, and the cutting, grinding, and polishing technology does not need to occupy much space. Therefore, the computation difficulty will dramatically decrease. Based on accumulated fine processing experience, the magnet poles with high-fineness surface are obtained by using the processing technology. The surface evenness of magnetic poles can be controlled in 0.3~0.1 μm, and so the magnetic field homogeneity of B_0 magnet will increase. The magnetic field after passive shimming needs further optimization by adding several groups of current coils on two-opposite-poles surface of magnet. The basic magnetic field is a constant field, and the scalar magnetic potential V satisfies Laplace equation; that is, $\Delta V = 0$. The expansion equation of magnetic field B_z in rectangular coordinate system is given as [38]

$$\begin{aligned} B_z(x,y,z) = {} & A_1^0 + 2A_2^0 + 3A_2^1 x + 3B_2^1 y \\ & + \frac{3}{2}A_3^0\left(2z^2 - x^2 - y^2\right) + 12A_3^1 zx \\ & + 12B_3^1 zy + 15A_3^2\left(x^2 - y^2\right) + 30B_3^2 xy \\ & + 4A_4^0 z\left[z^2 - \frac{2}{3}x^2 + y^2\right] \\ & + \frac{15}{2}A_4^1 x\left[4z^2 - x^2 - y^2\right] \\ & + \frac{15}{2}B_4^1 y\left[4z^2 - x^2 - y^2\right] + \cdots. \end{aligned} \tag{7}$$

Generally, only B_z is computed in the shimming. The first term in (7) is a uniformity field value preserved in shimming. The nonuniformity parts of the base magnetic field after passive shimming have usually a certain gradient. The second, third, and fourth terms denote linear gradients along x, y, and z coordinate axes, respectively. The fifth, sixth, seventh, and eighth terms are second-order nonuniformity parts. The ninth, tenth, eleventh, and twelfth terms are third-order nonuniformity parts. The developed high-order gradient coils still retain the early MRI technique characteristic of compensating the gradient of base magnetic field. When the magnetic field induced by these high-order gradient coils exactly offsets the gradient of main magnet itself in a specific direction, these high-order gradient coils are regarded as the shimming coils. In addition, when the resonance frequencies of these points in the high uniform magnetic field tend to be the same, the vibration amplitude of every point is the biggest, by which 27 groups of higher-order shimming coils including x, y, z, xy, yz, xz, $x^2 - y^2$, R^2, R^3, Rz^2, $(x^2 - y^2)z$, y^3, xyz, and other third-order parts are preliminary designed. The shimming method adding high-order current coils is named as the active shimming. In the study, a novel shimming scheme is based on passive shimming and active shimming. In addition, we took a year to track the imaging of small animal permanent magnet type MRI instrument and fulfill correction of magnetic poles continuously. A good shimming of permanent magnet is obtained when the high-order shimming coils reduce to 9 groups.

2.3. Eddy Current of Permanent Magnet. In the conventional permanent magnetic circuit, two possible magnetic flux routes generating gradient magnetic field are shown in Figure 6. Although the pole shoes are made from high permeability and impedance material, it is also very difficult for permanent magnetic poles to prevent the closed gradient magnetic flux passing through magnetic yokes. At present, adding an anti-eddy-current board between gradient coils and magnetic poles is the most mainstream and effective method of eliminating the eddy current in permanent magnetic circuit. However, the anti-eddy-current board will occupy large working space. It is also not an ideal method of reducing eddy current. In order to eliminate the eddy current, we replaced pole pieces and anti-eddy-current board with an alloy magnetic pole. These magnetic induction lines of magnetic circuits 1 and 2 in Figure 7 interrupt in nonspherical curved-surface alloy magnetic poles, which may effectively prevent generation of eddy current. Considering the symmetry of the magnetic circuit, the upper part of the magnetic circuit schematic diagram was given in Figures 6 and 7.

The medical magnetic resonance imaging system can be regarded as the magnetic field stacking a rapidly changed gradient magnetic field based on the uniform magnetic field. The system consists of X, Y, Z three groups of gradients. The spatial information is determined by changing the sizes of X, Y, Z gradients. So the accuracy and switching speed of the gradient magnetic field determine the imaging quality. The main factor affecting the accuracy and switching speed of the gradient magnetic field is the eddy current inducing

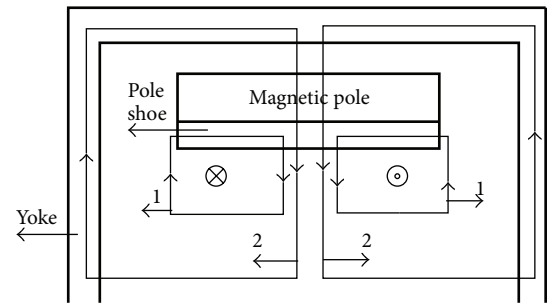

Figure 6: Magnetic circuits with traditional gradient coils.

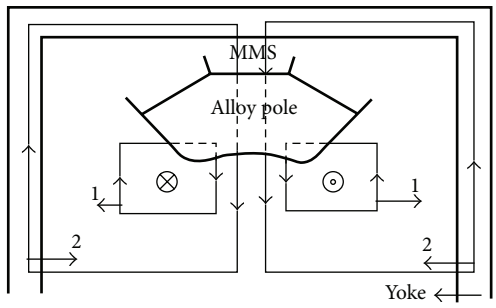

Figure 7: High-impedance special alloy magnetic poles without pole shoes. The magnetic circuit may block the gradient pulse and prevent the eddy currents.

the nearest magnetic poles extreme. The eddy current is a result of the interaction between the magnetic field and the current inducing the conductor in the variable magnetic field. Adding the active self-shielding coils is an effective method of reducing the eddy currents in superconducting magnetic circuit to date. Moreover, it is not very ideal for permanent magnetic circuit to add the active self-shielding coils. The active self-shield coils will take up too much space and need to pay a high price [31]. At present, making magnetic poles with the amorphous magnetic material, sheet lamination and silicon steel splicing are the popular solution methods of eliminating the eddy current. The above schemes can only be used below the 1.0 T magnetic resonance system owing to the low saturation magnetic intensity. In order to eliminate the eddy currents, the magnetic resonance imaging dedicated alloy with high-saturation magnetic field induction intensity and high electrical resistivity is developed, and nonspherical curved-surface magnetic poles made of the dedicated alloy replaced traditional magnetic poles and pole pieces which are easy to induce the eddy currents. A preparation method of the magnetic resonance imaging dedicated alloy is given as follows. The dedicated alloy is Fe-Co-Al fe-co-based alloy, the mass percent of the Co content is 5%–35%, the mass percent of Al content is 2%–6%, the mass percent of Si content is 0.5%–1%, the mass percent of Mo content is 2%-3%, required impurities include C, P, S, and Ni which are smaller than 0.01%, and the rest is Fe. The electrical resistivity of the alloy is larger than $50 * 10^{-8}$ Ω/m, the saturation flux density is larger than 1.4–2.3 T, the initial permeability is larger than 2000, the magnetic permeability at 1.0–1.5 T is larger than 10000, and preparation is performed by a vacuum metallurgy method.

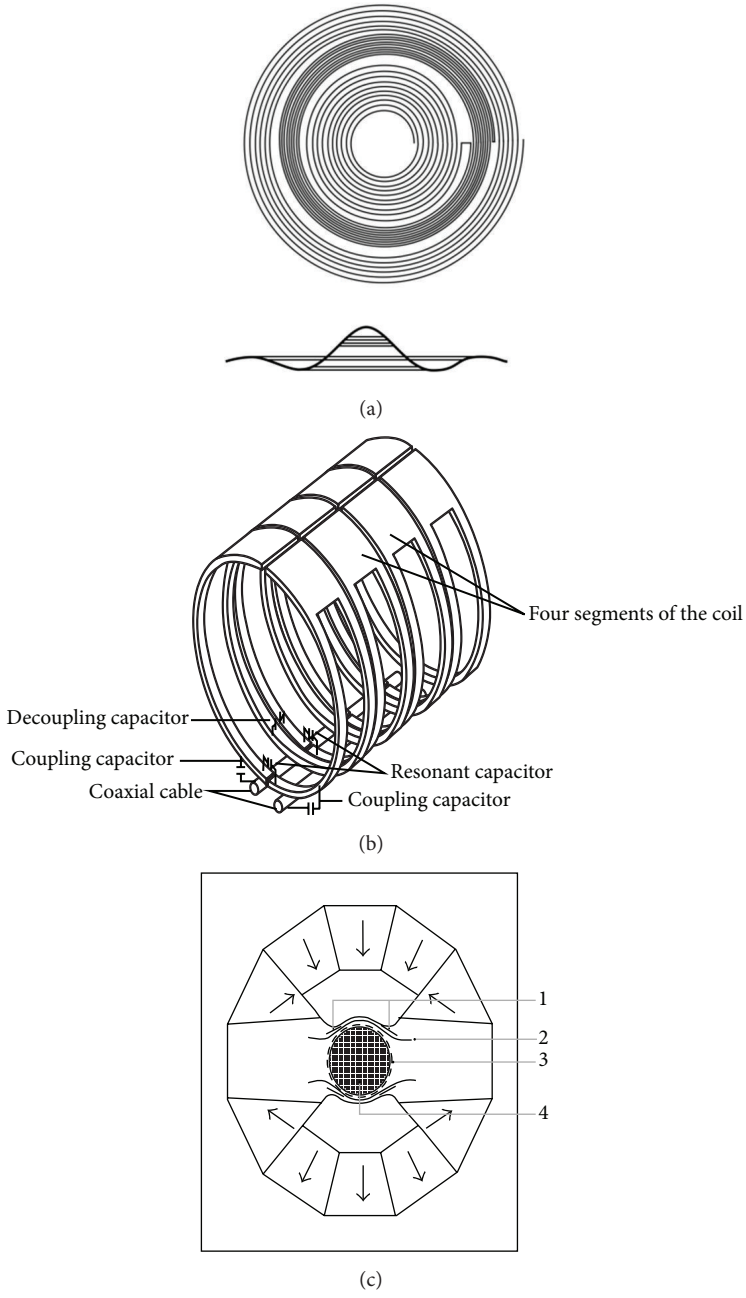

Figure 8: (a) Gradient coil. (b) RF coil. (c) The optimal allocation of all kinds of coil. 1, shimming coil. 2, gradient coil. 3, RF coil. 4, DSV.

According to the magnetic resonance imaging dedicated alloy and the preparation method, high-saturation magnetic field induction intensity and high electrical resistivity can be achieved, the alloy is a magnetic pole material that is used for 1.0 T–2.1 T permanent magnet magnetic resonance imager, and the anti-eddy effect is good.

2.4. Gradient Coil, RF Coil, and Temperature Control. We developed a self-shielding gradient coil with straw-hat curved-surface shape. The self-shielding gradient coil with high linearity, high efficiency, and small size is not only different from cylindrical superconducting gradient coil, but also different from the planar gradient coils. The eddy currents are effectively minimized by installing three groups of high-order gradient coils in small animal permanent MRI system at 0.5 T [40]. When the main magnetic field strength is up to 1.5 T [41], the stronger eddy current which worsens the linearity of the gradient magnetic field cannot effectively be eliminated by only adding self-shielding gradient coils. In addition, the magnetic resonance imaging dedicated alloy replaced traditional magnetic poles and pole pieces which are easy to induce the eddy currents. The self-shielding gradient coil picture is shown in Figure 8(a). Self-developed RF coil not only absorbs the advantage in which the saddle-shaped

coil can provide the uniform RF field in the vertical direction of B_0 magnetic field, but also absorbs the advantage of the solenoid-shaped coil with high sensitivity and uniformity field. The single-channel integral coil formed orthogonal transmitter coil and receiver coil avoids the complex array coil circuit. The single-channel integral coil has a faster imaging speed owing to selecting higher magnetic field strength and superior gradient coils. The RF coil picture is also shown in Figure 8(b). For improving the space utilization of magnetic poles gap and reducing the volume of B_0 magnet, all kinds of coils were arranged scientifically in Figure 8(c). Taking the curved type gradient coils, for example, three groups of coils were placed in the remaining gaps between the uniform field coils. This design not only obtained the self-shielding gradient coil, but also did not take up too much space.

The spatial distribution of the magnetic field may also vary with temperature. The stability of B_0 magnetic field determines the image quality. Therefore, the frequency or current compensation is an effective method of obtaining the stable magnetic field. Haishi et al. [42] developed a 1.0 T MR microscope using a NdFeB permanent magnet, and they developed an internal NMR locking technique or the imaging sequences because the magnetic field of the permanent magnet had a large temperature coefficient (−1200 ppm/deg.). In the study, the temperature drift can be effectively controlled by using a high quality temperature controller and "deuterium external locking" technique. The "deuterium external locking" technique is a method of compensating the magnetic field drift by the additional magnetic field inducing the current of the lock field coil, and the current of the lock field coil is adjusted by detecting the deuterium signal. The temperature drift is controlled around 1 ppm in 10 minutes (2~3 ppm/h) in imaging experiments.

3. Discussion

As the experiment, two kinds of permanent magnetic circuits are developed. One magnetic circuit is with a main magnetic field strength 1.5 T, a magnetic gap 43 mm, a cylinder shimming space with 35 mm (diameter) × 60 mm (height), and a space utilization efficiency of 81% (the space utilization efficiency is the ratio of the volume of the working space to the volume between magnetic poles); the static homogeneity is 1 ppm homogeneity over 20 mm DSV. According to the data in Table 2, the specific dimensions of the 1.5 T permanent magnetic circuit are given in Figure 9. The other one is with a main magnetic field strength 1.2 T, a magnetic gap 70 mm, a cylinder shimming space with 60 mm (diameter) × 100 mm (height), and a space utilization efficiency of 85%; the static homogeneity is 1 ppm homogeneity over 20 mm DSV. According to the data in Table 3, the specific dimensions of the 1.2 T permanent magnetic circuit are given in Figure 10. 1.2 T and 1.5 T permanent magnetic circuits, gradient coils, RF coils, and integrated software systems with independent intellectual property rights are assembled into 1.2 T and 1.5 T MRI instruments. The high quality images of mice are obtained by using self-developed two kinds of Micro-MRI instruments. The 1.2 T and 1.5 T Micro-MRI instruments are demonstrated in Figure 1.

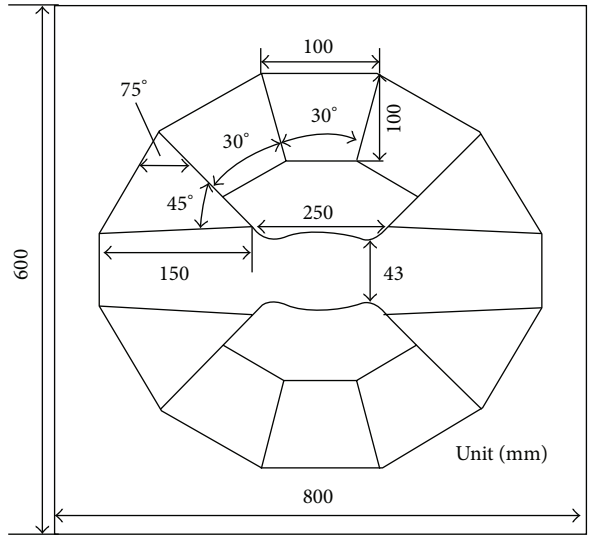

Figure 9: The size of each part of 1.5 T permanent magnetic circuit.

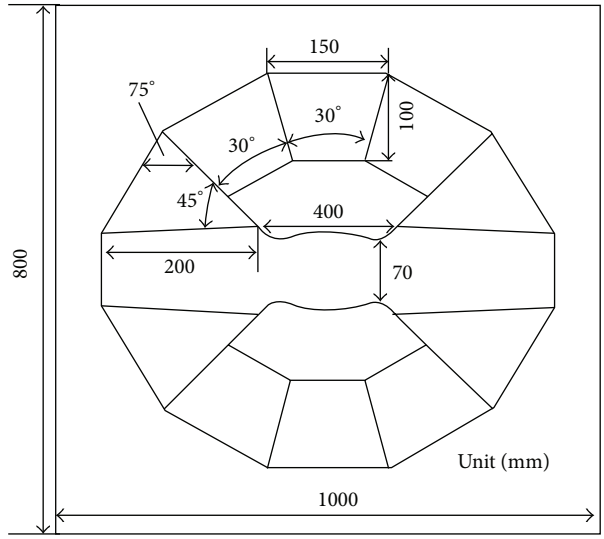

Figure 10: The size of each part of 1.2 T permanent magnetic circuit.

In order to implement mice imaging, 12 healthy male mice with the age of 4 weeks were obtained from Shanghai Experimental Animal Center. Their masses are between 17 and 20 grams. With the approval of the Ethical Committee of North China University of Science and Technology, the experiment of live mice and the injection of carcinogenic urethane to live mice were performed. The dosage of urethane anesthesia injecting into the abdomen of the healthy male mice is 1 g/kg. It took 4 minutes to 10 minutes for one 3D-T1 data set of one mouse under the anesthesia. The imaging scans of mice were performed after 5 minutes. The coronal images of a live mouse are obtained by using the 1.2 T small animal MRI instrument. The cross-sectional images of a dead mouse are obtained by using the 1.5 T small animal MRI instrument.

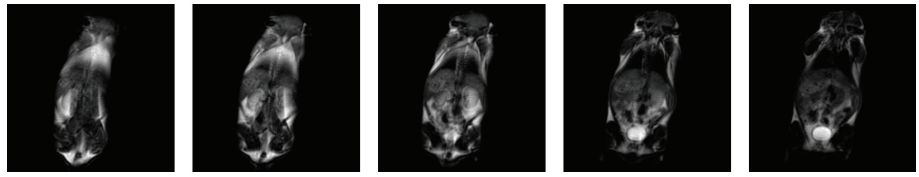

Figure 11: Coronal images of the 51st, 53rd, 55th, 57th, and 59th layer slices on live mice are demonstrated from left to right. Parameters of MRI at 1.2 T: TR/TE = 100 ms/15 ms, cylindrical shimming volume 60 mm × 100 mm, FOV = 60 mm × 100 mm, slice thickness 0.3 mm, data matrix 512 × 36 × 256, and imaging matrix 1024 × 1024.

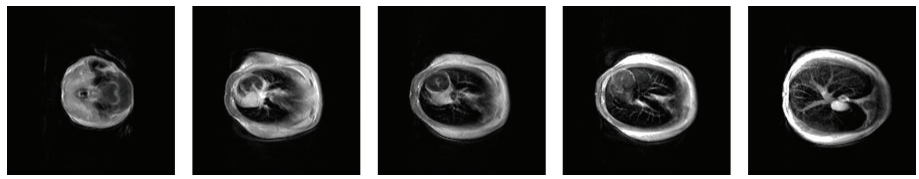

Figure 12: Cross-sectional images of the 60th, 90th, 93rd, 96th, and 104th layer slices on a dead mouse are demonstrated from left to right. Parameters of MRI at 1.5 T: TR/TE = 200 ms/15 ms, cylindrical shimming volume 35 mm × 60 mm, FOV = 35 mm × 60 mm, slice thickness 0.4 mm, data matrix 32 × 512 × 256, and imaging matrix 512 × 512.

The SE sequence and T1-weighted images of mice are obtained by using self-developed 1.2 T and 1.5 T small animal MRI instruments. x and y direction phase codes, z direction frequency code, and sinc form RF pulse are selected in coronal and cross-sectional scans of several mice. The 128 layers images of a live mouse are obtained in every imaging experiment. The imaging parameters of 1.2 T and 1.5 T MRI instruments are set as follows, respectively. (1) Coronal imaging parameters on the 1.2 T MRI instrument: TR/TE = 100 ms/15 ms, cylindrical shimming volume is 60 mm × 100 mm, the field of view (FOV) = 60 mm × 100 mm, slice thickness is 0.3 mm, data matrix is 512 × 36 × 256, and imaging matrix is 1024 × 1024. The 51st, 53rd, 55th, 57th, and 59th layer coronal images of a live mouse were demonstrated in Figure 11. These randomly selected coronal images of mice from head to tail can be clearly observed. (2) Cross-sectional imaging parameters on the 1.5 T MRI instrument: TR/TE = 200 ms/15 ms, cylindrical shimming volume is 35 mm × 60 mm, FOV = 35 mm × 60 mm, slice thickness is 0.4 mm, data matrix is 32 × 512 × 256, and imaging matrix is 512 × 512. The randomly selected 60th, 90th, 93rd, 96th, and 104th layer cross-sectional images of a dead mouse were demonstrated in Figure 12. The internal organs of the dead mouse can be clearly observed in Figure 12. The results show that higher field intensity of permanent magnet may improve greatly the imaging quality of small animals.

4. Conclusions

In the study, we developed a magnetic resonance imaging dedicated alloy with high-saturation magnetic field induction intensity and high electrical resistivity, and high-field permanent magnetic circuits of 1.2 T and 1.5 T with novel magnetic focusing and curved-surface correction. The nonspherical curved-surface magnetic poles made of the dedicated alloys are two saddle-type rotary curved surfaces, have the same shapes, and are symmetrically distributed at the center of the magnetic yoke. A new magnetic pole is formed by connecting the nonspherical curved-surface alloy magnetic pole with main magnetic steel together, which replaced traditional magnetic pole and poles pieces easily induced the eddy currents. The plugging magnetic steel is deviated from the center position and is, respectively, positioned behind the two magnetic poles and positioned on the two side surfaces of the main magnetic steel; the side magnetic steel is, respectively, positioned on the side surfaces of the two magnetic poles and arranged on the outer side of the plugging magnetic steel; the main magnetic steel and the plugging magnetic steel are made of permanent magnet materials with high coercive force; the side magnetic steel is made of permanent magnet materials with higher coercive force; the coercive force of the side magnetic steel is over 20 percent higher than that of the main magnetic steel. By the adoption of a magnetic focusing technology, high-field 1.2–2.1 T intensity can be achieved, and the uniform field of a magnet is corrected by the curved surfaces. In terms of shimming, the conventional passive shimming field method adding shim pieces is abandoned, and a telescope aspheric cutting, grinding, and fine processing technology of the nonspherical curved-surface magnetic poles is used. Meanwhile, the active shimming technology adding higher-order gradient coils is adopted, which effectively corrects the uniform field of B_0 magnet. Based on accumulated fine processing experience, the magnet poles with high-fineness surface are obtained by using the telescope aspheric cutting, grinding, and fine processing technology. The surface evenness of magnetic poles can be controlled in 0.3~0.1 μm. After adding third-order shimming coils, the static homogeneity is 1 ppm homogeneity over 20 mm DSV. In addition, the large temperature coefficient problem of permanent magnet

can be effectively controlled by using a good temperature controller and "deuterium external locking" technique; the new magnetic poles and gradient coils are optimally designed in terms of shape and structure. The shimming coils occupy the space between gradient coil and concave magnetic poles. Therefore, all the parts are optimally arranged and occupy the smallest magnetic field space. Combining our patents such as gradient coil, RF coil, and integration computer software, 1.2 T and 1.5 T small animal Micro-MRI instruments are developed, by which the high quality coronal and cross-sectional images of mice are obtained. Therefore, it is very necessary to strengthen the study of permanent magnet system for updating small animal MRI instruments.

Conflict of Interests

The authors declare that there is no conflict of interests regarding the publication of this paper.

Acknowledgment

This work was supported by The Scientific and Technological Department Foundation of Hebei Province (08202133D and 13202001D).

References

[1] C.-N. Chen, V. J. Sank, S. M. Cohen, and D. I. Hoult, "The field dependence of NMR imaging. I. Laboratory assessment of signal-to-noise ratio and power deposition," *Magnetic Resonance in Medicine*, vol. 3, no. 5, pp. 722–729, 1986.

[2] Y. Lvovsky, E. W. Stautner, and T. Zhang, "Novel technologies and configurations of superconducting magnets for MRI," *Superconductor Science and Technology*, vol. 26, no. 9, Article ID 093001, 2013.

[3] C. K. Kang, M. K. Woo, S. M. Hong, Y. B. Kim, and Z. H. Cho, "Intracranial microvascular imaging at 7 T MRI with transceiver RF coils," *Magnetic Resonance Imaging*, vol. 32, no. 1, pp. 1133–1138, 2014.

[4] T. Tominaka, M. Okamura, and T. Katayama, "Analytical field calculation of helical magnets with an axially symmetric iron yoke," *Nuclear Instruments and Methods in Physics Research Section: A*, vol. 484, no. 1–3, pp. 36–44, 2002.

[5] Z. Jin, X. Tang, B. Meng, D. L. Zu, and W. M. Wang, "A SQP optimization method for shimming a permanent MRI magnet," *Progress in Natural Science*, vol. 19, no. 10, pp. 1439–1443, 2009.

[6] Y. Cheng, W. He, L. Xia, and F. Liu, "Design of shimming rings for small permanent MRI magnet using sensitivity-analysis-based particle swarm optimization algorithm," *Journal of Medical and Biological Engineering*, vol. 35, no. 4, pp. 448–454, 2015.

[7] D.-H. Kim, B.-S. Kim, J.-H. Lee, W.-S. Nah, and I.-H. Park, "3-D optimal shape design of ferromagnetic pole in MRI magnet of open permanent-magnet type," *IEEE Transactions on Applied Superconductivity*, vol. 12, no. 1, pp. 1467–1470, 2002.

[8] U. Rapport, "Field adjusting mechanisms and methods for permanent magnet arrangement with backplate," US Patent, US20020097122 A1, 2002-07-25.

[9] T. Shirai, T. Haishi, S. Utsuzawa, Y. Matsuda, and K. Kose, "Development of a compact mouse MRI using a yokeless permanent magnet," *Magnetic Resonance in Medical Sciences*, vol. 4, no. 3, pp. 137–143, 2005.

[10] Q. L. Wang, W. H. Yang, Z. P. Ni et al., "Advances in NMRI technology," *High-Technology & Industrialization*, vol. 211, no. 12, pp. 46–53, 2013.

[11] D. L. Longo, F. Arena, L. Consolino et al., "Gd-AAZTA-MADEC, an improved blood pool agent for DCE-MRI studies on mice on 1 T scanners," *Biomaterials*, vol. 75, pp. 47–57, 2016.

[12] S. Kännälä, T. Toivo, T. Alanko, and K. Jokela, "Occupational exposure measurements of static and pulsed gradient magnetic fields in the vicinity of MRI scanners," *Physics in Medicine and Biology*, vol. 54, no. 7, pp. 2243–2257, 2009.

[13] M. Yamada, K. Takano, Y. Kawai, and R. Kato, "Hemodynamic-based mapping of neural activity in medetomidine-sedated rats using a 1.5T compact magnetic resonance imaging system: a preliminary study," *Magnetic Resonance in Medical Sciences*, vol. 14, no. 3, pp. 243–250, 2015.

[14] T. Haishi, M. Aoki, and E. Sugiyama, "Development of a 2.0 Tesla permanent magnetic circuit for NMR/MRI," in *Proceedings of the International Society for Magnetic Resonance in Medicine (ISMRM '13)*, vol. 13, p. 869, May 2005.

[15] D. Tamada, K. Kose, and T. Haishi, "Magnetic field shimming of a 2.0 T permanent magnet using a bi-planar single-channel shim coil," in *Proceedings of the International Society for Magnetic Resonance in Medicine (ISMRM '12)*, vol. 20, p. 2579, 2012.

[16] The Magnetic Materials Research Center of Shin-Etsu Chemical, "Development of world's largest Halbach-type magnetic circuit," http://www.shinetsu.co.jp/serem/e/rd/mc.html.

[17] C. Juchem, B. Muller-Bierl, F. Schick, N. K. Logothetis, and J. Pfeuffer, "Combined passive and active shimming for in vivo MR spectroscopy at high magnetic fields," *Journal of Magnetic Resonance*, vol. 183, no. 2, pp. 278–289, 2006.

[18] H. Sanchez, F. Liu, A. Trakic, and S. Crozier, "A magnetization mapping approach for passive shim design in MRI," in *Proceedings of the 28th Annual International Conference Engineering in Medicine and Biology Society (EMBS '06)*, vol. 1, pp. 1893–1896, New York, NY, USA, September 2006.

[19] B. Dorri, "Method for passively shimming a magnet," US Patent, US5677854A, 1995.

[20] K. M. Koch, P. B. Brown, D. L. Rothman, and R. A. de Graaf, "Sample-specific diamagnetic and paramagnetic passive shimming," *Journal of Magnetic Resonance*, vol. 182, no. 1, pp. 66–74, 2006.

[21] A. Belov, V. Bushuev, M. Emelianov et al., "Passive shimming of the superconducting magnet for MRI," *IEEE Transactions on Applied Superconductivity*, vol. 5, no. 2, pp. 679–681, 1995.

[22] B. Dorri, M. E. Vermilyea, and W. E. Toffolo, "Passive shimming of MR magnets: algorithm, hardware, and results," *IEEE Transactions on Applied Superconductivity*, vol. 3, no. 1, pp. 254–257, 1993.

[23] D. X. Xie, E. L. Wang, and Y. L. Zhang, "Passive shimming of permanent magnet for MRI based on dynamic programming," *Journal of Shenyang University of Technology*, vol. 29, no. 4, pp. 396–399, 2007.

[24] Z. Ren, D. Xie, and H. Li, "Shimming method for open MRI permanent main magnet," *Transactions of China Electrotechnical Society*, vol. 25, no. 3, pp. 1–5, 2010.

[25] X. F. You, Z. Wang, X. B. Zhang, W. Yang, and T. Song, "Passive shimming based on mixed integer programming for MRI magnet," *Science China Technological Sciences*, vol. 56, no. 5, pp. 1208–1212, 2013.

[26] G. Aubert, "Permanent magnet device for generating an offset uniform magnetic field," US Patent, US20130193973, 2013.

[27] Z. Jin, X. Tang, B. Meng, D. Zu, and W. Wang, "A SQP optimization method for shimming a permanent MRI magnet," *Progress in Natural Science*, vol. 19, no. 10, pp. 1439–1443, 2009.

[28] J. Lee and J. Yoo, "Topology optimization of the permanent magnet type MRI considering the magnetic field homogeneity," *Journal of Magnetism and Magnetic Materials*, vol. 322, no. 9–12, pp. 1651–1654, 2010.

[29] H. S. Lopez, F. Liu, E. Weber, and S. Crazier, "Passive shim design and a shimming approach for bi-planar permanent magnetic resonance imaging magnets," *IEEE Transactions on Magnetics*, vol. 44, no. 3, pp. 394–402, 2008.

[30] D. Tamada, K. Kose, and T. Haishi, "A new planar single-channel shim coil using multiple circular currents for magnetic resonance imaging," *Applied Physics Express*, vol. 5, no. 5, pp. 6701–6706, 2012.

[31] D. L. Zu, L. M. Hong, X. M. Cao et al., "Permanent magnet MRI pulsed eddy current magnetic field gradient background analysis," *Scientia Sinica Technologica*, vol. 40, no. 10, pp. 1221–1226, 2010.

[32] J. O. Nieminen, P. T. Vesanen, K. C. J. Zevenhoven et al., "Avoiding eddy-current problems in ultra-low-field MRI with self-shielded polarizing coils," *Journal of Magnetic Resonance*, vol. 212, no. 1, pp. 154–160, 2011.

[33] C. P. Bidinosti, I. S. Kravchuk, and M. E. Hayden, "Active shielding of cylindrical saddle-shaped coils: application to wire-wound RF coils for very low field NMR and MRI," *Journal of Magnetic Resonance*, vol. 177, no. 1, pp. 31–43, 2005.

[34] G. Sinha and S. S. Prabhu, "Analytical model for estimation of eddy current and power loss in conducting plate and its application," *Physical Review Special Topics—Accelerators and Beams*, vol. 14, no. 6, pp. 62401–62416, 2011.

[35] H. T. Xie, "Self-shielding gradient coils used in magnetic resonance imaging," CN, Patent, CN 202189140 U, 2012.

[36] H. T. Xie, "RF coil apparatus for magnetic resonance imaging," CN Patent, CN 202189138 U, 2012.

[37] H. T. Xie, *Huantong 3 Dimensional NMR Integration*, People's Republic of China National Copyright Administration of Integrated Software Computer, 2012.

[38] P. H. Xia, *The Permanent Magnet Mechanism*, Beijing Industrial University Press, 2000.

[39] Ningbo Jinyu Magnet, "N33–N52 Strong Rare Earth Sintered Neodymium Magnets Ring With Epoxy Coated," http://www.sinteredneodymiummagnets.com/sale-5908666-n33-n52-strong-rare-earth-sintered-neodymium-magnets-ring-with-epoxy-coated.html.

[40] S. L. Hou, H. T. Xie, W. Hou, S. Y. Li, and W. Chen, "Gradient coil of permanent magnet mini-magnetic resonance imager and image quality," *Chinese Journal of Magnetic Resonance*, vol. 29, no. 4, pp. 508–520, 2012.

[41] G. X. Wang, H. T. Xie, S. L. Hou, W. Chen, Q. Zhao, and S. Y. Li, "Development of the 1.2T ~ 1.5T permanent magnetic resonance imaging device and its application for mouse imaging," *BioMed Research International*, vol. 2015, Article ID 858694, 8 pages, 2015.

[42] T. Haishi, T. Uematsu, Y. Matsuda, and K. Kose, "Development of a 1.0 T MR microscope using a Nd-Fe-B permanent magnet," *Magnetic Resonance Imaging*, vol. 19, no. 6, pp. 875–880, 2001.

Hindawi Publishing Corporation
BioMed Research International
Volume 2016, Article ID 3749489, 6 pages
http://dx.doi.org/10.1155/2016/3749489

Research Article

Fast 3-Breath-Hold 3-Dimensional Tagging Cardiac Magnetic Resonance in Patients with Hypertrophic Myocardial Diseases: A Feasibility Study

Yasuo Amano,[1] Fumi Yamada,[1] Hidenobu Hashimoto,[1,2] Makoto Obara,[3] Kuniya Asai,[4] and Shinichiro Kumita[1]

[1]*Department of Radiology, Nippon Medical School, 1-1-5 Sendagi, Bunkyo-ku, Tokyo 113-8603, Japan*
[2]*Department of Cardiology, Toho University Omori Hospital, 6-11-1 Omori-Nishi, Tokyo 143-8541, Japan*
[3]*Philips Electronics Japan, 2-13-37 Konan, Minato-ku, Tokyo 108-8507, Japan*
[4]*Department of Cardiology, Nippon Medical School, 1-1-5 Sendagi, Bunkyo-ku, Tokyo 113-8603, Japan*

Correspondence should be addressed to Yasuo Amano; yas-amano@nifty.com

Received 21 November 2015; Revised 7 February 2016; Accepted 10 February 2016

Academic Editor: Jinyuan Zhou

Tagging CMR has been established as the standard reference for measurement of myocardial strain. The current 2D tagging technique requires multiple breath-holds to cover the whole heart and cannot show the 3D motions of the left ventricle. We performed fast 3-breath-hold 3D tagging with localized tagging preparation and complementary spatial modulation of magnetization in 10 patients with hypertrophic myocardial diseases and 6 normal volunteers. The left wall motion was observed at any view angle, which allowed for the identification of regional and global hypokinesis using the fast 3D tagging. Although a decrease in the circumferential strain and LGE were observed at the basal septum in hypertrophic cardiomyopathy, they were not located together in each patient. In hypertensive heart disease, the decrease in circumferential strain was observed more widely than LGE, and the summed strain of all segments was significantly decreased. The decrease in strain and LGE were observed diffusely in cardiac amyloidosis. In conclusion, fast 3-breath-hold 3D tagging is feasible for the regional and global strain analysis. The location of reduced circumferential strain is not necessarily the same as that of LGE and is related to the global cardiac function in patients with hypertrophic myocardial diseases.

1. Background

Myocardial hypertrophy is induced by genetic mutations, storage diseases, or reaction to hypertension, aortic valvular disorders, or obstruction of the left ventricular outflow tract. Myocardial hypertrophy may lead to a decrease in coronary reserve flow, which is related to adverse cardiac events [1, 2].

Cardiac magnetic resonance (CMR) is used to quantify regional and global cardiac function and myocardial thickness and mass and to detect myocardial scarring [3–5]. In particular, late gadolinium enhancement (LGE) CMR is valuable for the identification of the myocardial scarring associated with hypertrophic myocardial diseases including hypertrophic cardiomyopathy (HCM), hypertensive heart disease (HHD), and amyloidosis, and LGE is strongly related to serious complications and the prognosis of the patients [6–9]. Tagging CMR is another useful method that quantifies the regional or global strain related to myocardial fiber architecture, estimates cardiac dyssynchrony, and identifies subclinical systolic impairment [10–13]. In HCM and HHD, the regional heterogeneity of the strain, decrease in circumferential strain, or abnormal apical rotation is observed using tagging CMR [13, 14].

Although tagging CMR has been established as the standard reference for measurement of myocardial strain and motion, current 2-dimensional (2D) tagging CMR requires multiple breath-holds to cover the whole heart. The 2D imaging technique cannot show the 3-dimensional (3D) motions of the left ventricle. Ryf et al. [15] developed 3D tagging with complementary spatial modulation of magnetization

(CSPAMM). A detraction of 3D tagging is its lengthy scan time. Rutz et al. [16] developed fast 3D tagging by using line tagging in the 3 spatial directions, the spatial localized pulse for the second tagging preparation, and echo-planar imaging (EPI) readout. The fast 3D tagging allows for the whole heart to be imaged with 3D tagging with only 3-breath-holds and was applied to 5 patients with myocardial infarction. However, to our knowledge, there have been no previous studies to evaluate the myocardial strain with the fast 3D tagging technique in patients with nonischemic, hypertrophic myocardial diseases with myocardial stiffness and regional scarring.

In the present study, we sought to evaluate the feasibility of fast 3-breath-hold 3D tagging for the assessment of the circumferential strain in patients with hypertrophic myocardial diseases. We also compared the locations with the abnormal strain with those of LGE.

2. Methods

2.1. Subjects. Ten patients with a maximum wall thickness ≥ 15 mm were recruited between June 2014 and August 2015. They were 9 men and 1 woman ranging in age from 35 to 92 years (68.2 ± 16.1 years). They comprised 5 patients with HCM, 3 with HHD, and 2 with cardiac amyloidosis. One patient with HHD had associated myocardial infarction. The diagnosis of the hypertrophic myocardial diseases was made by endomyocardial biopsy or from a combination of family history of HCM, past history, electrocardiogram (ECG), and imaging studies [6–9]. For comparison, 6 healthy male volunteers (age: 30–61 years; 42.0 ± 14.4) underwent the fast 3D tagging. This study followed our institutional ethical guidelines given by the IRB.

2.2. CMR Protocol. CMR studies were performed using a 3.0 T unit (Achieva, Philips Healthcare, Best, The Netherlands). A cardiac phased-array coil was used for signal reception, and vector ECG was used for cardiac gating. After localizer scanning, short-axis 2D cine steady-state free precession was performed with the following image parameters: repetition time (TR), 4.1 ms; echo time (TE), 2.0 ms; flip angle, 45–55°; in-plane resolution, 1.6 × 1.7 mm^2; slice thickness, 8 mm with a 2 mm gap; and 20–24 phases per cardiac cycle. Thereafter, fast 3-breath-hold 3D tagging was performed with imaging parameters as follows: TR, 6.5 ms; TE, 3.0 ms; flip angle, 17°; EPI factor (i.e., echo train length), 7; in-plane resolution, 4.4 × 4.4 mm^2; slice thickness, 8.8 mm; slice partition, 14; and 24 phases per cardiac cycle. A ramped flip angle was used to prevent the tag fading. The line tagging with 8 mm spacing was applied in 3 orthogonal directions. The second tagging preparation was the spatial localized pulse, which allows for a half field-of-view without a wrapping-around artifact (Figure 1) [15–17]. The position of the diaphragm during 3-breath-holds was maintained identically using a navigator technique with a 15 mm window and a correction factor of 0.6 [18]. These imaging techniques in combination with CSPAMM induced fast 3-breath-hold 3D tagging of the whole heart (3D Tag, GyroTools, Zurich, Switzerland) [11, 15, 16]. Approximately 12 min after the injection of gadolinium-based contrast agent at a dose of 0.10–0.15 mmol/kg, LGE CMR was performed with the imaging parameters as follows: TR, 10 ms; TE, 2.9 ms; flip angle, 15°; pixel size, 1.8 × 1.2 mm^2; and slice thickness, 10 mm. The inversion time to null the signal from the normal myocardium was adjusted for each patient.

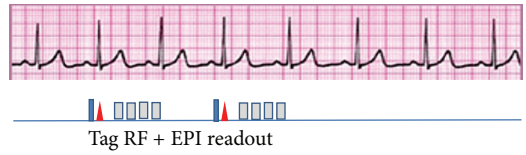

Figure 1: Imaging sequence for fast 3-breath-hold 3D tagging. The line tagging (blue box and red triangle) was applied in 3 orthogonal directions. The second tagging preparation (red triangle) was the spatial localized pulse, and its use and echo-planar imaging readout (gray box) in combination with CSPAMM allow for fast 3-breath-hold 3D tagging of the whole heart.

2.3. Image Analysis. Ejection fraction (EF), maximum wall thickness, and myocardial mass of the left ventricle were acquired from the cine data. The presence of myocardial LGE was determined when its mean signal intensity was above 6 SD of the mean signal intensity of the nullified myocardium. In cases of amyloidosis, the LGE was identified as global and diffuse LGE as it was in previous studies [9, 19].

One radiologist with 18-year experience of CMR analyzed the fast 3D tagging using dedicated software (TagTrack 3D, GyroTools, Zurich, Switzerland). The harmonic phase method was used to track the myocardial wall motion after the correction of magnetic inhomogeneity and smoothing the boundaries with a bandpass filter [16]. The midwall contour at the basal, middle, and apical levels was divided according to a 16-segment model from the American Heart Association [20]. The circumferential strain was defined as the fractional change (%) in the myocardial length in the direction tangential to the epicardial wall [13, 14] (Figure 2).

First, we assessed the technical feasibility of fast 3-breath-hold 3D tagging based on the success rates of the scanning, reconstruction of cine 3D surface representation, and acquisition of the quantitative regional strain data. Second, we compared the circumferential strain of the patients with those of the healthy volunteers at the 16 myocardial segments. In the present study, we defined the decrease in strain as being 20% less than the mean strain value of the normal volunteers. In addition, the comparison for circumferential strain was made between the normal volunteers and HCM patients at each segment, or the summed strain of all 16 segments was compared between the normal volunteers and patients with HCM, HHD, or cardiac amyloidosis. An unpaired t-test was used to assess the difference, and $P < 0.05$ was defined as statistically significant. Third, the circumferential strain was compared with the presence of LGE at each myocardial segment. A Fisher test was used to assess the relationship between the circumferential strain and LGE when appropriate, and $P < 0.05$ was considered significant.

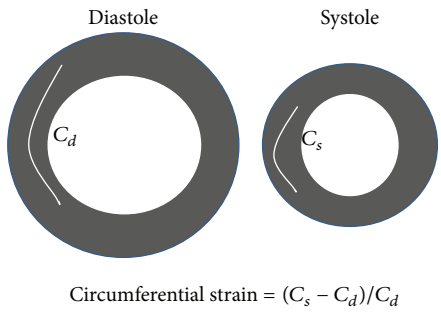

Figure 2: How circumferential strain is obtained is shown. C_d and C_s represent circumferential length at diastole and systole related to the strain, respectively.

3. Results

Fast 3-breath-hold 3D tagging was completed in all of the 10 patients and 6 healthy volunteers. The 3D surface representation in cine mode was successfully generated in all of the subjects. The circumferential strain was estimated in all of the myocardial segments of all subjects enrolled (Figure 3, Supplemental video in Supplementary Material available online at http://dx.doi.org/10.1155/2016/3749489, and Table 1).

Table 1 shows the circumferential strain in patients and controls. Because the normal strain values were below zero as expected [10–13], the decrease in strain was defined as that above zero or that being 20% less than the absolute value of the normal mean strain. In HCM, the circumferential strain reduced at the inferior septal segment at the basal level and apical septal segment. However, there were no significant differences in the strain between the normal volunteers and patients with HCM at any segments ($P > 0.14$). In HHD, the circumferential strain predominantly decreased at the mid septal and posterior segments and apical segments. The circumferential strain was also reduced at the basal anterior segment. The circumferential strain was decreased in 10 and 12 of the 16 segments in the 2 patients with cardiac amyloidosis. The summed strain of all segments was significantly decreased in patients with HHD (-8.3 ± 7.6; $P = 0.010$), but not in those with HCM (-17.3 ± 11.8) or those with amyloidosis (-11.0 ± 6.8), compared with the normal volunteers (-14.1 ± 18.4).

LGE was observed in HCM, whereas the segments with LGE were not identical to those with reduced circumferential strain in each patient. There was no relationship between the reduced circumferential strain and LGE in HCM patients ($P = 0.73$). In HHD, the segments with reduced circumferential strain were observed more widely than those with LGE. LGE was expectedly observed diffusely in cardiac amyloidosis.

4. Discussion

Fast 3-breath-hold 3D tagging successfully provided 3D surface representation in cine mode and circumferential strain data. Compared with the normal volunteers, the patients with HCM or HHD showed reduced circumferential strain at several myocardial segments. The segments showing reduced circumferential strain were not identical to those with LGE in HCM, and the reduced strain was distributed more widely than LGE in HHD. The reduced strain and LGE were observed extensively in patients with cardiac amyloidosis. Thus, the fast 3-breath-hold 3D tagging may be feasible for detection of the circumferential strain decrease, which is not necessarily associated with myocardial scarring in patients with hypertrophic myocardial diseases.

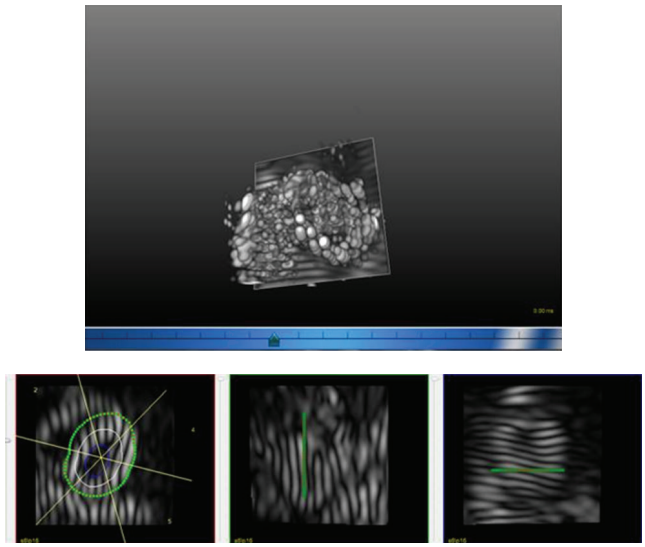

Figure 3: Reconstructed 3-dimensional image and source images in the 3 orthogonal directions are shown.

The scan time for 3D tagging was reduced by using line tagging in the 3 spatial directions, a spatial localized pulse for the second tagging preparation, and an EPI readout [16]. The position of the diaphragm during breath-hold was maintained identically during the 3-breath-holds using navigator technique [18]. Thereby, fast 3-breath-hold 3D tagging successfully provided 3D surface representation in cine mode and the regional circumferential strain in all of the subjects.

The circumferential strain deteriorated even in HCM patients with a preserved EF. A hypertrophied basal septum and apical septum tended to show a decrease in circumferential strain in HCM, which indicates the dominant changes in the septal myocardial architecture [21]. The segments with reduced circumferential strain were not concordant with those showing LGE. This result was not consistent with that of the previous study [22], partly because the patchy midwall LGE might not affect the circumferential strain in HCM. Aletras et al. [23] indicated that LGE does not necessarily explain reduced strain, which is estimated using displacement encoding with stimulated echoes, in HCM. When summing the strain at all segments, we did not find the reduction in circumferential strain in patients with HCM. Thus, the 3D tagging identified only regional wall abnormality in HCM patients with preserved EF.

Table 1: Circumferential Strain (%) Estimated by 3-Breath-Hold 3D Tagging CMR in Patients with Hypertrophic Myocardial Diseases and Normal Volunteers.

segment	1	2	3	4	5	6	7	8	9	10	11	12	13	14	15	16	EF (%)
	−14.0	−20.0	*28.0*	−10.0	−22.0	*23.0*	*6.8*	−33.0	−25.0	−15.0	−25.0	*17.0*	***−6.7***	**−24.0**	**−27.0**	−23.0	62.5
	−22.0	***−15.0***	**−14.0**	−7.9	−20.0	−11.0	**−35.0**	***−13.0***	−19.0	−23.0	**−25.0**	**−26.0**	*−15.0*	−25.0	−16.0	−25.0	79.7
HCM	−14.0	−22.0	*−10.0*	−13.0	*−5.4*	−14.0	−19.0	*−14.0*	−24.0	−12.0	−9.4	−14.0	*−12.0*	*−15.0*	−21.0	−27.0	67.1
	−10.0	**−22.0**	*6.0*	−12.0	−22.0	−22.0	−12.0	−18.0	**−23.0**	*−5.3*	−16.0	−25.0	*−14.0*	−22.0	−31.0	*−9.8*	54.0
	−16.8	−28.1	**−13.6**	−17.9	−21.5	−10.6	−22.6	**−17.6**	*−16.9*	−23.9	−31.7	−24.3	−35.7	−28.3	−18.2	−19.4	56.8
mean	−15.4	−21.4	−0.7	−12.2	−18.2	−6.9	−16.4	−19.1	−21.6	−15.8	−21.4	−14.5	−16.7	−22.9	−22.6	−20.8	64.0
	−1.6	**−17.0**	**−39.0**	*−6.5*	−13.0	***−1.6***	−16.0	*−9.9*	*−17.0*	*9.0*	***−4.2***	**−20.0**	*−6.7*	*−7.5*	*−12.0*	***−6.7***	22.7
HHD	*−10.0*	−20.0	*−8.6*	−6.9	*−5.3*	−14.0	6.9	*−9.2*	*−10.0*	*3.8*	*−4.0*	−12.0	*−5.2*	−19.0	*−12.0*	*−7.6*	13.8
	7.9	*−14.1*	*−7.1*	*8.0*	*−9.4*	−8.7	−14.0	*−9.1*	*−18.0*	−20.0	*10.0*	−16.0	*−8.4*	*−12.0*	*−11.0*	*−6.9*	33.5
Amyl	**−22.0**	***−10.0***	***−11.0***	***−4.8***	***−10.0***	**−15.0**	**−18.8**	***−9.9***	***−17.6***	***−3.9***	**−18.5**	**−18.2**	***−13.5***	**−22.0**	***−10.2***	***−17.1***	31.0
	0.3	*−7.6*	***0.6***	**−9.8**	***−2.4***	*−1.9*	*−1.9*	***−1.6***	*−14.0*	**−10.4**	***−3.0***	***−0.9***	*−0.7*	−21.9	***−12.7***	−20.4	60.8
Normal	−14.3	−20.3	−15.4	−8.4	−12.9	−9.5	−9.2	−18.5	−23.5	−11.0	−6.0	−8.6	−25.5	−22.7	−17.7	−23.7	NA

Italic: abnormal circumferential strain (%), bold: segments with late gadolinium enhancement (LGE). HCM: hypertrophic cardiomyopathy, HHD: hypertensive heart disease, Amyl: cardiac amyloidosis, Normal: normal volunteers, NA: not available. The mean value of circumferential strain was shown in normal volunteers. In HCM, the segments with LGE were not identical to those with reduced strain in each patient. In HHD with low ejection fraction, the segments with reduced strain were observed more widely than those with LGE. The reduction in strain and LGE were observed diffusely in cardiac amyloidosis.

In the 3 patients with HHD and low EF, the reduced strain was distributed more widely than LGE. The mid septal-to-posterior segments showed reduced circumferential strain in our study. These segments tend to have LGE in HHD patients with congestive heart failure [7, 9]. Foell et al. [24] showed a reduction in the radial and longitudinal strain of the mid posterior areas. Therefore, fast 3D tagging can identify the changes in myocardial architecture changes that preceded LGE in patients with HHD. In addition, the 3D tagging showed a decrease in the summed strain of all myocardial segments in patients with HHD, all of whom had decreased EF.

In cardiac amyloidosis, a decrease in circumferential strain and LGE were observed diffusely, as expected [9, 19].

There are several limitations to this study. First, the study population was small. The statistical analyses were affected by this limitation. In addition, almost all of the subjects were men because HCM and HHD are predominantly observed in men. Thus, the present results might not be possible to extrapolate the findings to female patients. Second, the volunteers were younger than the patients. Because there were some segments with reduced circumferential strain, subclinical myocardial disorders could not be excluded in the volunteers. The "normal" heterogeneity of the strain was also considered for the lower values of the strain [25]. Third, we defined the decrease in the strain as being 20% less than the mean strain value of the volunteers; this definition is somewhat arbitrary. Fourth, we investigated the whole left ventricular motion only in 3D surface representation and analyzed the regional strain only at 3 levels, because the volume of data acquired with 3D fast tagging was enormous relative to software capability. The development of sophisticated software to analyze 3 types of myocardial strain in all of the left ventricular regions (e.g., 6 segments × 14 slices × 24 cardiac phases) is warranted. Last, we did not compare the strain and histology. Endomyocardial biopsy provided a diagnosis of HHD or cardiac amyloidosis, whereas the biopsy was conducted without referring to the 3D fast tagging. Moreover, the circumferential strain data was acquired at the midwall, while the histological samples were acquired from the myocardium close to the ventricular cavity.

5. Conclusions

Fast 3-breath-hold 3D tagging allows for regional and global wall strain analysis. The location of reduced circumferential strain was not necessarily the same as that of LGE in patients with hypertrophic myocardial diseases. Fast 3D tagging may be feasible for the detection of myocardial strain changes which are not necessarily associated with myocardial scarring in the patients with HCM or HHD.

Abbreviations

CMR: Cardiac magnetic resonance
CSPAMM: Complementary spatial modulation of magnetization
ECG: Electrocardiogram
HCM: Hypertrophic cardiomyopathy
HHD: Hypertensive heart disease
LGE: Late gadolinium enhancement
3D: Three-dimensional.

Conflict of Interests

The authors declare that they have no competing interests.

Authors' Contribution

Yasuo Amano designed the research, analyzed the LGE and fast 3D tagging data, and drafted the paper. Both Fumi Yamada and Hidenobu Hashimoto performed CMR and analyzed the cine CMR data. Makoto Obara implemented and supported the software and algorithm of the research. Kuniya Asai enrolled the patients for this study. Shinichiro

Kumita applied for the ethical clearances and revised the paper.

Acknowledgments

The authors thank Gerard Crelier, Ph.D. (GyroTools, Zurich, Switzerland), for his development of fast 3D tagging and analysis software and for his helpful discussion. This study was supported in part by the Grants-in-Aid for Scientific Research (KAKENHI) from the Japan Society for the Promotion of Science: Kiban (C) 26461838.

References

[1] D. Levy, R. J. Garrison, D. D. Savage, W. B. Kannel, and W. P. Castelli, "Prognostic implications of echocardiographically determined left ventricular mass in the Framingham Heart Study," *The New England Journal of Medicine*, vol. 322, no. 22, pp. 1561–1566, 1990.

[2] M. L. Marcus, D. B. Doty, L. F. Hiratzka, C. B. Wright, and C. L. Eastham, "Decreased coronary reserve: a mechanism for angina pectoris in patients with aortic stenosis and normal coronary arteries," *The New England Journal of Medicine*, vol. 307, no. 22, pp. 1362–1366, 1982.

[3] R. J. Kim, E. Wu, A. Rafael et al., "The use of contrast-enhanced magnetic resonance imaging to identify reversible myocardial dysfunction," *The New England Journal of Medicine*, vol. 343, no. 20, pp. 1445–1453, 2000.

[4] M. L. Chuang, P. Gona, G. L. T. F. Hautvast et al., "CMR reference values for left ventricular volumes, mass, and ejection fraction using computer-aided analysis: the Framingham Heart study," *Journal of Magnetic Resonance Imaging*, vol. 39, no. 4, pp. 895–900, 2014.

[5] L. Wang, M. Pei, N. C. F. Codella et al., "Left ventricle: fully automated segmentation based on spatiotemporal continuity and myocardium information in cine cardiac magnetic resonance imaging (LV-FAST)," *BioMed Research International*, vol. 2015, Article ID 367583, 9 pages, 2015.

[6] R. H. Chan, B. J. Maron, I. Olivotto et al., "Prognostic value of quantitative contrast-enhanced cardiovascular magnetic resonance for the evaluation of sudden death risk in patients with hypertrophic cardiomyopathy," *Circulation*, vol. 130, no. 6, pp. 484–495, 2014.

[7] K. Andersen, M. Hennersdorf, M. Cohnen, D. Blondin, U. Mödder, and L. W. Poll, "Myocardial delayed contrast enhancement in patients with arterial hypertension: initial results of cardiac MRI," *European Journal of Radiology*, vol. 71, no. 1, pp. 75–81, 2009.

[8] H. Vogelsberg, H. Mahrholdt, C. C. Deluigi et al., "Cardiovascular magnetic resonance in clinically suspected cardiac amyloidosis," *Journal of the American College of Cardiology*, vol. 51, no. 10, pp. 1022–1030, 2008.

[9] M. Takeda, Y. Amano, M. Tachi, H. Tani, K. Mizuno, and S. Kumita, "MRI differentiation of cardiomyopathy showing left ventricular hypertrophy and heart failure: differentiation between cardiac amyloidosis, hypertrophic cardiomyopathy, and hypertensive heart disease," *Japanese Journal of Radiology*, vol. 31, no. 10, pp. 693–700, 2013.

[10] E. A. Zerhouni, D. M. Parish, W. J. Rogers, A. Yang, and E. P. Shapiro, "Human heart: tagging with MR imaging—a new method for noninvasive assessment of myocardial motion," *Radiology*, vol. 169, no. 1, pp. 59–63, 1988.

[11] L. Axel and L. Dougherty, "MR imaging of motion with spatial modulation of magnetization," *Radiology*, vol. 171, no. 3, pp. 841–845, 1989.

[12] C. C. Moore, C. H. Lugo-Olivieri, E. R. McVeigh, and E. A. Zerhouni, "Three-dimensional systolic strain patterns in the normal human left ventricle: characterization with tagged MR imaging," *Radiology*, vol. 214, no. 2, pp. 453–466, 2000.

[13] M.-Y. Jeung, P. Germain, P. Croisille, S. El Ghannudi, C. Roy, and A. Gangi, "Myocardial tagging with MR imaging: overview of normal and pathologic findings," *RadioGraphics*, vol. 32, no. 5, pp. 1381–1398, 2012.

[14] C. M. Kramer, N. Reichek, V. A. Ferrari, T. Theobald, J. Dawson, and L. Axel, "Regional heterogeneity of function in hypertrophic cardiomyopathy," *Circulation*, vol. 90, no. 1, pp. 186–194, 1994.

[15] S. Ryf, M. A. Spiegel, M. Gerber, and P. Boesiger, "Myocardial tagging with 3D-CSPAMM," *Journal of Magnetic Resonance Imaging*, vol. 16, no. 3, pp. 320–325, 2002.

[16] A. K. Rutz, S. Ryf, S. Plein, P. Boesiger, and S. Kozerke, "Accelerated whole-heart 3D SPAMM in myocardial motion quantification," *Magnetic Resonance in Medicine*, vol. 59, no. 4, pp. 755–763, 2008.

[17] M. T. Alley, J. M. Pauly, F. G. Sommer, and N. J. Pelc, "Angiographic imaging with 2D RF pulses," *Magnetic Resonance in Medicine*, vol. 37, no. 2, pp. 260–267, 1997.

[18] Y. Wang and R. L. Ehman, "Retrospective adaptive motion correction for navigator-gated 3D coronary MR angiography," *Journal of Magnetic Resonance Imaging*, vol. 11, no. 2, pp. 208–214, 2000.

[19] H. Mahrholdt, A. Wagner, R. M. Judd, U. Sechtem, and R. J. Kim, "Delayed enhancement cardiovascular magnetic resonance assessment of non-ischaemic cardiomyopathies," *European Heart Journal*, vol. 26, no. 15, pp. 1461–1474, 2005.

[20] M. D. Cerqueira, N. J. Weissman, V. Dilsizian V et al., "Standardized myocardial segmentation and nomenclature for tomographic imaging of the heart. A statement for healthcare professionals from the cardiac imaging committee of the council on clinical cardiology of the American Heart Association," *Circulation*, vol. 105, no. 4, pp. 539–542, 2002.

[21] S.-J. Dong, J. H. MacGregor, A. P. Crawley et al., "Left ventricular wall thickness and regional systolic function in patients with hypertrophic cardiomyopathy. A three-dimensional tagged magnetic resonance imaging study," *Circulation*, vol. 90, no. 3, pp. 1200–1209, 1994.

[22] Y. J. Kim, B. W. Choi, J. Hur et al., "Delayed enhancement in hypertrophic cardiomyopathy: comparison with myocardial tagging MRI," *Journal of Magnetic Resonance Imaging*, vol. 27, no. 5, pp. 1054–1060, 2008.

[23] A. H. Aletras, G. S. Tilak, L.-Y. Hsu, and A. E. Arai, "Heterogeneity of intramural function in hypertrophic cardiomyopathy mechanistic insights from MRI late gadolinium enhancement and high-resolution displacement encoding with stimulated echoes strain maps," *Circulation: Cardiovascular Imaging*, vol. 4, no. 4, pp. 425–434, 2011.

[24] D. Foell, B. Jung, E. Germann, F. Staehle, C. Bode, and M. Markl, "Hypertensive heart disease: MR tissue phase mapping reveals

altered left ventricular rotation and regional myocardial long-axis velocities," *European Radiology*, vol. 23, no. 2, pp. 339–347, 2013.

[25] I. Del-Canto, M. P. López-Lereu, J. V. Monmeneu et al., "Characterization of normal regional myocardial function by MRI cardiac tagging," *Journal of Magnetic Resonance Imaging*, vol. 41, no. 1, pp. 83–92, 2015.

Hindawi Publishing Corporation
BioMed Research International
Volume 2016, Article ID 3262795, 12 pages
http://dx.doi.org/10.1155/2016/3262795

Research Article

X-Ray Scatter Correction on Soft Tissue Images for Portable Cone Beam CT

Sorapong Aootaphao,[1] Saowapak S. Thongvigitmanee,[1] Jartuwat Rajruangrabin,[1] Chalinee Thanasupsombat,[1] Tanapon Srivongsa,[1] and Pairash Thajchayapong[2]

[1] *X-Ray CT and Medical Imaging Laboratory, National Electronics and Computer Technology Center, National Science and Technology Development Agency, 112 Thailand Science Park, Phahonyothin Road, Khlong Nueng, Khlong Luang, Pathum Thani 12120, Thailand*
[2] *National Science and Technology Development Agency, 111 Thailand Science Park, Phahonyothin Road, Khlong Nueng, Khlong Luang, Pathum Thani 12120, Thailand*

Correspondence should be addressed to Saowapak S. Thongvigitmanee; saowapak.thongvigitmanee@nectec.or.th

Received 11 September 2015; Revised 15 January 2016; Accepted 17 January 2016

Academic Editor: Steven Heymsfield

Soft tissue images from portable cone beam computed tomography (CBCT) scanners can be used for diagnosis and detection of tumor, cancer, intracerebral hemorrhage, and so forth. Due to large field of view, X-ray scattering which is the main cause of artifacts degrades image quality, such as cupping artifacts, CT number inaccuracy, and low contrast, especially on soft tissue images. In this work, we propose the X-ray scatter correction method for improving soft tissue images. The X-ray scatter correction scheme to estimate X-ray scatter signals is based on the deconvolution technique using the maximum likelihood estimation maximization (MLEM) method. The scatter kernels are obtained by simulating the PMMA sheet on the Monte Carlo simulation (MCS) software. In the experiment, we used the QRM phantom to quantitatively compare with fan-beam CT (FBCT) data in terms of CT number values, contrast to noise ratio, cupping artifacts, and low contrast detectability. Moreover, the PH3 angiography phantom was also used to mimic human soft tissues in the brain. The reconstructed images with our proposed scatter correction show significant improvement on image quality. Thus the proposed scatter correction technique has high potential to detect soft tissues in the brain.

1. Introduction

Cone beam computed tomography (CBCT) scanners have been initially developed for dental applications. Dental CBCT images usually represent only bone structures due to limited contrast resolution of X-ray detectors. In recent years, flat panel detectors (FPDs) were tremendously improved in their capability of detecting small differences in attenuation of X-ray beam, thus providing soft tissue detectability, such as tumor, muscle, and intracerebral hemorrhage (ICH) [1–4]. This particular FPD model has been introduced in portable CBCT scanners with large field of view (FOV) to cover the head region. The portable CBCT scanner can be freely moved where rapid diagnosis is needed such as in the emergency and operation rooms [2–4]. The scanner can perform patient screening before treatment, during operation, and after operation. For having a large FPD, soft tissue images from CBCT scanner are usually degraded as more artifacts occur such as lag, glare [5], motion artifact [4, 5], beam hardening effects (BHE) [4–6], and X-ray scattering effects [5–7]. However, it is well known that the most critical artifact is caused by the X-ray scattering effect which reduces image quality. X-ray scatter signals directly affect contrast and CT numbers of soft tissue images. The number of X-ray scatter signals is increased as an increase in FOV and object thickness [7].

There are many methods to reduce X-ray scatter signals in FPDs, such as antiscatter grid plate [8], beam stop array plate [9], primary modulation methods [10], Monte Carlo simulation (MCS) software [11, 12], and X-ray scattering models [13–18]. The antiscatter grid plate can reduce X-ray scatter signals to increase image quality; however, it is not sufficient for improving image quality on soft tissue images [8], and the apparent dose increase is always undesired.

A beam stop array plate [9] can be used for measuring X-ray scatter signals; however, this method is not practical in clinics. The primary modulation method was to place a high frequency attenuation plate between an X-ray source and an object to obtain a modulated projection image, and then this modulated projection image was filtered to eliminate low-frequency components due to X-ray scatter signals by a high-pass filter [10]. Monte Carlo simulation software based on Geant4 libraries [11, 12] has been used widely to design the simulated system for estimating high accuracy X-ray scatter signals. Generally, the MCS software usually utilized expensive computation time. The technique proposed by Star-Lack et al. [14] described efficient X-ray scattering correction on the large ellipse phantom using asymmetric kernels. Since our work aims to reduce the X-ray scatter signals in the patient's head only, symmetric kernels can be assumed. Several iterative techniques were proposed for scatter correction including subtraction from measured data [14, 15] and deconvolution by the statistical method [13, 16, 17]. The problem of the subtraction method is that the corrected value can become negative as discussed in [16].

In this work, we propose the X-ray scattering correction method for improving soft tissue images on the large flat panel detector of portable CBCT. We apply the deconvolution technique based on the maximum likelihood expectation maximization (MLEM) method [13, 16, 17] for estimating the primary signal. First, the MCS software is used to form the shape and the amplitude of the X-ray scatter signals as a point spread function (PSF) and a scatter fraction (SF) function according to actual parameters of the CBCT system. Second, we match equivalent thickness in projection images to obtain subprojection images. Third, those subprojection images are convolved with the prepared kernels or PSFs and combined to obtain a convolved projection image. Finally, the convolved projection image is used in the MLEM method to estimate the primary signal, and the process is iterated until convergence to FBCT data. Once the primary signal is estimated, the reconstruction algorithm based on filtered backprojection (FBP) technique [19] is employed. In the experiment, our proposed technique will be tested with the QRM-ConeBeam phantom by QRM GmbH, Germany [20], and the PH3 angiographic CT head phantom ACS by Kyoto Kagaku Co., Ltd., Japan [21]. The experimental results are compared with FBCT data.

2. Materials and Methods

2.1. Materials. Our prototype portable CBCT scanner prototype consists of the flat panel detector (Varian PaxScan 4030CB) and the high frequency X-ray source which shoots X-ray pulses by synchronizing with exposure time of the flat panel detector. The distance from source to detector (DSD) and the distance from source to an object (DSO) are 500 mm and 786 mm, respectively. The dynamic gain was operated for the pixel size of 0.388 mm. This system used 90 kVp, 9 mA, and the total filtration of 0.5 mm Aluminum. A full rotation of scanning was achieved. In this work, we used PSF and SF from MCS software to simulate X-ray scatter signals by using PMMA sheets with a pencil beam as shown in Figure 1.

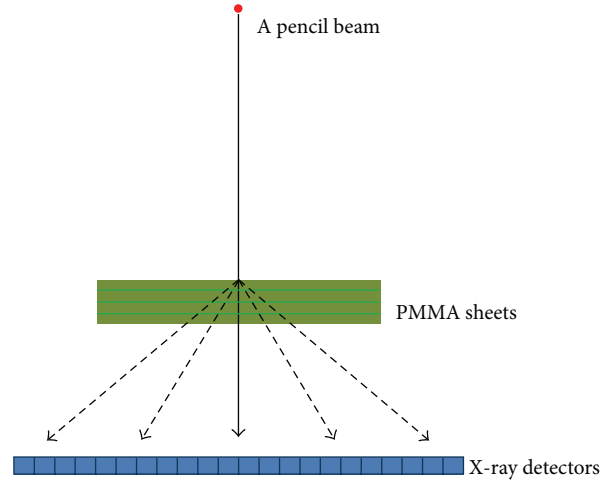

Figure 1: The X-ray scatter signal measurement model in the Monte Carlo simulation software.

The MCS software computed the X-ray scatter signals by simulating a pencil beam with the PMMA sheets; one set of the PMMA sheets was 38 mm thick and the total of 10 sets was used. The measured X-ray scatter signals at each thickness are interpolated to achieve X-ray scatter signals at thickness of 1 mm. We used 2 phantoms in the experiments: the QRM-ConeBeam phantom by QRM GmbH, Germany [20], is a cylindrical tissue equivalent phantom at 120 kVp with the diameter of 160 mm and the height of 160 mm and the PH3 angiographic CT head phantom ACS by Kyoto Kagaku Co., Ltd., Japan [21], is a life-size adult phantom made of Urethane base resin (SZ-50) and Epoxy base resin as shown in Figure 2.

2.2. Method. According to the fundamental law of physics, while the X-ray beam travels to penetrate each layer inside an object, there exist three phenomena of interactions: photoelectric effect, Compton scattering, and Rayleigh Scattering of X-ray photons. The Compton scattering effect is essential for cross section images reconstruction. The X-ray beam that penetrates an object and goes directly to the flat panel detector is desired; however, scattered X-rays from other directions are usually combined at the same sensor position of the flat panel detector. This degrades image quality, such as cupping artifacts, low contrast, and inaccurate CT numbers. We can write the measured X-ray signal model as follows:

$$I_m(x, y) = I_p(x, y) + I_s(x, y), \quad (1)$$

where I_m is the measured signal, I_p is the primary signal which is the expected signal to be used in cross section image reconstruction, I_s is the scatter signal, and (x, y) denotes the pixel coordinate in the projection image. The scatter signal can be written in the form of the primary signal convolved with the kernel function, K, as follows:

$$I_s(x, y) = K(x, y) ** I_p(x, y), \quad (2)$$

where $**$ denotes a 2D convolution operator. The statistical method is based on Bayes' rule as discussed in [13]. The average value of the statistical method is considered by the X-ray

(a) (b)

Figure 2: (a) QRM-ConeBeam phantom and (b) PH3 angiography CT head phantom.

photons behind an object as Poisson distribution [13]. The maximum likelihood is used to estimate the primary signal, I_p, and can be written in the form of the MLEM [13, 16, 17] algorithm as follows:

$$I_p^{n+1}(x,y) = \frac{I_p^n(x,y)\, I_m(x,y)}{I_p^n(x,y) + I_p^n * *K(x,y)}, \tag{3}$$

where I_p^n is the estimated primary signal at the nth iteration. The kernel measurement at different thickness, K_t, is obtained according to the thickness of the PMMA sheet, so I_p^n is divided according to thickness, $I_{p,t}^n$. We can rewrite the above equation as follows:

$$I_p^{n+1}(x,y) = \frac{I_p^n(x,y)\, I_m(x,y)}{I_p^n(x,y) + \sum_t I_{p,t}^n * *K_t(x,y)}. \tag{4}$$

The scatter correction method starts by creating a database of kernels according to thickness of PMMA sheets using the MCS software and initializing the primary signal, I_p^0. The next step is to match each pixel of the primary signal with the estimated PMMA equivalent thickness; that is, the projection image data are divided into different groups or subprojection image data according to thickness. The subprojection image data sets of the primary signal are convolved with the kernels and summed up to obtain the convolved projection image. Then the convolved projection image is used to perform deconvolution by the MLEM algorithm. Finally, we check the condition for convergence. If it does not converge, we will return to the thickness mapping process again. In summary, all steps of the scatter correction can be illustrated as in Figure 3.

2.2.1. Kernel Measurements. Kernel measurements in this work are obtained by measuring different thickness of the object. Generally, kernels can be measured from experiments or simulated by the MCS software. For accuracy of measuring the X-ray scatter signal, we used the MCS software to simulate

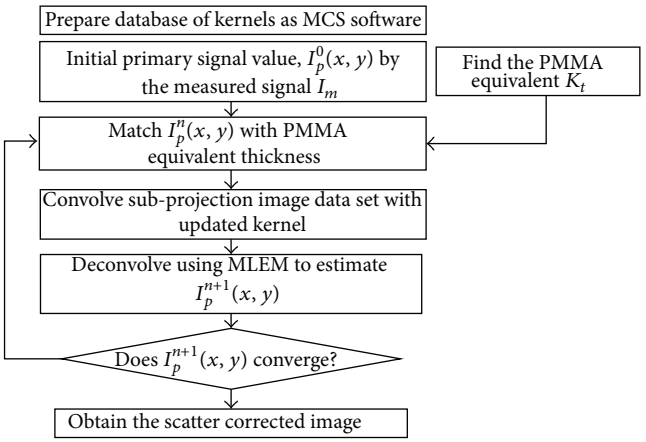

Figure 3: The scatter correction process.

the scatter signals according to the actual CBCT scanner system: 90 kVp Voltage as a pencil beam and the total flat filtration of 5.5 mm Al. The pencil beam penetrates through PMMA sheets. We used the total of 10 sets of PMMA sheets with the thickness of 38 mm each set. The measured scatter signals are interpolated to obtain the scatter signal at each 1 mm thickness, so the total of 380 scatter signals is obtained. The example of scatter signals using this work is shown in Figure 4. They are normalized to obtain the point spread function (PSF) according to thickness, PSF_t. The kernel at each thickness can be described as follows:

$$K_t(x,y) = A(t)\,\mathrm{SF}(t)\,\mathrm{PSF}_t(x,y), \tag{5}$$

where x and y denote the spatial coordinate, t is PMMA thickness, and A is the compensating value from the experiments, which depends on thickness. The values of A used in this work are shown in Table 1. Moreover, the scatter fraction values are measured as an average at the center region of each kernel for a suitable size of region of interest (ROI). In the experiments, we employ linear curve fitting to the measured

Table 1: Compensating value of A in each thickness range.

	$0 < t \leq 40$ mm	$40 < t \leq 80$ mm	$80 < t \leq 120$ mm	$120 < t \leq 160$ mm	160 mm $< t$
A	1.0	1.0	1.75	1.75	2.0

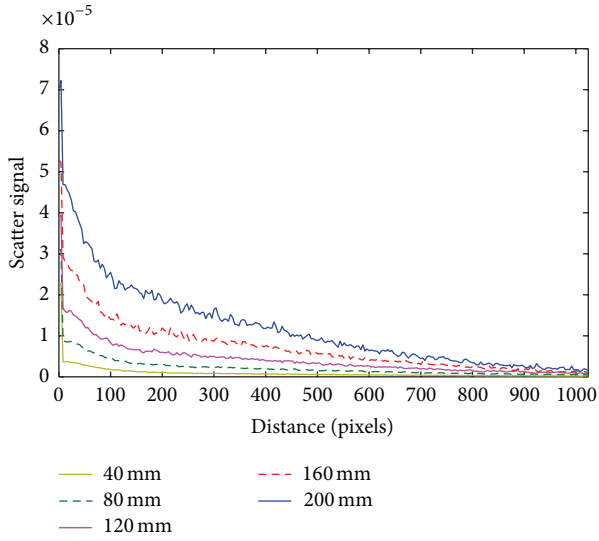

Figure 4: Profiles of scatter signals at each thickness of PMMA sheet.

average value of scatter fraction. The scatter fraction, I_s/I_m, can be described as follows:

$$\mathrm{SF}(t) = a_1 t + a_2, \tag{6}$$

where a_1 and a_2 are coefficients of the linear function. The SF value depends on object thickness and highly affects the amount of scatter correction.

2.2.2. Thickness Map Measurements. We match the projection image data to obtain the subprojection image data set according to PMMA thickness. First, we create the log signal function from pure PMMA plates for thickness mapping. We divide thickness of the projection image, t_{PMMA}, by using Beer's law [11, 12, 19] as follows:

$$t_{\mathrm{PMMA}} = \frac{1}{\mu_{\mathrm{PMMA}}} \log\left(\frac{I_{p,0}}{I_p}\right), \tag{7}$$

where μ_{PMMA} is the linear attenuation coefficient at the effective energy, $I_{p,0}$ is the measured primary signal without attenuation, and I_p is the primary signal. We divide the projection image data of the object into the subprojection image data set as the log signal function of PMMA sheet thickness. The measured primary signal I_p at different PMMA thickness from the MCS software can create the log signal function as the relationship between actual PMMA thickness and the log signal value. This function is used for transferring the log signal value to the equivalent value of PMMA thickness.

2.2.3. Evaluation. Evaluation in the experimental results starts as checking the performance of the MLEM method whether it converges according to the log likelihood function, L [13]. For simplicity, we ignore the insignificant terms as follows:

$$L = \sum_{x,y} \left[I_m(x,y) \log\left(I_p^n(x,y)\right) - I_p^n(x,y) \right]. \tag{8}$$

To verify our proposed algorithm, we will compare both projection images and cross section images with the FBCT data. The CT number in the reconstructed images is calibrated by using the water average value in the CT number section of the QRM-ConeBeam phantom as shown in Figure 5(a). Note that the water average value is measured by using FBCT instead of CBCT to avoid scatter effects. We can normalize the Hounsfield unit (HU) as follows:

$$\mathrm{CT\#} = 1000 \times \frac{\left(m_x - m_{\mathrm{water,FBCT}}\right)}{m_{\mathrm{water,FBCT}}}, \tag{9}$$

where m_x is the average value of any material in the cross section images and $m_{\mathrm{water,FBCT}}$ is the water average value from FBCT. To measure the low contrast detectability, we use Sections A, B, and C of the QRM-ConeBeam phantom. Section A has higher contrast between inserts and background than Sections B and C, while Section C has the lowest contrast. Here we measure the density value at numbers 1 to 4 as shown in Figure 5(b). Different gray level values represent different density values.

After estimating scatter correction, the contrast is increased; however, the noise signal value in the projection images is increased as well. In this study, we measure the contrast value between two different inserts and its contrast to noise ratio (CNR) as follows:

$$\mathrm{Contrast} = m_x - m_{\mathrm{background}},$$
$$\mathrm{CNR} = \frac{\left(m_x - m_{\mathrm{background}}\right)}{\sqrt{\sigma_x^2 + \sigma_{\mathrm{background}}^2}}, \tag{10}$$

where $m_{\mathrm{background}}$ is the average value in the background region and σ_x and $\sigma_{\mathrm{background}}$ are the standard deviation (STD) value of any insert material and the background, respectively. However, we also measure percentage of cupping in the cross section images in order to evaluate the proposed method and the remaining beam hardening effect as follows:

$$\%\ \mathrm{cupping} = \frac{\left(\mathrm{CT\#}_{\mathrm{edge}} - \mathrm{CT\#}_{\mathrm{center}}\right) \times 100}{\left(\mathrm{CT\#}_{\mathrm{edge}} + 1000\right)}, \tag{11}$$

where $\mathrm{CT\#}_{\mathrm{edge}}$ is an average CT number value from four peripheral ROIs in the uniform areas and $\mathrm{CT\#}_{\mathrm{center}}$ is the average CT number value at the center.

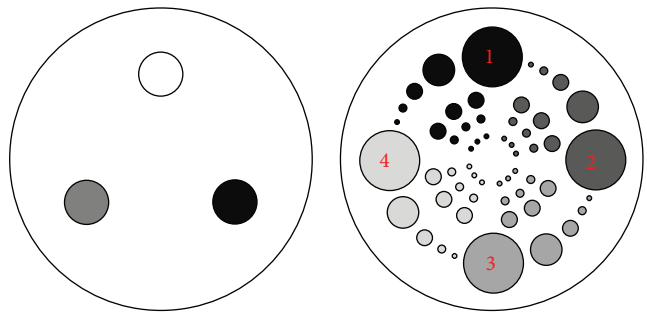

Figure 5: Sections in the QRM-ConeBeam phantom: (a) CT number section and (b) the pattern of low contrast section in Sections A, B, and C.

Table 2: Parameter setting for the proposed scatter correction method.

$SF(t) = a_1 \cdot t + a_2$	Thickness of each group	Number of groups
$a_1 = 0.0038$, $a_2 = 0.1$	40 mm	5

3. Results

All parameters used in this study are shown in Tables 1 and 2. Table 2 shows the implementation parameters including the coefficient values of the SF function: $a_1 = 0.0038$, $a_2 = 0.1$; number of groups: 5; and the thickness of each group: 40 mm. From the experiment, we tried dividing into different groups and found that five groups with 40 mm thickness in each group were sufficient for acceptable estimation of the primary signal. Moreover, according to the experiment, the proposed method did not introduce any additional artifacts.

3.1. Scatter Correction Results in the Projection Image. The scatter correction results in the projection images were compared with the FBCT data. FBCT was obtained from the narrow-collimated scan of the CBCT system. The collimation was made of 3 mm thick leaded blades with 3 mm opening in the vertical direction. Due to narrow collimation, the FBCT profile data contain less scatter signal than the profile data obtained from CBCT. In the experiment, we used the PMMA sheet (thickness of 60 mm) that is attached with the lead sheet (thickness of 3 mm) for measuring the scatter signal value and comparing its profile with FBCT as shown in Figure 6.

Ideally, the profile data obtained from FBCT should be almost identical to the actual primary signal; therefore, the FBCT data are used as the benchmark in comparison with the estimated data from CBCT. However, FBCT acquisition is limited to only a small strip around the center of the X-ray beam. Figure 7 shows comparison among uncorrected CBCT and corrected CBCT and FBCT profiles of the projection data acquired from the QRM-ConeBeam phantom. The log likelihood values calculated using (8) are plotted versus the number of iterations as shown in Figure 8. The log likelihood values seem to converge as the number of iterations increases. One of the stopping criteria can be monitored from the convergence of the log likelihood values. After the convergence of the log likelihood value, the reconstructed cross section images of the proposed scatter correction method should be close to the cross section image of the FBCT.

3.2. Measurements in the CT Number Section. Corrected projection images are reconstructed by the filtered back-projection method [19] using the Shepp Logan filter with the cutoff at 0.6 and the voxel size of 0.3 mm. The cross section images in the CT number section are measured and compared with FBCT data. Figure 9 shows the cross section images with and without scatter correction and their profiles comparison. All reconstructed images in Figure 9 are displayed with the window width and level (W/L) of 1500 and 1000, respectively.

The profile data comparison is plotted across the bone insert and the air hole in the CT number section as shown in Figure 9(d). The proposed profile is almost identical to the profile from FBCT as the cupping effect is reduced. The CT number values are calculated by using the average value of the water insert according to the QRM-ConeBeam phantom's specifications [20]. Since the X-ray spectrum we used cannot clearly discriminate the density value of water and soft tissue (background), we used the soft tissue value instead. In the experiment, we measured the CT numbers of three inserts up to 10 iterations as shown in Table 3.

The accuracy of the CT number value at each insert increases as the number of iterations increases; however, once convergence is reached the accuracy of CT number value stays the same even when we perform more number of iterations. These CT number values are considered to be valid for diagnosis after convergence is achieved. However, noise is also increased after scatter correction. We evaluated the contrast value between bone and soft tissue inserts and the influence of noise by measuring the contrast to noise ratio as shown in Table 4. In Table 5, to calculate percentage of cupping, we compare the center average value with the average value of four peripheral areas using (11).

From Table 5, the cupping artifacts are significantly reduced, comparing with FBCT data; however, the small effect from beam hardening is still present even with FBCT. As the log likelihood value is decreased, the CT number values of bone, air, and soft tissue as well as the contrast values

Table 3: CT number value comparison in the QRM-ConeBeam phantom.

	FBCT		No correction		Scatter correction at different iterations									
					2 iterations		4 iterations		6 iterations		8 iterations		10 iterations	
	HU	STD	HU	STD	HU	STD	HU	STD	HU	STD	HU	STD	HU	STD
Bone	752	122	141	82	436	105	648	128	713	139	736	145	742	148
Air	−1000	63	−760	57	−809	76	−905	77	−923	70	−940	67	−943	66
Soft tissue	0	112	−197	63	−60	85	−2	108	6	117	7	120	7	121

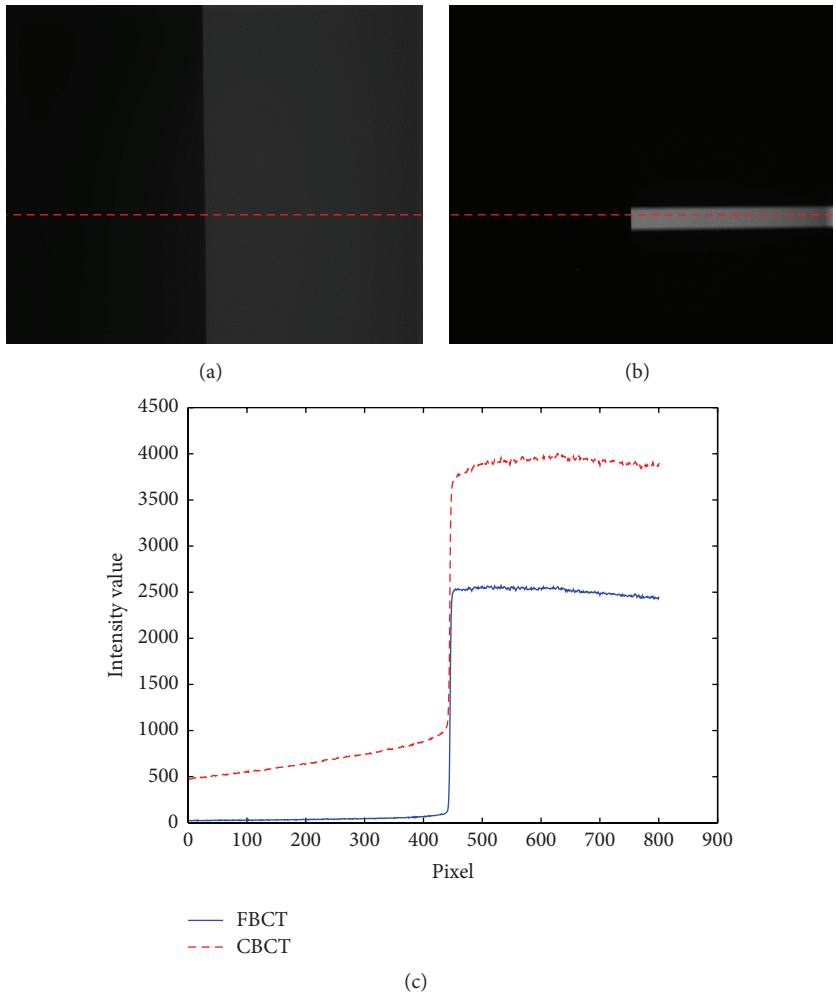

Figure 6: (a) The projection image from CBCT, (b) the projection image from FBCT, and (c) CBCT and FBCT profile data comparison.

are significantly improved; however, noise is also increased. In this study, we did not perform noise suppression after scatter correction, so this would affect the CNR.

3.3. Measurement Results in the Low Contrast Sections and the PH3 Phantom. There are three sections of low contrast detectability in the QRM-ConeBeam phantom, namely, Sections A, B, and C. They have the same pattern as shown in Figure 5(b), but the density values of the inserts within each section are different. The results of three low contrast sections after 5 iterations of scatter correction are reconstructed by the FBP method using the Hamming filter with the cutoff frequency of 0.6 and the voxel size of 0.6 mm and then compared with FBCT as shown in Figure 10. We measured the CT numbers in each section according to numbers 1 to 4 as shown in Figure 5(b) and the errors were calculated by using the absolute different value of the corrected results with FBCT.

The measured HU values in three sections of low contrast are shown in Tables 6–8. Note that one of the reasons that the error after scatter correction in Section A seems to be a little higher than Sections B and C might be because the position of Section A is further away from the central ray than Sections B and C.

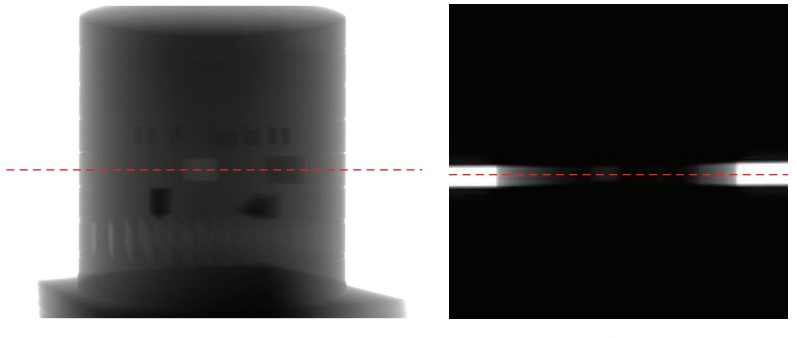

(a) (b)

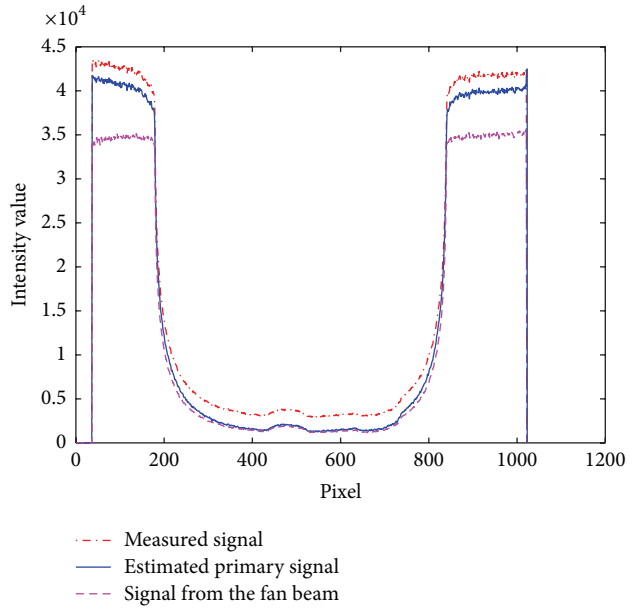

(c)

Figure 7: (a) The projection image of QRM-ConeBeam phantom in CBCT, (b) the projection image of the QRM-ConeBeam phantom in FBCT, and (c) comparison of profiles data before and after scatter correction with FBCT data.

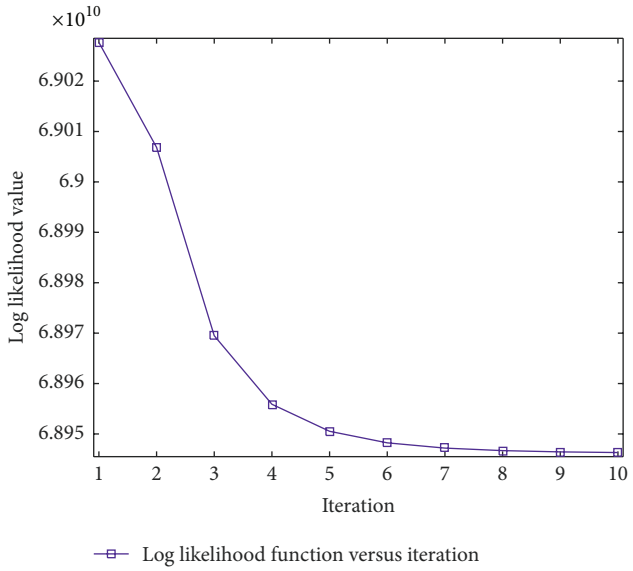

Figure 8: Log likelihood value versus number of iterations.

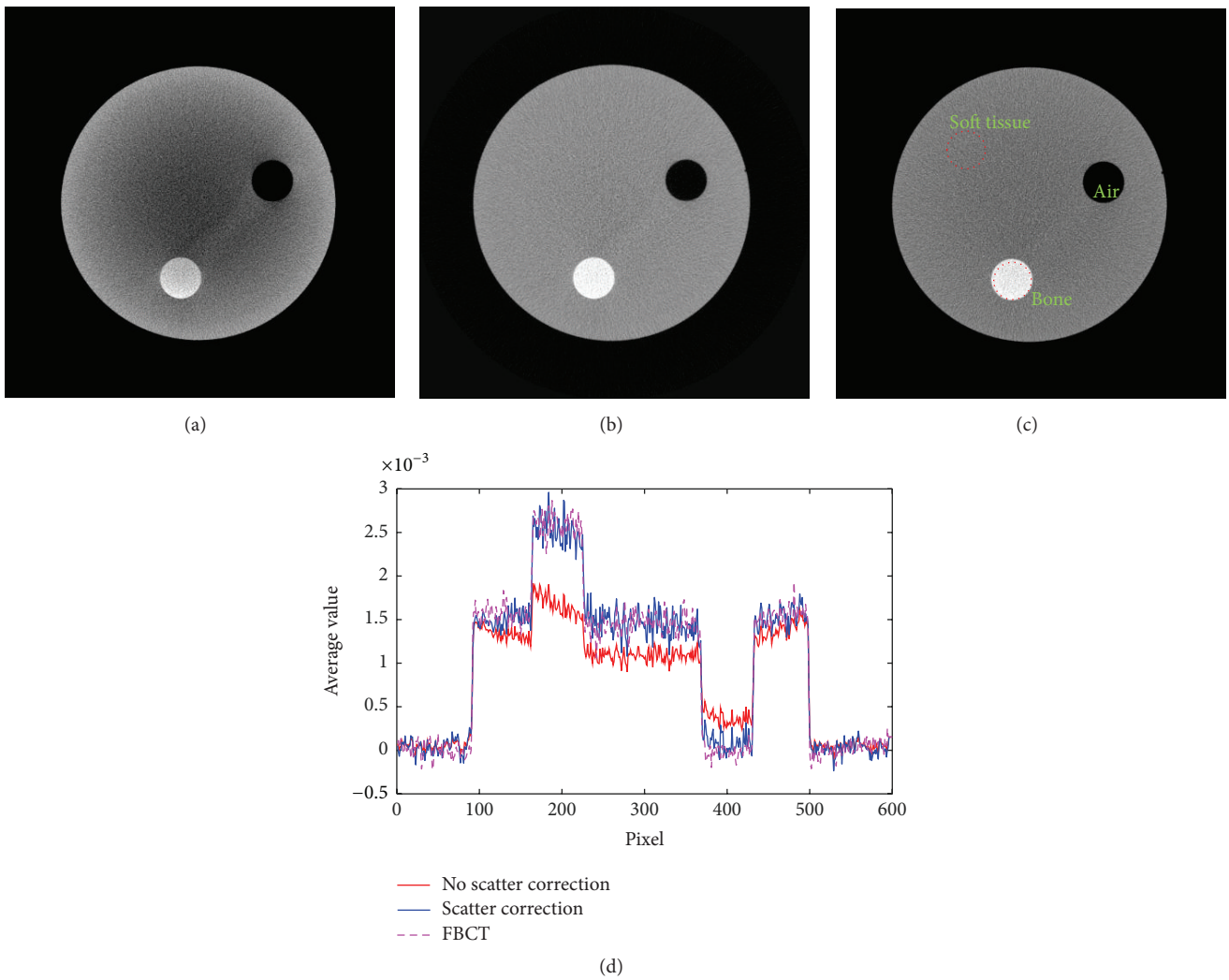

Figure 9: (a) Reconstructed image without scatter correction, (b) with scatter correction, (c) FBCT, and (d) comparison of profile data with and without scatter correction and FBCT data.

Table 4: Contrast and CNR values between bone and soft tissue.

	FBCT	No correction	Scatter correction at different iterations				
			2 iterations	4 iterations	6 iterations	8 iterations	10 iterations
Contrast	752	338	496	650	707	729	735
CNR	5.10	3.38	3.72	3.93	3.97	3.96	3.95

Table 5: Percentage of cupping artifacts.

	FBCT	No correction	Scatter correction at different iterations				
			2 iterations	4 iterations	6 iterations	8 iterations	10 iterations
% cupping	10	28.83	19.57	10.34	7.54	6.68	6.40

Table 6: HU values of different inserts in Section A of the QRM-ConeBeam phantom.

	FBCT	CBCT without correction		CBCT with scatter correction	
	Mean (HU)	Mean (HU)	Different value (HU)	Mean (HU)	Different value (HU)
A1	−165	−269	104	−187	22
A2	−91	−223	132	−112	21
A3	−69	−210	141	−90	21
A4	−45	−195	150	−68	23

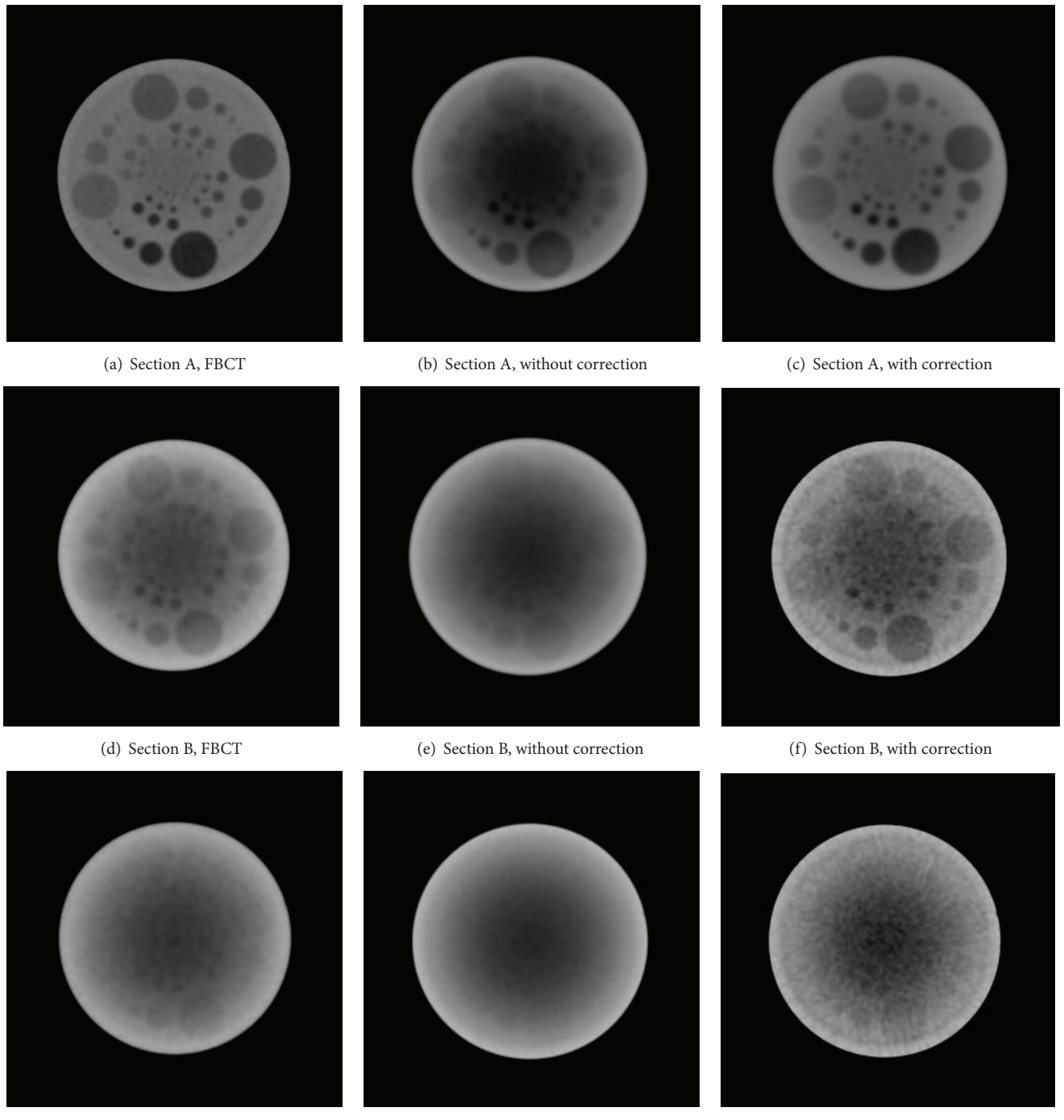

(a) Section A, FBCT (b) Section A, without correction (c) Section A, with correction

(d) Section B, FBCT (e) Section B, without correction (f) Section B, with correction

(g) Section C, FBCT (h) Section C, without correction (i) Section C, with correction

Figure 10: Result comparison between CBCT with and without scatter correction and FBCT in each section of low contrast detectability (window/level: 500/−50).

Table 7: HU values of different inserts in Section B of the QRM-ConeBeam phantom.

	FBCT	CBCT without correction		CBCT with scatter correction	
	Mean (HU)	Mean (HU)	Different value (HU)	Mean (HU)	Different value (HU)
B1	−8	−164	156	−6	2
B2	7	−156	149	8	1
B3	11	−154	143	12	1
B4	16	−148	132	17	1

Table 8: HU values of different inserts in Section C of the QRM-ConeBeam phantom.

	FBCT	CBCT without correction		CBCT with scatter correction	
	Mean (HU)	Mean (HU)	Different value (HU)	Mean (HU)	Different value (HU)
C1	17	−156	139	18	1
C2	21	−152	131	22	1

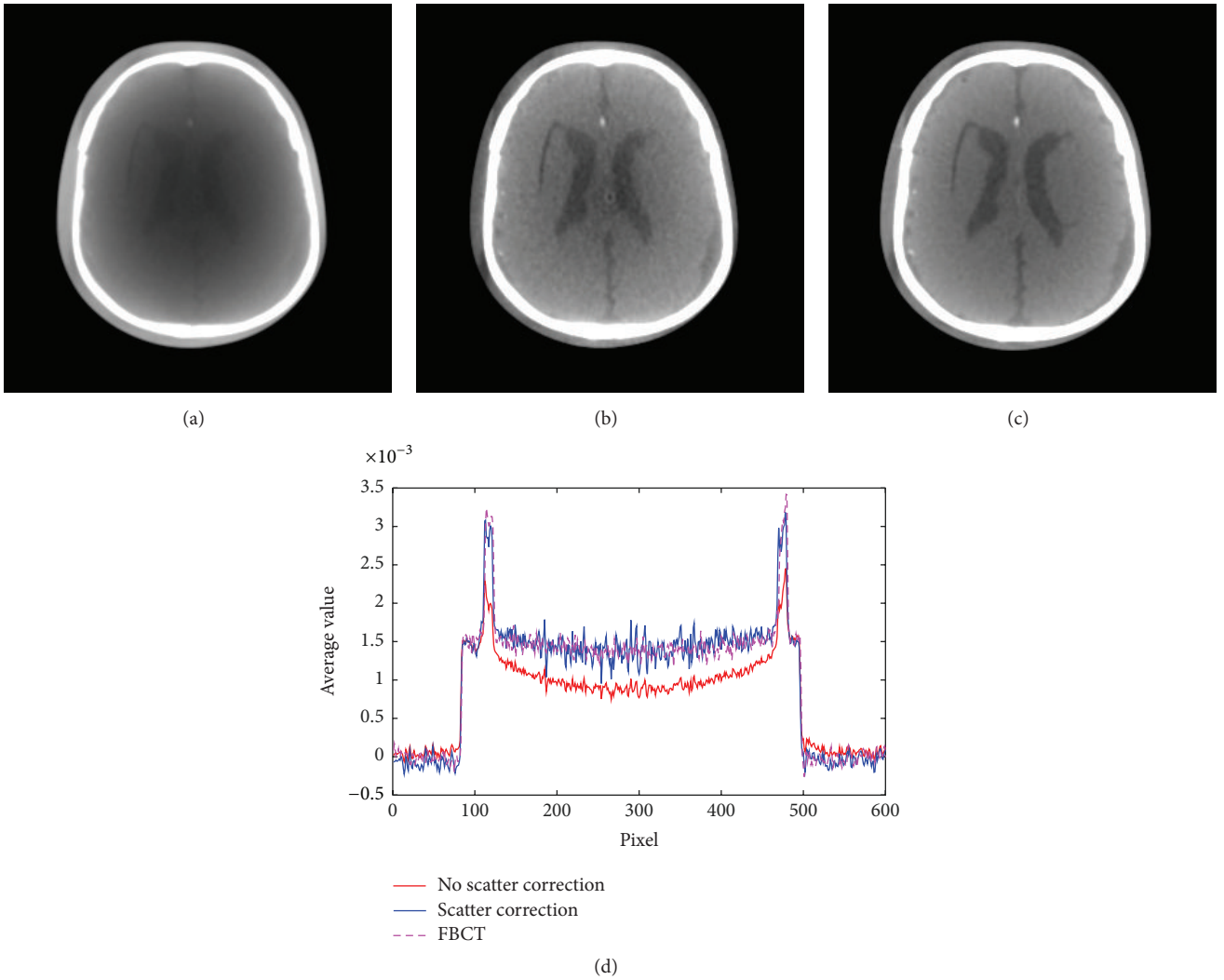

Figure 11: (a) CBCT without correction, (b) CBCT with correction, (c) FBCT, and (d) profile comparison.

Results in three sections of low contrast indicate better image quality. The low contrast values in three sections can be discriminated; thus the contrast is significantly improved. Moreover, some inserts appear after correction. In addition to the QRM-ConeBeam phantom, we applied the proposed method to another phantom using the same parameters and the results are shown in Figures 11 and 12. The reconstructed images in these two figures are displayed with the window width and level of 900 and −100, respectively. Figure 11 shows the cross section images of the PH3 phantom along with profile data comparison. The ventricles region in the PH3 angiographic CT head phantom is significantly improved as shown in Figure 11(b). The corrected profile in Figure 11(d) is very close to the FBCT profile. Figure 12 shows the reconstructed images with and without scatter correction in the coronal and sagittal planes. Although image quality is improved, the beam hardening effect still presents in these planes.

4. Discussion

Although the log likelihood function seems to converge as the number of iterations increases, image quality after scatter correction may not be approaching FBCT exactly according to the log likelihood function. The small change in the log

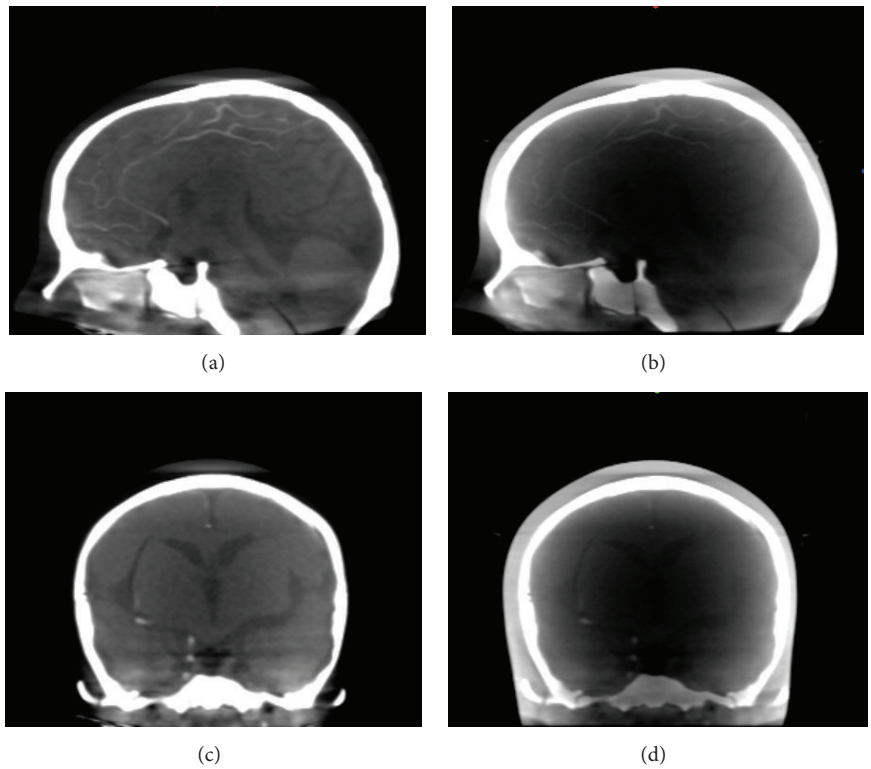

(a) (b) (c) (d)

Figure 12: (a) The sagittal plane with correction, (b) the sagittal plane without correction, (c) the coronal plane with correction, and (d) the coronal plane without correction.

likelihood value after several iterations may result in overcorrection in the reconstructed images as indicated by the percentage of cupping in Table 5. For example, the percentage of cupping at 10 iterations is smaller than that of FBCT. Therefore, to ensure convergence and avoid overcorrection, only 5 iterations seem to be sufficient (Figures 10–12). In this work, we attempt to improve image quality of low contrast by applying the proposed method to the three sections of low contrast in the QRM-ConeBeam phantom. The results of three sections in Figure 10 are significantly improved; that is, visibility of some inserts in Section C can be observed. Moreover, in Table 5, the percentage of cupping artifacts in FBCT is about 10% which means that other causes of cupping artifacts besides scattering are present. One of them could be beam hardening effects, which is ignored in this study.

5. Conclusions

In this paper, we propose the scatter correction method to improve image quality of soft tissue images acquired from portable CBCT. Our proposed technique is based on estimation of X-ray scatter signals using the MLEM method and kernel modeling with Monte Carlo simulation. By benchmarking with FBCT, the scatter correction results with CBCT show significant improvement on image quality. With the QRM-ConeBeam phantom, the cupping artifacts are reduced, CT numbers of inserts are approaching FBCT, contrast is increased, and low contrast detectability becomes more apparent. Moreover, scatter correction in the reconstructed images of the PH3 angiographic CT head phantom can bring out soft tissue structures prominently. Therefore, our proposed scatter correction method has a high possibility to detect soft tissue images using portable CBCT. For future work, we will test our proposed technique on real patient data.

Conflict of Interests

The authors declare that there is no conflict of interests regarding the publication of this paper.

Acknowledgment

The authors would like to thank the Faculty of Medicine, Prince of Songkla University, for research funding and feedbacks of the portable CBCT prototype.

References

[1] T. Struffert, G. Richter, T. Engelhorn et al., "Visualisation of intracerebral haemorrhage with flat-detector CT compared to multislice CT: results in 44 cases," *European Radiology*, vol. 19, no. 3, pp. 619–625, 2009.

[2] Z. Rumboldt, W. Huda, and J. W. All, "Review of portable CT with assessment of a dedicated head CT scanner," *American Journal of Neuroradiology*, vol. 30, no. 9, pp. 1630–1636, 2009.

[3] W. A. Kalender and Y. Kyriakou, "Flat-detector computed tomography (FD-CT)," *European Radiology*, vol. 17, no. 11, pp. 2767–2779, 2007.

[4] A. Shuaib, K. Khan, T. Whittaker, S. Amlani, and P. Crumley, "Introduction of portable computed tomography scanners, in the treatment of acute stroke patients via telemedicine in remote communities," *International Journal of Stroke*, vol. 5, no. 2, pp. 62–66, 2010.

[5] A. Sisniega, W. Zbijewski, J. Xu et al., "High-fidelity artifact correction for cone-beam CT imaging of the brain," *Physics in Medicine and Biology*, vol. 60, no. 4, pp. 1415–1439, 2015.

[6] W. Zbijewski and J. W. Stayman, "Volumetric soft tissue brain imaging on xCAT, a mobile flat-panel x-ray CT system," in *Medical Imaging: Physics of Medical Imaging*, vol. 7258 of *Proceedings of SPIE*, Lake Buena Vista, Calif, USA, March 2009.

[7] Y. Kyriakou and W. A. Kalender, "X-ray scatter data for flat-panel detector CT," *Physica Medica*, vol. 23, no. 1, pp. 3–15, 2007.

[8] S. Schafer, J. W. Stayman, W. Zbijewski, C. Schmidgunst, G. Kleinszig, and J. H. Siewerdsen, "Antiscatter grids in mobile C-arm cone-beam CT: effect on image quality and dose," *Medical Physics*, vol. 39, no. 1, pp. 153–159, 2012.

[9] J. S. Maltz, B. Gangadharan, M. Vidal et al., "Focused beam-stop array for the measurement of scatter in megavoltage portal and cone beam CT imaging," *Medical Physics*, vol. 35, no. 6, pp. 2452–2462, 2008.

[10] H. Gao, R. Fahrig, N. Robert Bennett, M. Sun, J. Star-Lack, and L. Zhu, "Scatter correction method for x-ray CT using primary modulation: phantom studies," *Medical Physics*, vol. 37, no. 2, pp. 934–946, 2010.

[11] M. Bertram, T. Sattel, S. Hohmann, and J. Wiegert, "Monte-Carlo scatter correction for cone-beam computed tomography with limited scan field-of-view," in *Proceedings of the Medical Imaging 2008: Physics of Medical Imaging*, vol. 6913 of *Proceedings of SPIE, Medical Imaging*, San Diego, Calif, USA, February 2008.

[12] S. Agostinelli, J. Allison, K. Amako et al., "GEANT4—a simulation toolkit," *Nuclear Instruments and Methods in Physics Research Section A: Accelerators, Spectrometers, Detectors and Associated Equipment*, vol. 506, pp. 250–303, 2003.

[13] A. H. Baydush and C. E. Floyd Jr., "Bayesian image estimation of digital chest radiography: interdependence of noise, resolution, and scatter fraction," *Medical Physics*, vol. 22, no. 8, pp. 1255–1261, 1995.

[14] J. Star-Lack, M. Sun, A. Kaestner et al., "Efficient scatter correction using asymmetric kernels," in *Medical Imaging: Physics of Medical Imaging*, vol. 7258 of *Proceedings of SPIE*, Lake Buena Vista, Fla, USA, March 2009.

[15] I. Reitz, B. M. Hesse, S. Nill, T. Tucking, and U. Oelfke, "Enhancement of image quality with a fast iterative scatter and beam hardening correction method for kV CBCT," *Medical Physics*, vol. 19, pp. 158–172, March 2009.

[16] J. S. Maltz, B. Gangadharan, S. Bose et al., "Algorithm for X-ray scatter, beam-hardening, and beam profile correction in diagnostic (kilovoltage) and treatment (megavoltage) cone beam CT," *IEEE Transactions on Medical Imaging*, vol. 27, no. 12, pp. 1791–1810, 2008.

[17] S. Aootaphao, S. S. Thongvigitmanee, J. Rajruangrabin, P. Junhunee, and P. Thajchayapong, "Experiment-based scatter correction for cone-beam computed tomography using the statistical method," in *Proceedings of the IEEE Engineering in Medicine and Biology Society*, pp. 5087–5090, Osaka, Japan, July 2013.

[18] S. K. Ahn, G. Cho, and H. Jeon, "A scatter correction using thickness iteration in dual-energy radiography," *IEEE Transactions on Nuclear Science*, vol. 53, no. 1, pp. 133–138, 2006.

[19] A. C. Kak and M. Slaney, *Principle of computed Tomographic Imaging*, IEEE Press, New York, NY, USA, 1988.

[20] QRM phantom specifications, http://www.qrm.de/content/pdf/QRM-ConeBeam-Phantom.pdf.

[21] PH3 angiography phantom specifications, http://www.kyotoka-gaku.com/products/detail03/pdf/ph-3_manual.pdf.

Hindawi Publishing Corporation
BioMed Research International
Volume 2016, Article ID 9578139, 9 pages
http://dx.doi.org/10.1155/2016/9578139

Research Article

Characterization of Enhancing MS Lesions by Dynamic Texture Parameter Analysis of Dynamic Susceptibility Perfusion Imaging

Rajeev K. Verma,[1,2] Johannes Slotboom,[1] Cäcilia Locher,[1] Mirjam R. Heldner,[3] Christian Weisstanner,[1] Eugenio Abela,[3] Frauke Kellner-Weldon,[1] Martin Zbinden,[1] Christian P. Kamm,[3] and Roland Wiest[1]

[1]*Support Center for Advanced Neuroimaging, University Institute of Diagnostic and Interventional Neuroradiology, Inselspital, University of Bern, 3010 Bern, Switzerland*
[2]*Tiefenau Hospital, Institute of Radiology, Spital-Netz Bern, 3004 Bern, Switzerland*
[3]*Department of Neurology, Inselspital, University of Bern, 3010 Bern, Switzerland*

Correspondence should be addressed to Roland Wiest; roland.wiest@insel.ch

Received 31 August 2015; Accepted 3 December 2015

Academic Editor: Guang Jia

Purpose. The purpose of this study was to investigate statistical differences with MR perfusion imaging features that reflect the dynamics of Gadolinium-uptake in MS lesions using dynamic texture parameter analysis (DTPA). *Methods*. We investigated 51 MS lesions (25 enhancing, 26 nonenhancing lesions) of 12 patients. Enhancing lesions ($n = 25$) were prestratified into enhancing lesions with increased permeability (EL+; $n = 11$) and enhancing lesions with subtle permeability (EL−; $n = 14$). Histogram-based feature maps were computed from the raw DSC-image time series and the corresponding texture parameters were analyzed during the inflow, outflow, and reperfusion time intervals. *Results*. Significant differences ($p < 0.05$) were found between EL+ and EL− and between EL+ and nonenhancing inactive lesions (NEL). Main effects between EL+ versus EL− and EL+ versus NEL were observed during reperfusion (mainly in mean and standard deviation (SD): EL+ versus EL− and EL+ versus NEL), while EL− and NEL differed only in their SD during outflow. *Conclusion*. DTPA allows grading enhancing MS lesions according to their perfusion characteristics. Texture parameters of EL− were similar to NEL, while EL+ differed significantly from EL− and NEL. Dynamic texture analysis may thus be further investigated as noninvasive endogenous marker of lesion formation and restoration.

1. Introduction

MR-based imaging biomarkers are integral parts of the diagnosis workup of multiple sclerosis since more than 20 years [1]. These biomarkers include baseline MRI lesion count, lesion load, and topography, as well as T1-associated signatures of axonal damage [2]. The most common phenotype of MS—relapsing-remitting MS—is characterized by recurrent perivenous inflammation and demyelination of brain tissue resulting in progressive neurological dysfunction triggered by immunopathogenic mechanisms that are not fully explored until now [3]. In particular, dysregulation and disruption of the blood-brain barrier (BBB) are a critical event in the pathological evolution of MS lesions [4]. Absence of Gd-enhancement does not preclude BBB breakdown and vice versa [5], although a temporal change of enhancement is frequently considered as a surrogate marker for BBB restoration. Thus, in daily clinical practice, most commonly the tissue is thus simply characterized as "enhancing" or "nonenhancing" and the dynamic aspects of lesion enhancement are frequently waived [6]. Beyond T1-weighted static MRI, perfusion imaging offers an alternative to quantify the amount of vascular permeability [7] and to analyze the time-dependency of the BBB disruption [8, 9]. Since perfusion imaging can be standardized according to the amount, flow, and timing of Gd-administration, lesion morphology may be reevaluated according to changes in microstructural perfusion and leakage during the first pass of the bolus passage. A recently proposed method, dynamic texture parameter analysis (DTPA), allows investigating these spatiotemporal

characteristics to describe specific features of enhancing and nonenhancing lesions in MS [10]. DTPA enables a quantitative grading of MS lesions and discriminates lesions according to their statistical metrics. In this study, we aimed to investigate whether contrast agent extravasation is associated with characteristic metrics derived from dynamic textures of histograms during the first pass of the perfusion and early reperfusion. We hypothesized (i) that microstructural perfusion analysis can be used to subcategorize enhancing lesions according to their vascular permeability [11] and (ii) that statistical texture analysis segregates enhancing MS lesions by lesion-specific time-dependent patterns.

2. Materials and Methods

2.1. Patients. 12 patients (9 women, 3 men) with relapsing-remitting MS (RR-MS, $n = 9$) and secondary progressive MS (SP-MS, $n = 3$) according to the revised McDonald criteria of 2010 [12] were included into this retrospective analysis. The 3 SPMS patients presented with an initial course of RRMS followed by stepwise deterioration with superimposed relapses. Median age was 43 y (range 23–74 years). All data were derived from an ongoing prospective study that incorporates perfusion MRI as part of the MS imaging protocol. Inclusion criteria were (i) at least one lesion with enhancement on T1-weighted images and (ii) at least one lesion without enhancement on T2/FLAIR images and normal hematocrit (0.34–0.47) [13]. The study was approved by the local ethics committee (Cantonal Ethics Commission Bern, Switzerland). All patients gave written informed consent to participate in this study.

2.2. MRI Sequences and Parameters. All subjects underwent an MRI examination with the same 3 T MRI system (Siemens Magnetom Trio, Siemens AG, Erlangen, Germany) equipped with a 32-channel head coil. The entire MS protocol encompassed (i) diffusion weighted imaging (TR 6100 ms, TE 102 ms, FoV read 230 mm, FoV phase 100%, voxel size 1.8 × 1.8 × 4.0 mm, acquisition time 1 : 45 min. 19 parallel images with a slice thickness of 4.0 mm), (ii) T1-weighted MPR pre- and postgadobutrol i.v. (TR 2530 ms, TE 2.96 s, FoV read 250 mm, FoV phase 87.5%, voxel size 1.0 × 1.0 × 1.0 mm, flip angle 7°, acquisition time 4 : 30 min, slices per slab 160, and slice thickness 1.0 mm), (iii) T2-weighted imaging (TR 6580 ms, TE 85 ms, FoV read 220 mm, FoV phase 87.5%, voxel size 0.7 × 0.4 × 3.0 mm, flip angle 150°, and acquisition time 6 : 03 min. 42 parallel images were acquired with a slice thickness of 3.0 mm), (iv) 3D FLAIR imaging (TR 5000 ms, TE 395 ms, FoV read 250 mm, FoV phase 100%, voxel size 1.0 × 1.0 × 1.0 mm, and acquisition time 6 : 27 min. 176 parallel images were acquired with a slice thickness of 1.0 mm), and (v) T1-weighted imaging postgadobutrol i.v. (TR 297 ms, TE 2.67 ms, FoV read 220 mm, FoV phase 87.5%, voxel size 0.8 × 0.6 × 3.0 mm, flip angle 70°, and acquisition time 4 : 14 min. Forty-two parallel images were acquired with a slice thickness of 3.0 mm). All patients received gadobutrol (Gadovist) 0.1 mL·kg^{-1} bodyweight. The flow rate was 5 mL/s, followed by 20 mL of sodium chloride with the same flow rate. Patients were positioned comfortably in the head coil and padding on either side of the head was used to help immobilization. The intravenous line with a long tube was put before examination to avoid unnecessary MRI table moving during data acquisition. Perfusion analysis was performed using DSC in addition to the standard sequences in all patients (TR 1400 ms, TE 29 ms, averages 1, FoV read 230 mm, FoV phase 100%, voxel size 1.8 × 1.8 × 5.0 mm, flip angle 90°, 80 repetitions, and acquisition time 1 : 59 min. 19 parallel images were acquired with a slice thickness of 5.0 mm).

2.3. Preclassification of Enhancing and Nonenhancing Lesions for Texture Analysis. Demyelinating lesions were identified on T2-weighted and fluid attenuated inversion recovery (FLAIR) MR-images. Further enhancing supratentorial lesions were identified in the T1-weighted sequence after Gd administration. To compare active lesions with inactive lesions in the perfusion images, at least one supratentorial nonenhancing lesion per patient was selected for comparison within the same vascular territory.

2.4. Preclassification of Gd-Enhancing Lesions according to Their Permeability. To determine the effect of leakage on postcontrast T1-weighted MPR images, we used a commercially available software (NordicIce Version 2.3; NordicNeuroLab AS, Bergen, Norway). We preselected enhancing MS lesions according to their leakage coefficient K2 following Boxerman et al. [11], a correction method in which contrast extravasation is estimated in each voxel by determining the voxel-wise deviation from a "nonleaky" reference tissue response curve. K2 refers to the leakage rate detected during DSC imaging. The method utilizes linear fitting to determine the leakage coefficient, a first-order estimate of vascular permeability proportional to the leakage, the product of permeability, and the surface area. In short, this method assumes that the contrast agent exhibits T2 or T2* effects ("negative contrast effect") in the intravascular compartment but assumes that the contrast effect is mainly driven by T1-shortening once the agent leaks into the extracellular space ("positive contrast effect"). The K2 measured with DSC perfusion MR imaging reflects a combination of all these factors on vascular leakiness. The K2 estimation has been previously employed to investigate differences in vascular permeability between gliomas of different grades and between primary CNS lymphomas and glioblastoma multiforme [7, 11]. For further texture analysis within the perfusion images, lesions were subdivided into enhancing lesions with a detectable K2 cutoff that exceeded 0.010, indicating increased permeability and enhancing lesions with a K2 cutoff lower than 0.010, indicating low permeability resembling normal appearing white matter, as suggested in a previous study of patients with cerebral gliomas [7] (see Figure 1).

2.5. Dynamic Texture Parameter Analysis. The concept of a texture refers to the appearance of a tissue defined by its shape, composition, arrangement, and proportion of its elementary parts. DTPA focuses on a quantification of regional tissue inhomogeneity according to its individual texture

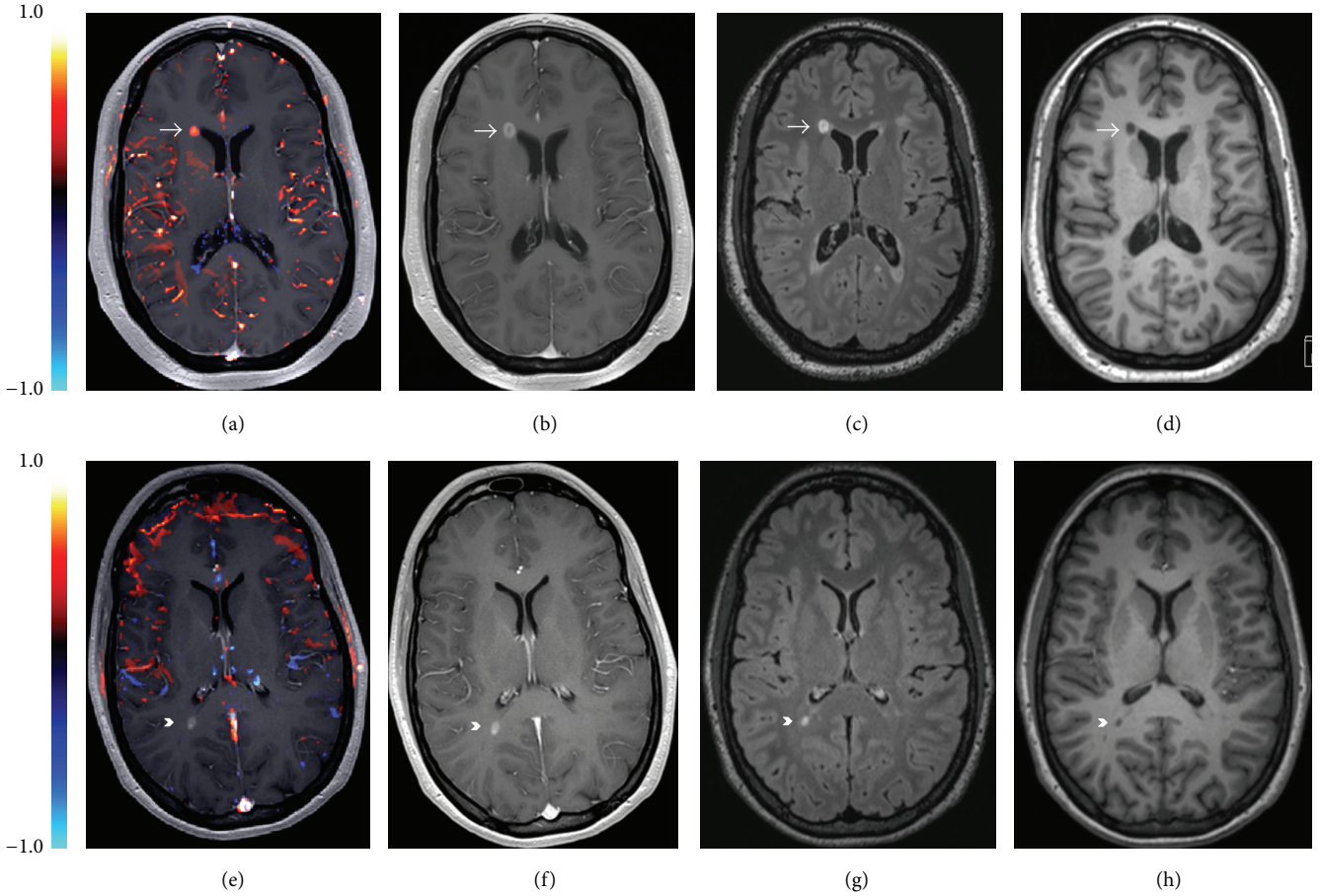

Figure 1: Prestratification of demyelinating lesions according to their leakiness. The upper row shows an enhancing lesion classified as EL+ (arrow), (a) T1w post-Gd after postprocessing with NORDIC Ice: the red area reflects the lesion with high permeability above the predefined cutoff value of 0.01; (b) T1w post-Gd; (c) FLAIR sequence; (d) T1w pre-Gd. The lower row shows an enhancing lesion classified as EL− (arrowhead); (e) T1w post-Gd, after postprocessing with NORDIC Ice: the lesion was classified as low permeability lesion below the predefined cutoff value of 0.01; (f) T1w post-Gd; (g) FLAIR sequence; (h) T1w pre-Gd.

during the bolus passage of Gd. The method uses a model-free approach to analyzing MR texture parameter maps at different time points between the first recorded image during the baseline and the subsequent images during bolus passage. The bolus passage was further divided into three epochs, namely, the inflow, the outflow, and the reperfusion time periods following a previous study to investigate lesion effects and leakage on the capillary level separately for arteries and veins [14]. The inflow and outflow time intervals are patient-dependent; they depend on the patient cardiac health state but also on the vascular state of the patient (e.g., stenosis). The inflow period was in the order 2 to 3 seconds; the outflow period was a little longer around 3–5 seconds. The baseline period was defined as the period between the start of the bolus injection and the time point where 2 subsequent data points exceeded 3 standard deviations of the concentration curve noise level. The inflow period was defined as end of the baseline period to the peak of the concentration time curve. The outflow period was defined as 1st time point after the peak maximum to the first local minimum. The recirculation period encompasses the 1st time point after the local minimum until the last image. To facilitate interindividual comparisons and to account for noise and image nonuniformity due to magnetic field inhomogeneity, a twofold normalization procedure has been performed. The normalization consisted of (i) a normalization of the normal appearing white matter (NAWM) in the frontal white matter reference region to the numerical value of 1000, followed by (ii) a normalization of the time integral of NAWM over encompassing the inflow and outflow period which was set to a reference value of 200. A detailed mathematical description of the computational procedure is provided in [10].

Texture parameter maps (TPMs) were computed from the *raw* DSCE-images using an in-house developed computer JAVA-application. The original raw DSC EPI image series constitutes a texture parameter map itself and was further denoted by "TPM-ORIG." The *difference* image time series computed from TPM-ORIG were denoted by "TPM-DIFF" and calculated by a subtraction of the first steady state baseline image from every subsequent image during

Table 1: Detailed patient information.

Pt. number	Sex	Diagnosis	Age (years)	EDSS	Disease duration	Therapy	Acute disease exacerbation/start before MRI	Symptoms of acute disease exacerbation
1	F	RR-MS	56	3	29 y	No	No	—
2	F	RR-MS	44	4	First relapse 5 months ago	No	No	—
3	F	RR-MS	23	1	4.5 months	No	No	—
4	F	SP-MS	35	5	14 y	No	Yes/5 months	Mild paresis left leg/impaired walking
5	F	RR-MS	42	4	5 months	No	Yes/2–5 months	Tetraspasticity/urinary urgency
6	F	SP-MS	60	7.5	19 y	No	Yes/2 d	Subacute hemiparesis left
7	F	RR-MS	50	3.5	8 y	Yes (interferon beta 1b)	No	—
8	M	SP-MS	74	7	25 y	No	Yes/1 d	Worsening of paraparesis
9	F	RR-MS	44	4	22 months	No	Yes/3 weeks	Vertigo, weakness in right leg, tongue sensation left
10	M	RR-MS	30	1.5	12 months	Yes (interferon beta 1b)	Yes/10 d	Weakness in left leg and arm
11	M	RR-MS	28	2.5	7 months	No	Yes/3 months	Retrobulbar pain, eye lid twinkles
12	F	RR-MS	24	3	3.5 y	Yes (glatiramer acetate)	Yes/1 month	Urinary urgency/vertigo

Note: RRMS: relapsing-remitting MS, SPMS: secondary progressive MS, and EDSS: Expanded Disability Status Scale.

bolus passage. Additionally, we calculated the TPM-standard deviation "TPM-SD" and TPM-variance "TPM-VAR" maps. The TPM-SD and TPM-VAR maps were computed from the TPM-DIFF map by computing pixel-by-pixel the pixels *local* standard deviation and *local* variance for a 5×5 pixel region. These maps are thus computed in the same fashion as one would compute a moving average filtered version of an image. The regions of interest (ROI) were manually segregated by a board certified neuroradiologist on the raw images and copied to the TPMs. For each TPM we calculated the following *statistical* parameters, that is, the mean intensity ("mean"), standard deviation ("SD"), variance ("VAR"), and variance of variance ("VARVAR"). For instance, the mean value of a region defined in the TPM-SD measures the average local standard deviation of the TPM-DIFF-map and hence may act as a surrogate marker for tissue heterogeneity. The other statistical parameters (SD, VAR, etc.) are features that measure higher order statistical properties of the TPMs.

2.6. Statistical Analysis. We used the statistical software SPSS (IBM Corp. Released 2011. IBM SPSS Statistics for Windows, Version 20.0. Armonk, NY: IBM Corp., USA) for the statistical analysis of the acquired data. We aimed to investigate which TPMs differentiate lesions according to severe versus marginal leakage.

Differences between nonenhancing inactive lesions (NEL), enhancing lesions with increased permeability (EL+), and enhancing lesions with subtle permeability (EL−) as determined by their K2 cutoff were analyzed. First, we analyzed the statistical distribution of all TPM in order to be able to select the correct test statistics. A WELCH-ANOVA was performed for all TPM within the prestratified epochs (baseline, inflow, outflow, and reperfusion period) due to heteroscedasticity. For post hoc multiple comparisons between NEL, EL+, and EL−, the Games-Howell method was selected for all texture parameters at a given p value of $p < 0.05$ in the WELCH-ANOVA.

3. Results

The Expanded Disability Status Scale (EDSS) of the 12 patients (9 female; median age 43 y) ranged between 1 and 7.5 (mean 3.83, SD 1.95). A detailed description of the clinical data is provided in Table 1. Nine of 12 patients were drug naive, the remaining 3 were treated with stable dosage of disease-modifying drugs (interferon 1b or glatiramer acetate). Eight of 12 patients showed acute neurological symptoms, while the remaining 4 showed none. The active lesions were located in the deep white matter (3), juxtacortical (6), and periventricular (16). The NEL were selected pairwise from the corresponding regions of the EL.

A total of 52 lesions were identified (26 EL and NEL). One EL had to be withdrawn from final analysis due to an equivocal Gd-uptake, resulting in 51 lesions available for final analysis. The 25 enhancing lesions were subdivided into 11 EL+ and 14 EL− according to a K2 cutoff value of 0.01. The

Table 2: One-way ANOVA of the texture parameter maps (TPMs): number of significant differences in the different time periods. A total of 19 out of 48 (12 × 4) tests revealed statistical significant differences.

	IF	OF	RP	Total
TPM-ORIG	0	0	2	2
TPM-DIFF	1	2	4	7
TPM-SD	0	1	4	5
TPM-VAR	0	2	3	5
Total	1	5	13	19

Note: ORIG: raw image, DIFF: difference image, SD: standard deviation, VAR: local variance, IF: inflow, OF: outflow, and RP: reperfusion.

average lesion size in this study was 146.62 mm^3 (±95.82) for NEL, 156.59 mm^3 (±154.29) for EL+, and 143.00 mm^3 (72.65) for EL−, with no significant volume differences among the three cohorts. The average lesion size was 9 voxels (1.8 × 1.8 × 5 mm). A multivariate analysis was performed on the features extracted from the four texture parameter maps (TPM-ORIG, TPM-DIFF, TPM-VAR, and TPM-SD): for this analysis the within-lesion mean intensity (mean), standard deviation (SD), variance (VAR), *skewness*, and *kurtosis* values were analyzed. A one-way ANOVA with Welch correction identified 19/48 TPM features that discriminated among the 3 lesion subtypes (Table 2).

The TPMs that appeared most sensitive to discriminate EL+ and EL− were TPM-DIFF (7 features), followed by TPM-SD (5 features) and TPM-VAR (5 features). The major effects were observed during late perfusion epochs, outflow (5), and reperfusion (13). A detailed description is provided in Table 4.

A post hoc Games-Howell test indicated significant differences between EL+ and NEL in 8 and between EL+ and EL− for 6 features (Table 3). The strongest discriminators between EL+ versus NEL and EL− were observed during reperfusion (9 features) and outflow (5 features). EL− and NEL were discriminated exclusively by the TPM-SD during outflow. No single test discriminated between all the three subgroups. The results are summarized in Table 3.

4. Discussion

DTPA enables a *quantitative* tissue characterization of MS lesions based on histogram-based textural features. Previous studies investigated the feasibility of contrast-free static and contrast-enhanced dynamic perfusion texture analyses to differentiate EL from NEL [10, 15]. Here, we demonstrated that EL can be further categorized into EL+ and EL− and that EL− behave similarly to NEL by post hoc analysis of texture parameters derived from DSC perfusion imaging. The dynamic texture features of EL+ and EL− correlated with the amount of vascular permeability, reflecting predominantly statistic differences in the local texture dynamics during outflow and reperfusion. The texture parameter changes are statistical measures that segregated lesions visually overall classified as "enhancing MS plaques." The mean contrast differences and standard deviations of the computed texture parameter maps were remarkably different between EL+ and EL− and the derived features reflect the net effect of the contrast extravasation on the dynamic signal intensity curves. In contrast, kurtosis and skewness did not differ between the two cohorts, indicating that only first- and second-order moments had discriminative power and that steepness and asymmetry of the contrast agent distribution played a less important role in our analysis. Beyond a statistically significant $T2^*$ effect caused by intralesional extravasation of Gd during outflow and reperfusion, significantly increased Gd concentrations and accelerated inflow were observed in EL+ compared to NEL. Both may reflect a net inflammation-related vasodilatation in acute and more aggressive lesions. There was a strong similarity in the textures of EL− and nonenhancing inactive lesions, reflecting a delayed Gd peak concentration during venous outflow (Figure 2(a)), with only subtle differences in the TPM-DIFF for "mean" and "SD."

Pathological features that encompass the evolution of acute versus subacute Gd-enhancing MS lesions have been recently investigated by high-resolution dynamic contrast-enhanced MRI [9]. Longitudinal enhancement dynamics of initially nodular lesions revealed a centrifugal pattern while older ring-like lesions enhanced centripetally with delayed lesion filling. The findings indicate lesions grow outward from a disrupted BBB along the central vein with a secondary opening of the BBB in peripheral vessels. Later, partial closure of BBB along the central vein and its contiguous vessels results in a reduction of the central enhancement and/or reduction in perfusion of the lesion core. The DTPA features may reflect similar changes in lesion formation from an early disruptive process continuously into the late stage of a hypometabolic plaque. The tissue response to plaque formation encompasses an inflammatory response and may end up in an impaired microcirculation in late stages of EL− and after closure of the BBB in nonenhancing inactive lesions. Dynamic enhancement data may thus offer a time-effective alternative for a more detailed characterization of the stages of lesion development.

This study has limitations: We have currently not investigated longitudinal DTPA characteristics to follow whether characteristics of EL+ turn into EL− and NEL over time, which will be substance of subsequent investigations. We selected a limited number of patients with RR-MS and relapsing SP-MS that were stratified into EL+ and EL− based on a preselection of T1 Gd-enhancing lesions according to their vascular permeability. This enabled us to identify texture features of lesions with high versus low- or nonpermeable lesions. DTPA does not require a perfusion model such as deconvolution methods or model-fitting of the bolus passage function for quantification of the DSC image series. However, the required normalization procedure may be affected by local T1 effects due to increased permeability in the periventricular NAWM. In order to minimize this effect, we normalized the data by setting the reference region for the normalization into the NAWM close to the gray/white matter border zone with a maximum spatial distance to the MS lesions.

DTPA features reflect statistic properties of enhancing MS lesions beyond descriptions of "*enhancement*" or "*no*

Table 3: Post hoc analysis (Games-Howell test) of all 19 texture parameter maps (TPMs) that discriminated significantly between EL+, EL−, and NEL in one-way ANOVA.

	Stat. par.	Time period	p values			
			ANOVA	EL+ versus EL−	EL+ versus NEL	EL− versus NEL
TPM-ORIG	SD	RP	**<0.001***	**0.018***	**0.035***	0.695
TPM-ORIG	VAR	RP	**<0.001***	**0.035***	0.05	0.82
TPM-DIFF	Mean	IF	**0.02***	0.117	**0.009***	0.356
TPM-DIFF	Mean	RP	**<0.001***	**0.018***	**0.019***	1
TPM-DIFF	SD	OF	**<0.001***	**0.029***	**0.003***	0.429
TPM-DIFF	SD	RP	**<0.001***	**0.044***	**0.030***	0.323
TPM-DIFF	VAR	OF	**0.03***	0.084	**0.030***	0.642
TPM-DIFF	VAR	RP	**0.006***	0.248	0.231	0.254
TPM-DIFF	VARVAR	RP	**0.039***	0.295	0.332	0.967
TPM-SD	Mean	OF	**<0.001***	0.2	**0.013***	**0.022***
TPM-SD	Mean	RP	**<0.001***	**0.032***	**0.012***	0.063
TPM-SD	SD	RP	**0.06***	0.247	0.209	0.641
TPM-SD	VAR	RP	**0.037***	0.396	0.388	0.786
TPM-SD	VARVAR	RP	**0.023***	0.412	0.301	0.295
TPM-VAR	Mean	OF	**0.006***	0.364	0.128	0.119
TPM-VAR	Mean	RP	**0.002***	0.201	0.167	0.11
TPM-VAR	SD	OF	**0.035***	0.479	0.231	0.372
TPM-VAR	SD	RP	**0.022***	0.353	0.331	0.385
TPM-VAR	VARVAR	RP	**0.03***	0.373	0.368	0.517

Note: ORIG: raw image, DIFF: difference image, SD: standard deviation, VAR: local variance, IF: inflow, OF: outflow, RP: reperfusion, EL+: enhancing lesions with increased permeability, EL−: enhancing lesions with subtle permeability, and NEL: nonenhancing inactive lesions; * $p < 0.05$.

enhancement" as currently used in daily routine. The technique identifies characteristic textural features that appear during lesion evolution from severe inflammation to recovery. Noteworthy, even though EL− are classified as active lesions in daily practice, their perfusion characteristics in terms of dynamic texture changes resemble that of NEL. This is a novel finding in MS that motivates the incorporation of these features into machine learning approaches, for example, into decision forest classifiers that can handle high-dimensional input data in larger datasets. Our data further support previous findings of tissue dependency in microcirculation [10] that may be further extended into the refinement and differentiation of white matter lesions other than MS in future.

Abbreviations

BBB: Blood brain barrier
CNS: Central nervous system
DIFF: Difference image
DSC: Dynamic susceptibility contrast perfusion imaging
DTPA: Dynamic texture parameter analysis
EDSS: Expanded Disability Status Scale
EL+: Enhancing lesions with increased permeability
EL−: Enhancing lesions with subtle permeability
FoV: Field of view
Gd: Gadolinium
IF: Inflow phase
T1w MPRage: T1-weighted magnetization prepared rapid gradient echo sequence
MS: Multiple sclerosis
NAWM: Normal appearing white matter
NEL: Nonenhancing lesions
OF: Outflow phase
ORIG: Raw image
RP: Reperfusion phase
RRMS: Relapsing remitting multiple sclerosis
SD: Standard deviation
SPMS: Secondary progressive multiple sclerosis
TE: Echo time
TPM: Texture parameter maps
TR: Repetition time
VAR: Variance
VARVAR: Variance of variance.

Disclosure

Rajeev K. Verma and Johannes Slotboom are both first co-authors.

Table 4: ANOVA of texture parameter map (TPM) between enhancing lesions with increased permeability (EL+), enhancing lesions with subtle permeability (EL−), and nonenhancing lesions (NEL) during the inflow, outflow, and reperfusion phase of Gadolinium.

	Inflow phase			Outflow phase			Reperfusion phase		
	EL+	EL−	NEL	EL+	EL−	NEL	EL+	EL−	NEL
TPM-ORIG mean	1304,21 (192,25)	1362,85 (255,7)	1355,87 (189,43)	1345,29 (168,13)	1323,95 (278,04)	1315,39 (184,87)	1471,50 (213.27)	1407,63 (249,18)	1371,52 (189,25)
TPM-ORIG SD	81,63 (35,88)	71,61 (25,22)	83,14 (23,29)	105,42 (47,76)	83,22 (24,63)	82,93 (24,08)	**104,67*** ** (36,23)**	**65,90*** ** (23,29)**	**71,70*** ** (18,79)**
TPM-ORIG VAR	8398,22 (7762,47)	6118,53 (3594,62)	7692,92 (4430,34)	14007,4 (13771,01)	7848,0 (4205,91)	7680,92 (4266,07)	**12839,71*** ** (8477,35)**	**5122,31*** ** (3449,82)**	**5762,78*** ** (2903,61)**
TPM-ORIG VARVAR	9,292E + 10 (2,135E + 11)	2,733E + 11 (5,176E + 11)	4,189E + 10 (1,042E + 11)	1,052E + 11 (2,371E + 11)	2,516E + 11 (4,952E + 11)	3,222E + 10 (7,731E + 10)	1,275E + 11 (2,783E + 11)	3,686E + 11 (7,462E + 11)	4,476E + 10 (1,103E + 11)
TPM-DIFF mean	**169,36*** ** (52,72)**	**125,37*** ** (53,97)**	**94,75*** ** (85,2)**	96,31 (76,2)	169,7 (76,13)	134,37 (87,81)	**−93,89*** ** (109,68)**	**17,27*** ** (24,99)**	**16,96*** ** (46,23)**
TPM-DIFF SD	63,13 (34,76)	53,11 (25,51)	44,18 (22,47)	**83,95*** ** (26,98)**	**57,61*** ** (20,25)**	**48,63*** ** (24,36)**	**97,74*** ** (76,73)**	**32,44*** ** (12,4)**	**26,98*** ** (9,42)**
TPM-DIFF VAR	5615,45 (5691,76)	4037,2 (3707,4)	2925,68 (3141,22)	**8298,77** ** (5176,78)**	**4283,61** ** (2875,78)**	**3338,1** ** (3687,26)**	**16077,65** ** (28558,66)**	**1317,18** ** (910,2)**	**890,35** ** (569,62)**
TPM-DIFF VARVAR	362978351 (781954883)	565232636 (1,2519E + 9)	81051320 (361085909)	158928026 (352922644)	579771510 (1,4200E + 9)	115586359 (491925502)	**11124685* (20663894)**	**1204394* (1989839)**	**1585312* (7228998)**
TPM-SD mean	82,02 (78,91)	61,28 (29,69)	46,59 (20,58)	**95,3*** ** (41,8)**	**70,25*** ** (21,55)**	**49,64*** ** (23,93)**	**90,54*** ** (57,66)**	**37,84*** ** (13,24)**	**28,11*** ** (11,25)**
TPM-SD SD	19,96 (20,99)	12,84 (6,88)	13,69 (12,19)	20,06 (11,41)	15,75 (7,15)	12,86 (6,74)	**18,19** ** (21,73)**	**6,92** ** (2,48)**	**6,16** ** (2,63)**
TPM-SD VAR	894,6 (2044,61)	278,93 (337,1)	383,08 (893,47)	608,14 (70,66)	363,77 (314,13)	244,75 (249,86)	**832,13* (1880,55)**	**60,47* (45,58)**	**50,63* (45,07)**
TPM-SD VARVAR	133699885 (432101281)	14178164 (44203559)	333236 (995759)	43079835 (126417365)	9755466 (21630255)	546108 (2004049)	**2789669* (5828131)**	**432494* (1010409)**	**24796* (82408)**
TPM-VAR mean	14218,05 (31070,18)	5783,47 (7305,58)	3360,02 (3458,39)	**12234,88** ** (13142,85)**	**6401,44** ** (4283,4)**	**3598,19** ** (4019,22)**	**12809,09** ** (19700,63)**	**1755,86** ** (1167,26)**	**1022,15** ** (871,07)**
TPM-VAR SD	6809,39 (15272,13)	2386,8 (2847,22)	2130,69 (3203,33)	**5052,86* (5789,93)**	**2865,72* (2165,8)**	**1916,57* (2061,01)**	**5659,71* (11524,87)**	**611,76* (395,44)**	**441,39* (377,58)**
TPM-VAR VAR	303820710 (973974129)	23181513,3 (62790956,2)	19406582,6 (57926284,0)	93586953,5 (243511997)	21479750,6 (40452799,7)	11376694,4 (23205702,7)	183622050 (557625048)	618965,14 (840273,06)	407992,02 (832069,7)
TPM-VAR VARVAR	4,156E + 18 (1,378E + 19)	6,431E + 16 (2,477E + 17)	4,414E + 14 (1,405E + 15)	7,405E + 17 (2,45E + 18)	2,636E + 16 (9,942E + 16)	1,017E + 15 (4,414E + 15)	**1,625E + 15* (3,8E + 15)**	**1,165E + 13* (3,658E + 13)**	**1,018E + 12* (4,554E + 12)**

Note: values are mean (SD); significant ANOVA results are marked with $*$ if $p < 0.05$ and with $**$ if $p < 0.01$ and with $***$ if $p < 0.001$.

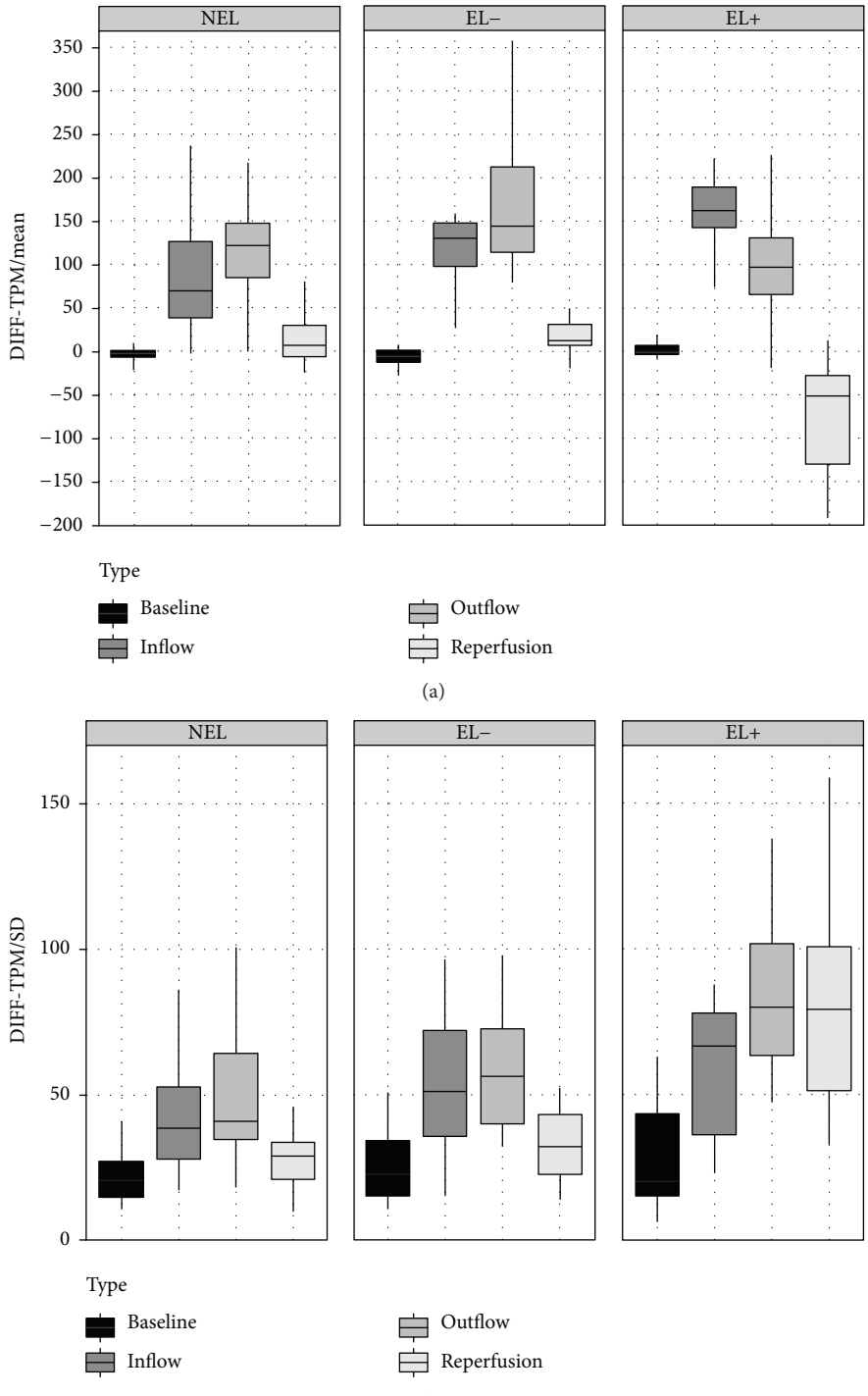

Figure 2: The averaged temporal dynamics of NEL, EL−, and EL+ are exemplarily provided for the mean (a) and SD (b) of the DIFF-TPM. (a) Mean of the DIFF-TPM for NEL, EL−, and EL+: the bars reflect the perfusion intensity of the lesion subtypes during baseline, inflow, outflow, and reperfusion. Significant differences between EL+ and NEL are detected during the inflow ($p = 0.009$) and between EL+ and EL− ($p = 0.018$) and EL+ and NEL ($p = 0.019$) during the reperfusion. The mean values for NEL and EL− increase until the end of the OF with subsequent normalization to baseline during the RP. In contrast the mean values of EL+ increase only until IF, followed by a decrease during outflow and reperfusion with negative values during reperfusion due to local leakage effects. (b) *SD* of the DIFF-TPM for NEL, EL−, and EL+: the bars reflect the perfusion homogeneity of the lesion subtypes during baseline, inflow, outflow, and reperfusion. The temporal dynamics of the EL− are similar to that of the NEL, indicating similar perfusion characteristics of EL− and NEL (n.s.). EL+ are characterized by increasing inhomogeneity during outflow and reperfusion. The SD segregated EL+ from EL− during OF ($p = 0.029$) and RP ($p = 0.044$) and EL+ from NEL during OF ($p = 0.003$) and RP ($p = 0.03$). The persistence of increased SD during RP indicates local leakage effects as observed in (a).

Conflict of Interests

The authors declare that they have no conflict of interests.

Authors' Contribution

Rajeev K. Verma and Johannes Slotboom contributed equally to the study.

Acknowledgments

This study was supported by the Swiss Multiple Sclerosis Society. The authors thank Pietro Ballinari for statistical analysis and Manuela Wapp for paper editing.

References

[1] H. F. McFarland, J. A. Frank, P. S. Albert et al., "Using gadolinium-enhanced magnetic resonance imaging lesions to monitor disease activity in multiple sclerosis," *Annals of Neurology*, vol. 32, no. 6, pp. 758–766, 1992.

[2] J. J. Graber and S. Dhib-Jalbut, "Biomarkers of disease activity in multiple sclerosis," *Journal of the Neurological Sciences*, vol. 305, no. 1-2, pp. 1–10, 2011.

[3] B. D. Trapp, J. Peterson, R. M. Ransohoff, R. Rudick, S. Mörk, and L. Bö, "Axonal transection in the lesions of multiple sclerosis," *The New England Journal of Medicine*, vol. 338, no. 5, pp. 278–285, 1998.

[4] M. I. Gaitán, P. Sati, S. J. Inati, and D. S. Reich, "Initial investigation of the blood-brain barrier in MS lesions at 7 tesla," *Multiple Sclerosis*, vol. 19, no. 8, pp. 1068–1073, 2013.

[5] M. Filippi and M. A. Rocca, "MR imaging of multiple sclerosis," *Radiology*, vol. 259, no. 3, pp. 659–681, 2011.

[6] A. Rovira, M. Tintoré, J. C. Álvarez-Cermeño, G. Izquierdo, and J. M. Prieto, "Recommendations for using and interpreting magnetic resonance imaging in multiple sclerosis," *Neurologia*, vol. 25, no. 4, pp. 248–265, 2010.

[7] C. H. Toh, K.-C. Wei, C.-N. Chang, S.-H. Ng, and H.-F. Wong, "Differentiation of primary central nervous system lymphomas and glioblastomas: comparisons of diagnostic performance of dynamic susceptibility contrast-enhanced perfusion MR imaging without and with contrast-leakage correction," *American Journal of Neuroradiology*, vol. 34, no. 6, pp. 1145–1149, 2013.

[8] Y. Lin, Y. Pan, M. Wang et al., "Blood-brain barrier permeability is positively correlated with cerebral microvascular perfusion in the early fluid percussion-injured brain of the rat," *Laboratory Investigation*, vol. 92, no. 11, pp. 1623–1634, 2012.

[9] M. I. Gaitán, C. D. Shea, I. E. Evangelou et al., "Evolution of the blood-brain barrier in newly forming multiple sclerosis lesions," *Annals of Neurology*, vol. 70, no. 1, pp. 22–29, 2011.

[10] R. K. Verma, J. Slotboom, M. R. Heldner et al., "Characterization of microcirculation in multiple sclerosis lesions by dynamic texture parameter analysis (DTPA)," *PLoS ONE*, vol. 8, no. 7, Article ID e67610, 2013.

[11] J. L. Boxerman, K. M. Schmainda, and R. M. Weisskoff, "Relative cerebral blood volume maps corrected for contrast agent extravasation significantly correlate with glioma tumor grade, whereas uncorrected maps do not," *American Journal of Neuroradiology*, vol. 27, no. 4, pp. 859–867, 2006.

[12] C. H. Polman, S. C. Reingold, B. Banwell et al., "Diagnostic criteria for multiple sclerosis: 2010 revisions to the McDonald criteria," *Annals of Neurology*, vol. 69, no. 2, pp. 292–302, 2011.

[13] K. Grgac, P. C. M. van Zijl, and Q. Qin, "Hematocrit and oxygenation dependence of blood ^1H_2O T_1 at 7 Tesla," *Magnetic Resonance in Medicine*, vol. 70, no. 4, pp. 1153–1159, 2013.

[14] J. Slotboom, R. Schaer, C. Ozdoba et al., "A novel method for analyzing DSCE-images with an application to tumor grading," *Investigative Radiology*, vol. 43, no. 12, pp. 843–853, 2008.

[15] O. Yu, Y. Mauss, G. Zollner, I. J. Namer, and J. Chambron, "Distinct patterns of active and non-active plaques using texture analysis on brain NMR images in multiple sclerosis patients: preliminary results," *Magnetic Resonance Imaging*, vol. 17, no. 9, pp. 1261–1267, 1999.

Hindawi Publishing Corporation
BioMed Research International
Volume 2015, Article ID 569367, 5 pages
http://dx.doi.org/10.1155/2015/569367

Research Article

Impact of Fibrotic Tissue on Shear Wave Velocity in Thyroid: An *Ex Vivo* Study with Fresh Thyroid Specimens

Takahiro Fukuhara,[1] Eriko Matsuda,[1] Yukari Endo,[2] Ryohei Donishi,[1] Shoichiro Izawa,[3] Kazunori Fujiwara,[1] Hiroya Kitano,[1] and Hiromi Takeuchi[1]

[1]*Department of Otolaryngology-Head and Neck Surgery, Tottori University Faculty of Medicine, 36-1 Nishicho, Yonago 683-8504, Japan*
[2]*Department of Pathology, Tottori University Faculty of Medicine, 36-1 Nishicho, Yonago 683-8504, Japan*
[3]*Endocrinology and Metabolism, Department of Molecular Medicine and Therapeutics, Tottori University Faculty of Medicine, 36-1 Nishicho, Yonago 683-8504, Japan*

Correspondence should be addressed to Takahiro Fukuhara; tfukuhara3387@med.tottori-u.ac.jp

Received 10 September 2015; Accepted 20 December 2015

Academic Editor: Guang Jia

We sought to elucidate the correlation between shear wave velocity (SWV) and fibrosis in thyroid by precisely assessing pathological structures inside $5 \times 5\,mm^2$ regions of interest (ROIs) of resected specimens, under conditions that excluded physical artifacts. The materials were unselected thyroid and lymph node specimens resected during thyroid surgery. Immediately after surgery, fresh unfixed thyroid and metastatic lymph node specimens were suspended in gel phantoms, and SWV was measured. Upon pathological examination of each specimen, the extent of fibrosis was graded as none, moderate, or severe. A total of 109 specimens were evaluated: 15 normal thyroid, 16 autoimmune thyroiditis, 40 malignant nodules, 19 benign thyroid nodules, and 19 metastatic lymph nodes. When all specimens were classified according to the degree of fibrosis determined by pathological imaging, the mean SWV was 1.49 ± 0.39 m/s for no fibrosis, 2.13 ± 0.66 m/s for moderate fibrosis, and 2.68 ± 0.82 m/s for severe fibrosis. The SWVs of samples with moderate and severe fibrosis were significantly higher than those of samples without fibrosis. The results of this study demonstrate that fibrosis plays an important role in determining stiffness, as measured by SWV in thyroid.

1. Introduction

Conventional elastography using manual compression evaluates stiffness of the target tissue relative to that of the surrounding tissue, whereas a recently developed elastography technique using acoustic radiation force impulse (ARFI) evaluates the local elastic characteristics of the target tissue itself [1]. In this method, a target region with fixed dimensions of $5 \times 5\,mm^2$ is identified as the region of interest (ROI), and shear wave velocity (SWV) is detected by a sonographic detection pulse in the ROI. The characteristics are expressed by the SWV of the tissue, which reflects tissue elasticity, as calculated using Young's modulus under the assumption that tissue density is $1\,g/cm^3$ and has Poisson's ratio of 0.5 [2, 3]. Thus, shear wave elastography (SWE) is thought to be useful for quantitatively evaluating tissue hardness. However, it remains unclear what types of pathology affect tissue hardness.

In liver, many clinical studies of SWE have been conducted, and SWV is thought to be affected by liver fibrosis [4, 5]. Currently, shear wave elastography is frequently used to evaluate liver fibrosis.

Many clinical studies have evaluated the usefulness of SWE for differentiating benign versus malignant thyroid nodules [6–10], and a recent report described the usefulness of SWE for diagnosing autoimmune thyroiditis [11, 12]. In a previous clinical study, we investigated the correlation between SWV and the pathological structure of thyroid lesions and reported that the shear wave is accelerated as the extent of elastic fibrosis increases [1]. Other authors also pointed out the possibility of elevated SWV in fibrotic thyroid tissue [13, 14]. In past reports, however, the assessment

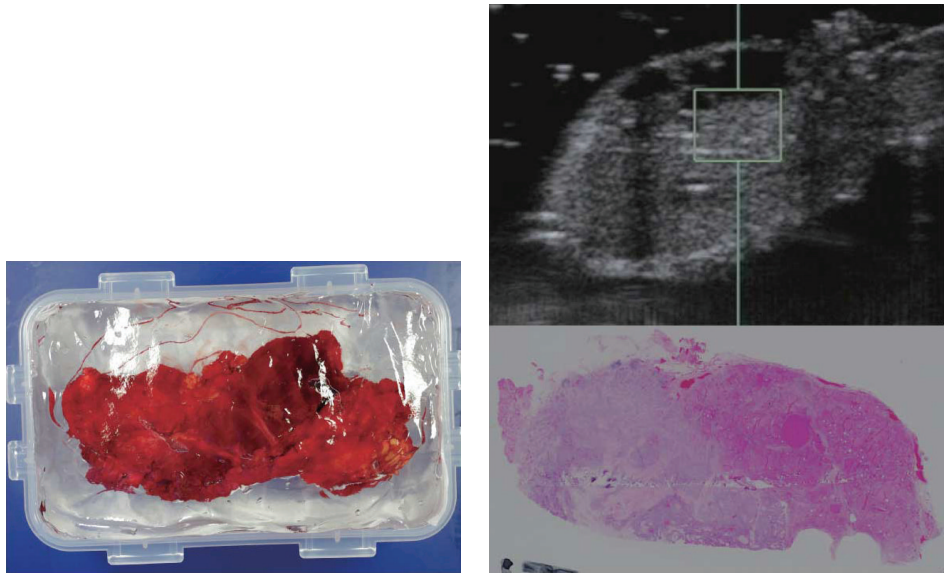

(a) (b)

Figure 1: (a) Fresh unfixed specimens were suspended in gel phantoms, and the SWV was measured. (b) Histologic slides were created in the same plane used for ultrasonography imaging.

of pathologies inside a $5 \times 5\,mm^2$ ROI, as reflected by measurement of SWV, may not be correct because the SWVs were measured *in vivo*. In particular, malignant tumors have multifaceted pathology, so it is possible that pathological structures change when the clinician's view is displaced by several millimeters. Indeed, SWVs measured in papillary thyroid cancer (PTC) tend to vary [1, 7, 9]. In light of these observations, in this study we sought to clarify the correlation between SWV and fibrotic pathology of thyroid specimens by precisely assessing the pathological structures inside a $5 \times 5\,mm^2$ ROI, as determined by SWV, under conditions that excluded physical artifacts. The results of this study indicate the most appropriate use of SWE in the thyroid.

2. Materials and Methods

2.1. Materials. Informed consent was obtained, and the study was performed in accordance with the ethical guidelines of the Helsinki Declaration. The ethics committee and the institutional review board of Tottori University approved the study protocol. The study period was from November 2011 to April 2014. The materials were unselected thyroid and lymph node specimens resected in thyroid surgery, at least 10 mm in diameter, so that they would encompass the entire ROI.

2.2. Methods. We used the Virtual Touch Quantification system (Siemens Medical Systems, Forchheim, Germany) to perform SWE using an ACUSON S2000 ultrasound system (Siemens Medical Systems) with a 9 MHz B-mode-ARFI combination linear transducer (ACUSON 2000; Siemens Medical Systems).

Immediately after surgery, fresh unfixed thyroid and metastatic lymph node specimens were suspended in gel phantoms and SWV generated by ARFI was measured (Figure 1). In each case, we scanned the specimens on B-mode, defined an ROI of $5 \times 5\,mm^2$, and measured SWV at the same point five times [15]. The $5 \times 5\,mm^2$ ROI was entirely within the thyroid specimen. Histologic slides corresponding to the ultrasonography imaging plane were created, and the degrees of fibrosis determined by imaging and SWV were compared.

2.3. Pathological Findings. All resected thyroid lesions and lymph nodes were analyzed pathologically. Collagen fiber on histologic slides was stained with Masson T stain (Figure 2), and the degree of fibrosis was assessed in $5 \times 5\,mm^2$ microscope fields in the plane used to measure SWV. Degree of fibrosis was classified into three groups: no fibrosis, moderate fibrosis, and severe fibrosis. The ImageJ software (version 1.48; Wayne Rasband, National Institutes of Health, Bethesda, MD, USA) was used to calculate the degree of fibrosis. Severe fibrosis was defined as extended fibrosis in over 50% of the area of $5 \times 5\,mm^2$ microscope fields, whereas moderate fibrosis indicated findings intermediate between no fibrosis and severe fibrosis. The correlation between SWV and the degree of fibrosis on pathological findings was evaluated.

2.4. Statistical Analysis. Statistical analysis was performed using SPSS software (version 22; IBM SPSS, Chicago, IL, USA). The SWVs of measured specimens (normal thyroid, autoimmune thyroiditis, benign nodule, malignant nodule, and metastatic lymph node) were expressed as the mean value ± standard deviation (SD) and compared using the Kruskal-Wallis test. The fibrosis grades of all targets were compared with their SWVs using the Kruskal-Wallis test. We then compared the SWVs between benign nodules and

Table 1: Number and characteristics of specimens of each lesion.

		Normal	AIT	Benign nodule	Malignant nodule	Lymph node
N		15	16	19	40	19
Measurable		15	16	19	36	16
SWV (mean ± SD)		1.40 ± 0.20	2.01 ± 0.42	1.34 ± 0.37	2.30 ± 0.82	1.72 ± 0.57
Fibrosis	No	15	3	19	12	9
	Moderate	0	8	0	20	8
	Severe	0	5	0	8	2

Note: SWV, shear wave velocity; SD, standard deviation; AIT, autoimmune thyroiditis.

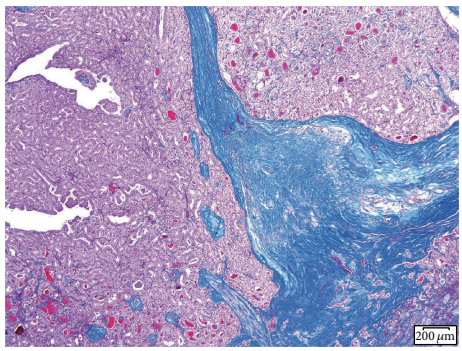

Figure 2: Collagen fibers were stained with Masson T stain.

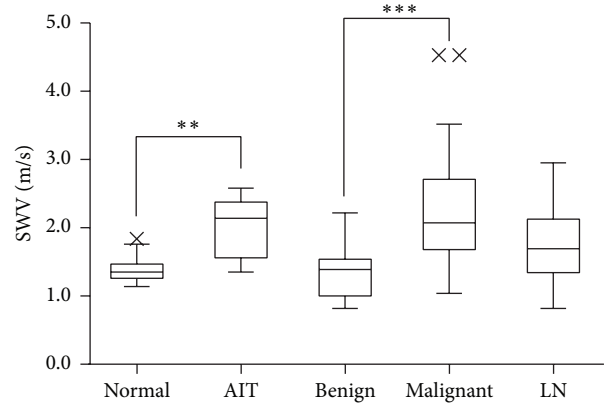

× Symbols indicate outliers
** $P < 0.01$
*** $P < 0.001$

Figure 3: Mean SWV of each lesion.

malignant nodules, depending on the fibrosis grade, using the Kruskal-Wallis test.

3. Results

A total of 109 specimens were evaluated: 15 normal thyroid, 16 autoimmune thyroiditis (AIT) (2 Hashimoto's thyroiditis and 14 Basedow disease), 40 malignant nodules (36 papillary thyroid carcinoma [PTC], 4 follicular carcinoma), 19 benign thyroid nodules, and 19 metastatic lymph nodes. Seven specimens were not measurable. The mean SWV was 1.40 ± 0.20 m/s for normal thyroid, 2.01 ± 0.42 m/s for autoimmune thyroiditis, 1.34 ± 0.37 m/s for benign nodule, 2.30 ± 0.82 m/s for malignant nodules, and 1.69 m/s for metastatic lymph node (Table 1, Figure 3). The SWVs of AIT and PTC were significantly higher than those of normal thyroid ($P = 0.009$ for AIT, $P < 0.001$ for PTC). Additionally, the SWVs of AIT and PTC were significantly higher than those of benign nodules ($P = 0.002$ for AIT, $P < 0.001$ for PTC). There was no difference in SWVs between normal thyroids and benign nodules.

When all specimens were classified according to the degree of fibrosis determined by pathological imaging, the mean SWV was 1.49 ± 0.39 m/s for no fibrosis, 2.13 ± 0.66 m/s for moderate fibrosis, and 2.68 ± 0.82 m/s for severe fibrosis (Figure 4). The SWVs of samples with moderate and severe fibrosis were significantly higher than those with no fibrosis, but there was no difference in SWV between samples with moderate fibrosis and severe fibrosis. SWV increased with fibrosis severity (Spearman's $\rho = 0.608$).

When SWVs of thyroid nodules were compared according to fibrotic grade, SWVs of malignant nodules with moderate or severe fibrosis were significantly higher than those of benign nodules with no fibrosis ($P < 0.001$) (Figure 5). There was no difference in SWVs between benign nodules without fibrosis and malignant nodules without fibrosis (Figure 5).

The pathologies of the 7 unmeasurable lesions were 3 calcifications, 2 cysts, and 2 heterogeneous tissues.

4. Discussion

We clarified the correlation between SWV and the precise pathological structure of targets inside the ROI by directly measuring resected thyroid specimens. The results revealed that fibrosis increased SWV, and that the variability of SWVs measured in malignant nodules was caused by variability in the fibrotic degree. Additionally, we showed that the results of SWV under conditions free of physical artifacts were similar to the results of previous clinical studies.

Shear waves are transverse waves that are very slow in comparison with acoustic waves and are therefore predicted to be easily affected by factors in the physiological environment such as carotid artery pulsation, respiratory movements, and reflections off the tracheal cartilage [1, 11, 16]. However, the degree to which such physical artifacts affect

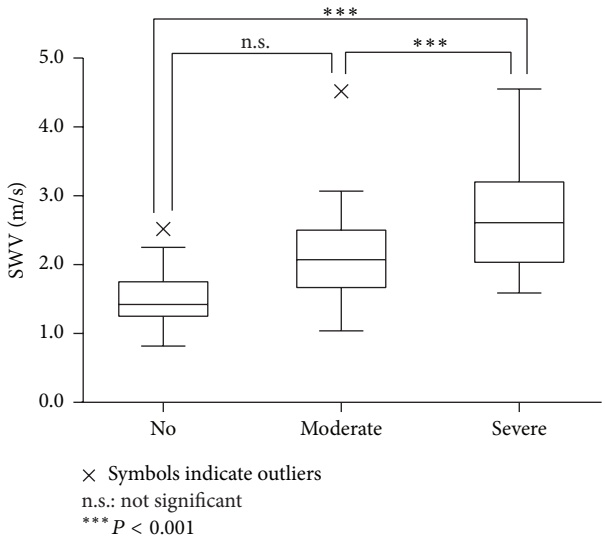

Figure 4: SWVs of specimens with no, moderate, and severe fibrosis when all specimens were classified according to the degree of fibrosis.

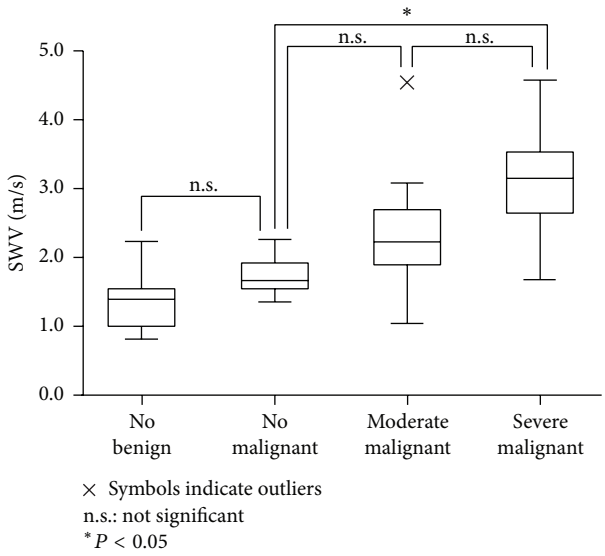

Figure 5: SWVs of thyroid nodules were compared according to fibrotic grade.

shear waves is unknown. The SWVs of each lesion, measured in resected specimens under conditions that excluded physical artifacts, were similar to the results of past clinical research in which SWVs were measured *in vivo* [1, 11, 12, 17–19]. The SWVs of AIT and PTC were significantly higher than those of normal thyroid or benign nodules, and there was no difference in SWVs between normal thyroids and benign nodules. Our results were also similar to the results of clinical studies [1, 9, 17–19]. The actual impact of the effect of the physiological environment upon SWV was judged to be negligible.

When the specimens were classified according to the degree of fibrosis determined by pathological imaging, and the SWVs of each fibrotic grade were compared, the results obviously showed that SWV increased with the severity of fibrosis. In this study, we observed no difference in SWV between moderate and severe fibrosis, probably because the moderate grade included a very wide range, from slight to 50%. There was no difference in SWV between normal thyroid and benign nodules, although the cell density obviously differed between these types of samples. As in a past study, the effect of cell density on SWV was thought to be small [1]. SWVs at solid cell patterns did not differ between normal controls, benign nodules, and PTCs. However, SWVs in fibrotic regions were significantly higher than those in non-fibrotic regions, and the SWV increased with fibrosis severity.

Several studies of SWV in the thyroid region have reported the usefulness of this technique for differentiating between benign and malignant thyroid nodules [8, 9, 20]. However, the SWVs of malignant nodules were variable. When we classified the malignant nodules according to the degree of fibrosis, the results revealed that the SWVs of malignant nodules differed significantly according to the degree of fibrosis. The SWVs of malignant nodules without fibrosis were not different from those of benign nodules. In general, benign nodules often have some fibrosis at the capsule. However, no fibrosis was observed in $5 \times 5\,\text{mm}^2$ microscope fields of benign nodules, because in this study we measured SWV inside the nodules and placed the $5 \times 5\,\text{mm}^2$ ROI entirely within the thyroid specimens. Fibrotic changes occur in most of PTC. Therefore, SWE may be helpful as an auxiliary diagnostic method for differentiating between benign and malignant nodules by measuring within an ROI encompassed within the thyroid nodule.

In this study, the SWVs of resected specimens were not measurable when the pathologies were calcifications, cysts, or heterogeneous tissues. Some authors also reported that these lesions were unmeasurable [1, 17, 18]. In the cases of calcifications or cysts, we believe that ARFI was not transmitted (due to reflection or absorption, resp.), and consequently no shear wave was generated. On the other hand, heterogeneous tissues were probably unmeasurable due to errors caused by the measurement principle of the ACUSON S2000 ultrasound system [1].

The findings of this study have potential clinical impact. In particular, measurement of SWV may be useful for choosing biopsy sites or predicting the extent of cancer invasion.

There were some limitations in this study. First, the efficiency of propagation of ARFI may differ in gel and *in vivo*. Consequently, the degree of generated SW may also differ between these conditions. Therefore, the proportion of unmeasurable samples was lower than in an *in vivo* study [1]. Second, the SWVs were measured in resected thyroid specimens under conditions very different from those that arise *in vivo*; in particular, there was no blood flow, and it is possible that this influenced the SWVs. Third, it is possible that unknown factors other than fibrosis and cell density influence SWV.

5. Conclusions

In this *ex vivo* study, we created histologic slides corresponding to the ultrasonography imaging plane. Comparison of

the imaging and SWV findings revealed that the SWV of the target tissue was affected by its pathology. Fibrosis played an important role in the stiffness, measured by SWV, in thyroid tissue.

Conflict of Interests

There is no conflict of interests to report.

Acknowledgment

This work was supported by JSPS KAKENHI Grant no. 26861385.

References

[1] T. Fukuhara, E. Matsuda, Y. Endo et al., "Correlation between quantitative shear wave elastography and pathologic structures of thyroid Lesions," *Ultrasound in Medicine & Biology*, vol. 41, no. 9, pp. 2326–2332, 2015.

[2] J. Benson and L. Fan, "Tissue strain analysis: a complete ultrasound solution for elastography," Medical Solutions—Siemens Healthcare Global, http://www.healthcare.siemens.com/.

[3] M. Kudo, T. Shiina, F. Moriyasu et al., "JSUM ultrasound elastography practice guidelines: liver," *Journal of Medical Ultrasonics*, vol. 40, no. 4, pp. 325–357, 2013.

[4] M. Friedrich-Rust, J. Nierhoff, M. Lupsor et al., "Performance of acoustic radiation force impulse imaging for the staging of liver fibrosis: a pooled meta-analysis," *Journal of Viral Hepatitis*, vol. 19, no. 2, pp. e212–e219, 2012.

[5] I. Sporea, R. Sirli, A. Popescu, and M. Danilă, "Acoustic Radiation Force Impulse (ARFI)—a new modality for the evaluation of liver fibrosis," *Medical Ultrasonography*, vol. 12, no. 1, pp. 26–31, 2010.

[6] J. Zhan, J. M. Jin, X. H. Diao, and Y. Chen, "Acoustic radiation force impulse imaging (ARFI) for differentiation of benign and malignant thyroid nodules-a meta-analysis," *European Journal of Radiology*, vol. 84, no. 11, pp. 2181–2186, 2015.

[7] A. Y. Park, E. J. Son, K. Han, J. H. Youk, J.-A. Kim, and C. S. Park, "Shear wave elastography of thyroid nodules for the prediction of malignancy in a large scale study," *European Journal of Radiology*, vol. 84, no. 3, pp. 407–412, 2015.

[8] P. Lin, M. Chen, B. Liu, S. Wang, and X. Li, "Diagnostic performance of shear wave elastography in the identification of malignant thyroid nodules: a meta-analysis," *European Radiology*, vol. 24, no. 11, pp. 2729–2738, 2014.

[9] T. Fukuhara, E. Matsuda, K. Fujiwara et al., "Phantom experiment and clinical utility of quantitative shear wave elastography for differentiating thyroid nodules," *Endocrine Journal*, vol. 61, no. 6, pp. 615–621, 2014.

[10] F. Sebag, J. Vaillant-Lombard, J. Berbis et al., "Shear wave elastography: a new ultrasound imaging mode for the differential diagnosis of benign and malignant thyroid nodules," *The Journal of Clinical Endocrinology & Metabolism*, vol. 95, no. 12, pp. 5281–5288, 2010.

[11] T. Fukuhara, E. Matsuda, S. Izawa, K. Fujiwara, and H. Kitano, "Utility of shear wave elastography for diagnosing chronic autoimmune thyroiditis," *Journal of Thyroid Research*, vol. 2015, Article ID 164548, 5 pages, 2015.

[12] K. Hekimoglu, D. Yildirim Donmez, S. Arslan, A. Ozdemir, C. Demir, and C. Yazici, "The role of shear wave elastography in the diagnosis of chronic autoimmune thyroiditis," *Medical Ultrasonography*, vol. 17, no. 3, pp. 322–326, 2015.

[13] F. Chamming's, H. Latorre-Ossa, M. A. Le Frère-Belda et al., "Shear wave elastography of tumour growth in a human breast cancer model with pathological correlation," *European Radiology*, vol. 23, no. 8, pp. 2079–2086, 2013.

[14] F. Magri, S. Chytiris, V. Capelli et al., "Shear wave elastography in the diagnosis of thyroid nodules: feasibility in the case of coexistent chronic autoimmune Hashimoto's thyroiditis," *Clinical Endocrinology*, vol. 76, no. 1, pp. 137–141, 2012.

[15] I. Sporea, R. Sirli, S. Bota, M. Vlad, A. Popescu, and I. Zosin, "ARFI elastography for the evaluation of diffuse thyroid gland pathology: preliminary results," *World Journal of Radiology*, vol. 4, no. 4, pp. 174–178, 2012.

[16] K. Nightingale, S. McAleavey, and G. Trahey, "Shear-wave generation using acoustic radiation force: *in vivo* and *ex vivo* results," *Ultrasound in Medicine and Biology*, vol. 29, no. 12, pp. 1715–1723, 2003.

[17] A. C. Calvete, J. D. B. Mestre, J. M. R. Gonzalez, E. S. Martinez, B. T. Sala, and A. R. Zambudio, "Acoustic radiation force impulse imaging for evaluation of the thyroid gland," *Journal of Ultrasound in Medicine*, vol. 33, no. 6, pp. 1031–1040, 2014.

[18] H. Grazhdani, V. Cantisani, P. Lodise et al., "Prospective evaluation of acoustic radiation force impulse technology in the differentiation of thyroid nodules: accuracy and interobserver variability assessment," *Journal of Ultrasound*, vol. 17, no. 1, pp. 13–20, 2014.

[19] T. Li, P. Zhou, X. Zhang, M. Ding, M. Yuchi, and Y. Li, "Diagnosis of thyroid nodules using virtual touch tissue quantification value and anteroposterior/transverse diameter ratio," *Ultrasound in Medicine and Biology*, vol. 41, no. 2, pp. 384–392, 2015.

[20] K. S. Bhatia, C. S. Tong, C. C. Cho, E. H. Yuen, Y. Y. Lee, and A. T. Ahuja, "Shear wave elastography of thyroid nodules in routine clinical practice: preliminary observation and utility for detecting malignancy," *European Radiology*, vol. 22, no. 11, pp. 2397–2406, 2012.

Hindawi Publishing Corporation
BioMed Research International
Volume 2015, Article ID 138060, 9 pages
http://dx.doi.org/10.1155/2015/138060

Research Article

Optimal Experiment Design for Monoexponential Model Fitting: Application to Apparent Diffusion Coefficient Imaging

Mohammad Alipoor,[1] Stephan E. Maier,[2] Irene Yu-Hua Gu,[1] Andrew Mehnert,[3] and Fredrik Kahl[1]

[1]*Department of Signals and Systems, Chalmers University of Technology, 41296 Gothenburg, Sweden*
[2]*Department of Radiology, Sahlgrenska University Hospital, Gothenburg University, 41345 Gothenburg, Sweden*
[3]*Centre for Microscopy, Characterisation and Analysis, The University of Western Australia, Perth, WA 6009, Australia*

Correspondence should be addressed to Mohammad Alipoor; alipoor@chalmers.se

Received 11 September 2015; Accepted 6 December 2015

Academic Editor: Guang Jia

The monoexponential model is widely used in quantitative biomedical imaging. Notable applications include apparent diffusion coefficient (ADC) imaging and pharmacokinetics. The application of ADC imaging to the detection of malignant tissue has in turn prompted several studies concerning optimal experiment design for monoexponential model fitting. In this paper, we propose a new experiment design method that is based on minimizing the determinant of the covariance matrix of the estimated parameters (D-optimal design). In contrast to previous methods, D-optimal design is independent of the imaged quantities. Applying this method to ADC imaging, we demonstrate its steady performance for the whole range of input variables (imaged parameters, number of measurements, and range of b-values). Using Monte Carlo simulations we show that the D-optimal design outperforms existing experiment design methods in terms of accuracy and precision of the estimated parameters.

1. Introduction

The monoexponential model has been used in many different engineering applications. It is frequently used in modeling biomedical phenomena to estimate biologically meaningful parameters. Its applications in quantitative biomedical imaging include apparent diffusion coefficient (ADC) imaging [1], monitoring metabolic reactions [2], and pharmacokinetics [3]. ADC imaging has a wide range of applications including the classification of brain disorders [4], detection of malignant breast lesions [5], identifying stages of cerebral infarction [6], and diagnostic imaging of the kidney [7, 8], prostate [9, 10], and ovaries [11, 12]. ADC imaging is also used to solve challenging clinical problems such as the differentiation of Parkinson's disease from multiple system atrophy and progressive supranuclear palsy [13].

The usefulness of ADC imaging as a quantitative imaging tool has motivated several studies that have investigated the reliability and reproducibility of ADC estimates [7, 14, 15]. From a mathematical point of view, the variance of the estimated ADC values can be minimized by optimizing experiment design. In the case of ADC imaging, experiment design equates to the choice of the b-values applied for measurements and their repetitions. In the case of enzyme kinetics, it equates to the sample collection time (t). The range of valid sampling points is determined by the biophysical aspects of the problem at hand. For instance, perfusion contamination at low b-values [15, 16] and SNR drop at high b-values [1] limit the applicable range of b-values. An intuitively appealing experiment design is the equidistant (ED) distribution of sampling points on a valid range of the independent variable (b or t). The ED experiment design method is widely used in the literature [7, 17–19]. However, many studies use nonsystematic and random experiment designs [9, 20] that can considerably influence the results.

Some studies have tried to find the optimal experiment design by empirically evaluating a variety of experiment designs [17]. In contrast, others have developed a theoretical

framework by minimizing the variance of the estimated parameters [21–23]. The former strategy may potentially miss the global optimum because of the discretization of the problem and a nonexhaustive search. On the other hand, studies pursuing the latter strategy are based on the Gaussian noise assumption. The Cramer-Rao lower bound (CRLB) of the ADC value is minimized in [23] assuming a Gaussian noise distribution. Hereinafter, we call this method GCRLB. The optimal experiment design in the GCRLB method (briefly described in Appendix B) depends on the ADC values to be imaged. Thus the optimal design must be revised for different applications and even for imaging different organs. Moreover, in applications where the noise assumption is violated, the GCRLB design becomes suboptimal. In this paper, we develop a theoretical framework for optimal experiment design of monoexponential model fitting problems with less restrictive assumptions on noise distribution. Our Monte Carlo simulations using the proposed design method for ADC imaging show that, in the presence of Rician noise, it outperforms the GCRLB and ED methods. In addition, the proposed design is independent of the imaged parameters and provides more robust results.

The remainder of the paper is organized as follows. The next section elaborates the proposed experiment design method. Section 3 presents results of extensive evaluations and comparisons. A discussion of different aspects and the potential impact of this work is given in Section 4. Finally the conclusion is presented in Section 5.

2. Proposed Experiment Design Method

Without loss of generality, hereinafter we focus on ADC imaging as an example of monoexponential model fitting problems. The model for ADC imaging is given by

$$m = m_0 \exp(-bD), \tag{1}$$

where m is the measured signal when the diffusion weighting factor b is applied, m_0 is the observed signal in the absence of such a weighting factor, and D is the apparent diffusion coefficient. The parameters to be estimated are m_0 and D. In ADC imaging the parameter of interest is D. However, there exist applications in which m_0 is also important such as (6) in [2]. Although mathematically two measurements suffice, in practice $N > 2$ measurements are acquired to maximize precision. Depending on the problem at hand, one is permitted to choose the independent variable (b in this case) such that $b_{\min} \le b \le b_{\max}$. Log-linear least square fitting is frequently used because of its computational efficiency [18]. It can be formulated as follows:

$$\ln m_i = \ln m_0 - b_i D, \quad \forall i = 1, \ldots, N. \tag{2}$$

For N measurements we obtain

$$\mathbf{y} = \mathbf{A}\mathbf{x}, \tag{3}$$

where $\mathbf{y} \in \mathbb{R}^N$ contains measurements ($\ln m_i$), $\mathbf{x} \in \mathbb{R}^2$ contains unknown parameters ($\mathbf{x} = [\ln m_0 D]^T$), and $\mathbf{A}$ is the design matrix below:

$$\mathbf{A} = \begin{bmatrix} 1 & -b_1 \\ \cdots & \cdots \\ 1 & -b_N \end{bmatrix}. \tag{4}$$

The least squares estimator (LSE) of $\mathbf{x}$ is given by $\hat{\mathbf{x}} = (\mathbf{A}^T\mathbf{A})^{-1}\mathbf{A}^T\mathbf{y}$. The precision of the estimation problem above is dependent on the experiment design $\mathbf{A}$. For independent and zero-mean measurement noise (on $\mathbf{y}$) with constant variance σ^2 the LSE is unbiased and has the following covariance matrix [24]:

$$\mathrm{Cov}(\hat{\mathbf{x}}) = \sigma^2 \mathbf{M}^{-1}, \tag{5}$$

where $\mathbf{M} = \mathbf{A}^T\mathbf{A}$ and is usually called the "*information matrix*." Optimal experiment design entails making the covariance matrix *small* in some sense. It is usual to minimize a scalar function of the covariance matrix. One design approach is to minimize the determinant of the information matrix (D-optimal design). In this paper, we solve the D-optimal experiment design problem for ADC imaging.

Remark 1. The noise distribution on the diffusion attenuated signal (denoted by m) is usually assumed to be Rician. To investigate the significance of our noise assumptions in the case of ADC imaging, we use Monte Carlo simulations. Let $|m + w|$ model the measured diffusion signal, where m is the true value of the signal and $w = w_R + jw_I$ is the complex-valued measurement noise. The noise components are Gaussian distributed: $w_R \sim \mathcal{N}(0, \sigma_G^2)$, $w_I \sim \mathcal{N}(0, \sigma_G^2)$. We perform Monte Carlo simulations with Rician noise (on m) and the following setup: number of Monte Carlo trials $N_{\mathrm{MC}} = 20000$, $\sigma_G = 20$, and m varies from 5 to $20\sigma_G$ with equal step size of 5. As can be seen in Figure 1, the zero-mean assumption (on $y_i = \ln m_i$) holds for SNR > 2 while the equal variance on log-measurements ($\mathbf{y}$) holds for SNR > 10. Overall, this shows that both zero-mean and equal variance assumptions hold for SNR > 10. Thus, we expect the proposed method to have diminished performance for high b-values and high D values.

2.1. D-Optimal Experiment Design for Monoexponential Model Estimation. The D-optimal experiment design is based on minimizing the determinant of the covariance matrix of the LSE. The D-optimal experiment design for ADC imaging can be written as follows:

$$\begin{aligned} &\min \quad \det\left(\mathbf{M}^{-1}\right) \\ &\text{s.t.:} \quad \mathbf{M} \ge 0, \\ &b_{\min} \le b_i \le b_{\max}, \quad i = 1, \ldots, N, \end{aligned} \tag{6}$$

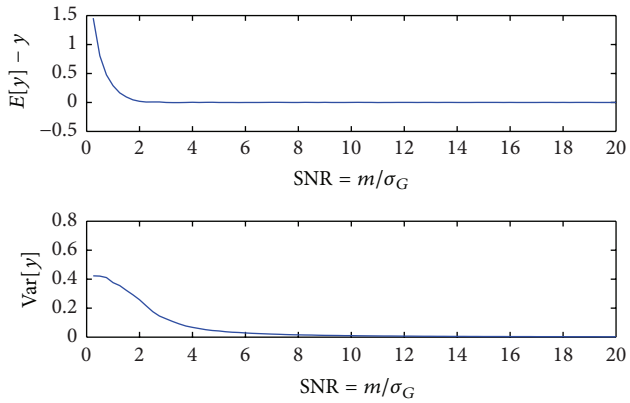

Figure 1: Results of Monte Carlo simulations show that if SNR > 10, then zero-mean and equal variance noise assumptions hold for ADC imaging. Simulation setup: number of Monte Carlo trials N_{MC} = 20000, σ_G = 20, and m varies from 5 to 20σ_G (equal step size of 5).

where the explicit expression for $\mathbf{M}$ is

$$\mathbf{M} = \begin{bmatrix} N & -\sum_{i=1}^{N} b_i \\ -\sum_{i=1}^{N} b_i & \sum_{i=1}^{N} b_i^2 \end{bmatrix}. \quad (7)$$

Noting that minimizing $\det(\mathbf{M}^{-1})$ is equivalent to maximizing $\det(\mathbf{M})$ we obtain the following problem formulation:

$$\begin{aligned} \max \quad & \det(\mathbf{M}) \\ \text{s.t.:} \quad & \mathbf{M} \geq 0, \\ & b_{\min} \leq b_i \leq b_{\max}, \quad i = 1, \ldots, N. \end{aligned} \quad (8)$$

2.2. Solutions to the D-Optimal Design Problem. The explicit form of the objective function of the optimization problem in (8) is

$$\det(\mathbf{M}) = N\sum_{i=1}^{N} b_i^2 - \left(\sum_{i=1}^{N} b_i\right)^2. \quad (9)$$

It can be seen that, in contrast to previous studies, the D-optimal design is independent of the unknown parameters. Thus, it can be used when imaging different organs as well as in other applications. For $N = 2$ the objective function becomes $\det(\mathbf{M}) = (b_1 - b_2)^2$. Therefore the D-optimal design is $b_1 = b_{\min}$, $b_2 = b_{\max}$. For $N = 3$ the objective function becomes $\det(\mathbf{M}) = (b_1 - b_2)^2 + (b_1 - b_3)^2 + (b_3 - b_2)^2$. Consequently, the D-optimal design is $b_1 = b_2 = b_{\min}$, $b_3 = b_{\max}$ or equivalently $b_1 = b_2 = b_{\max}$, $b_3 = b_{\min}$. Generally, one can see that for arbitrary N the D-optimal experiment design is obtained when

$$\begin{aligned} b_i &= b_{\min} \quad \forall i = 1, \ldots, n, \\ b_i &= b_{\max} \quad \forall i = n+1, \ldots, N, \end{aligned} \quad (10)$$

where $n = N/2$ if N is even; otherwise $n = (N+1)/2$. In the next section we compare the D-optimal design with the ED and GCRLB designs.

3. Evaluation and Simulation Results

In this section we evaluate the proposed D-optimal experiment design method and compare it with existing optimal design methods. We run Monte Carlo simulations using the pseudo-algorithm given in Appendix A. In our simulations we use the Rician noise distribution. While this does not match the noise assumptions of our theoretical framework, it permits a more realistic evaluation of the results for ADC imaging. We use the range $[0.1, 3] \times 10^{-3}$ mm^2/s of D values that are reported for human brain studies [4, 23]. In abdominal organs the range extends up to 5×10^{-3} mm^2/s [7]. In the text to follow we note that (i) the units associated with D and b have been omitted for readability (all b-values are stated in s/mm^2) and (ii) $E(x) = (1/N_{MC})\sum_{i=1}^{N_{MC}} \hat{x}$. It is also noteworthy that we used LSE throughout the paper for parameter estimation.

3.1. Comparison to GCRLB. Given that the GCRLB method [23] is specifically designed for ADC estimation and is in good agreement with previous studies [21, 22], herein we compare the proposed D-optimal design with the GCRLB method. Figure 2 shows the standard deviation of estimated ADC values (σ_D) for a range of D values, where $N = 2$, $b_{\min} = 0$, $b_{\max} = 2000$, $m_0 = 500$, $N_{MC} = 20000$, and SNR = m_0/σ_G. According to table 3 in [23] the optimal two-point design for $D \in [0.1, 3] \times 10^{-3}$ is $b_1 = 0$, $b_2 = 820$ while the D-optimal method suggests $b_1 = 0$, $b_2 = b_{\max}$. Several key observations can be drawn from Figure 2. (i) Increasing the SNR from 4 to 10 significantly improves the performance of the GCRLB. In addition, the performance of the GCRLB is heavily dependent on the D values to be measured. In contrast, the performance of the D-optimal design is very consistent, demonstrating robustness to changes in SNR and D. (ii) The D-optimal design outperforms the GCRLB over the entire range of D values and SNRs. (iii) For small D values and high SNR, where the Rician distribution can be fairly approximated by a Gaussian distribution [25], the performance of the GCRLB is close to that of the D-optimal design. (iv) Though the Rician noise model does not match our theoretical noise assumption, the precision of $\widehat{D}$ is independent of its actual value, D.

Figure 3 compares the GCRLB and D-optimal designs in terms of error (computed as $|E(\widehat{D}) - D|$) and standard deviation of $\widehat{D}$ (illustrated as vertical bars for each D value), where $N = 10$, $b_{\min} = 0$, $b_{\max} = 2000$, $m_0 = 500$, $N_{MC} = 20000$, and SNR = $m_0/\sigma_G = 10$. According to table 3 in [23] the optimal ten-point design for $D \in [0.1, 3] \times 10^{-3}$ is $b_1 = b_2 = 0$, $b_3 = b_4 = \cdots = b_8 = 700$, and $b_9 = b_{10} = b_{\max}$ while the D-optimal design suggests $b_1 = \cdots = b_5 = 0$, $b_6 = \cdots = b_{10} = b_{\max}$. It can be seen in Figure 3 that the D-optimal design performs better in terms of accuracy and precision. Figure 4 shows, for the same test, plots of the bias (computed as $E(\widehat{m}_0) - m_0$) and standard deviation of $\widehat{m}_0$. It can be seen that the proposed method leads to both accurate and precise estimation of m_0. In addition, the D-optimal design shows very consistent performance over the whole range of D values. It is noteworthy that the GCRLB method severely underestimates m_0 for high D values.

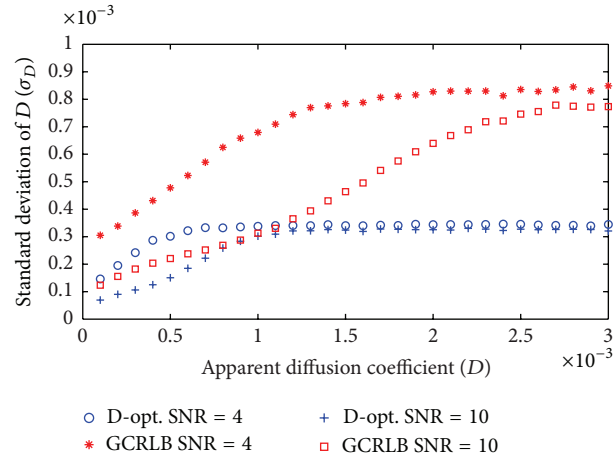

FIGURE 2: Standard deviation of estimated ADC values (σ_D) for a range of D values, where $N = 2$, $b_{\min} = 0$, $b_{\max} = 1500$, $m_0 = 500$, $N_{MC} = 20000$, and SNR $= m_0/\sigma_G$. The proposed D-optimal method is compared to GCRLB [23].

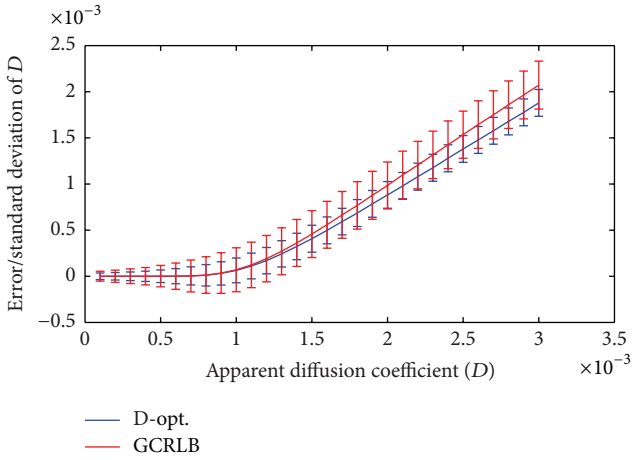

FIGURE 3: Error and standard deviation of estimated ADC values (vertical bars) for a range of D values, where $N = 10$, $b_{\min} = 0$, $b_{\max} = 1500$, $m_0 = 500$, $N_{MC} = 20000$, and SNR $= m_0/\sigma_G = 10$. The proposed D-optimal method is compared to GCRLB [23].

3.2. Sensitivity Analysis and Comparison to the ED Design. In this section we evaluate the sensitivity of the D-optimal design to changes in input parameters such as D, N, $b_{\max}$, and SNR. The input variable $b_{\min}$ is not considered because it is usually set to $b_{\min} = 0$.

The ADC value may vary depending on tissue type, pathological/developmental changes, and aging. The error and standard deviation of $\widehat{D}$ and $\widehat{m}_0$ are illustrated in Figure 5 for the range $D \in [0.1, 5] \times 10^{-3}$, where $N = 10$, $b_{\min} = 0$, $b_{\max} = 2000$, $m_0 = 500$, $N_{MC} = 20000$, and SNR $= m_0/\sigma_G = 10$. It can be seen that the D-optimal design outperforms the ED design in terms of accuracy and precision. Notably, the difference in estimation of m_0 is extremely large. This can have a significant impact on studies that use the diffusion signal itself as a biomarker (as in [14]). Note that, for the D-optimal design, the variance of σ_D is almost fixed for

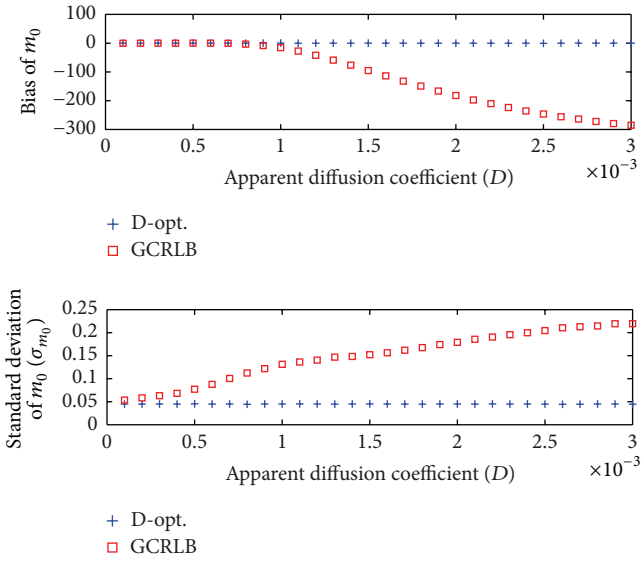

FIGURE 4: Bias and standard deviation of the estimated m_0 values for a range of D values, where $N = 10$, $b_{\min} = 0$, $b_{\max} = 1500$, $m_0 = 500$, $N_{MC} = 20000$, and SNR $= m_0/\sigma_G = 10$. The proposed D-optimal method is compared to GCRLB [23].

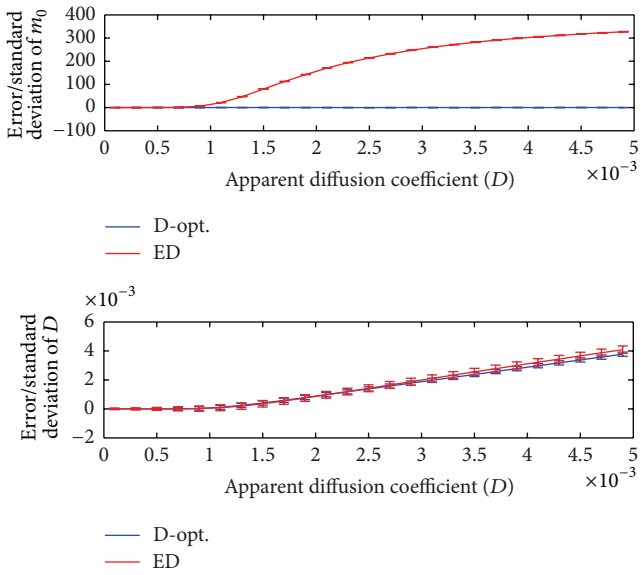

FIGURE 5: Error and standard deviation of $\widehat{D}$ and $\widehat{m}_0$ for the range $D \in [0.1, 5] \times 10^{-3}$, where $N = 10$, $b_{\min} = 0$, $b_{\max} = 2000$, $m_0 = 500$, $N_{MC} = 20000$, and SNR $= m_0/\sigma_G = 10$. The D-optimal design is compared to the ED design (where b_is are equidistantly distributed between $b_{\min}$ and $b_{\max}$).

$D \in [1, 5] \times 10^{-3}$. This consistency of performance is also apparent in the estimation of m_0.

The number of measurements is in general limited by the available clinical scan time. Here, we consider a range of N that is feasible for clinical studies according to the literature. The error and standard deviation of $\widehat{D}$ and $\widehat{m}_0$ are illustrated in Figure 6 for the range $N = 2$ to $N = 20$, where $D = 1 \times 10^{-3}$, $b_{\min} = 0$, $b_{\max} = 2000$, $m_0 = 500$, $N_{MC} = 20000$, and

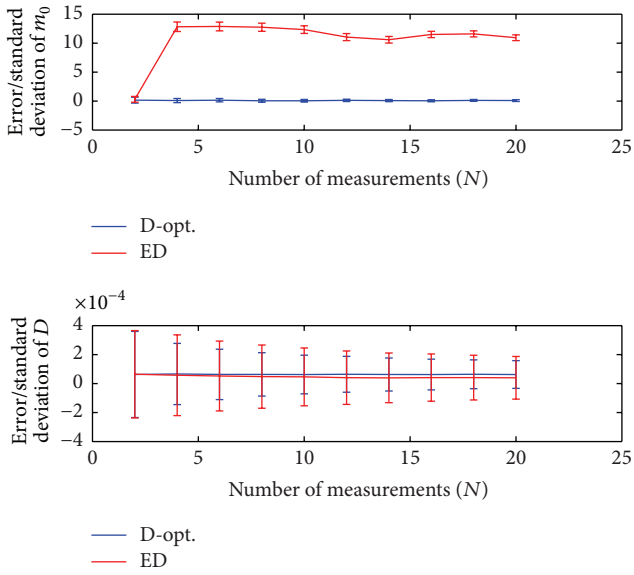

FIGURE 6: Error and standard deviation of $\widehat{D}$ and $\widehat{m}_0$ for the range $N = 2$ to $N = 20$, where D $= 1 \times 10^{-3}$, $b_{\min} = 0$, $b_{\max} = 2000$, $m_0 = 500$, $N_{\mathrm{MC}} = 20000$, and SNR $= m_0/\sigma_G = 10$. The D-optimal design is compared to the ED design.

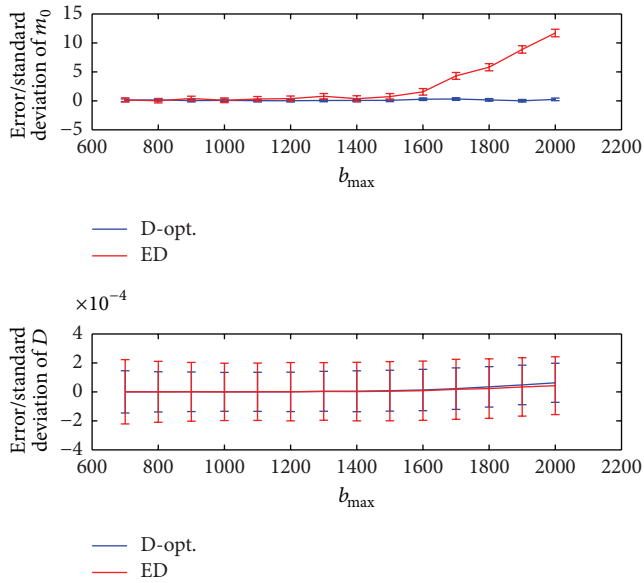

FIGURE 7: Error and standard deviation of $\widehat{D}$ and $\widehat{m}_0$ as a function of $b_{\max}$, where $D = 1 \times 10^{-3}$, $N = 10$, $b_{\min} = 0$, $m_0 = 500$, $N_{\mathrm{MC}} = 20000$, and SNR $= m_0/\sigma_G = 10$. The D-optimal design is compared to the ED design.

SNR $= m_0/\sigma_G = 10$. It shows that the D-optimal design outperforms the ED design in terms of standard deviation (vertical bars) of $\widehat{D}$ and $\widehat{m}_0$. As N increases, the variance of the estimated parameters decreases for both design methods while the accuracy is almost constant. Note that for $N = 2$ the two design methods lead to the same solution. Deviating from D-optimal solution, accuracy/precision of $\widehat{m}_0$ for the ED method considerably decreases even with higher number of measurements (cf. $N = 2$ with $N = 4$).

Different $b_{\max}$ values are recommended in the literature for different target organs/tissues. For example, [1] suggests $b_{\max} = 700$ for kidney while $b_{\max} = 1500$ is used for head and neck imaging [20] and $b_{\max} = 2000$ for brain imaging [18]. The error and standard deviation of $\widehat{D}$ and $\widehat{m}_0$ are illustrated in Figure 7 for the range $b_{\max} = 700, 800, \ldots, 2000$, where $D = 1 \times 10^{-3}$, $N = 10$, $b_{\min} = 0$, $m_0 = 500$, $N_{\mathrm{MC}} = 20000$, and SNR $= m_0/\sigma_G = 10$. It can be seen that the D-optimal design outperforms the ED design in terms of standard deviation (vertical bars) of $\widehat{D}$ and $\widehat{m}_0$. For the ED design, as $b_{\max}$ increases it does not make a considerable difference to the estimation of D but it does negatively impact on the estimation of m_0 producing increasingly larger errors for values of $b_{\max}$ beyond 1600. In contrast, the D-optimal design shows a better and relatively consistent performance over the whole range (with almost constant accuracy and precision).

The signal-to-noise ratio also affects the accuracy and precision of the estimation problem. We investigate the effect of SNR on the proposed experiment design as follows. The error and standard deviation of $\widehat{D}$ and $\widehat{m}_0$ are illustrated in Figure 8 as a function of SNR (defined as m_0/σ_G), where $D = 1 \times 10^{-3}$, $N = 10$, $b_{\min} = 0$, $b_{\max} = 2000$, $m_0 = 500$, and $N_{\mathrm{MC}} = 20000$. It shows that, over the whole range of SNR values, the

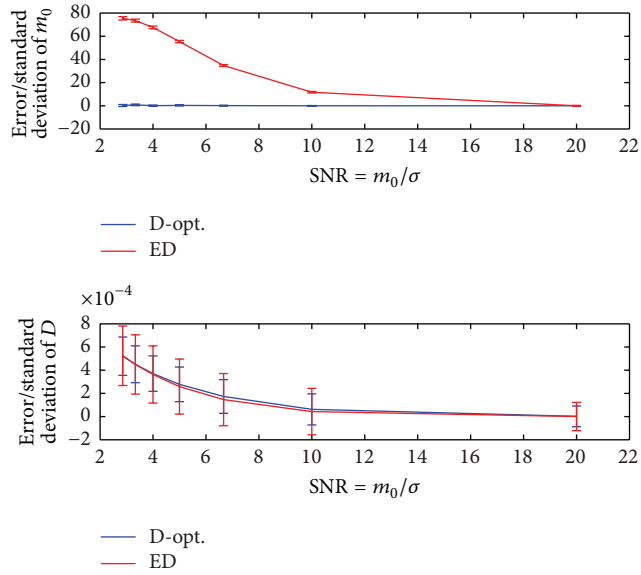

FIGURE 8: Error and standard deviation of $\widehat{D}$ and $\widehat{m}_0$ as a function of SNR (defined as m_0/σ_G), where $D = 1 \times 10^{-3}$, $N = 10$, $b_{\min} = 0$, $b_{\max} = 2000$, $m_0 = 500$, and $N_{\mathrm{MC}} = 20000$. The D-optimal design is compared to the ED design.

D-optimal design leads to minimum variance estimation of the unknown parameters. For ED design, the accuracy and precision of both $\widehat{D}$ and $\widehat{m}_0$ improve with increasing SNR while for the D-optimal design an improvement is only seen for $\widehat{D}$.

3.3. Tests on a Mean Diffusivity Map. To illustrate the impact that experiment design may have on diffusion-weighted

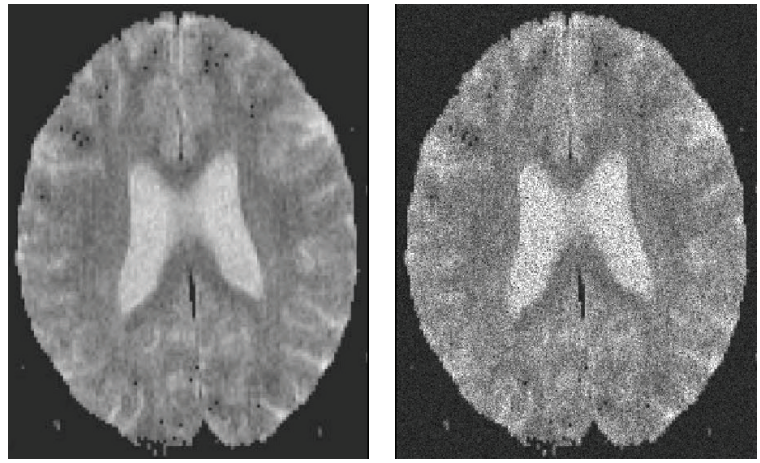

(a) (b)

Figure 9: Original mean diffusivity map considered as ground truth (a) and an example noisy image produced by adding Rician distributed noise, where SNR = 5 (b). The original image is taken from [18].

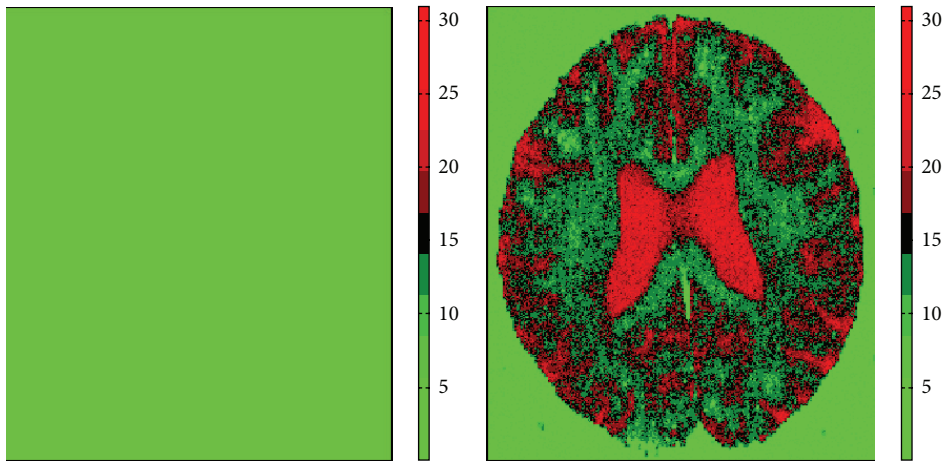

(a) (b)

Figure 10: Error in estimation of diffusion signal computed as $|E(\widehat{m}_0) - m_0|$ for the D-optimal (a) and ED (b) design methods. The color bar ranges from 0 to 31.

images, we perform the following test. We take figure 4.(a) in [18] as the ground truth image. Then we add Rician distributed noise pixelwise (SNR = 5). The original image and an example of noisy images are shown in Figure 9.

Let $I(i, j)$ denote a pixel intensity in the original image. Then we run Algorithm 1 with the following setting for all pixels: $m_0 = I(i, j)$, SNR $= m_0/5$, $N = 20$, $D = 1 \times 10^{-3}$, $b_{\min} = 0$, $b_{\max} = 2000$, and $N_{\mathrm{MC}} = 20000$. The resultant images computed as error in estimation of $\widehat{m}_0$ ($|E(\widehat{m}_0) - m_0|$) and its standard deviation are shown in Figures 10 and 11, respectively. Figure 10 shows that one can accurately estimate diffusion signal using the D-optimal design. The accuracy is almost independent of the signal level. In contrast, the ED design produces large errors for high signal levels. In applications that consider statistics in small ROIs (such as [11]) this may be misleading.

The optimal experiment design is fundamentally based on improving the precision of the estimation problem. This can be seen in Figure 11, where we illustrate the standard deviation of $\widehat{m}_0$. It can be seen that the D-optimal design consistently produces lower variance than the ED design. It is noteworthy that Figures 10 and 11 represent the sensitivity analysis with respect to m_0 and confirm the stable performance of the D-optimal design.

4. Discussions

Although the current work focuses on ADC imaging, the proposed method can be applied in experiment design for other applications of the monoexponential model. As an example, empirical evaluations in [17] show that adding more measurements on $b_{\min}$ improves the results of model fitting

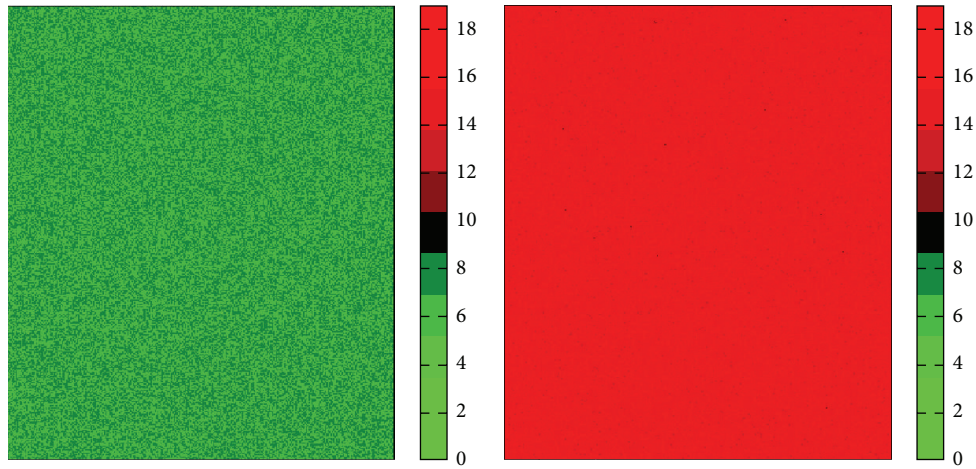

(a) (b)

Figure 11: Standard deviation in estimation of $\widehat{m}_0$. The D-optimal design (a) produces more precise estimates compared to the ED design (b). Note that the standard deviation is multiplied by 100 to enhance the visualization.

Data: D, m_0, N, $b_{\min}$, $b_{\max}$, σ_G and N_{MC}, number of Monte Carlo trials.
Result: Mean value and standard deviation of $\widehat{D}$ and $\widehat{m}_0$
(i) Choose an algorithm ED/GCRLB/D-opt. to assign $b_i \, \forall i = 1, \ldots, N$.
(ii) Set $m_i = m_0 \exp(-b_i D)$.
for $r = 1$ **to** N_{MC} **do**
(i) Add Rician distributed noise to m_is to obtain SNR $= m_0/\sigma_G$;
(ii) Compute the unknown parameters $\widehat{D}$ and $\widehat{m}_0$;
(iii) Record the mean value and standard deviation of $\widehat{D}$ and $\widehat{m}_0$.

Algorithm 1: Pseudo-algorithm to evaluate an experiment design.

in enzyme kinetics (compared to the ED design). This is in agreement with our findings.

Comparing the proposed method to previous studies, we see that it (i) is based on less restrictive noise assumptions and thus covers a wider range of applications, (ii) shows that the optimal design is not necessarily dependent on the imaged parameters, (iii) outperforms the ED and GCRLB methods (based on evaluations using simulated data), and (iv) is applicable even if the noise assumptions are partly violated.

Figures 3 and 5 show that (i) in contrast to the findings in [23] there exist D-independent optimal designs that minimize variance of the estimated ADC values and (ii) even using optimal designs D values greater than 1.1×10^{-3} cannot be estimated accurately. In other words, the error of $\widehat{D}$ is larger than 10% when $D > 1.1 \times 10^{-3}$. This means that ADC values reported for cartilage, muscle [23], and normal white matter [4] are accurate/reliable while high ADC values reported for normal kidney [7] should arguably be treated with caution. This warrants further investigation using real data.

Noise Distribution. The noise assumptions (independency and equal variance) are necessary for tractable theoretical derivations but do not necessarily limit the proposed method to Gaussian noise. For example, these assumptions hold for scenarios with independent but nonidentical noise distributions provided that they have equal variances. We have evaluated the proposed method in realistic cases (independent Rician noise with nonequal variances). However, in modern scanners with phased arrays and multicoil acquisition [26], the noise is noncentrally χ-distributed [27]. The D-optimal design problem for such kind of noise distributions is intractable. In addition, relaxing the "*equal variance*" condition, the D-optimal design becomes dependent on the imaged parameters. Thus, we can not find an optimal design that performs well over the whole range of the imaged parameters.

Estimation Method. One can use other estimation methods instead of LSE. Possibilities include the median estimator [18], maximum likelihood estimator (MLE), and weighted least squares (WLS) [28]. The exact formulation of the D-optimal design problem for these estimation techniques is dependent on the noise distribution and often becomes intractable. In the case of Gaussian noise the MLE leads to the same solution as LSE.

Physical Considerations. Given that the proposed method takes the minimum and maximum b-values as the input, one can adjust the range to avoid the signal distortion caused by physical phenomena such as the perfusion effect at low b-values and non-Gaussian behavior at high b-values.

5. Conclusion

The need for precise estimation of biomedical quantities has given rise to studies concerning optimal experiment design for monoexponential model fitting. In this paper, we formulated the problem as a D-optimal design problem that is a convex optimization problem. In contrast to previous studies, we did not restrict our theoretical framework to model fitting in the presence of Gaussian noise. Solving this problem and evaluating the results for ADC imaging on simulated data, we showed that the optimal design is independent of the imaged parameters. Furthermore, Monte Carlo simulations showed that the D-optimal design outperforms the ED and GCRLB methods. Moreover the proposed method is applicable to a wider range of problems because of its less restrictive noise assumptions. Our evaluations show that it is applicable even if the noise assumptions are partly violated. An important practical result is that accurate estimation of high ADC values is not possible even using optimal experiment design.

Appendices

A. Evaluation of an Experiment Design

Here we provide a pseudo-code for the algorithm used in Section 3 (see Algorithm 1).

B. GCRLB Experiment Design

In an estimation problem, the lower bound of the variance of a parameter x_j, $\sigma^2(x_j)$, is given by the corresponding diagonal element of the inverse of the Fisher information matrix:

$$\sigma^2\left(x_j\right) \geq \left(\mathbf{F}^{-1}\right)_{jj}. \tag{B.1}$$

This is known as the Cramer-Rao lower bound (CRLB). Assuming zero-mean Gaussian noise on m in (1), one can obtain the following Fisher information matrix for ADC imaging [23]:

$$\mathbf{F} = \frac{1}{\sigma_G}\begin{bmatrix} \sum_{i=1}^{N} \exp\left(-2b_iD\right) & -\sum_{i=1}^{N} b_iS_0 \exp\left(-2b_iD\right) \\ -\sum_{i=1}^{N} b_iS_0 \exp\left(-2b_iD\right) & \sum_{i=1}^{N} b_i^2S_0^2 \exp\left(-2b_iD\right) \end{bmatrix}. \tag{B.2}$$

In the derivation above $\mathbf{x} = [S_0 \quad D]$. The GCRLB experiment design entails minimizing the CRLB of D, $(\mathbf{F}^{-1})_{22}$, with respect to b_is for a given value/range of D. The reader is referred to [23] for more details.

Conflict of Interests

The authors declare that there is no conflict of interests regarding the publication of this paper.

References

[1] D. M. Koh and H. C. Thoeny, *Diffusion-Weighted MR Imaging: Applications in the Body*, Springer, Berlin, Germany, 2010.

[2] E. Sjögren, H. Lennernäs, T. B. Andersson, J. Gråsjö, and U. Bredberg, "The multiple depletion curves method provides accurate estimates of intrinsic clearance (CL_{int}), maximum velocity of the metabolic reaction (V_{max}), and michaelis constant (K_m): accuracy and robustness evaluated through experimental data and monte carlo simulations," *Drug Metabolism and Disposition*, vol. 37, no. 1, pp. 47–58, 2009.

[3] R. Urso, P. Blardi, and G. Giorgi, "A short introduction to pharmacokinetics," *European Review for Medical and Pharmacological Sciences*, vol. 6, no. 2, pp. 33–44, 2002.

[4] R. N. Sener, "Diffusion MRI: apparent diffusion coefficient (ADC) values in the normal brain and a classification of brain disorders based on ADC values," *Computerized Medical Imaging and Graphics*, vol. 25, no. 4, pp. 299–326, 2001.

[5] W. Abdulghaffar and M. M. Tag-Aldeen, "Role of diffusion-weighted imaging (DWI) and apparent diffusion coefficient (ADC) in differentiating between benign and malignant breast lesions," *The Egyptian Journal of Radiology and Nuclear Medicine*, vol. 44, no. 4, pp. 945–951, 2013.

[6] J.-M. Shen, X.-W. Xia, W.-G. Kang, J.-J. Yuan, and L. Sheng, "The use of MRI apparent diffusion coefficient (ADC) in monitoring the development of brain infarction," *BMC Medical Imaging*, vol. 11, article 2, 2011.

[7] J. L. Zhang, E. E. Sigmund, H. Chandarana et al., "Variability of renal apparent diffusion coefficients: limitations of the monoexponential model for diffusion quantification," *Radiology*, vol. 254, no. 3, pp. 783–792, 2010.

[8] C. Göya, C. Hamidi, Y. Bozkurt et al., "The role of apparent diffusion coefficient quantification in differentiating benign and malignant renal masses by 3 Tesla magnetic resonance imaging," *Balkan Medical Journal*, vol. 32, no. 3, pp. 273–278, 2015.

[9] S. Emad-Eldin, M. Halim, L. I. A. Metwally, and R. M. Abdel-Aziz, "Diffusion-weighted MR imaging and ADC measurement in normal prostate, benign prostatic hyperplasia and prostate carcinoma," *The Egyptian Journal of Radiology and Nuclear Medicine*, vol. 45, no. 2, pp. 535–542, 2014.

[10] M. A. Jacobs, R. Ouwerkerk, K. Petrowski, and K. J. MacUra, "Diffusion-weighted imaging with apparent diffusion coefficient mapping and spectroscopy in prostate cancer," *Topics in Magnetic Resonance Imaging*, vol. 19, no. 6, pp. 261–272, 2008.

[11] N. Mukuda, S. Fujii, C. Inoue et al., "Apparent diffusion coefficient (ADC) measurement in ovarian tumor: effect of region-of-interest methods on ADC values and diagnostic ability," *Journal of Magnetic Resonance Imaging*, 2015.

[12] K. A. Ahmad and A. Abdrabou, "The significance of added ADC value to conventional MR imaging in differentiation between benign and malignant ovarian neoplasms," *The Egyptian Journal of Radiology and Nuclear Medicine*, vol. 45, no. 3, pp. 997–1002, 2014.

[13] K. Tsukamoto, E. Matsusue, Y. Kanasaki et al., "Significance of apparent diffusion coefficient measurement for the differential diagnosis of multiple system atrophy, progressive supranuclear

palsy, and Parkinson's disease: evaluation by 3.0-T MR imaging," *Neuroradiology*, vol. 54, no. 9, pp. 947–955, 2012.

[14] Y. Lei, H. Wang, H.-F. Li et al., "Diagnostic significance of diffusion-weighted MRI in renal cancer," *BioMed Research International*, vol. 2015, Article ID 172165, 12 pages, 2015.

[15] A. Ogura, K. Hayakawa, T. Miyati, and F. Maeda, "Imaging parameter effects in apparent diffusion coefficient determination of magnetic resonance imaging," *European Journal of Radiology*, vol. 77, no. 1, pp. 185–188, 2011.

[16] T. Yoshikawa, H. Kawamitsu, D. G. Mitchell et al., "ADC measurement of abdominal organs and lesions using parallel imaging technique," *American Journal of Roentgenology*, vol. 187, no. 6, pp. 1521–1530, 2006.

[17] E. Sjögren, J. Nyberg, M. O. Magnusson, H. Lennernäs, A. Hooker, and U. Bredberg, "Optimal experimental design for assessment of enzyme kinetics in a drug discovery screening environment," *Drug Metabolism and Disposition*, vol. 39, no. 5, pp. 858–863, 2011.

[18] A. Kristoffersen, "Diffusion measurements and diffusion tensor imaging with noisy magnitude data," *Journal of Magnetic Resonance Imaging*, vol. 29, no. 1, pp. 237–241, 2009.

[19] J. Yuan, D. K. W. Yeung, G. S. P. Mok et al., "Non-Gaussian analysis of diffusion weighted imaging in head and neck at 3T: a pilot study in patients with nasopharyngeal carcinoma," *PLoS ONE*, vol. 9, no. 1, Article ID e87024, 2014.

[20] J. F. A. Jansen, H. E. Stambuk, J. A. Koutcher, and A. Shukla-Dave, "Non-gaussian analysis of diffusion-weighted MR imaging in head and neck squamous cell carcinoma: a feasibility study," *American Journal of Neuroradiology*, vol. 31, no. 4, pp. 741–748, 2010.

[21] Y. Bito, S. Hirata, and E. Yamamoto, "Optimum gradient factors for apparent diffusion coefficient measurements," in *Proceedings of the SMR/ESMRMB Joint Meeting*, p. 913, Nice, France, August 1995.

[22] D. Xing, N. G. Papadakis, C. L.-H. Huang, V. M. Lee, T. A. Carpenter, and L. D. Hall, "Optimised diffusion-weighting for measurement of apparent diffusion coefficient (ADC) in human brain," *Magnetic Resonance Imaging*, vol. 15, no. 7, pp. 771–784, 1997.

[23] O. Brihuega-Moreno, F. P. Heese, and L. D. Hall, "Optimization of diffusion measurements using Cramer-Rao lower bound theory and its application to articular cartilage," *Magnetic Resonance in Medicine*, vol. 50, no. 5, pp. 1069–1076, 2003.

[24] J. J. Ye and J. Zhou, "Minimizing the condition number to construct design points for polynomial regression models," *SIAM Journal on Optimization*, vol. 23, no. 1, pp. 666–686, 2013.

[25] M. Björk, *Contributions to signal processing for MRI [Ph.D. thesis]*, Uppsala University, 2015.

[26] C. D. Constantinides, E. Atalar, and E. R. McVeigh, "Signal-to-noise measurements in magnitude images from NMR phased arrays," *Magnetic Resonance in Medicine*, vol. 38, no. 5, pp. 852–857, 1997.

[27] J. Veraart, J. Rajan, R. R. Peeters, A. Leemans, S. Sunaert, and J. Sijbers, "Comprehensive framework for accurate diffusion MRI parameter estimation," *Magnetic Resonance in Medicine*, vol. 70, no. 4, pp. 972–984, 2013.

[28] J. Veraart, J. Sijbers, S. Sunaert, A. Leemans, and B. Jeurissen, "Weighted linear least squares estimation of diffusion MRI parameters: strengths, limitations, and pitfalls," *NeuroImage*, vol. 81, pp. 335–346, 2013.

Hindawi Publishing Corporation
BioMed Research International
Volume 2015, Article ID 672520, 9 pages
http://dx.doi.org/10.1155/2015/672520

Research Article

Enhanced Classification of Interstitial Lung Disease Patterns in HRCT Images Using Differential Lacunarity

Verónica Vasconcelos,[1,2] João Barroso,[1,3] Luis Marques,[2] and José Silvestre Silva[4]

[1] *INESC TEC, Campus da FEUP, Rua Dr. Roberto Frias, 4200-465 Porto, Portugal*
[2] *Coimbra Institute of Engineering, Polytechnic Institute of Coimbra, Rua Pedro Nunes, Quinta da Nora, 3030-199 Coimbra, Portugal*
[3] *School of Science and Technology, University of Trás-os-Montes e Alto Douro, Apartado 1013, 5001-801 Vila Real, Portugal*
[4] *Military Academy Research Center, Avenida Conde Castro Guimarães, 2720-113 Amadora, Portugal*

Correspondence should be addressed to Verónica Vasconcelos; veronica@isec.pt

Received 11 September 2015; Accepted 18 November 2015

Academic Editor: Yukihisa Takayama

The analysis and interpretation of high-resolution computed tomography (HRCT) images of the chest in the presence of interstitial lung disease (ILD) is a time-consuming task which requires experience. In this paper, a computer-aided diagnosis (CAD) scheme is proposed to assist radiologists in the differentiation of lung patterns associated with ILD and healthy lung parenchyma. Regions of interest were described by a set of texture attributes extracted using differential lacunarity (DLac) and classical methods of statistical texture analysis. The proposed strategy to compute DLac allowed a multiscale texture analysis, while maintaining sensitivity to small details. Support Vector Machines were employed to distinguish between lung patterns. Training and model selection were performed over a stratified 10-fold cross-validation (CV). Dimensional reduction was made based on stepwise regression (F-test, p value < 0.01) during CV. An accuracy of $95.8 \pm 2.2\%$ in the differentiation of normal lung pattern from ILD patterns and an overall accuracy of $94.5 \pm 2.1\%$ in a multiclass scenario revealed the potential of the proposed CAD in clinical practice. Experimental results showed that the performance of the CAD was improved by combining multiscale DLac with classical statistical texture analysis.

1. Introduction

Interstitial lung disease (ILD) is a common name for a heterogeneous group of complex disorders affecting lung parenchyma. The ILD affects similar lung regions and has identical clinical, radiological, and functional tests which hinder the differential diagnosis. However, ILD subtypes have different prognoses and treatments, so a correct diagnosis is essential [1]. High-resolution computed tomography (HRCT) imaging of the chest can offer such good image quality that it has become essential in the detection, diagnosis, and follow-up of ILD [2]. HRCT images of patients affected with ILD have specific patterns whose distribution and visual content analysis is particularly relevant in elaborating an accurate diagnosis [3].

Multidetector row computed tomography (CT) scanners generate a huge volume of data that must be visually examined by radiologists. This task is very time-consuming and requires experience, especially in the presence of ILD. Computer-aided diagnosis (CAD) for ILD is seen as a necessary tool to reduce interobserver and intraobserver variations, as well as to improve diagnostic accuracy by assisting radiologists in the detection, characterization, and quantification of pathological regions [3–13].

In this paper, a CAD scheme is presented allowing for a classification of regions of interest (ROIs), from HRTC images, in four classes of lung patterns: normal (NOR), ground glass (GG), honeycombing (HC), and emphysema (EMP). A scenario of binary differentiation, NOR class versus pathological class, is also considered. A generic flowchart of the proposed approach is shown in Figure 1. Classical statistical methods were used to extract and quantify texture information. The first-order (FO) analysis, the Spatial Gray Level Dependence Method (SGLDM), and the Gray Level Run-Length Method (GLRLM) allowed the estimate of statistical properties of individual pixel values and of the

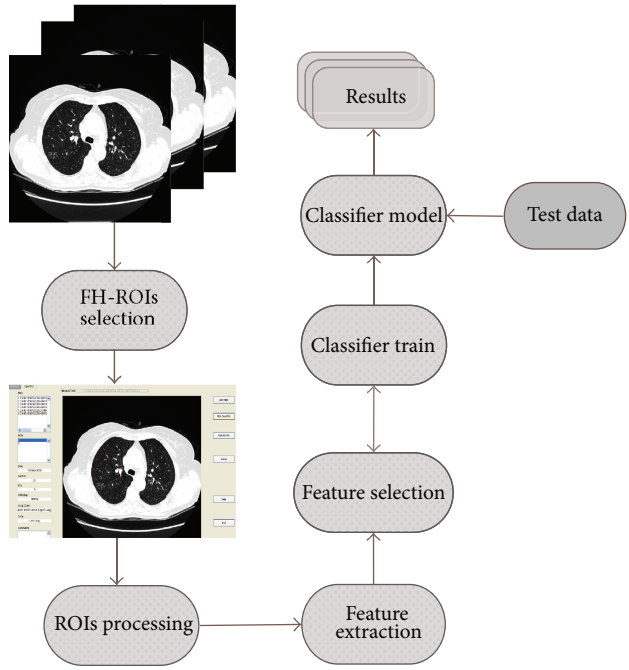

Figure 1: The proposed CAD scheme.

spatial interaction between two or more pixel values. These methods have frequently been used in texture analysis of medical images, namely, in the description of ILD patterns [4, 8–13]. Given the heterogeneity of lung parenchyma in healthy subjects or in the presence of pathologies, a multiscale texture analysis was proposed using differential lacunarity (DLac). Lacunarity has been successfully used in analyzing medical images of different organs or structures, acquired by different types of equipment. In [14, 15], fractal lacunarity analysis was applied to lumbar vertebra magnetic resonance images in order to extract relevant parameters, allowing for differentiation among three types of trabecular bone structure, from female subjects with different age and physiopathological status. In [16], lacunarity was combined with mean fractal dimension to differentiate between aggressive and nonaggressive malignant lung tumors, in sequence of contrast-enhanced CT images. An 83.3% accuracy can be valuable information in the choice of the appropriate treatment procedure. In [17], lacunarity analysis was applied for discriminating endoscopic images, obtained through a wireless capsule endoscopy technique, related to a common interstitial disease: ulceration. A promising classification accuracy of over 97% was obtained. In [18], lacunarity was applied to HRCT images of the chest to differentiate between normal and emphysematous regions of lung parenchyma. The preliminary results showed the potential of the proposed lacunarity features.

After a feature selection procedure, the obtained features were used to classify each ROI through a Support Vector Machines (SVM) algorithm. This learning algorithm has its origin in statistical learning theory and structural risk minimization [19, 20]. It emerged as an efficient technique for solving classification problems. A comparative study between SVM and other popular classifiers was performed by Meyer et al. [21]. The results highlight that SVM classifiers are among the best. In [5], five common classifiers were compared according to their ability to differentiate six lung tissue patterns in HRCT images. The results showed that SVM provides the best trade-off between the error rate and the capacity for generalization, an important aspect to take into consideration given the diversity of pulmonary patterns.

2. Materials and Methods

2.1. Texture Analysis. Texture is a major component in the interpretation of HRTC images in the presence of ILD. The most difficult aspect of texture analysis is to define a set of meaningful features that describe the texture associated with different lung patterns. Each ROI of $M \times N$ pixels was represented by a set of m features extracted using the methods described in the sections below.

2.1.1. First-Order Statistics Analysis. The CT attenuation of each ROI was described through FO statistical features extracted from ROI normalized histogram. Considering that L is the number of gray levels used in ROI quantization, the normalized histogram $h(z_i)$, $0 \leq i < L$, gives the probability of observing the gray level z_i in the ROI. From $h(z_i)$, six statistics features were computed: the mean, variance, skewness, kurtosis, energy, and entropy [22].

2.1.2. Spatial Gray Level Dependence Method. The method of texture analysis proposed by Haralick et al. [23] describes the spatial dependence of gray level distribution between neighboring pixels. In the SGLDM, the second-order joint conditional probability distribution $p(i, j \mid dx, dy)$ can be

estimated for a defined length and along a defined direction given by offsets in x and y direction: dx and dy. So, $p(i, j \mid dx, dy)$ is the probability that two pixels at a distance given by (dx, dy) have the gray levels i and j. The function $p(i, j \mid dx, dy)$ is defined as follows:

$$p(i, j \mid dx, dy) = \frac{\sum_{k=1}^{M} \sum_{q=1}^{N} \delta(i, \mathrm{ROI}(k, q)) \cdot \delta(j, \mathrm{ROI}(k + dx, q + dy))}{T(dx, dy)}, \quad \text{where } \delta(i, j) = \begin{cases} 1 & \text{if } i = j \\ 0 & \text{if } i \neq j. \end{cases} \tag{1}$$

$\mathrm{ROI}(k, q)$ is the intensity at pixel (k, q) and $T(dx, dy)$ is the total number of pixels pairs belonging to the ROI in the length and direction given by (dx, dy). The functions $p(i, j \mid dx, dy)$ can be written in matrix form $\Omega(dx, dy) = p(i, j \mid dx, dy)$, $0 \leq i, j < L$, where L is the maximum gray level of the ROI. For each pair (dx, dy), a different matrix $\Omega(dx, dy)$ can be computed. Often, each matrix $\Omega(dx, dy)$ is calculated taking into account a given offset and its opposite, giving rise to symmetrical matrices. In this study, from each matrix, six textural measures were extracted: angular second moment, entropy, inverse difference moment, correlation, contrast, and variance [23, 24].

2.1.3. Gray Level Run-Length Method. Run-length primitives were computed by the GLRLM [25]. A run-length primitive is a consecutive and collinear set of pixels with the same gray level. These primitives can be characterized by their length, direction, and gray level. Each chosen direction gives rise to a run-length matrix $\Psi(\theta)$ whose elements represent the number of runs with gray level intensity a and length r, along the direction θ:

$$\Psi(\theta) = M(a, r \mid \theta), \quad 0 \leq a < L, \ 0 < r \leq N_r, \tag{2}$$

where L is the number of gray levels and N_r is the possible maximum run-length in ROI along θ direction. From each run-length matrix $\Psi(\theta)$, eleven features were extracted, listed, and described in [24–27].

2.1.4. Lacunarity Analysis. Most of the textures and natural surfaces tend to have a fractal dimension (FD) that can be seen as a measure of irregularity [28]. However, different textures and natural surfaces can share identical FD. In order to differentiate these types of fractal patterns, Mandelbrot [29] proposed lacunarity, a complementary measure of FD that describes the texture of a fractal or their deviation from translational invariance [30]. More recent studies introduced lacunarity analysis as a technique that can be used to describe general spatial patterns, regardless of whether it is a fractal [31]. By using lacunarity, it is possible to distinguish the texture of spatial patterns through the analysis of their distribution gap sizes, at different scales.

Due to the extensive range of gray levels used in CT images acquisition, an appropriate algorithm to calculate lacunarity is that proposed in [32], called DLac. It is based on the gliding box [33] and the differential box counting algorithms [34].

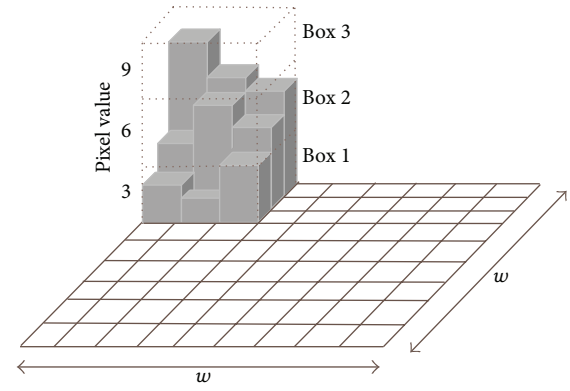

Figure 2: Differential box counting algorithm. A moving window of 9×9 pixels and a gliding box of 3×3 pixels are used to compute the box mass. A column of 3 cubic boxes is generated. The differential height of the column is $n(1, 1) = 3 - 1 - 1 = 1$.

According to DLac algorithm, the ROI is divided into overlapped windows of size $w \times w$ pixels, which scans the entire ROI, and a box of size $r \times r$ pixels, which scans each window ($r < w$). The box is placed on the left corner of the window w and a column of accumulated cubes of size $r \times r \times r$ is used to cover the ROI intensity surface in the box place (Figure 2). A sequential number is assigned to each cubic box, from bottom to top. Considering that the maximum and minimum pixel values lie in the cubic box v and u, respectively, the differential height of the column is given by $n(i, j) = v - u - 1$, where (i, j) is the box position. The box mass M of the window w, at specific coordinates, is obtained gliding the box inside the entire window w:

$$M = \sum_{i,j} n(i, j). \tag{3}$$

Considering $n(M, r)$, the number of windows w with box mass M calculated through a box r, the respective probability function $Q(M, r)$ is obtained by dividing $n(M, r)$ by the total number of windows. The DLac of the ROI for a box r, given a window w, is defined as follows:

$$\Lambda(r) = \frac{\sum_M M^2 Q(M, r)}{\left[\sum_M M Q(M, r)\right]^2}. \tag{4}$$

2.2. Feature Selection. After performing feature extraction, it is important to proceed with the selection of the most informative features. The resulting set of optimal features improves the classifier performance, while providing a reduction of the general data, as well as a better understanding of the data. The feature selection methods can be divided into two main groups: the filter methods and the wrapper methods. In the filter methods, the features are ordered based on a relevance index. In the wrapper methods, the process of feature selection involves the predictor. In these methods, subsets of features are scored during the learning machine training according to their predictive power [35].

In this work, the reduction of dimensionality was performed using the filter method stepwise regression [36]. In this systematic method, terms are added or removed from the multilinear model based on their statistically significant p value of F-statistics. The method begins with an initial model to which terms that have p values less than an entrance tolerance are added, step by step, and the model terms with p values greater than an exit tolerance are removed from the model.

2.3. Support Vector Machines. The reduced number of parameters that need to be tuned as well as the good trade-off between the error rate and the capability of generalization of SVM classifier algorithm was decisive for its choice in the classification of lung patterns [5, 21].

The SVM strategy, known as the kernel trick, is to map the input data space into a higher dimension feature space, via a nonlinear function kernel $\Phi : \Re^m \rightarrow \Im$, where separability between classes is improved. The distance between the nearest points of the two classes (*margin*) is maximized, creating an optimal separating hyperplane (OSH).

Considering the training data $\{\mathbf{x}_i, y_i\}$, $i = 1, \ldots, l$, $\mathbf{x}_i \in \Re^m$, $y_i \in \{+1, -1\}$, each instance $\mathbf{x}_i$ is characterized by a vector of m features (or attributes) and is associated with a class +1 or −1. The SVM machine learning solves the following quadratic optimization problem:

$$\begin{aligned} \min_{w,b,\xi} \quad & \frac{1}{2}\|\mathbf{w}\|^2 + C\sum_{i=1}^{l}\xi_i \\ \text{subject to} \quad & y_i\left(\mathbf{w}\cdot\Phi\left(\mathbf{x}_i\right) + b\right) \geq 1 - \xi_i \\ & \xi_i \geq 0, \ i = 1, \ldots, l, \end{aligned} \tag{5}$$

where $\mathbf{w}$ is a normal vector to OSH and b is the bias. In *hard margin* SVM all the examples have to stay outside the margin and be well classified. However, in real datasets, it is necessary to deal with outliers that can be inside the margin or on the wrong side of the classification boundary. The solution proposed in [37], as the *soft margin* SVM, is to introduce constraint slack variables ξ_i in the optimization problem. Ideally, these variables should be zero or have small values. So, to minimize the contribution of the slack variables, a penalty term C is added to the objective function (5). This parameter is a trade-off between the maximization of the margin and the minimization of training errors. For a test example $\mathbf{x}$, the decision function is given by

$$f\left(\mathbf{x}\right) = \operatorname{sgn}\left(\mathbf{w}\cdot\Phi\left(\mathbf{x}\right) + b\right). \tag{6}$$

There are several functions kernels $K(\mathbf{x}, \mathbf{x}_i) = \Phi(\mathbf{x})\cdot\Phi(\mathbf{x}_i)$ which can be selected to solve nonlinear problems. In this work, the Gaussian Radial Basis Function (RBF) was used: $K(\mathbf{x}, \mathbf{y}) = \exp(-\|\mathbf{x} - \mathbf{y}\|^2)/(2\sigma^2)$. This function only has one parameter (σ) that has to be tuned during the classifier training and model selection.

As the standard SVM is a binary classifier, several methods were developed to extend SVM to an n-class problem. Typically, these methods are based on combinations of binary classifiers such as one-versus-all and one-versus-one. In the one-versus-all approach, n binary classifiers are trained. For example, the model of the nth classifier is trained using the training instances of the n-class as positive and all the instances of the other classes as negative. To classify a new instance, all the n classifiers are run on this instance. The assigned class corresponds to the classifier which returns the largest distance from the separating hyperplane. In the one-versus-one approach $n(n-1)/2$ classifiers are trained in a pairwise methodology, where each takes one class as positive and the other class as negative. To classify a new example, each classifier is run and a count is assigned to each class selected by the classifier. The new instance is classified as belonging to the class which obtains the greatest number of wins, such as in a winner-takes-all voting scheme [38].

2.4. Dataset. The dataset $\mathscr{D}$ used in this work was acquired in Radiology Department of Coimbra Hospital and Universitary Centre, Coimbra, Portugal. It contains examples of representative regions associated with GG, HC, EMP, and NOR lung patterns, obtained from the daily practice of the hospital. The examples were acquired from subjects that agreed with the use of their images for research purposes by a written consent.

A user friendly software was developed to visualize CT exams, to outline freehand ROIs (FH-ROIs), and to label and to characterize each FH-ROI [39]. HRCT scans were acquired using multidetector row CT LightSpeed VCT 64, from General Electric Healthcare, with an average voxel size of $0.7 \times 0.7 \times 1.3\ \text{mm}^3$, without contrast agent. Each image was stored in a matrix of 512 × 512 pixels, with 16-bit gray level, using DICOM standard. Each image was displayed using a lung window with a centre in −700 Hounsfield Units (HU) and a width of 1500 HU. From CT images of 57 subjects (#29 female; #28 male) with an average age of 61 ± 16 years, radiologists outlined FH-ROIs from patients in different stages of disease.

The area and shape of each FH-ROI depend on the size and localization of the lung patterns. No more than one FH-ROI was selected from each side of the lungs. The lung region of each FH-ROI was sampled and covered with contiguous, nonoverlapping ROIs of 40 × 40 pixels [24]. Each FH-ROI was sequentially numbered and each ROI holds the reference of the FH-ROI from where it was extracted. For example, the FH-ROI*x*S*y* corresponds to ROI y extracted from FH-ROI x. Only the ROIs one hundred percent inside the FH-ROI boundary were considered in the train and test of the classifier; all the other ROIs were discarded. For example, in Figure 3 only the ROIs 8, 13, 14, and 18 respect the constraint. Table 1 resumes the dataset used to train and evaluate the proposed CAD system.

2.5. Model Selection and Performance Evaluation. The dataset $\mathscr{D}$ (#1261 ROIs) was divided into a training set and a testing set in a proportion of 2/3–1/3, respectively. The samples were randomly selected using a holdout strategy with stratification, which ensures mutually exclusive partitions where the class proportions are roughly the same as those in the original dataset $\mathscr{D}$ [40]. The holdout procedure was based on FH-ROIs in order to ensure that ROIs extracted from the same FH-ROI are placed on only one of the sets, train or test.

Table 1: Dataset used to train and evaluate the CAD system.

Class	Normal	Ground glass	Honeycombing	Emphysema
Visual aspect	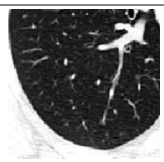	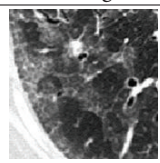	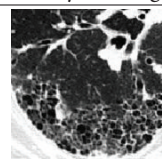	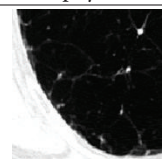
# of patients	16	20	7	14
# of freehand ROIs	87	166	72	92
# of ROIs	253	396	217	395

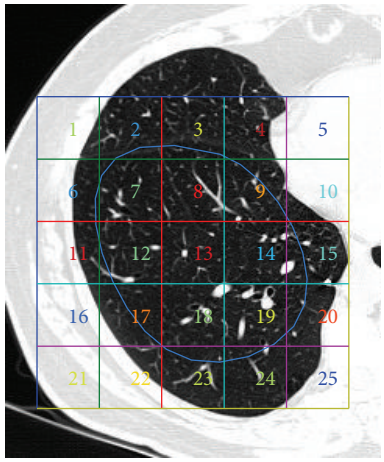

Figure 3: Example of FH-ROI and the grid that allows the extraction of ROIs. Only ROIs of one hundred percent inside FH-ROI boundary were kept.

During SVM training, a search was carried out to find optimal parameters to create the classifier model. In the case of the selected RBF kernel function, the parameters that have to be tuned were σ and C, the regularization parameter that corresponds to a penalty over the training errors. The search for the optimal parameters was done using a grid search methodology in the hyperparameter space. So, for every point of the hyperparameter space, a k-fold stratified cross-validation (CV) was performed, with $k = 10$ [40, 41]. The train set was randomly split into k mutually exclusive folds $F_1, F_2, \ldots, F_k$, with approximately the same proportion of each class as in $\mathcal{D}$. During CV, the classifier was trained and tested k times. In each iteration, it was trained on $k - 1$ folds and tested in the remaining fold F_t, with $t \in \{1, 2, \ldots, k\}$. The average of the k-fold accuracy corresponds to CV accuracy. To avoid the model overfitting, the feature selection procedure was included in CV loop [35]. The parameters and features that allow the best CV accuracy were selected and a fine grid search was carried out around the selected parameters, for refinement. The final classifier model was built using all the training set, the selected features, and the optimal parameters previously found. The obtained model was evaluated in the test set, which was not used during classifier training.

Table 2: Generic contingency table for n-class scenario.

Actual	Predicted		
	Class 1	$\cdots$	Class n
Class 1	a_{11}	$\cdots$	a_{1n}
$\vdots$	$\vdots$	$\ddots$	$\vdots$
Class n	a_{n1}	$\cdots$	a_{nn}

The performance evaluation of the classifier was performed based on a contingency table, as exemplified in Table 2 for n-class. Each matrix element has two indices; the first one corresponds to actual disease, while the second one corresponds to predicted disease. The elements of the main diagonal have equal indices representing correct classifications. All the other elements of the matrix correspond to incorrect classifications. For example, a_{31} means that a patient with disease 3 was misclassified as having disease 1. In the case of a binary classification, there are only normal and pathological classes, in a one-versus-all configuration.

After classification, the contingency table was filled with the obtained results. From these values, it is possible to compute a set of metrics allowing for the evaluation of the classifier performance. A common performance evaluation is overall accuracy, which measures the proportion of correctly classified instances for all the classes. Sensitivity of class i measures the fraction of actual positive instances of that class that are correctly classified, while precision measures the correctness of the predictions for class i. Specificity of class i measures the fraction of actual negative instances of class i that are correctly classified. These metrics can be computed by the following expressions [42]:

$$\begin{aligned}
\text{Sensitivity}\,(i) &= \frac{a_{ii}}{\sum_j a_{ij}},\\
\text{Precision}\,(i) &= \frac{a_{ii}}{\sum_j a_{ji}},\\
\text{Specificity}\,(i) &= \frac{1 - \sum_j a_{ij} - \sum_{j \neq i} a_{ji}}{1 - \sum_j a_{ij}},\\
\text{Overall Accuracy} &= \frac{\sum_{i=j} a_{ij}}{\sum_i \sum_j a_{ij}}.
\end{aligned} \tag{7}$$

2.6. Feature Settings. Each ROI was characterized by a feature vector extracted using FO, SGLDM, GLRLM, and DLac.

The ROIs were quantized to 32 gray levels before the extraction of FO, SGLDM, and GLRLM features. The minimum and maximum HU values were calculated for all ROIs of $\mathscr{D}$ and each ROI was quantized according to this range. In SGLDM and GLRLM, the directions $\theta = \{0^\circ, 45^\circ, 90^\circ, 135^\circ\}$ were considered. In GLDM, the distance between neighboring pixels was $d = 1$, in the four directions.

A multiscale approach was required due to the high variability of the appearance of lung patterns, even for the same pattern. The selected approach to calculate DLac allows a texture analysis at different scales by changing the value of w, for a box size r. The size of the window w determines the coarseness of the scale. The size of r should be relatively small in order to maintain sensitivity to small details present in the neighboring areas. Equation (8) illustrates the proposed approach to extract DLac features:

$$\Lambda(w, r) = \frac{\sum_M M^2 Q(M, r, w)}{\left[\sum_M MQ(M, r, w)\right]^2}. \quad (8)$$

DLac was computed for every box-window combination, subject to the condition $r < w$, in order to evaluate the DLac features that better differentiate the lung patterns. A DLac curve $\Lambda(w, r = \text{const})$ can be obtained by keeping the size of the gliding box r constant and by changing the size of the window w. To assure a common referential, DLac values were normalized in relation to the DLac value corresponding to the smallest window w: $\Lambda(w_{\min}, r = \text{const})$ [43]. In order to take advantage of the extensive scale used in CT images, the curves of normalized DLac were computed using Hounsfield scale [−1000 UH; +1000 UH].

3. Results and Discussion

Two scenarios were considered in order to evaluate the potential of the proposed CAD and the importance of DLac features in the CAD performance improvement. In the first approach, the differentiation between normal and ILD patterns was considered. The next step was the differentiation of the four classes. In both cases, the feature vector was obtained using two different sets. Set 1 includes the features from FO + SGLDM + GLRLM. Set 2 also englobes DLac features.

The DLac features were extracted from DLac normalized curves. Various experiments have been conducted computing DLac curves for every box-window size for $r = [2–34]$ pixels and $w = [3–35]$ pixels. The ability to differentiate the four classes was evaluated. The best results were obtained for DLac normalized curves for $r = 4$ pixels and $w = [5–35]$ pixels.

Figure 4 shows the average of normalized DLac curves for patterns of all the dataset $\mathscr{D}$. The results show that the DLac normalized curves are able to distinguish between lung patterns, being suitable to extract informative features.

The multiclass classification was performed using one-versus-one implementation [44]. In the case of the RBF kernel function, the parameters optimization was performed for the pair (C, σ). First, the parameters were evaluated using a coarse grid for $C = 2^{-5}, 2^{-4.5}, \ldots, 2^{15}$ and

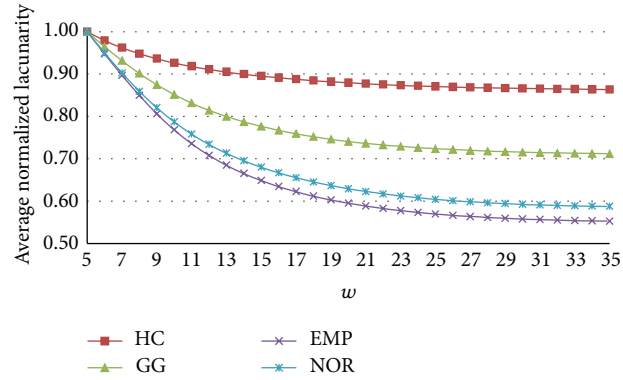

Figure 4: Averaged normalized DLac curves obtained for $r = 4$ pixels and $w = [5–35]$ pixels.

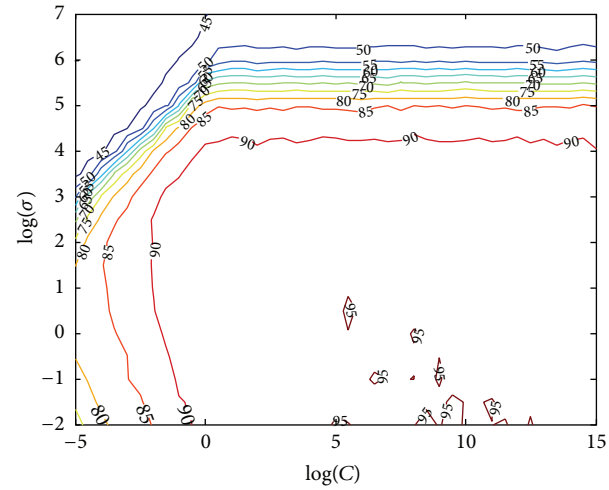

Figure 5: Example of 10-fold CV accuracy (%) obtained along the hyperparameter space for finding optimal parameters (C, σ). Results were obtained using Set 1, for the binary classification scenario.

$\sigma = 2^{-2}, 2^{-1.5}, \ldots, 2^7$. Figure 5 depicts a graphic of contours of CV accuracy, obtained over a 10-fold CV using features of Set 1, for the binary classification scenario. A heuristic analysis of these curves provides a clear understanding of the influence of the parameters in the classifier performance, as well as clues to reduce search space. The results showed the importance of fine tuning the SVM parameters during the classifier training phase to achieve an optimized model. After some experiments, the search grid was reduced to $C = 2^3, 2^{3.5}, \ldots, 2^{13}$ and $\sigma = 2^{-2}, 2^{-1.5}, \ldots, 2^1$. For every coordinate of the hyperparameter space, a k-fold CV was performed, with $k = 10$. In each of the k iterations feature selection was performed (F-test, p value < 0.01) in the $k - 1$ training folds. If the coordinates $(2^c, 2^\sigma)$ generate the best CV accuracy, a finer search was performed around these values with a step of 0.25 upward and downward.

After the classifier training, the selected model was evaluated in the testing set. The training and testing of the classifier were repeated over fifty iterations. So, the training and evaluation of the classifier were performed in fifty different sets.

Table 3: Mean (SD) accuracy, sensitivity, precision, and specificity using Set 1 and Set 2, for the binary classification (normal versus pathologic). Values in percentage, obtained for 50 iterations.

	Set 1	Set 2
Accuracy	94.4 (2.0)	95.8 (2.2)
Sensitivity	96.7 (1.2)	97.9 (1.1)
Precision	96.0 (2.1)	96.9 (2.1)
Specificity	84.8 (8.6)	88.1 (8.0)

Table 4: Mean (SD) of class-specific sensitivity, precision, and specificity using Set 1, for the multiclass classification. Values in percentage, obtained for 50 iterations.

	Classes			
	NOR	GG	HC	EMP
Sensitivity	87.2 (4.6)	92.5 (2.4)	89.4 (4.6)	96.9 (1.7)
Precision	89.6 (3.8)	84.7 (4.5)	93.5 (2.6)	99.8 (0.5)
Specificity	97.3 (1.1)	93.4 (2.3)	98.6 (4.6)	99.9 (0.2)

The presented metrics are the average of the results obtained over all the iterations.

In the binary classification scenario, the ROIs with normal pattern (#253) were considered as negative instances and the other ones as positive instances (#1008). In Table 3, the mean and standard deviation (SD) of overall accuracy, sensitivity, precision, and specificity are shown. The classifier performance obtained using features of Set 1 was 94.4 ± 2.0% for accuracy, 96.7 ± 1.2% for sensitivity, 96.0 ± 2.1% for precision, and 84.8 ± 8.6% for specificity. Using Set 2, the results increased to 95.8 ± 2.2% for accuracy, 97.9 ± 1.1% for sensitivity, 96.9 ± 2.1% for precision, and 88.1 ± 8.0% for specificity. High sensitivity and small SD values showed that the proposed CAD has the ability to signal the presence of abnormal patterns using both sets of features; that is, the number of false negatives is low. The integration of DLac features has primarily increased the specificity value, 3.3% on average, reducing the number of false positives. However, the SD value remains high (8.0). The correct classification of NOR class instances is not easy due the high variability of healthy lung tissue.

The classifier performance in the multiclass scenario was also improved using Set 2 (Tables 4 and 5). The overall accuracy increased from 91.9±1.9% to 94.5±2.1%. Moreover, the class-specific metrics for NOR, GG, and HC improved in a higher or lower percentage. For class EMP sensitivity slightly increased from 96.9% to 97.3%, the precision and the specificity maintained excellent values of 99.9%. Sensitivity of NOR class was the metric that most improved with a mean increase of about 5.3%, changing from 87.2% to 92.5%. In the case of NOR class these results mean that class-specific false negatives decreased; that is, the number of instances of NOR class that were categorized as pathological instances is smaller. In a clinical environment, this means that fewer patients are subjected to the stress of unnecessary additional medical exams. NOR class-specific precision and specificity improved from 89.6% to 92.3% and from 97.3% to 97.9%, respectively. These results mean that the number of false positives for NOR class, that is, pathological instances classified as normal, decreased with Set 2. This type of misclassification has a serious meaning; that is, the CAD system does not signal the presence of a pathological pattern. The number of false negatives and false positives of GG and HC classes also decreased with the presence of DLac features increasing the correct classification of GG and HC instances. SD decreases in all metrics and classes, except for sensitivity of EMP class. So, the DLac features also improved the classifier stability.

Table 5: Mean (SD) of class-specific sensitivity, precision, and specificity using Set 2, for the multiclass classification. Values in percentage, obtained for 50 iterations.

	Classes			
	NOR	GG	HC	EMP
Sensitivity	92.5 (3.8)	96.7 (3.0)	92.3 (4.0)	97.3 (1.8)
Precision	92.3 (3.4)	88.9 (3.9)	97.5 (2.5)	99.9 (0.3)
Specificity	97.9 (1.1)	95.2 (1.8)	99.5 (4.0)	99.9 (0.1)

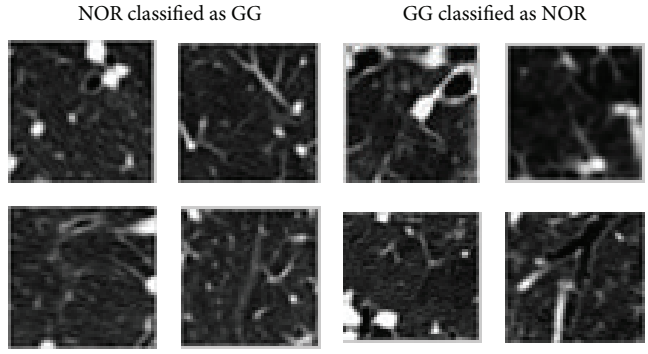

Figure 6: Examples of misclassified ROIs between GG and NOR classes.

The highest percentage of misclassified examples occurred among NOR and GG classes. Almost fifty percent (47.8%) of all the classification errors were due to incorrect classifications between these two classes. Figure 6 illustrates some random examples of normal ROIs that were classified as GG, on left column, and examples of ROIs with GG pattern that were classified as NOR, on right column. Although GG opacities are characterized by areas of increased attenuation, sometimes they are not dense enough to "hide" the bronchovascular markings, especially in the initial phases of ILD diseases, associated with the presence of GG patterns.

4. Conclusions

A CAD scheme applied to HRCT images of the chest was proposed for the classification of healthy lung regions and with the presence of ILD. A texture analysis was performed to describe the lung patterns in study. Texture information of each ROI was represented by features extracted using a multiscale DLac approach combined with features obtained by classical statistical texture analysis methods. Feature selection and SVM training was performed over a 10-fold stratified

CV. The performance evaluation of the classifier model was assessed using an independent test set.

Experimental results showed that DLac features improve the performance of the proposed CAD system in both suggested scenarios: normal versus pathological and multiclass. In this case, the number of false negatives and false positives of NOR class decreased, as well as the misclassification between instances of pathological classes. Differentiating the normal pattern from pathological patterns, the classifier accuracy improved with an average of 1.4% when DLac features were considered, resulting in a correct classification of 95.8 ± 2.2% of all instances. In the multiclass scenario the overall accuracy was improved from 91.9 ± 1.9% to 94.5 ± 2.1% due to the presence of DLac features. The performance of the proposed CAD highlights the good discriminatory properties of extracted DLac features, making it suitable to integrate clinical applications for the classification of patterns associated with ILD.

Conflict of Interests

The authors declare that they have no conflict of interests.

Acknowledgments

The authors thank Dr. Luísa Teixeira and Dr. Miguel Sêco from Radiology Department of Coimbra Hospital and Universitary Centre, for their medical knowledge and assistance. This work is financed by the FCT-Fundação para a Ciência e a Tecnologia (Portuguese Foundation for Science and Technology) within Project UID/EEA/50014/2013.

References

[1] E. A. Hoffman, J. M. Reinhardt, M. Sonka et al., "Characterization of the interstitial lung diseases via density-based and texture-based analysis of computed tomography images of lung structure and function," *Academic Radiology*, vol. 10, no. 10, pp. 1104–1118, 2003.

[2] J. A. Verschakelen and W. D. Wever, *Computed Tomography of the Lung—A Pattern Approach*, Springer, Berlin, Germany, 2007.

[3] I. Sluimer, A. Schilham, M. Prokop, and B. Van Ginneken, "Computer analysis of computed tomography scans of the lung: a survey," *IEEE Transactions on Medical Imaging*, vol. 25, no. 4, pp. 385–405, 2006.

[4] R. Uppaluri, E. A. Hoffman, M. Sonka, P. G. Hartley, G. W. Hunninghake, and G. McLennan, "Computer recognition of regional lung disease patterns," *American Journal of Respiratory and Critical Care Medicine*, vol. 160, no. 2, pp. 648–654, 1999.

[5] A. Depeursinge, J. Iavindrasana, A. Hidki et al., "Comparative performance analysis of state-of-the-art classification algorithms applied to lung tissue categorization," *Journal of Digital Imaging*, vol. 23, no. 1, pp. 18–30, 2010.

[6] W. Zhao, R. Xu, Y. Hirano, R. Tachibana, and S. Kido, "Classification of diffuse lung diseases patterns by a sparse representation based method on HRCT images," in *Proceedings of the 35th Annual International Conference of the IEEE Engineering in Medicine and Biology Society*, pp. 5457–5460, IEEE, July 2013.

[7] M. Anthimopoulos, S. Christodoulidis, A. Christe, and S. Mougiakakou, "Classification of interstitial lung disease patterns using local DCT features and random forest," in *Proceedings of the 36th Annual International Conference of the IEEE Engineering in Medicine and Biology Society (EMBC '14)*, pp. 6040–6043, IEEE, Chicago, Ill, USA, August 2014.

[8] M. Anthimopoulos, S. Christodoulidis, A. Christe, and S. Mougiakakou, "Computer-aided diagnosis of interstitial lung diseases based on computed tomography image analysis," in *Computational Optical Biomedical Spectroscopy and Imaging*, pp. 175–200, CRC Press, 2015.

[9] S. Delorme, M.-A. Keller-Reichenbecher, I. Zuna, W. Schlegel, and G. Van Kaick, "Usual interstitial pneumonia: quantitative assessment of high-resolution computed tomography findings by computer-assisted texture-based image analysis," *Investigative Radiology*, vol. 32, no. 9, pp. 566–574, 1997.

[10] S. Delorme, M. A. Keller-Reichenbecher, I. Zuna, W. Schlegel, and G. V. Kaick, "Interstitial lung disease a quantitative study using the adaptive multiple feature method," *American Journal of Respiratory and Critical Care Medicine*, vol. 159, no. 2, pp. 519–1073, 1999.

[11] F. Chabat, G.-Z. Yang, and D. M. Hansell, "Obstructive lung diseases: texture classification for differentiation at CT," *Radiology*, vol. 228, no. 3, pp. 871–877, 2003.

[12] I. C. Sluimer, P. F. van Waes, M. A. Viergever, and B. van Ginneken, "Computer-aided diagnosis in high resolution CT of the lungs," *Medical Physics*, vol. 30, no. 12, pp. 3081–3090, 2003.

[13] Y. Xu, M. Sonka, G. McLennan, A. J. Guo, and E. A. Hoffmam, "Computer-aided classification of interstitial lung diseases via MDCT: 3D adaptive multiple feature method (3D AMFM)," *IEEE Transactions on Medical Imaging*, vol. 16, no. 8, pp. 969–987, 2006.

[14] A. Zaia, R. Eleonori, P. Maponi, R. Rossi, and R. Murri, "MR imaging and osteoporosis: fractal lacunarity analysis of trabecular bone," *IEEE Transactions on Information Technology in Biomedicine*, vol. 10, no. 3, pp. 484–489, 2006.

[15] A. Zaia, "Fractal lacunarity of trabecular bone and magnetic resonance imaging: new perspectives for osteoporotic fracture risk assessment," *World Journal of Orthopedics*, vol. 6, no. 2, pp. 221–235, 2015.

[16] O. S. Al-Kadi and D. Watson, "Texture analysis of aggressive and nonaggressive lung tumor CE CT images," *IEEE Transactions on Biomedical Engineering*, vol. 55, no. 7, pp. 1822–1830, 2008.

[17] V. S. Charisis, L. J. Hadjileontiadis, and G. D. Sergiadis, "Enhanced ulcer recognition from capsule endoscopic images using texture analysis," in *New Advances in the Basic and Clinical Gastroenterology*, T. Brzozowski, Ed., pp. 185–210, InTech, Rijeka, Croatia, 2012.

[18] V. Vasconcelos, L. Marques, J. S. Silva, and J. Barroso, "Lacunarity analysis of pulmonary emphysema in high-resolution CT images," in *Proceedings of the 8th Iberian Conference on Information Systems and Technologies (CISTI '13)*, pp. 1–5, Lisboa, Portugal, June 2013.

[19] V. N. Vapnik, *The Nature of Statistical Learning Theory*, Springer, New York, NY, USA, 1995.

[20] C. J. C. Burges, "A tutorial on support vector machines for pattern recognition," *Data Mining and Knowledge Discovery*, vol. 2, no. 2, pp. 121–167, 1998.

[21] D. Meyer, F. Leisch, and K. Hornik, "The support vector machine under test," *Neurocomputing*, vol. 55, no. 1-2, pp. 169–186, 2003.

[22] R. C. Gonzalez and R. E. Woods, *Digital Image Processing*, Addison-Wesley, New York, NY, USA, 2nd edition, 2002.

[23] R. Haralick, K. Shanmugam, and I. H. Dinstein, "Textural features for image classification," *IEEE Transactions on Systems, Man, and Cybernetics*, vol. 3, no. 6, pp. 6l0–621, 1973.

[24] V. Vasconcelos, J. Silva, L. Marques, and J. Barroso, "Statistical textural features for classification of lung emphysema in CT images: a comparative study," in *Proceedings of the 5th Iberian Conference on Information Systems and Technologies*, pp. 1–5, Santiago de Compostela, Spain, June 2010.

[25] M. M. Galloway, "Texture analysis using gray level run lengths," *Computer Graphics and Image Processing*, vol. 4, no. 2, pp. 172–179, 1975.

[26] A. Chu, C. M. Sehgal, and J. F. Greenleaf, "Use of gray value distribution of run lengths for texture analysis," *Pattern Recognition Letters*, vol. 11, no. 6, pp. 415–419, 1990.

[27] B. V. Dasarathy and E. B. Holder, "Image characterizations based on joint gray level—run length distributions," *Pattern Recognition Letters*, vol. 12, no. 8, pp. 497–502, 1991.

[28] B. B. Mandelbrot, *The Fractal Geometry of Nature*, Freeman, New York, NY, USA, 1983.

[29] B. B. Mandelbrot, "A fractal's lacunarity, and how it can be tuned and measured," in *Fractals in Biology and Medicine*, T. F. Nonnenmacher, G. A. Losa, and E. R. Weibel, Eds., Mathematics and Biosciences in Interaction, pp. 8–21, Birkhäuser, Boston, Mass, USA, 1994.

[30] Y. Gefen, Y. Meir, B. B. Mandelbrot, and A. Aharony, "Geometric implementation of hypercubic lattices with noninteger dimensionality by use of low lacunarity fractal lattices," *Physical Review Letters*, vol. 50, no. 3, pp. 145–148, 1983.

[31] R. E. Plotnick, R. H. Gardner, W. W. Hargrove, K. Prestegaard, and M. Perlmutter, "Lacunarity analysis: a general technique for the analysis of spatial patterns," *Physical Review E*, vol. 53, no. 5, pp. 5461–5468, 1996.

[32] P. Dong, "Test of a new lacunarity estimation method for image texture analysis," *International Journal of Remote Sensing*, vol. 21, no. 17, pp. 3369–3373, 2000.

[33] C. Allain and M. Cloitre, "Characterizing the lacunarity of random and deterministic fractal sets," *Physical Review A*, vol. 44, no. 6, pp. 3552–3558, 1991.

[34] N. Sarkar and B. B. Chaudhuri, "An efficient approach to estimate fractal dimension of textural images," *Pattern Recognition*, vol. 25, no. 9, pp. 1035–1041, 1992.

[35] G. Dreyfus and I. Guyon, "Assessment methods," in *Feature Extraction: Foundations and Applications*, I. Guyon, M. Nikravesh, S. Gunn, and L. A. Zadeh, Eds., vol. 207 of *Studies in Fuzziness and Soft Computing: I*, pp. 65–86, Springer, Berlin, Germany, 2006.

[36] N. R. Draper and H. Smith, *Applied Regression Analysis*, Wiley-Interscience, Hoboken, NJ, USA, 1998.

[37] C. Cortes and V. Vapnik, "Support-vector networks," *Machine Learning*, vol. 20, no. 3, pp. 273–297, 1995.

[38] C.-W. Hsu and C.-J. Lin, "A comparison of methods for multiclass support vector machines," *IEEE Transactions on Neural Networks*, vol. 13, no. 2, pp. 415–425, 2002.

[39] V. Vasconcelos, J. S. Silva, and J. Barroso, "CAD lung system: texture based classifier of pulmonary pathologies," in *Proceedings of the 8th Iberian Conference on Information Systems and Technologies*, pp. 383–386, June 2009.

[40] R. Kohavi, "A study of cross-validation and bootstrap for accuracy estimation and model selection," in *Proceedings of the 14th International Joint Conference on Artificial Intelligence (IJCAI '95)*, vol. 2, pp. 1137–1143, Montreal, Canada, August 1995.

[41] G. C. Cawley and N. L. Talbot, "On over-fitting in model selection and subsequent selection bias in performance evaluation," *Journal of Machine Learning Research*, vol. 11, pp. 2079–2107, 2010.

[42] Y. Lee, J. B. Seo, J. G. Lee, S. S. Kim, N. Kim, and S. H. Kang, "Performance testing of several classifiers for differentiating obstructive lung diseases based on texture analysis at high-resolution computerized tomography (HRCT)," *Computer Methods and Programs in Biomedicine*, vol. 93, no. 2, pp. 206–215, 2009.

[43] L. J. Hadjileontiadis, "A texture-based classification of crackles and squawks using lacunarity," *IEEE Transactions on Biomedical Engineering*, vol. 56, no. 3, pp. 718–732, 2009.

[44] C.-C. Chang and C.-J. Lin, "LIBSVM: a Library for support vector machines," *ACM Transactions on Intelligent Systems and Technology*, vol. 2, no. 3, article 27, 2011.

Hindawi Publishing Corporation
BioMed Research International
Volume 2015, Article ID 154614, 13 pages
http://dx.doi.org/10.1155/2015/154614

Research Article

A Novel Statistical Approach for Brain MR Images Segmentation Based on Relaxation Times

Fabio Baselice,[1] Giampaolo Ferraioli,[2] and Vito Pascazio[1]

[1]*Dipartimento di Ingegneria, Università di Napoli Parthenope, Centro Direzionale di Napoli, Isola C4, 80143 Napoli, Italy*
[2]*Dipartimento di Scienze e Tecnologie, Università di Napoli Parthenope, Centro Direzionale di Napoli, Isola C4, 80143 Napoli, Italy*

Correspondence should be addressed to Fabio Baselice; fabio.baselice@uniparthenope.it

Received 11 September 2015; Revised 19 November 2015; Accepted 29 November 2015

Academic Editor: Jinyuan Zhou

Brain tissue segmentation in Magnetic Resonance Imaging is useful for a wide range of applications. Classical approaches exploit the gray levels image and implement criteria for differentiating regions. Within this paper a novel approach for brain tissue joint segmentation and classification is presented. Starting from the estimation of proton density and relaxation times, we propose a novel method for identifying the optimal decision regions. The approach exploits the statistical distribution of the involved signals in the complex domain. The technique, compared to classical threshold based ones, is able to globally improve the classification rate. The effectiveness of the approach is evaluated on both simulated and real datasets.

1. Introduction

In Magnetic Resonance Imaging (MRI) field, tissues segmentation can be helpful in several applications, such as image-guided interventions, surgical planning, and radiotherapy, but also in 2D/3D visualization, studying brain diseases, or clinical drug trials [1–3]. The aim of segmentation consists in identifying the different regions across the imaged slice. A step ahead is the classification which assigns each region to a class; that is, it identifies the involved tissues.

In this paper we restrict the analysis to MR images of brain. In this case, segmentation is a fundamental tool in quantification of white matter lesions in case of drug treatment assessment or in the study of temporal evolution of many disorders, such as multiple sclerosis, schizophrenia, epilepsy, or Alzheimer's disease. In particular, segmentation is able to provide the volumetric analysis of gray matter, white matter, and cerebrospinal fluid and to allow the morphological differences characterization between subjects.

Few decades ago, the manual delineation of MR images by a human expert was the main tool for segmenting tissues. Unfortunately, this approach is characterized by several disadvantages: the accurate delineation of complex 3D anatomical structures was very complex, results had a considerable inter- and intrarater variability, and it was very time consuming [4]. So in last decades big efforts for achieving effective automated procedures have been done [5].

Automatic segmentation techniques belong to two main categories: structural and statistical [6]. The former one is based on the recognition of anatomical shapes across the image, while the latter takes into account the statistical distribution of the acquired data. Among these two categories, the most used approaches are classification-based segmentation, region-based segmentation, and contour-based segmentation. Within this paper, we focus on classification-based approaches, that is, jointly segment and classify tissues across the imaged slice. In this kind of approach, voxels are classified and labeled as belonging to a particular tissue class according to a certain criterion. The simplest method is based on the application of a threshold. While this is a trivial operation, the determination of the proper thresholding value has to be carefully done. Thresholds are applied to a metric, which generally is the Euclidean distance of pixel gray level values. Basic approaches consider the Gaussian mixture model of tissues signal intensities, that is, a one-dimensional problem. If a proper postprocessing is not implemented, such approach produces poor results in case of low Signal to Noise Ratio (SNR) and tissues with similar signal intensities. Moreover, several artifacts could affect the images, such as the intensity

inhomogeneity that makes the ranges of the intensities in the regions to segment overlapped [7].

Within this paper we propose a brain joint segmentation and classification algorithm based on proton density (ρ) and relaxation times (T_1 and T_2), instead of the acquired gray level image. The idea of exploiting relaxation times for improving segmentation performances is not new, as methods based on single or multiple weighted images have been presented [4, 8]. The main limit of these approaches consists in computing the segmentation in a monodimensional space and eventually joining the results as a postprocessing step. What we propose is a segmentation in a 3D space, jointly based on ρ, T_1, and T_2 maps and not on weighted images. The physical parameters are first estimated from multiple acquired images and then used for the segmentation. As each voxel is segmented by considering three values (ρ, T_1, and T_2) instead of one (gray level), the approach works projecting each voxel in a 3D space (with coordinates ρ, T_1, and T_2) instead of a 1D one (with the gray level value as coordinate), proposing a new distance criterion, often referred to as metric. From a geometrical point of view, the projection of image points in a 3D space instead of a 1D line enlarges the distances between classes, making the segmentation and classification operations more accurate. In particular, the greater distances due to the 3D space are expected to reduce the wrong segmented points percentage. For the proposed approach, the ideal thresholds of the segmentation regions, which in this case are 3D curves, are automatically determined starting from the joint statistical distribution of the ρ, T_1, and T_2 estimators. The proposed metric is expected to have potentialities also in different frameworks, such as Magnetic Resonance Fingerprinting, which is capable of estimating proton density, T_1 and T_2, in a single scan [9].

Results on a simulated dataset are used to assess and quantitatively evaluate the proposed methodology. Results on a real dataset are used to show the effectiveness of the approach if compared with a standard distance based threshold technique, its robustness to intensity inhomogeneity fields, and its potentialities.

2. Methodology

Let us consider an MRI acquisition system using a Spin Echo imaging sequence. The amplitude of the recorded complex signal after image formation process, that is, after the computation of the 2D Fourier Transform, is related to the tissues parameters ρ, T_1, and T_2. By considering a single pixel, that is, one voxel of the slice, its intensity can be written as [10, 11]

$$f(\boldsymbol{\theta}) = \rho \exp\left(-\frac{T_E}{T_2}\right)\left(1 - \exp\left(-\frac{T_R}{T_1}\right)\right), \tag{1}$$

where T_E and T_R are the echo and repetition time, respectively, which are two imaging parameters that can be set in the MRI scanner and $\boldsymbol{\theta} = [\rho \;\; T_1 \;\; T_2]^T$ is the vector containing the tissue parameters we are interested in. The acquisition model reported in (1) is related to the noise-free case. Considering noise, in the complex domain the model becomes

$$y = y_R + iy_I = f(\boldsymbol{\theta}) \exp(i\phi) + (n_R + in_I), \tag{2}$$

where n_R and n_I are the real and imaginary parts of the noise samples, which are distributed as independent circularly Gaussian variables [12], and ϕ represents the angle of the complex data [13, 14].

We can estimate $\boldsymbol{\theta}$ by implementing an LS estimator [15, 16]:

$$\widehat{\boldsymbol{\theta}} = \arg\min_{\boldsymbol{\theta}} \sum_{k=1}^{M} \left(y_k - f(\boldsymbol{\theta}) e^{i\phi}\right), \tag{3}$$

where M is the number of images acquired with different T_E/T_R combinations.

As it is largely known from statistical estimation theory, in case of Gaussian noise, the LS estimator corresponds to the Maximum Likelihood (ML) one. So, if M is sufficiently large, the estimator becomes unbiased and optimal. This allows us to infer the statistical distribution of the estimated values $\widehat{\rho}$, $\widehat{T_1}$, and $\widehat{T_2}$. In particular, the estimators will be Gaussian distributed with known means and variances. As the estimators are unbiased the mean values μ_ρ, μ_{T_1}, and μ_{T_2} are equal to the unknown parameters, while, since they are optimal, the variances σ^2_ρ, $\sigma^2_{T_1}$, and $\sigma^2_{T_2}$ coincide with Cramer Rao Lower Bounds (CRLBs). Such bounds are related to the acquisition model and to involved noise and represent the lower achievable variance of any unbiased estimator, that is, a quality metric. In the considered acquisition model, CRLBs can be easily calculated numerically or analytically [17].

Thus, the statistical distributions of the random variables $\widehat{\rho}$, $\widehat{T_1}$, and $\widehat{T_2}$ are

$$\begin{aligned}
f_{\widehat{\rho}}(\widehat{\rho}) &= \frac{1}{\sqrt{2\pi\sigma^2_\rho}} \exp\left(-\frac{\left(\widehat{\rho} - \mu_\rho\right)^2}{2\sigma^2_\rho}\right),\\
f_{\widehat{T_1}}(\widehat{t_1}) &= \frac{1}{\sqrt{2\pi\sigma^2_{T_1}}} \exp\left(-\frac{\left(\widehat{t_1} - \mu_{T_1}\right)^2}{2\sigma^2_{T_1}}\right),\\
f_{\widehat{T_2}}(\widehat{t_2}) &= \frac{1}{\sqrt{2\pi\sigma^2_{T_2}}} \exp\left(-\frac{\left(\widehat{t_2} - \mu_{T_2}\right)^2}{2\sigma^2_{T_2}}\right).
\end{aligned} \tag{4}$$

In case different tissues are imaged within the same slice, the pdfs of each tissue have to be taken into account.

Starting from these distributions, the idea of the presented method consists in exploiting such pdfs, in order to find the optimal decision regions in a 3D space for joint segmentation and classification.

Within this framework, three different decision criteria have been developed, which are presented in the following.

2.1. Weighted Distance Based Criterion (WDC). By considering $\widehat{\rho}$, $\widehat{T_1}$, and $\widehat{T_2}$ estimators to be independent, we can derive the joint pdf by factorizing the marginal pdfs reported in

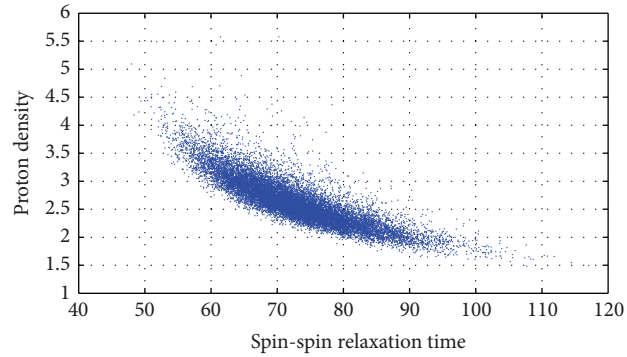

FIGURE 1: Estimated values projected on the (ρ, T_2) plane. T_2 values are in [ms]. Correlation between $\widehat{\rho}$ and $\widehat{T_2}$ estimators is −0.8443.

(4). A detector aimed at the maximization of the likelihood function has been implemented. This is equivalent to the maximization of the joint pdf or to the minimization of the negative exponential part:

$$\arg\min_{n} \left\{ \frac{\left[\widehat{\rho} - \boldsymbol{\mu}_{\rho}(n)\right]^2}{2\boldsymbol{\sigma}_{\rho}^2(n)} + \frac{\left[\widehat{t_1} - \boldsymbol{\mu}_{T_1}(n)\right]^2}{2\boldsymbol{\sigma}_{T_1}^2(n)} + \frac{\left[\widehat{t_2} - \boldsymbol{\mu}_{T_2}(n)\right]^2}{2\boldsymbol{\sigma}_{T_2}^2(n)} \right\}, \tag{5}$$

where $\boldsymbol{\mu}_{\rho}(n)$, $\boldsymbol{\mu}_{T_1}(n)$, and $\boldsymbol{\mu}_{T_2}(n)$ are the mean values of ρ, T_1, and T_2 estimators in case of the nth ($n = 1, \ldots, N$) class, while $\boldsymbol{\sigma}_{\rho}(n)$, $\boldsymbol{\sigma}_{T_1}(n)$, and $\boldsymbol{\sigma}_{T_2}(n)$ are their variances. In case of brain segmentation, $N = 3$ classes are commonly assumed: white matter (WM), gray matter (GM), and cerebrospinal fluid (CSF).

It can be noted that such criterion consists in assigning to each pixel the class related to the closest segmentation region centroid. This centroid is defined according to reference proton density and relaxation times values of involved tissues, which are reported in literature [18]. The distance is computed by considering as weights for ρ, T_1, and T_2 differences the inverse of variances of their estimators (i.e., σ_{ρ}^2, $\sigma_{T_1}^2$, and $\sigma_{T_2}^2$), which ensures that reliable values have a higher weight. A crucial point is the computation of weights: a good choice could be the Cramer Rao Lower Bounds (CRLBs) [17].

Practically, WDC approach, by evaluating the minimum distance class via (5), is equivalent to finding the class assignment with the highest probability. However, in some cases CRLBs are not the ideal choice because of external sources of noise. Often acquired images suffer from intensity inhomogeneity, which could be related to various factors, such as spatial variations in illumination and imperfections of imaging devices [7, 19, 20]. In the estimation of proton density and relaxation times, only the first one is affected by such problem, since T_1 and T_2 are related to a specific decay and thus are independent of the presence of an intensity bias. In this case, it is more effective to rely more on relaxation times than on the proton density. This can be achieved by applying a coefficient to σ_{ρ}^2. In other words, the segmentation is conducted by considering the ρ distance not as much reliable as T_1 and T_2. The weighting coefficient should be manually applied only in case of evident bias.

2.2. Statistical Correlation Based Criterion (StCC). The WDC is based on the assumption of statistical independence among the three estimators. Such hypothesis can be used in a simplified model. In order to generalize the approach, the mutual correlation among $\widehat{\rho}$, $\widehat{T_1}$, and $\widehat{T_2}$ has to be taken into account. To give an idea of such correlation, a Monte Carlo simulation has been considered. In each cycle, proton density and spin-spin relaxation time of a voxel are estimated. In Figure 1, one blue point for each Monte Carlo cycle is reported in a 2D Cartesian space. In particular, estimated T_2 is the horizontal axis coordinate, while estimated ρ is the vertical one. By looking at these projections of the estimators in (ρ, T_2) plane, we can easily note that a nonminimal correlation is present, as the cloud of points is not circular. The exploitation of such correlation leads to statistical correlation based criterion (StCC). In this case the covariance matrix $\boldsymbol{\Sigma}$ of multivariate Gaussian statistical distribution will be fully populated, leading to the following decision criterion:

$$\arg\min_{n} \left[\widehat{\mathbf{x}} - \boldsymbol{\mu}(n)\right]^T \boldsymbol{\Sigma} \left[\widehat{\mathbf{x}} - \boldsymbol{\mu}(n)\right] \tag{6}$$

with

$$\widehat{\mathbf{x}} = \begin{bmatrix} \widehat{\rho} \\ \widehat{T_1} \\ \widehat{T_2} \end{bmatrix},$$

$$\boldsymbol{\mu}(n) = \begin{bmatrix} \boldsymbol{\mu}_{\rho}(n) \\ \boldsymbol{\mu}_{T_1}(n) \\ \boldsymbol{\mu}_{T_2}(n) \end{bmatrix}, \tag{7}$$

$$\boldsymbol{\Sigma} = \begin{bmatrix} \sigma_{\rho}^2 & \mathrm{Cov}_{\rho,T_1} & \mathrm{Cov}_{\rho,T_2} \\ \mathrm{Cov}_{\rho,T_1} & \sigma_{T_1}^2 & \mathrm{Cov}_{T_1,T_2} \\ \mathrm{Cov}_{\rho,T_2} & \mathrm{Cov}_{T_1,T_2} & \sigma_{T_2}^2 \end{bmatrix},$$

where $\mathrm{Cov}_{i,j}$ is the covariance between the estimators of i and j parameters. Note that also $\boldsymbol{\Sigma}$ depends on tissue index n, but it has been neglected in the notation.

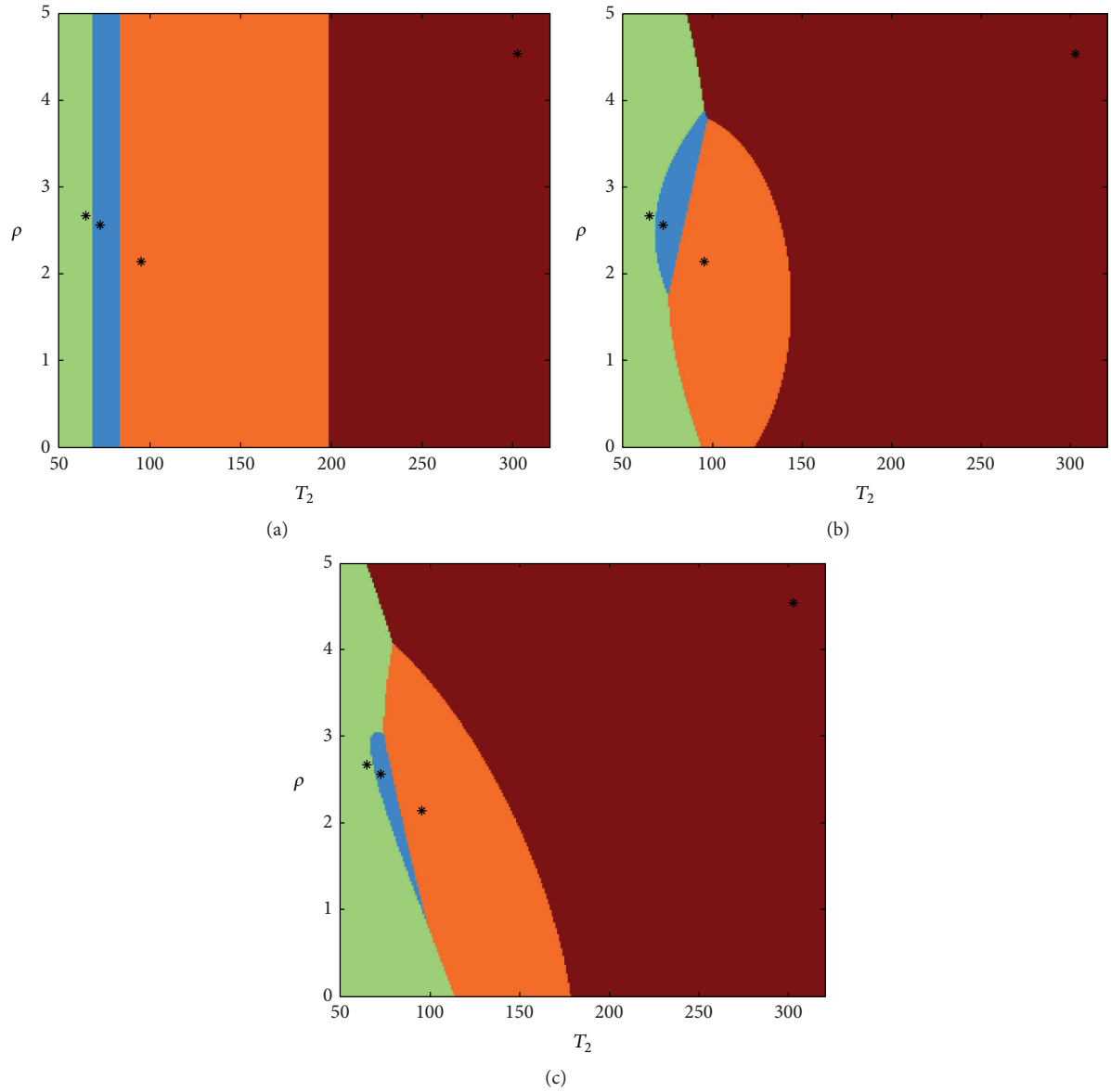

FIGURE 2: Decision regions computed with the minimum Euclidean distance criterion (a), with WDC (b), and with StCC (c). For each region, the centroid has been marked by an asterisk.

In this case, segmentation and classification are performed by minimizing (6). In order to give an idea of how the classification regions change when adopting such criteria, a comparison is reported in Figure 2. In this figure, four reference tissues are considered with different ρ-T_2 combinations (we considered the 2D case instead of the 3D, neglecting T_1 for simplicity); each one is characterized by an asterisk. For each point of the space, that is, for each ρ-T_2 pair, the distances from the four reference tissues are computed with the proposed metrics, and it is marked with a color corresponding to the closest class, providing the regions reported in Figure 2.

2.3. Spatial Correlation Based Criterion (SpCC). In order to improve results, a probabilistic regularization criterion has also been considered. Until now, detection and segmentation have been done by considering each pixel independently of

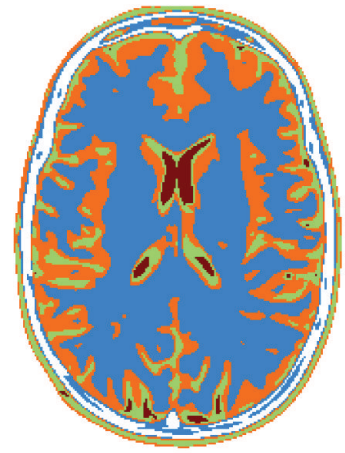

FIGURE 3: Reference head phantom composed of color coded 4 tissues.

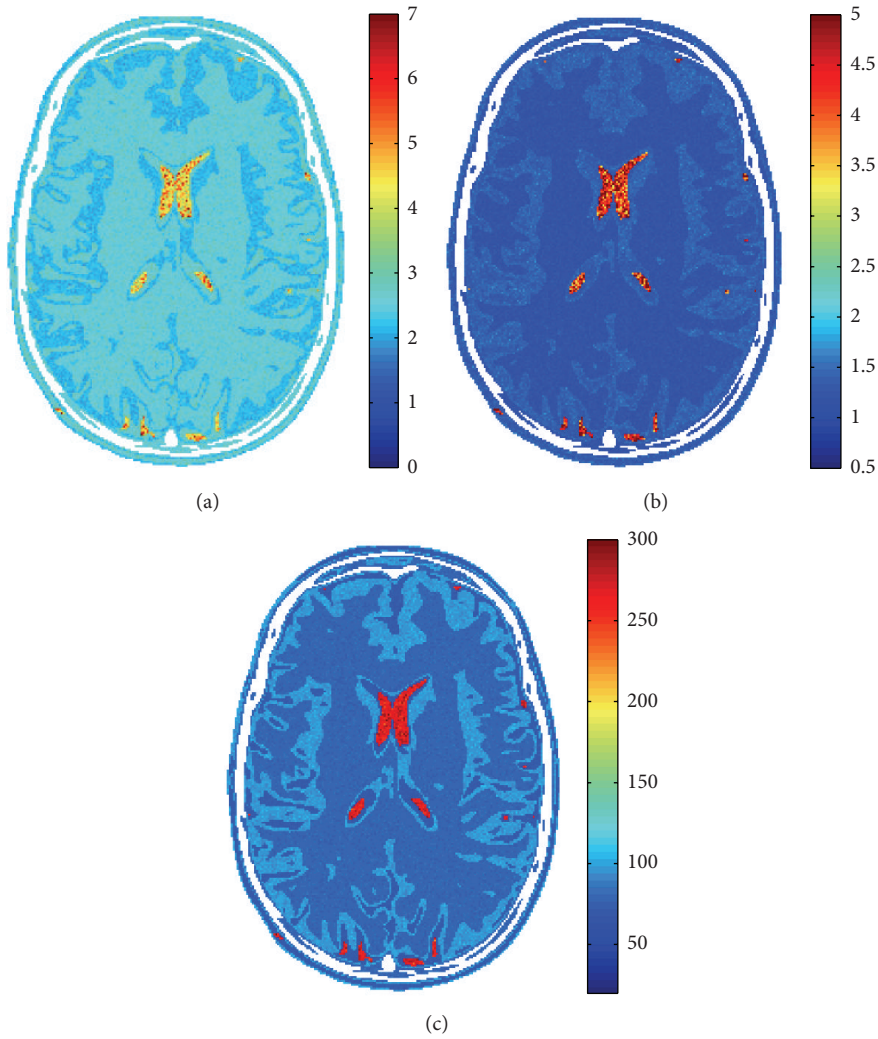

FIGURE 4: Estimated ρ (a), T_1 [s] (b), and T_2 [ms] (c) in case of 4 images and SNR = 30 dB.

all the others, that is, working pixelwise. Here we introduce a spatial dependency between each pixel and its neighborhood with the aim of improving the accuracy.

The spatial correlation based criterion (SpCC) is intended as a refinement of StCC solution. The processing chain consists in a two-step procedure: compute the StCC distances and the related classification and regularize using spatial correlation.

Let us focus on a single pixel and define a neighboring system Ω. It collects all the pixels that are close to the considered one. A typical Ω is the 8 neighbors, collecting the 8 adjacent pixels (i.e., the considered pixel is positioned in the center of a 3×3 window) [21].

Once StCC has been applied, we define d_0 as the minimum distance between the considered pixel and the centroid of the class assigned to it. We, also, define $\mathbf{p}(n)$ as the percentage of the pixels in Ω that have been associated with nth class. The idea is that if the majority of neighboring pixels belong to the same class, the distance from that class should be shortened in order to regularize the solution. As the distance cannot be negative, the reduction should be at most equal to the minimal distance d_0. Thus, the joint segmentation and classification are carried out by computing:

$$\arg \min_n \left\{ \left[\hat{\mathbf{x}} - \boldsymbol{\mu}(n) \right]^T \boldsymbol{\Sigma} \left[\hat{\mathbf{x}} - \boldsymbol{\mu}(n) \right] - \mathbf{p}(n)\, d_0 \right\}, \quad (8)$$

where the vector $\mathbf{p}(n)d_0$ is the metric reduction function for all classes. Note that its values are between 0 and d_0, as the probability values in $\mathbf{p}(n)$ are in the $[0, 1]$ range.

3. Results and Discussion

In order to quantitatively evaluate the advantage of the proposed method with respect to classical unsupervised criteria, a simulated case study has been considered. In particular, a brain slice phantom has been simulated [22]. Four tissues compose the phantom (white matter, subcortical white matter, gray matter, and cerebro spinal fluid) with $\rho = [2.56, 2.67, 2.14, 4.54]$, $T_1 = [1389, 1593, 1794, 7446]$ ms, and $T_2 = [72.4, 65.5, 95.2, 302]$ ms. Such values have been measured experimentally with a 3T scanner [23, 24]. A study

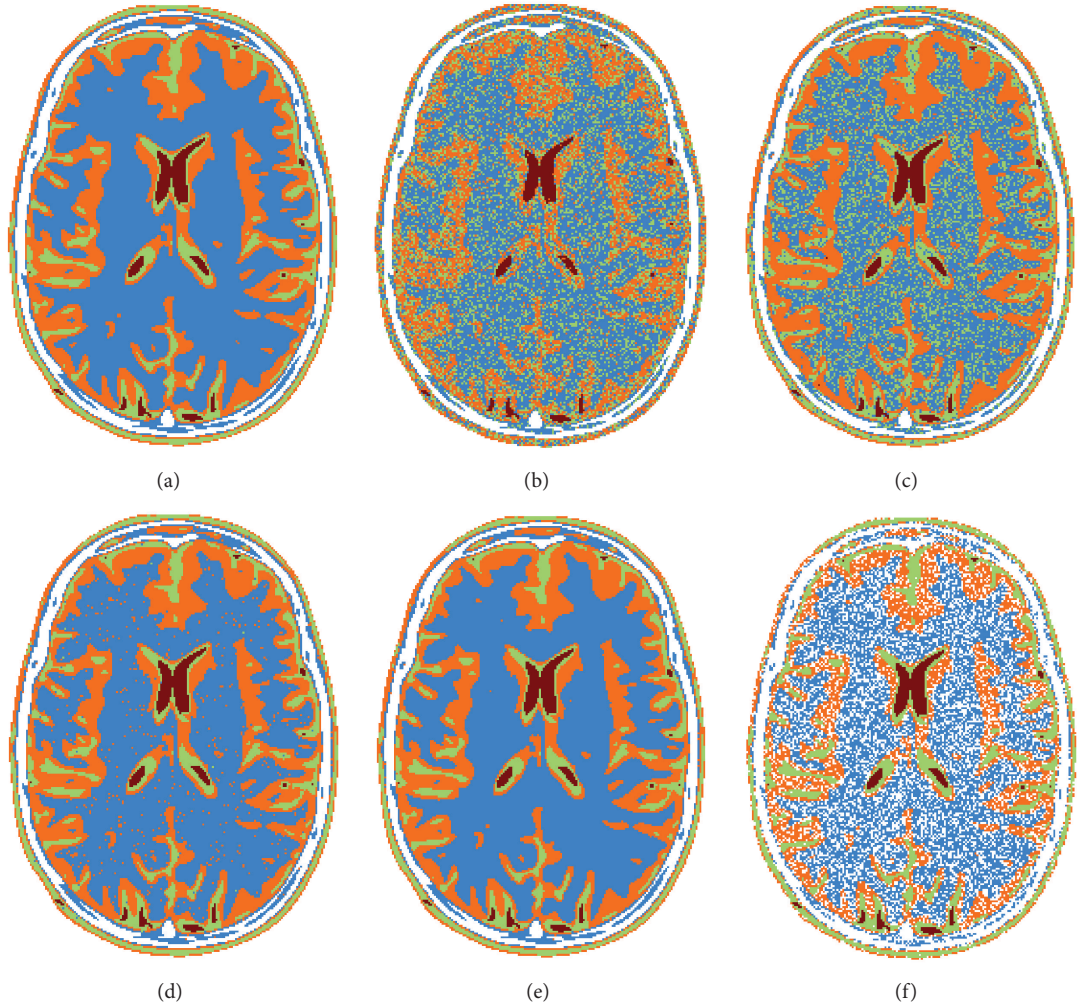

Figure 5: Segmentation and classification results: reference image (a), minimum Euclidean distance approach (b), WDM (c), StCC (d), SpCC (e), and K-means approach (f).

about the optimal acquisition parameter for the relaxation times estimation can be found in [17].

The reference phantom is reported in Figure 3, where the four tissues have been coded with blue, orange, green, and red color, respectively. Four images have been generated by simulating Spin Echo imaging sequence, with echo and repetition times of $(80, 3600)$, $(80, 500)$, $(155, 3600)$, and $(155, 500)$ [ms], respectively. Gaussian complex noise has been added to the data in order to achieve a mean SNR of 30 dB. Relaxation times have been estimated by using the LS approach [15, 23] of (3), producing ρ, T_1, and T_2 estimated maps reported in Figure 4.

The three approaches (WDC, StCC, and SpCC) previously presented have been applied to the considered data. In order to assess the obtained results, classification based on a classical minimum Euclidean distance from the expected values has been reported. Moreover, other methodologies present in literature, working on gray level images, have been investigated: seeded region growing algorithms family has not been considered, as it is supervised [25]; multithreshold maximum entropy has also not been considered due to its difficulty in classifying more than few classes [26]; K-means algorithm has been chosen as an interesting reference for the proposed technique [27]. Segmentation results are reported in Figure 5. It has to be considered that reported methodology requires multiple images, as the estimation of proton density and relaxation times is needed, while classical segmentation algorithms work on a single image. In order to have a fair comparison, K-means algorithm has been applied to a single image obtained from the estimated $\widehat{\rho}$, $\widehat{T_1}$, and $\widehat{T_2}$. Such image is characterized by an SNR higher than images of the starting dataset.

In order to give a quantitative performances evaluation, Jaccard indexes [28] and Sørensen-Dice coefficients [29, 30] have been computed and reported in Figure 6. Moreover, the stability of the approaches varying the SNR has been evaluated. Results are reported in Figure 7.

A second simulated case study has been considered. Four SE images have been downloaded from the BrainWeb (http://www.bic.mni.mcgill.ca/brainweb/) public archive with echo

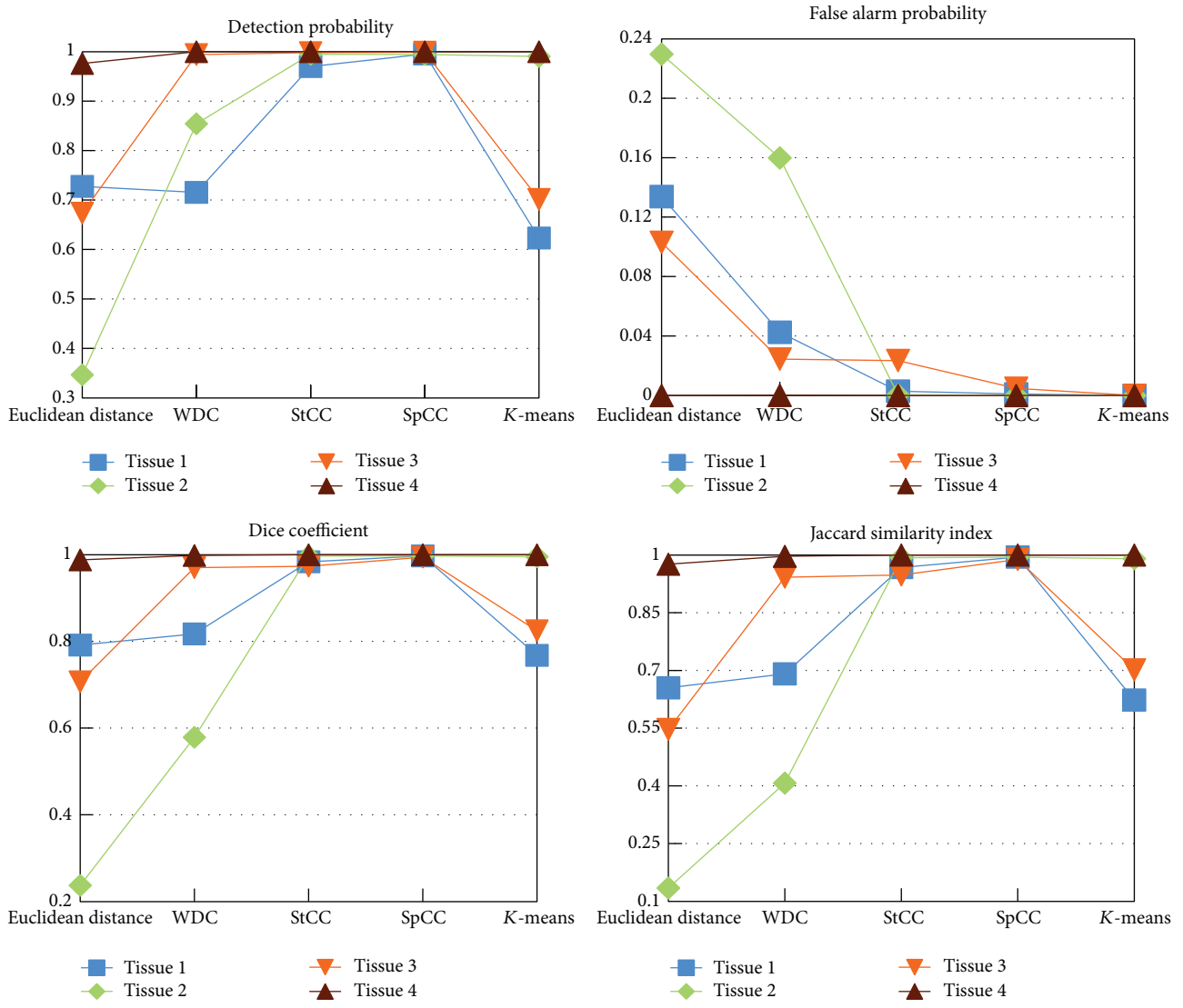

Figure 6: Performance indicator of the four considered methods in case of 4 tissues constituting brain phantom.

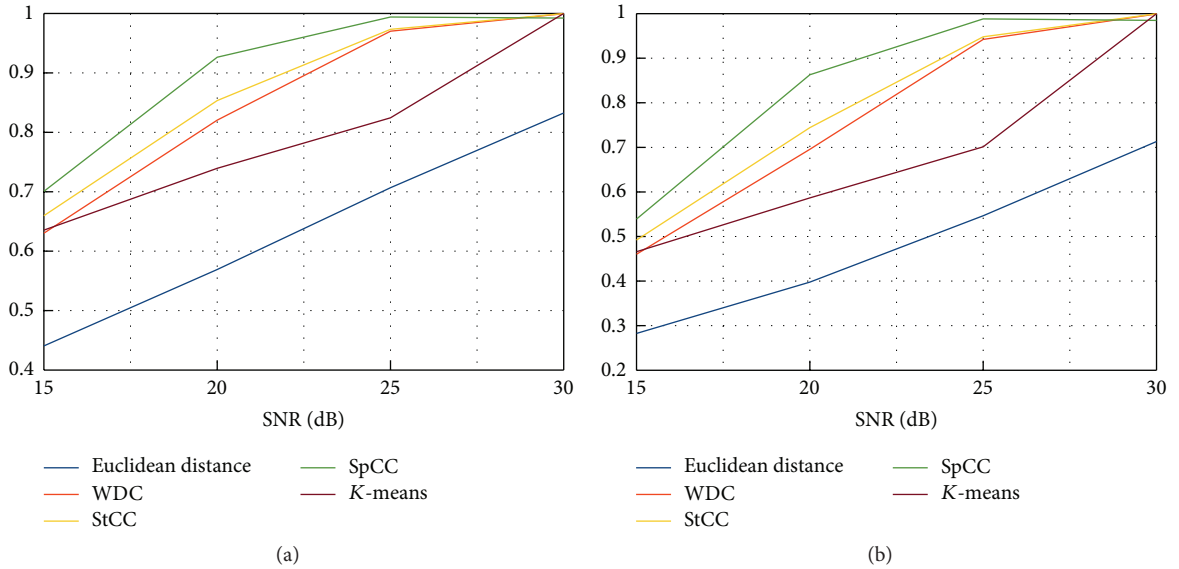

Figure 7: Dice coefficients (a) and Jaccard similarity indexes (b) in case of different SNR for all the considered methods.

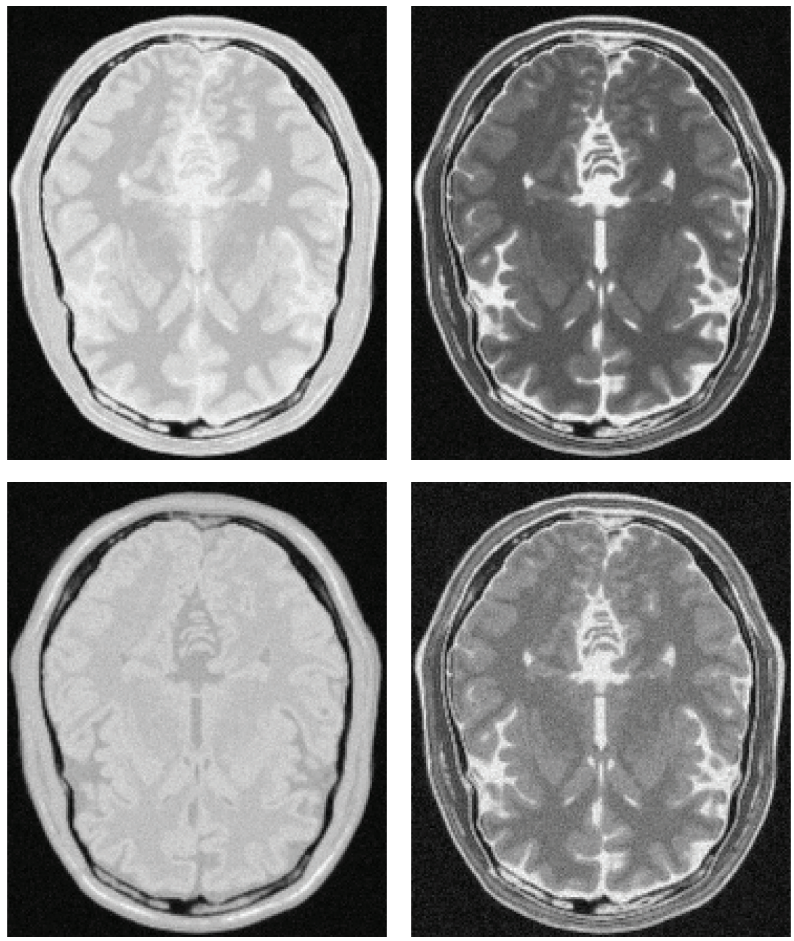

(a)

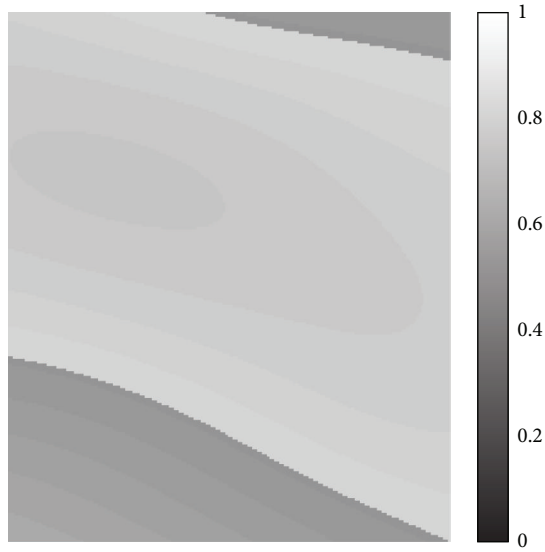

(b)

Figure 8: The four Spin Echo images from the BrainWeb database (a). The dataset has a field inhomogeneity of 20% (b).

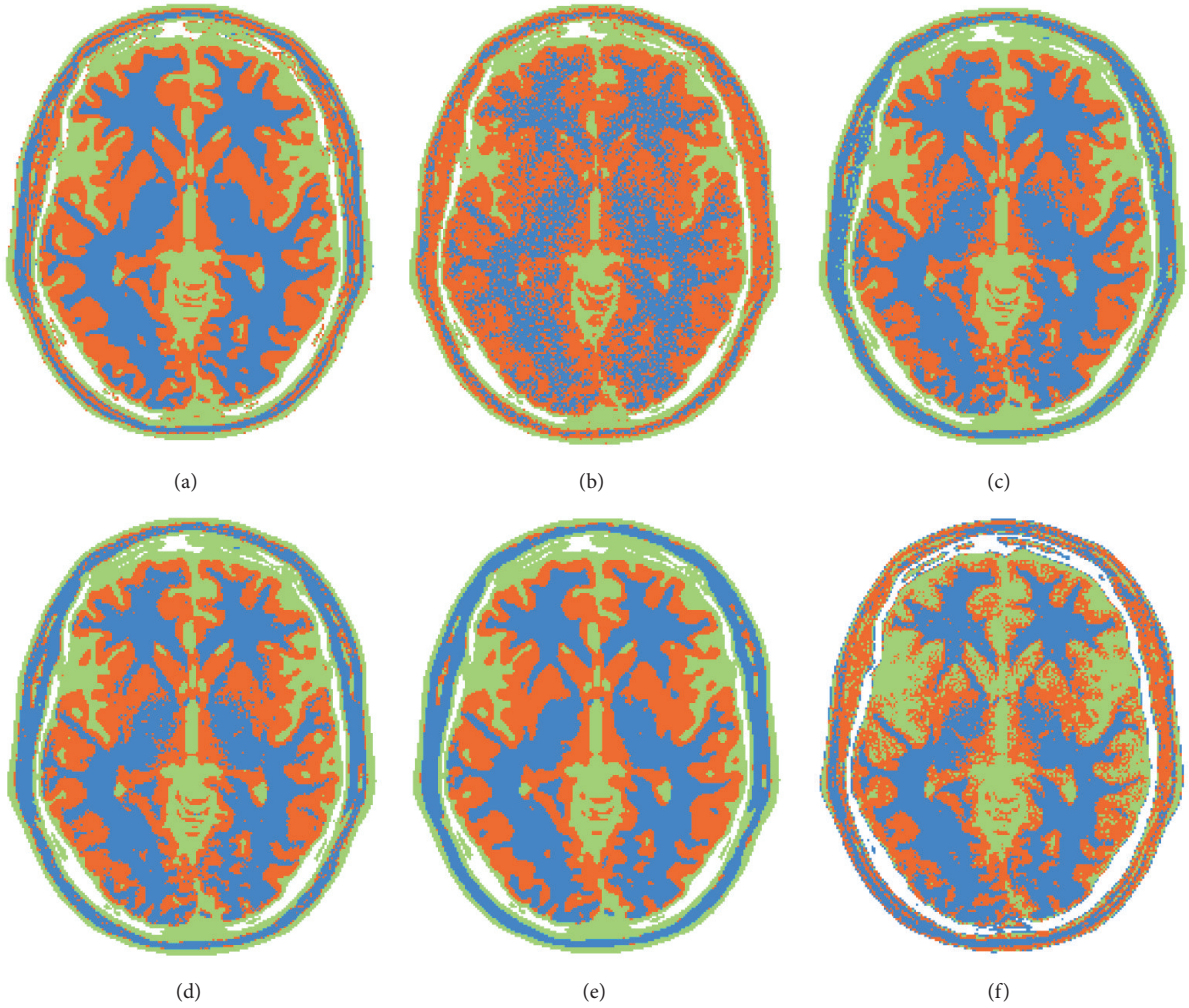

Figure 9: Segmentation and classification results for the BrainWeb phantom: reference image (a), minimum Euclidean distance approach (b), WDM (c), StCC (d), SpCC (e), and K-means approach (f).

and repetition times of $(20, 4000)$, $(100, 4000)$, $(20, 2000)$, and $(100, 2000)$ [ms] [31]. Reference ρ, T_1, and T_2 images have been obtained by performing the estimation in a noise-free test case. As a second step, an SNR equal to 30 dB together with a 20% intensity inhomogeneity field has been considered. The four images of the dataset are reported in Figure 8, together with the intensity inhomogeneity field. The considered segmentation approaches have been applied, producing results in Figure 9. In this case, a weight factor has been applied to the CRLB of ρ in order to improve the robustness taking into account the inhomogeneity fields (see Section 2.1).

Considered methodologies have also been tested on a real case. A male 31-year-old healthy volunteer has been considered. 4 Spin Echo images of a brain slice have been acquired with a 3T Philips Achieva MRI scanner. Acquisition details are reported in Table 1. In Figure 10 the acquired images are reported, while in Figure 11 the estimated proton density and relaxation times maps are shown. In this case, three segmentation classes have been considered, namely, white matter (WM), gray matter (GM), and cerebrospinal fluid (CSF).

Table 1: Real dataset, imaging protocol details.

MRI scanner	Philips Achieva
Field intensity	3.0 T
Coil	Bird cage, 8 channels
Sequence	Spin Echo
FOV	230 × 230 mm
Voxel size	0.45 × 0.45 × 3 mm
Image resolution	512 × 512 pixels
Number of images	4
Echo times [ms]	82.45, 82.45, 200, 200
Repetition times [ms]	700, 3500, 700, 3500

Simulated case results of Figure 5 clearly show that the more the statistical distribution of the data is exploited, the better the segmentation and classification accuracy is

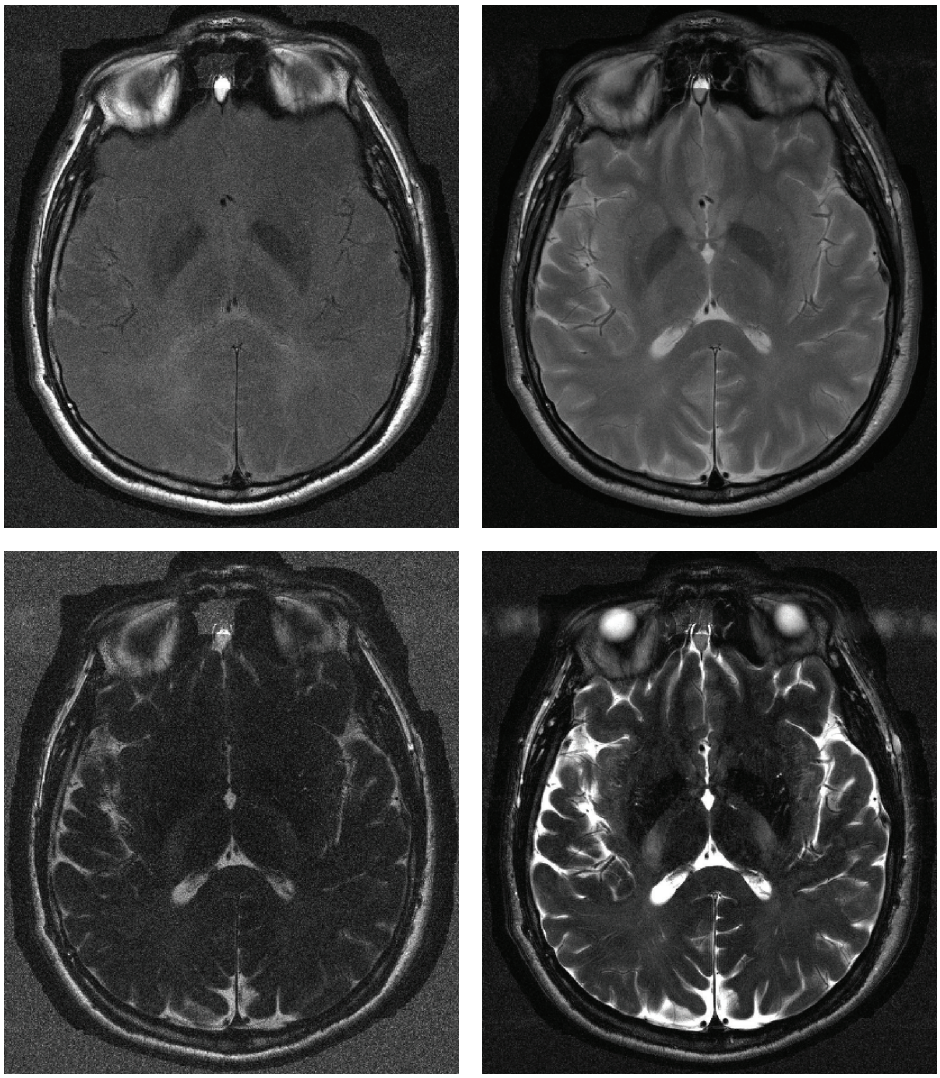

Figure 10: The four Spin Echo images composing the real dataset.

achieved. Specifically, the improvement can be evaluated by comparing the minimum Euclidean distance based classification (Figure 5(b)) with the WDC (Figure 5(c)) and with StCC (Figure 5(d)). In the latter approach, edges are well retrieved, small structures are preserved, and globally all the regions are correctly classified. Such trends are confirmed in all the synthetic quality criteria that have been chosen and reported in Figure 6, that is, detection probability, false alarm probability, Dice coefficient, and Jaccard similarity index. Errors appear mainly in the blue class, where some wrong isolated orange spots are present. This can be explained considering the closeness of blue and orange classes from Figure 2(c). In order to improve the capability of correctly discriminating blue and orange tissues, the spatial regularization criteria (SpCC) are applied, producing results of Figure 5(e). It is evident that most of isolated spots have been correctly classified without decreasing the segmentation performances of the other classes.

In order to give a reference, K-means methodology segmentation results are reported in Figure 5(f). With respect to proposed approach, some points are missing mainly in the blue and orange tissues, which are the most difficult to be discriminated, while good detection performances are achieved with red and green ones. Graphs of Figure 6 confirm such behavior. In particular, K-means is characterized by lower detection probability values compared to SpCC for blue and orange classes. On the other hand, SpCC shows good performances for all the four considered classes.

Results about robustness with respect to SNR are reported in Figure 7. In particular, Dice coefficients and Jaccard similarity indexes have been computed in case of Tissue 3 for the considered approaches with an SNR varying from 15 dB to 30 dB. The two graphs are similar, both confirming, as expected, a positive trend for all methodologies. Globally, SpCC is capable of good performances for the SNR values within the considered range, with the best improvement over the others in case of 20 dB. Moreover, at 25 dB a saturation appears, with results similar to 30 dB. On the other hand, the K-means approach reaches good performances only in case

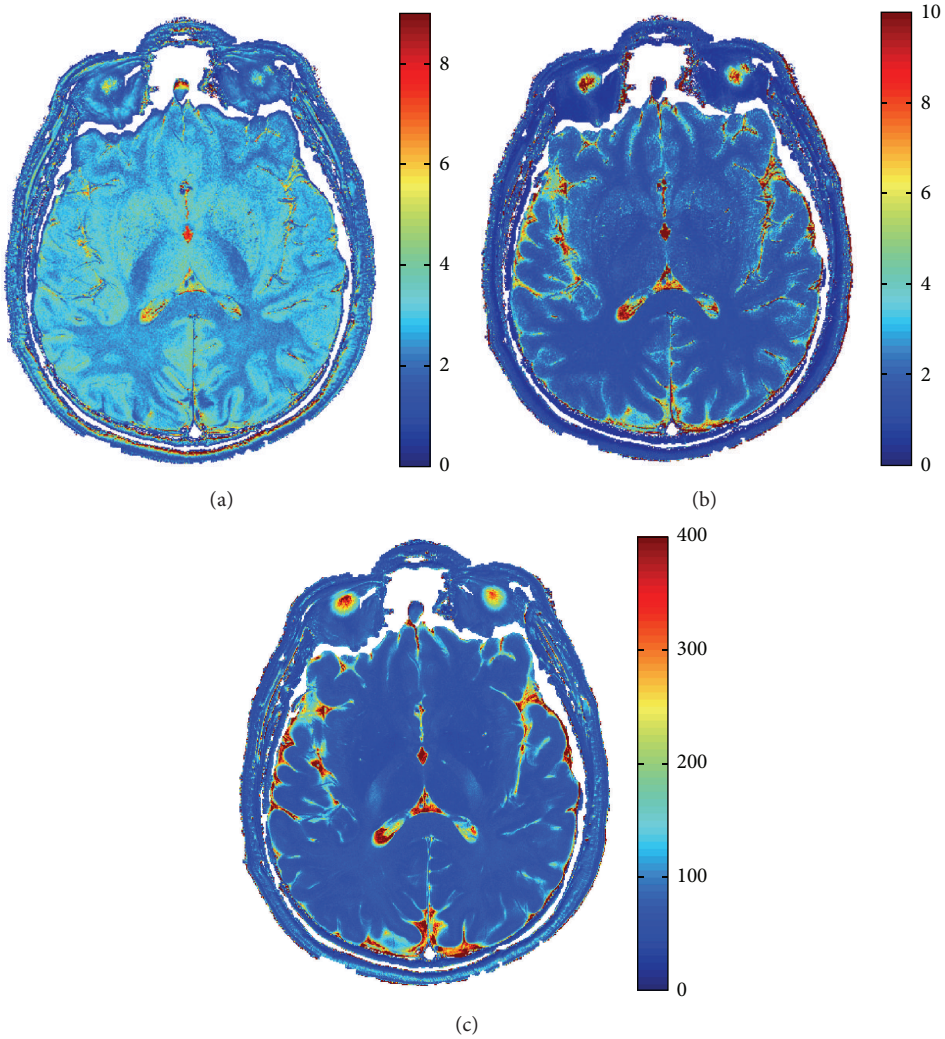

FIGURE 11: Real dataset estimated ρ (a), T_1 [s] (b), and T_2 [ms] (c) in case of 4 images.

of high SNR values, being very sensitive to noise at 25 dB and below.

Let us consider results related to the BrainWeb dataset reported in Figure 9. An intensity inhomogeneity affects such dataset, mainly in the bottom left region. It can be seen that K-means algorithm segmentation is deeply affected by the intensity inhomogeneity field, in particular where it is more severe, Figure 9(e), as in that region the green tissue is almost never detected. On the other hand, the performances of proposed methodologies are very close to the previous case study, confirming the effectiveness of the approach.

Moving to real dataset, among the three presented techniques, only SpCC methodology has been considered, being the most accurate, and compared with K-means approach. Results reported in Figure 12 show that both algorithms are able to detect the three regions: WM, GM, and CSF. K-means globally produces low regularized segmentation regions, with some classification errors in the retroocular region (GM map) and in the temporal area (CSF map). Moving to SpCC, segmented regions appear much more realistic, more regular, and without isolated spots. SpCC shows effective results especially in the retroocular region in the GM map and in the proximity of the insula region concerning CSF. However two WM nuclei have erroneously been included in the GM region. That said, it has to be underlined that the proposed unsupervised approach has substantial room for improvement if combined with more sophisticated regularization criteria, but it is evident how the proposed multidimensional distance metric is promising.

4. Conclusions

Within this paper a novel unsupervised approach for joint segmentation and classification in brain MRI has been presented. The peculiarity of the approach consists in detection criteria applied to the estimated proton density (ρ) and relaxation times (T_1 and T_2) maps, instead of to the acquired gray level image. It has to be pointed out that the effectiveness of the method is strictly related to the accuracy of adopted relaxation times estimator, which depends on several issues such as the number of images, the noise intensity, and the acquisition scheme [10, 32]. Moreover, the need of multiple images and of an estimation step implies longer

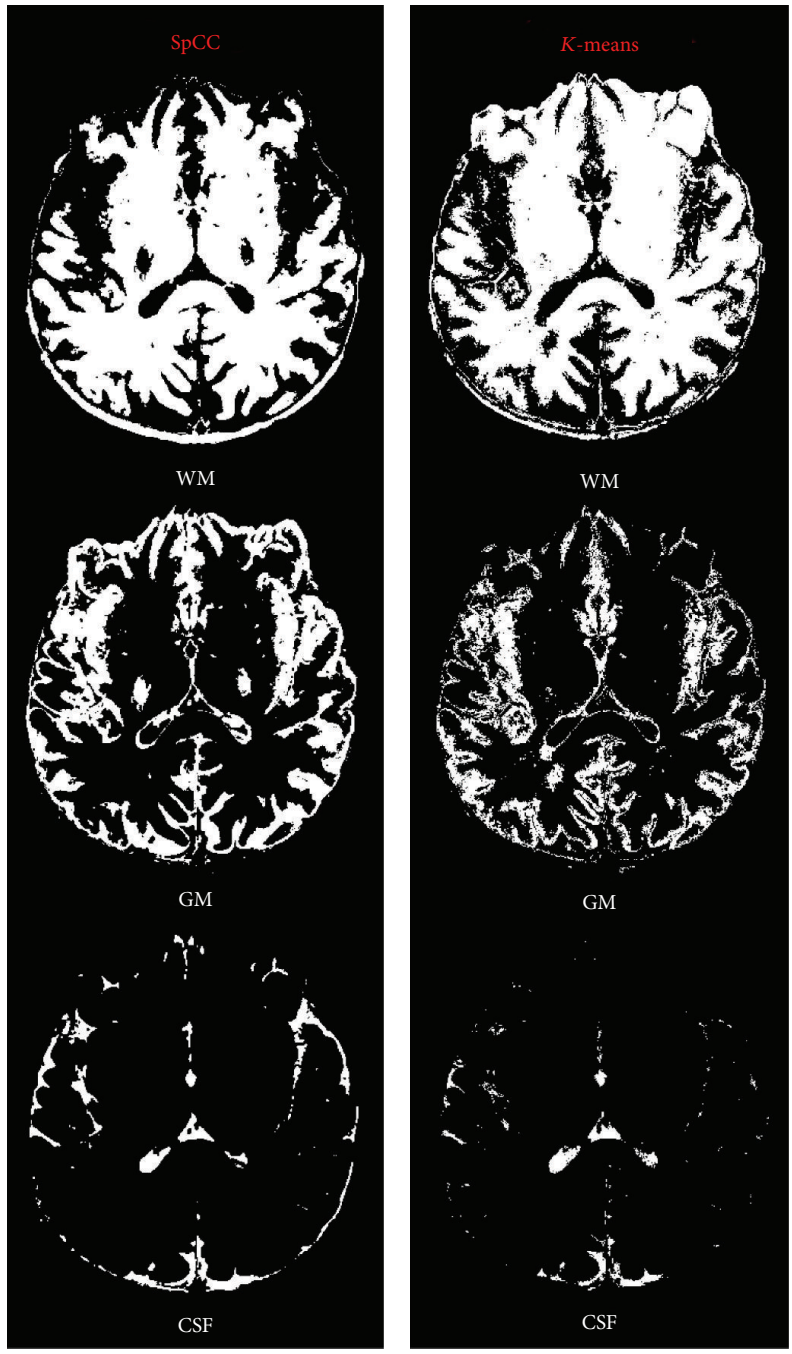

(a) (b)

Figure 12: Classification results of the proposed approach based on SpCC (a) and of K-means technique (b).

acquisition and computational times. After estimating the physical parameters from multiple scans, the segmentation is performed in a statistical framework. The aim of the paper is to show the feasibility of segmenting brain based on proton density and relaxation times. In particular, the paper focuses on the effectiveness of considering a 3D statistical metric for evaluating distances instead of a 1D one.

Results, validated on simulated datasets, are interesting and promising, greatly improving the detection rate with respect to a classical minimum distance based technique and other widely adopted segmentation methodologies. Moreover, results obtained on the real brain datasets appear reliable and consistent. A further refinement on the regularization criteria can be investigated in the future.

Conflict of Interests

The authors declare that there is no conflict of interests regarding the publication of this paper.

Acknowledgments

The authors would like to thank Rocchina Caivano and Aldo Cammarota, Department of Radiology, IRCSS CROB, Rionero in Vulture, Italy, for supplying real datasets.

References

[1] M. Kamber, R. Shinghal, D. L. Collins, G. S. Francis, and A. C. Evans, "Model-based 3-D segmentation of multiple sclerosis lesions in magnetic resonance brain images," *IEEE Transactions on Medical Imaging*, vol. 14, no. 3, pp. 442–453, 1995.

[2] M. R. Kaus, S. K. Warfield, A. Nabavi, P. M. Black, F. A. Jolesz, and R. Kikinis, "Automated segmentation of MR images of brain tumors," *Radiology*, vol. 218, no. 2, pp. 586–591, 2001.

[3] J. L. Tanabe, D. Amend, N. Schuff et al., "Tissue segmentation of the brain in Alzheimer disease," *American Journal of Neuroradiology*, vol. 18, no. 1, pp. 115–123, 1997.

[4] S. Widz, K. Revett, and D. Ślezak, "An automated multi-spectral MRI segmentation algorithm using approximate reducts," in *Rough Sets and Current Trends in Computing*, vol. 3066 of *Lecture Notes in Computer Science*, pp. 815–824, Springer, Berlin, Germany, 2004.

[5] L. P. Clarke, R. P. Velthuizen, M. A. Camacho et al., "MRI segmentation: methods and applications," *Magnetic Resonance Imaging*, vol. 13, no. 3, pp. 343–368, 1995.

[6] L. P. Clarke, R. P. Velthuizen, S. Phuphanich, J. D. Schellenberg, J. A. Arrington, and M. Silbiger, "MRI: stability of three supervised segmentation techniques," *Magnetic Resonance Imaging*, vol. 11, no. 1, pp. 95–106, 1993.

[7] C. Li, R. Huang, Z. Ding, J. C. Gatenby, D. N. Metaxas, and J. C. Gore, "A level set method for image segmentation in the presence of intensity inhomogeneities with application to MRI," *IEEE Transactions on Image Processing*, vol. 20, no. 7, pp. 2007–2016, 2011.

[8] W. Torres, M. Martín-Landrove, M. Paluszny, G. Figueroa, and G. Padilla, "Tumor segmentation of multiecho MR T2-weighted images with morphological operators," in *Medical Imaging 2009: Image Processing*, vol. 7259 of *Proceedings of SPIE*, March 2009.

[9] D. Ma, V. Gulani, N. Seiberlich et al., "Magnetic resonance fingerprinting," *Nature*, vol. 495, no. 7440, pp. 187–192, 2012.

[10] Z.-H. Cho, J. Jones, and M. Singh, *Foundations of Medical Imaging*, Wiley Interscience, 1993.

[11] G. A. Wright, "Magnetic resonance imaging," *IEEE Signal Processing Magazine*, vol. 14, no. 1, pp. 56–66, 1997.

[12] Y. Wang and T. Lei, "Statistical analysis of MR imaging and its applications in image modeling," in *Proceeedings of the IEEE International Conference Image Processing (ICIP '94)*, vol. 1, pp. 866–870, IEEE, Austin, Tex, USA, November 1994.

[13] F. Baselice, G. Ferraioli, and A. Shabou, "Field map reconstruction in magnetic resonance imaging using Bayesian estimation," *Sensors*, vol. 10, no. 1, pp. 266–279, 2010.

[14] H. Eggers, T. Knopp, and D. Potts, "Field inhomogeneity correction based on gridding reconstruction for magnetic resonance imaging," *IEEE Transactions on Medical Imaging*, vol. 26, no. 3, pp. 374–384, 2007.

[15] F. Baselice, G. Ferraioli, and V. Pascazio, "Relaxation time estimation from complex magnetic resonance images," *Sensors*, vol. 10, no. 4, pp. 3611–3625, 2010.

[16] F. Baselice, G. Ferraioli, and V. Pascazio, "A Bayesian approach for relaxation times estimation in MRI," *Magnetic Resonance Imaging*, 2015.

[17] F. Baselice, G. Ferraioli, A. Grassia, and V. Pascazio, "Optimal configuration for relaxation times estimation in complex spin echo imaging," *Sensors*, vol. 14, no. 2, pp. 2182–2198, 2014.

[18] J. P. Wansapura, S. K. Holland, R. S. Dunn, and W. S. Ball Jr., "NMR relaxation times in the human brain at 3.0 Tesla," *Journal of Magnetic Resonance Imaging*, vol. 9, no. 4, pp. 531–538, 1999.

[19] T. Zhan, J. Zhang, L. Xiao, Y. Chen, and Z. Wei, "An improved variational level set method for MR image segmentation and bias field correction," *Magnetic Resonance Imaging*, vol. 31, no. 3, pp. 439–447, 2013.

[20] Y. Chen, J. Zhang, and J. Yang, "An anisotropic images segmentation and bias correction method," *Magnetic Resonance Imaging*, vol. 30, no. 1, pp. 85–95, 2012.

[21] S. Z. Li, *Markov Random Field Modeling in Image Analysis*, Springer, Secaucus, NJ, USA, 2001.

[22] M. Guerquin-Kern, L. Lejeune, K. P. Pruessmann, and M. Unser, "Realistic analytical phantoms for parallel magnetic resonance imaging," *IEEE Transactions on Medical Imaging*, vol. 31, no. 3, pp. 626–636, 2012.

[23] F. Baselice, R. Caivano, A. Cammarota, G. Ferraioli, and V. Pascazio, "T_1 and T_2 estimation in complex domain: first results on clinical data," *Concepts in Magnetic Resonance Part A*, vol. 43, no. 5, pp. 166–176, 2014.

[24] F. Baselice, R. Caivano, A. Cammarota, G. Ferraioli, and V. Pascazio, "Relaxation times estimation in MRI," in *Medical Imaging 2014: Physics of Medical Imaging, 90332K*, vol. 9033 of *Proceedings of SPIE*, p. 6, March 2014.

[25] R. Adams and L. Bischof, "Seeded region growing," *IEEE Transactions on Pattern Analysis and Machine Intelligence*, vol. 16, no. 6, pp. 641–647, 1994.

[26] J. N. Kapur, P. K. Sahoo, and A. K. C. Wong, "A new method for gray-level picture thresholding using the entropy of the histogram," *Computer Vision, Graphics, and Image Processing*, vol. 29, no. 3, pp. 273–285, 1985.

[27] J. MacQueen, "Some methods for classification and analysis of multivariate observations," in *Proceedings of the Fifth Berkeley Symposium on Mathematical Statistics and Probability*, vol. 1 of *Statistics*, pp. 281–297, University of California Press, 1967.

[28] P. Jaccard, "Étude comparative de la distribution orale dans une portion des alpes et des jura," *Bulletin de la Société Vaudoise des Sciences Naturelles*, vol. 37, pp. 547–579, 1901.

[29] L. R. Dice, "Measures of the amount of ecologic association between species," *Ecology*, vol. 26, no. 3, pp. 297–302, 1945.

[30] T. Sørensen, "A method of establishing groups of equal amplitude in plant sociology based on similarity of species and its application to analyses of the vegetation on Danish commons," *Biologiske Skrifter*, vol. 5, pp. 1–34, 1948.

[31] R. K.-S. Kwan, A. C. Evans, and B. Pike, "MRI simulation-based evaluation of image-processing and classification methods," *IEEE Transactions on Medical Imaging*, vol. 18, no. 11, pp. 1085–1097, 1999.

[32] M. D'Arco, M. Genovese, E. Napoli, and M. Vadursi, "Design and implementation of a preprocessing circuit for bandpass signals acquisition," *IEEE Transactions on Instrumentation and Measurement*, vol. 63, no. 2, pp. 287–294, 2014.

Hindawi Publishing Corporation
BioMed Research International
Volume 2015, Article ID 693206, 6 pages
http://dx.doi.org/10.1155/2015/693206

Research Article

Brain Parenchymal Fraction: A Relatively Simple MRI Measure to Clinically Distinguish ALS Phenotypes

Venkateswaran Rajagopalan[1,2] and Erik P. Pioro[3,4]

[1] *Department of Electrical and Electronics Engineering, Birla Institute of Technology and Science, Pilani, Hyderabad Campus, Hyderabad 500078, India*
[2] *Department of Biomedical Engineering, ND2, Lerner Research Institute, Cleveland Clinic, Cleveland, OH 44195, USA*
[3] *Neuromuscular Center and Department of Neurology, Neurological Institute, Cleveland Clinic, Cleveland, OH 44195, USA*
[4] *Department of Neurosciences, Lerner Research Institute, Cleveland Clinic, Cleveland, OH 44195, USA*

Correspondence should be addressed to Erik P. Pioro; pioroe@ccf.org

Received 19 July 2015; Revised 19 November 2015; Accepted 23 November 2015

Academic Editor: Yukihisa Takayama

Even though neuroimaging and clinical studies indicate that amyotrophic lateral sclerosis (ALS) manifests with distinct clinical phenotypes, no objective test exists to assess upper motor degeneration in ALS. There is great interest in identifying biomarkers of ALS to allow earlier diagnosis and to recognize disease subtypes. Current quantitative neuroimaging techniques such as T2 relaxometry and diffusion tensor imaging are time-consuming to use in clinical settings due to extensive postprocessing requirements. Therefore, we aimed to study the potential role of brain parenchymal fraction (BPF) as a relatively simple quantitative measure for distinguishing ALS phenotypes. T1-weighted MR images of brain were obtained in 15 neurological controls and 88 ALS patients categorized into 4 distinct clinical phenotypes, upper motor neuron- (UMN-) predominant ALS patients with/without corticospinal tract (CST) hyperintensity on T2/PD-weighted images, classic ALS, and ALS with frontotemporal dementia (ALS-FTD). BPF was calculated using intracranial grey matter, white matter, and cerebrospinal fluid volumes obtained in control and ALS subgroups using SPM8 software. Only ALS-FTD patients had significant reduction in BPF when compared to controls and nondemented ALS patients. Correlation of clinical measures such as disease duration with BPF further supports the view that the BPF could be a potential biomarker for clinical diagnosis of ALS-FTD patients.

1. Introduction

Amyotrophic lateral sclerosis (ALS) is a progressive degeneration of motor neurons in brain and spinal cord of unknown cause [1]. Growing evidence from neuroimaging and clinical studies indicates that ALS manifests with distinct clinical phenotypes identified by extent of upper motor neuron (UMN) dysfunction [2], cognitive impairment (ALS patients with frontotemporal lobe dementia, ALS-FTD), and variable degrees of lower motor neuron dysfunction. According to the revised El Escorial criteria [3], the diagnosis of ALS is based on the presence of both UMN and LMN symptoms and signs. Whereas electromyography (EMG) is an objective test for LMN degeneration [4], no easily accessible equivalent exists to objectively identify UMN dysfunction in ALS, contributing to incorrect or delayed diagnoses [5]. There is great interest in identifying biomarkers of ALS to allow earlier diagnosis, recognize disease subtypes (which exist phenotypically), monitor disease progression, and assess the efficacy of therapeutic interventions.

Even though ALS patients have clinical evidence of both UMN and LMN dysfunction, a percentage of patients begin with UMN abnormalities before developing identifiable LMN signs. We have observed that some patients with predominantly UMN signs have bilateral corticospinal tract (CST) hyperintensities visible on conventional T2-, proton density-, and FLAIR-weighted image, while others with similar clinical features do not [2]. Why some patients with UMN-predominant ALS possess CST hyperintensities and others do not is unknown. Also, cognitive impairment in some patients

with ALS affects predominantly frontotemporal areas to cause frontotemporal dementia (FTD) while prominent LMN dysfunction with UMN signs occurs in patients with classic ALS. Based on such observations, one can hypothesize different pathological mechanisms of ALS in UMN-predominant patients with or without CST hyperintensity, as well as those with combined UMN and LMN dysfunction or those with FTD.

Currently neuroimaging studies especially using MRI (because of versatile contrasts) to evaluate UMN dysfunction have provided better understanding of pathophysiological changes brought out by the ALS disease process. However, techniques such as T2 relaxometry, diffusion tensor imaging, and quantitative assessment of T1-weighted images using techniques such as voxel based morphometry (VBM) and cortical thickness analysis are time-consuming due to extensive postprocessing requirements. Therefore, these techniques have less widespread application clinically as opposed to research setting. On the other hand, measures such as brain parenchymal fraction (BPF) are not only quantitative but also simple and easy to calculate in clinical settings. Two previous studies in ALS [6, 7] found significant reduction in BPF of ALS patient brain; however, they did not categorize or classify ALS patients by their clinical phenotypes. Furthermore, they did not study the role of BPF as a potential clinical quantitative measure for distinguishing ALS phenotypes. We hypothesize that categorizing ALS patients by their clinical phenotype would reveal quantitative differences in BPF between such ALS subgroups and may identify the potential of BPF for distinguishing ALS phenotypes.

2. Methods

2.1. Demographics. MRI data obtained at 1.5 T during routine clinical neuroimaging were approved by the Cleveland Clinic Institutional Review Board for storage and analysis as deidentified images after patients (or their legal representative when they were cognitively impaired) provided verbal consent. The data were analyzed in the following patient groups: (1) neurologic disease controls (associated diagnoses indicated in Table 1); (2) UMN-predominant ALS patients with CST hyperintensity on T2/PD-weighted images (ALS-CST+) (this hyperintense signal is predominantly seen in posterior limb of the internal capsule (corresponding to corticospinal tract) and was identified by a blinded evaluator); (3) UMN-predominant ALS patients without CST hyperintensity identified on T2/PD-weighted images (ALS-CST–); (4) classic ALS (ALS-Cl); and (5) ALS with frontotemporal dementia (ALS-FTD). Representative demographics of the above patient populations are given in Table 2.

Patients who were identified by one of us (EPP) during clinical evaluation as having cognitive or behavioral impairment (e.g., disturbances of impulse control, executive function, and language) underwent formal neuropsychometric testing in most cases. Eighteen ALS patients met Neary criteria of FTD [8] after testing by an experienced neuropsychologist ($n = 11$) or bedside evaluation with MoCA ($n = 7$) and were included in the ALS-FTD subgroup. Table 3 gives details of the domains affected in each of the ALS-FTD patients and their FTD subtype UMN-predominant ALS patients were defined as those with no lower motor neuron (LMN) signs or if present then these were restricted to only one neuraxial level (bulbar, cervical, thoracic, or lumbosacral) at the time of MRI. Classic ALS (ALS-Cl) had combined UMN and LMN features at one or more levels and did not display hyperintensity of CST. None of the ALS patients in the non-ALS-FTD subgroups had clinical evidence of FTD.

Table 1: Clinical diagnoses of neurologic disease controls.

Subject	Clinical diagnosis
1	Severe fatigue, headache
2	Stiff person syndrome
3	Myasthenia gravis
4	Parkinson's disease
5	Depression, headache, and fibromyalgia-like syndrome
6	Fibromyalgia-like syndrome, headache
7	Painful sensory polyneuropathy
8	Insomnia, headache
9	Parkinson's disease
10	Cervical radiculopathy
11	Non-length-dependent small fiber sensory neuropathy
12	Headache, pain in lower leg
13	Small fiber neuropathy, headache
14	Large fiber neuropathy
15	Fibromyalgia-like syndrome, headache

2.2. Clinical Data. Clinical measures of revised ALS functional rating scale (ALSFRS-R), disease duration (duration of symptoms prior to MRI), and disease progression rate were also measured and are given in Table 2. Disease progression rate was calculated by dividing the number of points ALSFRS-R score decreased from normal (i.e., 48) at the time of neuroimaging by symptom duration in months [9].

2.3. MR Image Acquisition. Structural high-resolution 3D T1-weighted MR images of head were obtained on a 1.5 T system (Siemens Symphony, Erlangen, Germany) using magnetization-prepared rapid gradient echo (MPRAGE) sequence. Imaging parameters were as follows: 160 slices, 1 mm thick, with 1.0×1.0 mm in-plane resolution; pulse sequence parameters were as follows: TR = 1970 ms; TE = 4.38 ms; number of averages = 1; and scan time = 6.45 minutes. T2- and PD-weighted images were also obtained using dual-echo FSE sequence to assess hyperintense signal changes along corticospinal tract in ALS patients. Imaging parameters include the following: 40 contiguous slices; slice thickness = 4 mm; in-plane resolution = 0.9×0.9 mm; pulse sequence parameters were as follows: repetition time (TR) = 3900 ms; echo time (TE) = 26 ms and 104 ms; echo train length or turbo factor = 7; and number of averages = 1; total scan time = 3.5 minutes. Although this dataset was used in our previous VBM studies [9], we did not study brain parenchymal fraction and so applied it to this study.

Table 2: Demographics and clinical measures of neurologic disease controls and ALS patients.

Clinical measure/ALS subgroups	Neurologic disease controls	ALS-CST+	ALS-CST−	ALS-Cl	ALS-FTD
n	15	21	26	23	18
Age (years) (mean ± SD)	57.1 ± 19.2	52.3 ± 11.02	60.1 ± 11.8	58.5 ± 12.6	66.4 ± 9.2
Age range (years)	28–95	32–75	32–76	39–84	52–87
Gender	10 men, 5 women	14 men, 7 women	13 men, 13 women	13 men, 10 women	5 men, 13 women
Duration of symptom prior to MRI (months) (mean ± SD)		9.6 ± 5.5	36.4 ± 44.2	29.1 ± 27.3	37.5 ± 25.2
ALSFRS-R score ($N = 48$) (mean ± SD)		34.6 ± 7.8	34.1 ± 8.1	37.2 ± 8.5	30.7 ± 7.1
Disease progression rate (mean ± SD)		1.38 ± 1.64	0.46 ± 0.43	0.68 ± 0.77	0.59 ± 0.33

Table 3: Clinical characteristics of ALS patients with FTD.

Patient	Gender	Age (yr)	Site of onset	Features of FTD	
				Extent	Domain affected (at time of MRI)
1	F	67	Speech	Mild	bv., ex., l.
2	F	75	UE	Mild	ex., l.
3	F	60	Speech	Mod.	bv., ex.
4	F	58	Speech	Mod.	bv., l.
5	F	60	Cognitive	Mod.	bv.
6	M	63	Speech	Severe	bv., l. (PNFA)
7	M	75	Cognitive	Severe	bv., mem.
8	F	53	Speech	Severe	bv., l.
9	F	52	Speech	Severe	g.
10	M	59	Cognitive	Severe	g.
11	M	87	UE, LE	Severe	g.
12	F	69	Cognitive	Severe	bv., l.
13	F	68	Cognitive	Severe	bv., ex.
14	F	67	LE	Severe	ex., l. (sem.), mem.
15	F	65	Cognitive	Severe	bv., l.
16	F	63	LE	Severe	bv., ex., l.
17	F	77	Speech	Severe	bv., ex., l.
18	M	78	LE	Severe	g.

bv. = behavior; Cog. = cognitive; ex. = executive; g. = global (bv. + ex. + l. + mem. present); l. = language; LE = lower extremity; mem. = memory; PNFA = progressive nonfluent aphasia; sem. = semantic; and UE = upper extremity.

2.4. Brain Parenchymal Fraction Measurement. Whole brain intracranial GM, WM, and CSF volumes from T1-weighted images were obtained for control and the ALS subgroups using SPM8 software (http://www.fil.ion.ucl.ac.uk/spm). Since segmentation algorithms are automatic and are dependent on high GM/WM contrast, careful postsegmentation quality-checks were performed by an experienced neuroanatomist (EPP). BPF (in percentage) was obtained by taking ratio of brain parenchyma to the total brain intracranial volume [10] as given in

$$\text{Brain parenchymal fraction (BPF)} = \frac{\text{Volume of (GM + WM)}}{\text{Volume of (GM + WM + CSF)}} \times 100. \quad (1)$$

As seen from (1), change in BPF could result from one or both of the GM and WM parenchymal components. In order to further elucidate this, we studied separately the parenchymal fractions of GM and WM with respect to total intracranial brain, as given in (2). We have termed these as grey matter parenchymal fraction (GMPF) and white matter parenchymal fraction (WMPF):

$$\begin{aligned} &\text{Grey matter parenchymal fraction (GMPF)} = \frac{\text{Volume of GM}}{\text{Volume of (GM + WM + CSF)}} \times 100, \\ &\text{White matter parenchymal fraction (WMPF)} = \frac{\text{Volume of WM}}{\text{Volume of (GM + WM + CSF)}} \times 100. \end{aligned} \quad (2)$$

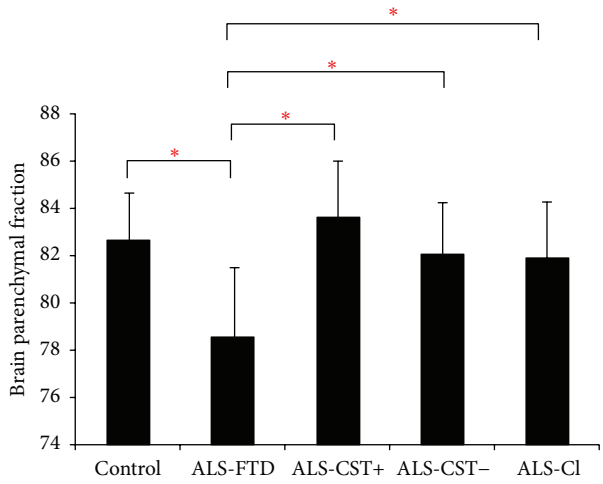

Figure 1: Brain parenchymal fraction values are significantly lower in patients with ALS-FTD compared to neurologic controls and other ALS subgroups. $^{*}P < 0.05$.

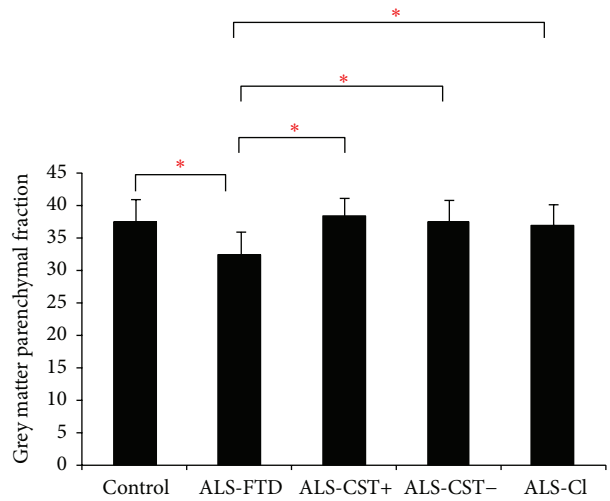

Figure 2: Grey matter parenchymal fraction values are significantly lower in patients with ALS-FTD compared to controls and other ALS subgroups. $^{*}P < 0.05$.

2.5. Statistical Analysis. Clinical measures of revised ALS functional rating scale (ALSFRS-R), disease duration, and disease progression rate were compared between ALS subgroups using Kruskal-Wallis test with post hoc Mann-Whitney U test (using Bonferroni correction). BPF, GMPF, and WMPF measures were compared between control and ALS subgroups using ANCOVA by regressing out age, ALSFRS-R score, and disease duration. Multiple comparison corrections using Sidak test were performed with $P < 0.05$. Correlations between clinical measures (disease duration, ALSFRS-R, and disease progression rate) and BPF in ALS patients were performed using Spearman's rank correlation coefficient.

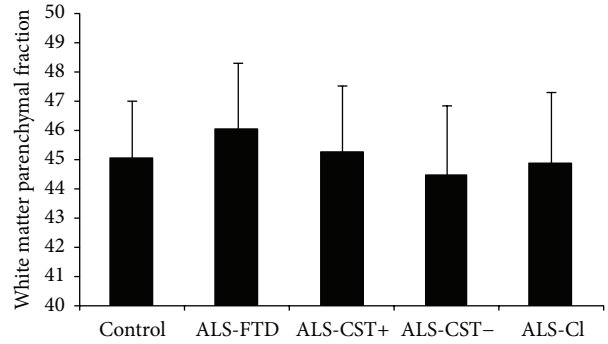

Figure 3: White matter brain parenchymal fraction values are not significantly different in any ALS patient subgroups compared to controls.

3. Results

Significant ($P < 0.05$) reductions in BPF and GMPF were observed only between control and ALS-FTD groups as shown in Figures 1 and 2. Similar reductions in BPF and GMPF were significant in ALS-FTD patients when compared to other ALS subgroups (ALS-CST+, ALS-CST−, and ALS-Cl). However, WMPF showed no significant difference between controls and any of the ALS subgroups (Figure 3). Inability to discriminate the other patient groups from neurological controls may arise from some of these controls having a degree of cerebral atrophy from other neurodegenerative conditions (e.g., two with Parkinson disease). In order to evaluate this, statistical analysis was performed with the two parkinsonian patients excluded from the neurologic control group. However, we still failed to observe any significant differences between the control and other ALS subgroups/phenotypes, and the results remained the same whether Parkinson disease patients were excluded or not from the neurologic control group. Correlation between BPF and clinical measures revealed moderately significant positive correlation ($r = 0.287$, $P = 0.005$) between BPF and disease duration. No significant correlation was found between BPF and ALSFRS-R score ($r = 0.143$, $P = 0.197$), BPF and disease progression rate ($r = 0.072$, $P = 0.521$). No significant correlation was observed between WMPF and any of the clinical measures, that is, WMPF versus disease duration ($r = -0.021$, $P = 0.843$), WMPF versus ALSFRS-R score ($r = 0.025$, $P = 0.816$), and WMPF versus disease progression rate ($r = 0.016$, $P = 0.886$). No significant correlation was found between GMPF and disease duration ($r = -0.197$, $P = 0.061$), GMPF and ALSFRS-R score ($r = 0.062$, $P = 0.55$).

4. Discussion

The main findings of this study are as follows: (1) BPF was significantly reduced in ALS-FTD patients when compared to controls and nondemented ALS patients; (2) this reduction primarily arose from changes in the grey matter parenchymal fraction (GMPF) and not the white matter parenchymal fraction (WMPF); (3) BPF significantly correlated with clinical disease duration but not with ALSFRS-R score or with disease progression rate.

The present BPF results align with our previous findings of significant GM atrophy in only ALS-FTD patients as measured by VBM [9]. BPF reduction in ALS-FTD patients appears to result entirely from GMPF changes with no significant decrease in WMPF. The preferential reduction of GMPF in ALS-FTD patients also supports our previous hypothesis that GM atrophy results from a dying forward "neuronopathy" in such patients [9]. WMPF on the other hand is actually slightly *increased* in the ALS-FTD group (mean WMPF in neurological controls equals 45.06%, whereas in ALS-FTD patients it equals 46.05%), although not reaching statistical significance. This increase in WMPF could be due to gliosis that results in response to damage of WM axons and/or myelin. Similarly, our previous VBM analyses failed to reveal significant changes of subcortical WM in brain regions of ALS patients compared to control individuals [9]. In addition, we observed WM abnormalities in diffusion tensor imaging (DTI) metrics at rostral but not caudal levels of the corticospinal tract (CST) in nondemented ALS patients as revealed by fractional anisotropy (FA), axial diffusivity, and radial diffusivity values [11]. Lack of concordance between the DTI studies and WMPF findings in ALS patients may occur because (1) WMPF and WM VBM detect macroscopic changes whereas DTI identifies more microscopic changes resulting in earlier and more sensitive detection of pathology than do volumetric measures and (2) WMPF represents whole brain WM tracts while only the CST fiber tracts are included in our DTI findings. Taken together, abnormalities of CST DTI metrics (demonstrated previously) but not abnormalities of BPF, including GMPF measures (demonstrated in the present study), suggest that ALS-CST+, ALS-CST–, and ALS-Cl patients have less cortical pathology than do ALS-FTD patients.

In contrast to our findings, previous VBM studies in ALS found significantly reduced grey matter volume in nondemented ALS patients [6, 7], although at least some of these patients showed cognitive impairment clinically. Other possible reasons for these disparate results include the following: (i) combining various clinical phenotypes of ALS patients into the same group for analysis [6] rather than separating by distinct clinical phenotypes as in our study; (ii) studying patients with extensive disease burden and more advanced disease, for example, all with definite ALS [7] rather than ALS subgroups with relatively restricted LMN abnormalities (as in our study with patients average El Escorial score = 2, indicating laboratory-supported probable ALS); (iii) using neurologic disease controls rather than healthy controls, which may have introduced some degree of abnormality (e.g., atrophy) into our "control" group but alternatively represented a more appropriate ("real world") comparison with ALS patients. Only healthy controls have been used in all other studies, making ours the first we know to have used neurologic disease controls.

Overall, ALSFRS-R values showed little difference among ALS subgroups suggesting that data were collected from patients with relatively similar degrees of functional impairment. However, significant differences were observed in disease duration among ALS subgroups. BPF and GMPF in ALS patients were significantly correlated with clinical markers of disease, including disease duration and disease progression rate. For example, positive correlation between disease duration and BPF suggests that shorter disease duration may be associated with worse disease and indicate both GM and WM damage.

Limitations of our study include the following: (1) lack of estimating the sensitivity and specificity of BPF, GMPF, and WMPF measures and (2) not evaluating changes in BPF, GMPF, and WMPF over time because of the cross-sectional nature of this study. Future longitudinal studies with larger sample sizes could confirm our findings.

MR imaging studies using techniques such as VBM, cortical thickness, and DTI showed significant GM and WM damage in ALS patients [6, 7, 12]. Although these techniques can certainly reveal abnormalities in *specific* brain regions as compared to BPF, which is a whole brain measure, they require extensive postprocessing of MR images, which is impractical in a clinical setting. Techniques such as VBM require robust registration to a template which in various pathological conditions (e.g., ventriculomegaly) may cause suboptimal normalization and segmentation leading to spurious results [13]. On the other hand Juengling and Kassubek [14] reported that BPF can not only be used for objective assessment of cerebral atrophy but can be included in MR reports of patients in routine diagnosis for neurodegenerative diseases. Along these lines we explored the use of BPF as a relatively quick and easy volumetric measure to distinguish ALS patients from controls as well as within ALS subgroups. Our results suggest that BPF, along with GMPF and WMPF, could serve as a potential MRI biomarker to distinguish ALS-FTD from other ALS subgroups in a clinical setting.

5. Conclusion

ALS patients with frontotemporal dementia have greatest reduction in brain parenchyma among ALS patients without dementia. Significant reduction in the GMPF and not the WMPF component of BPF suggests cortical atrophy and possibly a neuronopathy, in patients with ALS-FTD. Correlation of clinical disease duration with BPF further supports our suggestion that BPF and its individual components, GMPF and WMPF, may be useful MRI biomarkers for the clinical diagnosis of the ALS-FTD phenotype.

Conflict of Interests

The authors declare no conflict of interests regarding the publication of this paper.

Authors' Contribution

Venkateswaran Rajagopalan was responsible for designing the study, data collection, processing, analysis, and writing the paper. Erik P. Pioro was responsible for conceiving the study, data collection, and significant revision of the paper.

Acknowledgments

The authors thank all the patients and their caregivers who participated in this study. Support of this work was through funding from the Bright Side of the Road Foundation, the Fight ALS Fund, and the Frankino Foundation.

References

[1] S. Cluskey and D. B. Ramsden, "Mechanisms of neurodegeneration in amyotrophic lateral sclerosis," *Molecular Pathology*, vol. 54, no. 6, pp. 386–392, 2001.

[2] G. P. Matte and E. P. Pioro, "Clinical features and natural history in ALS patients with upper motor neuron abnormalities on conventional brain MRI," *Neurology*, vol. 74, supplement 2, p. A216, 2010.

[3] B. R. Brooks, R. G. Miller, M. Swash, and T. L. Munsat, "El Escorial revisited: revised criteria for the diagnosis of amyotrophic lateral sclerosis," *Amyotrophic Lateral Sclerosis and Other Motor Neuron Disorders*, vol. 1, no. 5, pp. 293–299, 2000.

[4] B. R. Brooks, "Diagnostic dilemmas in amyotrophic lateral sclerosis," *Journal of the Neurological Sciences*, vol. 165, supplement 1, pp. S1–S9, 1999.

[5] P. Kaufmann, S. L. Pullman, D. C. Shungu et al., "Objective tests for upper motor neuron involvement in amyotrophic lateral sclerosis (ALS)," *Neurology*, vol. 62, no. 10, pp. 1753–1757, 2004.

[6] D. M. Mezzapesa, A. Ceccarelli, F. Dicuonzo et al., "Whole-brain and regional brain atrophy in amyotrophic lateral sclerosis," *American Journal of Neuroradiology*, vol. 28, no. 2, pp. 255–259, 2007.

[7] J. Kassubek, A. Unrath, H.-J. Huppertz et al., "Global brain atrophy and corticospinal tract alterations in ALS, as investigated by voxel–based morphometry of 3–D MRI," *Amyotrophic Lateral Sclerosis and Other Motor Neuron Disorders*, vol. 6, no. 4, pp. 213–220, 2005.

[8] D. Neary, J. S. Snowden, L. Gustafson et al., "Frontotemporal lobar degeneration: a consensus on clinical diagnostic criteria," *Neurology*, vol. 51, no. 6, pp. 1546–1554, 1998.

[9] V. Rajagopalan and E. P. Pioro, "Distinct patterns of cortical atrophy in ALS patients with or without dementia: an MRI VBM study," *Amyotrophic Lateral Sclerosis & Frontotemporal Degeneration*, vol. 15, no. 3-4, pp. 216–225, 2014.

[10] M. D. Phillips, R. I. Grossman, Y. Miki et al., "Comparison of T2 lesion volume and magnetization transfer ratio histogram analysis and of atrophy and measures of lesion burden in patients with multiple sclerosis," *American Journal of Neuroradiology*, vol. 19, no. 6, pp. 1055–1060, 1998.

[11] V. Rajagopalan, G. H. Yue, and E. P. Pioro, "Brain white matter diffusion tensor metrics from clinical 1.5T MRI distinguish between ALS phenotypes," *Journal of Neurology*, vol. 260, no. 10, pp. 2532–2540, 2013.

[12] R. Walhout, H.-J. Westeneng, E. Verstraete et al., "Cortical thickness in ALS: towards a marker for upper motor neuron involvement," *Journal of Neurology, Neurosurgery and Psychiatry*, vol. 86, no. 3, pp. 288–294, 2015.

[13] A. Mechelli, C. Price, K. Friston, and J. Ashburner, "Voxel-based morphometry of the human brain: methods and applications," *Current Medical Imaging Reviews*, vol. 1, no. 2, pp. 105–113, 2005.

[14] F. D. Juengling and J. Kassubek, "Standardized calculation of brain parenchymal fraction: an approach to objective assessment of cerebral atrophy," *American Journal of Neuroradiology*, vol. 24, no. 7, pp. 1492–1493, 2003.

Hindawi Publishing Corporation
BioMed Research International
Volume 2015, Article ID 634275, 5 pages
http://dx.doi.org/10.1155/2015/634275

Research Article

Development of a Rapid Cartilage Damage Quantification Method for the Lateral Tibiofemoral Compartment Using Magnetic Resonance Images: Data from the Osteoarthritis Initiative

Ming Zhang,[1] Jeffrey B. Driban,[1] Lori Lyn Price,[2,3] Grace H. Lo,[4,5] Eric Miller,[6] and Timothy E. McAlindon[1]

[1]*Division of Rheumatology, Tufts Medical Center, 800 Washington Street, P.O. Box 406, Boston, MA 02111, USA*
[2]*The Institute for Clinical Research and Health Policy Studies, 800 Washington Street, P.O. Box 63, Boston, MA 02111, USA*
[3]*Tufts Medical Center and Tufts Clinical and Translational Science Institute, Tufts University, 800 Washington Street, P.O. Box 63, Boston, MA 02111, USA*
[4]*Medical Care Line and Research Care Line, Houston Health Services Research and Development (HSR&D) Center of Excellence Michael E. DeBakey VAMC, Houston, TX 77030, USA*
[5]*Section of Immunology, Allergy, and Rheumatology, Baylor College of Medicine, 1 Baylor Plaza, BCM-285, Houston, TX 77030, USA*
[6]*Department of Electrical and Computer Engineering, Tufts University, 216 Halligan Hall, Medford, MA 02155, USA*

Correspondence should be addressed to Timothy E. McAlindon; tmcalindon@tuftsmedicalcenter.org

Received 9 September 2015; Accepted 19 November 2015

Academic Editor: Yukihisa Takayama

The purpose of this study was to expand and validate the cartilage damage index (CDI) to detect cartilage damage in the *lateral* tibiofemoral compartment. We used an iterative 3-step process to develop and validate the lateral CDI: development (100 knees), testing (80 knees), and validation (100 knees). The validation set included 100 knees from the Osteoarthritis Initiative that was enriched to include all grades of lateral joint space narrowing (JSN, 0–3). Measurement of the CDI was rapid at 7.4 (s.d. 0.73) minutes per knee pair (baseline and follow-up of one knee). The intratester reliability is good (intraclass correlation coefficient (3, 1 model) = 0.86 to 0.98). At baseline, knees with greater KL grade and lateral JSN had a lower mean CDI (i.e., greater cartilage damage). Baseline lateral CDI is associated with both lateral JSW (r = 0.81 to 0.85, $p < 0.01$) and HKA (r = −0.30 to −0.33, $p < 0.05$). The SRM is good (lateral femur SRM = −0.76; lateral tibia SRM = −0.73; lateral tibiofemoral total SRM = −0.87). The lateral tibiofemoral CDI quantification allows for rapid evaluation and is reliable and responsive, with good construct validity. It may be an efficient method to measure lateral tibiofemoral articular cartilage in large clinical and epidemiologic studies.

1. Introduction

Cartilage morphometry on magnetic resonance (MR) images is important for the assessment of structural progression of knee osteoarthritis (OA). However, manually obtaining accurate and reproducible cartilage data on one set of images can take many hours [1]. To reduce the time and cost of measuring cartilage on MR images, there remains a great need to design a rapid quantification method which has good reproducibility, validity, and sensitivity to change [2].

In our previous study, we developed the cartilage damage index (CDI) for the *medial* knee compartment and demonstrated it to be an efficient, reliable, valid, and sensitive method to measure changes of articular cartilage in the *medial* tibiofemoral compartment. This new study builds on our previously published paper by adapting and testing the CDI to the *lateral* tibiofemoral compartment. It is important to note that we needed to modify the CDI because the medial and lateral tibiofemoral compartments have different articular surface shape [3], loading [4], and distributions of

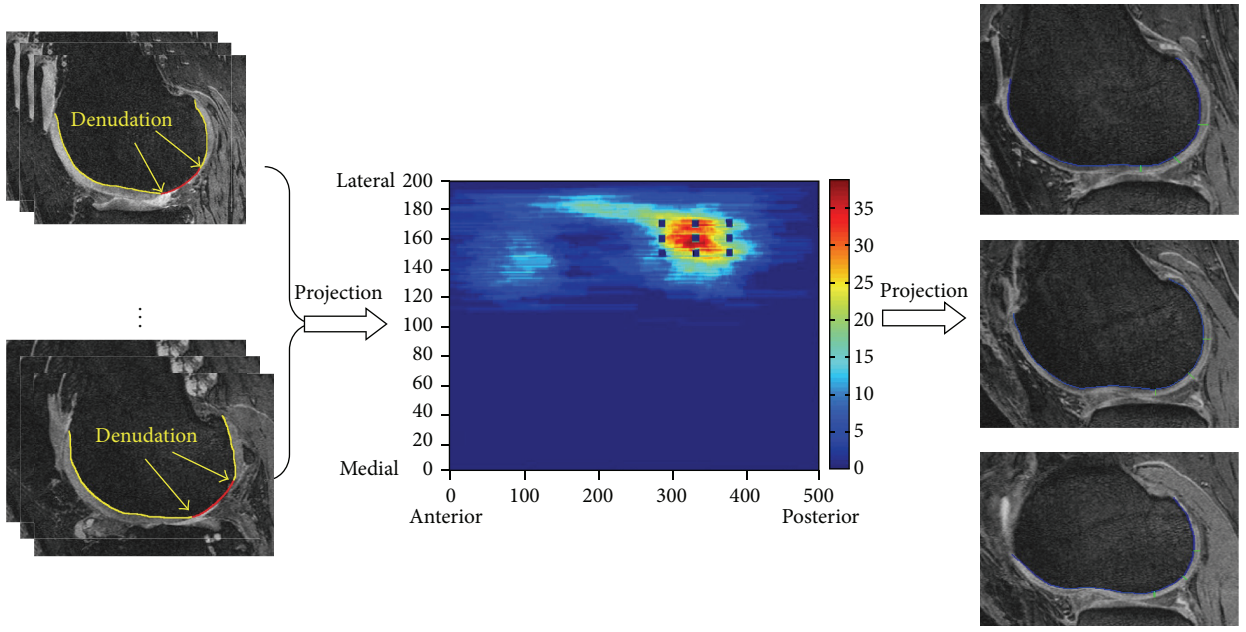

FIGURE 1: (a) Manual lateral femur cartilage mark. (b) Heat map of lateral femur denudation projection. (c) Lateral femur CDI measurement on 3 selected slices.

full thickness cartilage defects [5]. Because of the differences between compartments, we needed to identify new informative locations that are specific to the lateral tibiofemoral compartment and test whether these new locations could offer an efficient, reliable, valid, and sensitive method to measure changes of articular cartilage in the lateral tibiofemoral compartment. Hence, the purpose of this study was to adapt and validate the CDI to detect cartilage damage in the lateral tibiofemoral compartment.

2. Methods

2.1. Study Design. We developed, validated, and assessed reliability of the CDI in the lateral tibiofemoral compartment. Sampling from the Osteoarthritis Initiative (OAI), we created 4 datasets: (1) a development dataset (n = 100 knees), (2) a test dataset (n = 80 knees), (3) a validation dataset (n = 100 knees), and (4) a reliability dataset (n = 20 knees).

2.2. MR Image Assessments. To deploy the CDI, we focused on the OAI 3D sagittal water-excitation dual-echo steady state (DESS) images, which were acquired using the OAI MR imaging protocol [6]. The OAI has institutional review board approval (IRB) from the coordinating centers and the four clinical centers (University of Maryland and Johns Hopkins comprise a single recruitment center, Brown University, Ohio State University, and University of Pittsburgh). All participants provided informed consent to participate in the OAI. The 3D DESS sequences were acquired using the following parameters: field of view = 140 mm, slice thickness = 0.7 mm, skip = 0 mm, flip angle = 25 degrees, echo time = 4.7 ms, recovery time = 16.3 ms, 307 × 384 matrix, x resolution = 0.365 mm, y resolution = 0.456 mm, and total slice number = 160. The acquisition time for 3D DESS sequence is 11 minutes.

2.3. Development Dataset. For the development dataset, we selected 100 knees from OAI baseline that included an equivalent number of knees with the different grades of lateral joint space narrowing (JSN, grades 0–3). We used three steps to develop the lateral tibiofemoral CDI based on areas commonly affected by denudation. (1) One reader manually marked the lateral cartilage denudation on each knee (Figure 1(a)). (2) We designed a pair of two-dimensional, rectangular, universal coordinate systems to represent the articular surface on the distal lateral femur and the proximal lateral tibia (Figure 1(b)). (3) We projected the regions of denudation onto a coordinate system and constructed a figure illustrating the frequency distribution of denudation in a three-dimensional representation of the lateral compartment. We used this to evenly select 9 informative locations on the tibia and femur (18 locations in total) in and around the regions that most frequently exhibited denudation (Figure 1(b)). We hypothesize that this region has more frequent cartilage damage.

2.4. Lateral Tibiofemoral CDI Measurement. There are three steps to measure the lateral CDI. (1) The reader determines the medial-lateral width of the femur by selecting the most medial and lateral MR image slices possessing bone. These images represent the y-axis (medial-to-lateral) of the coordinate system (Figure 1(b)). The software automatically indicates the slices that contain the informative locations based on the coordinate system. (2) The reader manually marks the bone-cartilage boundary on the selected slices (Figure 1(c)).

The software then projects the bone-cartilage to x-axis (anterior-to-posterior) of coordinate system and indicates the predefined informative location on the MR slices. (3) The reader measures the cartilage thickness at those informative locations (Figure 1(c)). The software then computed the CDI by summing the products of cartilage thickness, cartilage length (anterior-posterior), and voxel size from each informative location. To normalize for body size, the CDI for the lateral tibia and femur was divided by the individual's height.

2.5. Test Dataset. We performed preliminary tests to explore face and construct validity by selecting 80 participants from the OAI. These 80 knees all had publicly available manual cartilage segmentation on baseline and 12-month follow-up MR images (Imorphics Ltd; the dataset originally included 88 knees but we excluded 8 knees with missing height or hip-knee-ankle (HKA) angle). These participants also had height data available at each visit. One reader used customized software to measure the CDI in the lateral femur and tibia cartilage in the testing dataset.

2.6. Validation Dataset. To test the validity of the lateral tibiofemoral CDI—the main purpose of this study—we selected 100 knees with baseline and 24-month MR images from the OAI. The validation samples were chosen to represent a wide range of disease severity. The dataset was selected to include all grades of lateral JSN (n = 25 knees per lateral JSN grade) and knees with and without lateral JSN progression (JSN grade change between baseline and follow-up visit). None of these knees was included in the development or test datasets. The first ten ids were used to record the measurement time.

2.7. Reliability Dataset. In addition to the final validation set, we identified 20 other knees to assess intratester reliability (two measurements separated by at least 72 hours). The reliability set was selected based on baseline lateral JSN grade (5 knees per lateral JSN grade).

2.8. Radiographic Assessments. Participants had bilateral weight-bearing, posterior-anterior, semiflexed knee radiographs at each annual OAI visit. Central readers provided Kellgren-Lawrence (KL) grade and the modified OARSI-atlas based assessment of lateral JSN score [7, 8]. The radiographs, central readings, and protocols are publicly available at the OAI website (kxr_sq_bu_00 (version 0.5) and kxr_sq_bu_03 (version 3.5); http://oai.epi-ucsf.org/; reliability for these readings was kappa = 0.70 to 0.88).

The same bilateral knee radiographs were also used to provide central measurements of lateral tibiofemoral joint space width (JSW). We selected lateral JSW at one fixed location (x = 0.725). JSW data and descriptions of the methods are publicly available on the OAI website (kxr_qjsw_duryea_00 (version 0.5) and kxr_qjsw_duryea_03 (version 3.4); http://oai.epi-ucsf.org/; reliability for these readings was ICC > 0.93).

Finally, we used publicly available measures of static alignment (HKA angle) that was measured by a third investigator. The HKA angles were measured on full limb films primarily at the 12-month or 24-month OAI visits. The HKA data and descriptions of the methods are publicly available on the OAI website (flXR_KneeAlign_Cooke01 (version 1.2) and flXR_KneeAlign_Cooke03 (version 3.1); http://oai.epi-ucsf.org/; reliability for these readings was ICC > 0.99).

2.9. Statistical Analyses. We validated the lateral CDI by examining the Spearman correlations between baseline (month 0) lateral CDI, lateral joint space width (JSW), and static alignment (HKA angle). Scatter plots were generated using the ranking (from smallest to largest) of lateral CDI, JSW, and HKA angle measurements. Tests for trend were used to examine associations of lateral CDI with baseline JSN and KL grade. We calculated standard response mean (SRM) for lateral CDI change between baseline and 24 months. To evaluate the intratester reliability, we calculated intraclass correlation coefficients with a 3,1 model [9].

3. Results

3.1. Test Dataset (n = 80). We found a good correlation between baseline lateral CDI and lateral cartilage volume (manual segmentation) in this test dataset (lateral femur: spearman correlation = 0.74; lateral tibia: spearman correlation = 0.77; lateral tibiofemoral: r = 0.80, all $p < 0.0001$).

3.2. Validation Dataset Characteristics (n = 100). The final validation set included 100 knees with a mean age = 64.4 (SD = 9.3) years, 59% females, mean BMI = 28.7 (SD = 4.2) kg/m^2, mean JSW = 4.4 (SD = 2.3) mm, mean HKA = 3.0° (SD = 4.7°), and a diverse range of baseline lateral JSN grades (0 to 3). The distribution of baseline KL and lateral JSN grades is provided in Table 1. Forty-eight knees had lateral JSN progression over 24 months.

3.3. Measurement Time. We recorded the measurement time for the first 10 knees. The average CDI measurement time of 10 knees was 7.4 minutes (SD = 0.73) per pair of knees (baseline and 24-month scans).

3.4. Assessment of Reliability. Intratester (ICC (3, 1 model)) reliability for baseline lateral femur, lateral tibia, and total lateral tibiofemoral ranged from 0.86 to 0.98.

3.5. Relationship of Lateral CDI to Radiographic Severity. At baseline, knees with greater lateral JSN and KL had lower mean CDI (i.e., greater cartilage damage, Table 1). Baseline lateral femur CDI, baseline lateral tibia CDI, and baseline lateral tibiofemoral CDI are associated with both lateral JSW and static alignment (see Table 2 and Supplementary Figures 1 and 2 in Supplementary Material available online at http://dx.doi.org/10.1155/2015/634275).

3.6. Sensitivity to Change. The sensitivity to change is good (SRM = −0.76 for lateral femur; SRM = −0.73 for lateral tibia; SRM = −0.87 for lateral tibiofemoral total).

Table 1: Baseline lateral cartilage damage index stratified by baseline lateral joint space narrowing (JSN) and Kellgren-Lawrence (KL) grade.

(a) Lateral joint space narrowing (JSN)

Cartilage measure	JSN = 0 (n = 25) mean	JSN = 1 (n = 25) mean	JSN = 2 (n = 25) mean	JSN = 3 (n = 25) mean	p value for trend
Lateral femur CDI	2969.3	3003.2	2184.4	1542.0	<0.001
Lateral tibia CDI	1154.9	889.9	663.8	392.7	<0.001
Lateral tibiofemoral CDI	4124.3	3893.0	2848.2	1934.6	<0.001

(b) Kellgren-Lawrence (KL)

Cartilage measure	KL = 0 (n = 10) mean	KL = 1 (n = 6) mean	KL = 2 (n = 32) mean	KL = 3 (n = 26) mean	KL = 4 (n = 26) mean	p value for trend
Lateral femur CDI	2718.7	2831.5	3061.0	2254.0	1605.3	<0.001
Lateral tibia CDI	1229.3	994.1	946.3	690.4	424.7	<0.001
Lateral tibiofemoral CDI	3948.0	3825.5	4007.3	2944.4	2030.0	<0.001

Table 2: Correlation between lateral CDI and baseline HKA and lateral JSW.

	Spearman correlation	
	Lateral JSW	HKA
Femur CDI (baseline)	0.81 ($p < 0.01$)*	−0.31 ($p < 0.01$)*
Tibia CDI (baseline)	0.81 ($p < 0.01$)*	−0.30 ($p = 0.01$)*
Tibiofemoral CDI (baseline)	0.85 ($p < 0.01$)*	−0.33 ($p < 0.01$)*

Notes: * $p < 0.05$; HKA = hip-knee-ankle; JSW = joint space width.

4. Discussion

This study demonstrates that the CDI can be adapted for use in the lateral tibiofemoral compartment by identifying informative locations that are unique to the lateral femur and tibia. This study also shows that the lateral CDI is quick to perform, reliable, and responsive and has good construct validity.

Testing the lateral CDI was important because the lateral denudation regions were in different locations than the medial tibiofemoral compartment [10]. The lateral denudation region is more posterior (both femur and tibia) than medial compartment region. The size of the denudation region is smaller in the lateral compartment compared to the medial compartment.

The lateral CDI had good construct validity relative to other established radiographic measures of knee OA severity and risk factors including lateral tibiofemoral JSN (a semiquantitative scale), lateral JSW (continuous), KL grade (a global semiquantitative score), and knee alignment (continuous). Radiographic JSN and JSW are generally attributed, at least in part, to articular cartilage damage among knees with OA [11]. For example, Bruyere et al. found that lateral tibiofemoral JSW was significantly correlated with baseline lateral tibial cartilage volume ($r = 0.48$, $p < 0.01$) and thickness ($r = 0.58$, $p < 0.01$) [12]. While we only used 18 informative locations, our baseline lateral tibiofemoral CDI had a better correlation with lateral JSW ($r = 0.81$, $p < 0.0001$). We did not look at the correlations with CDI change because Bruyere et al. found that there were no significant correlations between cartilage/thickness loss and lateral JSW [12]. In addition to verifying that the lateral CDI was associated with radiographic OA severity, we also demonstrated that the lateral CDI is related to knee alignment ($r = -0.30$ to -0.33, $p = 0.004$ to 0.01), which is a strong risk factor for knee OA progression [2, 13].

We also found that lateral CDI is sensitive to change over 24 months. One other OAI study found that knees with lateral JSN had more lateral tibiofemoral cartilage loss in 1 year than knees without lateral JSN (SRM = −0.48 versus SRM = −0.09 for total lateral tibiofemoral cartilage thickness change) [14]. Our lateral CDI had a comparable sensitivity (SRM = −0.87 for two-year lateral tibiofemoral change).

The CDI is an efficient method of measuring cartilage damage. The proficient operator can measure the lateral tibiofemoral CDI of a pair of knee MRIs in about 7 minutes. In contrast, the manual MR-based cartilage measurement method may take up to 6 hours per knee [1]. Due to the time and cost of measuring cartilage, most studies only focus on medial tibiofemoral unicompartmental measurements. Using the CDI measurement instead of full manual segmentation represents substantial time and resource savings. Our group plans to complete CDI development to include a comprehensive assessment of knee articular cartilage including medial tibiofemoral, lateral tibiofemoral, and patellofemoral compartments. Such efforts will help develop a quantitative understanding of OA disease progression in a compartment-by-compartment basis.

This study is limited because our validation dataset did not include lateral cartilage segmentation values. However, we found a good correlation between baseline lateral CDI and lateral cartilage volume (manual segmentation) in our test dataset ($r = 0.74$ to 0.80, $p < 0.0001$). Another limitation of CDI is the possibility that the informative locations may not include all cartilage damage. This limitation is similar to other methods that focus on specific articular surface regions [6, 15]. Despite this limitation, we demonstrated that the lateral CDI has good construct validity with radiographic data, which is a common strategy to assess lateral tibiofemoral cartilage data [12, 14, 16].

In summary, the lateral tibiofemoral CDI quantification allows for rapid evaluation and is reliable and responsive, with good construct validity. It may be an efficient method to measure lateral tibiofemoral articular cartilage in large clinical and epidemiologic studies.

Conflict of Interests

The authors declare that there is no conflict of interests regarding the publication of this paper.

Acknowledgments

The OAI is a public-private partnership comprised of five contracts (N01-AR-2-2258; N01-AR-2-2259; N01-AR-2-2260; N01-AR-2-2261; N01-AR-2-2262) funded by the National Institutes of Health, a branch of the Department of Health and Human Services, and conducted by the OAI Study Investigators. Private funding partners include Pfizer, Inc., Novartis Pharmaceuticals Corporation, Merck Research Laboratories, and GlaxoSmithKline. Private sector funding for the OAI is managed by the Foundation for the National Institutes of Health. The test dataset of 80 knees was provided for public access by Imorphics. Jeffrey Duryea measured JSW and HKA data. Dr. Zhang is supported by Scientist Development grant from Rheumatology Research Foundation.

References

[1] J. L. Jaremko, R. W. T. Cheng, R. G. W. Lambert, A. F. Habib, and J. L. Ronsky, "Reliability of an efficient MRI-based method for estimation of knee cartilage volume using surface registration," *Osteoarthritis and Cartilage*, vol. 14, no. 9, pp. 914–922, 2006.

[2] D. J. Hunter, W. Zhang, P. G. H. Conaghan et al., "Systematic review of the concurrent and predictive validity of MRI biomarkers in OA," *Osteoarthritis and Cartilage*, vol. 19, no. 5, pp. 557–588, 2011.

[3] A. Gulati, R. Chau, D. J. Beard, A. J. Price, H. S. Gill, and D. W. Murray, "Localization of the full-thickness cartilage lesions in medial and lateral unicompartmental knee osteoarthritis," *Journal of Orthopaedic Research*, vol. 27, no. 10, pp. 1339–1346, 2009.

[4] M. K. Harman, G. D. Markovich, S. A. Banks, and W. A. Hodge, "Wear patterns on tibial plateaus from varus and valgus osteoarthritic knees," *Clinical Orthopaedics and Related Research*, no. 352, pp. 149–158, 1998.

[5] J. Weidow, "Lateral osteoarthritis of the knee. Etiology based on morphological, anatomical, kinematic and kinetic observations," *Acta Orthopaedica. Supplementum*, vol. 77, no. 322, pp. 3–44, 2006.

[6] W. Wirth, M. Nevitt, M.-P. H. Le Graverand et al., "Sensitivity to change of cartilage morphometry using coronal FLASH, sagittal DESS, and coronal MPR DESS protocols—comparative data from the osteoarthritis initiative (OAI)," *Osteoarthritis and Cartilage*, vol. 18, no. 4, pp. 547–554, 2010.

[7] R. D. Altman and G. E. Gold, "Atlas of individual radiographic features in osteoarthritis, revised," *Osteoarthritis Cartilage*, vol. 15, supplement A, pp. A1–A56, 2007.

[8] D. T. Felson, M. C. Nevitt, M. Yang et al., "A new approach yields high rates of radiographic progression in knee osteoarthritis," *The Journal of Rheumatology*, vol. 35, no. 10, pp. 2047–2054, 2008.

[9] P. E. Shrout and J. L. Fleiss, "Intraclass correlations: uses in assessing rater reliability," *Psychological Bulletin*, vol. 86, no. 2, pp. 420–428, 1979.

[10] J. D. Harris and D. C. Flanigan, "Management of knee articular cartilage injuries," in *Modern Arthroscopy*, J. L. Dragoo, Ed., chapter 6, InTech, Rijeka, Croatia, 2001.

[11] W. P. Chan, G.-S. Huang, S.-M. Hsu, Y.-C. Chang, and W.-P. Ho, "Radiographic joint space narrowing in osteoarthritis of the knee: relationship to meniscal tears and duration of pain," *Skeletal Radiology*, vol. 37, no. 10, pp. 917–922, 2008.

[12] O. Bruyere, H. Genant, M. Kothari et al., "Longitudinal study of magnetic resonance imaging and standard X-rays to assess disease progression in osteoarthritis," *Osteoarthritis and Cartilage*, vol. 15, no. 1, pp. 98–103, 2007.

[13] L. Sharma, J. Song, D. T. Felson, S. Cahue, E. Shamiyeh, and D. D. Dunlop, "The role of knee alignment in disease progression and functional decline in knee osteoarthritis," *Journal of the American Medical Association*, vol. 286, no. 2, pp. 188–195, 2001.

[14] W. Wirth, M. Nevitt, M.-P. Hellio Le Graverand et al., "Lateral and medial joint space narrowing predict subsequent cartilage loss in the narrowed, but not in the non-narrowed femorotibial compartment—data from the Osteoarthritis Initiative," *Osteoarthritis and Cartilage*, vol. 22, no. 1, pp. 63–70, 2014.

[15] J. Duryea, C. Ratzlaff, T. Iranpour-Boroujeni et al., "Responsiveness of a semi-automated novel method of measuring cartilage loss in knee osteoarthritis over two years using 3.0T DESS 3D MRI," *Osteoarthritis Cartilage*, vol. 20, article S221, 2012.

[16] F. Eckstein, W. Wirth, M. Hudelmaier et al., "Patterns of femorotibial cartilage loss in knees with neutral, varus, and valgus alignment," *Arthritis Care & Research*, vol. 59, no. 11, pp. 1563–1570, 2008.

Hindawi Publishing Corporation
BioMed Research International
Volume 2015, Article ID 482017, 6 pages
http://dx.doi.org/10.1155/2015/482017

Research Article

Quantitative Evaluation of Growth Plates around the Knees of Adolescent Soccer Players by Diffusion-Weighted Magnetic Resonance Imaging

Zmago Krajnc,[1] Mitja Rupreht,[2,3] and Matej Drobnič[4]

[1]*Department of Orthopaedic Surgery, University Medical Centre Maribor, Maribor, Slovenia*
[2]*Department of Radiology, University Medical Centre Maribor, Maribor, Slovenia*
[3]*Medical Faculty, University of Maribor, Maribor, Slovenia*
[4]*Department of Orthopaedic Surgery, University Medical Centre Ljubljana, Ljubljana, Slovenia*

Correspondence should be addressed to Mitja Rupreht; mitja.rupreht@guest.arnes.si

Received 7 September 2015; Revised 25 October 2015; Accepted 9 November 2015

Academic Editor: Jinyuan Zhou

Purpose. To quantitatively evaluate growth plates around the knees in adolescent soccer players utilizing the diffusion-weighted MR imaging (DWI). *Methods*. The knees and adjacent growth plates of eleven 14-year-old male soccer players were evaluated by MRI before (end of season's summer break) and after two months of intense soccer training. MRI evaluation was conducted in coronal plane by PD-FSE and DWI. All images were screened for any major pathological changes. Later, central growth plate surface area (CGPSA) was measured and the apparent diffusion coefficient (ADC) values were calculated in two most central coronal slices divided into four regions: distal femur medial (DFM), distal femur lateral (DFL), proximal tibia medial (PTM), and proximal tibia lateral (PTL). *Results*. No gross pathology was diagnosed on MRI. CGPSA was not significantly reduced: DFM 278 versus 272, DFL 265 versus 261, PTM 193 versus 192, and PTL 214 versus 210. ADC decrease was statistically significant only for PTM: DFM 1.27 versus 1.22, DFL 1.37 versus 1.34, PTM 1.13 versus 1.03 ($p = 0.003$), and PTL 1.28 versus 1.22. *Conclusions*. DWI measurements indicate increased cellularity in growth plates around knees in footballers most prominent in PTM after intense training. No detectable differences on a standard PD-FSE sequence were observed.

1. Introduction

Soccer is the most popular and widely played sport worldwide, especially among children and adolescents [1]. The players are notorious for their bow-legs and this general observation has recently been proven scientifically: studies by Chantraine and Witvrouw et al. confirmed an evident association between soccer playing and genu varum [2, 3]. Soccer playing, particularly at higher competition levels on a daily basis, induces an inordinate amount of load and torque in the involved extremity [2, 3]. In a growing skeleton, these forces are transferred further onto growth plates that are subsequently asymmetrically activated [4–6]. Varus deformity in boys typically arises between the ages of 13 to 15, when the skeletal growth spurt is reached [2, 3, 7, 8]. Varus causes medial knee compartment overloading and increases a risk for an early cartilage failure [9–12]. Bow-legs additionally predispose athletes to patellofemoral pain syndrome and meniscal lesions [8]. Current musculoskeletal MRI techniques may detect acute physeal injuries and their late consequences [13, 14], but they are not able to reveal chronic physeal dysfunction induced by the repetitive loading. Diffusion-weighted MR imaging (DWI) is a novel addition to the MR sequences which provides quantitative information on microscopic movements of water at the cellular level [15]. In musculoskeletal system, DWI has been particularly useful for the differentiation of metastatic from osteoporotic vertebral fractures, for the evaluation of bone marrow pathology, such as infection and haematological malignancies, and also for the detection of bone metastases and their response to treatment [15–20]. The aim of the current study was to evaluate usage of DWI in the chronic,

Table 1: General and anthropometric data of adolescent soccer players enrolled in the study ($N = 11$). Data are presented as mean (SD).

Data	Values (SD)
Height (cm)	169.2 (4.9)
Weight (kg)	59.3 (4.1)
BMI (kg/m^2)	20.7 (1.3)
Lower limb alignment (mm)*	23.6 (16.2)
Years of training	6 (1.3)
KOOS score SPORT	100 (0)
Tegner Lysholm Knee Score	100 (0)

*Average intracondylar (positive for varus) or intramalleolar (negative for valgus) distance.

sports activity-related disturbances of growth plates. To the best of our knowledge, this is the first time DWI was used for evaluation of the growth plates around the knees. We hypothesized that DWI-MRI is able to detect and quantify water diffusibility changes in growth plates around the knees of adolescent soccer players before and after intensive sports participation.

2. Materials and Methods

The study was designed as a 4-month single-centre case series. The protocol was approved by the National Medical Ethics Committee (number 86/02/13). The work was conducted in accordance with the Declaration of Helsinki (1964).

2.1. Participants and Sports Activity. The study group comprised eleven asymptomatic junior members U14 of the soccer club NK Maribor, Slovenia, who had a history of soccer training for a minimum of 3 years. Informed consent was obtained from all individual participants and their parents. The following exclusion criteria were set: history of lower limb surgery or any serious knee injury, musculoskeletal abnormalities or systemic disease with a possible impact on joints, or presence of metallic foreign bodies that would had prevented MRI examination. Players' general data and physical examination (height, weight, hip, and knee range of motion measurements) were acquired upon inclusion. Clinical measurements of lower limb mechanical alignment were conducted in a weight-bearing position with a calliper, similarly as previously described [7, 21]. Demographic and anthropometric data are summarized in Table 1.

The initial examinations and baseline MRIs were performed at the end of "summer soccer vacation," which had lasted from mid-May 2014 till mid-June 2014. During this one-month period the players were not involved in any systematic soccer training. They were allowed to conduct only low intensity running, swimming, and cycling. No cutting and pivoting sports were performed during this period. The players were asked to fill in daily activities diary. After this quiet period, the players were enrolled into preparations for the new season. They followed an intense practice routine of circuit training workouts, aerobic and anaerobic exercises with and without the ball, high intensity running (sprinting and jogging), plyometric and isometric exercises, and soccer training skills (kicking, ball control, heading, dribbling, passing, and tackling). They were also involved in the preparation matches. Participants were active in the training process between 1.5 and 3.5 hours daily, 6 days a week. The second MRI was conducted after two months of such training, within 24 hours after their last sporting activity.

2.2. MRI Acquisition. Both MRI scans were performed on a 3 T Signa Excite (General Electric, Waukesha, WI, USA) MRI scanner using eight-channel transmit-receive knee coil. Both knees were scanned in 7 players and only dominant leg was scanned in 4 players due to limited parent consent. MRI examinations were first performed in the proton-density fast spin-echo (PD-FSE) sequence with eighteen fat-suppressed slices in the coronal plane: TR (repetition time) = 2080 ms, TE (echo time) = 11 ms, ETL = 6, ST (slice thickness) = 3 mm, spacing = 0.3 mm, FOV (field of view) = 18 cm, and matrix = 384 × 384 (Figure 1). This pulse sequence has an excellent spatial and contrast resolution and it is one of the most commonly used in the routine knee MRI. It is clinically utilized for diagnosing the areas of bone marrow oedema (BME) as well as the analysis of the articular cartilage, menisci, and cruciate ligaments. DWI was performed with the echo-planar imaging (EPI) method. Ten 7 mm slices were acquired with 1 mm gap, using the spin-echo single shot technique at TR/TE = 8000/75 ms, 20 cm FOV, and 160 × 256 matrix. Two image acquisitions were performed for each DWI: one without ($b = 0$ s/mm^2) and the other with diffusion weighting ($b = 400$ s/mm^2) with the inferior-superior direction of gradient orientation. FOV included the distal femur and proximal tibia in a coronal plane thereby including the distal femoral and proximal tibial metaphysis (Figure 2).

2.3. MRI Analysis. All MRI analyses and measurements were performed by consensus of a musculoskeletal radiologist with 10 years of experience (MR) and an orthopaedic surgeon (ZK) being blind to the study group and the examination time. They were performed 2 months after the last MRI to minimize bias resulting from the consensus reading.

Coronal fat-suppressed PD-FSE images were first analysed for any gross pathology in and around the knee. Screening for BME was then performed. BME was defined as an area of visually detected clearly increased signal intensity in the bone marrow at least on two consecutive PD-FSE images, measuring between 0.5 cm^2 and 1.5 cm^2. Larger homogenous areas of slightly increased signal intensities, found predominantly in the diaphysis of femur and tibia, were not considered as BME, since they represent areas of active red marrow, which may be normally present in this age group [22].

For DWI analyses, the region of interest (ROI) encircled the border of the growth plates of femur and tibia in two consecutive most central coronal slices. At each slice, ROIs were divided into medial and lateral half (Figure 2) yielding four regions: distal femur medial (DFM), distal femur lateral

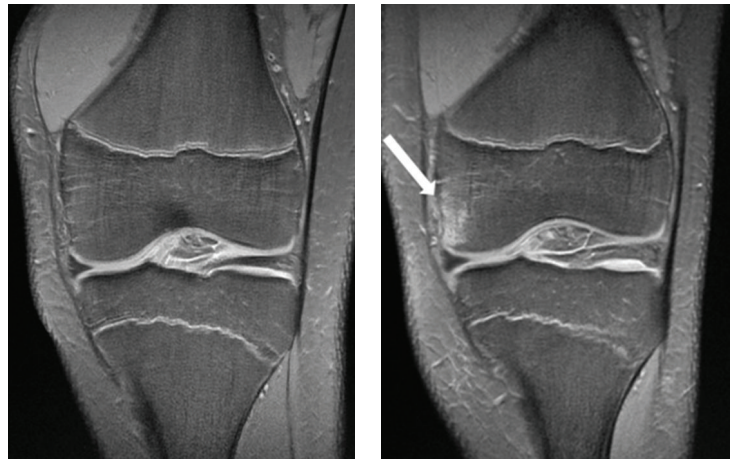

(a) (b)

Figure 1: Coronal PD fat-saturated FSE images show left knee of a 14-year-old soccer player before (a) and two months after (b) seasonal training. Note the area of the increased signal intensity in the anterior aspect of the medial femoral condyle in (b) (arrow) compared to (a) representing bone marrow oedema reflecting stress reaction or contusion during the training.

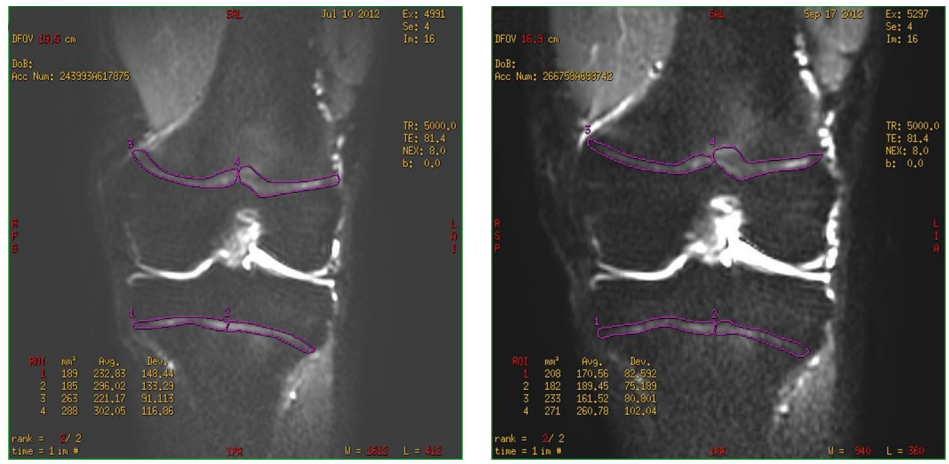

(a) (b)

Figure 2: A sample of DWI analysis in a 14-year-old soccer player before (a) and two months after (b) sport activity. First, the coronal surfaces in the most central MRI were encircled (purple line). Each growth plate surface area was then halved to form four regions of interest for the analysis. An apparent diffusion coefficient (ADC) was calculated in each of these regions.

(DFL), proximal tibia medial (PTM), and proximal tibia lateral (PTL). In the follow-up examination, the same slices were meticulously chosen for the analyses. From two DWI image sets of different b values, apparent diffusion coefficient (ADC) maps were calculated. This was followed by the calculation of ADC values (mm/s $\times 10^{-3}$) for each region with the subsequent average of both slices. Also, the area of each region was recorded and the average was calculated from both consecutive slices representing the central growth plate surface area (CGPSA) value (mm^2).

2.4. Data Analysis. All the data are presented as mean values with SD. Preactivity to postactivity values of *CGPSA* and the ADC in each of the growth plate regions were compared by Student's t-test for paired samples with a statistical significance set to $P < 0.05$. The computer software IBM SPSS Statistics, Version 20, was used. Post hoc power analysis of ADC preactivity to postactivity values in the proximal tibia medial growth plate (PTM) showed an effect size of 0.80 and a statistical power of 0.95 (calculated with G*Power 3.1.7, Universität Kiel, Germany).

3. Results

There was no gross pathology of cartilage, bone, ligaments, or menisci diagnosed on preactivity or on postactivity images. No intra-articular effusion was found in any case. Bone marrow oedema was detected in three knees of different individuals, always in the medial femoral condyle (Figure 1).

Table 2: Measured values of the central growth plate surface area (CGPSA) in mm^2 and the calculated apparent diffusion coefficient (ADC) values in $mm/s \times 10^{-3}$ around the knees ($N = 18$) of adolescent soccer players before and after an intensive activity. Data is presented as mean (SD); statistically significant pairs are marked with $*$.

Growth plate region	Central growth plate surface area		Apparent diffusion coefficient	
	Preactivity	Postactivity	Preactivity	Postactivity
Distal femur medial	265.28	261.17	1.3679	1.3473
Distal femur lateral	277.67	272.28	1.2749	1.2202
Proximal tibia medial	193.33	191.67	1.1333*	1.0317*
Proximal tibia lateral	213.72	210.39	1.2759	1.2177

In one knee, it was present before and after the soccer training, whereas in the other two it was diagnosed only at the follow-up examinations. CGPSA of all growth plates was not significantly reduced: DFM 278 versus 272; DFL 265 versus 261; PTM 193 versus 192; and PTL 214 versus 210. A decrease of ADC in all four growth plates occurred during the follow-up but it was statistically significant only for PTM: DFM 1.27 versus 1.22; DFL 1.37 versus 1.34; PTM 1.13 versus 1.03 ($p = 0.003$); and PTL 1.28 versus 1.22 (Table 2 and Figure 2).

4. Discussion

The aetiology of genu varum in soccer is thought to be multifactorial: ranging from natural selection of players with a genetic predisposition to varus (varus knees have some advantages for soccer performance) to mechanical overload of proximal medial tibial physis [7]. The susceptibility of growth plates to injury appears to be especially pronounced during the period of rapid pubescent growth spurt [13, 23]. An accumulating number of clinical reports indicate that intensive sport training may precipitate pathological changes of the growth plate and even produce growth disturbance [13]. An increased varus deviation around the knees of soccer players in comparison to the same aged peers was also observed during this time period [3, 7, 8, 10, 24]. Clinically measured axial deviations of lower extremities in our study group (mean ICD was 24 mm) were comparable to the reports of other authors (ICD from 22 to 33 mm) for the age matched soccer players [3, 7, 8]. Proximal tibial growth changes due to repeated stress over the open growth plates may be a possible mechanism of this axis deviation. Several factors other than running and cutting manoeuvres unique to the soccer may play a role as deforming forces of which the ball kicking deserves special attention for its additional torque movement which is unique to soccer when compared to other sports. However, the exact mechanism or activity that leads to increased medial growth plate stress remains enigmatic.

The histological evaluation of growth plates in humans is limited to the material retrieved at the surgical procedure, epiphysiodesis, which cannot be used for systematic studies of sporting population. Conventional radiography, CT, and MRI had been used in the assessment of growth plates injuries in the past [13, 25, 26]. Radiological diagnoses were based on the widening of the physis, irregularity of the metaphyseal line, and fragmentation or separation of the metaphysis [13, 14]. These radiological findings become visible only after a period of a pain interval when an athlete is brought to the radiological examination [13]. On the contrary, they fail to show any changes in asymptomatic adolescent athletes. To the best of our knowledge, DWI has not been utilized for the evaluation of the growth plates around the knees yet. It represents a novel diagnostic tool in which image contrast is related to the random motion of water protons, which differs in various tissue environments. It therefore noninvasively reflects the tissue organizational features, principally its cellularity [15]. Diffusion weighting in the spin-echo echo-planar T2 weighted sequence is achieved by two additional gradient pulses of equal magnitude and polarity symmetrically positioned relative to the refocusing RF pulse. The degree of diffusion weighting (b value) is determined by the amplitude of the gradient pulses, as well as by their duration and spacing. Two DWI acquisitions with different b values enable calculation of ADC map. Higher ADC values correspond to elevated diffusion in the extracellular space; the motion of water is less restricted [20]. In areas with high cellularity, molecular water mobility is impeded, yielding lower ADC values [20]. One of the most important findings of this study is the feasibility of DWI-MRI to detect subtle, activity-related changes in the growth plates around the knees of adolescent soccer players. The calculated ADC values in the growths plates were lower than mean values for free water (2.80×10^{-3} mm^2/s at 37°C) [16], but higher than ADC values for normal bone marrow (0.15 to 0.23×10^{-3} mm^2/s) [16, 17]. Decreasing ADC values at the follow-up examinations of adolescent soccer players, although not statistically significant, may reflect an increased cellularity in the growth plates, possibly owing to the maturation. Significantly lower ADC values in PTM growth plate disclose additional reduction of water mobility in the extracellular space in this region. This suggests that cellular structures in this zone are even higher packed as a response to the extreme repetitive rotational and pressure forces on the physes. This is consistent with histological findings in animal studies (more numerous chondrocytes, a notable increase in the hypertrophic cell zone, and a progressive disorganization of the layers and chondrocyte columns) after their growth plates were exposed

to a compressive external impact [27, 28]. Consequently, we can presume that higher cellularity in medial tibial growth plate indicates the greatest impact of soccer training on the medial tibial growth plate. This is in accordance with the higher incidence of varus angulation among soccer players at the end of growth spurt [3, 7, 8]. It is also in line with general varus deformity of the knee, which is typically caused by deficiency in the medial tibia plateau, since distal femoral surface usually remains in valgus to neutral alignment to the long axis of femur [29]. Preserved CGPSA during the follow-up could be probably related to a relatively short follow-up period. This finding further emphasizes the importance of DWI for detection of cellularity, which seems to be more sensitive indicator of growth plate activity than its surface area.

BME signal is an unspecific MRI finding showing increased water content in the bone marrow accompanying fracture, stress reaction, bone contusion, inflammation, or tumour. Therefore the correlation with other imaging and clinical findings is necessary. The few areas of BME, found in three cases, most probably represent an unspecific stress reaction that was previously already described by Soder et al. in their study of asymptomatic adolescent soccer players [30]. Preserved integrity of menisci as well as the lack of larger joint effusion, cartilage, or cruciate lesion is in accordance with previous studies of MRI findings in asymptomatic junior athletes [31, 32].

The presented study has the following limitations. The study group was rather small therefore necessitating the confirmation of the results by a prospective study on a larger number of sporting and nonsporting adolescent subjects. To minimize bias resulting from consensus analyses by the MSK radiologist and the orthopaedic surgeon, MRI analyses were performed 2 months after the last MRI. Still, this might represent another study limitation. DWI with low b value (so-called "black blood" images) is susceptible to influences related to perfusion and T2. However we were cautious not to lose signal also in the growth plates with higher b values, being aware of biexponential behaviour of the signal intensity decay observed with increasing b values [15], in particular in the context of a limited experience in DWI of growth plates. Calculating the average ADC and growth plate area from several slices could be more accurate, but it would be also time-consuming and more complex for data analyses. The main advantage of DWI is in its quantitative nature that limits the observer's variability only to ROI delineation. In clinical routine, the articular cartilage, menisci, effusion, and cruciate ligaments are evaluated in both coronal and sagittal plane in one of standard sequences. We did not perform PD sequence in the sagittal plane for the time reasons; therefore some smaller lesions and effusions could have been missed. However, they were not clinically considered in any of the participants. To date, we have no data available on the kinetics and duration of ADC changes in the growth plates after an activity. To answer this question properly, a continuous daily scanning would be required. We currently also do not have any data on the normal values of ADC in growth plates of certain age groups; however, pre- and postactivity imaging allowed us to detect relative changes in ADC.

5. Conclusions

The presented study confirmed the feasibility of DWI in the evaluation of growth plates. Quantitative DWI measurements indicate increased cellularity in the medial part of the proximal tibial growth plate around the knee linked to intense soccer training in asymptomatic adolescent players. This suggests an asymmetric growth plate involvement that may consequently lead to bow-leg deformity. No detectable differences on a standard PD-FSE sequence were observed. Having a quantitative imaging tool for growth plates evaluation is important to delineate harmful sporting activities and to avoid or modify them accordingly to prevent long-term impacts on the growing skeleton.

Conflict of Interests

The authors declare that they have no conflict of interests.

Authors' Contribution

The authors agree that all of them contributed equally to the presented work and therefore all shall be regarded as the leading authors.

References

[1] J. Dvorak, A. Junge, T. Graf-Baumann, and L. Peterson, "Football is the most popular sport worldwide," *The American Journal of Sports Medicine*, vol. 32, no. 1, supplement, pp. 3S–4S, 2004.

[2] A. Chantraine, "Knee joint in soccer players: osteoarthritis and axis deviation," *Medicine and Science in Sports and Exercise*, vol. 17, no. 4, pp. 434–439, 1985.

[3] E. Witvrouw, L. Danneels, Y. Thijs, D. Cambier, and J. Bellemans, "Does soccer participation lead to genu varum?" *Knee Surgery, Sports Traumatology, Arthroscopy*, vol. 17, no. 4, pp. 422–427, 2009.

[4] C. Heuter, "Antomical study of the limb joints of newborns and adults," *Virchows Archiv*, vol. 25, no. 5-6, pp. 572–599, 1862.

[5] R. Volkmann, "Impairments of the musculoskeletal system," in *Handbook for Common and Special Surgery*, B. Pitha, Ed., pp. 845–920, Ferdinand Enkle, Stuttgart, Germany, 1869.

[6] H. M. Frost, "A chondral modeling theory," *Calcified Tissue International*, vol. 28, no. 3, pp. 181–200, 1979.

[7] M. Yaniv, T. Becker, M. Goldwirt, S. Khamis, D. M. Steinberg, and S. Weintroub, "Prevalence of bowlegs among child and adolescent soccer players," *Clinical Journal of Sport Medicine*, vol. 16, no. 5, pp. 392–396, 2006.

[8] Y. Thijs, J. Bellemans, L. Rombaut, and E. Witvrouw, "Is high impact sports participation associated with bowlegs in adolescent boys?" *Medicine and Science in Sports and Exercise*, vol. 44, no. 6, pp. 993–998, 2012.

[9] G. M. Brouwer, A. W. Van Tol, A. P. Bergink et al., "Association between valgus and varus alignment and the development and progression of radiographic osteoarthritis of the knee," *Arthritis and Rheumatism*, vol. 56, no. 4, pp. 1204–1211, 2007.

[10] D. D. Wu, D. B. Burr, R. D. Boyd, and E. L. Radin, "Bone and cartilage changes following experimental varus or valgus tibial angulation," *Journal of Orthopaedic Research*, vol. 8, no. 4, pp. 572–585, 1990.

[11] J. D. Metzl and L. J. Micheli, "Youth soccer: an epidemiologic perspective," *Clinics in Sports Medicine*, vol. 17, no. 4, pp. 663–673, 1998.

[12] D. Hayashi, M. Englund, F. W. Roemer et al., "Knee malalignment is associated with an increased risk for incident and enlarging bone marrow lesions in the more loaded compartments: the MOST study," *Osteoarthritis and Cartilage*, vol. 20, no. 11, pp. 1227–1233, 2012.

[13] D. Caine, J. DiFiori, and N. Maffulli, "Physeal injuries in children's and youth sports: reasons for concern?" *British Journal of Sports Medicine*, vol. 40, no. 9, pp. 749–760, 2006.

[14] L. F. Rogers and A. K. Poznanski, "Imaging of epiphyseal injuries," *Radiology*, vol. 191, no. 2, pp. 297–308, 1994.

[15] M. M. Y. Khoo, P. A. Tyler, A. Saifuddin, and A. R. Padhani, "Diffusion-weighted imaging (DWI) in musculoskeletal MRI: a critical review," *Skeletal Radiology*, vol. 40, no. 6, pp. 665–681, 2011.

[16] N. Gašperšič, I. Serša, V. Jevtič, M. Tomšič, and S. Praprotnik, "Monitoring ankylosing spondylitis therapy by dynamic contrast-enhanced and diffusion-weighted magnetic resonance imaging," *Skeletal Radiology*, vol. 37, no. 2, pp. 123–131, 2008.

[17] R. Bammer, A. M. Herneth, S. E. Maier et al., "Line scan diffusion imaging of the spine," *American Journal of Neuroradiology*, vol. 24, no. 1, pp. 5–12, 2003.

[18] M. H. Pui, A. Mitha, W. I. D. Rae, and P. Corr, "Diffusion-weighted magnetic resonance imaging of spinal infection and malignancy," *Journal of Neuroimaging*, vol. 15, no. 2, pp. 164–170, 2005.

[19] W. M. Byun, S. O. Shin, Y. Chang, S. J. Lee, J. Finsterbusch, and J. Frahm, "Diffusion-weighted MR imaging of metastatic disease of the spine: assessment of response to therapy," *American Journal of Neuroradiology*, vol. 23, no. 6, pp. 906–912, 2002.

[20] M. Rupreht, V. Jevtič, I. Serša, M. Vogrin, and M. Jevšek, "Evaluation of the tibial tunnel after intraoperatively administered platelet-rich plasma gel during anterior cruciate ligament reconstruction using diffusion weighted and dynamic contrast-enhanced MRI," *Journal of Magnetic Resonance Imaging*, vol. 37, no. 4, pp. 928–935, 2013.

[21] C. H. Heath and L. T. Staheli, "Normal limits of knee angle in white childrenβgenu varum and genu valgum," *Journal of Pediatric Orthopaedics*, vol. 13, no. 2, pp. 259–262, 1993.

[22] G. C. Dooms, M. R. Fisher, H. Hricak, M. Richardson, L. E. Crooks, and H. K. Genant, "Bone marrow imaging: magnetic resonance studies related to age and sex," *Radiology*, vol. 155, no. 2, pp. 429–432, 1985.

[23] T. Sasaki, Y. Ishibashi, Y. Okamura, S. Toh, and T. Sasaki, "MRI evaluation of growth plate closure rate and pattern in the normal knee joint," *The Journal of Knee Surgery*, vol. 15, no. 2, pp. 72–76, 2002.

[24] K. Ecklund and D. Jaramillo, "Patterns of premature physeal arrest: MR imaging of III children," *American Journal of Roentgenology*, vol. 178, no. 4, pp. 967–972, 2002.

[25] M. Nanni, S. Butt, R. Mansour, T. Muthukumar, V. N. Cassar-Pullicino, and A. Roberts, "Stress-induced Salter-Harris I growth plate injury of the proximal tibia: first report," *Skeletal Radiology*, vol. 34, no. 7, pp. 405–410, 2005.

[26] T. Laor, E. J. Wall, and L. P. Vu, "Physeal widening in the knee due to stress injury in child athletes," *American Journal of Roentgenology*, vol. 186, no. 5, pp. 1260–1264, 2006.

[27] F. Arriola, F. Forriol, and J. Cañadell, "Histomorphometric study of growth plate subjected to different mechanical conditions (compression, tension and neutralization): an experimental study in lambs mechanical growth plate behavior," *Journal of Pediatric Orthopaedics—Part B*, vol. 10, no. 4, pp. 334–338, 2001.

[28] J. Trueta and A. Trias, "The vascular contribution to osteogenesis. IV. The effect of pressure upon the epiphysial cartilage of the rabbit," *The Journal of Bone & Joint Surgery—British Volume*, vol. 43, no. 4, pp. 800–813, 1961.

[29] L. A. Whiteside, *Ligament Balancing in Total Knee Arthroplasty. An Instructional Manual*, Springer, New York, NY, USA, 2004.

[30] R. B. Soder, J. D. Simões, J. B. Soder, and M. Baldisserotto, "Study MRI of the knee joint in asymptomatic adolescent soccer players: a controlled study," *American Journal of Roentgenology*, vol. 196, no. 1, pp. W61–W65, 2011.

[31] W. Krampla, R. Mayrhofer, J. Malcher, K. H. Kristen, M. Urban, and W. Hruby, "MR imaging of the knee in marathon runners before and after competition," *Skeletal Radiology*, vol. 30, no. 2, pp. 72–76, 2001.

[32] C. Schueller-Weidekamm, G. Schueller, M. Uffmann, and T. R. Bader, "Does marathon running cause acute lesions of the knee? Evaluation with magnetic resonance imaging," *European Radiology*, vol. 16, no. 10, pp. 2179–2185, 2006.

Hindawi Publishing Corporation
BioMed Research International
Volume 2015, Article ID 731903, 5 pages
http://dx.doi.org/10.1155/2015/731903

Research Article

Magnetic Resonance Image Sequence Influences the Relationship between Bone Marrow Lesions Volume and Pain: Data from the Osteoarthritis Initiative

Ming Zhang,[1] Jeffrey B. Driban,[1] Lori Lyn Price,[2] Grace H. Lo,[3,4] and Timothy E. McAlindon[1]

[1] *Division of Rheumatology, Tufts Medical Center, 800 Washington Street, Box No. 406, Boston, MA 02111, USA*
[2] *The Institute for Clinical Research and Health Policy Studies, Tufts Medical Center and Tufts Clinical and Translational Science Institute, Tufts University, 800 Washington Street, Box No. 63, Boston, MA 02111, USA*
[3] *Medical Care Line and Research Care Line, Houston VA HSR&D Center for Innovations in Quality, Effectiveness and Safety, Michael E. DeBakey VAMC, Houston, TX 77030, USA*
[4] *Section of Immunology, Allergy, and Rheumatology, Baylor College of Medicine, 1 Baylor Plaza, BCM-285, Houston, TX 77030, USA*

Correspondence should be addressed to Timothy E. McAlindon; tmcalindon@tuftsmedicalcenter.org

Received 17 August 2015; Revised 16 October 2015; Accepted 19 October 2015

Academic Editor: Yukihisa Takayama

Subchondral bone marrow lesions (BMLs) are related to structural and symptomatic osteoarthritis progression. However, it is unclear how sequence selection influences a quantitative BML measurement and its construct validity. We compared quantitative assessment of BMLs on intermediate-weighted fat suppressed (IW FS) turbo spin echo and 3-dimensional dual echo steady state (3D DESS) sequences. We used a customized software to measure 30 knees' (24- and 48-month MR images) BMLs on both sequences. The results showed that the IW FS sequences have much larger BML volumes (median: IW FS = 1840 mm^3; DESS = 191 mm^3) and BML volume change (between 24 and 48 months) than DESS sequence and demonstrate more BML volume change. The 24-month BML volume on IW FS is correlated with BML volume on DESS (r_s = 0.83). BML volume change on IW FS is not significantly correlated with change on DESS. The 24-month WOMAC pain is correlated with the 24-month BMLs on IW FS (r_s = 0.39) but not DESS. The change in WOMAC pain is correlated with BML volume change on IW FS (r_s = 0.37) but not DESS. Overall, BML quantification on IW FS offers better validity and statistical power than BML quantification on a 3D DESS sequence.

1. Introduction

Subchondral bone marrow lesions (BMLs) are common findings on magnetic resonance (MR) images of knees with osteoarthritis (OA) and relate to structural and symptomatic progression of OA [1–3]. While BMLs are often assessed on intermediate-weighted fat suppressed (IW FS) or similar sequences [4] some researchers have also evaluated BMLs on 3-dimensional dual echo steady state (3D DESS) sequences or other similar sequences that are used for cartilage measurements [5]. The latter approach enables a time- and cost-efficient method to assess changes in BMLs and cartilage on the same sequence [6]. One prior study provided a head-to-head cross-sectional comparison using a semiquantitative measure of BML and demonstrated that IW FS sequences are more sensitive to detecting BMLs [7]. No studies to our knowledge have evaluated the measures longitudinally nor have any studies compared the association of BMLs measured with the two different sequences as they relate with pain, which would provide insight into the construct validity of the BMLs measured using the two different sequences [7]. The purpose of this study was to compare assessment of BMLs on IW FS and 3D DESS sequences both cross-sectionally and longitudinally using quantitative assessments and to evaluate their construct validity against knee pain. We anticipated that BML volumes and change of volumes would be larger on IW FS than on a 3D DESS sequence but that construct validity would be similar.

2. Methods

2.1. Participants. We chose 30 knees from the Osteoarthritis Initiative (OAI) with 24- and 48-month MR images as well as complete data from the OAI Bone Ancillary Study (i.e., subchondral bone mineral density, MR-based trabecular morphometry, meniscal readings, and cartilage damage). We enriched the study sample by selecting knees with or without medial joint space narrowing to increase the heterogeneity of BML size and BML change. Fifteen knees were selected among those with an increase in medial joint space narrowing (OARSI score) between the 24- and 48-month OAI visits. An additional 15 knees with no increase in medial joint space narrowing were also selected. Increase in joint space narrowing was defined as any increase in OARSI joint space narrowing score [8] including within-grade changes.

2.2. MR Images. All of the knees had IW FS and 3D DESS MR images. The IW FS turbo spin echo and 3D DESS sequences were acquired using the OAI MR imaging protocol [9]. The IW FS sequence with field of view = 160 mm, slice thickness = 3 mm, skip = 0 mm, flip angle = 180 degrees, echo time = 30 ms, recovery time = 3200 ms, 313×448 matrix, x resolution = 0.357 mm, y resolution = 0.511 mm, and total slice number = 37. The 3D DESS sequence with field of view = 140 mm, slice thickness = 0.7 mm, skip = 0 mm, flip angle = 25 degrees, echo time = 4.7 ms, recovery time = 16.3 ms, 307 × 384 matrix, x resolution = 0.365 mm, y resolution = 0.456 mm, and total slice number = 160.

2.3. Semiautomated BML Segmentation. We designed a customized semiautomatic software to measure BMLs on both sequences. "BMLs are characterized as areas of high-signal intensity within bone on fat suppressed MR images [10, 11]. One reader used the software to place a large region of interest (ROI) around a BML. The software first applies threshold filter to convert selected ROI into binary image. The threshold is calculated based on the intensity histogram distribution within the region of interest. The follow-up slice used the same threshold on the corresponding baseline slice. Then a dilation filter is used to merge connected regions. Finally, the software removes small noise pixels. The user performs a final quality control to ensure the BMLs had been correctly segmented on each slice. The user can manually adjust the threshold and remove non-BML regions. To colocate the corresponding BMLs on baseline and follow-up images, we used dual screens to display simultaneously baseline and follow-up MR images." We summed the femur and tibia BMLs to generate a whole knee BML volume.

We first measured 30 pairs (baseline and follow-up) of IW FS images and then 30 pairs of 3D DESS images. We randomly selected 15 knees from the analytic dataset to assess intratester reliability. The two measurements were separated by at least 72 hours. Intratester (ICC [3, 1 model] [12]) reliability for IW FS baseline is 0.99 and IW FS change is 0.84; the reliability for 3D DESS baseline is 0.97 and 3D DESS change is 0.93.

2.4. Clinical Data. Knee pain was measured using the Western Ontario and McMaster University (WOMAC) pain score [13]. Radiographic measure of joint space narrowing (JSN) has been previously described in detail [14]. The radiographs, central readings, and protocols are publicly available at the OAI website (kxr_sq_bu_00 [version 0.5] and kxr_sq_bu_03 [version 3.5]; http://oai.epi-ucsf.org/; reliability for these readings was good with kappa = 0.70 to 0.88.)

2.5. Statistical Analyses. An *a priori* power calculation revealed 30 participants were needed to detect a Pearson correlation of 0.50 with $\alpha = 0.05$ and 80% power. A post hoc power calculation showed that, using the same parameters, we have >75% power to detect a Spearman correlation >0.50. To determine the distribution of whole knee BML volumes on each sequence we calculated medians and the 25th, 75th percentiles for BML volumes on both sequences. We performed a Wilcoxon signed rank sum test to compare BML volumes on the IW FS and 3D DESS sequences. Bland-Altman-like plots [15] were generated using the median (rather than the mean) of the difference for the horizontal line. We calculated Spearman correlations (r_s) to assess the relationship of 24-month BML volume and BML volume change (48-month BMLs minus 24-month BMLs) between IW FS and 3D DESS sequences. Finally, to determine construct validity we calculated Spearman correlations between 24-month BMLs on both sequences with 24-month WOMAC pain score. We also calculated the Spearman correlations of BML volume change on both sequences with WOMAC pain change (48-month WOMAC pain score minus 24-month WOMAC pain score).

3. Results

The study sample consisted of 30 right knees among 16 males and 14 females. The mean age was 64.0 (SD 9.4) years and mean body mass index was 30.7 (SD 5.3) kg/m^2, with a mean WOMAC pain score of 4.4 (3.9) and an average change in WOMAC pain of 0.7 (3.7) over 24 months of follow-up. Twenty-five knees (83%) had radiographic OA (Kellgren-Lawrence grade ≥ 2).

3.1. BMLs on IW FS and 3D DESS Sequences. There were 87 BMLs on IW FS 24-month visit. 3D DESS detected 75% of them (65 out of 87 BMLs). BMLs measured on the IW FS sequences had statistically significantly larger volumes than those measured on 3D DESS sequences ($p < 0.0001$, 24-month BMLs IW FS = 1840 (median) [290, 3588] (25th and 75th percentiles) mm^3; 3D DESS = 191 [40, 1048] mm^3; Figure 1(a)). The difference in BML volumes between sequences is greater among knees with larger BMLs than knees with smaller BMLs (the larger the BMLs, the greater the difference between sequences, Figure 1(b)).

The IW FS sequence generally demonstrated more BML volume change (BMLs change between 24-month and 48-month: IW FS = 27 [−320, 2166] mm^3; DESS = 2 [−110, 187] mm^3) than 3D DESS sequence (Figure 1(c)). The difference of BML volume change between the two sequences was greatest among knees with larger BML volume change (Figure 1(d)).

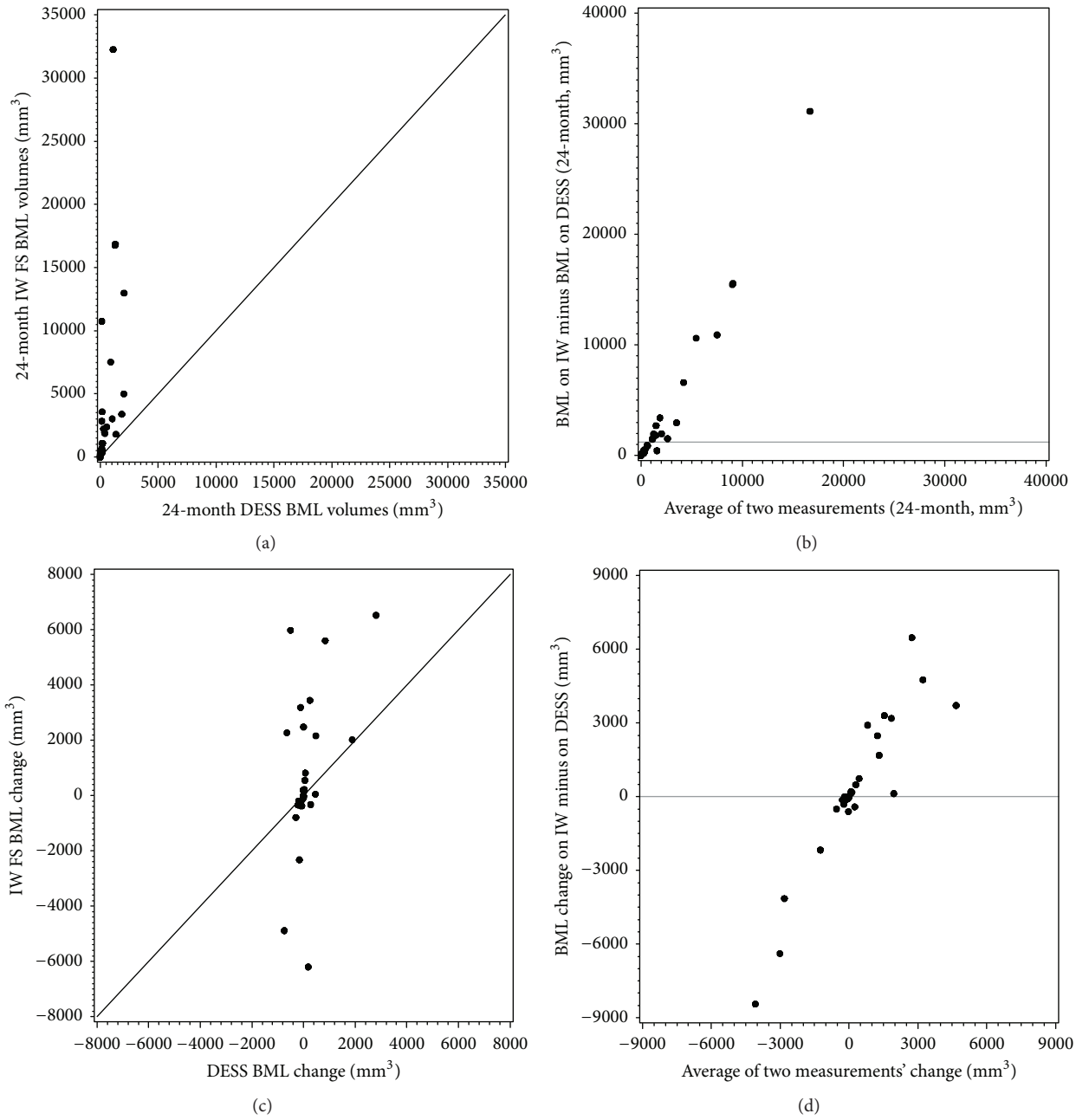

Figure 1: (a) Scatter plot of baseline BML volumes on IW FS versus 3D DESS. (b) Modified Bland-Altman plot of IW FS minus 3D DESS. (c) Scatter plot of BML volume change on IW FS versus 3D DESS. (d) Modified Bland-Altman plot of BML volume change on IW FS minus change on 3D DESS.

The 24-month BML volume on IW FS was correlated with the 24-month BML volume on 3D DESS (Figure 1(a), r_s = 0.83, 95% confidence interval [95% CI] = 0.66 to 0.91). However, BML volume change on IW FS was not significantly correlated with the BML volume change on 3D DESS (Figure 1(c), r_s = 0.33, 95% CI = −0.04 to 0.61).

Three knees did not have any BML volume detected by either sequence at either time point. IW FS detected a larger absolute change than DESS in 26 of the 27 knees that had BMLs.

3.2. BMLs and WOMAC Pain. The 24-month WOMAC pain was statistically significantly correlated with the 24-month BML volume on IW FS (r_s = 0.39, 95% CI = 0.02 to 0.65; see Supplemental Figure 1(A) in Supplementary Material available online at http://dx.doi.org/10.1155/2015/731903) but not the 24-month BML volume on 3D DESS (r_s = 0.27, 95% CI = −0.11 to 0.57; see Supplemental Figure 1(B)). The change in WOMAC pain was correlated with BML volume change on IW FS (r_s = 0.37, 95% CI = 0.01 to 0.64) but not with BML volume change on 3D DESS (r_s = −0.19, 95% CI = −0.51 to 0.19).

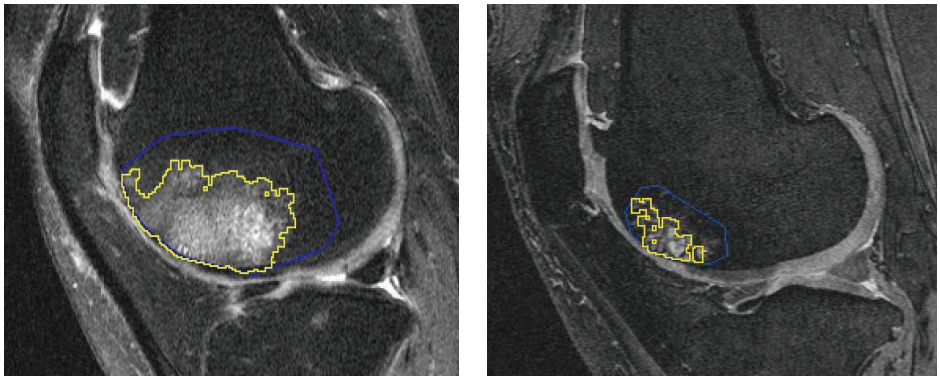

(a) (b)

Figure 2: (a) BML on IW FS sequence. (b) Same BML on 3D DESS sequence.

4. Discussion

This study confirms that the selection of appropriate MR pulse sequence to measure BMLs is important. We verified our hypothesis that IW FS sequences are more sensitive in detecting BMLs as compared to DESS sequences, sequences that are optimized to evaluate articular cartilage, as expected. We also found that the correlation between BML volume and knee pain was *qualitatively* greater in magnitude and statistically significant when using BML measurements from the IW FS sequences compared to those measured using DESS sequences. Although evaluating BMLs on 3D DESS sequences would enable a time- and cost-efficient method to assess changes in BMLs and cartilage on the same sequences, our results indicate that a study doing so may require a larger sample size to overcome the lack of sensitivity for measuring BMLs, especially those of larger volume, and decreased correlations with pain.

In a recent published paper [16], there were 74% BMLs on T2-weighted sequences which were also seen on T1-weighted sequences, similar to our results (75% BMLs on IW FS sequence were detected on 3D DESS sequence). We also found that the sizes of BML measured on IW FS generally are larger than those measured on 3D DESS (Figure 2). The cross-sectional study by Hayashi et al., using a semiquantitative BML assessment, similarly found that measurements taken using IW FS sequences demonstrate larger subchondral BMLs in 186 (93%) subregions when compared to the DESS sequences [7].

BMLs are an important feature of knee OA that is associated with pain [1, 17, 18]. In this study, we found BML volume and BML volume change on IW FS sequence had stronger associations with knee pain and knee pain fluctuation than when BMLs were measured on 3D DESS sequences.

An important limitation of this study is its small sample size. However, by selecting a small sample size, this allowed us to detect differences in the strength of associations between both cross-sectional and longitudinal change in BML volumes measured using the two sequences as compared with WOMAC pain.

5. Conclusions

Generally, BMLs are detected on both IW FS and 3D DESS sequences. There is an association of BML volumes on both sequences at baseline though the point estimates are smaller when assessing BML volume change. IW FS sequence usually has larger BML volumes than DESS sequence and may be more sensitive to change. The quantitative BMLs measurement on IW FS sequence also provided larger correlation coefficients with pain than the 3D DESS both cross-sectionally and longitudinally. Overall, these results do not support the use of DESS sequences as optimal sequence to measure BMLs. While it is feasible, BMLs measured on 3D DESS sequences will underestimate BML size, BML change, and some associations (e.g., with knee pain).

Disclaimer

The content is solely the responsibility of the authors and does not necessarily represent the official views of the National Institute of Arthritis and Musculoskeletal and Skin Diseases, the National Institutes of Health, or the Department of Veterans Affairs. The views expressed in this paper are those of the authors and do not necessarily represent the views of the Department of Veterans Affairs, the National Institutes of Health, or the US government.

Conflict of Interests

There was no financial support or other benefits from commercial sources for the work reported in this paper. No authors declare that they have conflict of interests with regard to the work.

Authors' Contribution

Ming Zhang contributed to the conception and design, acquisition of data, analysis, interpretation of data, drafting/revision of the paper, and final approval of the paper. Jeffrey B. Driban contributed to the conception and design, acquisition of data, analysis and interpretation of data, drafting/revision of the paper, and final approval of the paper. Lori Lyn Price

contributed to the conception and design, acquisition of data, analysis, interpretation of data, drafting/revision of the paper, and final approval of the paper. Grace H. Lo contributed to interpretation of data. Timothy E. McAlindon contributed to the conception and design, analysis and interpretation of data, drafting/revisions of the paper, and final approval of the paper. All authors read and approved the final paper.

Acknowledgments

The OAI is a public-private partnership comprised of five contracts (N01-AR-2-2258; N01-AR-2-2259; N01-AR-2-2260; N01-AR-2-2261; N01-AR-2-2262) funded by the National Institutes of Health, a branch of the Department of Health and Human Services, and conducted by the OAI Study Investigators. Private funding partners include Pfizer, Inc.; Novartis Pharmaceuticals Corporation; Merck Research Laboratories; and GlaxoSmithKline. Private sector funding for the OAI is managed by the Foundation for the National Institutes of Health. Dr. Zhang is supported by Scientist Development grant from Rheumatology Research Foundation. This work was supported in part by Rapid Quantitative Composite MRI Measurement of Knee OA Structural Progression (NIH/NIAMS Grant 1U01AR067168-01). Periarticular Bone Density as a Biomarker for Early Knee Osteoarthritis was sponsored by NIH/NIAMS (McAlindon R01 AR 060718). Dr. Lo is supported by K23 AR062127, an NIH/NIAMS funded mentored award. This work is supported in part by resources at the VA HSR&D Center for Innovations in Quality, Effectiveness and Safety (no. CIN 13-413), at the Michael E. DeBakey VA Medical Center, Houston, TX.

References

[1] G. H. Lo, T. E. McAlindon, J. Niu et al., "Bone marrow lesions and joint effusion are strongly and independently associated with weight-bearing pain in knee osteoarthritis: data from the osteoarthritis initiative," *Osteoarthritis and Cartilage*, vol. 17, no. 12, pp. 1562–1569, 2009.

[2] S. K. Tanamas, A. E. Wluka, J.-P. Pelletier et al., "Bone marrow lesions in people with knee osteoarthritis predict progression of disease and joint replacement: a longitudinal study," *Rheumatology*, vol. 49, no. 12, pp. 2413–2419, 2010.

[3] M. F. Sower, C. Hayes, D. Jamadar et al., "Magnetic resonance-detected subchondral bone marrow and cartilage defect characteristics associated with pain and X-ray-defined knee osteoarthritis," *Osteoarthritis and Cartilage*, vol. 11, no. 6, pp. 387–393, 2003.

[4] C. G. Peterfy, G. Gold, F. Eckstein, F. Cicuttini, B. Dardzinski, and R. Stevens, "MRI protocols for whole-organ assessment of the knee in osteoarthritis," *Osteoarthritis and Cartilage*, vol. 14, supplement 1, pp. 95–111, 2006.

[5] Y. Wang, A. E. Wluka, J.-P. Pelletier et al., "Meniscal extrusion predicts increases in subchondral bone marrow lesions and bone cysts and expansion of subchondral bone in osteoarthritic knees," *Rheumatology*, vol. 49, no. 5, pp. 997–1004, 2010.

[6] M. Zhang, J. B. Driban, L. L. Price et al., "Development of a rapid knee cartilage damage quantification method using magnetic resonance images," *BMC Musculoskeletal Disorders*, vol. 15, article 264, 2014.

[7] D. Hayashi, A. Guermazi, C. K. Kwoh et al., "Semiquantitative assessment of subchondral bone marrow edema-like lesions and subchondral cysts of the knee at 3T MRI: a comparison between intermediate-weighted fat-suppressed spin echo and Dual Echo Steady State sequences," *BMC Musculoskeletal Disorders*, vol. 12, article 198, 2011.

[8] R. D. Altman and G. E. Gold, "Atlas of individual radiographic features in osteoarthritis, revised," *Osteoarthritis and Cartilage*, vol. 15, supplement A, pp. A1–A56, 2007.

[9] C. G. Peterfy, E. Schneider, and M. Nevitt, "The osteoarthritis initiative: report on the design rationale for the magnetic resonance imaging protocol for the knee," *Osteoarthritis and Cartilage*, vol. 16, no. 12, pp. 1433–1441, 2008.

[10] C. G. Peterfy, A. Guermazi, S. Zaim et al., "Whole-organ magnetic resonance imaging score (WORMS) of the knee in osteoarthritis," *Osteoarthritis and Cartilage*, vol. 12, no. 3, pp. 177–190, 2004.

[11] L. Xu, D. Hayashi, F. W. Roemer, D. T. Felson, and A. Guermazi, "Magnetic resonance imaging of subchondral bone marrow lesions in association with osteoarthritis," *Seminars in Arthritis and Rheumatism*, vol. 42, no. 2, pp. 105–118, 2012.

[12] P. E. Shrout and J. L. Fleiss, "Intraclass correlations: uses in assessing rater reliability," *Psychological Bulletin*, vol. 86, no. 2, pp. 420–428, 1979.

[13] N. Bellamy, W. W. Buchanan, C. H. Goldsmith, J. Campbell, and L. W. Stitt, "Validation study of WOMAC: A health status instrument for measuring clinically important patient relevant outcomes to antirheumatic drug therapy in patients with osteoarthritis of the hip or knee," *The Journal of Rheumatology*, vol. 15, no. 12, pp. 1833–1840, 1988.

[14] D. T. Felson, M. C. Nevitt, M. Yang et al., "A new approach yields high rates of radiographic progression in knee osteoarthritis," *Journal of Rheumatology*, vol. 35, no. 10, pp. 2047–2054, 2008.

[15] J. M. Bland and D. G. Altman, "Statistical methods for assessing agreement between two methods of clinical measurement," *The Lancet*, vol. 1, no. 8476, pp. 307–310, 1986.

[16] A. E. Wluka, A. J. Teichtahl, R. Maulana et al., "Bone marrow lesions can be subtyped into groups with different clinical outcomes using two magnetic resonance imaging (MRI) sequences," *Arthritis Research & Therapy*, vol. 17, article 270, 2015.

[17] D. T. Felson, C. E. Chaisson, C. L. Hill et al., "The association of bone marrow lesions with pain in knee osteoarthritis," *Annals of Internal Medicine*, vol. 134, no. 7, pp. 541–549, 2001.

[18] Y. Zhang, M. Nevitt, J. Niu et al., "Fluctuation of knee pain and changes in bone marrow lesions, effusions, and synovitis on magnetic resonance imaging," *Arthritis and Rheumatism*, vol. 63, no. 3, pp. 691–699, 2011.

Hindawi Publishing Corporation
BioMed Research International
Volume 2015, Article ID 517369, 7 pages
http://dx.doi.org/10.1155/2015/517369

Research Article

Hepatic and Splenic Acoustic Radiation Force Impulse Shear Wave Velocity Elastography in Children with Liver Disease Associated with Cystic Fibrosis

Teresa Cañas,[1] Araceli Maciá,[2] Rosa Ana Muñoz-Codoceo,[1] Teresa Fontanilla,[3] Patricia González-Rios,[1] María Miralles,[3] and Gloria Gómez-Mardones[1]

[1]*Hospital Universitario Infantil Niño Jesús, 28009 Madrid, Spain*
[2]*Universidad Nacional de Educación a Distancia (UNED), 28040 Madrid, Spain*
[3]*Hospital Universitario Puerta de Hierro, 28222 Majadahonda, Spain*

Correspondence should be addressed to Teresa Cañas; tcanasmacia@yahoo.es

Received 9 September 2015; Accepted 15 October 2015

Academic Editor: Yukihisa Takayama

Background. Liver disease associated with cystic fibrosis (CFLD) is the second cause of mortality in these patients. The diagnosis is difficult because none of the available tests are specific enough. Noninvasive elastographic techniques have been proven to be useful to diagnose hepatic fibrosis. Acoustic radiation force impulse (ARFI) imaging is an elastography imaging system. The purpose of the work was to study the utility of liver and spleen ARFI Imaging in the detection of CFLD. *Method*. 72 patients with cystic fibrosis (CF) were studied and received ARFI imaging in the liver and in the spleen. SWV values were compared with the values of 60 healthy controls. *Results*. Comparing the SWV values of CFLD with the control healthy group, values in the right lobe were higher in patients with CFLD. We found a SWV RHL cut-off value to detect CFLD of 1.27 m/s with a sensitivity of 56.5% and a specificity of 90.5%. CF patients were found to have higher SWC spleen values than the control group. *Conclusions*. ARFI shear wave elastography in the right hepatic lobe is a noninvasive technique useful to detect CFLD in our sample of patients. Splenic SWV values are higher in CF patients, without any clinical consequence.

1. Introduction

Hepatic chronic disease associated with cystic fibrosis is the second cause of mortality in cystic fibrosis (CF) patients. The real prevalence of cystic fibrosis liver disease (CFLD) is unknown (it is estimated between 13 and 25%) owing to its difficult diagnosis because none of the available tests are specific or sensitive enough and also because there is a discrepancy between the ultrasound findings, the laboratory tests, and the clinical manifestations [1, 2].

CFLD usually appears during childhood, with a peak incidence in teenage years, and usually has a progressive and slow course. Clinical manifestations of the disease are varied and include neonatal cholestasis, asymptomatic hepatomegaly, liver steatosis, biliary tract complications, and portal hypertension, which may require hepatic transplantation [3–5].

CFLD happens more frequently in males, in patients with severe mutations, and in patients with pancreatic insufficiency, with a poor nutritional status, and with a history of neonatal meconium ileus. No specific mutation has been associated with the presence and severity of CFLD [2, 6, 7].

Transaminase levels are altered when the disease is advanced. This is due to the fact that the primary involvement of the disease is biliary, and transaminase values are related to hepatocyte injury rather than to biliary function. For this reason, hepatic involvement is usually subclinical and a combination of clinical examination and different laboratory and imaging techniques is required to make the diagnosis. Dr. Colombo et al. [6] criteria have been accepted for diagnosing CFLD and consist in two of the following findings which are seen at least during two consecutive visits in one year:

(1) Hepatomegaly, with liver edge >2 cm below costal margin in the midclavicular line and confirmed by ultrasound,

(2) at least 2 of the 3 of AST, ALT, and GGTP above the upper limit of normal.

Ultrasound altered parenchymal pattern (diffuse high echogenicity suggestive of steatosis) is not considered a diagnostic criterium.

The use of hepatic biopsy is controverted in these patients because it is an invasive technique which may have complications and also because there is a 20% of interobserver variability [8]. Furthermore, biliary focal fibrosis, which is the typical pathologic lesion in CFLD, has a patchy liver involvement, which may be related to false negative results after liver biopsy. Because of these reasons biopsy is not used as a screening technique to estimate fibrosis [6, 9, 10], but rather it is used just in dubious cases or when cirrhosis is suspected.

During the last years noninvasive elastographic techniques have been developed and have been proven to be useful to diagnose hepatic fibrosis. Acoustic radiation force impulse (ARFI) imaging (Siemens-ACUSON) is an ultrasound elastographic technique which is integrated in an ultrasound device, based on the measurement of shear wave velocity (SWV) in a ROI (region of interest). SWV is related to mechanic tissue properties; the higher the shear wave speed, the higher the rigidity of the tissue [11].

So far, the authors have found a few articles that report the usefulness of ARFI in the detection of CFLD, in which [9, 12–16] higher SWV values are found in patients with a higher risk of hepatic involvement. However, these studies did not have a group of healthy controls to compare the SWV values. Recently some articles have been published reporting the usefulness of hepatic and splenic ARFI in predicting the risk of portal hypertension and the appearance of oesophageal varices or variceal bleeding in adults [17–20]. However, we have not found studies concerning the usefulness of splenic ARFI in the detection of CFLD.

The aim of the present study is to evaluate the usefulness of hepatic and splenic ARFI in the detection of CFLD.

2. Materials and Methods

The study was performed during July 2015. Seventy-two patients with CF disease (45 boys and 27 girls) between 9 months and 18 years old were included. The study was approved by the local ethical committee and written informed consent was obtained in all cases. All patients received the same day abdominal ultrasound, Doppler study, and hepatic and splenic ARFI study and laboratory blood tests within one month. Dr. Colombo et al. criteria were used to diagnose CFLD [6, 9].

SWV values were compared with the values of healthy controls previously studied by the authors [21, 22].

Anthropometric and other data of the patient were saved and studied, including age, gender, body mass index (BMI), history of neonatal meconium ileus, presence of pancreatic insufficiency, treatment with ursodeoxycholic acid, laboratory tests results, and pulmonary function (FEV1). Exclusion criteria were coinfection by hepatotropic viruses, hepatic disease of other causes, and hepatic surgery history. No patient of the selected group was excluded.

Table 1: Williams ultrasound score [23].

Points	1	2	3
Parenchyma	Normal	Coarse	Irregular
Echogenicity (periportal fibrosis)	None	Moderate	Severe
Liver edge	Smooth	Irregular	Nodular
Score	3 (normal)	>4 (hepatopathy)	9 (cirrhosis)

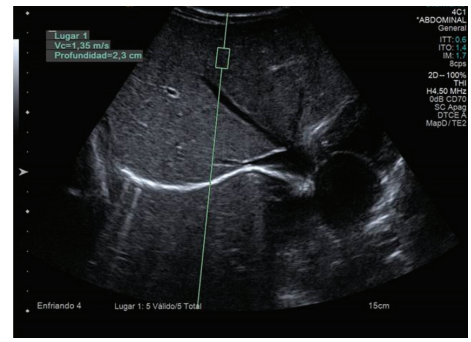

Figure 1: Shear wave velocity (SWV) measurement with the 4 C1 probe in a region of interest 1 × 0.5 cm at a depth of 2,3 cm. SWV = 1.35 m/s.

2.1. Ultrasound. All patients received an ultrasound examination of the abdomen, a portal and splenic color and spectral Doppler examination, and left hepatic vein color and spectral Doppler examination using a convex ultrasound-probe (4C1-probe, Siemens-ACUSON S2000, Mountain View, CA, USA). The abdominal ultrasound included a detailed examination of the liver, and hepatic involvement was graded according to Williams scale [23], Table 1. This scale considers hepatic echotexture, periportal echogenicity, and hepatic surface nodularity and scores the findings, 3 normal, over 4 suggestive of hepatopathy, and 9 suggestive of cirrhosis. Signs of portal hypertension, presence of ascites, and focal liver lesions were evaluated.

2.2. ARFI. ARFI hepatic and splenic elastography was performed using a convex multifrequency probe (4C1) on an ACUSON S2000 device (Siemens Medical Solutions, Mountain View, CA, USA) with the specific software for generating and tracking shear waves Virtual Touch Tissue Quantification. All studies were performed by a radiologist with 3 years of experience in performing ARFI. SWV was measured in several ROIs within the liver and the spleen. A rectangular ROI with fixed dimensions (1 × 0.5 cm) was adjusted under ultrasound control in the liver and in the spleen to avoid identifiable blood vessels and biliary structures (Figure 1).

Patients were supine and breathing normally when measurements were performed. For children younger than 7 years old, a subcostal approach was used; in children over 7 years

Table 2: Liver and spleen ARFI shear wave velocity normal values [21, 22].

	Mean (SD)	95% confidence interval
SWV right hepatic lobe (m/s)	1.19 (0.13)	1.15–1.23
SWV left hepatic lobe (m/s)	1.27 (0.19)	1.22–1.32
SWV spleen (m/s)	2.17 (0.35)	2.08–2.26

old, an intercostal approach was used. Minimal scanning pressure was applied by the operator. Five valid measurements of SWV were performed in each hepatic lobe (right hepatic lobe (RHL) and left hepatic lobe (LHL)) deeper than 1 cm from the probe; and five valid measurements were performed in the spleen. SWV means and standard deviations were calculated for each hepatic lobe and for the spleen in each patient; the results were expressed in meters per second (m/s). Unreliable velocity measurements caused the machine to automatically display XXXX and were not taken into consideration in shear wave velocity calculations. The number of nonvalid measurements was not registered. Measurements were repeated until five reliable values for a complete examination were obtained. The range of depths between which the measurements were taken was 2,55–5,86 cm in the RHL, 1,96–5,40 cm in the LHL, and 1,72–4,73 cm in the spleen.

Liver and spleen SWV values were compared to those obtained and published by the authors in healthy children [21, 22], Table 2.

2.3. Laboratory Tests. Blood tests were performed to all patients either the same day of the ultrasound and ARFI or after one month. The tests included determination of necrobiosis enzymes, alanine-aminotransferase (ALT or GPT) and aspartate-aminotransferase (AST or GOT); of cholestasis enzymes γ-glutamyl-transpeptidase, alkaline phosphatase (AP), and total and direct and indirect bilirubin; of hepatic synthesis markers: glucose, albumin, and cholinesterase; and also of prothrombin time.

2.4. Statistical Analysis. SPSS 21.0 (IBM, Armonk, NY) was used for statistical analysis. P values < 0.05 were considered to indicate statistical significance. Normal distribution was tested using Kolmogorov-Smirnov test. Data followed normal distribution and parametric test was used. To make comparison between two groups Student's t-test was used. To make comparison across groups ANOVA test and Bonferroni test were used. Correlations were assessed by Pearson's correlation coefficient. Moreover the areas under the ROC (AUROC) curves were calculated. Cut-off values for the prediction CFLD were defined using Youden's index. The optimal cut-off was defined as the cut-off with the highest sum of sensitivity and specificity.

3. Results

Seventy-two patients with CF were studied. Patient characteristics are shown in Table 3. Fifty-four patients with CF without LD (75%) and 20 with CFLD (86,95%) had pancreatic insufficiency. Ten patients with CF without LD (13,88%) and five with CFLD (21,73%) had a history of meconium ileum. Pulmonary function mean (FEV1) in CFLD patients was 91% and that of patients with CF without CFLD was 87,85%.

3.1. Ultrasound. Based on Williams ultrasound score patients were divided into score 3 (normal ultrasound) and scores 4–9 (mild to moderate hepatopathy), Table 2. In the group of patients with CFLD there were 12 patients with normal ultrasound and 11 patients with altered ultrasound. In the group of patients without liver involvement 39 of the patients had a normal ultrasound and 10 patients had altered ultrasound. None of the patients had cirrhosis ultrasound criteria or ascites.

3.2. Hepatic ARFI. No statistically significant difference was found between both SWV in the right hepatic lobe and SWV in left hepatic lobe between healthy children ($n = 60$) and the global CF group ($n = 72$) (RHL $P = 0.386$ and LHL $P = 0.578$). In CF patients SWV values were higher in the LHL than in the RHL ($\overline{x} = 1.29$ m/s and $\overline{x} = 1.22$ m/s, resp., $P = 0.019$), as happens in healthy children [12, 21].

Results of the ANOVA test are shown in Table 4. Comparing the SWV values of RHL in the three groups (group I: healthy children; group II: children with CF without liver disease; group III: children with CFLD) we found a significant value of F ($P = 0.003$). The post hoc comparisons indicate that the differences are due to the comparison between group III (CFLD) and groups I (control healthy group) and II (CF without liver disease) because values in the RHL were higher in patients with CFLD. However, no difference was found comparing LHL values ($P = 0.397$).

When we calculate the area under the ROC curve, we found a SWV RHL cut-off value to detect CFLD of 1.27 m/s, with a sensitivity of 56,5% and a specificity of 90,5% (Figure 2). The AUROC for SWV in the RHL was 0.746 $P < 0.001$ (95% CI 0.61–0.88). The AUROC curve (0.529) for SWV in the LHL was not significant.

3.3. Splenic ARFI. CF patients were found to have higher SWV than the control group of healthy children ($P < 0.0001$). No significant difference was found when comparing patients with CFLD ($n = 23$) with those CF patients without hepatic involvement ($n = 49$), Table 4.

3.4. Laboratory Tests. Pearson correlation was calculated between RHL SWV and the following variables: BMI, FEV 1, GOT, GPT, GGT, FA, bilirubin, glucose, cholinesterase, and prothrombin time. A negative correlation was found with the BMI (−0.239, $P = 0.044$) and a positive correlation was found with GOT (0.397, $P = 0.001$) and GGT (0.386, $P = 0.001$). No other significant correlation was found. Pearson correlation was calculated between splenic SWV and the same variables, and no significant correlation was found.

No significant differences were found in the laboratory variables, BMI and FEV1, between patients with CFLD and patients with CF without CFLD, Table 4.

Table 3: Patient characteristics.

	Patients without CFLD	Patients with CFLD	All patients with CF
N	49	23	72
Sex: H–M	28–21	17–6	45–27
Age: mean (SD) (95% CI)	9,99 (5,3); 0,9–18	10,56 (4,41); 0,9–18	10,18 (5,02); 0,9–18
BMI: mean (SD); 95% CI	17,67 (2,92); 9,5–23	17,3 (3,2); 12,8–26,5	17,56 (2,99); 9,5–26,5
Patients with pancreatic insufficiency	34	20	54
Patients with history of neonatal meconium ileus	5	5	10
Pulmonary function: FEV1: mean (SD)	87,85 (15,21)	91,04 (16,17)	88,96 (15,5)
Williams ultrasound score			
(i) Points <3	39	12	51
(ii) Points between 4 and 8	10	11	21

Table 4: Comparison between healthy patients and patients with CF with or without CFLD. ANOVA test and post hoc (Bonferroni) for SWV in right hepatic lobe (RHL), left hepatic lobe (LHL), and spleen. Student's *t*-test for the main variables, BMI and FEV1.

	Group I Healthy children *N* = 60 Mean (SD)	Group II Patients with CF without liver disease *N* = 49 Mean (SD)	Group III Patients with CFLD *N* = 23 Mean (SD)	*F*/*t*	*P*	Post hoc comparison
RHL	1.19 (0.13)	1.18 (0.18)	1.31 (0.16)	6.023	**0.003**	Group I–group III Group II-group III
LHL	1.27 (0.19)	1.27 (0.24)	1.34 (0.30)	0.930	0.397	
Spleen	2.16 (0.35)	2.51 (0.30)	2.51 (0.31)	18.154	<**0.0001**	Group I-group II Group I–group III
FEV1		87.85 (15.21)	91.05 (16.17)	−0.777	0.440	
BMI		17.67 (2.92)	17.30 (3.19)	0.48	0.633	
GOT		33.94 (13.03)	64.17 (114.47)	−1.82	0.073	
GPT		27.5 (14.08)	54.13 (101.43)	−1.79	0.077	
GGT		15.5 (14.56)	79.79 (272.87)	−1.64	0.106	
AP		187.89 (61.79)	189.65 (73.82)	−0.105	0.917	
TB		0.63 (0.54)	0.31 (0.16)	1.229	0.223	
Glu		93.79 (10.37)	95.26 (16.75)	−0.454	0.651	
Albu		4.03 (0.30)	3.97 (0.27)	0.943	0.349	
Colin		9370.23 (2051.30)	8493.68 (1398.98)	1.693	0.096	

RHL = right hepatic lobe; LHL = left hepatic lobe; FEV1 = pulmonary function; BMI = body mass index; GOT = aspartate-aminotransferase; GPT = alanine-aminotransferase; GGT = γ-glutamyl-transpeptidase; AP = alkaline phosphatase; TB = total bilirubin; Glu = glucose; Albu = albumin; Colin = cholinesterase.

4. Discussion

Owing to the increasing life expectancy of CF patients, CFLD has more time to appear and progress and it is nowadays the second cause of death in CF patients. The mechanisms involved in the pathogenesis of liver disease in CF are largely unknown. The absence or dysfunction of the fibrosis regulator protein (CFTR) is thought to be key in the pathogenetic sequence of cystic fibrosis associated liver disease. CFTR is expressed in the membrane of the intrahepatic and extrahepatic biliary canaliculi cells and in the gallbladder epithelial cells, but it is not present in the hepatocytes, so the damage in this condition is primary biliary and causes increased bile viscosity. This leads to bile duct plugging, and biliary obstruction and chronic cholestasis ensue. Associated pathological findings include inflammation, paraductal mucinous cysts, mural fibrosis, biliary ductal proliferation, and periportal fibrosis [2, 24]. Secondary hepatocyte injury eventually occurs.

The histologic typical lesion is focal biliary fibrosis (Figure 3). Lesions may be confluent and eventually progress to multilobular cirrhosis. In it, lobules are not equally involved and relatively normal lobules can be found among involved ones. The left hepatic lobe may be more involved than the right one [2]. CFLD diagnosis is difficult and the use of hepatic biopsy is controverted, so noninvasive techniques are being investigated and used, among them elastographic techniques.

ARFI is an elastography imaging system based on SWV measurement that has been found to be a reliable tool for estimating fibrosis in adults, with good accuracy in the diagnosis of significant liver fibrosis and excellent accuracy in the diagnosis of significant fibrosis and cirrhosis [11, 25]. Most of the published articles are based on findings in HCV

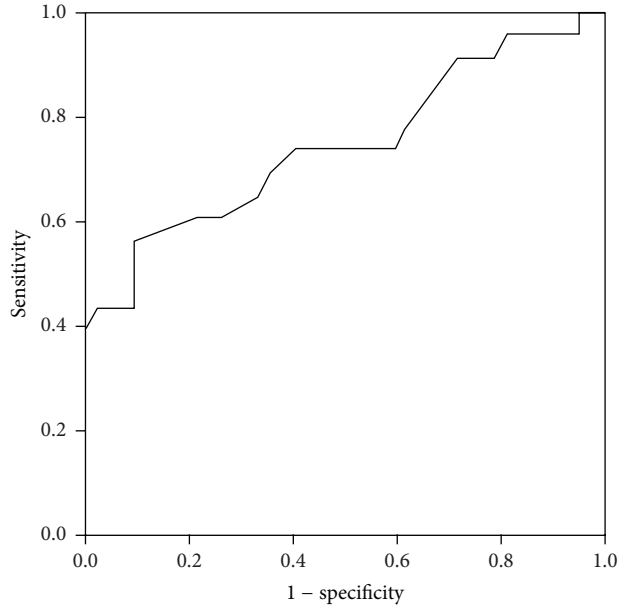

Figure 2: ROC curve for SWV in the RHL.

patients, or else mixed groups of patients including HCV and HBV [26, 27]. Articles based on studies on children are scarce, and in them the sample of patients usually is heterogeneous with different causes of liver disease [28–30]. Since SWV values may be different in different liver diseases, it seems reasonable to study SWV in each disease separately. The main purpose of this study was to find SWV values in CFLD in children and to compare them with CF without liver disease, using as reference of normality the results of previous study of the authors in healthy children [21, 22]. The range of normal values in healthy children was 1.15–1.23 m/s. The results of the present study obtain a cut-off value of 1.27 m/s to detect CFLD, with a sensibility of 56,5% and a specificity of 90,5%. Friedrich-Rust et al. [16] propose a cut value of 1.42 m/s in adult patients with CF with a sensibility of 54.17% and a specificity of 93.90%. The higher cut value obtained by Friedrich may be related to the fact that the studied patients were adult, possibly with more advanced liver involvement. A value of 1.27 m/s really is not very far from a value of 1.23 m/s, with the first considered the cut value for abnormality and the second considered the upper range limit for the mean of SWV in healthy children. This may pose a problem for result interpretation. Studies with larger samples may adjust the values further. In this sense, it would be of interest to carry out a longitudinal study of the values in CF with the same patients. It would be interesting to find if SWV values change along time in CFLD. Presumably SWV values will increase with time in CFLD and in those patients in which LD develops, but this has to be studied specifically.

This study was designed to measure SWV in both hepatic lobes separately. On one hand ARFI systematic study has been agreed in the literature to be performed in the RHL because SWV LHL values are higher than RHL values both in healthy adults and children; in adults LHL values are also more disperse. It is thought that this difference may be due to the closeness of the heart and its pressure on the liver [31, 32]. On the other hand, liver involvement is patchy in CF patients and it has been reported that the LHL may be more affected than the RHL. So another purpose of this work was to study if there are differences between SWV values in both hepatic lobes in CF patients. Our results show that LHL SWV are higher in CF patients, but we have not found difference between patients with and patients without CFLD. So in the same way as Friedrich-Rust et al. [16] we do not think it necessary to measure LHL SWV in the evaluation of liver involvement in CFLD.

Necrobiosis enzymes (AST and ALT) and cholestasis enzymes (GGT and FA) allow detecting hepatic involvement which is not evident at exploration and even with ultrasound. On the other hand, there may be hepatic involvement with normal enzymes. In this study a significant positive correlation has been found between RHL SWV and GOT and GPT values. This association between high transaminase levels and high SWV values has been described in the literature [33] and indeed it is considered a confounder in the estimation of hepatic fibrosis in chronic liver disease in adults, so the recommendation in adults is to perform the evaluation for fibrosis estimation avoiding periods with transaminase flares. It seems reasonable to think that this must be considered also when evaluating CFLD.

Another aim of the present study was to evaluate splenic SWV, taking into account the hemodynamic relationship between liver and spleen, and the secondary splenic involvement of the spleen in chronic liver disease. Considering the spleen, there are a few published articles that report about the higher spleen SWV values and the usefulness of this finding to predict the risk of portal hypertension and the presence of varices and of variceal bleeding in adults [17–20]. In our study splenic SWV values were found to be significantly higher in CF patients than in the control group. However, this finding did not have any clinical consequence or association, there was no plaquetopenia or more frequent infections, and there were no splenomegaly and no ultrasound or Doppler findings suggestive of portal hypertension. Without having histologic confirmation and without any reference in the literature of splenic involvement in CF, it is not possible to ascertain the nature of the splenic high SWV; this could be due to a direct involvement of the disease, but further study of the splenic SWV in these patients is needed.

This study has some limitations; the main one is that there has not been comparison of the diagnosis of hepatic involvement with a gold standard such as the histologic analysis after biopsy. However, the use of an invasive test which is so far not included as a routine procedure in the management or follow-up of CF patients is not justifiable. Also, the healthy reference group was studied by four authors of these articles (Teresa Cañas, Araceli Maciá, Teresa Fontanilla, and María Miralles) in another hospital, though with the same device and convex probe and including children of all ages, so the authors think that those values can still be used as a reference of normality in this study.

The main conclusion of this study is that ARFI shear wave elastography in the RHL was useful to detect CFLD in our sample of patients, and thus it has the potential to be a useful

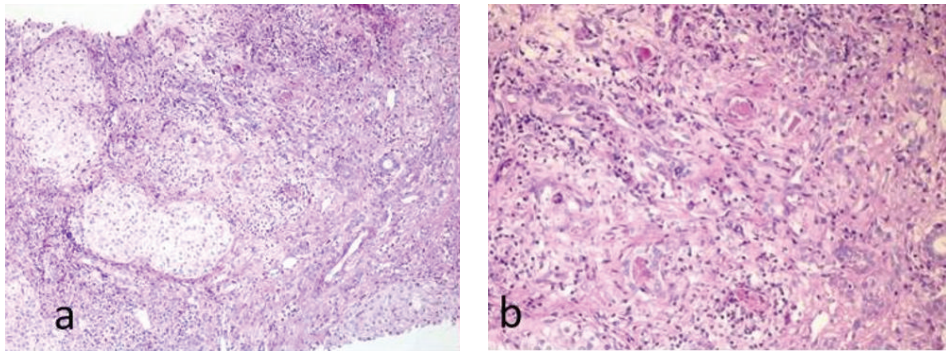

(a) (b)

Figure 3: (a) Hepatic parenchyma altered structure: an expanded portal area is shown, with fibrous septa and hepatocytes enclosed in them. Inflammatory cells and ductular proliferation are seen, with positive Periodic Acid Schiff (PAS) content inside several proliferated biliary ducts. (b) Close-up view of the portal area in which four biliary ducts are seen (3 in the top half of the image and one in the lower half of the image) with PAS positive plugging inside. Images lent by Dr. Daniel Azorín, pathology department.

tool in the followup of CFLD patients as a noninvasive technique to evaluate liver involvement and disease progression. Another conclusion is that splenic SWV values are higher in CF patients, without any clinical consequence or association. Further study of splenic SWV is needed.

Conflict of Interests

The authors declare that there is no conflict of interests regarding the publication of this paper.

Acknowledgment

This work has been possible thanks to Siemens collaboration, which has facilitated the use of ACUSON S2000 device (Siemens Medical Solutions, Mountain View, CA, USA) with the specific software for generating and tracking shear waves Virtual Touch Tissue Quantification.

References

[1] A. S. Aguirre and C. B. García, "La fibrosis quística en la actualidad (I): aspectos digestivos," *Acta Pediátrica Española*, vol. 68, no. 11, pp. 555–560, 2010.

[2] M. M. Gómez and RM. Codoceo, "Fibrosis quística: manifestaciones digestivas," *Pediatría Integral*, vol. 11, no. 2, pp. 121–133, 2007.

[3] M. Miralles, G. Gonzalez, C. Serrano, J. Manzanares, and T. Berrocal, "Diagnostic imaging of digestive tract involvement in cystic fibrosis. Part 1: hepatobiliary disease," *Radiologia*, vol. 40, no. 9, pp. 577–586, 1998.

[4] L. Stewart, "The role of abdominal ultrasound in the diagnosis, staging and management of cystic fibrosis liver disease," *Journal of the Royal Society of Medicine, Supplement*, vol. 98, no. 45, pp. 17–27, 2005.

[5] H. P. Haber, "Cystic fibrosis in children and young adults: findings on routine abdominal sonography," *American Journal of Roentgenology*, vol. 189, no. 1, pp. 89–99, 2007.

[6] C. Colombo, P. M. Battezzati, A. Crosignani et al., "Liver disease in cystic fibrosis: a prospective study on incidence, risk factors, and outcome," *Hepatology*, vol. 36, no. 6, pp. 1374–1382, 2002.

[7] U. Herrmann, G. Dockter, and F. Lammert, "Cystic fibrosis-associated liver disease," *Best Practice & Research: Clinical Gastroenterology*, vol. 24, no. 5, pp. 585–592, 2010.

[8] H. Matos, M. J. Noruegas, I. Gonçalves, and C. Sanches, "Effectiveness and safety of ultrasound-guided percutaneous liver biopsy in children," *Pediatric Radiology*, vol. 42, no. 11, pp. 1322–1325, 2012.

[9] D. Debray, D. Kelly, R. Houwen, B. Strandvik, and C. Colombo, "Best practice guidance for the diagnosis and management of cystic fibrosis-associated liver disease," *Journal of Cystic Fibrosis*, vol. 10, pp. S29–S36, 2011.

[10] D. Borowitz, K. A. Robinson, M. Rosenfeld et al., "Cystic fibrosis Foundation evidence-based guidelines for management of infants with cystic fibrosis," *The Journal of Pediatrics*, vol. 155, no. 6, supplement, pp. S73–S93, 2009.

[11] M. Friedrich-Rust, J. Nierhoff, M. Lupsor et al., "Performance of Acoustic Radiation Force Impulse imaging for the staging of liver fibrosis: a pooled meta-analysis," *Journal of Viral Hepatitis*, vol. 19, no. 2, pp. e212–e219, 2012.

[12] P. Witters, K. De Boeck, L. Dupont et al., "Non-invasive liver elastography (Fibroscan) for detection of cystic fibrosis-associated liver disease," *Journal of Cystic Fibrosis*, vol. 8, no. 6, pp. 392–399, 2009.

[13] T. Rath, L. Hage, M. Kügler et al., "Serum proteome profiling identifies novel and powerful markers of cystic fibrosis liver disease," *PLoS ONE*, vol. 8, no. 3, Article ID e58955, 2013.

[14] L. Monti, M. Manco, C. Lo Zupone et al., "Acoustic radiation force impulse (ARFI) imaging with Virtual Touch Tissue Quantification in liver disease associated with cystic fibrosis in children," *Radiologia Medica*, vol. 117, no. 8, pp. 1408–1418, 2012.

[15] C. B. Behrens, J. H. Langholz, J. Eiler et al., "A pilot study of the characterization of hepatic tissue strain in children with cystic-fibrosis-associated liver disease (CFLD) by acoustic radiation force impulse imaging," *Pediatric Radiology*, vol. 43, no. 5, pp. 552–557, 2013.

[16] M. Friedrich-Rust, N. Schlueter, C. Smaczny et al., "Non-invasive measurement of liver and pancreas fibrosis in patients with cystic fibrosis," *Journal of Cystic Fibrosis*, vol. 12, no. 5, pp. 431–439, 2013.

[17] S. Bota, I. Sporea, R. Sirli et al., "Spleen assessment by Acoustic Radiation Force Impulse Elastography (ARFI) for prediction of

liver cirrhosis and portal hypertension," *Medical Ultrasonography*, vol. 12, no. 3, pp. 213–217, 2010.

[18] S. Bota, I. Sporea, R. Şirli et al., "Can ARFI elastography predict the presence of significant esophageal varices in newly diagnosed cirrhotic patients?" *Annals of Hepatology*, vol. 11, no. 4, pp. 519–525, 2012.

[19] I. Grgurevic, I. Cikara, J. Horvat et al., "Noninvasive assessment of liver fibrosis with acoustic radiation force impulse imaging: increased liver and splenic stiffness in patients with liver fibrosis and cirrhosis," *Ultraschall in der Medizin*, vol. 32, no. 2, pp. 160–166, 2011.

[20] Y. Furuichi, F. Moriyasu, J. Taira et al., "Noninvasive diagnostic method for idiopathic portal hypertension based on measurements of liver and spleen stiffness by ARFI elastography," *Journal of Gastroenterology*, vol. 48, no. 9, pp. 1061–1068, 2013.

[21] T. Fontanilla, T. Cañas, A. Macia et al., "Normal values of liver shear wave velocity in healthy children assessed by acoustic radiation force impulse imaging using a convex probe and a linear probe," *Ultrasound in Medicine and Biology*, vol. 40, no. 3, pp. 470–477, 2014.

[22] T. Cañas, T. Fontanilla, M. Miralles, A. Maciá, A. Malalana, and E. Román, "Normal values of spleen stiffness in healthy children assessed by acoustic radiation force impulse imaging (ARFI): comparison between two ultrasound transducers," *Pediatric Radiology*, vol. 45, no. 9, pp. 1316–1322, 2015.

[23] S. G. J. Williams, J. E. Evanson, N. Barrett, M. E. Hodson, J. E. Boultbee, and D. Westaby, "An ultrasound scoring system for the diagnosis of liver disease in cystic fibrosis," *Journal of Hepatology*, vol. 22, no. 5, pp. 513–521, 1995.

[24] S. Tabernero da Veiga, Y. González Lama, R. Lama More, M. C. Martínez Carrasco, M. C. Antelo Landeria, and P. Jara Vega, "Hepatopatía crónica asociada a fibrosis quística: gasto energético en reposo, factores de riesgo y repercusión en la evolución de la enfermedad," *Nutrición Hospitalaria*, vol. 19, no. 1, pp. 19–27, 2004.

[25] S. Bota, I. Sporea, R. Sirli, A. Popescu, and O. Gradinaru-Tascau, "How useful are ARFI elastography cut-off values proposed by meta-analysis for predicting the significant fibrosis and compensated liver cirrhosis?" *Medical Ultrasonography*, vol. 17, no. 2, pp. 200–205, 2015.

[26] L. Rizzo, V. Calvaruso, B. Cacopardo et al., "Comparison of transient elastography and acoustic radiation force impulse for non-invasive staging of liver fibrosis in patients with chronic hepatitis C," *The American Journal of Gastroenterology*, vol. 106, no. 12, pp. 2112–2120, 2011.

[27] I. Sporea, S. Bota, M. Peck-Radosavljevic et al., "Acoustic Radiation Force Impulse elastography for fibrosis evaluation in patients with chronic hepatitis C: an international multicenter study," *European Journal of Radiology*, vol. 81, no. 12, pp. 4112–4118, 2012.

[28] S. Hanquinet, A.-L. Rougemont, D. Courvoisier et al., "Acoustic radiation force impulse (ARFI) elastography for the noninvasive diagnosis of liver fibrosis in children," *Pediatric Radiology*, vol. 43, no. 5, pp. 545–551, 2013.

[29] C. O. Marginean and C. Marginean, "Elastographic assessment of liver fibrosis in children: a prospective single center experience," *European Journal of Radiology*, vol. 81, no. 8, pp. e870–e874, 2012.

[30] M. J. Noruegas, H. Matos, I. Gonçalves, M. A. Cipriano, and C. Sanches, "Acoustic radiation force impulse-imaging in the assessment of liver fibrosis in children," *Pediatric Radiology*, vol. 42, no. 2, pp. 201–204, 2012.

[31] T. Karlas, C. Pfrepper, J. Wiegand et al., "Acoustic radiation force impulse imaging (ARFI) for non-invasive detection of liver fibrosis: Examination standards and evaluation of interlobe differences in healthy subjects and chronic liver disease," *Scandinavian Journal of Gastroenterology*, vol. 46, no. 12, pp. 1458–1467, 2011.

[32] T. Toshima, K. Shirabe, K. Takeishi et al., "New method for assessing liver fibrosis based on acoustic radiation force impulse: a special reference to the difference between right and left liver," *Journal of Gastroenterology*, vol. 46, no. 5, pp. 705–711, 2011.

[33] E. B. Tapper, E. B. Cohen, K. Patel et al., "Levels of alanine aminotransferase confound use of transient elastography to diagnose fibrosis in patients with chronic hepatitis C virus infection," *Clinical Gastroenterology and Hepatology*, vol. 10, no. 8, pp. 932.e1–937.e1, 2012.

Hindawi Publishing Corporation
BioMed Research International
Volume 2015, Article ID 373716, 11 pages
http://dx.doi.org/10.1155/2015/373716

Research Article

Parameterization of the Age-Dependent Whole Brain Apparent Diffusion Coefficient Histogram

Uwe Klose, Marion Batra, and Thomas Nägele

Department of Diagnostic and Interventional Neuroradiology, University Hospital Tübingen, Tübingen, Germany

Correspondence should be addressed to Uwe Klose; uwe.klose@med.uni-tuebingen.de

Received 7 July 2015; Revised 4 September 2015; Accepted 10 September 2015

Academic Editor: Jinyuan Zhou

Purpose. The distribution of apparent diffusion coefficient (ADC) values in the brain can be used to characterize age effects and pathological changes of the brain tissue. The aim of this study was the parameterization of the whole brain ADC histogram by an advanced model with influence of age considered. *Methods*. Whole brain ADC histograms were calculated for all data and for seven age groups between 10 and 80 years. Modeling of the histograms was performed for two parts of the histogram separately: the brain tissue part was modeled by two Gaussian curves, while the remaining part was fitted by the sum of a Gaussian curve, a biexponential decay, and a straight line. *Results*. A consistent fitting of the histograms of all age groups was possible with the proposed model. *Conclusions*. This study confirms the strong dependence of the whole brain ADC histograms on the age of the examined subjects. The proposed model can be used to characterize changes of the whole brain ADC histogram in certain diseases under consideration of age effects.

1. Introduction

Diffusion-weighted imaging provides additional image contrast in MR imaging of the brain and has become an important part of clinical MR diagnostics. Data evaluation is usually performed directly in the diffusion-weighted images or in calculated apparent diffusion coefficient (ADC) maps. In addition to the analysis of images and maps, the distribution of ADC values in selected region of the brain can be used to characterize the examined tissue. This was shown, for example, for stroke lesions (lesions with subsequent hemorrhagic transformation could be identified by the ADC histogram) [1], for multiple sclerosis patients [2], for low-grade and high-grade gliomas [3, 4], and for epilepsy [5]. In addition, histograms from the whole brain can be used to characterize global changes of the brain tissue. This possibility was introduced by Mascalchi et al. [6, 7] and also by Molko et al. [8]. Mascalchi et al. found a correlation of the median ADC value with a disease score in patients with leukoaraiosis, while Molko et al. examined patients with cerebral autosomal dominant arteriopathy with subcortical infarcts and leukoencephalopathy (CADASIL) and found that the histogram parameters mean ADC value, peak height, and peak locations were significantly correlated with both the Minimental State Examination score and Rankin Scale score in the patient group. These parameters were also examined in other studies [9–14]. In more sophisticated studies, further parameters such as 25th and 75th percentile, kurtosis and skewness were evaluated [5, 15]. All groups excluded pixel outside the skull; some groups also excluded pixels containing cerebrospinal fluid (CSF) and extracerebral tissue based on a manual [8, 10] or automated segmentation [11]; and others excluded CSF by an ADC threshold [7, 12]. Only few groups performed a modelling of the ADC histogram: Pope et al. suggested a two-mixture normal distribution [16], and Dyke et al. and Zhang et al. used a model consisting of two normal distributions for the brain tissue and CSF and an additional distribution for partial volume of the brain tissue and CSF [17, 18]. All these groups did not include an age dependence of the ADC histogram in their model estimations. Recent studies showed a strong influence of age on the shape of the whole brain histogram [19, 20]. In particular, the relative content of cerebrospinal fluid in the brain is increasing with age and this has an effect on the ADC histogram. The examination in this

study was performed with a large number of datasets. This allowed the calculation of highly reliable average histograms for different age classes.

The aim of this study was the development of a model for the fitting of the ADC histogram. The contribution of brain tissue (gray and white matter) is responsible for the left part of the histogram. In a first step, a model for the large maximum of the ADC histogram should be developed and, in a second step, a model for the right part of the ADC histogram was searched. In both cases, the influence of age was considered.

Such models of the description of the ADC histogram in normal subjects should be helpful for the description of changes of the ADC histogram in patients with certain pathologies.

2. Methods

2.1. Subjects and Data Acquisition. All examinations were performed with a conventional 3T MR whole-body scanner Skyra (Siemens Erlangen, Germany) equipped with a 20-channel head coil as part of the standard routine examination of patients with neuroradiological report requests from several departments of the University Hospital of Tübingen. Informed consent was obtained after the nature of the procedure had been fully explained. The local Ethics Committee approved of this retrospective study.

Data were acquired between August 2012 and July 2014. In all cases, the diffusion-weighted readout-segmented echo planar imaging (rs-EPI) sequence was applied with identical measurement parameters: repetition time (TR) 6.3 s, echo time (TE) 73 ms, b-values 0 and 1000 mm/s^2, matrix 224 $*$ 224, FOV 230 mm, slice thickness 4 mm, slice gap 0.8 mm, 30 slices, number of segments of the segmented EPI-sequence 5, and diffusion gradient scheme: three-scan trace. All measurements were performed in axial orientation parallel to the line through anterior commissure and posterior commissure (AC-PC line). All DWI data were carefully examined and data with pathological changes or with artifacts were excluded from evaluation. The exclusion of datasets was based on the decision of two neuroradiologists with more than 10 years of experience in the MR examination of patients.

The total number of examinations was 1327 patient examinations, and after the data exclusion 891 remained (448 females, 443 males). From all patient data, seven age classes were built: 10–20 years (group 1, n = 75, 28 females, 47 males), 20–30 years (group 2, n = 104, 63 females, 41 males), 30–40 years (group 3, n = 103, 61 females, 42 males), 40–50 years (group 4, n = 155, 86 females, 69 males), 50–60 years (group 5, n = 161, 78 females, 83 males), 60–70 years (group 6, n = 134, 51 females, 83 males), and 70–80 years (group 7, n = 113, 62 females, 51 males).

The age was calculated by the difference between date of measurement and date of birth and used as a decimal number. Patients of the first class had a calculated age equal to or larger than 10.00 years and lower than 20.00 years. The separation into the six other age groups was correspondingly calculated. Patients with age lower than 10 and those older than 80 years were not included in this evaluation, since the number of these patients' groups was too small and their ages were not equally distributed within these groups.

2.2. Calculation of ADC Histograms. For each of the age groups, average ADC histograms were calculated for all patients and for female and male separately and a fitting procedure was performed (described in the following). In addition to the age-dependent evaluation of the whole group of examinations, three subgroups of datasets were built and all fitting procedures were applied to each of the subgroups. The results from these three additional evaluations allow an estimation of the reliability of the obtained results of the whole group evaluation.

Each subset was built from patient examinations from a certain range of measurement dates. The number of datasets within the subgroups was 298 (147 females, 151 males), 298 (141 females, 157 male), and 295 (160 females, 135 males). The mean age of the whole group was 47.7 years; the mean age of the three subgroups was 47.5, 47.7, and 48.0 years.

All fitting procedures were also performed for these subsets to have a possibility to estimate the stability of the fitting results. Typical images with the applied sequence are shown in Figure 1. All 30 slices of the b0-images (Figure 1(a)) and the dw-images (Figure 1(b)) are shown.

Scaling of the acquired data was not consistent. Therefore, a histogram of values in the dw-images was evaluated for each patient on the basis of all 30 slices. The maximum of the smoothed histogram was estimated. The signal intensities of the acquired b0 and dw data were divided by a scale factor derived as the quotient of this median intensity and an arbitrarily chosen value of 250.

Noise pixels and pixels from the skull were excluded by applying a combined threshold derived from b0- and dw-images: pixels with a dw-value lower than 130 and b0-value lower than 600 were selected for exclusion. This procedure avoids the exclusion of pixels containing CSF with low dw-values and allows the exclusion of lipid pixels from the skull.

For the remaining pixels, the ADC value was calculated and histograms of all ADC values were evaluated for each patient. The histograms were normalized to the number of pixels exceeding the noise threshold. This normalization compensates for different head sizes.

2.3. Models for the Fitting of the ADC Histograms. From an average ADC histogram over all groups, the position and the height of the peak were evaluated. Next, the positions of the ADC values at the half-peak height (full width at half maximum, FWHM) below and above the peak position were evaluated and named as ADC_50%_below and ADC_50%_above. The position of the ADC_50%_above

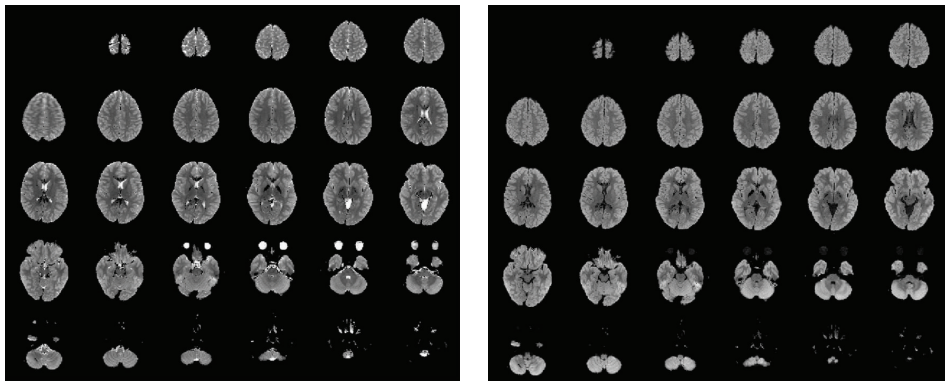

(a) (b)

Figure 1: Example of acquired data from one patient: b0-images (a) and dw-images (b).

value was used to split the mean histograms of all seven groups in two parts, hist1 and hist2, which were separately fitted to model functions. The first part of the histogram was approximated by two models: a single Gaussian curve and a combination of two Gaussian curves:

$$\text{Model 1: hist1} = A * \frac{1}{\sigma\sqrt{2*\pi}} * \exp -\frac{1}{2}\left(\frac{(\text{ADC}-\mu)}{\sigma}\right)^2,$$

$$\text{Model 2: hist1} = \text{hist1a} + \text{hist1b}$$

$$\text{hist1a} = A_1 * \frac{1}{\sigma_1\sqrt{2*\pi}} * \exp -\frac{1}{2}\left(\frac{(\text{ADC}-\mu_2)}{\sigma_2}\right)^2$$

$$\text{hist1b} = A_2 * \frac{1}{\sigma_2\sqrt{2*\pi}} * \exp -\frac{1}{2}\left(\frac{(\text{ADC}-\mu_1)}{\sigma_1}\right)^2. \quad (1)$$

The second part of the histograms, hist2, showed a decreasing behavior and was therefore approximated by a two-exponential decay curve (starting at the first point of hist2) and a decreasing straight line. In addition, the contribution of the CSF spaces was approximated by a Gaussian curve:

$$\text{hist2} = \text{hist2a} + \text{hist2b} + \text{hist2c} + \text{hist2d}$$

$$\text{hist2a} = A_3 * \exp\left(-\frac{(\text{ADC}-\text{ADC\_50\%})}{k_3}\right)$$

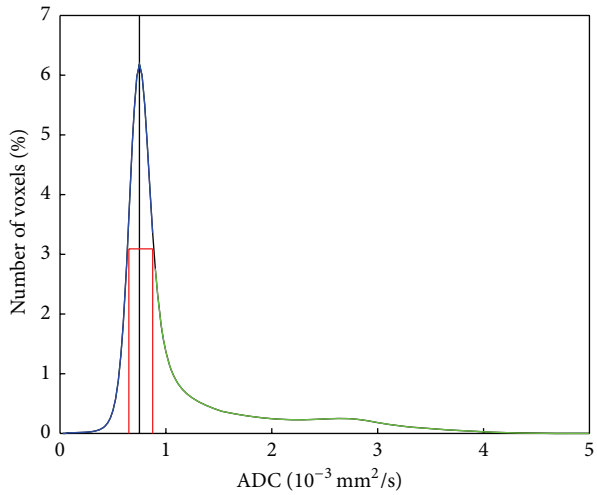

Figure 2: Histogram of ADC values from all patients. The position of the peak is marked by a black line; the position of the ADC values where the FWHM is reached is marked by red lines (ADC_50%_below and ADC_50%_above). The histogram was split into a first part (lower values than ADC_50%_above, blue) and a second part (larger values than ADC_50%_above, green). The value of ADC_50%_above lies between two data points; therefore the part of the histogram between the highest data point of the first point and the lowest part of the second point is shown in black.

$$\text{hist2b} = A_4 * \exp\left(-\frac{(\text{ADC}-\text{ADC\_50\%})}{k_4}\right)$$

$$\text{hist2c} = A_5 - m_5 * (\text{ADC}-\text{ADC\_50\%})$$

$$\text{hist2d} = A_6 * \frac{1}{\sigma_6\sqrt{2*\pi}} * \exp -\frac{1}{2}\left(\frac{(\text{ADC}-\mu_6)}{\sigma_6}\right)^2. \quad (2)$$

The fitting of the first and second part of the histogram was performed for all seven age classes. The similarity between the respective part of the histogram and the fitted

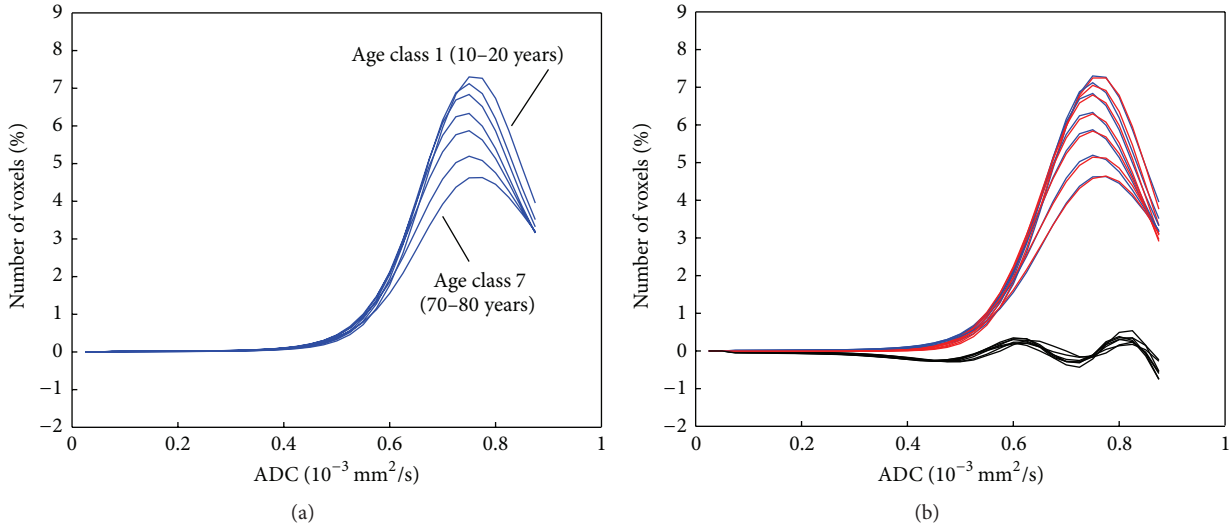

FIGURE 3: First part of the histograms of all seven age groups (a) in blue and with superposed fitted curve (based on model 1) in red (b). In addition, the differences between histograms and fitted curves are shown in black, magnified by a factor of 3. The histograms of the seven age classes follow a continuous order.

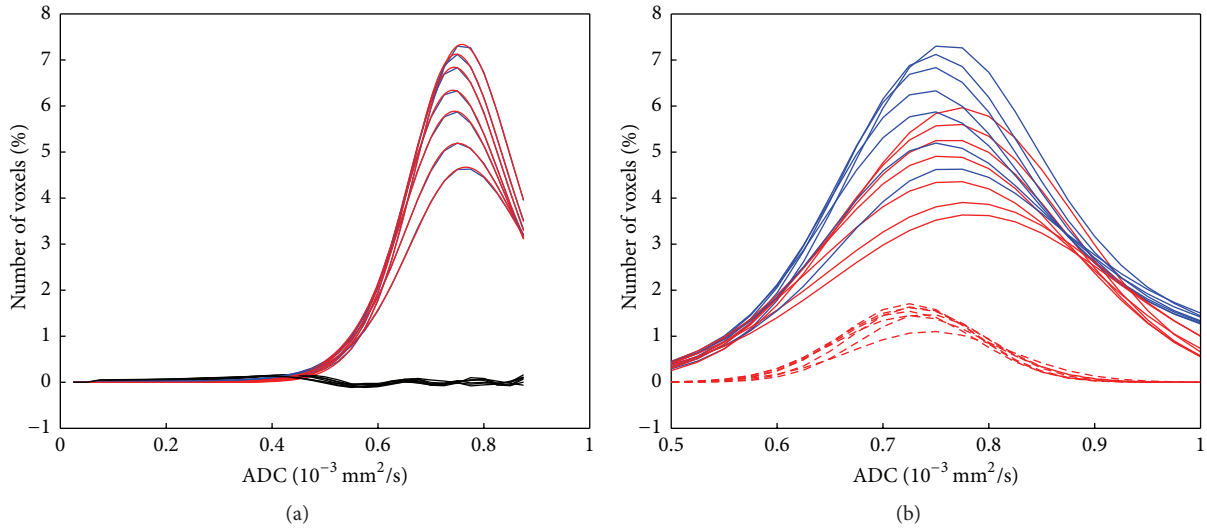

FIGURE 4: First part of the histograms of all seven age groups in blue and with superposed fitted curve (based on model 2) in red (a). The differences between histograms and fitted curves are shown in black, magnified by a factor of 3. The two Gaussian curves of the fit are separately shown in (b). The blue curves in (b) are again the calculated histograms.

curve was described by the root mean square deviation (rmsd). In addition, the relative rmsd (rmsd divided by the mean value of the respective part of the histogram) was calculated.

Calculations were performed by a computer program using MATLAB (MathWorks, Natick MA, USA) written by one of the authors.

3. Results

The calculated mean ADC histogram over all seven groups is shown in Figure 2.

The peak was at $0.75 \cdot 10^{-3}$ mm^2/s and the ADC_50%_above value at half-peak height was at $0.875 \cdot 10^{-3}$ mm^2/s. This was the value where the mean ADC histograms were split.

The first part of the mean histograms for the seven age classes is shown in Figure 3.

The results of the fitting of the first part of the histogram using model 1 and the deviations are shown in Supplementary Table 1 (Supplementary Material available online at http://dx.doi.org/10.1155/2015/373716). In Figure 3(b), the fitted curves for all seven classes due to model 1 are overlaid in red. The amplitude A_1 of the Gaussian curves is continuously

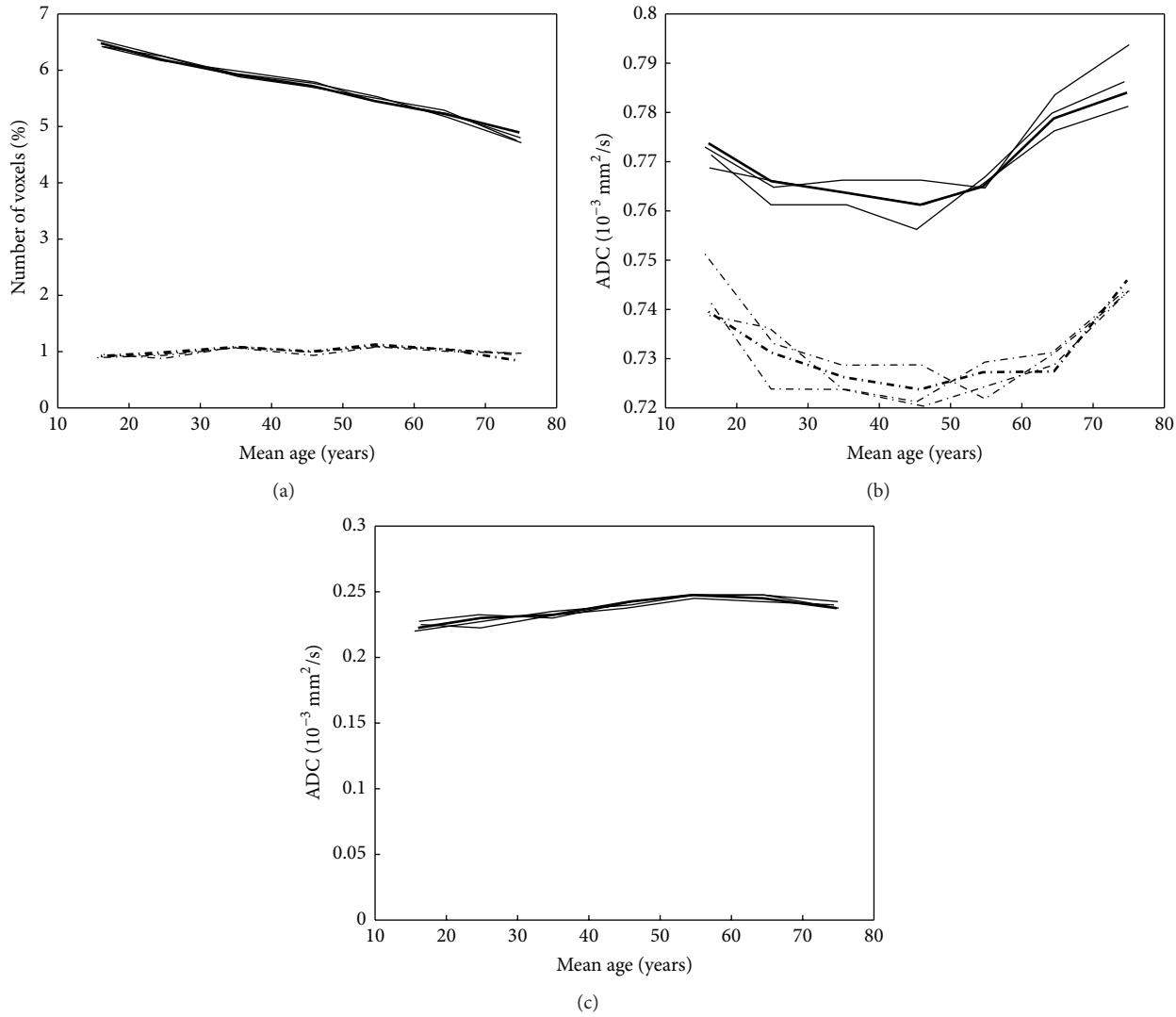

Figure 5: Fitted parameters of the first part of the histogram (based on model 2) for the different age groups: amplitudes of both Gaussian curves (a) and peak positions of both Gaussian curves (b) and of the width (FWHM) of the fitted curve (c). In all cases, the parameters are shown for all selected patients (bold line) and for the results of the three subsets of patients.

decreasing with the mean age of the seven classes. The fitting procedure was repeated for males only and females only in the seven age classes. The deviation of evaluated histograms and fitted curves are shown in Figure 3(b), in black. These difference curves show a unique behavior for all seven age classes (the maxima and minima of the difference curve are at the same position for all seven age classes). This shows that the used model 1 is incomplete.

The results of the fitting of the first part of the histogram using model 2 and the deviations are shown in Supplementary Table 2. The histograms and the fitted curves based on model 2 are shown in Figure 4(a). The difference curves between the histograms of the seven groups and the fitted curves in Figure 4(a) have all a much smaller maximum than those in Figure 3(b) and they do not show a systematic shape as the difference curves in Figure 3(b). The two Gaussian curves that were fitted to the histograms are shown in Figure 4(b). In all seven age classes, a larger Gaussian curve with a higher mean ADC value and a smaller one with a lower mean ADC value were obtained. The obtained values for the fit parameters are shown in Figure 5. In addition to the results from all patients (shown as bold lines), the results from the seven age classes from the three subsets of patients are shown.

The obtained amplitudes A_1 and A_2 are shown in Figure 5(a). The mean positions $\mu_1$and $\mu_1$for the seven age classes are shown in Figure 5(b), and the widths of the fits calculated from the sum of both Gaussian curves are given in Figure 5(c).

Figure 6 shows the results for the separate evaluation for females and males again for all patients (bold lines) and results from the three subsets of patients. The only clear difference is a larger peak ADC position of men in the age range from 30 to 50 years.

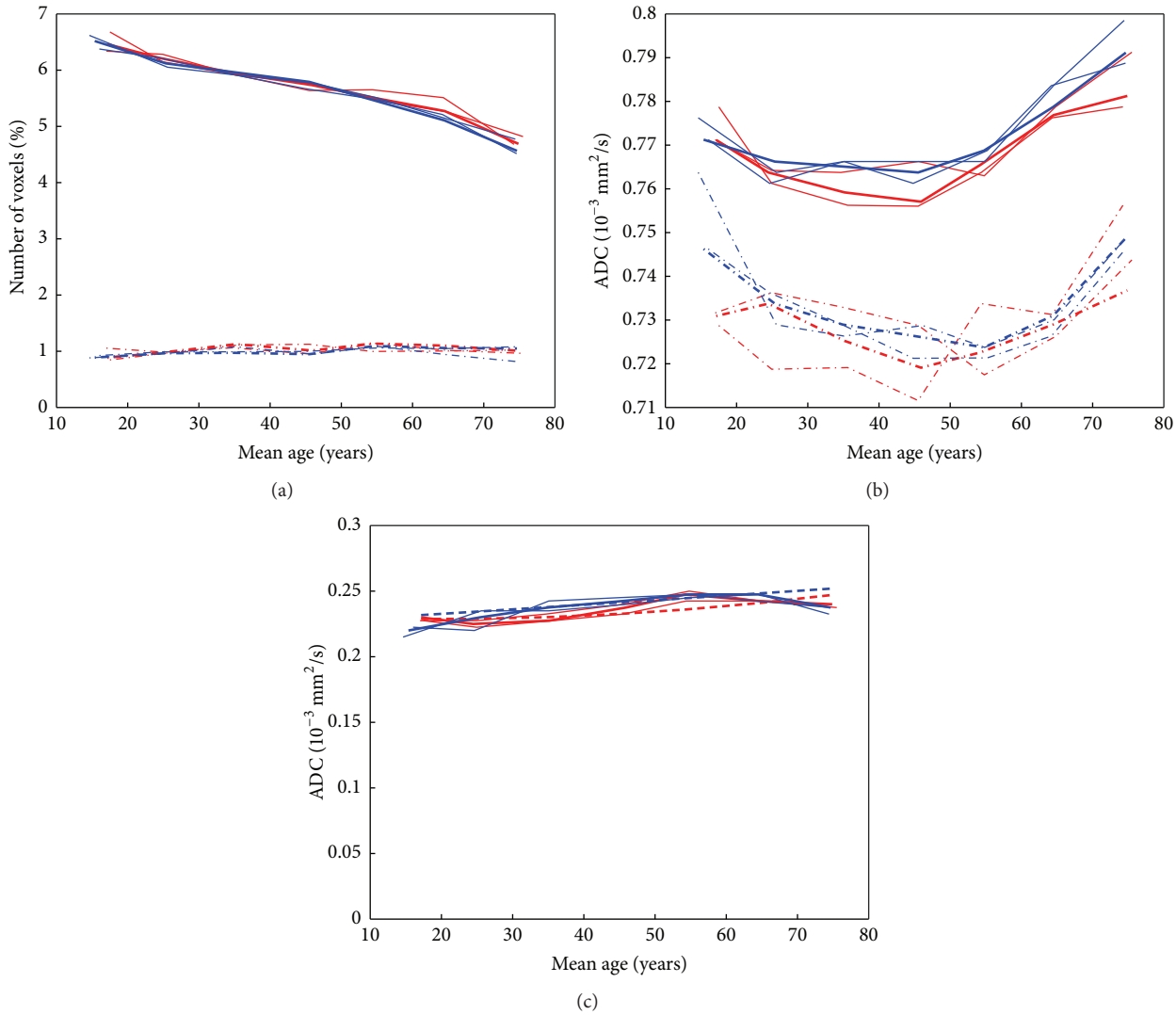

FIGURE 6: Fitted parameters of the first part of the histogram (based on model 2) for the different age groups: amplitudes of both Gaussian curves (a) and peak positions of both Gaussian curves (b) and of the width (FWHM) of the fitted curve (c). In all cases, the parameters are shown for female (red) and male (blue).

The results of the fitting of the second part of the histogram using and the deviations are shown in Supplementary Table 3. The comparison of the second part of the mean histograms for the seven age classes with the fitted curves is shown in Figure 7(a). The fitted curves consist of three different components: the biexponential decay, a Gaussian curve to describe the local maximum at $2.8 \cdot 10^{-3}$ mm^2/s, and a straight line with a negative slope and a foot point at $4.3 \cdot 10^{-3}$ mm^2/s. These components are shown in Figure 7(b). The variation of the fitted parameters of the second part of the histogram for the different age classes is shown in Figure 8 again for all datasets in bold and in addition for the three subsets. The evaluation for male and female separately (Figure 9) showed no clear difference between the evaluated parameters. The comparison of the complete histograms with both parts of the fitted curves is shown in Figure 10(a). The small step between the fitted curves of hist1 and hist2 can be seen in Figure 10(b).

4. Discussion

This study confirms the strong dependency of the whole brain ADC histograms on the age of the examined subjects. Any comparison between different groups of subjects should therefore consider this influence. On the other hand, the shape of the mean whole brain ADC histograms of the different age classes can be described by the same model using different parameters. The model used in this paper has the same main components as that of previous studies: a brain tissue part, a pure CSF part, and a part describing the partial volume between the brain tissue and CSF. In the first approach, the brain tissue part was approximated by a single Gaussian function, as it was suggested by previous studies [17, 18]. In this case, the residuum of the ADC histograms of all age classes had a very similar shape (Figure 3(b)), indicating that the first part of the histogram is described incompletely. The position of the peak of the

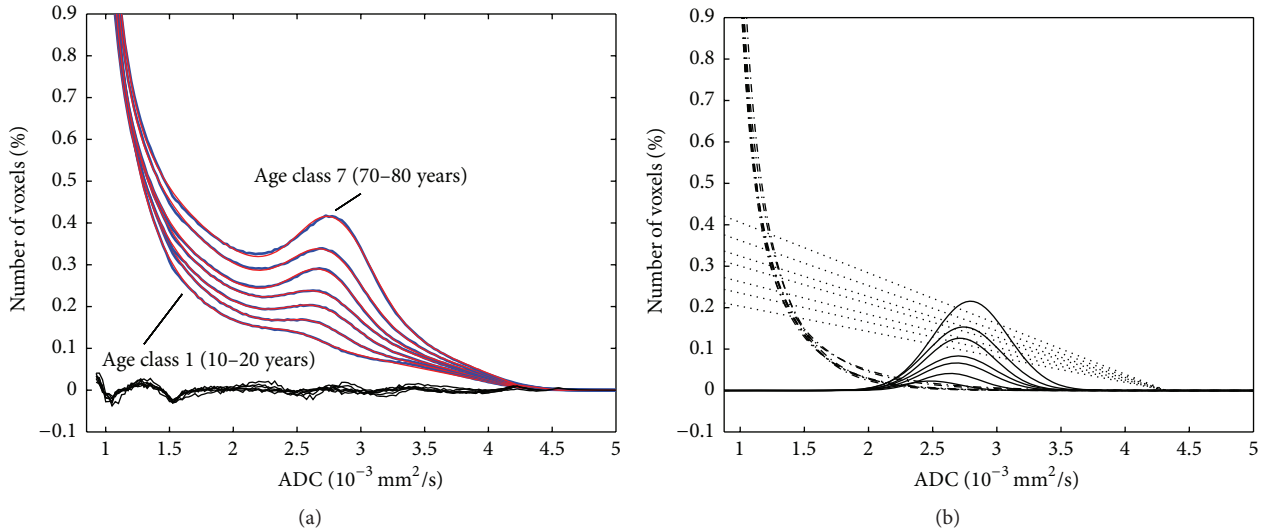

FIGURE 7: Second part of the histograms of all seven age classes in blue and with superposed fitted curve in red (a). The differences between histograms and fitted curves are shown in black, magnified by a factor of 3. The biexponential decays, the Gaussian curves for the CSF component, and the straight lines are separately shown in (b). The histograms of the seven age classes follow a continuous order.

Gaussian function is changing in a very similar way as it was described by Watanabe et al. [19] (Figure 5(b)) and the increase of the width of the fitted curve with age was also found as described by Watanabe et al. In addition to their work, we also analyzed the age-dependent amplitudes of the Gaussian curves that were used to approximate the evaluated histograms.

The residuum could be considerably reduced in all age classes by the introduction of a combination of two Gaussian curves for the first part of the histogram (Figure 4(a)). In this case, both peaks showed a U-shaped behaviour in their age dependency (Figure 5(b)) with an almost constant difference for all ages of approximately $0.04 \cdot 10^{-3}$ mm^2/s. This difference is similar to the difference of the mean ADC values of white and gray matter in a recent study of Baumann et al. [21]. They found mean values of $0.713 \cdot 10^{-3}$ mm^2/s for white matter and $0.743 \cdot 10^{-3}$ mm^2/s for parietal gray matter (difference $0.030 \cdot 10^{-3}$ mm^2/s). The Gaussian curve with the lower peak position can therefore be assumed to be representative of white matter. This assumption is confirmed by the age dependence of the peak heights (Figure 6(a)): the peak of the first Gaussian curve is almost constant while the second curve decreases from 6.5% to 5% in the age range from 15 to 75 years. These results correspond to a decreasing relative gray matter volume and slightly increasing relative white matter volume over lifespan observed by Ziegler et al. [22] (Supplementary Material, Figure S2) and by Hasan et al. [23].

The second part of the whole brain histogram consists of a decreasing component and a Gaussian shape with a peak at about $2.8 \cdot 10^{-3}$ mm^2/s. The position of this Gaussian shape was similar to the CSF component in the work of Dyke et al. [17]. However, the decreasing part could not be described by an additional Gaussian curve; instead, we used a combination of a biexponential decay and a decreasing straight line. The foot point of the straight line was at $4.3 \cdot 10^{-3}$ mm^2/s. This value is much larger as the peak of the CSF Gaussian curve and might represent the apparent diffusion coefficient of moving CSF. The decreasing straight line is characterized by its value at the position $0.875 \cdot 10^{-3}$ mm^2/s, which shows a linear increase with age (Figure 8(a)). The Gaussian curve, representing the pixels of mainly CSF, has an amplitude that is increasing linearly up to the age of 45 years. With higher ages, the increase is larger. The shift of the peak of the Gaussian curve to larger ADC values with age might also be an effect of the changing moving characteristics of CSF molecules.

The amplitudes of both exponential decay curves are decreasing with age. The curves represent voxel with partial volume of CSF and brain tissue and the decrease of their amplitude corresponds to the decrease of the brain tissue components in the first part of the histogram. The similar shape of the residuum, the difference between the calculated histograms, and the fitted curve in Figure 6(a) for all age classes is a hint that this modeling of the second part of the whole brain histogram is still incomplete. However, for all age classes, the amplitude of the residuum is very small (it is magnified by a factor of three in Figure 6(a)).

With the proposed model for the whole brain ADC histogram, it was possible to fit the histograms of seven age classes and to demonstrate systematic changes of the histogram with age. This model can be used to characterize changes of the whole brain ADC histogram in certain diseases. The sensitivity for such changes was already shown by previous studies [6–8]. The differentiation of a normal and a pathologically changed ADC histogram needs a consideration of the subject's age and can be improved by using the proposed ADC histogram model. An ADC histogram characterization by this model may replace the use

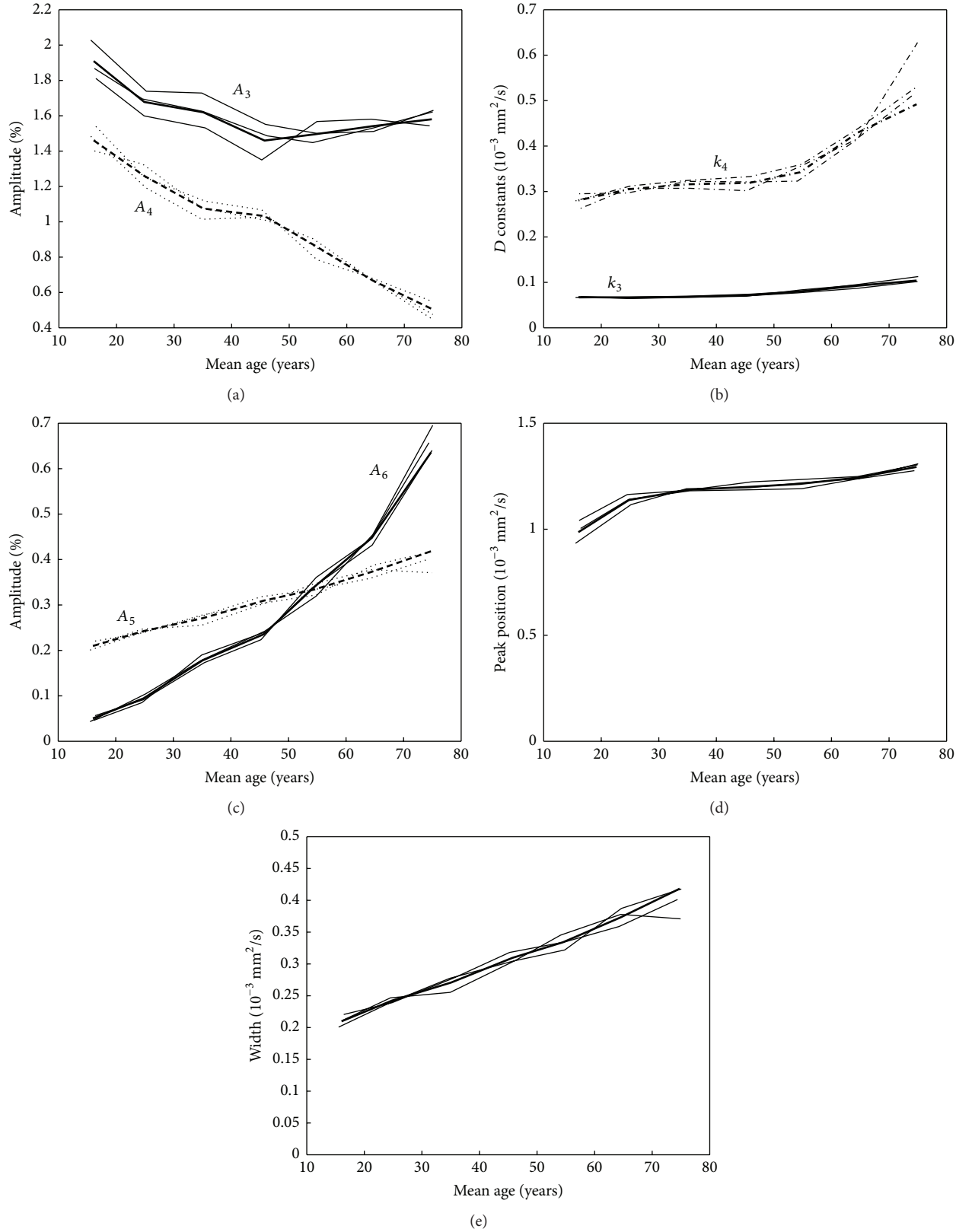

FIGURE 8: Fitted parameters of the second part of the histogram for the different age classes: amplitudes A_3 (-) and A_4 (- -) of the exponential decay curves (a), the diffusion constants k_3 and k_4 of the exponential decays (b), the amplitude A_6 of the Gaussian curve for the CSF component (-) and the value A_5 of the straight line at the position $0.875 \cdot 10^{-3}$ mm^2/s (- -) (c), the peak position μ_6 (d) and the width (FWHM) (e) of the Gaussian curve for the CSF component. In all cases, the parameters are shown for all selected patients (bold line) and for the results of the three subsets of patients.

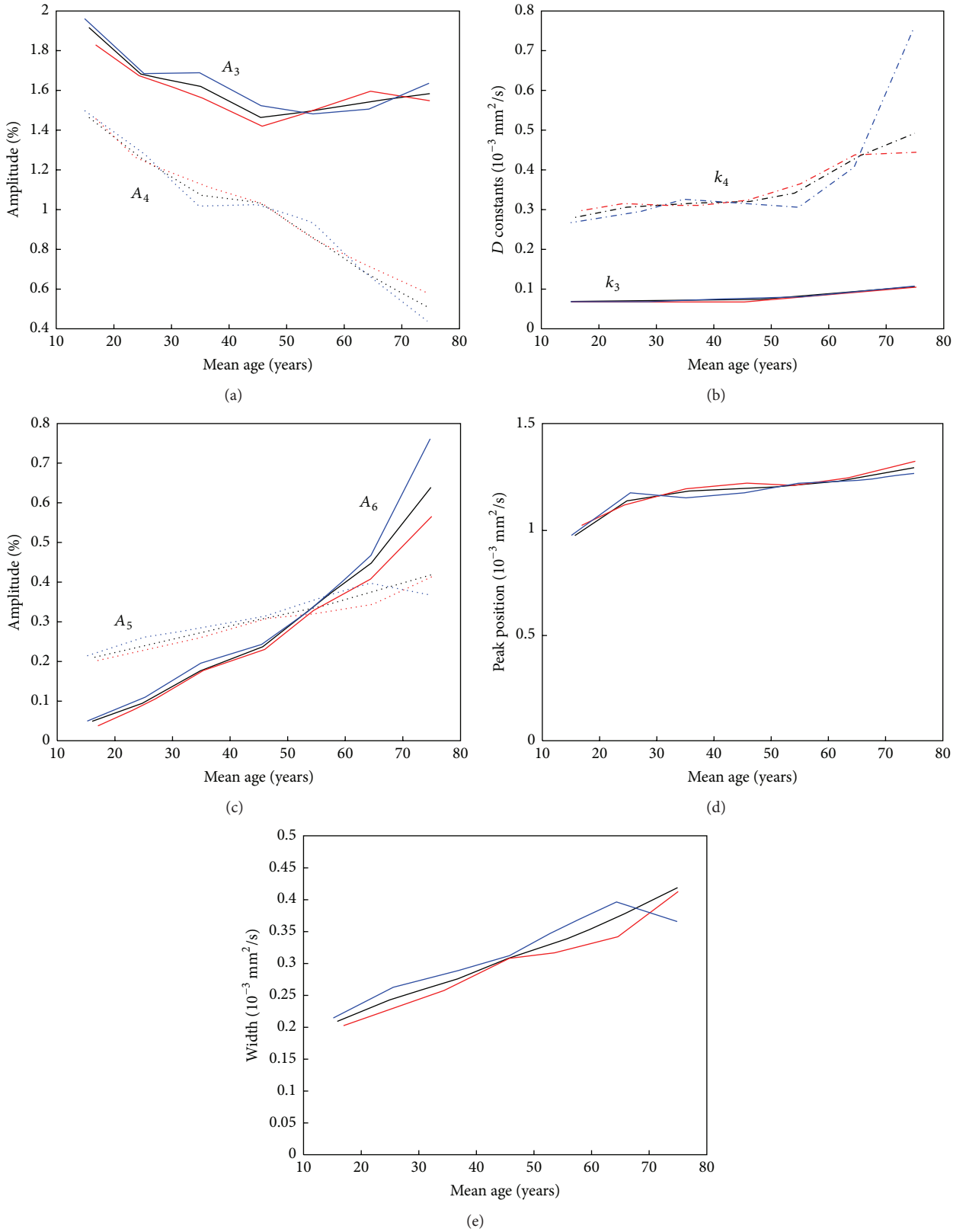

FIGURE 9: Fitted parameters of the second part of the histogram for the different age classes: amplitudes A_3 (-) and A_4 (- -) of the exponential decay curves (a), the diffusion constants k_3 and k_4 of the exponential decays (b), the amplitude A_6 of the Gaussian curve for the CSF component (-) and the value A_5 of the straight line at the position $0.875 \cdot 10^{-3}$ mm^2/s (- -) (c), the peak position μ_6 (d) and the width (FWHM) (e) of the Gaussian curve for the CSF component. In all cases, the parameters are shown for women (red), men (blue), and all patients (black).

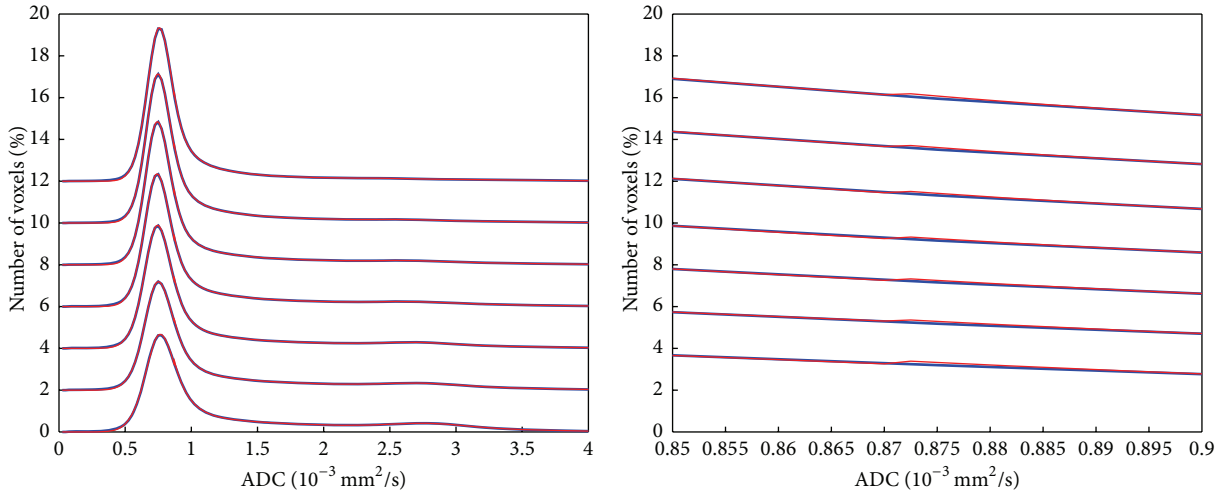

FIGURE 10: Complete histograms with both parts of the fitted curves with different vertical offsets for different age classes (2% between successive groups). The age class of 10–20 years is shown at the top, and the age class of 70–80 years is shown at the bottom. Whole ADC range (a) and reduced ADC range to visualize the step between the fitted curves of hist1 and hist2 (b).

of derived parameters as percentiles and skewness of the ADC histogram.

Conflict of Interests

The research was conducted in the absence of any commercial or financial relationships that could be construed as a potential conflict of interests.

References

[1] D. C. Tong, A. Adami, M. E. Moseley, and M. P. Marks, "Relationship between apparent diffusion coefficient and subsequent hemorrhagic transformation following acute ischemic stroke," *Stroke*, vol. 31, no. 10, pp. 2378–2384, 2000.

[2] M. Wilson, P. S. Morgan, X. Lin, B. P. Turner, and L. D. Blumhardt, "Quantitative diffusion weighted magnetic resonance imaging, cerebral atrophy, and disability in multiple sclerosis," *Journal of Neurology Neurosurgery and Psychiatry*, vol. 70, no. 3, pp. 318–322, 2001.

[3] D. J. Tozer, H. R. Jäger, N. Danchaivijitr et al., "Apparent diffusion coefficient histograms may predict low-grade glioma subtype," *NMR in Biomedicine*, vol. 20, no. 1, pp. 49–57, 2007.

[4] J. Lee, S. H. Choi, J.-H. Kim, C.-H. Sohn, S. Lee, and J. Jeong, "Glioma grading using apparent diffusion coefficient map: application of histogram analysis based on automatic segmentation," *NMR in Biomedicine*, vol. 27, no. 9, pp. 1046–1052, 2014.

[5] R. Della Nave, A. Magaudda, R. Michelucci et al., "Whole-brain histogram and voxel-based analyses of apparent diffusion coefficient and magnetization transfer ratio in celiac disease, epilepsy, and cerebral calcifications syndrome," *American Journal of Neuroradiology*, vol. 28, no. 3, pp. 479–485, 2007.

[6] M. Mascalchi, M. Moretti, R. Della Nave et al., "Longitudinal evaluation of leukoaraiosis with whole brain ADC histograms," *Neurology*, vol. 59, no. 6, pp. 938–940, 2002.

[7] M. Mascalchi, C. Tessa, M. Moretti et al., "Whole brain apparent diffusion coefficient histogram: a new tool for evaluation of leukoaraiosis," *Journal of Magnetic Resonance Imaging*, vol. 15, no. 2, pp. 144–148, 2002.

[8] N. Molko, S. Pappata, J.-F. Mangin et al., "Monitoring disease progression in CADASIL with diffusion magnetic resonance imaging: a study with whole brain histogram analysis," *Stroke*, vol. 33, no. 12, pp. 2902–2908, 2002.

[9] Y. Zhou, F.-C. Lin, J. Zhu et al., "Whole brain diffusion tensor imaging histogram analysis in vascular cognitive impairment," *Journal of the Neurological Sciences*, vol. 268, no. 1-2, pp. 60–64, 2008.

[10] M. Rovaris, G. Iannucci, M. Cercignani et al., "Age-related changes in conventional, magnetization transfer, and diffusion-tensor MR imaging findings: study with whole-brain tissue histogram analysis," *Radiology*, vol. 227, no. 3, pp. 731–738, 2003.

[11] S. C. A. Steens, F. Admiraal-Behloul, J. A. Schaap et al., "Reproducibility of brain ADC histograms," *European Radiology*, vol. 14, no. 3, pp. 425–430, 2004.

[12] T. Kin, M. Hirano, T. Taoka et al., "Global and region-specific analyses of apparent diffusion coefficient in dentatorubral-pallidoluysian atrophy," *American Journal of Neuroradiology*, vol. 27, no. 7, pp. 1463–1466, 2006.

[13] K. Shanmuganathan, R. P. Gullapalli, S. E. Mirvis, S. Roys, and P. Murthy, "Whole-brain apparent diffusion coefficient in traumatic brain injury: correlation with Glasgow Coma Scale score," *American Journal of Neuroradiology*, vol. 25, no. 4, pp. 539–544, 2004.

[14] R. C. Welsh, H. Rahbar, B. Foerster, M. Thurnher, and P. C. Sundgren, "Brain diffusivity in patients with neuropsychiatric systemic lupus erythematosus with new acute neurological symptoms," *Journal of Magnetic Resonance Imaging*, vol. 26, no. 3, pp. 541–551, 2007.

[15] P. G. Sämann, M. Knop, E. Golgor, S. Messler, M. Czisch, and F. Weber, "Brain volume and diffusion markers as predictors of disability and short-term disease evolution in multiple sclerosis," *American Journal of Neuroradiology*, vol. 33, no. 7, pp. 1356–1362, 2012.

[16] W. B. Pope, H. J. Kim, J. Huo et al., "Recurrent glioblastoma multiforme: ADC histogram analysis predicts response to bevacizumab treatment," *Radiology*, vol. 252, no. 1, pp. 182–189, 2009.

[17] J. P. Dyke, H. U. Voss, D. Sondhi et al., "Assessing disease severity in late infantile neuronal ceroid lipofuscinosis using quantitative MR diffusion-weighted imaging," *American Journal of Neuroradiology*, vol. 28, no. 7, pp. 1232–1236, 2007.

[18] L. Zhang, M. Harrison, L. A. Heier et al., "Diffusion changes in patients with systemic lupus erythematosus," *Magnetic Resonance Imaging*, vol. 25, no. 3, pp. 399–405, 2007.

[19] M. Watanabe, O. Sakai, A. Ozonoff, S. Kussman, and H. Jara, "Age-related apparent diffusion coefficient changes in the normal brain," *Radiology*, vol. 266, no. 2, pp. 575–582, 2013.

[20] U. Klose, M. Batra, and T. Nägele, "Age-dependent changes in the histogram of apparent diffusion coefficients values in magnetic resonance imaging," *Frontiers in Aging Neuroscience*, vol. 5, article 78, 2013.

[21] P. S. Baumann, L. Cammoun, P. Conus et al., "High b-value diffusion-weighted imaging: a sensitive method to reveal white matter differences in schizophrenia," *Psychiatry Research*, vol. 201, no. 2, pp. 144–151, 2012.

[22] G. Ziegler, R. Dahnke, L. Jäncke, R. A. Yotter, A. May, and C. Gaser, "Brain structural trajectories over the adult lifespan," *Human Brain Mapping*, vol. 33, no. 10, pp. 2377–2389, 2012.

[23] K. M. Hasan, I. S. Walimuni, L. A. Kramer, and R. E. Frye, "Human brain atlas-based volumetry and relaxometry: application to healthy development and natural aging," *Magnetic Resonance in Medicine*, vol. 64, no. 5, pp. 1382–1389, 2010.

Hindawi Publishing Corporation
BioMed Research International
Volume 2015, Article ID 141853, 5 pages
http://dx.doi.org/10.1155/2015/141853

Research Article

MR Prediction of Liver Function and Pathology Using Gd-EOB-DTPA: Effect of Liver Volume Consideration

Dai Shimamoto,[1] Akihiro Nishie,[1] Yoshiki Asayama,[1] Yasuhiro Ushijima,[1] Yukihisa Takayama,[1] Nobuhiro Fujita,[1] Ken Shirabe,[2] Tomoyuki Hida,[3] Yuichiro Kubo,[3] and Hiroshi Honda[1]

[1]*Department of Clinical Radiology, Graduate School of Medical Sciences, Kyushu University, 3-1-1 Maidashi, Higashi-ku, Fukuoka 812-8582, Japan*
[2]*Department of Surgery and Science, Graduate School of Medical Sciences, Kyushu University, 3-1-1 Maidashi, Higashi-ku, Fukuoka 812-8582, Japan*
[3]*Department of Anatomic Pathology, Graduate School of Medical Sciences, Kyushu University, 3-1-1 Maidashi, Higashi-ku, Fukuoka 812-8582, Japan*

Correspondence should be addressed to Akihiro Nishie; anishie@radiol.med.kyushu-u.ac.jp

Received 4 May 2015; Revised 12 October 2015; Accepted 13 October 2015

Academic Editor: Enzo Terreno

Purpose. To evaluate whether the diagnostic performance of Gd-EOB-DTPA-enhanced MRI in evaluating liver function and pathology is improved by considering liver volume (LV). *Methods*. This retrospective study included 104 patients who underwent Gd-EOB-DTPA-enhanced MRI before liver surgery. For each patient, using the precontrast and hepatobiliary phase images, we calculated the increase rate of the liver-to-spleen signal intensity ratio (LSR), that is, the "ΔLSR," and the increase rate of the liver-to-muscle signal intensity ratio (LMR), that is, the "ΔLMR." ΔLSR × LV and ΔLMR × LV were also calculated. The correlation of each MR parameter with liver function data or liver pathology was assessed. The correlation coefficients were compared between ΔLSR (ΔLMR) and ΔLSR (ΔLMR) × LV. *Results*. The correlation coefficient between ΔLSR (ΔLMR) × LV and cholinesterase was significantly higher than that between ΔLSR (ΔLMR) and cholinesterase. The correlation coefficient between ΔLSR (ΔLMR) × LV and the degree of fibrosis or necroinflammatory activity was significantly lower than that between ΔLSR (ΔLMR) and the degree of fibrosis or necroinflammatory activity. *Conclusion*. The inclusion of liver volume may improve Gd-EOB-DTPA-based predictions of liver function, but not in predictions of liver pathology.

1. Introduction

Gadolinium ethoxybenzyl diethylenetriamine penta-acetic acid (Gd-EOB-DTPA) is a liver-specific agent, and it is widely used to improve both the detection rate of focal liver lesions and the characterization of liver tumors on magnetic resonance imaging (MRI) [1, 2]. As Gd-EOB-DTPA is taken up specifically by hepatocytes, the measurement of the uptake of Gd-EOB-DTPA in the liver can be used to evaluate liver function [3–5]. A correlation between the uptake of Gd-EOB-DTPA and pathological liver fibrosis has also been reported [6, 7]. That is, the signal intensity itself or the signal intensity change in the hepatobiliary phase decreases as the liver function or fibrosis worsens. In these previous studies, only the degree of Gd-EOB-DTPA uptake on a single slice or several slices was considered as an indicator of liver function or fibrosis. However, the liver volume (LV) is quite different among individuals. We hypothesized that the liver function or fibrosis could be more precisely estimated by using a parameter including the LV, which would represent the whole liver function.

The purpose of the present study was to evaluate whether the diagnostic performance of Gd-EOB-DTPA-enhanced MRI in evaluating liver function or fibrosis is improved by considering the LV.

2. Methods

2.1. Patients. This study was approved by the institutional review board of our hospital. The requirements for informed consent were waived for this retrospective study. Referring to the medical data recorded at our hospital, we enrolled 129 consecutive patients who underwent Gd-EOB-DTPA-enhanced MRI and hepatic resection for a liver tumor or liver transplantation between June 2010 and May 2013. Of them, twelve, eight, and five patients were excluded due to a history of splenectomy, a history of right or left lobectomy, and poor image quality derived from respiratory artifacts, respectively. Finally, 104 patients were enrolled in this study. The 104 patients included 69 men and 35 women (age range, 32–86 years; mean age, 64.5 years). The hepatitis C virus antibody was present in 45 cases, the hepatitis B surface antigen in 17 cases, alcoholic hepatitis in five cases, nonalcoholic steatohepatitis in five cases, primary biliary cirrhosis in two cases, autoimmune hepatitis in one case, and primary sclerosing cholangitis in one case. The grading of liver dysfunction was preoperatively evaluated based on the Child-Pugh classification, and 86, seven, and 11 patients were categorized into Grades A, B, and C, respectively. The grading of liver function or severity of liver cirrhosis in patients with chronic liver disease was evaluated according to the Child-Pugh classification [8]. The classification is based on the following five factors, graded on a scale from 1 to 3: hepatic encephalopathy, ascites, total bilirubin level, albumin level, and prothrombin time. The liver function or severity of cirrhosis was classed into three groups according to the sum of the scores: Grade A, from 5 to 6; Grade B, from 7 to 9; Grade C, from 10 to 15. The laboratory data were obtained at least within one month before surgery. For each patient, the platelet count (Plt), albumin (Alb), total bilirubin (T-bil), lactate dehydrogenase (LDH), cholinesterase (ChE), Child-Pugh score, and model for end-stage liver disease (MELD) score were recorded. An MR examination was performed at least 3 months before the surgery. No treatment was performed between the MR examination and the surgery for any of the patients.

2.2. MR Imaging. MR imaging was performed on a whole-body 3.0 Tesla (T) scanner (Achieva 3.0Tx, Philips Medical Systems, Best, Netherlands). For the Gd-EOB-DTPA-enhanced MRI, axial 3D eTHRIVE (three-dimensional enhanced-T1 high-resolution isotropic volume excitation) was scanned before and 20 min after an intravenous injection of 0.1 mL/kg (total amount: 4 to 8 mL) of Gd-EOB-DTPA (Primovist; Bayer, Osaka, Japan). The detailed imaging parameters were as follows: 32-channel cardiac phased-array coil, TR/TE/FA = 3 ms/1.4 ms/10°, matrix 252 × 200, FOV 37.5 × 29.8 cm, SENSE factor 1.8, slice thickness = 3 mm, gap = −1.5 mm, linear *k*-space ordering, spectral attenuation with inversion recovery, acquired 133 sections, scan time 17.9 s, and breath-holding.

2.3. Liver Volume Measurement. For the LV measurement, the total of the MR images in the hepatobiliary phase was prepared for each patient. The LV of each patient was semiautomatically measured using the "liver analysis" function of the volume analyzer SYNAPSE VINCENT (Fuji Film Medical, Tokyo). A part of liver tumor was not considered as LV.

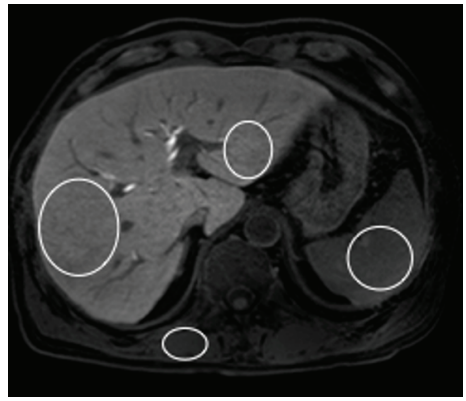

Figure 1: Hepatobiliary phase of Gd-EOB-DTPA-enhanced MRI. The signal intensities were measured by placing the largest possible regions of interest (ROIs) on the liver parenchyma, spleen, and erector spinae muscle, avoiding vessels, tumors, and artifacts. For the liver parenchyma, two round or oval ROIs were placed: one in the right lobe and the other in the left.

2.4. MR Image Analysis. The signal intensity of axial eTHRIVE on Gd-EOB-DTPA-enhanced MRI was measured on the same DICOM viewer. First, two abdominal radiologists with six and 19 years of experience together selected three slices without significant artifacts. On the same slices they measured the signal intensities by placing the largest possible region of interest (ROI) on the liver parenchyma, spleen, and erector spinae muscle, avoiding vessels, tumors, and artifacts in a consensus manner (Figure 1). For the liver parenchyma, two round or oval ROIs were placed: one in the right lobe and the other in the left. The averages of the six signal intensities of the liver parenchyma and the three signal intensities of the spleen or the erector spinae muscle were calculated.

Based on these average values, the liver-to-spleen ratio (LSR) and the liver-to-muscle ratio (LMR) before and after the administration of Gd-EOB-DTPA were recorded for each patient. The same size and shape of ROI were placed at the same position for the images before and after the administration of Gd-EOB-DTPA. As indicators of liver function, the increase rates of the LSR (LMR) in the hepatobiliary phase compared with the precontrast image were calculated using the following equation: (LSR (LMR) on the hepatobiliary phase − LSR (LMR) on the precontrast image)/LSR (LMR) on the precontrast image [3, 4]. We named "the increase rate of LSR (LMR)" as "ΔLSR (ΔLMR)." We also set the parameter "ΔLSR (LMR) × LV" (unit; liter) for the analysis.

2.5. Pathologic Analysis. One pathologist with 4 years of experience who was unaware of the imaging data reviewed the hematoxylin-eosin-stained glass slides of each patient and referred to the official pathological report to determine

the histological findings of the liver parenchyma. When the results were discordant, another experienced pathologist with 17 years of experience was consulted. The degree of liver fibrosis was classified into five groups according to the New Inuyama Classification: F0 (no fibrosis), F1 (fibrous portal expansion), F2 (bridging fibrosis), F3 (bridging fibrosis with architectural distortion), and F4 (liver cirrhosis) [9]. Similarly, the grade of necroinflammatory activity was scored as A0 (no necroinflammatory reaction), A1 (mild), A2 (moderate), and A3 (severe) [9].

2.6. Statistical Analysis. We used a linear regression analysis to examine the correlations between ΔLSR (ΔLMR) and ΔLSR (ΔLMR) × LV and the laboratory data corresponding to liver function (including Plt, Alb, T-bil, LDH, and ChE). The correlations of these four parameters with the Child-Pugh score, MELD score, the degree of liver fibrosis, and the grade of necroinflammatory activity were each examined using Spearman's rank correlation test. We also compared the correlation coefficients between ΔLSR and ΔLSR × LV and between ΔLMR and ΔLMR × LV. The statistical significance was evaluated using the following method: when the dependence of a variable (y, z) on a single independent variable (x) was observed, we calculated the correlation coefficient (Rxy, Rxz), and we tested the significance of the Rxy, Rxz coefficient by means of the modified t-test, the number of degrees of freedom being $f = n - 3$, using the following formula (n = sample number):

$$t\text{-statistic} = (Ryz - Rxz) \cdot \sqrt{\frac{(n-3)(1+Ryz)}{2\left(1 - Rxy^2 - Rxz^2 - Ryz^2 + 2RxyRyzRxz\right)}} \quad (1)$$

(see [10]).

For all tests, a p value of <0.05 indicated a significant difference.

3. Results

The number of patients in each grade of fibrosis and necroinflammatory activity was as follows: F0 ($n = 33$), F1 ($n = 11$), F2 ($n = 11$), F3 ($n = 12$), and F4 ($n = 37$) and A0 ($n = 30$), A1 ($n = 38$), A2 ($n = 32$), and A3 ($n = 4$). The average LVs ± standard deviation (SD) in F0, F1, F2, F3, and F4 were 1.09 ± 0.24, 1.06 ± 0.26, 1.15 ± 0.17, 1.13 ± 0.26, and 1.06 ± 0.34, respectively. The average LVs ± SD in A0, A1, A2, and A3 were 1.08 ± 0.23, 1.04 ± 0.29, 1.13 ± 0.29, and 1.19 ± 0.30, respectively. The average values and SD of ΔLSR, ΔLSR × LV, ΔLMR, and ΔLMR × LV were 0.53 ± 0.30, 0.59 ± 0.37, 0.64 ± 0.29, and 0.70 ± 0.35, respectively. All four parameters (ΔLSR, ΔLSR × LV, ΔLMR, and ΔLMR × LV) were significantly correlated with all laboratory data, the grade of fibrosis, and necroinflammatory activity ($p < 0.05$ in each case).

Table 1 shows the correlation coefficients between ΔLSR or ΔLSR × LV and the laboratory data or pathologic factors. The correlation coefficient between ΔLSR × LV and ChE was significantly higher than that between ΔLSR and ChE ($p < 0.05$). The correlation coefficients between ΔLSR × LV and Plt, Alb, LDH, Child-Pugh score, or MELD score tended to be higher than those between ΔLSR and Plt, Alb, LDH, Child-Pugh score, or MELD score. However, the correlation coefficient between ΔLSR × LV and the degree of fibrosis or necroinflammatory activity was significantly lower than that between ΔLSR and the degree of fibrosis or necroinflammatory activity ($p < 0.01$). The correlation coefficient between ΔLSR × LV and T-bil tended to be lower than that between ΔLSR and T-bil.

Table 1: Correlation coefficients between ΔLSR or ΔLSR × LV and the laboratory or pathologic data.

Parameter	ΔLSR	ΔLSR × LV	p value
Plt	0.498	0.522	0.49
Alb	0.624	0.646	0.49
T-bil	0.364	0.330	0.40
LDH	0.238	0.244	0.88
ChE	0.577	0.649	<0.05
Child-Pugh score	−0.592	−0.641	0.12
MELD score	−0.471	−0.478	0.85
Fibrosis	−0.492	−0.383	<0.01
Necroinflammation	−0.451	−0.341	<0.01

The data are correlation coefficients. LSR: the liver-to-spleen ratio; ΔLSR: the increase rate of LSR on the hepatobiliary phase compared with the precontrast image. Plt: platelet count; Alb: albumin; T-bil: total bilirubin; LDH: lactate dehydrogenase; ChE: cholinesterase. ΔLSR and ΔLSR × LV were calculated as described in Section 2.

Table 2: Correlation coefficients between ΔLMR or ΔLMR × LV and the laboratory or pathologic data.

Parameter	ΔLMR	ΔLMR × LV	p value
Plt	0.405	0.457	0.22
Alb	0.668	0.701	0.22
T-bil	0.400	0.382	0.69
LDH	0.211	0.249	0.41
ChE	0.590	0.681	<0.01
Child-Pugh score	−0.599	−0.655	0.12
MELD score	−0.433	−0.477	0.29
Fibrosis	−0.493	−0.395	<0.05
Necroinflammation	−0.462	−0.324	<0.01

The data are correlation coefficients. LMR: the liver-to-erector spinae muscle; ΔLMR: the increase rate of LMR on the hepatobiliary phase compared with the precontrast image. ΔLMR and ΔLMR × LV were calculated as described in Section 2.

Table 2 shows correlation coefficients between ΔLMR or ΔLMR × LV and the laboratory data or pathologic factors. The correlation coefficient between ΔLMR × LV and ChE was significantly higher than that between ΔLMR and ChE ($p < 0.01$) (Figure 2). The correlation coefficients between ΔLMR × LV and Plt, Alb, LDH, Child-Pugh score, or MELD score tended to be higher than those between ΔLMR and Plt, Alb, LDH, Child-Pugh score, or MELD score. However, the correlation coefficient between ΔLMR × LV and the degree of fibrosis or necroinflammatory activity was significantly lower than that between ΔLMR and the degree of fibrosis ($p < 0.05$) or necroinflammatory activity ($p < 0.01$). The correlation

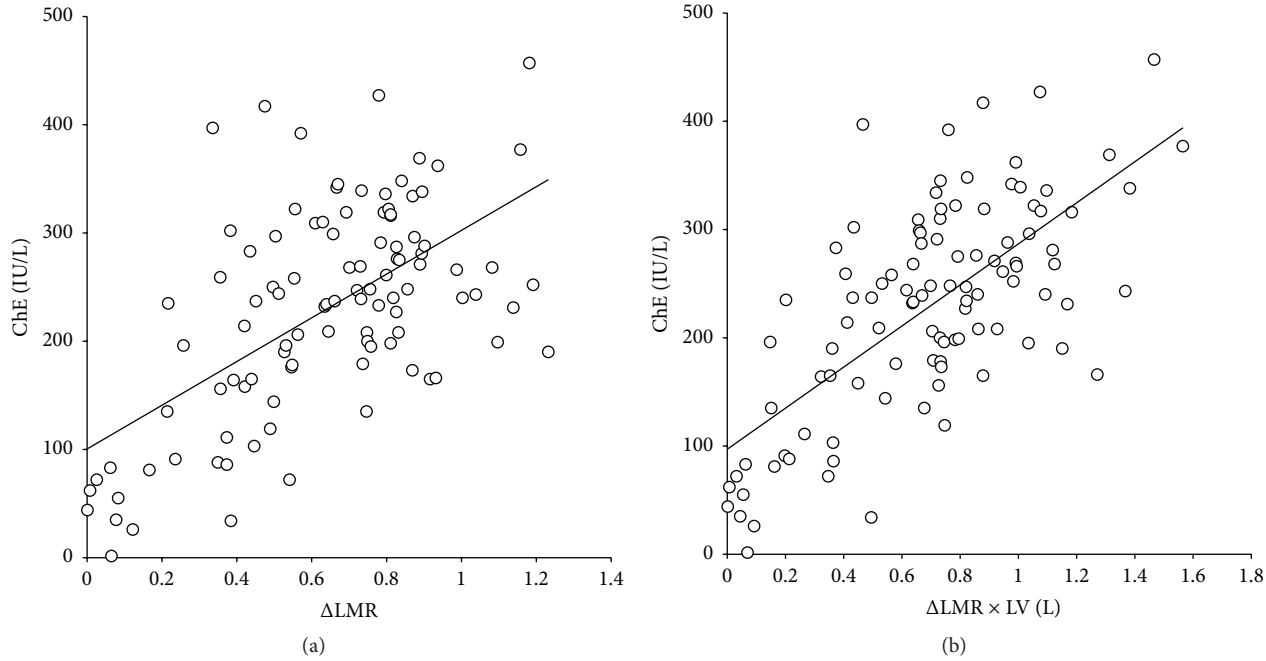

Figure 2: Scatterplot showing the relationship between (a) ΔLMR and ChE and (b) ΔLMR × LV and ChE ($n = 103$). (a) The regression analysis yielded the following standard formula (solid line): ChE = 201.9 × ΔLMR + 100.5 (correlation coefficient = 0.590; $p < 0.01$). (b) The regression analysis yielded the following standard formula (solid line): ChE = 189.7 × ΔLMR × LV + 97.0 (correlation coefficient = 0.681; $p < 0.01$). The correlation coefficient between ΔLMR × LV and ChE was significantly higher than that between ΔLMR and ChE.

coefficient between ΔLMR × LV and T-bil tended to be lower than that between ΔLMR and T-bil.

4. Discussion

In our study using 3T-MRI, significant correlations between the uptake of Gd-EOB-DTPA and liver function, fibrosis, and necroinflammatory activity were obtained, as reported previously [4–7]. In light of this result, we feel that our radiological assessment is valid for evaluating liver function, fibrosis, and necroinflammatory activity. In addition, the correlation coefficient between ΔLSR (LMR) × LV and ChE was significantly higher than that between ΔLSR (LMR) and ChE. The correlation coefficients between ΔLSR (LMR) × LV and Plt, Alb, LDH, Child-Pugh score, or MELD score tended to be higher than those between ΔLSR (LMR) and Plt, Alb, LDH, Child-Pugh score, or MELD score, suggesting that we should consider "liver volume" in addition to the uptake of Gd-EOB-DTPA for setting the MR parameters. Recently, some articles have reported that the relationship between the uptake of Gd-EOB-DTPA and indocyanine green test can be improved by considering liver volume [11–13] and supports our result or hypothesis.

In general, liver function data are evaluated with a blood test, which includes a "whole liver" element. Therefore, the consideration of liver volume in the MR parameter could enable the correlation with liver function to be more intensive. We found in the present study that the correlation coefficient between ΔLSR (LMR) × LV and T-bil tended to be lower than that between ΔLSR (LMR) and T-bil, although the difference was only slight. T-bil includes both unconjugated and conjugated bilirubin, and the T-bil value can be affected by a number of factors including prehepatic or posthepatic disorders, hemolysis, and constitutional predisposition. Therefore, considering "liver volume" in the MR parameter might not be effective for the correlation with T-bil.

We also found that the correlation coefficients between ΔLSR (LMR) × LV and the degree of fibrosis or necroinflammatory activity were significantly lower than those between ΔLSR (LMR) and the degree of fibrosis or necroinflammatory activity. That is, the consideration of liver volume in addition to the uptake of Gd-EOB-DTPA for setting the MR parameters was not useful. Although this result was beyond the scope of our hypothesis, we propose two plausible reasons why this result was obtained. One is that fibrosis and necroinflammatory activity represent the local state of the liver parenchyma. Therefore, the consideration of "liver volume" might worsen the correlation with liver pathology. Another possible reason is that the LV does not always decrease gradually as the degree of fibrosis progresses. A report on LV change in patients with hepatic fibrosis is available [14]. The LV tends to increase with the severity of fibrosis since the number of hepatic cells accounts for 70%–80% of the liver parenchyma and then decrease. The presumed reason for the hepatic volume increase would be the ballooning of hepatocytes along with the increased fibrotic component.

We obtained a similar result; that is, LV tends to increase with the severity of fibrosis from F0 to F2 but decrease at F3 to F4, which would affect the rank correlation between ΔLSR

(LMR) × LV and the degree of fibrosis. It was reported that the LV tends to increase with the aggravation of inflammatory activity (the increase of necroinflammatory activity) [14]. In our study we obtained a similar result; that is, the LV tends to increase as the degree of necroinflammatory activity advances from A1 to A3. Therefore, the LV consideration would have the opposite effect on the correlation with the degree of necroinflammatory activity. We thus suggest that "liver volume" should not be considered among the MR parameters when evaluating liver pathology using Gd-EOB-DTPA-enhanced MRI.

Our study had several limitations. First, the trial was a study with a limited patient population, and the number of cases with each degree of fibrosis and necroinflammatory activity was not uniform. Second, we used two organs, the spleen and erector spinae muscle, as signal intensity references of the liver parenchyma. As there may be persistence of contrast enhancement in the spleen and muscle, these organs might be limitations for analyses of LSR and LMR as well as motion artifacts and partial volume effects. Although a T1 map might be preferable for the quantitative analysis of the uptake of Gd-EOB-DTPA, it was difficult to generate such a map with our scanner. Third, we could not evaluate indocyanine green test results as a laboratory datum corresponding to liver function. Although 80 patients underwent this test preoperatively, the Child-Pugh classification for all of them was Grade A. That is, patients with moderate or severe liver dysfunction were not included. We judged that we should not juxtapose the comparison with ICG test to those with other liver function parameters in our study, because of the difference in patient population. Finally, tumor volumes of small lesions in the liver were not excluded from measured LV for technical difficulty, which may have led to minor overestimation of LV in some patients.

5. Conclusion

We have demonstrated that the inclusion of liver volume may improve Gd-EOB-DTPA-based predictions of liver function, but not in predictions of liver pathology.

Conflict of Interests

The authors declare that there is no conflict of interests regarding the publication of this paper.

Acknowledgments

The authors thank Dr. Yoshihiko Maehara, Department of Surgery and Science, Kyushu University, for providing the clinical information for this paper. They also thank Dr. Yoshinao Oda, Department of Anatomic Pathology, Kyushu University, for providing the pathological information for this paper. This study was supported in part by Grant-in-Aid for Scientific Research (C), JSPS KAKENHI Grant no. 26461796.

References

[1] S. Kogita, Y. Imai, M. Okada et al., "Gd-EOB-DTPA-enhanced magnetic resonance images of hepatocellular carcinoma: correlation with histological grading and portal blood flow," *European Radiology*, vol. 20, no. 10, pp. 2405–2413, 2010.

[2] T. Ichikawa, K. Saito, N. Yoshioka et al., "Detection and characterization of focal liver lesions: a Japanese phase III, multicenter comparison between gadoxetic acid disodium-enhanced magnetic resonance imaging and contrast-enhanced computed tomography predominantly in patients with hepatocellular carcinoma and chronic liver disease," *Investigative Radiology*, vol. 45, no. 3, pp. 133–141, 2010.

[3] B. Hamm, T. Staks, A. Mühler et al., "Phase I clinical evaluation of Gd-EOB-DTPA as a hepatobiliary MR contrast agent: safety, pharmacokinetics, and MR imaging," *Radiology*, vol. 195, no. 3, pp. 785–792, 1995.

[4] A. Nishie, Y. Ushijima, T. Tajima et al., "Quantitative analysis of liver function using superparamagnetic iron oxide- and Gd-EOB-DTPA-enhanced MRI: comparison with Technetium-99m galactosyl serum albumin scintigraphy," *European Journal of Radiology*, vol. 81, no. 6, pp. 1100–1104, 2012.

[5] U. Motosugi, T. Ichikawa, H. Sou et al., "Liver parenchymal enhancement of hepatocyte-phase images in Gd-EOB-DTPA-enhanced MR imaging: which biological markers of the liver function affect the enhancement?" *Journal of Magnetic Resonance Imaging*, vol. 30, no. 5, pp. 1042–1046, 2009.

[6] A. Nishie, Y. Asayama, K. Ishigami et al., "MR prediction of liver fibrosis using a liver-specific contrast agent: superparamagnetic iron oxide versus Gd-EOB-DTPA," *Journal of Magnetic Resonance Imaging*, vol. 36, no. 3, pp. 664–671, 2012.

[7] S. Nojiri, A. Kusakabe, K. Fujiwara et al., "Noninvasive evaluation of hepatic fibrosis in hepatitis C virus-infected patients using ethoxybenzyl-magnetic resonance imaging," *Journal of Gastroenterology and Hepatology*, vol. 28, no. 6, pp. 1032–1039, 2013.

[8] R. N. H. Pugh, I. M. Murray Lyon, and J. L. Dawson, "Transection of the oesophagus for bleeding oesophageal varices," *British Journal of Surgery*, vol. 60, no. 8, pp. 646–649, 1973.

[9] Y. Tomimaru, Y. Sasaki, T. Yamada et al., "Fibrosis in non-cancerous tissue is the unique prognostic factor for primary hepatocellular carcinoma without hepatitis B or C viral infection," *World Journal of Surgery*, vol. 30, no. 9, pp. 1729–1735, 2006.

[10] H. Ikeda, "Chapter II-37, test of the difference between two correlation coefficients," in *Statistical Guidebook*, Shin-Yo-Sha, Tokyo, Japan, 1989 (Japanese).

[11] A. Yamada, T. Hara, F. Li et al., "Quantitative evaluation of liver function with use of gadoxetate disodium-enhanced MR imaging," *Radiology*, vol. 260, no. 3, pp. 727–733, 2011.

[12] T. Yoneyama, Y. Fukukura, K. Kamimura et al., "Efficacy of liver parenchymal enhancement and liver volume to standard liver volume ratio on Gd-EOB-DTPA-enhanced MRI for estimation of liver function," *European Radiology*, vol. 24, no. 4, pp. 857–865, 2014.

[13] M. Haimerl, M. Schlabeck, N. Verloh et al., "Volume-assisted estimation of liver function based on Gd-EOB-DTPA-enhanced MR relaxometry," *European Radiology*, 2015.

[14] P. Liu, P. Li, W. He, and L.-Q. Zhao, "Liver and spleen volume variations in patients with hepatic fibrosis," *World Journal of Gastroenterology*, vol. 15, no. 26, pp. 3298–3302, 2009.

Hindawi Publishing Corporation
BioMed Research International
Volume 2015, Article ID 824525, 6 pages
http://dx.doi.org/10.1155/2015/824525

Research Article

The Preoperative CT-Scan Can Help to Predict Postoperative Complications after Pancreatoduodenectomy

Femke F. Schröder,[1,2] Feike de Graaff,[1,2] Donald E. Bouman,[3] Marjolein Brusse-Keizer,[4] Kees H. Slump,[2] and Joost M. Klaase[1]

[1]*Department of Surgery, Medical Spectrum Twente, Haaksbergerstraat 55, 7513 ER Enschede, Netherlands*
[2]*Faculty of Science and Technology, University of Twente, Netherlands*
[3]*Department of Radiology, Medical Spectrum Twente (MST), Enschede, Netherlands*
[4]*Twente Medical School, Medical Spectrum Twente (MST), Enschede, Netherlands*

Correspondence should be addressed to Joost M. Klaase; j.klaase@mst.nl

Received 10 July 2015; Accepted 15 October 2015

Academic Editor: Guang Jia

After pancreatoduodenectomy, complication rates are up to 40%. To predict the risk of developing postoperative pancreatic fistula or severe complications, various factors were evaluated. 110 consecutive patients undergoing pancreatoduodenectomy at our institute between January 2012 and September 2014 with complete CT scan were retrospectively identified. Pre-, per-, and postoperative patients and pathological information were gathered. The CT-scans were analysed for the diameter of the pancreatic duct, attenuation of the pancreas, and the visceral fat area. All data was statistically analysed for predicting POPF and severe complications by univariate and multivariate logistic regression analyses. The POPF rate was 18%. The VFA measured at umbilicus (OR 1.01; 95% CI = 1.00–1.02; $P = 0.011$) was an independent predictor for POPF. The severe complications rate was 33%. Independent predictors were BMI (OR 1.24; 95% CI = 1.10–1.42; $P = 0.001$), ASA class III (OR 17.10; 95% CI = 1.60–182.88; $P = 0.019$), and mean HU (OR 0.98; 95% CI = 0.96–1.00; $P = 0.024$). In conclusion, VFA measured at the umbilicus seems to be the best predictor for POPF. BMI, ASA III, and the mean HU of the pancreatic body are independent predictors for severe complications following PD.

1. Introduction

In Netherlands, each year more than 2000 patients are diagnosed with pancreatic cancer, mostly located in the pancreatic head [1]. The only curative treatment is a pancreatoduodenectomy (PD). Complication rates after pancreatic resections are up to 40%. Currently, BMI (>25 kg/m^2) is considered as an easy to measure patient related factor associated with an increased risk of postoperative morbidity and mortality [2]. Since BMI does not necessarily reflect the distribution of fat, recent studies investigated the predicting probability of visceral fat area (VFA) and this measure seemed to be a more promising parameter to predict surgical outcome after pancreatic resection [2–5].

Another well-known factor associated with postoperative complications is a small pancreatic duct [6, 7]. Roberts et al. [7] developed a predictive score for complications following PD with an accuracy of 75% combining size of the pancreatic duct with BMI. Other investigations have shown that a fatty pancreas, also called pancreatic steatosis, is a risk factor for postoperative complications [3, 6]. Mathur et al. [6] examined the histology of the pancreas and found that a fatty pancreas was related to complications following PD.

The aim of the present study was to develop a predictive score for POPF and severe postoperative complications following PD. Therefore, the impact of different patient, tumour, and CT-derived data was analysed.

2. Methods

Patients undergoing PD or pylorus preserving PD (PPPD) at Medical Spectrum Twente between January 2012 and

September 2014 were retrospectively identified from the hospital's medical database ($n = 134$). Patients from whom preoperative CT imaging was unavailable or incomplete were excluded from the study ($n = 24$). Preoperative data was gathered for each patient including gender, age, BMI, Charlson index, ASA score, and CT-data. Perioperative data included type of operation, duration of surgery, and perioperative blood loss. Postoperative data included localization of the tumour, histology of the tumour, radicality of resection, duration of the hospital stay, intensive care unit (ICU) admission, readmission, and complications up to 30 days after surgery. POPF was scored according to the classification system of the International Study Group of Pancreatic Fistula (ISGPF) [8]. The severity of complications was scored using the Clavien-Dindo classification of surgical complications [9, 10]. In this study, severe complications were defined as a Clavien-Dindo score grade IIIa or higher.

All used CT scans were postcontrast in the portovenous phase, with slice thickness ranging from 1 to 5 mm. The diameter of the pancreatic duct, attenuation of pancreatic tissue calculated as HU of the head, body, and tail of the pancreas, and the VFA were measured with a software program for CT, TeraRecon (Aquarius; TeraRecon, USA). This software enables semiautomatic measurements of a specific region with specified HU. The diameter of the pancreatic duct was measured perpendicular to the duct in the neck of the pancreas, obtained at the level of the confluence of the superior mesenteric and portal veins. The mean HU of the pancreas head, body, and tail was measured by manually drawing a region of interest (ROI) in these regions. The ROI was in the proximity, but did not include the pancreatic duct. The minimum size of the ROI was 1 cm^2, but it preferably included an area as large as possible of homogeneous pancreatic tissue. VFA measurements were performed at three different levels, at the coeliac trunk, umbilicus, and top of the iliac crest.

Statistical Analysis. Data was analysed with IBM SPSS statistics version 22. Continuous data are presented with mean and standard deviation (STD) when normally distributed or median and range (IQR) when not normally distributed. Categorical data are summarized by frequency and percentage within each cohort. The univariate associations between variables and the different groups (no POPF versus POPF and nonsevere versus severe complications) were assessed using student's t-test or Mann-Whitney U tests for continuous variables. Categorical variables were compared by Pearson chi-square and Fischer's exact test. A $P < 0.05$ was considered statistically significant. Variables with a $P < 0.15$ in univariate analysis were entered in a forward stepwise multivariate logistic regression analysis to identify independent predictors for POPF or severe complications, based on the variables that were included in the multivariate model when they increased the fit of the model (based on the −2 log likelihood).

Per- and postoperative variables such as blood loss, length of stay, and readmission were not included in the multivariate logistic regression model, because these factors will not contribute to a preoperative risk prediction.

3. Results

The study cohort consists of 110 patients, 62% male, with a mean age of 66 years (±9.3). In the cohort, 47% of patients had a normal BMI (<25 kg/m^2), 42% were overweight (25–30 kg/m^2) and 11% were obese (>30 kg/m^2). Of the patients, 36% underwent PD and 64% PPPD. The median operation time was 156 min (140–179 min) with an intraoperative blood loss of 500 mL (300–763 mL). The majority of patients had a pancreatic adenocarcinoma (47%) or periampullary carcinoma (35%). Other patients had neuroendocrine tumours (4%), or other (14%). The overall rate of POPF was 18%. Of all pancreatojejunostomy anastomotic leaks, 2 of them were graded POPF A, 9 of them POPF B, and 9 of them POPF C. By definition for POPF C reintervention was required; this group is within the severe complication group. No or nonsevere complications (Clavien-Dindo grades I-II) were seen in 67% of the patients. Severe complications, Clavien-Dindo grade ≥ IIIa, occurred in 33%. The postoperative mortality rate was 6.4%. Patient cohort characteristics are given in Table 1. There were no statistical differences in baseline characteristics between patients with and without POPF. However, for the selection of variables for the multivariate model to predict the occurrence of POPF ($P < 0.15$), BMI showed to be somewhat higher in patients with POPF ($P = 0.13$).

In univariate analysis, patients who experienced severe complications were more likely to have a higher BMI ($P < 0.01$). Patients who encountered severe complications had an increased median length of stay from 12 to 22 days ($P < 0.01$) and an increased risk of mortality from 0 to 19% ($P < 0.01$).

Preoperative CT measured values and resulting POPF and no/nonsevere or severe complications are given in Table 2.

Patients who developed POPF were more likely to have a higher VFA measured at the level of the coeliac trunk, umbilicus, and top of iliac crest (all $P < 0.05$). Patients who developed severe complications were more likely to have a lower mean HU of the pancreas head, body, and tail (all $P < 0.05$). Furthermore, patients with severe complications were more likely to have a higher VFA measured at the level of the coeliac trunk, umbilicus, and top of iliac crest (all $P < 0.05$). Pancreatic duct diameter was not associated with POPF or severe complications ($P = 0.444$ and $P = 0.420$).

BMI (OR 1.24; 95% CI = 1.09–1.42; $P = 0.001$), ASA class III (OR 17.10; 95% CI = 1.60–182.88; $P = 0.019$), and mean HU of the body of the pancreas (OR 0.98; 95% CI = 0.96–1.00; $P = 0.024$) were independent predictors for postoperative severe complications after multivariate analysis. With these variables, a risk score is developed as follows:

$$\frac{e^{(-4.801+0.215[\text{BMI}]+2.839[\text{ASA}]-0.02[\text{HU body}])}}{1+e^{(-4.801+0.215[\text{BMI}]+2.839[\text{ASA}]-0.02[\text{HU body}])}}. \quad (1)$$

The risk score is based on the coefficient of the variables and the constant coefficient of the multivariate model (Table 3). To use this risk score the BMI, ASA score, and the mean HU of the body of the pancreas of the patient are needed. For correct use, ASA I and ASA II are filled in as 0 and ASA III as 1, and then a risk score between 0 and 1 is calculated.

Table 1: Patients cohort characteristics for POPF and nonsevere versus severe complications.

Factor	All	POPF			Postoperative complications		
	($n = 110$) (100%)	No ($n = 90$) (82%)	Yes ($n = 20$) (18%)	P value	No or nonsevere ($n = 74$) (67%)	Severe ($n = 36$) (33%)	P value
Age, years, mean (STD)	66 (9.29)	66 (9.15)	65 (10.1)	0.733	65 (9.3)	68 (9.1)	**0.148**
Gender, *n* (%)				0.853			0.915
Male	68 (61.8)	56 (62.3)	12 (60)		46 (62.2)	22 (61.1)	
Female	42 (38.2)	34 (37.8)	8 (40)		28 (37.8)	14 (38.9)	
BMI (kg/m^2), *n* (%)	25 (3.65)	24.8 (3.65)	26.2 (3.48)	**0.131**	24.4 (3.44)	26.8 (3.49)	**<0.001***
ASA, *n* (%)				0.402			**0.076**
I	5 (4.5)	4 (4.4)	1 (5)		4 (5.4)	1 (2.8)	
II	100 (90.9)	83 (92.2)	17 (85)		69 (93.2)	31 (86.1)	
III	5 (4.5)	3 (3.3)	2 (10)		1 (1.4)	4 (11.1)	
Charlson, *n* (%)				0.876			0.204
0	55 (50)	46 (51.1)	9 (45)		38 (51.4)	17 (47.2)	
1	31 (28.2)	25 (27.8)	6 (30)		23 (31.1)	8 (22.2)	
≥2	24 (21.8)	19 (21.1)	5 (25)		13 (17.6)	11 (30.6)	
Procedure, *n* (%)				0.639			0.169
PD	39 (35.5)	31 (34.4)	8 (40)		23 (31.1)	16 (44.4)	
PPPD	71 (64.5)	59 (65.6)	12 (60)		51 (68.9)	20 (55.6)	
Diagnosis, *n* (%)				0.196			0.972
Pancreatic adenocarcinoma	52 (47.3)	46 (51.1)	6 (30.0)		36 (48.6)	16 (44.4)	
Periampullary carcinoma	39 (35.5)	30 (33.3)	9 (45)		25 (33.8)	14 (38.9)	
Neuroendocrine tumour	4 (3.6)	4 (4.4)	0 (0)		3 (4.1)	1 (2.8)	
Benign diseases or tumour	11 (10.0)	7 (7.8)	4 (20)		7 (9.5)	4 (11.1)	
Other	4 (3.6)	3 (3.3)	1 (5)		3 (4.1)	1 (2.8)	
Radically, *n* (%)				0.24			0.641
R0	33 (30)	31 (34.4)	2 (10)		26 (35.2)	8 (22.2)	
R1	55 (50)	44 (48.9)	11 (55)		35 (47.3)	19 (52.8)	
R2	11 (10)	8 (8.9)	3 (15)		6 (8.1)	5 (13.9)	
n/a	11 (10)	7 (7.8)	4 (20)		7 (9.5)	4 (11.1)	
Surgical duration, min, median (IQR)	156 (140–179)	155 (140–179)	159 (145–174)	0.975	158 (142–179)	153 (138–177)	0.381
Blood loss, mL, median (IQR)	500 (300–763)	500 (300–700)	300 (550–975)	0.369	500 (300–663)	600 (400–975)	0.057
Length of stay, days, median (IQR)	12 (9–18)	11 (8–17)	17 (23–38)	<0.001*	10.5 (8–14)	22 (14.5–34.5)	<0.001*
Readmission, *n* (%)	27 (24.5)	23 (25.6)	4 (20)	0.602	14 (18.9)	13 (36.1)	0.049*
Mortality, *n* (%)	7 (6.4)	5 (5.6)	2 (10)	0.609	0 (0)	7 (19.4)	<0.001*

BMI: body mass index, ASA: American Society of Anesthesiologist, PD: pancreaticoduodenectomy, PPPD: pylorus preserving pancreaticoduodenectomy, STD: standard deviation, and IQR: interquartile range. $^*P < 0.05$ and bold are $P < 0.015$ and are included in the multivariate analysis.

The risk score was validated with a 1000-sample bootstrap analysis (Table 4). These values were comparable to the values of BMI, ASA III, and HU in the multivariate model.

4. Discussion

This study reviewed various factors associated with the occurrence of POPF and severe complications after PD or PPPD. The main findings were that VFA measured at the umbilicus is the best predictor for POPF. BMI, ASA class III, and the mean HU of the pancreas body were independent predictors for postoperative severe complications.

The appearance of POPF is comparable to the rates found in previous studies [2, 5, 7]. However, POPF rates found in the literature range between 3.7% and 39%, which is probably caused by the various interpretations of POPF, despite an international consensus. However, as was stated by Gebauer et al. [11], there are some limitations in applying this fistula classification [8, 12]. Because of the differences in reporting of POPF, it is believed that the well-defined Clavien-Dindo classification is a more valuable tool to score postoperative

Table 2: CT measured values for POPF and nonsevere versus severe complications.

Factor	All	POPF			Postoperative complications		
	($n = 110$) (100%)	No ($n = 90$) (82%)	Yes ($n = 20$) (18%)	P value	No or nonsevere ($n = 74$) (67%)	Severe ($n = 36$) (33%)	P value
HU pancreas, HU, and median (IQR)							
Head	82 (69.4–98.6)	84.3 (70.2–98.4)	77.5 (63.4–98.9)	0.443	86.1 (73.5–99.7)	74.6 (58.1–93.5)	**0.017***
Body	79.4 (61.1–92.9)	79.4 (61.6–92.9)	76.8 (55.6–94.1)	0.541	80.5 (67.3–97.2)	74.5 (55–85)	**0.014***
Tail	80.4 (64.3–97.4)	79 (63.6–98.6)	81 (71.4–94)	0.947	83.2 (66.2–99.4)	74.1 (60–91.3)	**0.089**
Pancreatic duct, mm, median (IQR)	3.25 (0–5.06)	3.4 (0–5.1)	2.1 (0–4.8)	0.316	3.55 (0–5.1)	2.75 (0–4.79)	0.289
VFA, cm^2, median (IQR)							
Truncus coeliacus	95.5 (59–142.5)	88 (50–135.8)	105.5 (85.6–178)	**0.036***	84 (48.3–129.8)	112 (75.5–155.3)	**0.012***
Umbilicus	130.5 (92.7–166)	119.5 (90–152.5)	157 (121.5–210.8)	**0.008***	118.5 (87.5–155)	147.5 (108.3–197.8)	**0.016***
Top of iliac crest	139 (96–204.3)	127.5 (93.8–184)	188.5 (118.8–242.8)	**0.013***	121 (89.8–182.3)	157 (116.3–232)	**0.006***

HU: Hounsfield units, IQR: interquartile range, and VFA: visceral fat area. *$P < 0.05$ and bold are $P < 0.015$ and are included in the multivariate analysis.

Table 3: Multivariate analysis to predict severe complications.

Logistic regression for complications	Univariate			Multivariate			
	OR	95% CI	P value	OR	95% CI	P value	Coefficient
Age	1.034	(0.988–1.082)	0.149				
BMI	1.227	(1.084–1.390)	0.001	1.240	(1.086–1.415)	0.001	0.215
ASA I/II	ref (1.0)	—	—	—	—	—	
ASA III	9.000	(0.957–83.742)	0.054	17.095	(1.598–182.884)	0.019	2.839
Age	1.034	(0.988–1.082)	0.149				
HU pancreas							
Head	0.983	(0.967–0.999)	0.033	—	—	—	
Body	0.981	(0.966–0.997)	0.024	0.980	(0.962–0.997)	0.024	−0.020
Tail	0.985	(0.969–1.001)	0.062	—	—	—	
VFA							
Truncus coeliacus	1.007	(1.001–1.014)	0.030	—	—	—	
Umbilicus	1.009	(1.002–1.016)	0.016	—	—	—	
Top of iliac crest	1.007	(1.002–1.013)	0.011	—	—	—	
Constant						0.010	−4.801

BMI: body mass index, ASA: American Society of Anesthesiologist, VFA: visceral fat area, HU: Hounsfield units, OR: odds ratio, and CI: confidence interval.

Table 4: Bootstrap analysis to validate the risk score.

Bootstrap (1000 samples)	OR	95% CI	P value	Coefficient
BMI	1.240	(1.119–1.461)	0.001	0.215
ASA III	17.099	(1.629–162.00)	0.009	2.839
HU pancreas (body)	0.980	(0.954–0.998)	0.045	−0.020
Constant			0.004	−4.801

BMI: body mass index, ASA: American Society of Anesthesiologist, HU: Hounsfield units, OR: odds ratio, and CI: confidence interval.

complications as this classification tool is less subject to interpretation than the scoring of POPF.

The postoperative severe complication rate of 33% in this study was higher than the rates of 16.7–27.1% reported in literature [5, 13–15]. Multiple factors were significant after univariate analysis for nonsevere versus severe complications (Tables 1 and 2). After multivariate analysis (Table 3), BMI, ASA class III, and mean HU of the body of the pancreas remained predictors for developing severe complications after PD or PPPD. A risk score based on these three factors was made (1) and validated with a bootstrap analysis (Table 4). The advantage of these three factors as predictors is that these factors are preoperatively known or easy to measure. Currently, BMI and ASA are defined by the anaesthesiologist before surgery. Preoperative CT-scans are almost always available as part of preoperative staging. The HU of the pancreatic body can be easily measured by the surgeon or radiologist. Knowledge of a presumed high risk for POPF and/or severe complications could lead to change in intraoperative steps as performing pancreatogastric instead

of pancreatojejunal anastomosis or using an isolated roux limb for the pancreatic anastomosis [16, 17]. Another possibility is a prehabilitation program to increase the anaerobic threshold, which might reduce the chance of complications [18, 19].

The BMI of the patients who developed severe complications was significantly higher. After multivariate analysis, BMI remained a valuable predictor for postoperative severe complications. This is in accordance with the expectations and literature [2, 5, 7, 20, 21]. In this study population, there were only 5 patients with an ASA class III classification, of whom 4 developed severe complications. However, to be able to say more about the quality of ASA class III as a predictor, more patients in the ASA class III category are needed. In other studies, investigating risk factors for the development of severe complications following PD or PPPD, ASA score is not frequently mentioned [2–5, 7]. Braga et al. [14] measured ASA score and analysed it for severe complications following PD. After multivariate analysis, ASA class III was found to be a significant predictor for developing postoperative severe complications.

This study showed that the mean HU of the body of the pancreas of patients who developed severe complications was significantly lower, compared to patients who did not. In a comparable study of McAuliffe et al. [5], nonenhanced CT-scans were measured and analysed to predict complications with Clavien-Dindo classes I–V. The mean HU of the pancreas for patients with complications scored Clavien-Dindo classes I–V was decreased but not significant ($P = 0.130$). This is probably due to the different classification of complications, McAuliffe et al. studied overall complications instead of severe complications. In the study of Roberts et al. [22], nonenhanced CT-scans were measured, the mean HU of the pancreas was found to be a significant predictor for POPF. As was the case in our present study, contrast enhanced images were used in the study of Hashimoto et al. [21]. They found the mean HU of the pancreas as a significant predictor for pancreatic anastomotic failure.

Next to the differences observed in the associations between complications and HU in the studies mentioned above, also the cause of lower HU can have various reasons. It is still unclear if fatty infiltration or steatosis, measured as a lower mean HU, is the cause of this phenomenon: washin and washout of contrast agent, namely, vary depending on the pathology of tissue and according to local blood flow mechanics [5]. Thus, the decreased HU could be attributed not only to steatosis or fatty infiltration of the pancreas but also to other reasons, such as a poorer blood flow and low cardiac output. Future studies should focus on noncontrast and postcontrast venous phase CT-scans and compare the measured HU of the pancreas.

Postoperatively, 18% of the patients developed POPF. After univariate and multivariate analyses, only the VFA remained as a significant predictor. In various studies, VFA was found to be a predictor for POPF [2–4, 20, 23]. However, in the majority of these studies, other factors were identified as predictors as well. Regularly, BMI and the pancreatic duct diameter were found to be predictors for POPF [7, 21, 22, 24]. A study by Roberts et al. [7] showed that a pancreatic duct diameter smaller than 3 mm increases the risk of POPF. In the present study population, the mean pancreatic duct diameter of the patient with POPF was smaller than the diameter of patients without POPF, although not significant. The literature is divided, since some studies indeed confirm a small pancreatic duct to be a significant predictor for POPF [6, 7, 24]. While others do not find a relation with POPF, even when the duct diameter is measured durante operationem [2, 4].

Despite the interesting and useful findings of our study, the present study also has several limitations. Firstly, the study included a variation of imaging protocols since patients were admitted from other different regional hospitals. The scans were obtained with different CT-scanners and the scan protocols varied depending on the patients referring hospital. Ideally, the measurement protocol uses a fixed scan delay with a specific contrast injection rate. Secondly, the effect of small timing differences between performance of scan and arrival of contrast in the structures was not taken into account. Thirdly, the used CT-scans had slice thickness ranging from 1 to 5 mm. For fat, muscle or HU measurement 5 mm slices were detailed enough. However, exact measurement of such small structures as the pancreatic duct may be diminished due to partial volume effects. Fourthly, from some patients, CT-scans were unavailable or incomplete; these patients were excluded. This could lead to a selection bias.

In conclusion, this study analysed preoperative CT images of patients who underwent PD or PPPD and investigated predictors for POPF and postoperative severe complications. VFA was found to be a significant predictor for POPF. The most significant factors to predict severe complications appear to be BMI, ASA, and the mean HU of the body of the pancreas. Based on these three variables, a risk score for postoperative severe complications after PD or PPPD was developed. To validate these results, a prospective study is required.

Conflict of Interests

The authors declare that there is no conflict of interests regarding the publication of this paper.

References

[1] EUCAN: Most frequent cancers in the Netherlands, 2012, http://eco.iarc.fr/EUCAN/Country.aspx?ISOCountryCd=528.

[2] M. G. House, Y. Fong, D. J. Arnaoutakis et al., "Preoperative predictors for complications after pancreaticoduodenectomy: impact of BMI and body fat distribution," *Journal of Gastrointestinal Surgery*, vol. 12, no. 2, pp. 270–278, 2008.

[3] H. Tranchart, S. Gaujoux, V. Rebours et al., "Preoperative CT scan helps to predict the occurrence of severe pancreatic fistula after pancreaticoduodenectomy," *Annals of Surgery*, vol. 256, no. 1, pp. 139–145, 2012.

[4] C. M. Park, J. S. Park, E. S. Cho, J. K. Kim, J. S. Yu, and D. S. Yoon, "The effect of visceral fat mass on pancreatic fistula after pancreaticoduodenectomy," *Journal of Investigative Surgery*, vol. 25, no. 3, pp. 169–173, 2012.

[5] J. C. McAuliffe, K. Parks, P. Kumar, S. F. McNeal, D. E. Morgan, and J. D. Christein, "Computed tomography attenuation and patient characteristics as predictors of complications after pancreaticoduodenectomy," *HPB*, vol. 15, no. 9, pp. 709–715, 2013.

[6] A. Mathur, H. A. Pitt, M. Marine et al., "Fatty pancreas: a factor in postoperative pancreatic fistula," *Annals of Surgery*, vol. 246, no. 6, pp. 1058–1064, 2007.

[7] K. J. Roberts, J. Hodson, H. Mehrzad et al., "A preoperative predictive score of pancreatic fistula following pancreatoduodenectomy," *HPB*, vol. 16, no. 7, pp. 620–628, 2014.

[8] W. J. Tan, A. W. Kow, and K. H. Liau, "Moving towards the New International Study Group for Pancreatic Surgery (ISGPS) definitions in pancreaticoduodenectomy: a comparison between the old and new," *HPB*, vol. 13, no. 8, pp. 566–572, 2011.

[9] P. A. Clavien, J. Barkun, M. L. de Oliveira et al., "The Clavien-Dindo classification of surgical complications: five-year experience," *Annals of Surgery*, vol. 250, no. 2, pp. 187–196, 2009.

[10] D. Dindo, N. Demartines, and P.-A. Clavien, "Classification of surgical complications: a new proposal with evaluation in a cohort of 6336 patients and results of a survey," *Annals of Surgery*, vol. 240, no. 2, pp. 205–213, 2004.

[11] F. Gebauer, K. Kloth, M. Tachezy et al., "Options and limitations in applying the fistula classification by the international study group for pancreatic fistula," *Annals of Surgery*, vol. 256, no. 1, pp. 130–138, 2012.

[12] M. W. Büchler, M. Wagner, B. M. Schmied, W. Uhl, H. Friess, and K. Z'graggen, "Changes in morbidity after pancreatic resection: toward the end of completion pancreatectomy," *Archives of Surgery*, vol. 138, no. 12, pp. 1310–1314, 2003.

[13] D. Y. Greenblatt, K. J. Kelly, V. Rajamanickam et al., "Preoperative factors predict perioperative morbidity and mortality after pancreaticoduodenectomy," *Annals of Surgical Oncology*, vol. 18, no. 8, pp. 2126–2135, 2011.

[14] M. Braga, G. Capretti, N. Pecorelli et al., "A prognostic score to predict major complications after pancreaticoduodenectomy," *Annals of Surgery*, vol. 254, no. 5, pp. 702–708, 2011.

[15] M. L. DeOliveira, J. M. Winter, M. Schafer et al., "Assessment of complications after pancreatic surgery: a novel grading system applied to 633 patients undergoing pancreaticoduodenectomy," *Annals of Surgery*, vol. 244, no. 6, pp. 931–939, 2006.

[16] A. McKay, S. Mackenzie, F. R. Sutherland et al., "Meta-analysis of pancreaticojejunostomy *versus* pancreaticogastrostomy reconstruction after pancreaticoduodenectomy," *British Journal of Surgery*, vol. 93, no. 8, pp. 929–936, 2006.

[17] C. D. Sutton, G. Garcea, S. A. White et al., "Isolated roux-loop pancreaticojejunostomy: a series of 61 patients with zero postoperative pancreaticoenteric leaks," *Journal of Gastrointestinal Surgery*, vol. 8, no. 6, pp. 701–705, 2004.

[18] C. P. Snowden and G. Minto, "Exercise: the new premed," *British Journal of Anaesthesia*, vol. 114, no. 2, pp. 186–189, 2014.

[19] A. F. O'Doherty, M. West, S. Jack, and M. P. W. Grocott, "Preoperative aerobic exercise training in elective intra-cavity surgery: a systematic review," *British Journal of Anaesthesia*, vol. 110, no. 5, pp. 679–689, 2013.

[20] S. Gaujoux, J. Torres, S. Olson et al., "Impact of obesity and body fat distribution on survival after pancreaticoduodenectomy for pancreatic adenocarcinoma," *Annals of Surgical Oncology*, vol. 19, no. 9, pp. 2908–2916, 2012.

[21] Y. Hashimoto, G. M. Sclabas, N. Takahashi et al., "Dual-phase computed tomography for assessment of pancreatic fibrosis and anastomotic failure risk following pancreatoduodenectomy," *Journal of Gastrointestinal Surgery*, vol. 15, no. 12, pp. 2193–2204, 2011.

[22] K. J. Roberts, R. Storey, J. Hodson, A. M. Smith, and G. Morris-Stiff, "Pre-operative prediction of pancreatic fistula: is it possible?" *Pancreatology*, vol. 13, no. 4, pp. 423–428, 2013.

[23] D. P. O'Leary, D. O'Neill, P. McLaughlin et al., "Effects of abdominal fat distribution parameters on severity of acute pancreatitis," *World Journal of Surgery*, vol. 36, no. 7, pp. 1679–1685, 2012.

[24] F. Muscari, B. Suc, S. Kirzin et al., "Risk factors for mortality and intra-abdominal complications after pancreatoduodenectomy: multivariate analysis in 300 patients," *Surgery*, vol. 139, no. 5, pp. 591–598, 2006.

Hindawi Publishing Corporation
BioMed Research International
Volume 2015, Article ID 764383, 9 pages
http://dx.doi.org/10.1155/2015/764383

Research Article

Self-Trained Supervised Segmentation of Subcortical Brain Structures Using Multispectral Magnetic Resonance Images

Michele Larobina,[1] Loredana Murino,[2] Amedeo Cervo,[3] and Bruno Alfano[1]

[1]*Istituto di Biostrutture e Bioimmagini, CNR, Via Tommaso De Amicis 95, 80145 Napoli, Italy*
[2]*Istituto per le Applicazioni del Calcolo "Mauro Picone", CNR, Via Pietro Castellino 111, 80131 Napoli, Italy*
[3]*Dipartimento di Scienze Biomediche Avanzate, Università "Federico II", Via Sergio Pansini 5, 80131 Napoli, Italy*

Correspondence should be addressed to Michele Larobina; michele.larobina@cnr.it

Received 15 June 2015; Accepted 4 August 2015

Academic Editor: Guang Jia

The aim of this paper is investigate the feasibility of automatically training supervised methods, such as *k*-nearest neighbor (*k*NN) and principal component discriminant analysis (PCDA), and to segment the four subcortical brain structures: caudate, thalamus, pallidum, and putamen. The adoption of supervised classification methods so far has been limited by the need to define a representative training dataset, operation that usually requires the intervention of an operator. In this work the selection of the training data was performed on the subject to be segmented in a fully automated manner by registering probabilistic atlases. Evaluation of automatically trained kNN and PCDA classifiers that combine voxel intensities and spatial coordinates was performed on 20 real datasets selected from two publicly available sources of multispectral magnetic resonance studies. The results demonstrate that atlas-guided training is an effective way to automatically define a representative and reliable training dataset, thus giving supervised methods the chance to successfully segment magnetic resonance brain images without the need for user interaction.

1. Introduction

Brain tissue classification is an important topic in magnetic resonance (MR) brain image analysis. In the last years, the major tissues such as gray matter (GM), white matter (WM), and cerebrospinal fluid (CSF) have been largely studied with particular attention on volumetric variations due to the aging process or the evolution of degenerative diseases. In the recent years, a growing interest in the classification of minor brain structures has emerged [1–5]. The segmentation of the minor brain structures presents a higher degree of difficulty due to a variable and often lower contrast between these structures and adjacent tissues, which limits intensity-based classification even in the presence of multispectral data [6–8].

Supervised classification methods have shown very good results for the segmentation of MR brain images; they require the construction of a training dataset to learn how to classify new data. This represents a time consuming and expensive task, which can be achieved only by expert operators who should manually label a certain number of MR studies. Moreover, in this way, the methods tend to perform well only for studies acquired using the same acquisition protocol of the training dataset. Nowadays, the huge amount of MR brain data generated in large-scale clinical studies has prompted the development of automatic classification which should avoid or minimize the human intervention. The aim of the present work is to develop and test a completely automatic procedure to build training datasets for the classification of MR brain images using supervised methods. The method is based on the use of probabilistic atlases to guide the selection of a training dataset within the same MR study to be classified.

The idea to automatically train a supervised classification scheme using an atlas was first presented by Cocosco et al. and later by Vrooman et al. [9–11]. These authors focused primarily on segmenting brain MR images into WM, GM, CSF, and white matter lesions. They used a *k*-nearest neighbor

(*k*NN) working only with MR intensity information for segmentation and lesion detection. A combination of spatial and local features using a *k*NN classifier for the segmentation of the caudate was presented by Arzhaeva et al. with a manually defined training set [12]. Various different approaches have been followed so far to segment subcortical regions but, to the best of our knowledge, the potential classification ability of *k*NN and discriminant analysis methods were not fully explored. Recently the MICCAI 2012 Gran Challenge Workshop focused on the multiatlas labeling segmentation approach, presenting the results obtained by numerous research groups using a common dataset of 35 T1 MR images from the publicly available OASIS database [13]. This dataset that contains 14 manually segmented subcortical structures to be used as reference does not include multispectral data [14]. Among the most widely used and freely available software we find two automatic methods: FreeSurfer (Martinos Center for Biomedical Imaging, Charlestown, Massachusetts, USA) [15] and FSL-First (Centre for Functional Magnetic Resonance Imaging of the Brain, Oxford, UK) [16, 17]. Both of these software packages that need only T1w images to achieve the segmentation are often used for comparison in the evaluation of new developed methods.

In this paper we present results from *k*NN and principal component discriminant analysis (PCDA) segmentation methods. The methods utilize an atlas-guided automatic training selection and work with a combination of voxel spatial locations and intensities using multispectral data. By using nonlinear spatial registration of the tissue probability atlases to the subject, the training set is tailored to the target study. The spatial a priori information of the atlas guides the choice of a representative number of voxels that serve as intensity and spatial location sample information for each of the four structures to be segmented: caudate, thalamus, pallidum, and putamen.

We present and discuss experiments conducted on 20 real studies selected from two publicly available sources of multispectral magnetic resonance studies. Fourteen studies from the IXI database of the Imperial College in London consist of T1-, T2-, and PD-weighted images. The remaining six studies (3 subjects scanned twice) were taken from the Kirby21 database of the Kirby Research Center in Baltimore, from which we selected T1- and T2-weighted and fluid attenuation inversion recovery (FLAIR) images. The scan-rescan data of three subjects served two purposes: first, to test the reproducibility of segmentation methods in providing volume estimates in subjects who were scanned twice within the same day and, second, to demonstrate that the automatically trained segmentation methods considered can work well with other acquisition sequences and can hence be thought as sequence independent. Differences in the behavior of the methods with respect to training are described. The relative performance of the autotrained *k*NN and PCDA methods is shown and discussed. The accuracy of both methods was assessed on the fourteen IXI datasets based on visual analysis of the segmentation results by an expert observer. These results are also compared with those obtained with the FSL-First software in terms of volume differences and percent of volume overlap.

2. Materials and Methods

Two supervised segmentation methods were considered in this work.

(i) k-Nearest Neighbor (kNN). The implemented *k*NN classifier was carried out using the *knnclassify* function of the Matlab package (The Mathworks, Inc.). The algorithm combines intensity and spatial features as described in the work of Anbeek et al. [18]. Briefly, for each brain voxel to be classified the three spatial coordinates and the multispectral intensity information (the number of components depends on how many different contrast-weight MR images have been considered as input) have been considered. Based on these features, each voxel was assigned to the brain tissue class that, according to a distance measure, receives the largest vote amongst the k-nearest neighbor belonging to the training [19]. For all the experiments we considered the Euclidean distance and a value of $k = 40$. The value of k has been set on the base of the observations reported by other research groups for the brain tissue segmentation task [11, 20] and our numerical experiments.

(ii) Principal Component Discriminant Analysis (PCDA). The segmentation algorithm, belonging to the family of discriminant analysis methods [21], was implemented using an in-house software written in Matlab (see Appendix B for a description of the function). Starting from the training, the method performs a nonparametric estimate of tissue's probability density functions. The original components were transformed into principal components prior to estimating the probability densities. Each brain voxel was then assigned to one of the brain tissues applying the Bayes decision rule. Intensity values (the number of components depends on how many different contrast-weight MR images have been considered as input) and spatial coordinates of the voxels have been considered by the classifier as discriminant features.

For both segmentation methods, all feature values were shifted and rescaled to have zero mean and unit variance.

2.1. MRI Data. We used two different datasets of images for method set-up and evaluation, for a total of 20 MRI studies.

(1) Image Dataset I. Fourteen subjects with no evidence of pathology, age range: 25–82 (6 M, 8 F), were selected from the publicly available IXI database (see Appendix A). Seven subjects were acquired at 1.5T and seven at 3T, in two different hospitals. The data from each subject consists of T1w, T2w, and PDw images. The scanning parameters for the 1.5T studies were T1w (TR/TE = 9.8/4.6 ms, flip angle 8°, voxel size 0.94 × 0.94 × 1.20 mm) and PD-T2w (TR/TE = 8178/8.0 − 100.0 ms, voxel size 0.94 × 0.94 × 1.25 mm); the scanning parameters for the 3T studies were T1w (TR/TE = 9.6/4.6 ms, flip angle 8°, voxel size 0.94 × 0.94 × 1.25 mm) and PD-T2w (TR/TE = 5725/8.0 − 100.0 ms, voxel size 0.94 × 0.94 × 1.25 mm).

(2) Image Dataset II. Three subjects with no history of neurological disease, age range: 25–30 (2 M, 1 F), were selected from

Figure 1: An axial, coronal, and sagittal slice of the subcortical structures probabilistic atlas: caudate (yellow), thalamus (cyan), pallidum (red), and putamen (green).

the publicly available Kirby21 database (see Appendix A). Each subject was scanned twice with a protocol from which we selected T1w, T2w, and FLAIR as input for the classifiers; thus, this dataset consists of six MR studies. Images were acquired on a 3T scanner and the scan parameters were T1w MPRAGE (TR/TE/TI = 6.8/3.1/842 ms, flip angle 8°, voxel size 1.0 × 1.0 × 1.2 mm, sense acceleration factor = 2), T2w 3D TSE (TR/TE = 2500/287 ms, voxel size 0.9375 × 0.9375 × 1.0 mm), and FLAIR (TR/TE/TI = 8000/331/2400 ms, voxel size 0.417 × 0.417 × 0.55 mm, sense acceleration factor = 2).

2.2. Preprocessing. Before starting the training and subsequent classification step, the MR images of each subject were coregistered and/or resliced when necessary. With *Image dataset I*, where the T1w images were acquired in the sagittal plane and T2w and PDw in the axial plane, T1 images were resliced to the axial orientation. With *Image dataset II*, FLAIR and T2w images were coregistered and resliced to the image space of the MPRAGE images. All datasets were corrected for MR field inhomogeneity using SPM12 (http://www.fil.ion.ucl.ac.uk/spm) bias correction function with very light regularization. Then, all the tissue probabilistic atlases were reported into the Montreal Neurological Institute (MNI) space. The matrix of the nonlinear transformation that maps the MR study onto the MNI space was estimated by means of the SPM12 segment function and used to map tissue probabilistic atlases to the subject with the SPM12 inverse deformations utility.

Training was then performed for each tissue class (and for each MR contrast) as described in Training Data. These training datasets were used by the algorithms for the segmentation of the subjects intracranial brain volume after the nonbrain structures were removed using the Brain Extraction Tool FSL-BET [22].

2.3. Training Data. To automatically select training data from each subject, the segmentation framework presented requires a probability map for each intracranial tissue or structure to be segmented. A unique probabilistic atlas including all four subcortical tissues was constructed grouping information from the following atlases available in the literature: the International Consortium for Brain Mapping (ICBM) deep nuclei probabilistic atlas for the putamen, thalamus, and caudate [23]; and the Colin27 high-resolution single subject template to map the pallidum [24]. Figure 1 shows an axial, coronal, and sagittal slice of the obtained subcortical tissues probabilistic atlas. To discriminate subcortical structures from the underlying WM, GM, and CSF, a training is required to construct the density functions of these three major brain tissues. For this task we take into account both the ICBM452 probabilistic tissue atlas and the result of a reference segmentation method like SPM.

After the coregistration of all the probability maps to the subject (see Section 2.2), the atlas was constructed superimposing on the probability map of GM, WM, and CSF the subcortical tissue atlases in the following order: pallidum, putamen, thalamus, and caudate. Due to the heterogeneous nature of the database some overlaps of the maps can occur. In these cases a voxel is assigned to the last superimposed layer. All the atlases were initially rescaled in the range $[0, 1]$.

The training was then defined on the target study to be segmented in the following way. First, tissue probability maps were coregistered to the T1w of the subject and thresholded before automatically selecting the training samples for each tissue class. Four different threshold values have been evaluated in the range of 0.6 to 0.9. A threshold of 0.8 has been recognized as optimal value; lower threshold values lead to greater inaccuracy (noisy classification) while a threshold value of 0.9 may reduce too much the number of points for some of the tissues. Second, the voxels selected for training samples for each tissue class were chosen randomly. Figure 2 shows the trainings points overlapped to an axial slice for one of the studies of the *Image dataset I*. Spatial coordinates of the training samples and the corresponding multispectral intensities were used by the *k*NN and PCDA classifiers for the learning step.

2.4. Processing and Analysis. Several experiments were conducted to optimize parameters and training selection and then to assess the accuracy and the robustness of the two automatically trained classifiers.

The first experiment conducted on the *Image dataset I* allowed us to (i) establish the optimal threshold for the tissue probabilistic atlases, (ii) find the optimal number of training

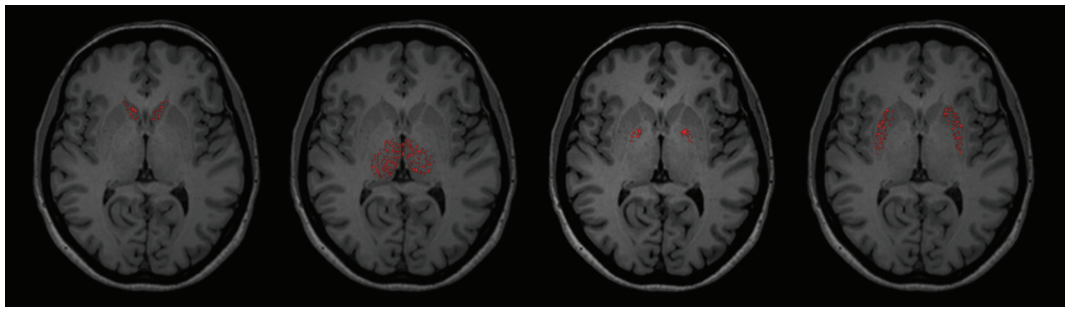

Figure 2: The randomly generated trainings points (in red) overlapped to a T1w axial slice for one of the studies of the *Image dataset I* (IXI002-Guys-0828). Spatial coordinates and the corresponding multispectral intensities of these points were used by the classifiers for the learning phase.

samples to be used by the classifiers and to assess the behavior of the two methods considered with respect to the training, and (iii) realize that for the three main tissues the use of a reference segmentation as tissue probability map in place of a smoothed atlas such as the ICBM452 gives more stability and accuracy for segmentation of minor structures. After this first experiment, we focused our attention on the segmentation of subcortical structures using the segmentation of the three main brain tissues achieved with the SPM software as preprocessing. Our choice of the SPM software was because this software package was used to coregister tissue probability maps to the subject in our processing pipeline. As the SPM segmentation output is probabilistic, the same threshold value of 0.8 was applied for the training definition of GM, WM, and CSF.

The second experiment, always conducted on the *Image dataset I*, was aimed at evaluating the accuracy of the segmentation of the four subcortical structures. As a reference standard was not available for these studies, a semiquantitative evaluation of segmentation results based on visual analysis by an expert observer (Amedeo Cervo) was performed. For each MR study the visual inspection was performed slice by slice using the OsiriX software (http://www.osirix-viewer.com/), keeping the segmented structure on one series and the MR images, mainly the T1w, on another series and using the image fusion utility to view, with a user selectable fusion percentage, the segmented result overlapped to the MR signal. A score on a 5-point rating scale (very poor, poor, fair, good, and very good) was assigned for each structure and for each of the two methods, *k*NN and PCDA. From the table containing these annotations we calculated the median value and the first and third quartile for each of the four subcortical structures and for each of the two methods.

The third experiment was a reproducibility test conducted on the *Image dataset II* representing MR images from three subjects that underwent the MR scan twice in the same day. The reproducibility was evaluated by computing, for each tissue, the volume difference between the two repeated imaging sessions for both *k*NN and PCDA classifiers. The availability of FLAIR images (that condense the T2/PD information) allowed us to also investigate the response of the classifiers when only two MR contrasts instead of three (i.e., T1w and FLAIR) were considered as input.

3. Results

The fourteen studies of *Image dataset I* (with images weighted in T1, T2, and PD) were used for training optimization, evaluation of segmentation accuracy, and comparison with an existing method (FSL-First). The six studies of *Image dataset II* (with T1w, T2w, and FLAIR images) were used for the reproducibility test.

3.1. Training Optimization. The *k*NN and PCDA methods exhibit different behaviors with respect to the training. PCDA is less sensitive to the number of training samples for each class. A number of voxels corresponding to roughly the 10% of the volume of each tissue allow the PCDA to work well. No significant variations were observed by increasing the number of training samples. For the *k*NN method, a number of training points equal to the 10% of the volume were not an optimal choice, regardless of the tissue. We experimentally verified that an increase of the number of samples for the small structures leads to a significant improvement. For the caudate, thalamus, pallidum, and putamen, we selected a number of voxels corresponding to roughly the 20% of the volume as optimal parameter. This corresponded to a training size ranging from 500 to 2,000 voxels (corresponding to a volume from 0.5 cc to 2.0 cc at a resolution of $1 \times 1 \times 1\,\text{mm}^3$). Moreover, for the *k*NN an unbalanced sample size for the major tissue training has a negative impact on the estimation of some minor structures, since the GM is the tissue with the greater volume and a number of training points proportional to the volume lead to an overestimation of the GM. Experiments revealed that *k*NN works better when GM, WM, and CSF have the balanced number of training samples that was set to 50,000 voxels (corresponding to a volume of 50 cc at a resolution of $1 \times 1 \times 1\,\text{mm}^3$).

3.2. Segmentation Accuracy. A visual analysis of the segmentation results for the four subcortical structures was performed for both *k*NN and PCDA methods. Figure 3 shows the segmented images at the level of basal ganglia for one of the studies of the *Image dataset I*. Classification results are listed in Table 1 which shows the differences in the performance of the two considered methods. For the caudate, thalamus, pallidum, and putamen, the *k*NN exhibits scores

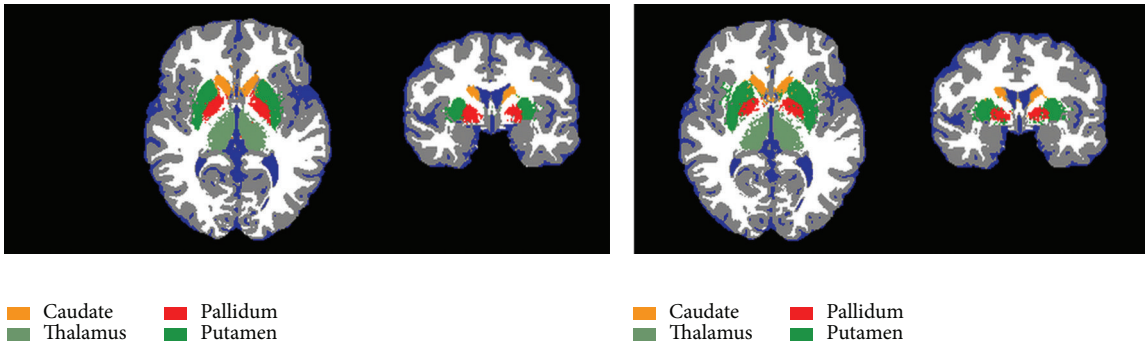

Figure 3: Segmentation results of the automatically trained *k*NN (axial and coronal sections on the left) and PCDA (axial and coronal sections on the right) classifier for one of the studies of the *Image dataset I* (IXI002-Guys-0828).

Table 1: Evaluation of segmentation algorithms in the 14 MR studies of the *Image dataset I* performed by visual assessment. 1 = very poor, 2 = poor, 3 = fair, 4 = good, 5 = very good; Q1: 1st quartile and Q3: 3rd quartile.

	*k*NN			PCDA		
	Median	Q1	Q3	Median	Q1	Q3
Caudate	4	4.0	4.25	3	2.0	3.0
Thalamus	4	3.0	4.0	3	2.0	3.0
Pallidum	4	3.0	4.0	3	3.0	3.5
Putamen	4	4.0	4.0	3	3.0	3.0

from 3 to 5 on the 5-point rating scale with a median value of 4. The PCDA performs worse than *k*NN, with a grade range from 2 to 4 and a median value of 3.

3.3. Reproducibility Test. Reproducibility was evaluated by computing the volume differences between scan-rescan imaging sessions. Results are reported in Table 2 for the *k*NN and Table 3 for the PCDA. In the case of the *k*NN algorithm, caudate, thalamus, and putamen were classified with a volume variation less than 5%, for the classifier working with T1 and FLAIR as input, and less than 3.5% when the classifier works with T1, T2, and FLAIR as input. Pallidum shows variability up to 11% in both cases. PCDA exhibits greater instability and less reproducibility in the measurements.

3.4. Comparison with an Existing Method. Segmentation results provided by the best performing algorithm (*k*NN) were compared with those obtained with the FSL-First software. Mean volume and the percent of volume overlap have been calculated for caudate, thalamus, pallidum, and putamen, in the 14 MR studies of the *Image dataset I*. Results are summarized in Table 4 and Figure 4. The mean overlap indices were 0.87 for thalamus (range: 0.81–0.90), 0.83 for caudate (range: 0.73–0.88), 0.81 for putamen (range: 0.74–0.86), and 0.76 for pallidum (range: 0.70–0.86).

3.5. Execution Times. Both methods considered in this study are computationally efficient. The execution time for the segmentation of a subject is below 8 minutes on a desktop PC with an Intel Core i7 processor, 16 GB RAM, and operating Windows 7.

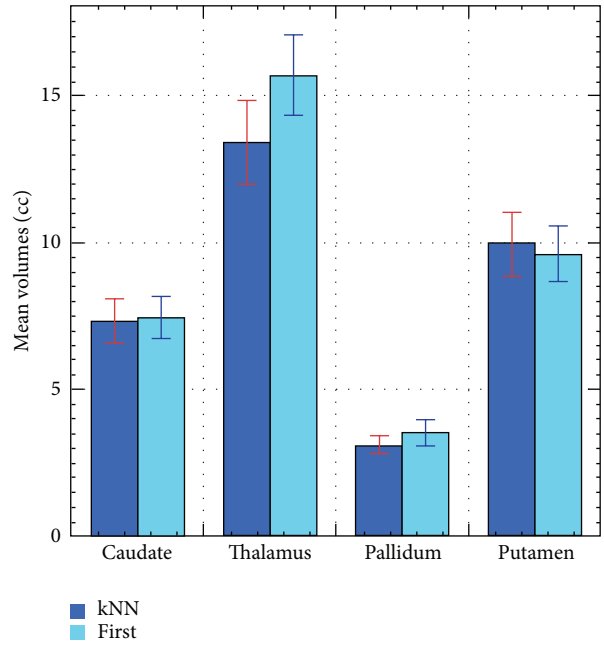

Figure 4: Bar graph showing the mean volume estimates of the automatically trained *k*NN *versus* the FSL-First software for caudate, thalamus, pallidum, and putamen, in the 14 MR studies of the *Image dataset I*. Numerical data are reported in Table 4.

4. Discussion

The objective of this paper is twofold: (1) to study the feasibility of automatically defining a representative training by registering an atlas to the target study and (2) to assess the performance of two atlas-guided trained supervised methods on real MRI data. Training selection is based on thresholded tissue probability atlases coregistered to the subject to define, in intensity and spatial locations, the training dataset of each subcortical structure. The subsequent segmentation by applying supervised methods such as *k*NN and PCDA is in principle feasible for each tissue or structure for which

Table 2: Results of the reproducibility test for the automatically trained *k*NN algorithm. Volume estimates of the scan and rescan sessions in the case of an input with three and two contrast image types.

		Subject 1			Subject 2			Subject 3		
		Scan (cc)	Rescan (cc)	Δ (%)	Scan (cc)	Rescan (cc)	Δ (%)	Scan (cc)	Rescan (cc)	Δ (%)
*k*NN (T1w, T2w, and FLAIR)	Caudate	8.28	8.18	1.2	6.92	7.02	1.4	7.11	7.08	0.4
	Thalamus	13.58	14.02	3.2	12.87	12.82	0.4	13.98	14.31	2.3
	Pallidum	2.61	2.33	11.3	2.42	2.26	6.8	3.04	2.99	1.7
	Putamen	10.31	10.60	2.8	11.54	11.42	1.0	13.06	12.84	1.7
*k*NN (T1w, FLAIR)	Caudate	9.17	8.92	2.8	7.78	7.97	2.4	8.18	8.17	0.1
	Thalamus	13.49	13.62	1.0	13.04	13.10	0.5	14.42	14.76	2.3
	Pallidum	2.41	2.17	10.5	2.50	2.41	3.7	2.83	2.76	2.5
	Putamen	9.92	10.39	4.6	11.16	11.24	0.7	12.55	12.40	1.2

Table 3: Results of the reproducibility test for the automatically trained PCDA algorithm. Volume estimates of the scan and rescan sessions in the case of an input with three and two contrast image types.

		Subject 1			Subject 2			Subject 3		
		Scan (cc)	Rescan (cc)	Δ (%)	Scan (cc)	Rescan (cc)	Δ (%)	Scan (cc)	Rescan (cc)	Δ (%)
PCDA (T1w, T2w, and FLAIR)	Caudate	7.89	7.52	4.8	6.50	6.44	0.9	5.76	7.2	22.2
	Thalamus	13.92	15.63	11.6	12.40	12.38	0.2	12.34	13.75	10.8
	Pallidum	2.17	2.27	4.5	1.74	1.92	9.8	2.47	2.48	0.4
	Putamen	8.41	9.64	13.6	9.89	10.62	7.1	10.79	10.95	1.5
PCDA (T1w, FLAIR)	Caudate	7.19	7.26	1.0	5.57	5.89	5.6	4.52	5.43	18.3
	Thalamus	8.72	10.23	15.9	7.55	8.79	15.2	9.66	11.00	13.0
	Pallidum	1.90	2.12	10.9	2.35	1.92	20.1	2.48	2.44	1.6
	Putamen	6.35	7.06	10.6	7.93	7.87	0.8	8.61	9.05	5.0

Table 4: Comparison of subcortical volume estimates provided by *k*NN and FSL-First in terms of mean value and standard deviation for the 14 MR studies of the *Image dataset I*.

	*k*NN		FSL-First	
	Mean (cc)	Std. dev.	Mean (cc)	Std. dev.
Caudate	7.33	0.77	7.45	0.70
Thalamus	13.41	1.43	15.70	1.36
Pallidum	3.12	0.30	3.56	0.45
Putamen	9.96	1.06	9.63	0.93

a probability atlas is available. The autotraining is likely applicable to other supervised methods. This is the first study that investigated the ability of automatically trained *k*NN and discriminant analysis methods that combine voxel intensities and spatial coordinates for the classification of subcortical brain structures. A *k*NN classifier trained in a fully automated way using an atlas was initially proposed by Cocosco et al. [9] and Vrooman et al. [11] for the classification of the three major tissues from MR brain images, mainly using intensity information. The combination of intensity and spatial coordinates to be used as features for a *k*NN classifier was instead first proposed by Anbeek et al. [18, 20] and applied to the segmentation of adult and neonatal MR brain images. We focused our attention on the recognition of four subcortical brain structures: caudate, thalamus, pallidum, and putamen. In our approach, the training is not derived on a subset of MR studies with the intent to be performed only once and then used as reference dataset but is always selected on the target study.

A successful supervised segmentation of subcortical structures first requires the definition of a well-founded training of the three main brain tissues in order to derive the corresponding probability density functions; otherwise it will be impossible to differentiate minor structures from underlying tissues. In this study we found that the selection of the training of GM, WM, and CSF on a segmented target study volume achieved with a widely used software (e.g., SPM) allows for obtaining better results than an averaged atlas like ICBM452 coregistered to the subject, providing in addition a superior stability against anatomical variability. Probably, the average and smoothing of the atlas impact the selection of GM, WM, and CSF training samples, leaving the training classes to be nonpure on both spatial location and intensity, thus introducing a bias in the classification process that affects the quality of the segmentation of subcortical structures. For this reason it is important to achieve a reference segmentation of the three main brain tissues in the target study, before starting the subcortical segmentation.

The optimization of the training dataset required an extensive number of tests to select the more appropriate

```
% PCDA Performs Principal Component Discriminant Analysis
%
% USAGE:
%   strike=pcda(test,train,class,ndis,plflag,prflag);
%
% INPUTS:
%   test  : an (m x p) array of test data to classify
%           m is the number of test data to classify
%           p is the number of variates
%   train: an (n x p) array of data used for training
%           n is the number of data of the training set
%   class: an (n x 1) vector with the class of the train dataset
%           as an integer ranging from 1 to the number of classes
%   ndis  : optional integer number specifying the procedure used for
%           the density estimation by Kernel regression for each class:
%           n(k) <= ndis ==> estimate of the density function for each sample
%                            computed from the whole training dataset by Kernel regression
%           n(k) > ndis  ==> estimate of the density function computed once from
%                            the training set on an equispaced grid with approximately
%                            ndis points by Kernel regression; then for each
%                            test data, density is computed by linear interpolation.
%                            This option speeds up computations
%           ndis < 0 or missing always implies the first option
%           (n(k) is the number of training data belonging to class k)
%   plflag: optional flag for producing plots:
%           plflag = 0 ==> no plot
%           plflag = 1 ==> summary plots
%           plflag = 2 ==> detailed plots
%           plflag < 0 or missing ==> no plot
%   prflag: optional flag for prior:
%           prflag = 0 ==> uniform prior
%           prflag = 1 ==> class frequencies estimated on the training set
%
%
% OUTPUTS
%   strike: an (m x 1) vector containing the class of the test dataset as
%           assigned by the method
%
% Example:
%   train = [mvnrnd([ 1 1], eye(2), 100); ...
%             mvnrnd([-1 -1], 2*eye(2), 100)];
%   class = [repmat(1,100,1); repmat(2,100,1)];
%   test  = unifrnd(-5, 5, 100, 2);
%   strike = pcda(test,train,class);
%
% Copyright 2002-2008 Umberto Amato, Istituto per le Applicazioni del Calcolo
% 'Mauro Picone' CNR, Napoli (Italy) and Anestis Antoniadis, Laboratoire de
% Modelisation et Calcul IMAG, Universite 'J. Fourier', Grenoble (France)
```

Algorithm 1

threshold value and the number of samples to be used in the learning phase of the classification process. In particular, for each setting we systematically checked (1) the confusion matrix for the classification of the subvolume formed by the only voxels coincident with the training, (2) the histograms of the intensity features for each tissue, (3) the correspondence between training samples and anatomy (goodness of coregistration), and (4) the final segmented images and the relative volume estimates. Overall, the *k*NN classifier showed a superior stability with respect to small changes in the automatic selection of the training set.

The evaluation of the accuracy of segmentation results in the absence of a reference standard was performed visually by an expert. Results highlighted that caudate, thalamus, pallidum, and putamen received a median rating *good* for the *k*NN, with grades between *fair* and *very good*; for the PCDA the median rating was *fair* with scores ranging from *poor* to *good*.

The reproducibility test, with the limitation to be conducted on a restricted number of studies, showed the best results for the *k*NN method. The tissue with greater variability was the pallidum. The test also highlighted that the *k*NN is able to perform well even with only two contrast types as input, confirming that the essential classification information resides in the T1 and FLAIR channels and consequently that the incorporation of T2 contrast is almost redundant.

The comparison of our results with the well-known and freely available FSL-First software was intended to do a preliminary verification of the agreement of the volume estimates provided by the best performance of the two methods considered in this paper. It should be noted that the approach is different as our segmentation is voxel based while FSL-First defines an enclosed surface shaped to the structure of interest. Table 4 shows that the volumes estimated by the automatically trained *k*NN and the FSL-First software are comparable. Overall, the FSL-First yielded a very good result, with a segmented image less noisy than that provided by *k*NN, although it tends, in some cases, to overestimate the thalamus volume.

The methods considered in this work require multispectral data but not specific acquisition sequences. The experiments conducted on publicly available data acquired in different centers with different scanners and sequences exemplify the generality of the considered approach. The automated training defined by registering an atlas to the target study has been demonstrated to be valid and reliable. This work did not consider the multiatlas approach [25] that hence could be explored as a refinement step in the atlas-guided selection of the training set. The inclusion of additional features for the *k*NN classifier may also be investigated as a possible way to further improve the overall segmentation accuracy.

5. Conclusions

Atlas-guided training is a valid and reliable strategy to automatically define a representative training dataset for the segmentation of subcortical structures with supervised methods. Using this training approach, a *k*-nearest neighbor classifier is able to successfully segment caudate, thalamus, pallidum, and putamen from multispectral magnetic resonance brain images without the need of user interaction.

Appendices

A. MR Data Sources

The IXI database (http://biomedic.doc.ic.ac.uk/brain-development/index.php?n=Main.Datasets) is a publicly available collection of nearly 600 MRI scans from normal, healthy subjects.

The fourteen MR studies selected for this work have the following ID: IXI002-Guys-0828, IXI087-Guys-0768, IXI136-HH-1452, IXI143-Guys-0785, IXI176-HH-1604, IXI263-HH-1684, IXI320-Guys-0902, IXI327-HH-1999, IXI351-Guys-0914, IXI499-Guys-1004, IXI562-Guys-1131, IXI567-HH-2536, IXI608-HH-2599, and IXI613-HH-2734.

The Kirby21 database (http://mri.kennedykrieger.org/databases.html) is a publicly available collection of scan-rescan imaging sessions on 21 healthy volunteers with no history of neurological disease. Subjects were imaged twice using the same scanner and acquisition protocol with a complete repositioning of the subject between the first and the second imaging session. The database includes a wide range of MRI sequences as described in [26], from which we selected T1w, T2w, and FLAIR for our segmentation.

The MR studies considered in this work have been downloaded from the NITRC website of Multi-Modal MRI Reproducibility Resource, at http://www.nitrc.org/projects/multimodal.

The six MR studies selected have the following ID: Subject ID 679 (Sessions 03 and 22), Subject ID 913 (Sessions 05 and 31), and Subject ID 492 (Sessions 18 and 38).

B. Description of the In-House Developed PCDA Function Written in Matlab

See Algorithm 1.

Conflict of Interests

The authors declare that there is no conflict of interests regarding the publication of this paper.

Acknowledgment

The authors acknowledge the support of the Italian Ministry of Instruction, University and Research, Projects MERIT RBNE08E8CZ and PRIN 2010XE5L2R.

References

[1] G. J. M. Parker and D. T. Chard, "Volume and atrophy," in *Quantitative MRI of the Brain: Measuring Changes Caused by Disease*, P. Tofts, Ed., pp. 533–558, John Wiley & Sons, Chichester, UK, 2004.

[2] L. W. de Jong, K. van der Hiele, I. M. Veer et al., "Strongly reduced volumes of putamen and thalamus in Alzheimer's disease: an MRI Study," *Brain*, vol. 131, part 12, pp. 3277–3285, 2008.

[3] X. Long, W. Liao, C. Jiang, D. Liang, B. Qiu, and L. Zhang, "Healthy aging: an automatic analysis of global and regional morphological alterations of human brain," *Academic Radiology*, vol. 19, no. 7, pp. 785–793, 2012.

[4] D. Unay, "Local and global volume changes of subcortical brain structures from longitudinally varying neuroimaging data for dementia identification," *Computerized Medical Imaging and Graphics*, vol. 36, no. 6, pp. 464–473, 2012.

[5] M. C. Keuken, P.-L. Bazin, L. Crown et al., "Quantifying inter-individual anatomical variability in the subcortex using 7T structural MRI," *NeuroImage*, vol. 94, pp. 40–46, 2014.

[6] B. Fischl, D. H. Salat, E. Busa et al., "Whole brain segmentation: automated labeling of neuroanatomical structures in the human brain," *Neuron*, vol. 33, no. 3, pp. 341–355, 2002.

[7] K. O. Babalola, B. Patenaude, P. Aljabar et al., "An evaluation of four automatic methods of segmenting the subcortical

structures in the brain," *NeuroImage*, vol. 47, no. 4, pp. 1435–1447, 2009.

[8] L. Murino, D. Granata, M. F. Carfora et al., "Evaluation of supervised methods for the classification of major tissues and subcortical structures in multispectral brain magnetic resonance images," *Computerized Medical Imaging and Graphics*, vol. 38, no. 5, pp. 337–347, 2014.

[9] C. A. Cocosco, A. P. Zijdenbos, and A. C. Evans, "A fully automatic and robust brain MRI tissue classification method," *Medical Image Analysis*, vol. 7, no. 4, pp. 513–527, 2003.

[10] H. A. Vrooman, C. A. Cocosco, R. Stokking et al., "kNN-based multi-spectral MRI brain tissue classification: manual training versus automated atlas-based training," in *Medical Imaging: Image Processing*, vol. 6144 of *Proceedings of SPIE*, 2006.

[11] H. A. Vrooman, C. A. Cocosco, F. van der Lijn et al., "Multi-spectral brain tissue segmentation using automatically trained k-Nearest-Neighbor classification," *NeuroImage*, vol. 37, no. 1, pp. 71–81, 2007.

[12] Y. Arzhaeva, E. M. van Rikxoort, and B. van Ginneken, "A multi-atlas approach to automatic segmentation of the caudate nucleus in MR brain images," in *3D Segmentation in the Clinic: A Gran Challenge*, T. Heimann, M. Styner, and B. van Ginneken, Eds., Image Sciences Institute, 2007.

[13] D. A. Dickie, D. E. Job, I. Poole et al., "Do brain image databanks support understanding of normal ageing brain structure? A systematic review," *European Radiology*, vol. 22, no. 7, pp. 1385–1394, 2012.

[14] B. A. Landman and S. K. Warfield, Eds., *MICCAI 2012 Workshop on Multi-Atlas Labeling*, 2012, https://masi.vuse.vanderbilt.edu/workshop2012/index.php/Workshop_Proceedings.

[15] B. Fischl, A. J. van der Kouwe, C. Destrieux et al., "Automatically parcellating the human cerebral cortex," *Cerebral Cortex*, vol. 14, no. 1, pp. 11–22, 2004.

[16] B. Patenaude, S. M. Smith, D. N. Kennedy, and M. Jenkinson, "A Bayesian model of shape and appearance for subcortical brain segmentation," *NeuroImage*, vol. 56, no. 3, pp. 907–922, 2011.

[17] M. Jenkinson, C. F. Beckmann, T. E. J. Behrens, M. W. Woolrich, and S. M. Smith, "FSL," *NeuroImage*, vol. 62, no. 2, pp. 782–790, 2012.

[18] P. Anbeek, K. L. Vincken, G. S. van Bochove, M. J. P. van Osch, and J. van der Grond, "Probabilistic segmentation of brain tissue in MR imaging," *NeuroImage*, vol. 27, no. 4, pp. 795–804, 2005.

[19] A. R. Webb, *Statistical Pattern Recognition*, John Wiley & Sons, New York, NY, USA, 2nd edition, 2002.

[20] P. Anbeek, I. Išgum, B. J. M. van Kooij et al., "Automatic segmentation of eight tissue classes in neonatal brain MRI," *PLoS ONE*, vol. 8, no. 12, Article ID e81895, 2013.

[21] U. Amato, M. Larobina, A. Antoniadis, and B. Alfano, "Segmentation of magnetic resonance brain images through discriminant analysis," *Journal of Neuroscience Methods*, vol. 131, no. 1-2, pp. 65–74, 2003.

[22] S. M. Smith, "Fast robust automated brain extraction," *Human Brain Mapping*, vol. 17, no. 3, pp. 143–155, 2002.

[23] J. Mazziotta, A. Toga, A. Evans et al., "A probabilistic atlas and reference system for the human brain: International Consortium for Brain Mapping (ICBM)," *Philosophical Transactions of the Royal Society B: Biological Sciences*, vol. 356, no. 1412, pp. 1293–1322, 2001.

[24] C. J. Holmes, R. Hoge, L. Collins, R. Woods, A. W. Toga, and A. C. Evans, "Enhancement of MR images using registration for signal averaging," *Journal of Computer Assisted Tomography*, vol. 22, no. 2, pp. 324–333, 1998.

[25] A. J. Asman and B. A. Landman, "Non-local statistical label fusion for multi-atlas segmentation," *Medical Image Analysis*, vol. 17, no. 2, pp. 194–208, 2013.

[26] B. A. Landman, A. J. Huang, A. Gifford et al., "Multi-parametric neuroimaging reproducibility: a 3-T resource study," *NeuroImage*, vol. 54, no. 4, pp. 2854–2866, 2011.

Hindawi Publishing Corporation
BioMed Research International
Volume 2015, Article ID 808625, 5 pages
http://dx.doi.org/10.1155/2015/808625

Research Article

Availability of Software-Based Correction of Mandibular Plane for the Vertical Measurement of the Mandible in Cone Beam Computed Tomography

Sang-Sun Han,[1] Kwang-Min Lee,[2] and Kee-Deog Kim[2]

[1]*Department of Oral and Maxillofacial Radiology, College of Dentistry, Yonsei University, Seoul 03722, Republic of Korea*
[2]*Department of Advanced General Dentistry, College of Dentistry, Yonsei University, Seoul 03722, Republic of Korea*

Correspondence should be addressed to Kee-Deog Kim; kdkim@yuhs.ac

Received 10 September 2015; Accepted 8 October 2015

Academic Editor: Guang Jia

Objectives. To investigate the availability of correction of mandibular plane using software for vertical measurements in cone beam computed tomography (CBCT) according to the sites of the mandible. *Methods*. CBCT scans of six dry mandibles were performed at 0-, 5-, 10-, 15-, and 20-degree angles relative to CBCT scanning table. Using the imaging software, mandibular planes of the different angles were corrected to that of 0-degree angle on the CBCT images. Before and after correction of the mandibular planes, the distance from the mandibular canal to the alveolar crest was measured at M1, M2, and M3 areas of the mandible and vertical measurements were statistically compared with those of 0-angle location using the paired t-test. *Results*. Prior to correction, the vertical measurements increased as the angle increased. The greatest differences of measurements were observed in M3 areas ($P < 0.05$). After correction, a strong correlation was found in measurements between the 0-degree angle and the other angles in all sites of the mandible ($P > 0.05$). *Conclusions*. The vertical measurements of CBCT were significantly influenced by mandibular positioning. When CBCT scans are performed at angles other than 0-degree angle, software-based correction of the mandibular plane can be a reliable tool for the accurate vertical measurements in CBCT.

1. Introduction

The assessment of the available bone height is one of the significant factors which influences the decision regarding the length of the implant prior to dental implant placement [1]. Computed tomography (CT) is an accurate imaging modality for the evaluation of preimplant sites in the mandibles [2]. Cone beam computed tomography (CBCT) also enables measurement of the distance between the alveolar crest and the mandibular canal so that impingement of the inferior alveolar nerve can be avoided [3–6].

Recently, due to the advantages of low radiation exposure and relatively low cost, CBCT scans have come to be preferred over CT for evaluations of bone quantity prior to dental implant placement [4, 7, 8]. Additionally, CBCT is known to provide measurements with submillimeter accuracy [9].

Our previous study reported that vertical measurements based on CT scans can be significantly influenced by mandibular positioning angle [10]. In CBCT, the accuracy of the measurements is affected by the CBCT system and software, patient motion during the scan, and the clinician's skill in interpreting the images [3]. However, we were unable to identify any study that focused on the influence of changes in the mandibular position on the vertical measurements from CBCT scans.

An imaging software program has been developed to improve the applicability of CBCT imaging for dental treatments [8, 11, 12]. Today, this software program has the functionality to make the adjustment of the axes of CBCT data that are obtained at angles other than the 0-degree angle. We thought that such functionality would make it possible to obtain the accurate vertical measurements regardless of the mandibular positions. However, no study has addressed the correction of mandibular plane using the software.

This study aimed at evaluating the influence of mandibular position changes on the vertical measurements from

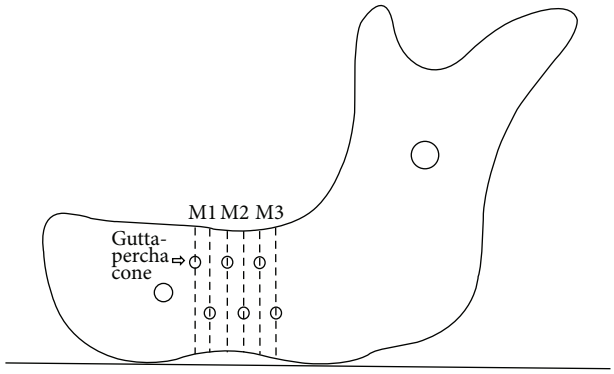

Figure 1: Marked sites of the mandible for the measurements.

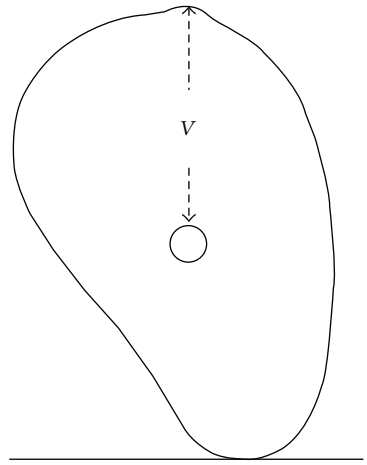

Figure 2: Measurement of the distance (V) from the top of the mandibular canal to the alveolar crest on cross-sectional image.

CBCT scans and investigating the availability of software-based correction of mandibular plane on CBCT images for vertical measurements according to the sites of the mandible.

2. Materials and Methods

2.1. CBCT Scans. The CBCT scans were conducted with reference to the experimental procedure that we have previously reported for CT scans [10]. Six dry mandibles in partially edentulous states were used. To evaluate the measurement differences according to sites of the mandibles, gutta-percha cones (1 × 1 mm) were attached as references to the areas at points M1 (5 and 10 mm distal to the mental foramen), M2 (15 and 20 mm distal to the mental foramen), and M3 (25 and 30 mm distal to the mental foramen) on the right and left buccal surfaces of the mandibles (Figure 1). To ensure the reproducibility of the CBCT scans with regard to different angles, the inferior border of the mandible was set on a 30 mm thick styrofoam plate that was fixed to an acrylic plate. To evaluate the influence of mandibular positional changes on the vertical measurements, the CBCT scans were performed in the positions described below.

The inferior border of the mandible (mandibular plane) was positioned parallel to the CBCT scanning table of 0-degree location and at the following positions:

(1) At a positive 5-degree angle to the scanning table (5-degree location).

(2) At a positive 10-degree angle to the scanning table (10-degree location).

(3) At a positive 15-degree angle to the scanning table (15-degree location).

(4) At a positive 20-degree angle to the scanning table (20-degree location).

An Alphard 3030 CBCT unit (ASAHI Co., Tokyo, Japan) was used. All images were recorded at 80 kVp and 5 mA over 17 s using a 102 × 102 mm field of view and an axial slice thickness of 0.2 mm. To obtain accurate results, the images of the remnant teeth and the extraction sockets were excluded.

2.2. Vertical Measurements of the CBCT Images before Correction of the Mandibular Plane. Before the correction of the mandibular plane, a total of 56 areas (18 M1 areas, 20 M2 areas, and 18 M3 areas) were obtained, and the 280 cross-sectional images taken from the 56 areas at 0-, 5-, 10-, 15-, and 20-degree angles were used.

Using the In2Guide software OnDemand3D (Cybermed Inc., Seoul, Korea), the distances from the top of the mandibular canal to the alveolar crest were measured on the cross-sectional images at the marked areas at which the gutta-percha was highly visible (M1, M2, and M3) at the 0-, 5-, 10-, 15-, and 20-degree angles (Figure 2). All measurements from CBCT images were performed twice with an interval of three weeks by a single experienced oral and maxillofacial radiologist and the means of these measurements were adopted for analysis.

2.3. Vertical Measurements of the CBCT Images after Correction of the Mandibular Plane. The imaging software OnDemand3D has the functionality to make the adjustment of the axes of CBCT data. This function is used for correction of the mandibular planes of CBCT images that are obtained at angles other than the 0-degree angle. In the adjustment of CBCT data, the base plane is dragged to reslice as newly aligned DICOM data. Rotation degrees will be shown on the 3D plane automatically. The mandibular planes in the CBCT images taken at the 5-, 10-, 15-, and 20-degree angles were corrected to that of the 0-degree position for M1, M2, and M3 areas of the mandibles using the software program (Figure 3) and 224 cross-sectional images were added. The vertical measurements were performed using the same method that was applied to the CBCT images prior to correction.

2.4. Statistical Analyses. To assess intraobserver difference, Wilcoxon matched-pairs test was used for repeated measurements of the same observer. All vertical measurements before and after correction were statistically compared with those obtained at 0-degree location according to the M1, M2, and M3 areas using the paired t-test ($P < 0.05$). The data set was analyzed using the Statistical Package for Social Science software ver. 19.0 (SPSS, Chicago, IL).

Table 1: Means and standard deviations of vertical measurements according to mandibular angles before correction (mm).

	0°	5°	10°	15°	20°
M1 ($n = 18$)	11.79 ± 1.44	11.84 ± 1.43	11.98 ± 1.38	12.12 ± 1.36	12.27 ± 1.46
M2 ($n = 20$)	10.12 ± 1.30	10.23 ± 1.30	10.56 ± 1.49	11.04 ± 1.54	11.34 ± 1.75
M3 ($n = 18$)	9.22 ± 1.64	9.45 ± 1.64	9.93 ± 1.87	10.52 ± 1.95	11.00 ± 2.12

Table 2: Means and standard deviations of vertical measurements according to mandibular angles after correction (mm).

	0°	5°	10°	15°	20°
M1 ($n = 18$)	11.79 ± 1.44	11.77 ± 1.51	11.78 ± 1.53	11.83 ± 1.46	11.76 ± 1.41
M2 ($n = 20$)	10.12 ± 1.30	10.21 ± 1.28	10.17 ± 1.32	10.18 ± 1.28	10.21 ± 1.28
M3 ($n = 18$)	9.22 ± 1.64	9.18 ± 1.74	9.19 ± 1.78	9.25 ± 1.71	9.25 ± 1.67

Table 3: Mean error and standard deviation between measurements at 0° location and others before correction (mm).

	5°	10°	15°	20°
M1 ($n = 18$)	0.04 ± 0.24	0.18 ± 0.48	0.29 ± 0.96	0.33 ± 0.58
M2 ($n = 20$)	0.10 ± 0.26	0.21 ± 0.55	0.91 ± 0.45*	1.21 ± 0.69*
M3 ($n = 18$)	0.19 ± 1.05	0.71 ± 0.54*	1.31 ± 0.71*	1.79 ± 0.94*

*Statistically significant difference at $P < 0.05$.

Table 4: Mean error and standard deviation between measurements at 0° location and others after correction (mm).

	5°	10°	15°	20°
M1 ($n = 18$)	0.02 ± 0.21	0.02 ± 0.29	0.04 ± 0.20	0.04 ± 0.25
M2 ($n = 20$)	0.09 ± 0.20	0.04 ± 0.18	0.06 ± 0.20	0.09 ± 0.24
M3 ($n = 18$)	0.04 ± 0.32	0.03 ± 0.32	0.03 ± 0.27	0.03 ± 0.23

3. Results

There was no statistically significant intraobserver difference in repeated measurements of CBCT images ($P > 0.05$). Intraobserver consistency was rated at 95% between two measurements.

Before the correction of the mandibular plane, the value of vertical measurements increased as the angle between the mandibular plane and the scanning table increased (Table 1). The vertical measurements between the 0-degree and 5-degree angles were not statistically significant different in any site of the mandible ($P > 0.05$). However, at the 15-degree and 20-degree angles, there were statistically significant differences for the M2 and M3 areas ($P < 0.05$; Table 3).

The differences of vertical measurements were more pronounced in the M3 areas than in the M2 areas and the differences in M2 areas were greater than those in M1 areas (Table 3). In the M3 areas, statistically significant differences at 10-, 15-, and 20-degree angles were observed ($P < 0.05$). However, in the M1 area, there were no statistically significant differences between 0-degree angle and the other angles ($P > 0.05$; Table 3).

In contrast, after the correction of the mandibular plane with software, the vertical measurements were relatively constant across different angles of the mandibular planes regardless of sites of the mandible (Table 2). There was no statistically significant difference in the measurements between the 0-degree angle and the other angles ($P > 0.05$). Regarding the marked areas of the mandible, there was no statistically significant effect in the M1, M2, and M3 areas ($P > 0.05$; Table 4).

4. Discussion

During evaluations of preimplant sites of the mandible, accurate measurements of the distance from the mandibular canal to the alveolar crest on radiographs have been linked to primary implant success [13]. Insertion of an inadequately long implant can injure the inferior alveolar nerve resulting in permanent hypoesthesia of the lower lip [14].

Prior to the correction of mandibular planes, the vertical measurements based on CBCT scans were affected by changes in the position of the mandible. As the angle between the mandibular plane and the CBCT scanning table increased, the vertical measurements increased. Because the cross sections of CBCT images that were taken at angles other than the 0-degree angle were not perpendicular to the long axis of the mandible, the vertical measurements from the CBCT images taken at different angles might be overestimated compared to those at 0-degree angle location of the mandible.

Regarding the sites of the mandible, before correction, the greatest differences of vertical measurements were observed in the posterior regions, and the difference of measurements decreased toward the more anterior regions. Because the M3 areas are the farthest from the axis of rotation in terms of angle, the cross-sectional images of the areas were oblique to the long axis of the mandible. So the measurements in the M3 areas were likely greater than those of the other sites in the mandibles.

Large errors in measurements of available bone height might cause nerve injury during the insertion of the implant. When patients are not accurately positioned in CBCT scans, CBCT rescans might be necessary for accurate evaluations of preimplant site. When patients are not accurately positioned in CBCT scans, CBCT rescan might be necessary for accurate evaluation of preimplant site, and it results in unnecessary radiation exposure to the patient.

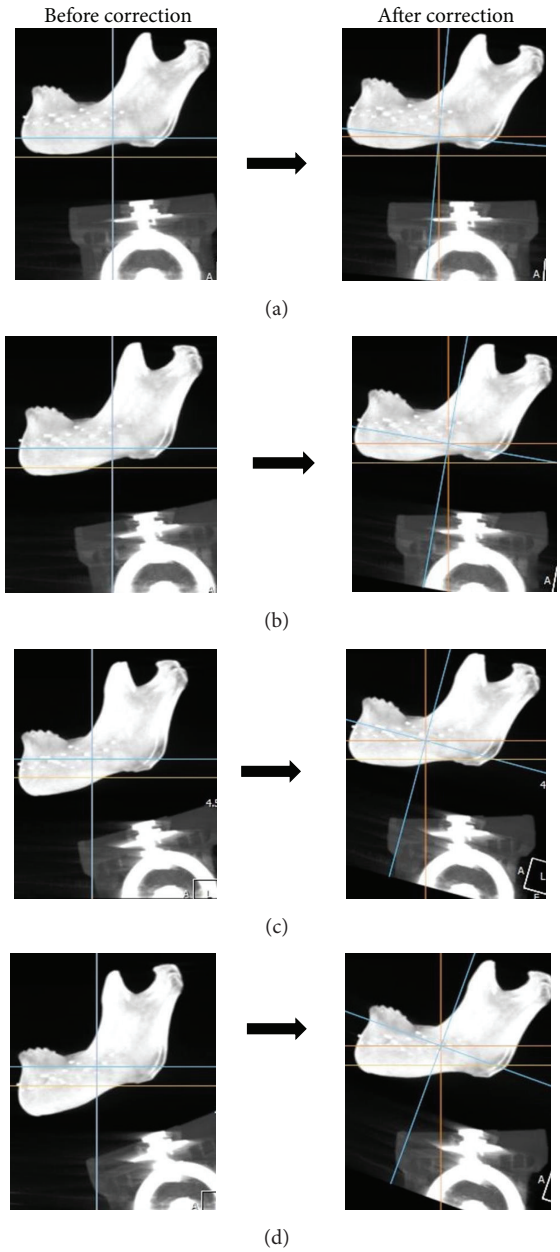

Figure 3: CBCT images before and after the correction of the mandibular planes. The inferior border of the mandible (mandibular plane) was positioned at 5-, 10-, 15-, and 20-degree angles relative to CBCT scanning table, and the mandibular planes at different angles were corrected to the 0-degree position using the software. (a) Five-degree angle location. (b) Ten-degree angle location. (c) Fifteen-degree angle location. (d) Twenty-degree angle location.

Today, imaging software has been developed for dental treatment, and the software has the functionality to rotate the axis of CBCT image. We thought that this function should be used for the correction of mandibular plane on all CBCT images that were at angles other than the 0-degree angle. After correction, the vertical measurements at different angles corresponded relatively well with those at the 0-degree angle. Additionally, a strong correlation was found in the vertical measurements between the 0-degree angle and the other angles in all sites of the mandible. Therefore, the correction of the mandibular plane using software is thought to be a reliable tool for the accurate measurements of the vertical distance in preimplant site of CBCT images.

In conclusion, changes of mandibular position in CBCT scan affected the vertical measurements from the cross-sectional images according to the sites of the mandible. However, when CBCT scans are performed at angles other than the 0-degree angle, software-based correction of the mandibular plane can provide satisfactory information about the vertical measurements without requiring an additional CBCT scanning.

Conflict of Interests

The authors declare that there is no conflict of interests regarding the publication of this paper.

References

[1] H. H. Zadeh, "Implant site development: clinical realities of today and the prospects of tissue engineering," *Journal of the California Dental Association*, vol. 32, no. 12, pp. 1011–1020, 2004.

[2] M. G. P. Cavalcanti, J. Yang, A. Ruprecht, and M. W. Vannier, "Accurate linear measurements in the anterior maxilla using orthoradially reformatted spiral computed tomography," *Dentomaxillofacial Radiology*, vol. 28, no. 3, pp. 137–140, 1999.

[3] M. Halperin-Sternfeld, E. E. Machtei, and J. Horwitz, "Diagnostic accuracy of cone beam computed tomography for dimensional linear measurements in the mandible," *The International Journal of Oral & Maxillofacial Implants*, vol. 29, no. 3, pp. 593–599, 2014.

[4] J. Gupta and S. P. Ali, "Cone beam computed tomography in oral implants," *National Journal of Maxillofacial Surgery*, vol. 4, no. 1, pp. 2–6, 2013.

[5] K. B. Waltrick, M. J. Nunes de Abreu Junior, M. Corrêa, M. D. Zastrow, and V. D'Avila Dutra, "Accuracy of linear measurements and visibility of the mandibular canal of cone-beam computed tomography images with different voxel sizes: an in vitro study," *Journal of Periodontology*, vol. 84, no. 1, pp. 68–77, 2013.

[6] K. Kamburoğlu, C. Kiliç, T. Özen, and S. P. Yüksel, "Measurements of mandibular canal region obtained by cone-beam computed tomography: a cadaveric study," *Oral Surgery, Oral Medicine, Oral Pathology, Oral Radiology and Endodontology*, vol. 107, no. 2, pp. e34–e42, 2009.

[7] L.-G. Chen, T. Lundgren, H. Hallström, and F. Cherel, "Comparison of different methods of assessing alveolar ridge dimensions prior to dental implant placement," *Journal of Periodontology*, vol. 79, no. 3, pp. 401–405, 2008.

[8] K. Abramovitch and D. D. Rice, "Basic principles of cone beam computed tomography," *Dental Clinics of North America*, vol. 58, no. 3, pp. 463–484, 2014.

[9] M. Loubele, N. Van Assche, K. Carpentier et al., "Comparative localized linear accuracy of small-field cone-beam CT and multislice CT for alveolar bone measurements," *Oral Surgery, Oral Medicine, Oral Pathology, Oral Radiology and Endodontology*, vol. 105, no. 4, pp. 512–518, 2008.

[10] K.-D. Kim, H.-G. Jeong, S.-H. Choi, E.-H. Hwang, and C.-S. Park, "Effect of mandibular positioning on preimplant site measurement of the mandible in reformatted CT," *The International*

Journal of Periodontics & Restorative Dentistry, vol. 23, no. 2, pp. 177–183, 2003.

[11] P. Tarazona-Álvarez, J. Romero-Millán, D. Peñarrocha-Oltra, M.-Á. Fuster-Torres, B. Tarazona, and M. Peñarrocha-Diago, "Comparative study of mandibular linear measurements obtained by cone beam computed tomography and digital calipers," *Journal of Clinical and Experimental Dentistry*, vol. 6, no. 3, pp. e271–e274, 2014.

[12] R. Jacobs and M. Quirynen, "Dental cone beam computed tomography: justification for use in planning oral implant placement," *Periodontology 2000*, vol. 66, no. 1, pp. 203–213, 2014.

[13] V. Braut, M. M. Bornstein, U. Kuchler, and D. Buser, "Bone dimensions in the posterior mandible: a retrospective radiographic study using cone beam computed tomography. Part 2—analysis of edentulous sites," *The International Journal of Periodontics and Restorative Dentistry*, vol. 34, no. 6, pp. 639–647, 2014.

[14] L. Vazquez, Y. Nizamaldin, C. Combescure et al., "Accuracy of vertical height measurements on direct digital panoramic radiographs using posterior mandibular implants and metal balls as reference objects," *Dentomaxillofacial Radiology*, vol. 42, no. 2, Article ID 20110429, 2013.

Hindawi Publishing Corporation
BioMed Research International
Volume 2015, Article ID 595742, 5 pages
http://dx.doi.org/10.1155/2015/595742

Research Article

Smooth Muscle Cells of Penis in the Rat: Noninvasive Quantification with Shear Wave Elastography

Jia-Jie Zhang, Xiao-Hui Qiao, Feng Gao, Ming Bai, Fan Li, Lian-Fang Du, and Jin-Fang Xing

Department of Medical Ultrasound, Shanghai General Hospital, Shanghai Jiao Tong University School of Medicine, Shanghai 200080, China

Correspondence should be addressed to Jin-Fang Xing; xingshi70188@163.com

Received 5 August 2015; Revised 22 September 2015; Accepted 28 September 2015

Academic Editor: Guang Jia

Purpose. Smooth muscle cells (SMCs) of cavernosum play an important role in erection. It is of great significance to quantitatively analyze the level of SMCs in penis. In this study, we investigated the feasibility of shear wave elastography (SWE) on evaluating the level of SMCs in penis quantitatively. *Materials and Methods*. Twenty healthy male rats were selected. The SWE imaging of penis was carried out and then immunohistochemistry analysis of penis was performed to analyze the expression of alpha smooth muscle actin in penis. The measurement index of SWE examination was tissue stiffness (TS). The measurement index of immunohistochemistry analysis was positive area percentage of alpha smooth muscle actin (AP). *Results*. Sixty sets of data of TS and AP were obtained. The results showed that TS was significantly correlated with AP and the correlation coefficient was −0.618 ($p < 0.001$). The result of TS had been plotted against the AP measurements. The relation between the two results has been fitted with quadric curve; the goodness-of-fit index was 0.364 ($p < 0.001$). *Conclusions*. The level of SMCs in penis was successfully quantified *in vivo* with SWE. SWE can be used clinically for evaluating the level of SMCs in penis quantitatively.

1. Introduction

The special structure in cavernosum is the key structure for erectile function. In cavernosum, smooth muscle cells (SMCs) account for about 40–52% of cells [1] and the level of SMCs can directly affect the erectile function. Blood flows into sinusoids during the relaxation of SMCs; this is the key process of penile erection. So the blood flow of cavernosum under the erectile condition is directly determined by the number of SMCs. The decrease of SMCs will directly lead to the erectile hypofunction. Studies have found that, with age increasing, the smooth muscle tissue will gradually atrophy, cells will decrease, fibrous tissue will proliferate, and consequently the erectile function will decline [2]. The number of SMCs of cavernosum is also closely related with the sex hormone levels. Testosterone can promote the generation of SMCs and enhance the cell vitality. Cell vitality and proliferation of SMCs decline with testosterone decrease, which can lead to their atrophy and reduction in the number and the decline of erectile function [3]. Some diseases can also lead to the change of the number of SMCs. For example, Peyronie's disease can cause abnormal fibrosis of cavernosum and the decline of SMCs-fibroblasts ratio and consequently affect the erectile function [4]. Therefore, it is of great significance to quantitatively analyze the level of SMCs in penis. At present, the level of SMCs can be quantitatively analyzed only by penis biopsy and immunohistochemistry [5, 6]. But this method is not suitable for clinical expansion because of many side effects; a new technology is in urgent need.

Shear wave elastography (SWE) is a new ultrasound technology. It uses probe to emit safe acoustic radiation force impulses which can focus consecutively on different depth of tissue to cause the tissue particles to vibrate and generate shear waves. The ultrafast imaging system can precisely measure the shear wave velocity, and then the tissue stiffness (TS) can be calculated with shear wave velocity in system and can accomplish real time imaging [7–12]. Since TS is determined by cell types and amount of tissue, theoretically, SWE can be used to analyze cell types and level. Also, SWE is noninvasive, of low cost, and easy to handle. It may become a new method to diagnose pathological changes of cavernosum tissues and take the place of biopsy.

In this study, twenty rats with different level of SMCs in penis were imaged by SWE and TS was measured. Then we analyzed the correlation of TS with the amount of SMCs and investigated the feasibility of SWE on evaluating the level of SMCs in penis quantitatively and noninvasively.

2. Materials and Methods

2.1. Animals. All animal experiments were approved by Institutional Animal Care and Use Committee. Twenty healthy male Sprague Dawley rats (1.5–14 months) obtained from the Animal Breeding Center were randomly sampled. The rats' weight was 337.12 ± 102.64 g, and length of body was 13.43 ± 4.92 cm.

2.2. Reagents. The anti-alpha actin antibody [SA-20] (ab 82247) and rabbit anti-rat IgG H&L (HRP) (ab 6734) were obtained from Abcam (Shanghai, China).

2.3. SWE Examination. All rats were anesthetized with sodium pentobarbital (30 mg/kg, ip), and anesthesia was maintained with supplemental sodium pentobarbital as needed. The penis of rat was in a flaccid state below narcotism. The ultrafast ultrasound device Aixplorer (SuperSonic Imagine, Aix-en-Provence, France) was used for SWE imaging and the probe selected was SuperLinear SL15-4. The four limbs of the rat were fixed supinely after it was anesthetized and the two-dimensional ultrasonography was performed after penis was fully exposed. The transverse section was selected for scanning. Then SWE was carried out after penis was shown clearly and the SWE imaging box should be larger than the transverse section of penis. The near glans, mid, and the near root segment of penis were, respectively, selected for SWE imaging and the images were saved in real time. The information regarding the Aixplorer settings was as follows: the focal depth was 1-2 cm, the gain was 30%, the frame for averaging was 12 Hz, and the penetration mode selection of SWE was "Pen."

After SWE examination, the saved images were used for measurement. Q-Box was used to measure TS in SWE imaging box. The delineated standard of the Q-Box (circle) was surrounding penis on the largest scale with the capsule as the outer boundary. Therefore, the diameter of Q-Box was different for each rat; it was determined by the size of penis. TS of the near glans, mid, and near root segment of penis was, respectively, measured. The unit was kilopascal (kPa).

2.4. Histological Examination. Each rat was killed immediately after SWE examination. Penis was cut off at the root and fixed in 4% paraformaldehyde for 12–24 hours. After dehydration through graded concentrations of ethanol and transparence in xylene, penis was embedded in paraffin. The paraffin-embedded tissue was cut into 5 μm sections and adhered to SuperFrost Plus slides. These prepared sections were used for hematoxylin-eosin (HE) and immunohistochemical staining.

The sections were stained with hematoxylin for 10 min, followed by being rinsed several times with flowing water, and then they were stained with eosin for 20–30 s. After dehydration through graded alcohol and transparence in xylene, the sections were mounted with neutral gum and baked at the temperature of 37°C for drying.

After heat drying, the sections were deparaffinized in xylene and subsequently rehydrated in gradients of ethanol. The sections were treated with 3% hydrogen peroxide to inactivate endogenous peroxidase, and then the antigen was retrieved at 95°C for 10 min. The sections were incubated with the normal goat serum at 37°C for 15 min and then primary antibody, anti-alpha actin antibody (1 : 50), was applied, and the sections were incubated at 4°C overnight. Subsequently, the sections were incubated with rabbit anti-rat secondary antibody for 15 min and then incubated with streptavidin-peroxidase complex for 15 min. Colored reactions were developed by incubating with $3'3'$-diaminobenzidine and subsequently counterstained with hematoxylin. After dehydration and transparence, the sections were mounted with neutral gum. Between all reaction steps, the slides were rinsed with 0.1 M phosphate buffered saline (pH 7.4).

2.5. Image Collection and Analysis. The sections with HE staining were observed under light microscope and the color image analysis system was used to analyze immunohistochemical images. The image analysis and data measurement were performed by professional pathologists with more than 5 years of experiences. The positive area percentage of alpha-smooth muscle actin (AP) of the near glans, mid, and near root segment of penis was, respectively, measured by the software of Leica QWin Plus (Wetzlar, Germany).

2.6. Statistical Analysis. The Kolmogorov-Smirnov (K-S) test was used to determine whether the data sets (TS and AP of rats) followed normal distribution. If necessary, the nonparametric method (Spearman test) would be used to analyze the correlation of TS with AP. The statistical analyses were performed by SPSS software (v. 18.0 for Windows; SPSS Inc., Chicago, USA). A p value of < 0.05 was considered statistically significant.

3. Results

3.1. SWE Imaging. All rats' penises were imaged successfully (Figure 1). The two-dimensional images showed that the transverse section of penis was oval with clear boundary and intact capsule and was uniformly hypoechoic inside. The SWE images showed that each area of penis was filled with color, the image was like an oil painting, and there were no mosaic-like points (area without SWE signal). TS of all rats was 9.10 ± 1.63 kPa.

3.2. HE Staining and Immunohistochemistry Analysis. The rats' penile tissue mainly included SMCs and fibroblasts (Figure 2). The sections with immunohistochemical staining were obtained successfully. Figure 3 shows the expression of alpha-actin of penis. AP of all rats was 10.55 ± 9.13%, AP of the near glans segment of all rats was 10.60 ± 8.93%, AP of

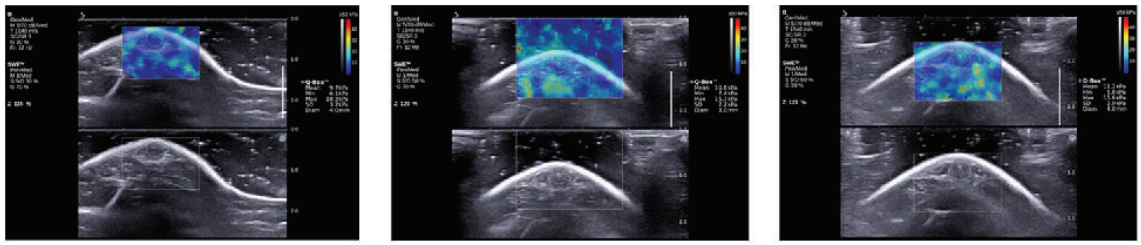

Figure 1: SWE imaging of penis. The two-dimensional image (lower) shows that the transverse section of penis is oval with intact capsule and uniformly hypoechoic inside. The SWE image (upper) shows that each area of penis is filled with color, the image is like an oil paint, and there are no mosaic-like points. Q-Box was a circle depicted with tunica albuginea as the boundary. (Q-Box, measurement results of TS; Min, minimum; Max, maximum; SD, standard deviation; Diam, diameter.)

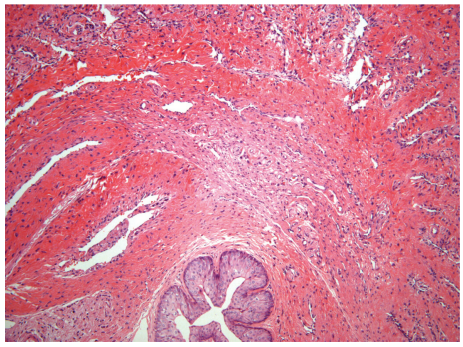

Figure 2: Sections of rat's penile tissue (HE 100x). The outer layer is the corpus cavernosum; the inner layer is the corpus spongiosum. At the center of the corpus spongiosum is the urethra (cavity) which is covered with urethral epitheliums (blue staining). The penile tissue is mainly composed of SMCs and fibroblasts and the arrangement.

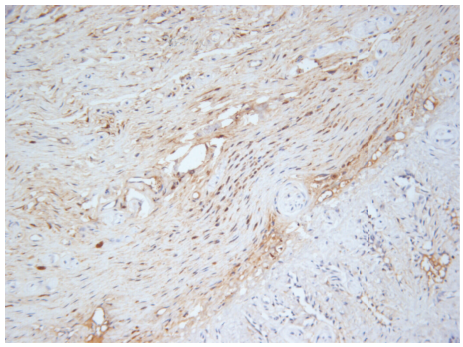

Figure 3: The expression of alpha-actin in rats' penile tissue. The brown color shows the positive cell in this area. In this figure, the positive cells are smooth muscle cells (400x).

the mid segment was 10.77 ± 10.02%, and AP of near the root segment was 10.27 ± 8.87%.

3.3. Correlation Analysis. For each rat, the near glans, mid, and near root segment of penis were, respectively, selected for the measurement of TS and histological examinations. Sixty sets of data of TS and AP were obtained. We found that the data of TS followed normal distribution ($p = 0.909$), but

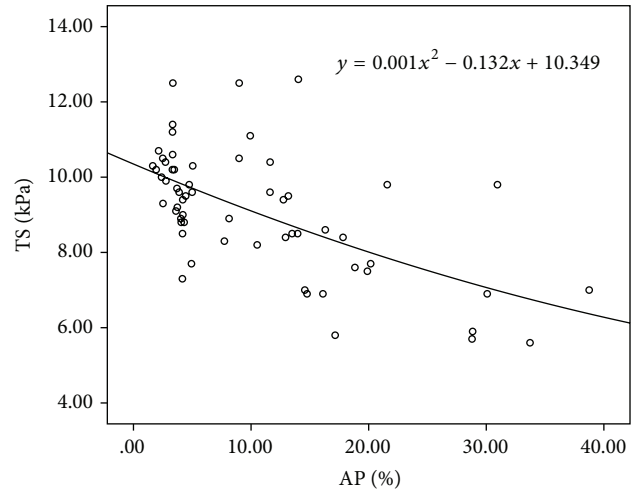

Figure 4: The result of TS plotted against the AP measurements of each rat. The relation between the two results has been fitted with quadric curve.

the data of AP did not. So the Spearman test was used to analyze the correlation between TS and AP. The result showed that TS was significantly correlated with AP ($p < 0.001$); the correlation coefficient was −0.618. The result of TS has been plotted against the AP measurements of each rat (Figure 4). The relation between the two results has been fitted with quadric curve ($y = 0.001x^2 - 0.132x + 10.349$); the goodness-of-fit index was 0.364 ($p < 0.001$).

4. Discussion

Penis is mainly composed of corpora cavernosa and corpus spongiosum, and the cell types include SMCs and fibroblasts. SMCs are the structural basis of cavernosum relaxation and account for about 40–52% in cavernosum. The main process of penile erection is as follows: with sexual stimulation, SMCs relax and then corpora cavernosum penis congests and swells followed by the gradual increase of intracavernous pressure. At the same time, the subalbugineous veniplex is compressed which can lead to the decrease of blood reflux. When the intracavernous pressure is high enough, the inflow of penis arteries stops and there is no outflow. Thus the penis is under

a fully closed condition and achieves full erection [13, 14]. Meanwhile, the effective venoocclusion is directly affected by the SMCs-fibroblasts ratio. Therefore, the level of SMCs can directly impact the erectile function.

So far, the only way to evaluate the level of SMCs in penis is obtaining samples by penis biopsy and quantifying cell amount by immunohistochemistry. The mechanism of quantifying the amount of SMCs by immunohistochemistry is as follows: SMCs in penis include cavernosum SMCs and vascular SMCs, mainly cavernosum SMCs [1], which have the function of contraction and contain alpha-actin. And anti-alpha actin antibody can serve as the marker of SMCs. But this method needs high technical conditions when drawing materials and is invasive and liable to cause some severe side effects including penis pain and penile induration. Therefore, it is difficult to be accepted by patients and the clinical application has been greatly restricted. It is necessary to explore a noninvasive method that can be applied on clinical evaluation of the level of SMCs in penis.

SWE is a new technology which can be used to analyze TS clinically. Since TS is closely associated with cell types and level of tissue, SWE can be used to analyze cell types and level. SWE uses the ultrafast imaging system to precisely record the tissue movement induced by the propagation of shear waves and the velocity of the tissue movement is quantified using tissue Doppler techniques; thus the propagation of shear waves through the scanning plane can be monitored in real time. The shear wave velocity getting through each particle of tissue is estimated using cross correlation algorithms. Then the TS can be calculated with shear wave velocity in system. At the same time, the TS can be color coded and superimposed on a B-mode image, and then a real time TS map of *in vivo* tissue is formed [1, 11, 12]. Since SWE is hopeful to be a new method for analyzing types and level of cells, we attempted to analyze the level of SMCs in penis with SWE.

In this study, anti-alpha actin antibody was selected to quantitatively measure the amount of SMCs and the measurement index was AP. Then the correlation of TS with AP was analyzed. The result showed that TS was significantly negatively correlated with AP of all rats. It suggests that there is a significant negative correlation of TS with SMCs in penis. This finding just fits with the common understanding that more SMCs in penis means better elasticity and lower TS of penis. At the same time, we got the quantitative relationship between AP and TS of penis for the first time. The curve-fitting equation was $TS = 0.001AP^2 - 0.132AP + 10.349$. Therefore, SWE is promising to be a new noninvasive method of evaluating the level of SMCs and it deserves further study.

The transverse section was used for SWE measurements in this study as we considered the anisotropy of SMCs. Based on the anisotropy of SMCs, the shear wave speed along the fiber could be significantly higher than that across the fiber. When SWE imaging was carried out, shear waves would propagate along the fiber if the section was parallel to the fiber, and shear waves would travel across the fiber if the section was perpendicular (or nearly perpendicular) to the fiber. Therefore, when the longitudinal section was used for SWE imaging, the influence of the anisotropy of the SMCs for shear wave velocity could not be avoided because it was impossible to ensure that each section was parallel to the fiber in practice. When the transverse section was selected, the influence of the anisotropy of the SMCs for shear wave velocity could be overcome effectively because it was possible to ensure that each section was perpendicular (or nearly perpendicular) to all fibers.

There are some limitations in this study. We could not identify the corpus spongiosum and the corpus cavernosum of rats in the two-dimensional ultrasonography, so we measured the TS of the whole penis. But the cell types of the corpus spongiosum are close to the corpus cavernosum, mainly including SMCs and fibroblasts, so our result is also suitable for the corpus cavernosum. Furthermore, since the corpus spongiosum and the corpus cavernosum of human beings can be clearly divided in the two-dimensional ultrasonography, it would not happen when this technology is used clinically.

5. Conclusion

In our research, the level of SMCs in penis was successfully quantified *in vivo* with SWE. SWE can be used clinically for evaluating the level of SMCs in penis quantitatively, and it deserves further study.

Conflict of Interests

The authors report no conflict of interests.

Authors' Contribution

Jia-Jie Zhang and Xiao-Hui Qiao contributed equally to this study and should share first authorship. Jin-Fang Xing and Lian-Fang Du contributed equally to this study.

Acknowledgment

This work was supported by the Science Foundation of School of Medicine, Shanghai Jiao Tong University (Grant no. 4XJ10075).

References

[1] A. Nehra, I. Goldstein, A. Pabby et al., "Mechanisms of venous leakage: a prospective clinicopathological correlation of corporeal function and structure," *Journal of Urology*, vol. 156, no. 4, pp. 1320–1329, 1996.

[2] B. Liu, J.-H. Liu, T. Wang et al., "Effects of testosterone on the proliferation of rat corpus cavernosum cells in vitro," *National Journal of Andrology*, vol. 14, no. 6, pp. 524–526, 2008.

[3] N. Tomada, I. Tomada, F. Cruz, P. Vendeira, and D. Neves, "Characterization of VEGF and angiopoietins expression in human corpus cavernosum during aging," *Journal of Sexual Medicine*, vol. 7, no. 4, part 1, pp. 1410–1418, 2010.

[4] J. P. Langston and C. C. Carson, "Peyronie's disease: review and recent advances," *Maturitas*, vol. 78, no. 4, pp. 341–343, 2014.

[5] G. Falke, J. J. Yoo, T. G. Kwon, R. Moreland, and A. Atala, "Formation of corporal tissue architecture *in vivo* using human cavernosal muscle and endothelial cells seeded on collagen matrices," *Tissue Engineering*, vol. 9, no. 5, pp. 871–879, 2003.

[6] T.-Y. Shin, J.-K. Ryu, H.-R. Jin et al., "Increased cavernous expression of transforming growth factor-β1 and activation of the smad signaling pathway affects erectile dysfunction in men with spinal cord injury," *Journal of Sexual Medicine*, vol. 8, no. 5, pp. 1454–1462, 2011.

[7] J.-L. Gennisson, M. Muller, P. Gabor et al., "Quantification of elasticity changes in the myometrium during labor using supersonic shear imaging: a feasibility study," *Ultrasonics*, vol. 56, pp. 183–188, 2015.

[8] A. P. Sarvazyan, O. V. Rudenko, S. D. Swanson, J. B. Fowlkes, and S. Y. Emelianov, "Shear wave elasticity imaging: a new ultrasonic technology of medical diagnostics," *Ultrasound in Medicine and Biology*, vol. 24, no. 9, pp. 1419–1435, 1998.

[9] K. Nightingale, S. McAleavey, and G. Trahey, "Shear-wave generation using acoustic radiation force: *in vivo* and *ex vivo* results," *Ultrasound in Medicine and Biology*, vol. 29, no. 12, pp. 1715–1723, 2003.

[10] J. Bercoff, M. Tanter, and M. Fink, "Supersonic shear imaging: a new technique for soft tissue elasticity mapping," *IEEE Transactions on Ultrasonics, Ferroelectrics, and Frequency Control*, vol. 51, no. 4, pp. 396–409, 2004.

[11] M. Tanter, J. Bercoff, A. Athanasiou et al., "Quantitative assessment of breast lesion viscoelasticity: initial clinical results using supersonic shear imaging," *Ultrasound in Medicine and Biology*, vol. 34, no. 9, pp. 1373–1386, 2008.

[12] Jeremy Bercoff (Engineer of SuperSonic Imagine, Aix en Provence, France), White paper of ShearWave Elastography.

[13] S. L. Archer, "Potassium channels and erectile dysfunction," *Vascular Pharmacology*, vol. 38, no. 1, pp. 61–71, 2002.

[14] A. D. Seftel, "Erectile dysfunction in the elderly: epidemiology, etiology and approaches to treatment," *Journal of Urology*, vol. 169, no. 6, pp. 1999–2007, 2003.